# Development of Biomimetic Systems for the Transportation of Ions and Water across Lipid Bilayer Membranes

**A Thesis**

**Submitted in Partial Fulfillment of the Requirements of the Degree of**

**Doctor of Philosophy**

**By**


**Debashis Mondal**

**ID: 20163427**


**Research Supervisor**

**Prof. Pinaki Talukdar**





**Indian Institute of Science Education and Research Pune**


**(2022)**

*Dedicated to…*

*Maa Baba*

# CERTIFICATE

Certified that the work incorporated in the thesis entitled "**Development of Biomimetic Systems for the Transportation of Ions and Water across Lipid Bilayer Membranes**" Submitted by Debashis Mondal was carried out by the candidate, under my supervision. The work presented here or any part of it has not been included in any other thesis submitted previously for the award of any degree or diploma from any other University or institution.

Pinaki Talukdar

Date: 28/12/2021

Place: Pune

Prof. Pinaki Talukdar

(Research Supervisor)

## Declaration

I declare that this written submission represents my ideas in my own words and where others' ideas have been included, I have adequately cited and referenced the original sources. I also declare that I have adhered to all principles of academic honesty and integrity and have not misrepresented or fabricated or falsified any idea/data/fact/source in my submission. I understand that violation of the above will be cause for disciplinary action by the Institute and can also evoke penal action from the sources which have thus not been properly cited or from whom proper permission has not been taken when needed.

Debashis Mondal

Date: 28/12/2021

Place: Pune

Debashis Mondal

(ID No. 20163427)

## *Acknowledgement*

*Throughout my Ph.D. journey, I have had the privilege of getting acquainted with many great personalities whose encouragement and support helped me to complete this journey. So here in the forthcoming section, I would like to convey my sincere gratitude to them.*

*I express my sincere thanks to my thesis supervisor Prof. Pinaki Talukdar for accepting me as his student and introducing the fascinating field of supramolecular chemistry. I sincerely thank him for providing me the opportunity to work in his laboratory for completing my thesis work. His broad experience in the research field, constructive criticism, suggestion, encouragement, and persistent support are invaluable for completing my thesis work. I express my heartfelt gratitude to him for giving me enormous freedom in the laboratory and the way he guided me at every stage of my Ph.D. journey.*

*I am deeply grateful to my research advisory committee (RAC) members, Prof. Dilip D. Dhavale and Prof. Hosahudya N. Gopi, for their valuable suggestions during the RAC meetings of my Ph.D. tenure. I appreciate their precious time, efforts and feedback.*

*I would like to thank the former Director, Prof. K. N. Ganesh, and the current director Prof. Jayant B. Udgaonkar, for providing excellent infrastructure and world-class research facilities at the Indian Institute of science education and research Pune.*

*I would like to thank the former chairman of Chemistry department prof. M. Jayakannan, the current chairman Prof. Hosahudya N. Gopi, and all the faculty members and staff of the chemistry department for being extremely helpful.*

*I would like to express my sincere gratitude to Dr. Jagannath Mondal, TIFR Hyderabad, for his valuable discussions and support, which helped us to get the MD simulation model of the water channel and its permeability across the lipid bilayer membrane. I am also thankful to his student Mr. Bhupendra R. Dandekar, for his help. I would like to thank Prof. Aloke Das, IISER Pune, for his valuable suggestion in DFT calculation studies. I am also thankful to his student Mr. Prakash Panwaria for his valuable suggestion and help. I would like to thank Dr. Jeetender Chugh, IISER Pune, for his valuable discussion and help in the $^{1}H$ NMR-based binding calculation studies.*

*I would like to thank Prof. Thomas J. Pucadyil, IISER Pune, for allowing me to use the fluorescence instrument during the second year of my Ph.D. journey. I would also like to thank Prof. Jayant B. Udgaonkar, IISER Pune, for allowing me to use the stopped-flow instrument*

*for water transport studies. I am also thankful to his students Ms. Anushka Kaushik and Mr. Rupam Bhattacharjee for their valuable suggestion and help.*

*I would like to express my heartful thanks to my labmates Dr. Shard Deshmukh, Dr. Dinesh Chauhan, Dr. Tanmoy Saha, Dr. Arundhati Roy, Dr. Sopan Valiba Shinde, Dr. Harshali Khatod, Dr. Javid Ahmad Malla, Rashmi, Manzoor, Swati, Naveen, Avisikta, Anjana, Abhishek, Ravindra (Ravi), Anurag, Nihar, Sandip, Akram, Parappa, Debarati, Paras, Dipti, and Kshitij. They made a friendly and humorous environment in the laboratory, and without their cooperation, this work could not be accomplished.*

*I had a great time with my IISER friends Dr. Bappa Ghosh, Iranna Todkari, Yogesh Sutar, Aman Bajpai, Lakshman Sawase, Vikash Khade, Pankaj Dharpure, Anindita Adak, Sanjit Dey, Dr. Rahul Maiti, Soumodip Sur, and the entire chemistry department.*

*I sincerely thank Chinmoy Lowalekar, Ravinder Malothu, Sandeep Kanade, Nitin Dalvi, Dr. Sandeep Mishra, Mayuresh Kulkarni, Mahesh Jadav, Ganesh Dimbar, and Tushar Kurulkar for their support.*

*I would like to acknowledge University Grants Commission (UGC), India, and IISER-Pune for providing research fellowship during my entire research journey.*

*I am fortunate to have wonderful friends, Sabyasachi Das, Soumi Maji, Suparna Das, Abhijit Bera, Srikanta Jana, Pabitra Singha, Sujoy Bej, Bijoy Dey, Narugopal Manna, Sankar Khaskel, Amit Mondal, Gobonda Mondal, whose support and love blessed me to complete this unforgettable journey.*

*Finally, I am profoundly grateful to be blessed by the unconditional love, encouragement, and support from my family members, without whom it could not be possible for me to reach this milestone.*

# *Table of Contents*


**Chapter 1: Introduction to Membrane Transport**

1.1. Cell Membrane 1.1

1.2. Membrane Transport 1.2

1.3. Ion Transport across Bilayer Membrane 1.3

1.3.1. Importance of Ion Transport 1.4

1.3.2. Naturally Occurring Cation Transporters 1.4

1.3.3. Naturally Occurring Anion Transporter 1.5

1.3.4. The $Cl^-$ Ion Transport and Consequence 1.7

1.3.5. Artificial Anion Transporters 1.7

1.3.6. Technique for Measuring Ion Transport 1.10

1.4. Water Transport across Bilayer Membrane 1.12

1.4.1. Importance of Water Transport 1.13

1.4.2. Naturally Occurring Water Channels 1.14

1.4.3. Artificial Water Channel Systems 1.15

1.4.4. Technique for Measuring Water Permeability 1.15

1.5. References 1.16

**Chapter 2: Tripodal Cyanurates as Selective Transmembrane $Cl^-$ Transporters**

2.1. Introduction 2.1

2.2 Results and Discussions 2.2

2.2.1. Synthesis 2.2

2.2.2. The Comparison of pKa Values 2.3

2.2.3. The Solution State $Cl^-$ Ion Binding 2.3

2.2.4. Geometry Optimization and Binding Energy Calculations 2.4

2.2.5. Ion Transport Activity 2.5

2.3. Conclusion 2.9

2.4. Experimental Section 2.9

2.4.1. General Methods 2.9

2.4.2. Physical Measurements 2.10

2.4.3. Synthesis Procedures 2.10

2.4.4. $^{1}$H NMR Dilution Studies 2.16

2.4.5. $^{1}$H NMR Titration with TBACl 2.18

2.4.6. Theoretical Calculations 2.18

2.4.7. Ion Transport Activity Studies 2.30

2.5. NMR Spectra 2.38

2.6. References 2.48

**Chapter 3: Anion Induced Triazole Foldamers for Transport of $Cl^-$ ion across Phospholipid Membranes**

3.1. Introduction 3.1

3.2. Results and Discussions 3.3

3.2.1. Synthesis 3.3

3.2.2. Anion Binding Studies 3.3

3.2.3. Conformational Analysis 3.5

3.2.4. Ion Transport Activity 3.6

3.2.5. Geometry Optimization and Binding Energy Calculation 3.8

3.3. Conclusion 3.9

3.4. Experimental Section 3.9

3.4.1. General Methods 3.9

3.4.2. Synthesis Procedures 3.10

3.4.3. $^{1}$H NMR Dilution Studies 3.17

3.4.4. $^{1}$H NMR Titration 3.18

3.4.5. 2D NMR Studies 3.24

3.4.6. Ion Transport Activity Studies 3.27

3.5. Theoretical Calculations 3.35

3.6. NMR Spectra 3.57

3.7. References 3.66

**Chapter 4: Reversible Unwinding-Rewinding of Bis(indole) Double Helix to Chloride-coordinated Supramolecular Polymeric Anion Channel**

4.1. Introduction 4.1

4.2. Results and Discussions 4.2

| | | |
|---|---|---|
| 4.2.1. | Synthesis | 4.2 |
| 4.2.2. | Double Helix Conformation | 4.3 |
| 4.2.3. | Supramolecular Anionic Polymer Formation | 4.5 |
| 4.2.4. | Solid State Morphology Study | 4.6 |
| 4.2.5. | Solution Phase Anion Binding | 4.7 |
| 4.2.6. | Ion Transport Activity across Phospholipid Bilayer Membrane | 4.9 |
| 4.3. | Conclusion | 4.13 |
| 4.4. | Experimental Section | 4.13 |
| 4.4.1. | General Methods | 4.13 |
| 4.4.2. | Physical Measurements | 4.13 |
| 4.4.3. | Synthesis of Compounds | 4.14 |
| 4.4.4. | Crystallographic Measurement and Analysis | 4.19 |
| 4.4.5. | ESI-MS Experiment for **1a** and **1b** | 4.23 |
| 4.4.6. | Solution Phase NMR Studies | 4.25 |
| 4.4.7. | Field Emission Scanning Electron Microscopy (FESEM) | 4.28 |
| 4.4.8. | Atomic Force Microscopy (AFM) | 4.29 |
| 4.4.9. | High-Resolution Transmission Electron Microscopy (HRTEM) | 4.30 |
| 4.4.10. | ESI-MS Spectrum of $Cl^-$ bound Complex of **1b** | 4.31 |
| 4.4.11. | Solution Phase Anion Binding | 4.34 |
| 4.4.12. | 2D-DOSY NMR Experiment of Bis(indole) Compound **1c** | 4.35 |
| 4.4.13. | Ion Transport Studies | 4.38 |
| 4.4.14. | Planner Bilayer Conductance Measurement | 4.45 |
| 4.5. | NMR Spectra of Compounds | 4.47 |
| 4.7. | References | 4.54 |
| **Chapter 5:** | **Peptide Backbone-based 1,2-Diol Transports Water via Self-Assembled Barrel Rosette Water Channel** | |
| 5.1. | Introduction | 5.1 |
| 5.2. | Results and Discussions | 5.3 |
| 5.2.1. | Synthesis | 5.3 |

| | | |
|---|---|---|
| 5.2.2. | Morphology Analysis | 5.4 |
| 5.2.3. | Solid-state Structure Analysis | 5.4 |
| 5.2.4. | Water Permeability Studies across Lipid Bilayer Membrane | 5.6 |
| 5.2.5. | Water Permselectivity Studies across Lipid Bilayer Membrane | 5.7 |
| 5.2.6. | Ion Transport Studies across Lipid Bilayer Membrane | 5.8 |
| 5.2.7. | Molecular Dynamics Simulations Studies | 5.9 |
| 5.3. | Conclusion | 5.12 |
| 5.4. | Experimental Section | 5.12 |
| 5.4.1. | General Methods | 5.12 |
| 5.4.2. | Physical Measurements | 5.13 |
| 5.4.3. | Synthesis of Compounds | 5.13 |
| 5.4.4. | Field Emission Scanning Electron Microscopy (FESEM) | 5.26 |
| 5.4.5. | High-Resolution Transmission Electron Microscopy (HRTEM) | 5.27 |
| 5.4.6. | Crystallographic Measurement and Analysis | 5.28 |
| 5.4.7. | Water Transport Studies | 5.29 |
| 5.4.8. | Ion Transport Studies | 5.35 |
| 5.4.9. | MD Simulation Setup | 5.42 |
| 5.5. | NMR spectra of Compounds | 5.44 |
| 5.6. | References | 5.62 |

## A

| | |
|---|---|
| α | Alpha |
| Å | Angstrom |
| Ar | Aromatic |
| Ac | Acetyl |
| ATP | Adenosine Tri-Phosphate |

## B

| | |
|---|---|
| β | Beta |
| BLM | Black lipid membrane |

## C

| | |
|---|---|
| *c* | Concentration |
| cm | Centimeter |
| CF | Carboxyfluorescein |
| Calc. | Calculated |
| CFTR | Cystic Fibrosis Transmembrane Conductance Regulator |
| CLC | Chloride Channel |
| $CHCl_3$ | Chloroform |
| $CDCl_3$ | Deuterated chloroform |
| $CH_3CN$ | Acetonitrile |
| CsCl | Cesium chloride |
| CCDC | Cambridge Crystallographic Data Centre |

## D

| | |
|---|---|
| δ | Delta (Chemical shift) |
| °C | Degree Celsius |
| d | Doublet |
| dd | Doublet of doublet |
| dt | Doublet of triplet |
| DPhPC | 2-diphytanoyl-*sn*-glycero-3-phosphocholine |
| DMSO | Dimethylsulfoxide |

| | |
|---|---|
| DCM | Dichloromethane |
| DFT | Density Functional Theory |

## E

| | |
|---|---|
| EYPC | L-α-phosphatidylcholine from egg-yolk |
| $EC_{50}$ | Effective concentration at half maximal activity |
| EtOAc | Ethylacetate |
| EtOH | Ethanol |
| $Et_3N$ | Triethylamine |
| ESI | Electrospray ionization |
| EDC·HCl | 1-(3-Dimethylaminopropyl)-3-ethylcarbodiimide hydrochloride |

## F

| | |
|---|---|
| $F_t$ | Fluorescence intensity at time *t* |
| FCCP | Carbonyl cyanide-p-trifluoromethoxyphenylhydrazone |

## G

| | |
|---|---|
| $G_{hyd}$ | Free energy of hydration |

## H

| | |
|---|---|
| Hz | Hertz |
| h | Hour |
| HPTS | 8-Hydroxypyrene-1,3,6-trisulfonate trisodium salt |
| HOBt | Hydroxybenzotriazole |
| HEPES | 4-(2-hydroxyethyl)-1-piperazineethanesulfonic acid |
| HCl | Hydrochloric acid |
| HPLC | High performance liquid chromatography |
| HRMS | High Resolution Mass Spectrometry |

## I

| | |
|---|---|
| $I_F$ | Normalized Fluorescence Intensity |
| IR | Infrared spectroscopy |

| | |
|---|---|
| ISE | Ion selective electrode |

## J

| | |
|---|---|
| *J* | Coupling constant |

## K

| | |
|---|---|
| *k* | Rate constant |
| $K_a$ | Association constant |
| $K_2CO_3$ | Potassium carbonate |
| kcal | kilocalorie |
| KCl | Potassium chloride |
| KBr | Potassium bromide |
| KOH | Potassium Hydroxide |

## L

| | |
|---|---|
| λ | Lambda |
| LUV | Large unilamellar vesicle |
| logP | logarithmic form of a ratio of Partition Coefficient |
| LiCl | Lithium chloride |

## M

| | |
|---|---|
| m | Multiplet |
| M | Molar |
| μM | Micromolar |
| μL | Microliter |
| M.P. | Melting Point |
| MHz | Mega hertz |
| min | Minute(s) |
| max | Maximum |
| mg | Milligram(s) |
| mol | Mole |
| mmol | Millimole(s) |

| | |
|---|---|
| mM | Millimolar |
| mL | Milliliter |
| M. W. | Molecular weight |
| MeOH | Methanol |
| Me | Methyl |

## N

| | |
|---|---|
| *n* | Hill coefficient |
| nm | Nanometer |
| nM | nanomolar |
| NMR | Nuclear magnetic resonance |
| $Na_2SO_4$ | Sodium sulfate |
| NaF | Sodium fluoride |
| NaCl | Sodium chloride |
| NaBr | Sodium bromide |
| NaI | Sodium iodide |
| $NaNO_3$ | Sodium nitrate |
| $NaClO_4$ | Sodium perchlorate |
| NaSCN | Sodium thiocyanate |
| NaOAc | Sodium acetate |
| NaOH | Sodium hydroxide |

## O

| | |
|---|---|
| obs | Observed |
| ORTEP | Oak Ridge Thermal Ellipsoid plot |

## P

| | |
|---|---|
| Ph | Phenyl |
| ppm | Parts per million |

## R

| | |
|---|---|
| *R* | Ideal gas constant |
| ρ | Resistivity |

| | |
|---|---|
| rt | Room temperature |
| RbCl | Rubidium chloride |

## S

| | |
|---|---|
| *s* | singlet |
| s | Second(s) |
| SCXRD | Single crystal X-ray diffraction |

## T

| | |
|---|---|
| t | Triplet |
| td | Triplet of doublets |
| *t* | Time |
| Tx | Triton X-100 |
| TLC | Thin Layer Chromatography |
| THF | Tetrahydrofuran |
| TBA | Tetrabutyl ammonium |

## V

| | |
|---|---|
| Val | Valinomycin |

## Y

| | |
|---|---|
| *Y* | Fractional fluorescence intensity |

# *Synopsis*

The thesis entitled **"Development of Biomimetic Systems for the Transportation of Ions and Water across Lipid Bilayer Membranes"** comprises five chapters.

*The thesis aims to develop small molecule based artificial systems for selective transport of anion and water across the phospholipid membrane. The transport of essential solutes across the bilayer membrane is crucial for the smooth functioning of the cellular processes. Naturally occurring transporter systems perform this job for intracellular pH control, cell volume regulation, osmotic balance regulation, signal transduction, stabilization of resting potential, etc., and have shown promising application as antibacterial, antimalarial, antimicrobial, and anticancer agents, etc. Here we develop artificial carrier and channel forming molecules, which have the ability to mimic the roles of naturally occurring transport systems. The anion recognition behavior of the carrier molecules was confirmed by performing the solution phase NMR and computation studies, whereas the transportability of all transporters was evaluated across various lipid membranes, including vesicular and planar membranes. Additionally, we have developed water channel systems for selective translocation of water across phospholipid membranes, which can be applied in various applications, including the development of biomimetic RO membranes.*

**Chapter 1: Introduction to Membrane Transport**

Biological lipid membranes provide protective layers around cells and cell organelles, and are impervious to polar solutes. Nevertheless, the exchange of these polar solutes, such as cations, anions, water, amino acid, ATP, carbohydrates, etc., across cellular membranes is essential for the smooth functioning of the cellular processes. Therefore, nature has developed proteins that form channels and pores that facilitate the transport of these critical chemical species across the cell membranes and regulate the cellular pH, osmotic pressure, cell signaling, etc. Therefore, significant efforts have been dedicated to study their structures and mechanisms of action, and the outcome has attracted chemists to design artificial systems to mimic their natural congeners. Among the biological anions, chloride is the most abundant and essential anion inside the physiological systems transported by either membrane-embedded protein channels, ion carriers, or ion pumps. Mutations in these protein channels can perturb the ion homeostasis leading to multiple life-threatening diseases, such as *cystic fibrosis*, *Bartter syndrome*, *Dent's disease*, etc. Therefore, immense efforts have been made to develop synthetic chloride transporters, hoping to replace the faulty chloride channels through a process called 'channel

replacement theory'. Therefore, we aimed to design new artificial systems that can bind and selectively transport chloride ions across lipid membranes.

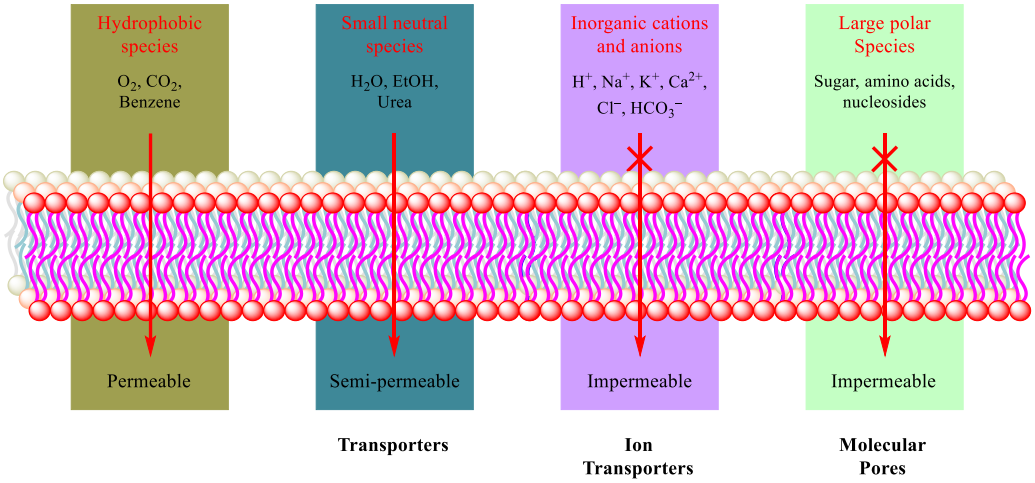



**Figure 1.** The schematic representation of membrane transport across the phospholipid membrane.

## Chapter 2: Tripodal Cyanurates as Selective Transmembrane $Cl^-$ Transporters

In this section, we have discussed a series of tris-carboxamide and tris-sulfonamide tripodal molecules having the cyanuric acid core and the evaluation of their selective transmembrane $Cl^-$ transport properties. These $C_{3v}$ symmetric tripodal receptors offer anion-π interaction from the electron deficient core, N–H···anion hydrogen bonding interactions from either carboxamide or sulfonamide moieties. In addition, the terminal aryl group offers either C–H···anion or anion-π interaction, depending on its substitution pattern. The $^1$H NMR-based apparent association constant calculation showed that the *p*-$CF_3$-phenyl-linked tris-carboxamide is a better receptor for $Cl^-$ compared to its tris-sulfonamide analogue.

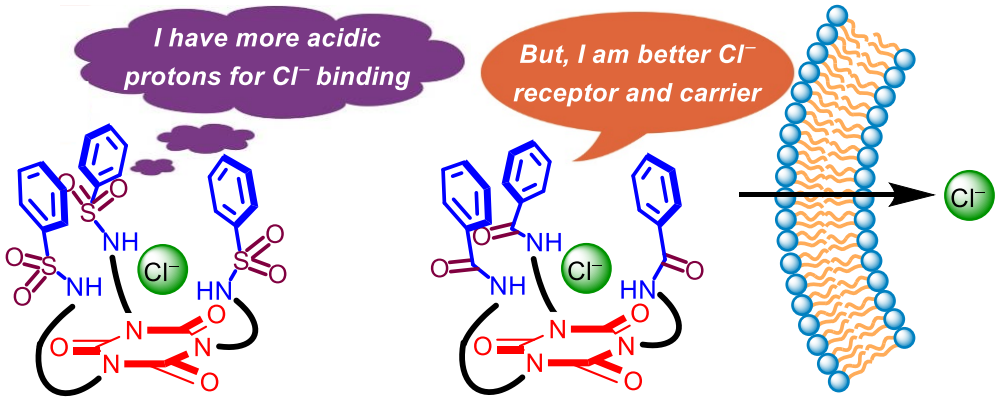



**Figure 2.** The schematic representation of tris-carboxamide and tris-sulfonamide tripodal molecules as transmembrane transporters.

The theoretical calculations confirmed that the binding of tris-carboxamide with $Cl^-$ is – 4.25 kcal $mol^{-1}$ more favorable compared to the corresponding tris-sulfonamide. The tris-carboxamide receptors exhibited significantly higher activity than their tris- sulfonamide analogues. Such results were corroborated to their better anion binding and membrane permeability. The most active receptor, consisting of pentafluoro carboxamide arms, was also established as a $Cl^-$/anion antiporter by fluorescence-based ion transport and U-tube experiments.

**Chapter 3: Triazole based Anion Induced Foldamer for Transmembrane Transport of $Cl^-$ across Phospholipid Membrane**

In this chapter, a series of triazole-cyanostilbene receptors were designed and synthesized. In the absence of anion, the receptor stays in a dynamic equilibrium of open and closed form, where the open form is largely populated, confirmed from theoretical calculations. However, in the presence of anion, the receptor forms a folded conformation where it binds with the anions through various CH···anion hydrogen bonding interactions. The strong binding was observed for $SO_4^{2-}$ anion followed by $Cl^-$, $Br^-$, $NO_3^-$, and $I^-$, calculated from $^1H$ NMR titration experiment. The NOESY NMR experiment of the receptor confirmed the formation of anion induced folded conformation. The CH···anion hydrogen bonding interactions mediated anion recognition, and foldamer formation was further confirmed from geometry optimization studies of the anion bound complex. The ion transport ability of the receptors was evaluated in vesicles based assay and found that the receptor transport $Cl^-$ anion efficiently compared to $SO_4^{2-}$ anion across the lipid bilayer membrane via mobile carrier mechanism.

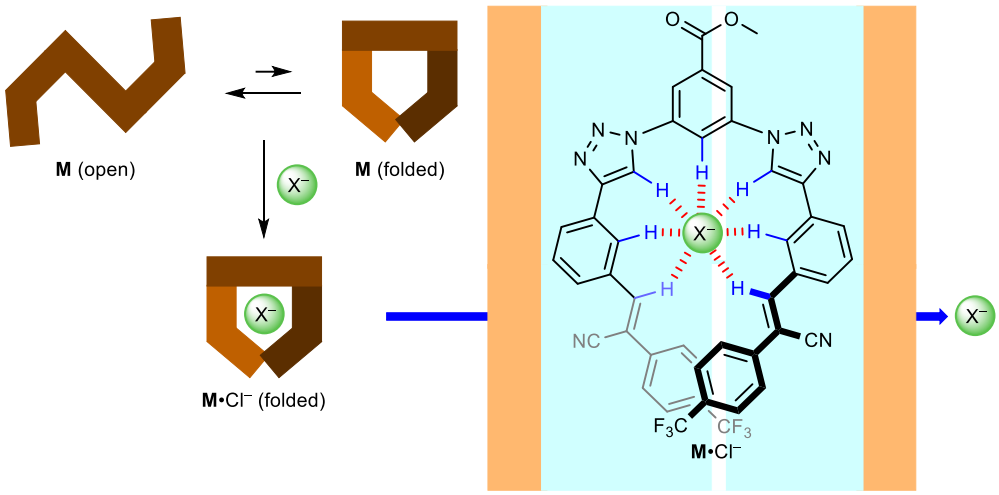



**Figure 3.** The schematic representation of anion induced foldamer formation and transport.

**Chapter 4: Reversible Unwinding-Rewinding of a Hydrogen Bonded Bis(indole) Double Helix to Chloride-coordinated Supramolecular Polymeric Anion Channel**

We report a series of bis(indole)-based biofunctional molecules that form a stable double helix structure in the solid state and solution phase. The unwinding of the double-helical structure with the treatment of chloride ions led to the formation of an anion coordinated supramolecular polymeric channel, which was confirmed by X-ray crystallography, mass spectrometry, and morphological studies. Restoration of the double-helical structure from the polymeric assembly upon the addition of Ag salts demonstrated the reversibility of the process. The supramolecular self-assembled polymeric channel forming motifs were further employed to study the ion transport activity across the artificial lipid bilayer membranes, which was evaluated through HPTS, and lucigenin based vesicular studies. The dose-dependent ion transport activity across the HPTS vesicles furnish the $EC_{50}$ value of 10.9 nM and Hill coefficient $n$ value of 1, indicating a stable supramolecular ion channel formation. Further, mechanistic ion transport studies confirmed the operation of an antiport mechanism via $Cl^-/NO_3^-$ exchange across the lipid bilayer. The planar bilayer conductance measurement confirmed the formation of an ion channel in the lipid bilayer.

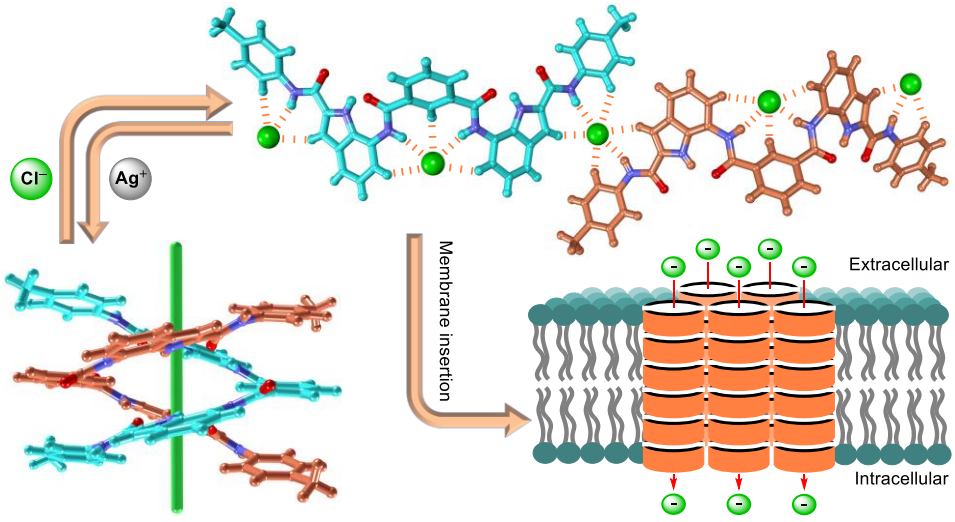



**Figure 4.** The reversible interchange between double helix to $Cl^-$ coordinated polymeric form and the schematic representation of ion channel formation.

**Chapter 5: Peptide Backbone-based 1,2-Diol Transports Water via Self-Assembled Barrel Rosette Water Channel**

Here, we have demonstrated the water channel behavior of two configurationally different peptide diol isomers that mimic the natural water channel system, i.e., Aquaporins. The solid-

state morphology studies showed the formation of self-assembled aggregated structure, and X-rays crystal structure analysis confirmed the construction of a water channel assembly, where a single self-assembled unit comprises two distinct water channels. The experimental analysis revealed that the molecules are able to transport the water across the lipid bilayer membrane with the highest permeability rate of $5.05 \times 10^8$ water molecules/s/channel, observed for the **4S** derivative. Most importantly, the precise single-channel diameter of 2.5 Å allows only water molecules selectively to pass through it while excluding the $Na^+$, $Cl^-$, and $H^+$, which are also confirmed from experimental and computational studies. The MD simulation studies for **4R** superstructure confirmed the formation of stable water channel assembly inside the bilayer membrane at ambient temperature and pressure, and more importantly, it transports the water through its 2 × 8 layers aggregated assembly.

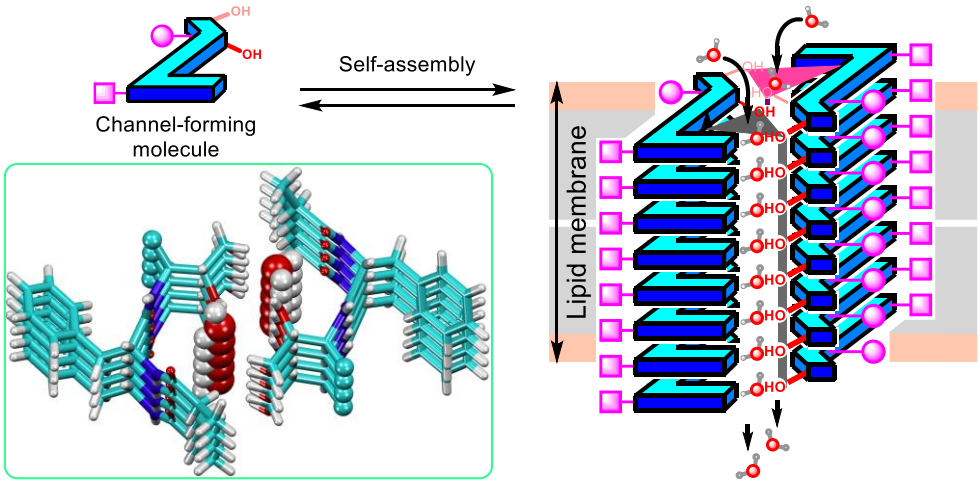
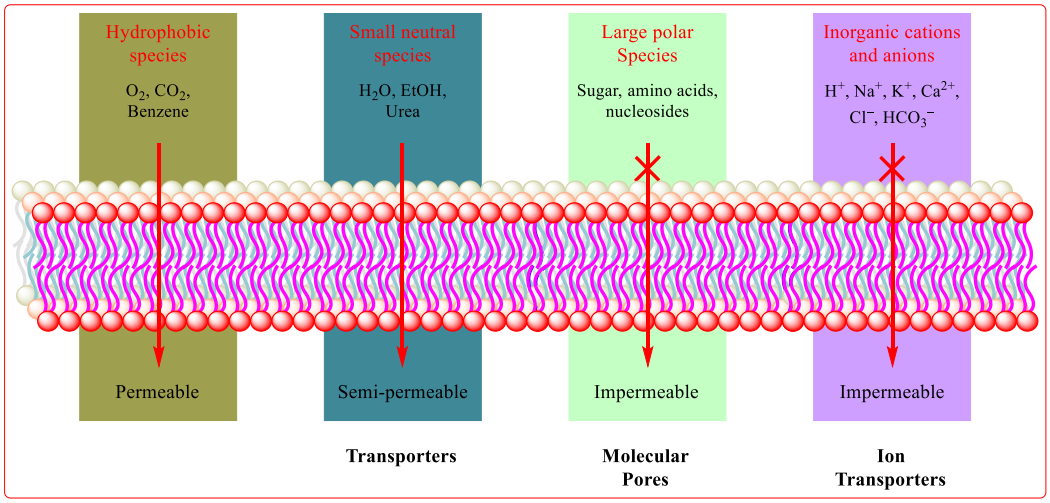



**Figure 5.** The schematic representation of water channel formation by peptide backbone-based 1,2-diol.

# Chapter 1

# Introduction to Membrane Transport



Cells are the fundamental and structural building blocks of all living organisms, from tiny living objects to giant animals. The cooperative action of the cells provides the structural shape to the body and carries out all complex processes to accomplish the survival of the organisms. The complex processes include energy production from the absorbed nutrients, transfer of the genetic information, signal transduction process for performing various functions, etc. The cellular structure is divided into three major components, i.e., the cytoplasm, the nucleus, and the cell membrane. The cytoplasm is a gel-like substance of the cell, where all the other components are in suspended condition for functioning their jobs. It contains various special compartments called cellular organelles like mitochondria, endoplasmic reticulum, chloroplasts, Golgi apparatus, lysosomes, etc. The nucleus, on the other hand, contains essential genetic information. The entire cytoplasmic constituents, including the subcellular organelles and nucleus, are surrounded by a flexible hydrophobic barrier called the plasma membrane, which acts as the protective barrier for the cellular compartments from the extracellular environment. Moreover, each subcellular organelles keep them separated from the cytosol by this specific membrane.[1]

## 1.1. Cell Membrane

Cell membranes provide protective layers around cells and cellular organelles and are impervious to highly polar solutes. These cell membranes are made up of three primary categories of lipids, such as phospholipids, cholesterol, and glycolipids, which have a hydrophilic head part and a hydrophobic tail part. The amphiphilic property of the lipid utilizes

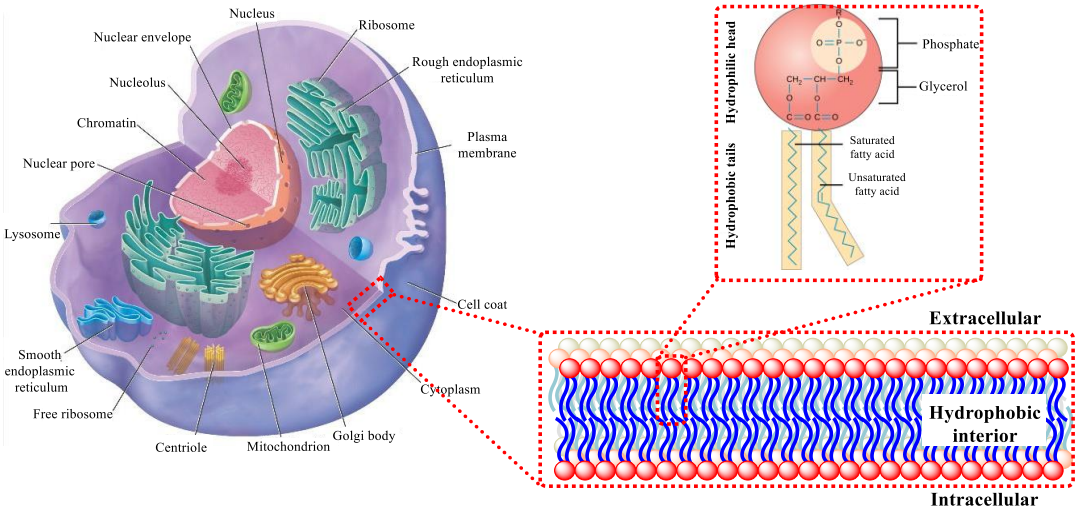



**Figure 1.1** The schematic representation of the cell membrane construction from the basic phospholipid units. The images have been accumulated from https://newbiescience.files.wordpress.com/2014/05/animal-cell.jpg.

numerous noncovalent supramolecular interactions among themself to form bilayer self-assembly with a hydrophobic thickness of 3–4 nm in aqueous media. The hydrophilic head part of the lipid in the self-assembled structure is oriented towards the inside and outside of the membrane wall, where the outer part interacts with the cell surrounding for communication and transport process. The amphipathic nature of the bilayer membrane protects the cell by allowing selective passage of required materials for its survival.[2-3]

## 1.2. Membrane Transport

As mentioned above, the interior of the cell is separated from the exterior environment with a specific barrier of the hydrophobic plasma membrane, and therefore, it allows particular solute particles to pass through it while restricting others to do so. The controlled exchange of the polar solutes such as small molecules (e.g., water, ethanol, urea, etc.), inorganic ions (e.g., $Na^+$, $K^+$, $Ca^{2+}$, $Cl^-$, $HCO_3^-$, $PO_4^{3-}$, etc.), large polar molecules (e.g., sugar, amino acid, nucleosides, etc.) and nonpolar solutes (e.g., $O_2$, $CO_2$, etc.) across the bilayer membrane is essential for smooth functioning of cellular processes. These cellular processes include intracellular pH control, cell volume regulation, osmotic balance regulation, signal transduction, stabilization of resting potential, etc. The hydrophobic nonpolar species can easily pass through the membrane via the diffusion process form higher concentration to the lower concentration. Small polar molecules such as water, ethanol, urea, etc., are also permeable through the membrane, but the diffusion rate is very slow. On the other hand, large polar molecules (e.g., sugars, ATP, amino acids, etc.) and ions are completely impermeable through the membrane due to the high thermodynamic barrier generated by the hydrophobic interior of the membrane.

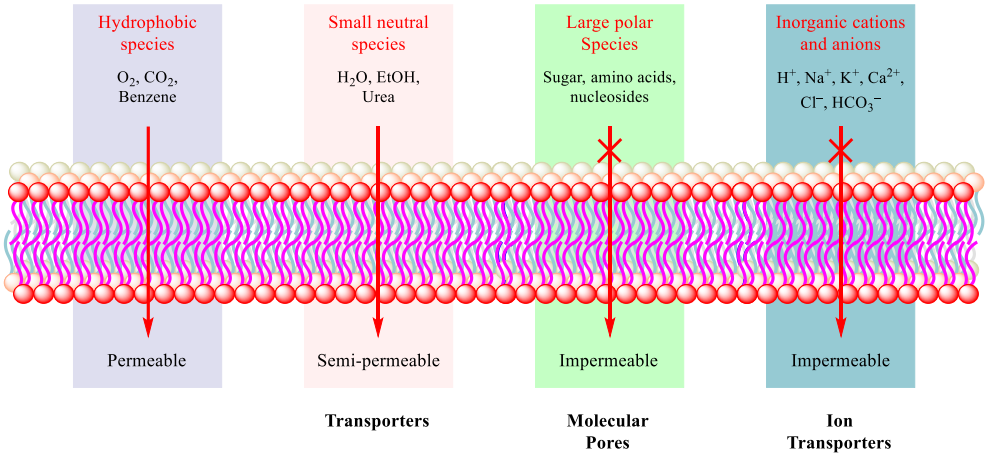



**Figure 1.2** The schematic representation of the relative permeability of the different polar and nonpolar solutes across the bilayer membrane.

As these substances are crucial for cellular functions, they are usually transported through some specific transmembrane proteins that form either the ion channels or pores inside the lipid membrane and provide a static hydrophilic path to assist the transport of these important solutes.[4]

### 1.3. Ion Transport across Bilayer Membrane

The transport of ions across the bilayer membrane, either along or against the electrochemical gradient is crucial for various cellular processes like intracellular pH regulation, maintaining osmotic balance, nutrient transport, cell volume regulation, cell proliferation, and signal transduction process in muscles, synapses, and nerves. The ion transport process across the cell membrane is usually mediated by families of protein and non-protein based entities called ion channels or ion carriers. The ion channels provide a static hydrophilic pathway across the membrane to drive the ion transport, and on the other hand, ion carriers are small molecules that can shuttle across the cell membrane and lead the ion transport across the cell membrane. Furthermore, the ion transport across the membrane can be divided into two different categories, namely passive transport, and active transport. The passive transport generally occurs along the concentration gradient without any expenditure of energy. On the other hand, in the case of active transport, ion transport occurs by the expenditure of energy in the form of ATP and drives the ion transport against the concentration gradient. This mode of ion transport usually occurs through specific types of machinery, called ion pumps.[5-6]

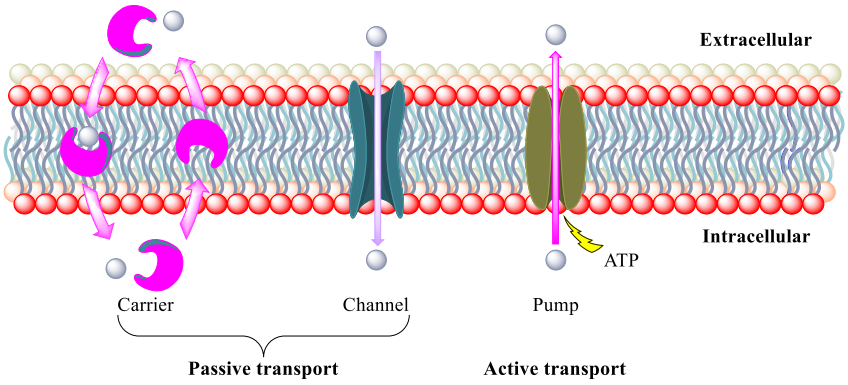



**Figure 1.3** The schematic representation of different categories of ion transport systems.

Depending upon the direction of the transport of ions, the transport process can be further classified into two major classes: uniport and co-transport. In the uniport mechanism, a particular single solute is transported from one side of the membrane to the other side, and this type of ion transport is usually driven through ion pumps by utilizing the energy source from ATP hydrolysis. On the other hand, in the co-transport mechanism, a minimum of two types

of solutes are involved, and this mode of ion transport can further be classified into two categories: symport ion transport, where two oppositely charged species transport in the same direction across the cell membrane, and antiport, where two similarly charged species are transported in opposite directions across the cell membrane (Figure 1.4.).[5, 7]

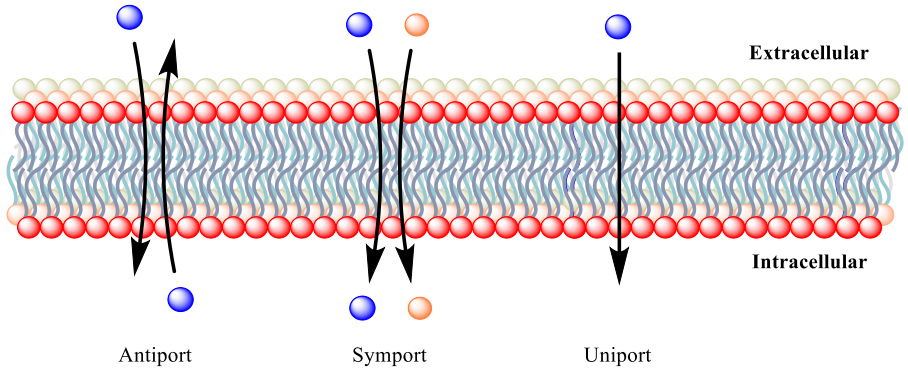



**Figure 1.4** The schematic representation of various mechanisms for transporting ions across the bilayer membrane.

### 1.3.1. Importance of Ion Transport

We have stated earlier that anions play a prerequisite role for cell survival, and their homeostasis is maintained by their transport across cellular membranes. Therefore, nature has developed proteins that form channels and pores that facilitate the transport of these critical chemical species across the cell membranes and regulate the cellular pH, osmotic pressure, cell signaling, etc. Any defects in these ion transport systems can lead to perturbed ion transport, leading to several life-threatening diseases, known as channelopathies.[8-9] For example, the $Cl^-$ ion channel malfunction leads to cystic fibrosis (CF), myotonia, Bartter syndrome, etc. Among these diseases, cystic fibrosis (CF) is caused by cystic fibrosis transmembrane conductance regulator (CFTR) mutations, also connected with the $HCO_3^-$ ion transport. The bicarbonate ion transporter, which transports $CO_2$ in the form of $HCO_3^-$ ions in the mitochondrial membrane of lungs and respiring tissues, has a vital role in maintaining pH homeostasis. Moreover, any mutations in the bicarbonate transport channels are linked to diseases in the heart, brain, bones, and CF disease.[10-11]

### 1.3.2. Naturally Occurring Cation Transporters

Natural ion channels are unique due to their structural and functional aspects. Mostly, protein-based ion transporters are found in cellular membranes of bacterial, plant, and animal cells, including the protein-based transporter, which transports cation across the bilayer membrane. The most well-known example of cation-selective transporter is gramicidin A (gA), a 15

peptide units based helical unit, where the two helical units interact face to face to form a dimeric peptide channel known to transport $K^+$ and $Rb^+$ over $Li^+$ and $Na^+$ or alkaline earth metals.[12-13] It also can transport protons across the bilayer for the destabilization of pH homeostasis. Similarly, valinomycin (Val) is a cation-selective dodecadepsipeptide found in the cell membrane of several Streptomyces transport monovalent cation across bilayer membrane. In terms of transmembrane transport, valinomycin is very selective for $K^+$ ion than the $Na^+$ ion, where binding studies suggest that the $K^+$ ion bound valinomycin complex is 10000 times more stable than that of $Na^+$ ion complex.[14] Both the peptide-based cation transporter, i.e., gA and Val, are used to study the ion transport mechanism of synthetic transporter molecules for their efficient transmembrane activity and selectivity. On the other hand, KcsA is a naturally occurring protein channel that transport $K^+$ ion at 10000 times more rate than that of $Na^+$ ion across the bilayer membrane and transport the $K^+$ ion with an exceptional speed of 108 ions per second.[15-16]

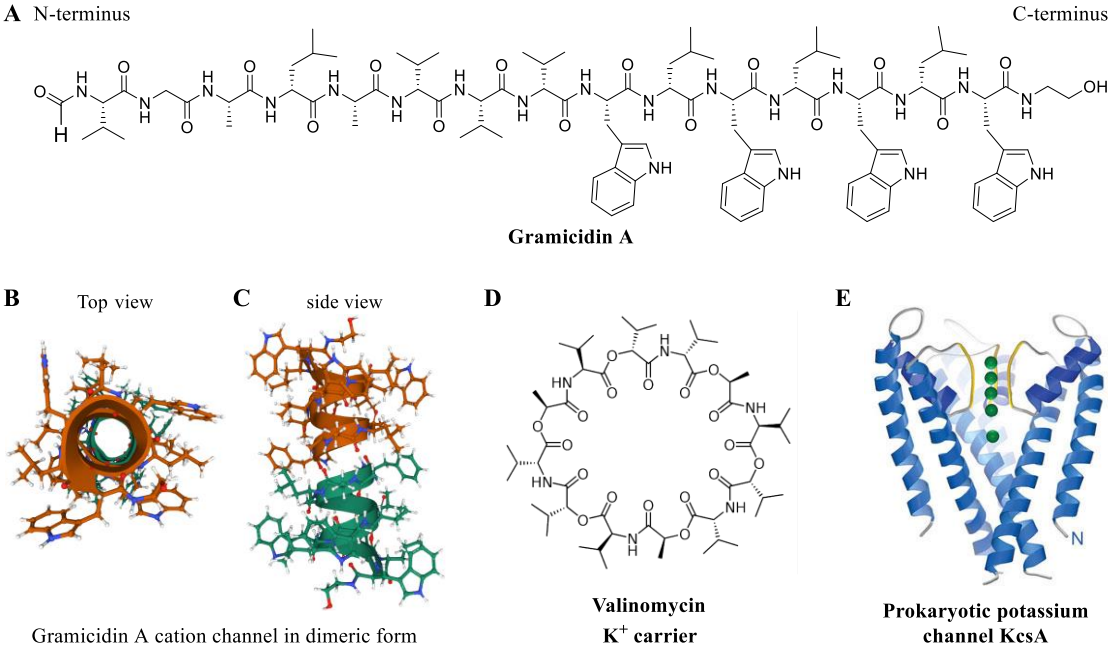



**Figure 1.5** The chemical structural representation of naturally occurring cation transporters.

### 1.3.3. Naturally Occurring Anion Transporter

Anion transporters are the entities that transport the anions across the bilayer membrane along the concentration gradient. Several naturally occurring anion transporter are reported to date and can be classified into two categories based on their structural unit: non-protein and protein-based anion channels. One well-known and widely studied nonprotein-based anion transporter system is Prodigiosin found in Gram-negative bacteria such as Serratia marcescens.[17] The

Prodigiosin has an optimal anion-binding site and is lipophilic in nature, which can bind the $Cl^-$ and $HCO_3^-$ in its cavity and transport the anion via $H^+/Cl^-$ symport and $Cl^-/HCO_3^-$ exchange with superfast permeability across the membrane.[18] This high ion transport activity of the prodigiosin molecule is believed to be one of the major factors that are responsible for the cytotoxic effects toward different cancer cells. Moreover, it has drawn significant attention in extensive biological applications including, antimalarial, immunosuppressive, and antifungal activities.[19] Tambjamines are the structural analogs of naturally occurring anion transporter Prodigiosin found from marine invertebrates and bacteria. The anion binding cavity of this series of molecules shows that it can bind the $Cl^-$ ion with a receptor to an anion binding ratio of 1:1 and transport the anion via $Cl^-/NO_3^-$ and $Cl^-/HCO_3^-$ exchange where higher N–H proton p$K_a$ help to prohibit the symport mechanism, unlike Prodigiosin.[20-22] Similar to Prodigiosin, the tambjamine series of molecules has also shown anticancer and antimicrobial activities.[23-24] The ceramides, a group of sphingolipid, are also naturally occurring anion transporter that participates in various signaling processes in eukaryotic cells by transporting the anion across the cell membrane via the anion-exchange mechanism. Interestingly, this class of molecules transports the anion via carrier mechanism at lower concentration whereas act as a channel at higher concentration.[25-27]

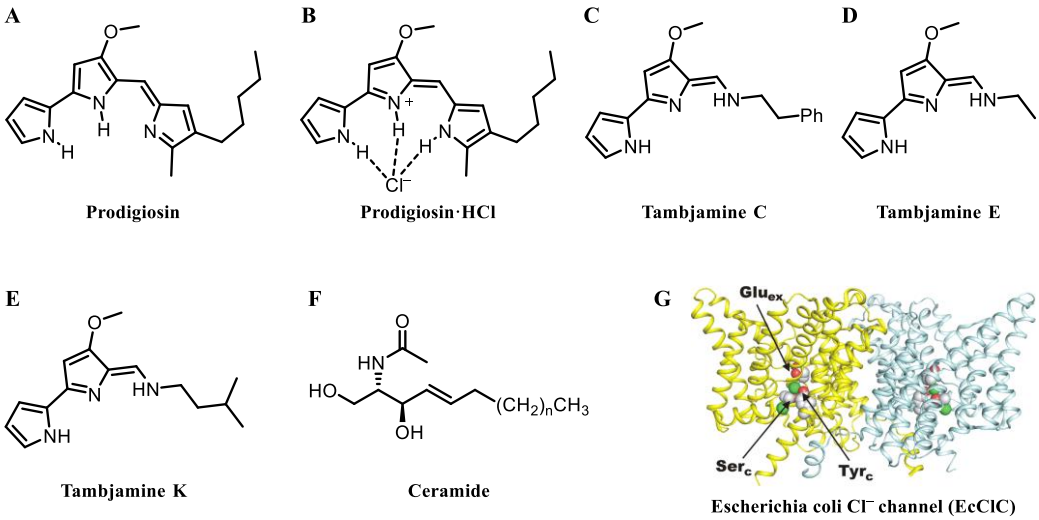



**Figure 1.6** The chemical structural representation of naturally occurring anion transporters.

On the other hand, EcClC from Escherichia coli is the protein-based naturally occurring dimeric channel. Each monomeric unit of this channel contains 473 amino acids that transport $Cl^-$ ion across the cell membrane with high precision and selectivity to maintain membrane potential and salts concentration gradient.[28-29]

### 1.3.4. The $Cl^-$ Ion Transport and Consequence

The $Cl^-$ ion is the most abundant and crucial one among the essential biologically relevant anions such as phosphate, bicarbonate, fluoride, acetate, etc. The concentration distribution of this anion in the intracellular and extracellular media of the cell are not same, which is important for signal transduction processes. It has been found that the extracellular $Cl^-$ ion concentration in the cell is 110 mM, whereas the intracellular concentration is extremely low, i.e., 5–15 mM. This concentration gradient is maintained by the combined effort of action ion pumps and passive $Cl^-$ channel. Any mutations in $Cl^-$ channels protein can perturb the ion homeostasis leading to multiple life-threatening diseases, such as *cystic fibrosis*, *Bartter syndrome*, *dents disease*, etc. Therefore, immense efforts have been made to develop synthetic chloride transporters, hoping to replace the faulty chloride channels through a process called 'channel replacement theory'. Moreover, studies on the development of artificial $Cl^-$ channels can give us a better understanding of the ion transport process and its mechanism.[4, 30]

### 1.3.5. Artificial Anion Transporters

#### 1.3.5.1. Synthetic Anion Carriers

The findings, as mentioned earlier, inspired the research community to develop artificial small molecule-based synthetic anion transport systems to gain more insights into ion transport processes. The artificial anion carriers are anion receptors whose amphiphilic nature makes them suitable for transporting anion across the bilayer membrane. As a primary requirement to function as an ion receptor, the molecules have to have a polar cavity engaging multiple ion binding sites. The outer surface of the receptor molecule has to be nonpolar in nature to interact with the hydrophobic tail of the lipid in the membrane. Moreover, the logP values of the receptors, which dictate the membrane permeability, have to be close to 5 for better transport activity according to lipinski's rule.[31-32] The typical designs of the ion carriers with their different structural diversities are bipodal, tripodal, foldameric, macrocyclic, and cage receptors.[33-35]

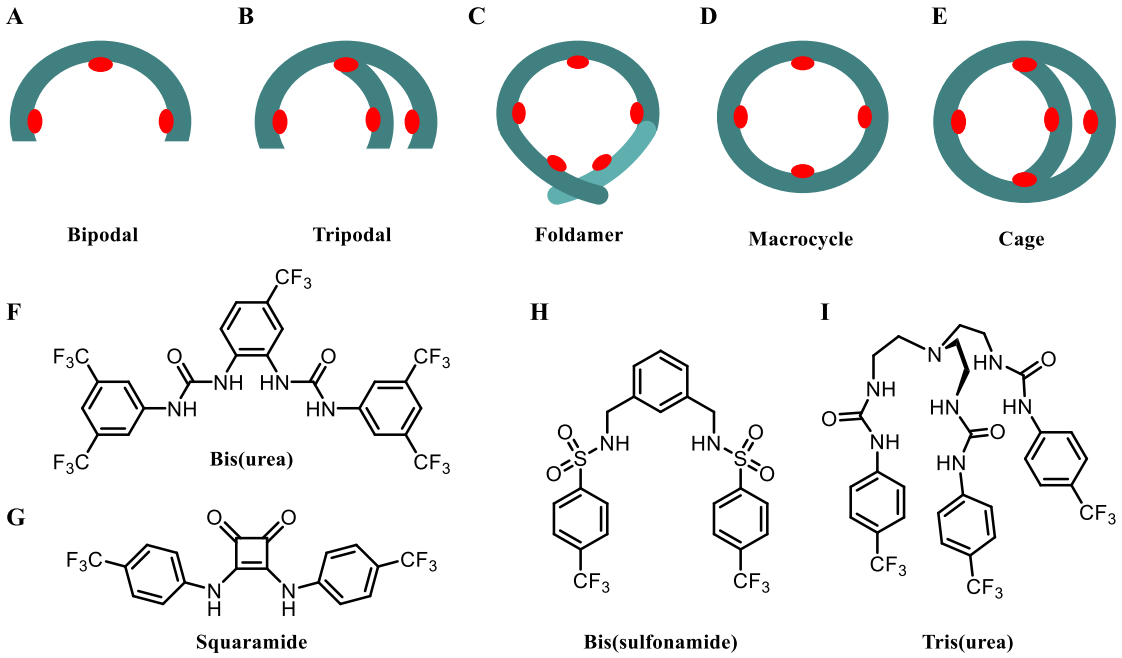



**Figure 1.7** The schematic representation of various strategies for designing ion channels and reported small molecule based synthetic anion channels.

The above mentioned design principles have lead scientists to develop various artificial ion carrier systems. The ortho-phenylene bis-urea receptor reported by Davis and co-workers has been shown to transport the $Cl^-$ ion via $Cl^-/NO_3^-$, $Cl^-/HCO_3^-$, and $Cl^-$/carboxylate antiport mechanism across the bilayer membrane.[36] In another report, Gale and co-workers have reported squaramide series[37] for their transmembrane $Cl^-$ transport activity via $Cl^-/NO_3^-$ and $Cl^-/HCO_3^-$ exchange. Similarly, the bis(sulfonamide) molecules[38] reported by Talukdar and co-workers and tripodal tris(urea)[39] designed by Gale and co-workers have been found to transport $Cl^-$ ion via $Cl^-/NO_3^-$ exchange across the bilayer membrane. Biological studies showed that this bis(sulfonamide) transporter molecule had shown apoptosis-inducing activity in the cancer cell lines.

### 1.3.5.2. Synthetic Anion Carriers

Unlike anion carriers, it is more challenging for the synthetic chemists to design and synthesize anion channels that can mimic the structure and functions of the membrane embedded protein molecules. For designing the synthetic channel, various noncovalent supramolecular interactions must be taken into account for creating a channel assembly that can form a proper channel lumen that can bind a specific type of ion. Enormous progress has been made to develop the synthetic

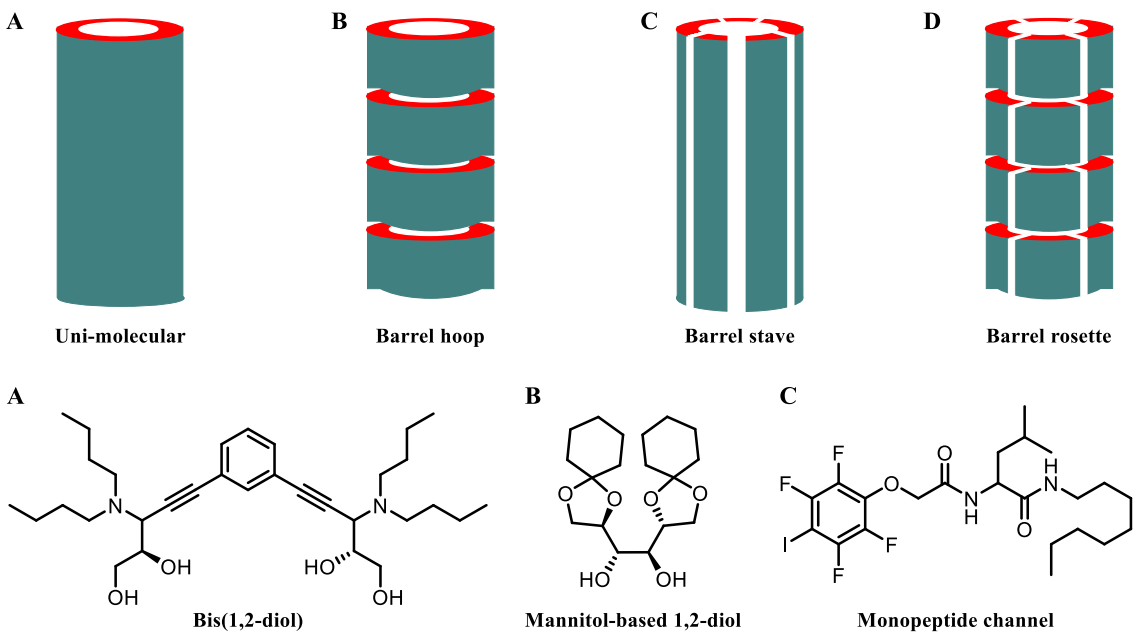



**Figure 1.8** The schematic representation of various strategies for designing ion channels and reported small molecule based synthetic anion channels.

channel systems considering the supramolecular interaction between their building block where each design follows some specific principles such as: (a) The vertical spanning the length of the channel in the membrane has to be more or equal to the thickness of the lipid membrane either by single or multiple self-assembled units of the channel-forming molecules, (b) The outer surface of the channel has to be hydrophobic so that it can easily be inserted into the lipophilic membrane, and (c) The inner pore surface of the channel has to be hydrophilic so that it can interact with the polar ion and allow it to pass through its channel lumen.

Considering the abovementioned points, supramolecular chemists have designed various channel structures such as unimolecular, barrel hoop, barrel stave, and barrel rosette channel.

Several synthetic channel systems have been reported in the literature which transport anion across bilayer membrane following various mechanisms. The mannitol-based 1,2-diol reported by Talukdar and co-workers have shown to form a barrel rosette channel across the bilayer membrane which transports the $Cl^-$ ion selectively via antiport mechanism. Details biological studies revealed that this mannitol transporter molecule shows apoptosis-inducing activity in the cancer cell line.[40] Similarly, the bis(1,2-diol) series of molecules have also been shown to transport $Cl^-$ ion via rosette ion channel for ion concentration decapitation across the bilayer membrane.[41] In another report, Zeng and co-workers reported a monopeptide-based

channel that transports anion via hooping mechanism employing the halogen bonding interactions as a key interaction.[42]

### 1.3.6. Technique for Measuring Ion Transport

Transport of ions across the bilayer membrane by the transporter molecule occurs along the concentration gradient for the dissipation of the gradient. To measure the ion transport behavior of a transporter molecule in terms of permeability and selectivity, it is essential to develop some accurate techniques that can give direct quantification. For this purpose, various liposome-based assays have been designed where large unilamellar vesicles (LUVs) are prepared using the EYPC lipid following the vortex, extrusion, and column chromatography process. A good quality lipid provided a stable barrier for ion movement after generating any gradient across the bilayer. A concentration gradient of a particular ion was then created across the extravesicular and intravesicular medium by the addition of various pulses, and the dissipation of the gradient was monitored in either of the following processes:

#### 1.3.6.1. Fluorescent Dye Based Assay

In fluorescence-based assays, various dyes such as 8-hydroxypyrene-1,3,6-trisulfonic acid trisodium salt (HPTS), lucigenin, 6-Carboxyfluorescein (CF), etc. are used. The HPTS is a pH-sensitive fluorescent dye with the p*K*a of 7.2, where the emission maximum of the deprotonated form of the molecule is 510 nm when excited at 450 nm.[43] This pH-sensitive fluorescence change behavior of the dye solution has been utilized for designing the transport measurement technique. In HPTS assay, vesicles are prepared by entrapping 1.0 mM HPTS dye solution, and after extrusion, the extravesicular dye is removed by size exclusion column chromatographic technique. In a typical assay condition, a pH gradient across the extravesicular and intravesicular medium by a base pulse was destructed by transporter molecule and measured by quantifying the fluorescence intensity change of the HPTS dye. This observation gives evidence in support of the ion transport process across the membrane assisted by the transporter molecules.[44] Similarly, lucigenin is a halide-sensitive fluorescent dye whose emission intensity decreases with increasing the halide ion concentration in its vicinity. The excited maximum of this dye is 535 nm while excited at 455 nm.[45] In assay conditions, the lucigenin dye is entrapped inside the vesicles. Then a halide concentration gradient is generated, which can be destroyed by the transport behavior of an active transporter by measuring the emission intensity change of the dye with time.[46] On the other hand, in CF dye-based assay, is used to check the membrane integrity of the vesicles in the presence of

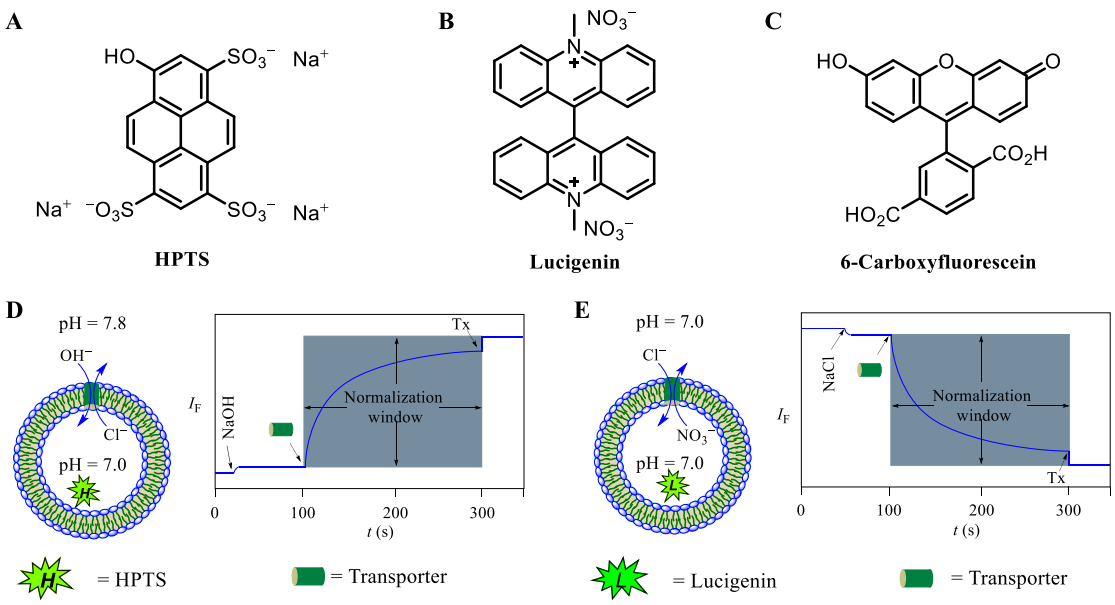



**Figure 1.9** The molecular structures of different fluorescent dyes used in ion transport assay. The schematic representation of vesicular structure in detail and assay conditions.

any active transporter. In a typical assay condition, the emission intensity of CF dye increases going from higher concentration to lower due to the leakage of the dye from the vesicles by the destruction of the membrane integrity by the transporter molecule.[47]

### 1.3.6.2. Ion Selective Electrode Based Assay

One electrode device is used in this assay, which detects the $Cl^-$ ion concentration of a particular solution by measuring the conductivity. The vesicles for this assay are prepared in nitrate buffer solution using EYPC lipid by entrapping $Cl^-$ ion solution following the extrusion and dialysis processes. Then the $Cl^-$ ion efflux by the transporter molecule was measured using the $Cl^-$ ion-selective electrode, which gives direct evidence about the transport activity and selectivity.[48] In another way, this electrode is also used in the U-tube experiment. The U-tube

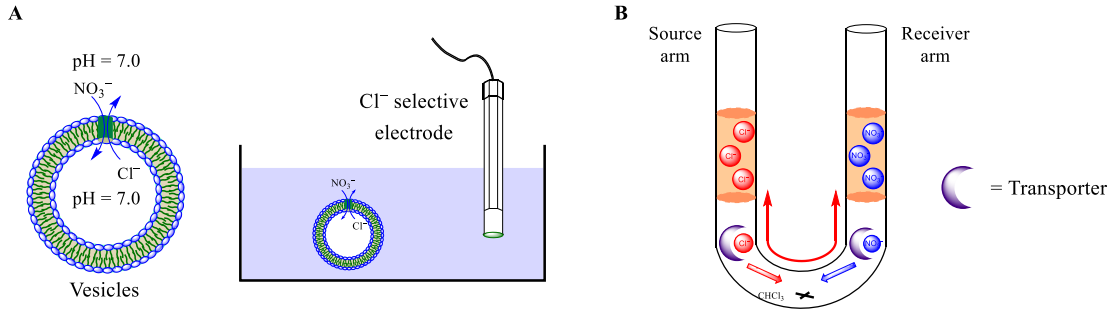



**Figure 1.10** The schematic representation of vesicles and assay details for ion selective electrode based experiment (A). The representation of U-tube experiment for carrier mechanism (B).

experiment is a setup where two different aqueous solutions (i.e., $NO_3^-$ and $Cl^-$ ions solutions) are placed on two sides of a hydrophobic $CHCl_3$ layer, and the increase of $Cl^-$ ion concentration measured at the receiver arm, gives direct proof of carrier mechanism by the transporter molecule.[49]

### 1.3.6.3. Conductance Measurement across Planar Lipid Bilayer

In this method, the electrical conductivity of an ion channel is measured across a planar lipid bilayer membrane, which separates two different chambers. For this purpose, a solution of diphytanoylphosphatidylcholine lipid (DPhPC) is painted to form a planar bilayer membrane across an aperture of 150 μm diameter in a polystyrene cup. Both the cis and trans chambers of the instrument are filled with a symmetrical solution containing 1 M KCl where the bilayer blocks the conducting path between the two sections. The channel-forming molecules can generate a conductive pathway by creating an ion channel for ion permeation. After applying a voltage gradient, channel opening and closing events indicate ion channel formation through the membrane.[50-51]

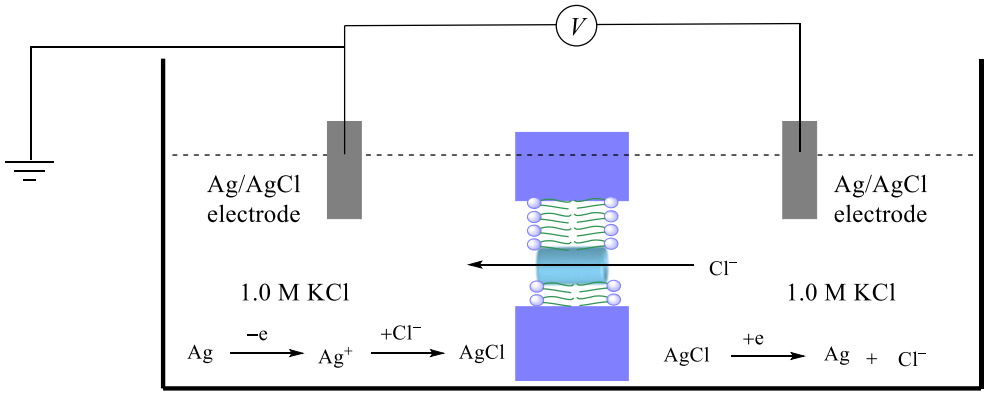



**Figure 1.11** The schematic representation of conductance measurement experiment across the planar lipid bilayer.

## 1.4. Water Transport across Bilayer Membrane

Even though the lipid bilayer membrane allows some amount of water to diffuse through it, the finite permeability via diffusion is insufficient for functioning cellular processes. The transport of water across the bilayer membrane through channels is crucial for functioning various cellular processes and is found to do its job by concentrating urine in the renal tubules of the kidney, secreting tears, generating saliva in the salivary gland, producing sweat. The diffusion of water across the membrane is a bidirectional process, whereas water transport via the channel is directed by an osmotic gradient and can be regulated by the inhibitor. In nature,

aquaporins (AQPs)-based protein channels are available, which are known to transport water across lipid bilayer membranes with high permeability and permselectivity.[52]

### 1.4.1. Importance of Water Transport

Water, the universal solvent for all living and non-living objects, is found in microbes, vertebrates, invertebrates, and plants occupy 70% of our body to perform fundamental processes, where aquaporin proteins serve as a plumbing system for water inside cells. Aquaporins are the specialized set of protein channels that form pores inside the lipid bilayer membrane and assist water transport across it. Any defects in aquaporins can lead to several diseases such as *nephrogenic diabetes insipidus* and *neuromyelitis optica*.[53-54] These aquaporin-based systems can also be used for the desalination of seawater to address the increasing demand for pure water supply in current days. However, the lack of stability and compatibility of aquaporins outside the cellular environment delimit its widespread use for water purification applications. Therefore, the development of biomimetic artificial water channels (AWCs) is fundamentally essential for studying their water transport behavior and is helpful for medical and water purification purposes.

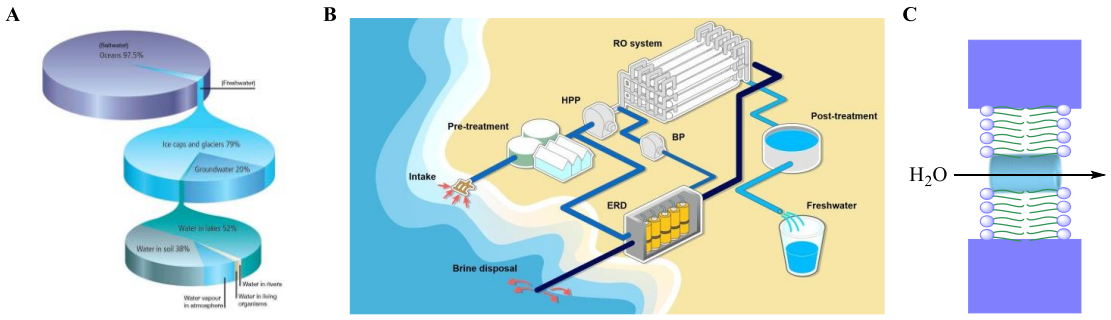



**Figure 1.12** The schematic representation of total water distribution on earth surface (A), water purification plant employing reverse technique (B), and water transport across the lipid bilayer through a water channel (C). The images was acquired from https://olc.worldbank.org/sites/default/files/sco/E7B1C4DE-C187-5EDB-3EF2-897802DEA3BF/Nasa/chapter1.html.

Even though 71% of the earth's surface is covered by water, over more than one-third of the world's population faces severe freshwater scarcity because a tiny percentage of the total is available as accessible freshwater.[55] This shortage of freshwater is not only incompetent to meet the drinking water issue but also pushes humankind to get infected with severe life-threatening diseases due to inadequate sanitation.[56] To solve this crisis, scientists have come up with various water purification techniques where 90% of the water purification plant work using reverse osmotic (RO) technique by desalination from seawater. In this regard, reverse

osmosis membrane or artificial water channels (AWCs), which have the ability to transport water selectively by excluding the salts and protons from the seawater, have an important role. However, one disadvantage of this technique is that the desalination process is very energy consuming. Therefore, an extremely sophisticated membrane material is required, which can complete the process by consuming less energy and making the process economical and available to all.[57-58]

### 1.4.2. Naturally Occurring Water Channels

In nature, aquaporin water channels are there, which facilitate water translocation through the cellular membrane. The AQPs are made up of six alpha-helixes proteins, which are embedded in the bilayer membrane. The transport rate of water through this channel is exceptionally high and very much selective for water, excluding salts and protons. In this context, the presence of arginine amino acid residue at the channel entrance helps it gain selectivity by prohibiting the proton transport, whereas precise channel lumen (with 3 Å diameter) allows it to achieve salts exclusions. There are various classes of aquaporins in nature, such as AQP1, AQP2, AQP3, AQP4, AQPZ, etc. Among them, the AQPZ transports water across the membrane with a permeability rate of $6 \times 10^9$ $H_2O$ molecules per second per channel.[59-60]

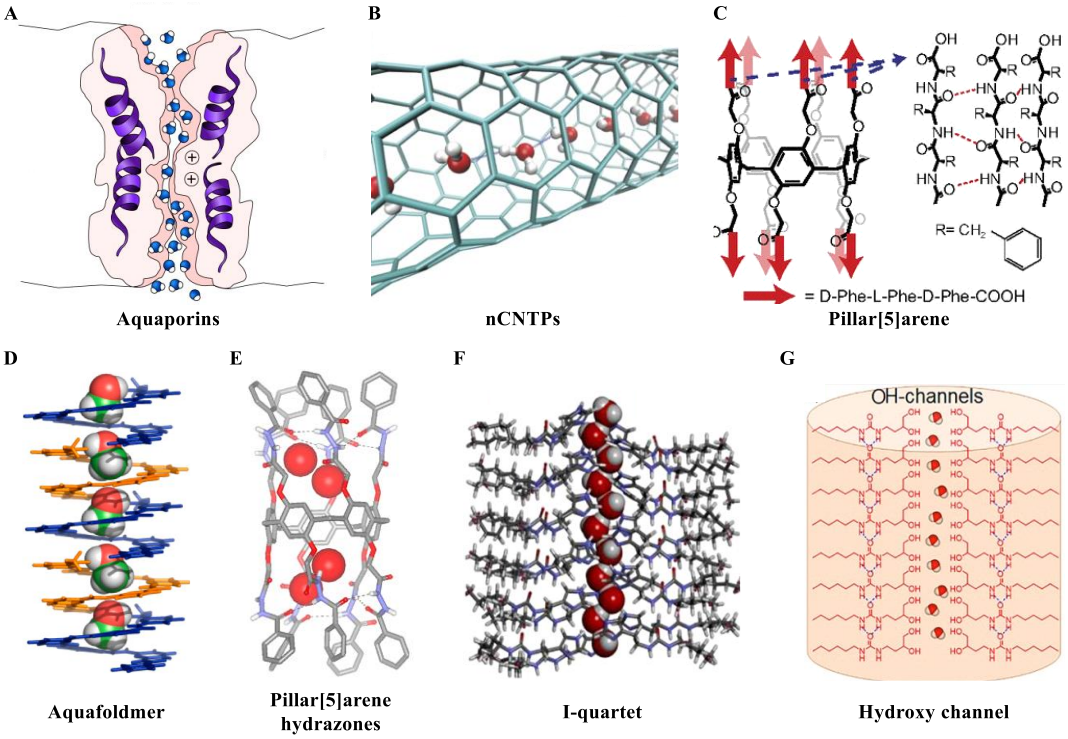



**Figure 1.13** The structure of naturally occurring aquaporin water channels showing water its translocation path (A). The structure of artificial water channels: nCNTPs (B)[61], pillar[5]arene (C)[62], aquafoldamer (D)[60], pillar[5]arene hydrazones (E)[63], imidazole I-quartet (F)[64], and hydroxyl channel (G).[65]

### 1.4.3. Artificial Water Channel Systems

Significant progress has been made to develop artificial water channels (AWCs) based on simple synthetic molecules, which can mimic the function of the structurally critical aquaporin protein channels for water transport. Some of them have even shown ultrafast water transport rates. For example, carbon nanotube porins (nCNTPs) transport water across the bilayer membrane with a transport rate of 6 times that of AQP1, a natural water channel protein. However, it also transports monovalent cations such as $Na^+$, $K^+$, and protons.[61] However, the exclusion of salts and protons by the channel-forming substrate is an indispensable criterion during the water transport process. Barboiu, Hou, and their co-workers have made a tremendous effort to develop synthetic channels for selective water transport, where the studies were further extended by Kumar, Zeng, and their co-workers. The I-quartet and the hydroxyl-based water channels reported by Barboiu and co-workers has shown selective and fast water permeation across the bilayer membrane.[64-66] The hydrazide-appended pillar[5]arene derivatives reported by Hou and co-workers has shown to transport water while excluding protons like the natural water channels.[62] Later, Kumar and co-workers has reported peptide-appended hybrid[4]arenes (PAH[4]s) based water transport system which transport water (water permeability > $10^9$ $H_2O$ $s^{-1}$ $channel^{-1}$) with comparable transport rate of AQPs while excluding salts.[63] The studies were further extended in recent reports by Zeng and co-workers, where they have reported several foldamer-based water channels that have shown excellent water permeability rate and exclude salts and protons during the transport process.[60, 67-68]

### 1.4.4. Technique for Measuring Water Permeability

Transport of water across the bilayer membrane by the channel-forming molecule occurs along the osmotic gradient. To measure a channel's water transport behavior, it is essential to develop some accurate techniques that can give direct qualitative and quantitative estimation. For this

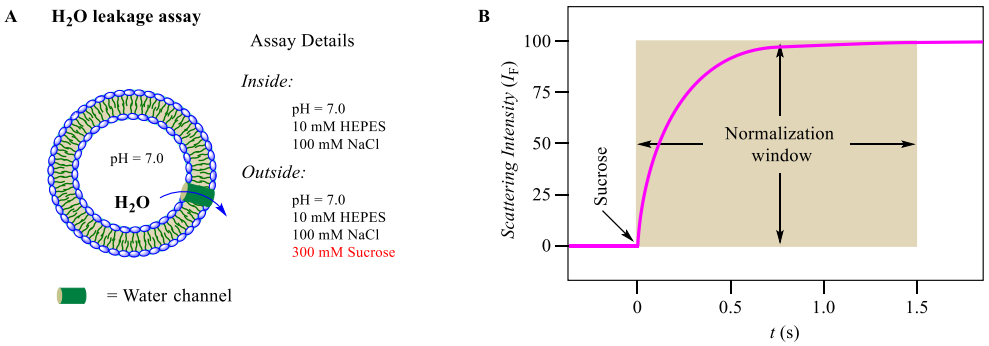



**Figure 1.14** The schematic representation of vesicular structure in detail (A) and assay conditions (B) for water permeability measurement.

purpose, liposome-based assays have been designed where large unilamellar vesicles (LUVs) are prepared using the DOPC lipid in NaCl solution following the vortex and extrusion process. An osmotic gradient was then created across the extravesicular and intravesicular medium by adding an equal volume of 300 mM sucrose solution, which leads to the efflux of water through the channel for the dissipation of the gradient monitored by measuring the scattering intensity change of the solution. A more abrupt change in scattering intensity in the presence of a channel-forming molecule compared to the blank test confirmed its transportability.[60]

## 1.5. References


1. Li, Y.; Zhao, D., Basics of Molecular Biology. In *Molecular Imaging: Fundamentals and Applications*, Tian, J., Ed. Springer Berlin Heidelberg: Berlin, Heidelberg, 2013; pp 541–601.
2. Enkavi, G.; Javanainen, M.; Kulig, W.; Róg, T.; Vattulainen, I. *Chem. Rev.* **2019**, *119*, 5607–5774.
3. Herrmann, T.; Leavitt, L.; Sharma, S., Physiology, Membrane. In *StatPearls*, StatPearls Publishing Copyright © 2021, StatPearls Publishing LLC.: Treasure Island (FL), 2021.
4. Davis, A. P.; Sheppard, D. N.; Smith, B. D. *Chem. Soc. Rev.* **2007**, *36*, 348–357.
5. Davis, J. T.; Okunola, O.; Quesada, R. *Chem. Soc. Rev.* **2010**, *39*, 3843–3862.
6. Fyles, T. M. *Chem. Soc. Rev.* **2007**, *36*, 335–347.
7. Hoffmann, E. K.; Keynes, R. D.; Ellory, J. C. *Philos. Trans. R. Soc. Lond., B, Biol. Sci.* **1982**, *299*, 519–535.
8. Ashcroft, F. M.; Roper, J. *Curr. Opin. Cell Biol.* **1993**, *5*, 677–683.
9. Dworakowska, B.; Dołowy, K. *Acta Biochim. Pol.* **2000**, *47*, 685–703.
10. Sheppard, D. N.; Rich, D. P.; Ostedgaard, L. S.; Gregory, R. J.; Smith, A. E.; Welsh, M. J. *Nature* **1993**, *362*, 160–164.
11. Choi, J. Y.; Muallem, D.; Kiselyov, K.; Lee, M. G.; Thomas, P. J.; Muallem, S. *Nature* **2001**, *410*, 94–97.
12. Kelkar, D. A.; Chattopadhyay, A. *Biochim. Biophys. Acta, Biomembr.* **2007**, *1768*, 2011–2025.
13. Harold, F. M.; Baarda, J. R. *J. Bacteriol.* **1967**, *94*, 53–60.
14. Bhattacharyya, P.; Epstein, W.; Silver, S. *Proc. Natl. Acad. Sci. U.S.A.* **1971**, *68*, 1488–1492.

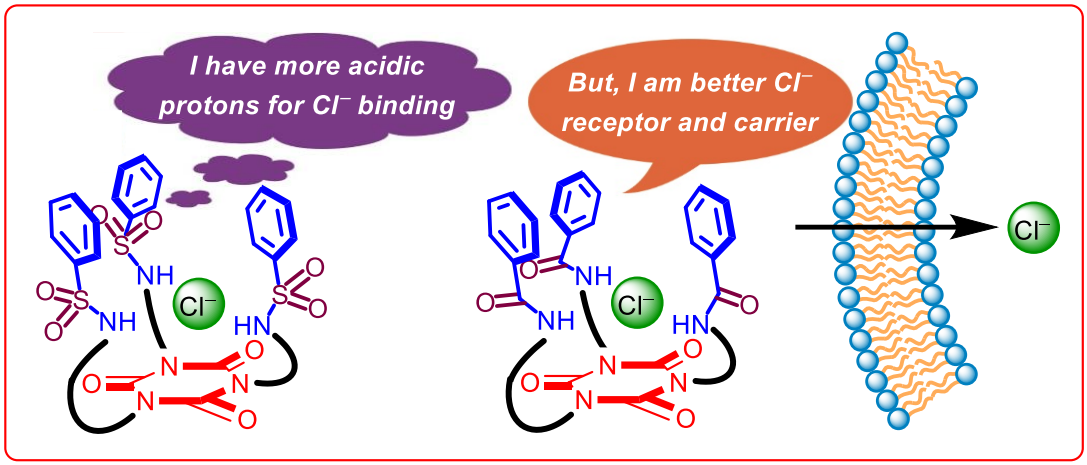
15. Shealy, R. T.; Murphy, A. D.; Ramarathnam, R.; Jakobsson, E.; Subramaniam, S. *Biophys. J.* **2003**, *84*, 2929–2942.
16. Kuang, Q.; Purhonen, P.; Hebert, H. *Cell. Mol. Life Sci.* **2015**, *72*, 3677–3693.
17. Haddix, P. L.; Shanks, R. M. Q. *Arch. Microbiol.* **2018**, *200*, 989–999.
18. Sato, T.; Konno, H.; Tanaka, Y.; Kataoka, T.; Nagai, K.; Wasserman, H. H.; Ohkuma, S. *J. Biol. Chem.* **1998**, *273*, 21455–21462.
19. Li, D.; Liu, J.; Wang, X.; Kong, D.; Du, W.; Li, H.; Hse, C.-Y.; Shupe, T.; Zhou, D.; Zhao, K. *Int. J. Mol. Sci.* **2018**, *19*, 3465.
20. Saggiomo, V.; Otto, S.; Marques, I.; Félix, V.; Torroba, T.; Quesada, R. *Chem. Commun.* **2012**, *48*, 5274–5276.
21. Melvin, M. S.; Ferguson, D. C.; Lindquist, N.; Manderville, R. A. *J. Org. Chem.* **1999**, *64*, 6861–6869.
22. Hernández, P. I.; Moreno, D.; Javier, A. A.; Torroba, T.; Pérez-Tomás, R.; Quesada, R. *Chem. Commun.* **2012**, *48*, 1556–1558.
23. Manuel-Manresa, P.; Korrodi-Gregório, L.; Hernando, E.; Villanueva, A.; Martínez-García, D.; Rodilla, A. M.; Ramos, R.; Fardilha, M.; Moya, J.; Quesada, R.; Soto-Cerrato, V.; Pérez-Tomás, R. *Mol. Cancer Ther.* **2017**, *16*, 1224–1235.
24. Pinkerton, D. M.; Banwell, M. G.; Garson, M. J.; Kumar, N.; de Moraes, M. O.; Cavalcanti, B. C.; Barros, F. W. A.; Pessoa, C. *Chem. Biodivers.* **2010**, *7*, 1311–1324.
25. Goñi, F. M.; Alonso, A. *Biochim. Biophys. Acta, Biomembr.* **2006**, *1758*, 1902–1921.
26. Yamaji, T.; Hanada, K. *Traffic* **2015**, *16*, 101–122.
27. Harrell, J. W. A.; Bergmeyer, M. L.; Zavalij, P. Y.; Davis, J. T. *Chem. Commun.* **2010**, *46*, 3950–3952.
28. Wang, C.-H.; Duster, A. W.; Aydintug, B. O.; Zarecki, M. G.; Lin, H. *Front. Chem.* **2018**, *6*, doi: 10.3389/fchem.2018.00062.
29. Dutzler, R. *FEBS Lett.* **2007**, *581*, 2839–2844.
30. Zaydman, M. A.; Silva, J. R.; Cui, J. *Chem. Rev.* **2012**, *112*, 6319–6333.
31. Lipinski, C. A.; Lombardo, F.; Dominy, B. W.; Feeney, P. J. *Adv. Drug Deliv. Rev.* **1997**, *23*, 3–25.
32. Keller, T. H.; Pichota, A.; Yin, Z. *Curr. Opin. Chem. Biol.* **2006**, *10*, 357–361.
33. Lang, C.; Zhang, X.; Luo, Q.; Dong, Z.; Xu, J.; Liu, J. *Eur. J. Org. Chem.* **2015**, *2015*, 6458–6465.

34. Shokri, A.; Deng, S. H. M.; Wang, X.-B.; Kass, S. R. *Org. Chem. Front.* **2014**, *1*, 54–61.
35. Helttunen, K.; Annala, R.; Suhonen, A.; Iloniemi, J.; Kalenius, E.; Aragay, G.; Ballester, P.; Tuononen, H. M.; Nissinen, M. *Chem. Asian J.* **2019**, *14*, 647–654.
36. Dias, C. M.; Li, H.; Valkenier, H.; Karagiannidis, L. E.; Gale, P. A.; Sheppard, D. N.; Davis, A. P. *Org. Biomol. Chem.* **2018**, *16*, 1083–1087.
37. Busschaert, N.; Kirby, I. L.; Young, S.; Coles, S. J.; Horton, P. N.; Light, M. E.; Gale, P. A. *Angew. Chem., Int. Ed.* **2012**, *51*, 4426–4430.
38. Saha, T.; Hossain, M. S.; Saha, D.; Lahiri, M.; Talukdar, P. *J. Am. Chem. Soc.* **2016**, *138*, 7558–7567.
39. Busschaert, N.; Wenzel, M.; Light, M. E.; Iglesias-Hernández, P.; Pérez-Tomás, R.; Gale, P. A. *J. Am. Chem. Soc.* **2011**, *133*, 14136–14148.
40. Saha, T.; Gautam, A.; Mukherjee, A.; Lahiri, M.; Talukdar, P. *J. Am. Chem. Soc.* **2016**, *138*, 16443–16451.
41. Saha, T.; Dasari, S.; Tewari, D.; Prathap, A.; Sureshan, K. M.; Bera, A. K.; Mukherjee, A.; Talukdar, P. *J. Am. Chem. Soc.* **2014**, *136*, 14128–14135.
42. Ren, C.; Ding, X.; Roy, A.; Shen, J.; Zhou, S.; Chen, F.; Yau Li, S. F.; Ren, H.; Yang, Y. Y.; Zeng, H. *Chem. Sci.* **2018**, *9*, 4044–4051.
43. Kano, K.; Fendler, J. H. *Biochim. Biophys. Acta, Biomembr.* **1978**, *509*, 289–299.
44. Roy, A.; Saha, D.; Mukherjee, A.; Talukdar, P. *Org. Lett.* **2016**, *18*, 5864–5867.
45. Biwersi, J.; Tulk, B.; Verkman, A. S. *Anal. Biochem.* **1994**, *219*, 139–143.
46. Roy, A.; Saha, D.; Mandal, P. S.; Mukherjee, A.; Talukdar, P. *Chem. – Eur. J.* **2017**, *23*, 1241–1247.
47. Roy, A.; Gautam, A.; Malla, J. A.; Sarkar, S.; Mukherjee, A.; Talukdar, P. *Chem. Commun.* **2018**, *54*, 2024–2027.
48. Wu, X.; Judd, Luke W.; Howe, Ethan N. W.; Withecombe, Anne M.; Soto-Cerrato, V.; Li, H.; Busschaert, N.; Valkenier, H.; Pérez-Tomás, R.; Sheppard, David N.; Jiang, Y.-B.; Davis, Anthony P.; Gale, Philip A. *Chem* **2016**, *1*, 127–146.
49. Shinde, S. V.; Talukdar, P. *Angew. Chem., Int. Ed.* **2017**, *56*, 4238–4242.
50. Malla, J. A.; Umesh, R. M.; Vijay, A.; Mukherjee, A.; Lahiri, M.; Talukdar, P. *Chem. Sci.* **2020**, *11*, 2420–2428.
51. Ren, C.; Zeng, F.; Shen, J.; Chen, F.; Roy, A.; Zhou, S.; Ren, H.; Zeng, H. *J. Am. Chem. Soc.* **2018**, *140*, 8817–8826.

52. Agre, P. *Angew. Chem., Int. Ed.* **2004**, *43*, 4278–4290.
53. Bichet, D. G. *Adv. Chronic Kidney Dis.* **2006**, *13*, 96–104.
54. Agre, P.; Kozono, D. *FEBS Lett.* **2003**, *555*, 72–78.
55. Czajkowski, A.; Remiorz, L.; Pawlak, S.; Remiorz, E.; Szyguła, J.; Marek, D.; Paszkuta, M.; Drabik, G.; Baron, G.; Paduch, J.; Antemijczuk, O. *Appl. Sci.* **2021**, *11*, 4081.
56. Byker, E. J.; Ezelle-Thomas, V. *J. Res. Child. Educ.* **2021**, *35*, 268–280.
57. Park, K.; Kim, J.; Yang, D. R.; Hong, S. *J. Membr. Sci.* **2020**, *595*, 117607.
58. El-Sayed, Y. M. *Desalination* **2001**, *134*, 129–158.
59. Connolly, D. L.; Shanahan, C. M.; Weissberg, P. L. *Int. J. Biochem. Cell Biol.* **1998**, *30*, 169–172.
60. Shen, J.; Ye, R.; Romanies, A.; Roy, A.; Chen, F.; Ren, C.; Liu, Z.; Zeng, H. *J. Am. Chem. Soc.* **2020**, *142*, 10050–10058.
61. Tunuguntla Ramya, H.; Henley Robert, Y.; Yao, Y.-C.; Pham Tuan, A.; Wanunu, M.; Noy, A. *Science* **2017**, *357*, 792–796.
62. Hu, X.-B.; Chen, Z.; Tang, G.; Hou, J.-L.; Li, Z.-T. *J. Am. Chem. Soc.* **2012**, *134*, 8384–8387.
63. Song, W.; Joshi, H.; Chowdhury, R.; Najem, J. S.; Shen, Y.-x.; Lang, C.; Henderson, C. B.; Tu, Y.-M.; Farell, M.; Pitz, M. E.; Maranas, C. D.; Cremer, P. S.; Hickey, R. J.; Sarles, S. A.; Hou, J.-l.; Aksimentiev, A.; Kumar, M. *Nat. Nanotechnol.* **2020**, *15*, 73–79.
64. Licsandru, E.; Kocsis, I.; Shen, Y.-x.; Murail, S.; Legrand, Y.-M.; van der Lee, A.; Tsai, D.; Baaden, M.; Kumar, M.; Barboiu, M. *J. Am. Chem. Soc.* **2016**, *138*, 5403–5409.
65. Huang, L.-B.; Hardiagon, A.; Kocsis, I.; Jegu, C.-A.; Deleanu, M.; Gilles, A.; van der Lee, A.; Sterpone, F.; Baaden, M.; Barboiu, M. *J. Am. Chem. Soc.* **2021**, *143*, 4224–4233.
66. Murail, S.; Vasiliu, T.; Neamtu, A.; Barboiu, M.; Sterpone, F.; Baaden, M. *Faraday Discuss.* **2018**, *209*, 125–148.
67. Shen, J.; Fan, J.; Ye, R.; Li, N.; Mu, Y.; Zeng, H. *Angew. Chem., Int. Ed.* **2020**, *59*, 13328–13334.
68. Roy, A.; Shen, J.; Joshi, H.; Song, W.; Tu, Y.-M.; Chowdhury, R.; Ye, R.; Li, N.; Ren, C.; Kumar, M.; Aksimentiev, A.; Zeng, H. *Nat. Nanotechnol.* **2021**, *16*, 911–917.

*Chapter 2*

# Tripodal Cyanurates as Selective Transmembrane $Cl^-$ Transporters

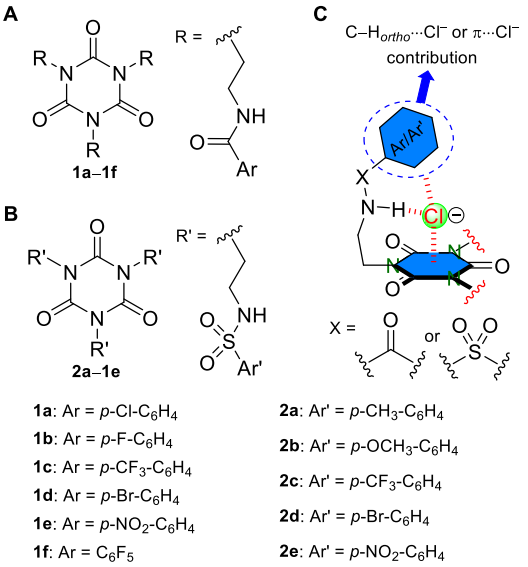


## 2.1. Introduction

We have already discussed earlier that nature has developed membrane proteins that form carriers, channels, and pumps to facilitate the controlled transport of ions. Such transport processes are critical for regulating cellular pH, osmotic pressure, cell signaling, etc. Therefore, significant efforts have been dedicated to studying their structures and mechanisms of action, and the outcome has attracted chemists to design artificial systems to mimic their natural congeners. In designing anion receptors, noncovalent interactions, such as electrostatic, hydrogen bond, halogen bond, anion-π, etc., are crucial. However, the critical challenge is to achieve selective $Cl^-$ recognition by exploiting these interactions and efficient transmembrane transport of the ion by the designed receptor.[1-5] In this context, tripodal transporters have attracted considerable attention for modulating their activity and selectivity in the anion transport process. The tripodal molecules act as excellent anion receptors for noncovalent bonding interactions by utilizing their three arms and the pre-organized cavity of these tripodal systems help them to overcome the energy loss due to conformational change during anion binding. Moreover, these receptors give the anion better shielding, making the anion complex easily permeable through the bilayer membrane. Tripodal receptors have also shown great promises in selective $Cl^-$ binding in the family of synthetic anion receptors.[6-7] The transmembrane $Cl^-$ transport by this class of receptors mostly occurs *via* the $Cl^-$/anion antiport and occasionally HCl symport.[8-12]

In this section, we report a series of tris-carboxyamide **1a**–**1f** (Figure 2.1A) and tris-sulfonamide **2a**–**2f** (Figure 2.1B) tripodal molecules having the cyanuric acid core and the evaluation of their selective transmembrane $Cl^-$ transport properties. These $C_{3v}$ symmetric tripodal receptors offer anion-π interaction from the electron deficient core, N–H···anion hydrogen bonding interactions from either carboxamide or sulfonamide moieties (Figure 2.1C). In addition, the terminal aryl group offers either C–H···anion or anion-π interaction, depending on its substitution pattern. Although anion binding studies with the tris-carboxamide **1f** and tris-sulfonamide **2e** were reported previously,[13-14] the efficiency of these classes of molecules as anion transporters required thorough attention. Ideally, it can be anticipated that the N–H proton of sulfonamide being more acidic than that of carboxamide should form a stronger N–H···anion bond. For example, Talukdar and co-workers reported a bis-sulfonamide receptor as better $Cl^-$ transporter compared to the corresponding bis-carboxamide receptor.[15] However,

the permeability of a free receptor and its anion bound complex in the lipid bilayer membrane is also crucial for an efficient ion transport process.




**1a**: Ar = *p*-Cl-$C_6H_4$
**1b**: Ar = *p*-F-$C_6H_4$
**1c**: Ar = *p*-$CF_3$-$C_6H_4$
**1d**: Ar = *p*-Br-$C_6H_4$
**1e**: Ar = *p*-$NO_2$-$C_6H_4$
**1f**: Ar = $C_6F_5$

**2a**: Ar' = *p*-$CH_3$-$C_6H_4$
**2b**: Ar' = *p*-$OCH_3$-$C_6H_4$
**2c**: Ar' = *p*-$CF_3$-$C_6H_4$
**2d**: Ar' = *p*-Br-$C_6H_4$
**2e**: Ar' = *p*-$NO_2$-$C_6H_4$

**D**

| Carboxyamide | p$K_{a1}$ [a,b] | logP [b] | Sulfonamide | p$K_{a1}$ [a,b] | logP [b] |
|---|---|---|---|---|---|
| **1a** | 14.25 | 4.08 | **2a** | 9.92 | 3.07 |
| **1b** | 14.27 | 2.69 | **2b** | 9.97 | 1.06 |
| **1c** | 14.26 | 4.90 | **2c** | 9.64 | 4.16 |
| **1d** | 14.30 | 4.57 | **2d** | 9.14 | 3.84 |
| **1e** | 13.38 | 2.02 | **2e** | 9.11 | 1.35 |
| **1f** | 10.17 | 4.40 | **2f** | 4.95 | 3.67 |

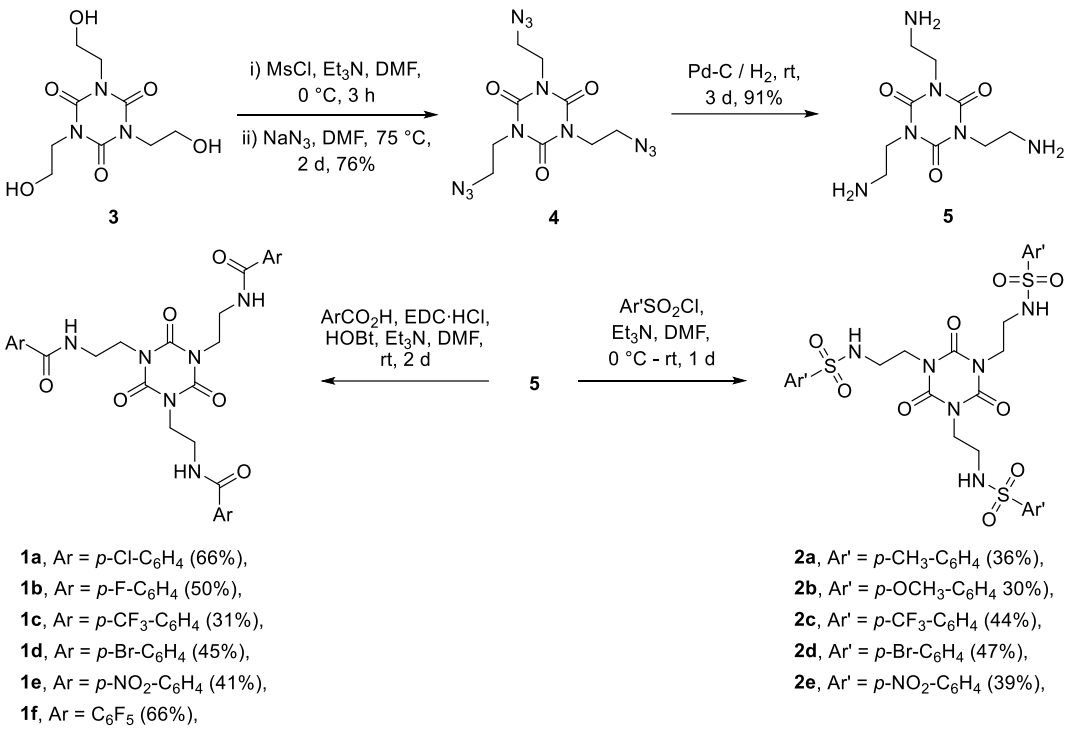
[a] The first p$K_a$ of N-H proton was considered. [b] The logP and p$K_{a1}$ values were calculated from calculator plugins of MarvinSketch program.

**Figure 2.1** Structures of tris-carboxyamides **1a**–**1f** (**A**) and tris-sulfonamides **2a**–**2f** (**B**). Representation of chloride binding with these receptors (**C**). Theoretical prediction of N–H proton acidity and logP values of the designed receptors (**D**).

## 2.2. Results and Discussions

### 2.2.1. Synthesis

The synthesis of the receptors was started form 1,3,5-tris(2-hydroxyethyl)-1,3,5-triazinane-2,4,6-trione **3**. At first, the hydroxyl cyanurate **3** was converted to corresponding trisamine **5** in two steps following the reported procedure.[16] The trisamine was then reacted with different aromatic carboxylic acids in the presence of EDC·HCl to get the carboxamide derivatives in 31-66% yield. On the other hand, the trisamine was then reacted with different aryl sulfonyl chlorides to furnish the sulfonamide derivatives in 30-47% yield.




**Scheme 2.1** The synthesis scheme of **1a**–**1f** and **2a**–**2e**.

### 2.2.2. The Comparison of p*K*a Values

The acidity (p$K_{a1}$) of the N–H proton (*i.e.*, first p$K_a$ value) and partition coefficient (logP) of these molecules were calculated theoretically using the calculator plugins of the MarvinSketch program (Figure 2.1D).[17] For carboxamides **1a**–**1f**, the p$K_{a1}$ values were 14.25, 14.27, 14.26, 14.30, 13.38, and 10.17, and corresponding logP values were 4.08, 2.69, 4.90, 4.57, 2.02, and 4.40. The p$K_{a1}$ = 9.92, 9.97, 9.64, 9.14, 9.11, and 4.95, and logP = 3.07, 1.06, 4.16, 3.84, 1.35, and 3.67 were calculated for **2a**–**2f**. These values suggested that for a particular aryl group, the acidity of N–H proton increases while the lipophilicity decreases if carboxamide moieties are replaced with sulfonamides. For **2f**, the p$K_{a1}$ = 4.95 indicated the deprotonation of the N–H proton at physiological pH, and therefore, this compound was excluded in the present study.

### 2.2.3. The Solution State $Cl^-$ Ion Binding

At first, the self-assembly of either **1c** or **2c** was studied by concentration-dependent $^1$H NMR spectroscopy. For each receptor, the NMR data showed a downfield shift and broadening of the N-H proton chemical shift upon diluting from 3.0 mM to 0.05 mM in acetonitrile-$d_3$ (Figure 2.7 and 2.8). As a result, the proper monomeric state could not be obtained due to the poor intensity of the N–H proton signal. Therefore, $Cl^-$ binding studies were done to determine the

apparent association constant values.[18-19] The addition of tetrabutylammonium chloride (TBACl) to each receptor (3.0 mM) resulted in the downfield shift of N–H as well as $C_{ortho}$–H protons, confirming the hydrogen bond mediated (N-H···$Cl^-$ and $C_{ortho}$–H···$Cl^-$ interactions) recognition of the anion (Figure 2.2A and 2.2C). Job's plot analysis confirmed 1:1 binding between a receptor and $Cl^-$ (Figure 2.2B and 2.2D). Based on this stoichiometry, the apparent association constant values 32876 (±23%) and 21678 (±19%) $M^{-1}$ were calculated for **1c** and **2c**, respectively (Figure 2.9A and 2.9B). Further, the competitive $^1$H NMR titrations were done for **1c**, **2c**, **1d**, **2d**, **1e** and **2e** (1 mM concentration of each receptor) with TBACl (0 – 4 mM). For a fixed *p*-substituent, the normalized chemical shift variation (i.e., $\Delta\delta/\Delta\delta_{max}$) was higher for the carboxamide derivative compared to its sulfonamide analog. This data also suggests that the tripodal carboxamides act as better receptors for $Cl^-$ ion.

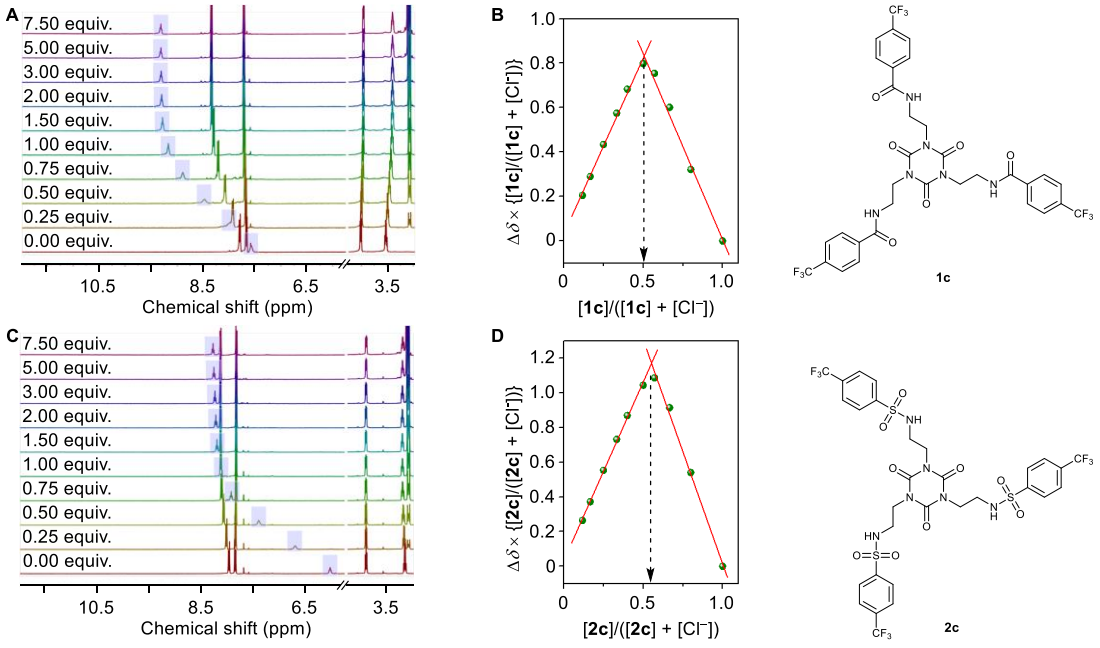



**Figure 2.2** The $^1$H NMR titration of **1c** with TBACl (**A**) and corresponding Job's plot analysis for N-H proton shift (**B**). The $^1$H NMR titration of **2c** with TBACl (**C**) and corresponding Job's plot analysis for N-H proton shift (**D**).

### 2.2.4. Geometry Optimization and Binding Energy Calculation

Due to the inaccessibility of accurate association constant values, the quantitative comparison of carboxamide and sulfonamide toward $Cl^-$ binding was not possible. This led us to investigate the theoretical estimation of binding energies of these receptors with $Cl^-$ ion, which were performed in the gas phase, i.e., without considering any solvents or other molecules in the

vicinity of the experimental object. At first, the most probable conformation of **1c**, [**1c**+$Cl^-$] complex, **2c**, and [**2c**+$Cl^-$] complexes were generated by using CONFLEX 8 program.[20-21] Subsequently, the generated conformations were optimized by Gaussian 09 program[22] using B3LYP functional and 6-31G basis set (Figure 2.3A, 2.3B, 2.3C, and 2.3D).[23] The geometry-optimized [**1c**+$Cl^-$] complex showed a $C_3$-symmetric conformation with $Cl^-$ ion bound within the cavity (Figure 2.3B). The anion was involved in N–H···$Cl^-$ and C–$H_{ortho}$···$Cl^-$ interactions with each carboxamide arm. Additionally, the ion was also involved in the $Cl^-$-π interaction with the central cyanurate ring. For [**2c**+$Cl^-$] complex, N–H···$Cl^-$ interaction with each sulfonamide arm and $Cl^-$-π interaction with the central cyanurate ring were observed (Figure 2.3D). In this complex, no C–$H_{ortho}$···$Cl^-$ interaction was observed. On the other hand, each C–$H_{meta}$ proton was involved in S=O···$H_{meta}$–C interaction with neighboring sulfonamide arm. For the complexes [**1c**+$Cl^-$] and [**2c**+$Cl^-$], the determination of binding energy provided *BE* = –51.83 and –47.58 kcal $mol^{-1}$, respectively. This data indicates that the binding of the tris-carboxamide **1c** with $Cl^-$ is more favorable (i.e., Δ*BE* = – 4.25 kcal $mol^{-1}$ compared to the tris-sulfonamide **2c** with the same anion. The above-mentioned calculations using the CONFLEX 8 and Gaussian program were performed in gas phase, i.e. without considering any solvents or other molecules in the vicinity of the experimental object.

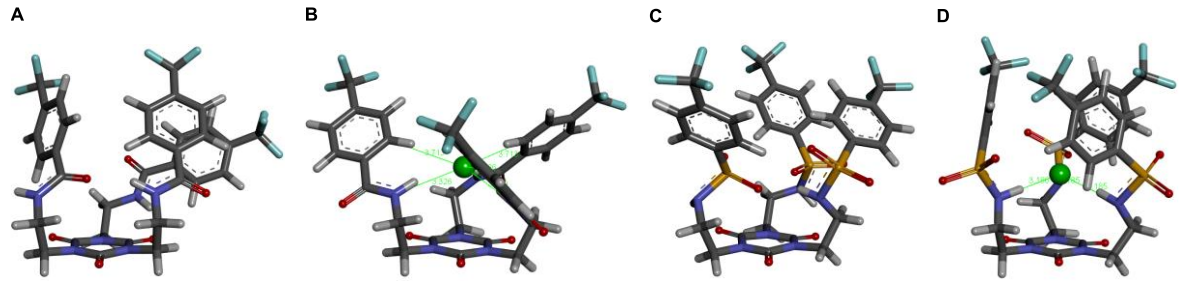



**Figure 2.3** The geometry optimized structures of **1c** (**A**), [**1c**+$Cl^-$] complex (**B**), **2c** (**C**), and [**2c**+$Cl^-$] complex (**D**).

### 2.2.5. Ion Transport Activity

In the next stage, ion transport activities of **1a**–**1f** and **2a**–**2e** across lipid bilayer membrane were determined. In these experiments, egg yolk phosphatidylcholine (EYPC) based large unilamellar vesicles (LUVs) were prepared by entrapping 8-hydroxypyrene-1,3,6-trisulfonate (HPTS, 1 mM) and applying a pH gradient prior to the addition of a transporter.[24-27] The destruction of the applied pH gradient, upon addition of a transporter, was monitored by fluorescence kinetics experiments. Ion transport data indicates that the tris-carboxamides **1a**–**1f**

displayed better activity compared to that of tris-sulfonamides **2a**–**2e** (Figure 2.4A and 2.4B), when studied at an identical concentration of 1 μM. For example, the activity of **1c** was 9.1–fold ($I_F$ values at 100 s after the compound addition were compared) higher than that of **2c** although, these compounds have identical aryl arms. Similarly, **1d** was 9.6-fold more active compared to **2d**, and **1e** was 11.4-fold more active compared to **2e**. Overall, such higher ion transport activity can be correlated to (a) better anion binding and (b) better permeability values of the carboxamide receptors compared to the sulfonamide receptors. The contribution of the permeability was also evident for **1a**–**1c**, which have similar p$K_{a1}$ values. For these compounds, the ion transport activity trend **1b** < **1a** < **1c** corresponds to their increasing trend of logP values. The highest activity of **1f** can be corroborated by its highest acidity as compared to the other tripodal receptors. Subsequently, concentration-dependent ion transport activities of compounds **1a**, **1c**–**1f** were measured and Hill analyses were done. For the most active compound **1f**, the study provided the effective concentration at 50% activity, $EC_{50}$ = 0.14 μM, and its Hill coefficient value $n$ ~ 1 indicated that one molecule is involved in the active transporter formation.

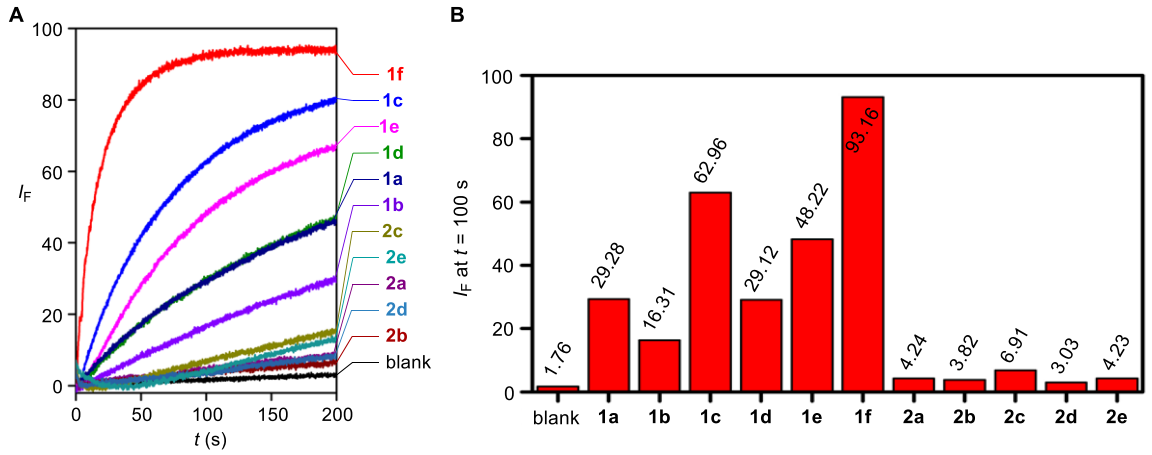



**Figure 2.4** Comparison of ion transport activities of **1a**–**1f** and **2a**–**2e** across EYPC vesicles with entrapped HPTS (A). Normalized fluorescence intensity value at 100 s after the addition of each transporter (1.0 μM) was used for the plot (B).

In the preceding ion transport experiments, the destruction of pH gradient is possible *via* either of four different mechanisms, such as (a) $OH^-/X^-$ antiport, (b) $H^+/X^-$ symport, (c) $H^+/M^+$ antiport, and (d) $OH^-/M^+$ symport. To identify the preferential ion transport mechanism, the ion transport activity of **1f** across EYPC-LUVs⊃HPTS was checked by varying either cations or anions in the extravesicular buffer. In this study, the ion transport activity was unaltered

when the assays were done by varying the extravesicular cations (Figure 2.5A) in the extravesicular salts MCl ($M^+$ = $Li^+$, $Na^+$, $K^+$, $Rb^+$, and $Cs^+$). Such unaltered ion transport activities imply that cations are not involved in ion transport process. But, variation of anions in the extravesicular salts, NaX ($X^-$ = $Cl^-$, $Br^-$, $I^-$, $NO_3^-$, $ClO_4^-$, $OAc^-$, and $SCN^-$) provided significantly different ion transport rates with the order $Cl^- > SCN^- > OAc^- > Br^- > NO_3^- > I^- > ClO_4^-$ (Figure 2.5B), which confirmed the participation of anions in the ion transport process. As there was no influence of alkali cations during the ion transport by **1f** (Figure 2.5A), so the $H^+/M^+$ antiport and $OH^-/M^+$ symport mechanisms are not operating in the ion transport process, and the transport mechanism is restricted to either $OH^-/X^-$ antiport or $H^+/X^-$ symport.

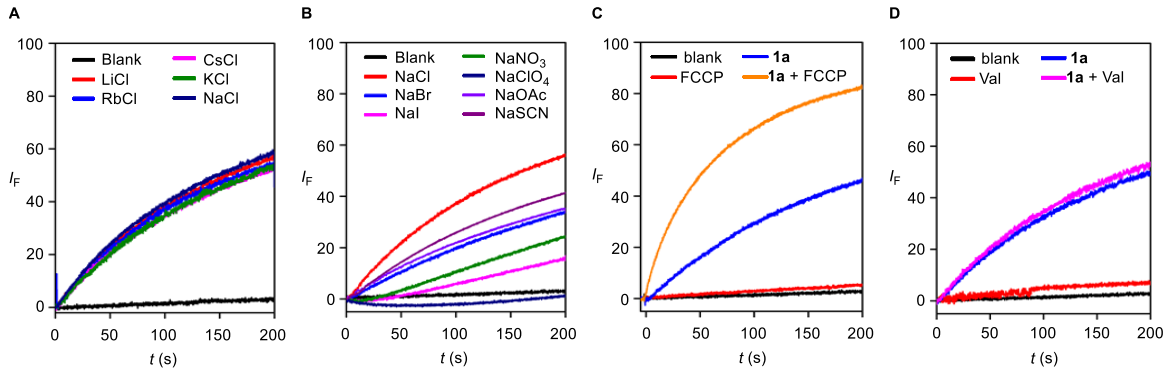



**Figure 2.5** Influence of extravesicular cations (**A**), and anions (**B**) in the ion transport by **1f** (0.16 μM) across EYPC vesicles with entrapped HPTS. Ion transport activity of **1f** (0.16 μM) determined in the absence and presence of FCCP (**C**). Ion transport activity of **1f** (0.16 μM) determined in the absence and presence of valinomycin (**D**).

Next, ion transport experiments were carried out in the presence of coupled ionophores. At first, carbonyl cyanide-4-(trifluoromethoxy)phenylhydrazone (FCCP), a selective $H^+$ carrier, was used.[28] Under the applied pH gradient conditions, FCCP is expected to facilitate the efflux of $H^+$ to the extravesicullar medium. When the ion transport activity of **1f** was measured in the presence of FCCP, an approximately 2.3-fold higher rate of pH gradient collapse was observed compared to the transport activity of **1f** alone (Figure 2.5C). The increased rate of pH gradient collapse by the transporter in the presence of FCCP indicates the co-operative effect of **1f** and FCCP during the ion transport process. The study suggested that the transport rate of $Cl^-$ by the **1f** is faster compared to that of $H^+$. Further, preferential ion selectivity between $OH^-$ and $Cl^-$ was determined by measuring the transport activity in the presence of valinomycin, a $K^+$ selective ionophore.[29] In a typical experiment, KCl was taken in the extravesicular buffer with iso-osmolar intravesicular NaCl and the collapse of applied

pH gradient by **1f** was monitored in the presence and absence of valinomycin. If compound **1f** allows better $OH^-$ transport over $Cl^-$ then, a positive cooperative effect in the pH gradient collapse rate is expected. On the other hand, if **1f** allows better $Cl^-$ transport, then no such cooperative effect would be observed. When the ion transport activity of **1f** was determined in the absence and presence of valinomycin comparable rates of pH gradient collapse were observed (Figure 2.5D). Therefore, the experiments indicated preferential selectivity of **1f** towards $Cl^-$ over the $OH^-$ , *i.e.*, $Cl^-$ >> $OH^-$.

The anion transport mechanism by **1f** was further evaluated by measuring the $Cl^-$ influx across EYPC liposomes with entrapped lucigenin dye in $NaNO_3$ and iso-osmolar extravesicular NaCl (Figure 2.20). The dye is known to show a quantitative fluorescence quenching in the presence of $Cl^-$.[30] The $Cl^-$ influx by different concentrations of **1f** was measured (Figure 2.6A) and the data provided an $EC_{50}$ = 1.58 μM and $n$ = 1.36 (Figure 2.21A and 2.21B). Variation of the cation in the extravesicular buffer ($M^+$ = $Li^+$, $K^+$, $Rb^+$, and $Cs^+$) did not provide any noticeable difference in the $Cl^-$ influx rate, which further excluded the possibility of $M^+/Cl^-$ symport during the transport process (Figure 2.6B). To get the direct evidence of anion antiport mechanism (*i.e.*, $Cl^-/X^-$) across the bilayer membranes, the lucigenin assay was done in the presence of valinomycin under external KCl and internal iso-osmolar $NaNO_3$ conditions. Significantly faster $Cl^-$ influx was observed after when **1f** and valinomycin were studied together compared to **1f** alone, suggesting a cooperative effect of two transporters (Figure 2.6C). This data established the $Cl^-/X^-$ antiport by the tris-carboxamide receptor.

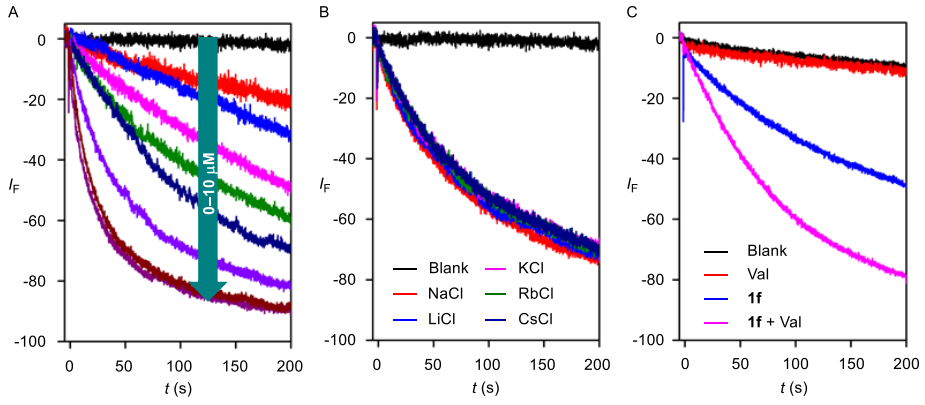



**Figure 2.6** Concentration dependent $Cl^-$ influx by **1f** (0 - 10 μM) into EYPC vesicles with entrapped lucigenin (**A**). Influence of extravesicular cations in the $Cl^-$ influx by **1f** (1.5 μM) (**B**). Influence of valinomycin (2.5 pM) in the $Cl^-$ influx by **1f** (0.7 μM) (**C**).

U-tube experiments were done to identify the ion transport machinery formed by **1f**. In this study, the lipid bilayer membrane was substituted by a chloroform layer, separating two aqueous layers. The compound **1f** (1 mM) and tetrabutylammonium hexafluorophosphate ($TBAPF_6$, 1 mM) were added to the chloroform layer. Then, two aqueous layers were added, one containing 500 mM NaCl (*i.e.*, $Cl^-$ source layer) while the other containing 500 mM $NaNO_3$ (*i.e.*, $Cl^-$ receiving layer), and $Cl^-$ concentration in the receiving aqueous layer was monitored using a chloride ion selective electrode (ISE) with time. The experiment was also carried out without adding **1f** in the chloroform layer to obtain the blank data. A significant increase in the $Cl^-$ concentration in the receiving layer was measured with time (Figure 2.22). As no ion channel that can span the chloroform layer is feasible, the observed $Cl^-$ transport to the receiving layer is corroborated to the mobile carrier as the active anion transporter.

## 2.3. Conclusion

In conclusion, we have synthesized a series of tris-carboxamide and tris-sulfonamide tripodal receptors consisting of the cyanuric acid core, and studied their $Cl^-$ binding and selective $Cl^-$ transport activity across lipid bilayer membranes. Both the tris-carboxamide and tris-sulfonamide remain in the self-aggregated state even in 0.05 mM concentration. However, the $^1H$ NMR-based apparent association constant calculation showed that the *p*-$CF_3$-phenyl-linked tris-carboxamide is a better receptor for $Cl^-$ compared to its tris-sulfonamide analog. The theoretical calculations confirmed that the binding of tris-carboxamide with $Cl^-$ is – 4.25 kcal $mol^{-1}$ more favorable compared to the corresponding tris-sulfonamide. The tris-carboxamide receptors exhibited significantly higher activity compared to their tris- sulfonamide analogs. Such results were corroborated by their better anion binding and membrane permeability. The most active receptor, consisting of pentafluoro carboxamide arms, was also established as a $Cl^-$/anion antiporter by fluorescence-based ion transport and U-tube experiments.

## 2.4. Experimental Section

### 2.4.1. General Methods

All reagents and compounds used for the synthesis were purchased either from Sigma-Aldrich, Avra chemicals, Spectrochem, Alfa Aesar and used without further purification. Dry solvents MeCN, $CH_2Cl_2$, and MeOH were purchased from commercially available source, Merck and used without further drying. All the reactions were performed under the nitrogen atmospheric environment using $N_2$ gas balloon and monitored by checking TLC, performed on pre-coated

aluminium plates of silica gel 60 $F_{254}$ (0.25 mm, E. Merck). Developed TLC plates were visualized either by ninhydrin staining followed by heating or under a short-wave UV lamp. Column chromatography for purifying the compound was performed using ethyl acetate in hexane or methanol in chloroform as solvents on silica gel (100–200 mesh). HEPES buffer, HPTS dye, Lucigenin dye, Triton X-100, NaOH, and all the inorganic salts (NaCl, $NaNO_3$, KCl, LiCl, CsCl, NaBr, NaI, etc.) were of molecular biology grade purchased from Sigma Aldrich. Egg yolk phosphatidylcholine (EYPC) lipid (25 mg/mL in chloroform), mini-extruder and polycarbonate membranes (100 and 200 nm) used for the preparation of large unilamellar vesicles (LUVs) were obtained from Avanti Polar Lipids.

### 2.4.2. Physical Measurements

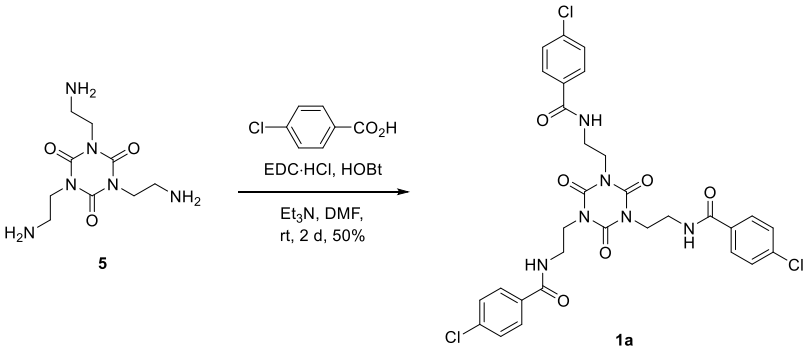
All $^1$H NMR (400 MHz) and $^{13}$C NMR (100 MHz) spectra were recorded on Bruker 400 MHz and Jeol 400 MHz spectrometers. The chemical shifts ($\delta$) in parts per million were referenced to the residual proton signal of deuterium solvents ($^1$H NMR $CDCl_3$: $\delta$ 7.26 ppm; $^{13}$C NMR $CDCl_3$: $\delta$ 77.2 ppm; $^1$H NMR $CD_3OD$: $\delta$ 3.31 ppm; $^{13}$C NMR $CD_3OD$: $\delta$ 49.2 ppm; $^1$H NMR DMSO-$d_6$: $\delta$ 2.5 ppm; $^{13}$C NMR DMSO-$d_6$: $\delta$ 39.5 ppm). The multiplicities of the peaks are s (singlet), d (doublet), t (triplet), q (quartet), dd (doublet of doublet), ddd (doublet of doublet of doublet), m (multiplet). Coupling constants are reported in Hertz. All the FT-IR spectra were taken and reported in wave numbers ($cm^{-1}$) using a solution of compound in MeOH/$CHCl_3$. High resolution mass spectra (HRMS) were acquired in the ESI (+ve) mode. Melting points for all the molecules were recorded in a Veego melting point apparatus and the values were uncorrected. The measurement of pH during the preparation of buffer solution was done by a Helmer pH meter. Fluorescence spectra were recorded on a Fluoromax-4 from JobinYvon Edison equipped with an injector port and a magnetic stirrer and data were processed in Origin 8.5 software. Chloride ion concentration in U-tube experiment was measured using chloride-selective electrode from Accumet.

### 2.4.3. Synthesis Procedures

**General procedure for carboxamides synthesis:** In a 25 mL round bottom flask, trisamine **5** (1.0 equiv.) was taken and dissolved the same in 5 mL of dry DMF. Then substituted benzoic acid (3.2 equiv.), HOBt (3.2 equiv.), EDC·HCl (3.2 equiv.) was added sequentially and the reaction mixture was stirred for 5 minutes. Then $Et_3N$ (3.2 equiv.) was added into this and then the whole mixture was allowed to stir under nitrogen atmosphere for 2 days at room temperature. The reaction was monitored in between by checking TLC. After completion of

reaction, the DMF was evaporated in high vacuum and the product was extracted into $CHCl_3$ by washing with saturated $NaHCO_3$ solution (10 mL) and water (3 × 10 mL), respectively and followed by brine solution (10 mL). The organic part was then separated from the aqueous layer, dried over $Na_2SO_4$ and the solvent was evaporated in a vacuum to get the crude product. The crude product was then purified using silica gel column chromatography (2–3% MeOH in $CHCl_3$) to obtain white solid compound **1a-f** in 31–66% yield.

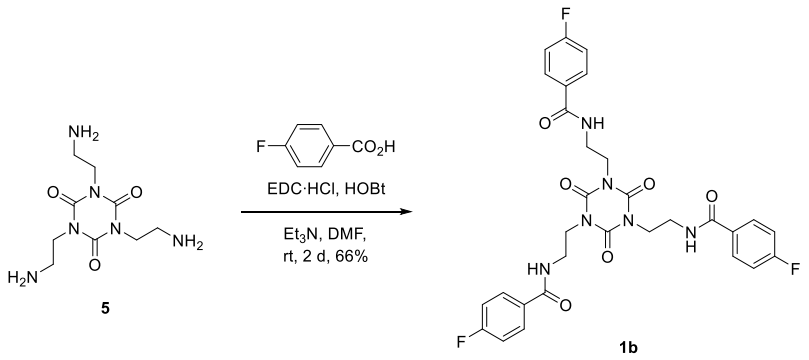
***N*,*N*',*N*''-((2,4,6-trioxo-1,3,5-triazinane-1,3,5-triyl)tris(ethane-2,1-diyl))tris(4-chloro-benzamide) ($C_{30}H_{27}Cl_3N_6O_6$) 1a:**




**Scheme 2.2** Synthesis of compound **1a**.

**Yield:** 50%. **M.p.:** 256 °C; **IR** (neat, ν/cm$^{-1}$)**:** 3856, 3752, 3305, 2103, 1687, 1639, 1546, 1460, 1311, 1181, 1094, 1015, 845, 758, 688; **$^1$H NMR (400 MHz, $CDCl_3$ : MeOH-*d*$_4$ = 4 : 1):** $\delta$ 7.64 (d, *J* = 16.9 Hz, 3H), 7.54 (d, *J* = 8.5 Hz, 6H), 7.25 (d, *J* = 8.5 Hz, 6H), 4.06 – 3.98 (m, 6H), 3.57 – 3.49 (m, 6H); **$^{13}$C NMR (101 MHz, $CDCl_3$ : MeOH-*d*$_4$ = 4 : 1):** $\delta$ 167.8, 149.6, 137.7, 132.3, 128.6, 128.3, 42.5, 37.9; **HRMS (ESI):** Calcd. $C_{30}H_{28}Cl_3N_6O_6$ $[M+H]^+$: 673.1135, Found: 673.1130, 675.1106.

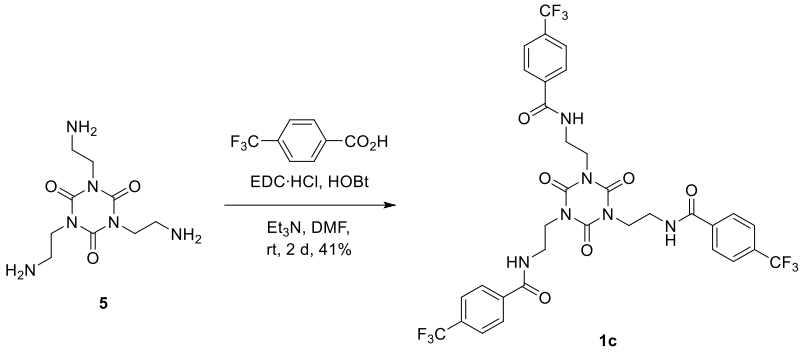
***N*,*N*',*N*''-((2,4,6-trioxo-1,3,5-triazinane-1,3,5-triyl)tris(ethane-2,1-diyl))tris(4-fluoro-benzamide) ($C_{30}H_{27}F_3N_6O_6$) 1b:**



**Scheme 2.3** Synthesis of compound **1b**.

**Yield:** 66 %. **M.p.:** > 260 °C; **IR** (neat, ν/cm$^{-1}$)**:** 3960, 3892, 3855, 3818, 3755, 3295, 2312, 2172, 1640, 1502, 1453, 1231, 1113, 1016, 759; **$^1$H NMR (400 MHz, DMSO-*d*$_6$):** $\delta$ 8.52 (t, *J* = 5.8 Hz, 3H), 7.81 (dd, *J* = 8.4, 5.7 Hz, 6H), 7.27 (t, *J* = 8.8 Hz, 6H), 3.92 (t, *J* = 5.8 Hz, 6H), 3.44 (dd, *J* = 11.5, 5.7 Hz, 6H).; **$^{13}$C NMR (101 MHz, DMSO-*d*$_6$):** $\delta$ 166.1, 165.5, 163.0, 149.6, 131.4, 131.3, 130.2, 130.1, 115.7, 115.5, 42.2, 37.25; **HRMS (ESI):** Calcd. $C_{30}H_{28}F_3N_6O_6$ $[M+H]^+$: 625.2022, Found: 625.2023.

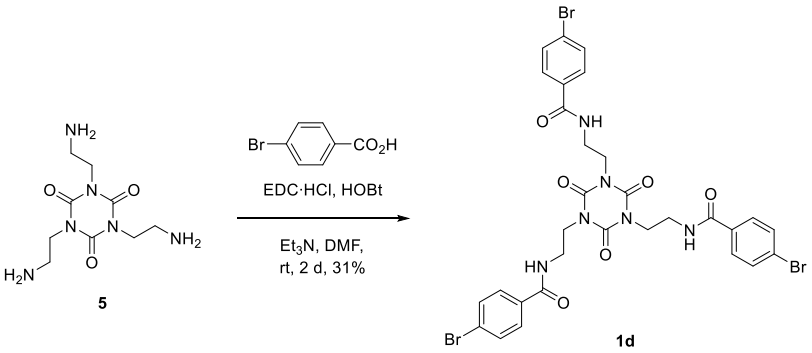
***N*,*N*',*N*''-((2,4,6-trioxo-1,3,5-triazinane-1,3,5-triyl)tris(ethane-2,1-diyl))tris(4-(trifluoro-methyl)benzamide) ($C_{33}H_{27}F_9N_6O_6$) 1c:**




**Scheme 2.4** Synthesis of compound **1c**.

**Yield:** 41%. **M.p.:** 183 °C; **IR** (neat, ν/cm$^{-1}$)**:** 3310, 2943, 2834, 1690, 1548, 1456, 1327, 1117, 1019, 754, 661; **$^1$H NMR (400 MHz, DMSO-*d*$_6$):** $\delta$ 8.71 (t, *J* = 5.8 Hz, 3H), 7.89 (d, *J* = 8.2 Hz, 6H), 7.79 (d, *J* = 8.3 Hz, 6H), 3.94 (t, *J* = 5.8 Hz, 6H), 3.46 (m, 6H); **$^{13}$C NMR (101 MHz, DMSO-*d*$_6$):** $\delta$ 165.9, 149.3, 138.3, 131.41, 131.0, 128.0, 125.6, 125.5, 125.3, 122.6; **HRMS (ESI):** Calcd. $C_{33}H_{28}F_9N_6O_6$ $[M+H]^+$: 775.1926, Found: 775.1929.

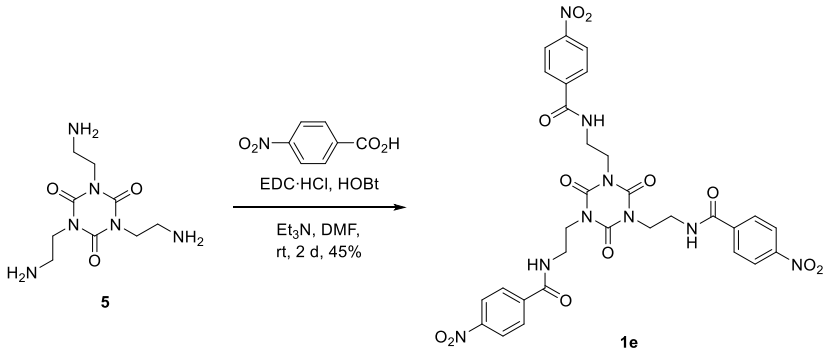
***N*,*N*',*N*''-((2,4,6-trioxo-1,3,5-triazinane-1,3,5-triyl)tris(ethane-2,1-diyl))tris(4-bromo-benzamide) ($C_{30}H_{27}Br_3N_6O_6$) 1d:**



**Scheme 2.5** Synthesis of compound **1d**.

**Yield:** 31 %. **M.p.:** 249 °C; **IR** (ν/cm$^{-1}$)**:** 3941, 3884, 3742, 3286, 2927, 2850, 2312, 1686, 1639, 1543, 1456, 1310, 1182, 1106, 1071, 1015, 910, 842, 754, 714, 661; **$^1$H NMR (400 MHz, DMSO-*d*$_6$):** δ 8.59 (t, *J* = 5.9 Hz, 3H), 7.70 – 7.62 (m, 12H), 3.92 (t, *J* = 5.9 Hz, 6H), 3.43 (dd, *J* = 11.8, 5.9 Hz, 6H); **$^{13}$C NMR (100 MHz, DMSO-*d*$_6$):** *δ* 165.9, 149.2, 133.5, 131.3, 129.2, 124.9, 41.7, 36.8; **HRMS (ESI):** Calcd. $C_{30}H_{28}Br_3N_6O_6$ [M+H]$^+$: 806.9599, Found: 806.9612.

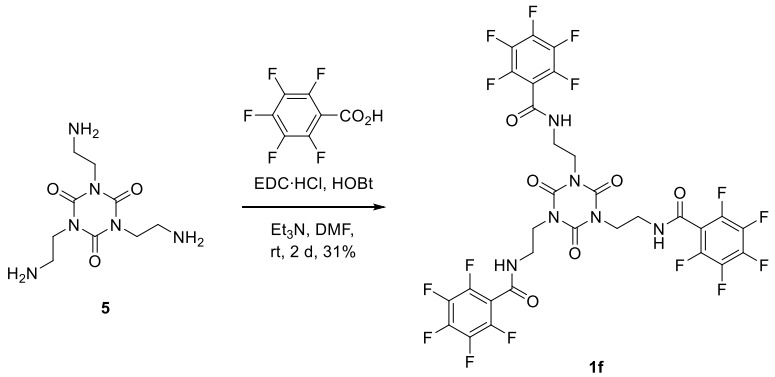
***N*,*N*',*N*''-((2,4,6-trioxo-1,3,5-triazinane-1,3,5-triyl)tris(ethane-2,1-diyl))tris(4-nitro-benzamide) ($C_{30}H_{27}N_9O_{12}$) 1e:**




**Scheme 2.6** Synthesis of compound **1e**.

**Yield:** 45%. **M.p.:** 239 °C; **IR** (neat, ν/cm$^{-1}$)**:** 3268, 2140, 1639, 1459, 1350, 1015, 697, 660; **$^1$H NMR (400 MHz, DMSO-*d*$_6$):** *δ* 8.82 (t, *J* = 5.9 Hz, 3H), 8.30 (d, *J* = 8.9 Hz, 6H), 7.96 (d, *J* = 8.9 Hz, 6H), 3.96 (t, *J* = 5.9 Hz, 6H), 3.46 (dd, *J* = 12.0, 6.1 Hz, 6H); **$^{13}$C NMR (101 MHz, DMSO-*d*6):** *δ* 165.2, 149.2, 149.0, 140.1, 128.6, 123.6, 41.6, 37.0; **HRMS (ESI):** Calcd. $C_{30}H_{28}N_9O_{12}$ [M+H]$^+$: 706.1857, Found: 706.1857.

***N*,*N*',*N*''-((2,4,6-trioxo-1,3,5-triazinane-1,3,5-triyl)tris(ethane-2,1-diyl))tris (2,3,4,5,6-pentafluorobenzamide) ($C_{30}H_{15}F_{15}N_6O_6$) 1f:[13]**

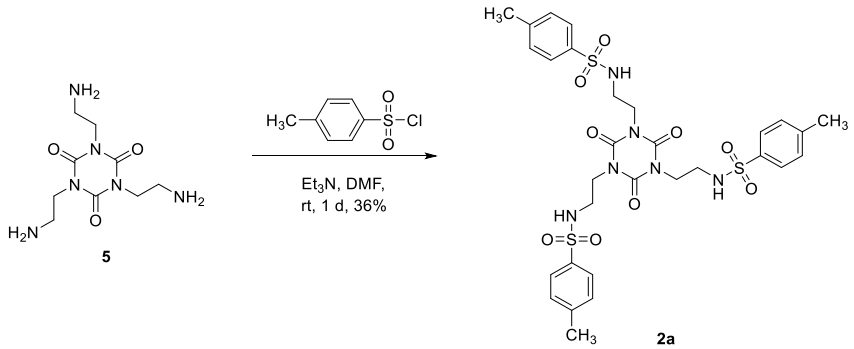


**Scheme 2.7** Synthesis of compound **1f**.

**Yield:** 31%. **M.p.:** 222 °C; **IR** (neat, ν/cm$^{-1}$)**:** 3303, 2945, 2833, 1657, 1456, 1114, 1018, 752, 522, 510, 474, 437; **$^1$H NMR (400 MHz, DMSO-*d*$_6$):** $\delta$ 9.01 (t, *J* = 6.0 Hz, 3H), 3.96 (t, *J* = 6.1 Hz, 6H), 3.51 (dd, *J* = 12.1, 6.0 Hz, 6H); **HRMS (ESI):** Calcd. $C_{30}H_{16}F_{15}N_6O_6$ $[M+H]^+$: 841.0892, Found: 841.0883.

**General procedure for sulfonamides synthesis:** In a 25 ml round bottom flask, trisamine **5** (1.0 equiv.) was taken and was dissolved in 2 mL of dry DMF. Triethylamine (3.2 equiv.) was added into it under nitrogen atmosphere. In another 10 mL round bottom flask benzenesulphonylchloride (3.2 equiv.) was taken and dissolved in dry DMF under nitrogen atmosphere. Later this solution was added to the previous solution drop wise at 0 °C for 10 minutes. Then the whole reaction mixture was allowed to stir under nitrogen atmosphere for 2 days at RT (reflux at 120 °C for nitro derivative). The reaction was monitored in between by checking TLC. After completion of the reaction, the reaction mixture was washed with water (3 × 10 mL) and then with a solution of brine (1 × 10 mL), after which it was extracted in $CHCl_3$ (50 mL). The solvent was then evaporated in a vacuum to get the crude product. The crude product was then purified using silica gel column chromatography (2–3% MeOH in $CHCl_3$) to obtain white solid compound **2a-e** in 30–47 % yield.

***N*,*N*',*N*''-((2,4,6-trioxo-1,3,5-triazinane-1,3,5-triyl)tris(ethane-2,1-diyl))tris(4-methyl-benzenesulfonamide) ($C_{30}H_{36}N_6O_9S_3$) 2a:**

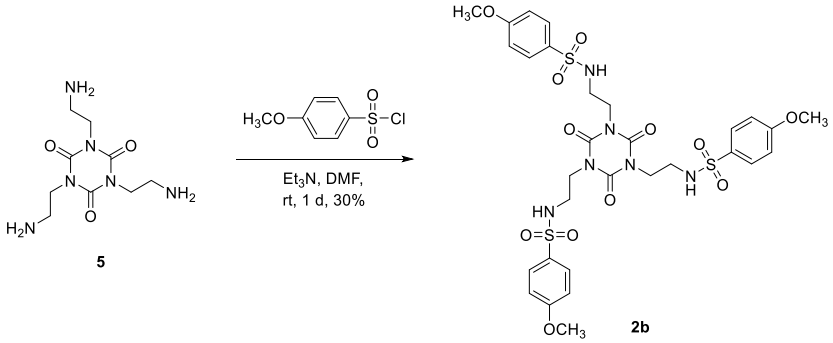



**Scheme 2.8** Synthesis of compound **2a**.

**Yield:** 36%. **M.p.:** 84 °C; **IR** (neat, ν/cm$^{-1}$)**:** 3304, 2944, 2834, 1687, 1461, 1324, 1219, 1155, 1097, 1020, 923, 815, 752, 662; **$^1$H NMR (400 MHz, $CDCl_3$):** $\delta$ 7.70 (d, *J* = 8.3 Hz, 6H), 7.25 (d, *J* = 8.1 Hz, 6H), 5.66 – 5.44 (m, 3H), 4.05 (t, *J* = 5.1 Hz, 6H), 3.29 (dd, *J* = 10.7, 6.0 Hz,

6H), 2.39 (s, 9H); **$^{13}$C NMR (101 MHz, $CDCl_3$):** $\delta$ 149.5, 143.6, 137.3, 129.8, 127.0, 42.8, 40.9, 21.6; **HRMS (ESI):** Calcd. $C_{30}H_{37}N_6O_9S_3$ $[M+H]^+$: 721.1783, Found: 721.1781.

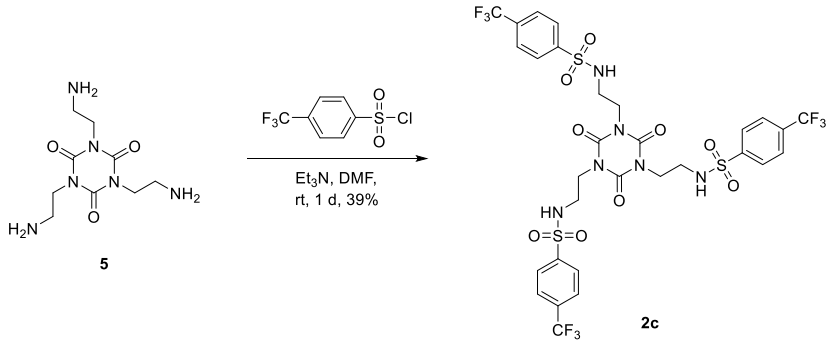
***N*,*N*',*N*''-((2,4,6-trioxo-1,3,5-triazinane-1,3,5-triyl)tris(ethane-2,1-diyl))tris(4-methoxy-benzenesulfonamide) ($C_{30}H_{36}N_6O_{12}S_3$) 2b:**




**Scheme 2.9** Synthesis of compound **2b**.

**Yield:** 30%. **M.p.: 97** $^o$C; **IR** (neat, $\nu$/cm$^{-1}$)**:** 3332, 2943, 2831, 1453, 1220, 1113, 1022, 750, 663; **$^1$H NMR (400 MHz, $CDCl_3$)**: $\delta$ 7.76 (d, $J$ = 8.9 Hz, 6H), 6.92 (d, $J$ = 8.9 Hz, 6H), 5.54 (t, $J$ = 6.4 Hz, 3H), 4.08 – 3.98 (m, 6H), 3.83 (s, 9H), 3.28 (dd, $J$ = 10.7, 6.1 Hz, 6H); **$^{13}$C NMR (101 MHz, $CDCl_3$):** $\delta$ 162.9, 149.5, 131.7, 129.1, 114.3, 55.7, 42.8, 40.8; **HRMS (ESI):** Calcd. $C_{30}H_{37}N_6O_{12}S_3$ $[M+H]^+$: 769.1631, Found: 769.1627.

***N*,*N*',*N*''-((2,4,6-trioxo-1,3,5-triazinane-1,3,5-triyl)tris(ethane-2,1-diyl))tris(4-(trifluoro-methyl)benzamide) ($C_{30}H_{27}F_9N_6O_9S_3$) 2c:**

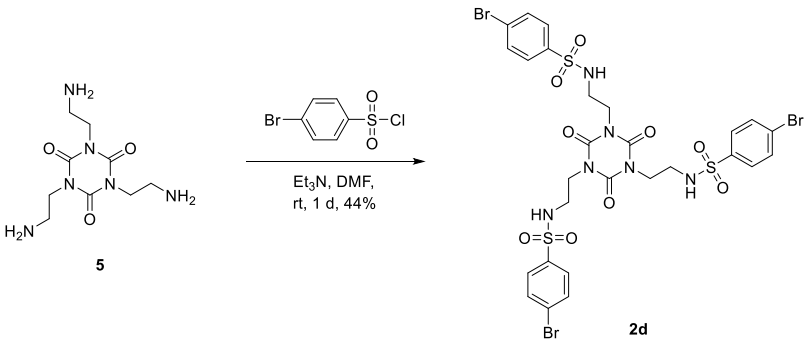



**Scheme 2.10** Synthesis of compound **2c**.

**Yield:** 39%. **M.p.:**125 °C; **IR** (neat, $\nu$/cm$^{-1}$)**:** 3313, 2943, 2832, 1689, 1455, 1326, 1221, 1166, 1111, 1020, 752, 663; **$^1$H NMR (400 MHz, $CDCl_3$):** $\delta$ 7.97 (d, $J$ = 8.2 Hz, 6H), 7.75 (d, $J$ = 8.3 Hz, 6H), 5.79 (t, $J$ = 6.0 Hz, 3H), 4.19 – 4.10 (m, 6H), 3.37 (dd, $J$ = 10.6, 6.3 Hz, 6H); **$^{13}$C**

**NMR (101 MHz, $CDCl_3$):** $\delta$ 149.6, 143.6, 134.7, 134.3, 127.4, 126.4, 124.5, 121.8, 42.8, 40.8; **HRMS (ESI):** Calcd. $C_{30}H_{28}F_9N_6O_9S_3$ $[M+H]^+$: 883.0935, Found: 883.0942.

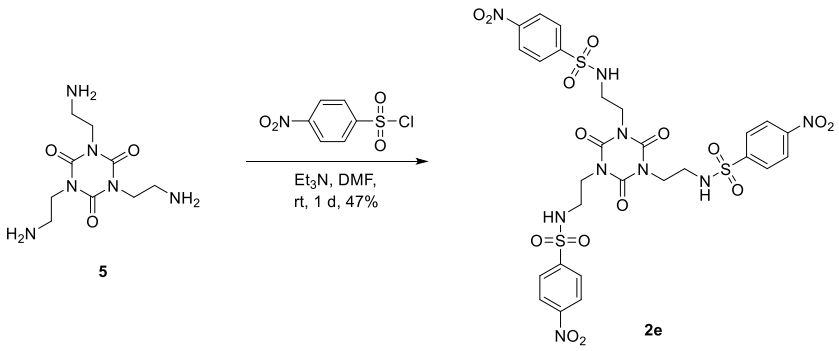
***N*,*N*',*N*''-((2,4,6-trioxo-1,3,5-triazinane-1,3,5-triyl)tris(ethane-2,1-diyl))tris(4-bromo-benzenesulfonamide) ($C_{27}H_{27}Br_3N_6O_9S_3$) 2d:**




**Scheme 2.11** Synthesis of compound **2d**.

**Yield:** 44%. **M.p.:** 197 °C; **IR** (neat, ν/$cm^{-1}$)**:** 3330, 2943, 2832, 1689, 1458, 1218, 1159, 1108, 1022, 749, 664; **$^1$H NMR (400 MHz, $CDCl_3$):** $\delta$ 7.69 (d, $J$ = 8.6 Hz, 6H), 7.62 (d, $J$ = 8.6 Hz, 6H), 5.56 (t, $J$ = 6.1 Hz, 3H), 4.15 – 4.07 (m, 6H), 3.33 (dd, $J$ = 10.5, 6.0 Hz, 6H); **$^{13}$C NMR (101 MHz, $CDCl_3$):** $\delta$ 149.5, 139.2, 132.6, 128.5, 127.9, 42.8, 40.9; **HRMS (ESI):** Calcd. $C_{27}H_{28}Br_3N_6O_9S_3$ $[M+H]^+$: 914.8609, Found: 914.8615, 916.8593.

***N*,*N*',*N*''-((2,4,6-trioxo-1,3,5-triazinane-1,3,5-triyl)tris(ethane-2,1-diyl))tris(4-nitro-benzenesulfonamide) ($C_{27}H_{27}N_9O_{15}S_3$) 2e:[14]**




**Scheme 2.12** Synthesis of compound **2e**.

**Yield:** 47% yield. **M.p.:** 125 °C; **IR** (neat, ν/$cm^{-1}$)**:** 3337, 2943, 2831, 1454, 1219, 1112, 1022, 749, 664; **HRMS (ESI):** Calcd. $C_{27}H_{28}N_9O_{15}S_3$ $[M+H]^+$: 814.0867, Found: 814.0887.

### 2.4.4. $^1$H NMR Dilution Studies

To check whether any self-association is present in **1c** and in **2c**, we have recorded a series of $^1$H NMR spectra by diluting the sample from 3.0 mM to 0.05 mM. In the dilution experiment, we have observed that the N–H proton chemical shift has gradually shifted to downfield region with the broadening of the peaks (Figure 2.7 and 2.8). These results suggested that self-association is present in both the compounds. These results also suggest that carboxyamide **1c** and sulfonamide **2c** are aggregating in different exchange rates, and we cannot predict at what concentration self-association will be stopped.

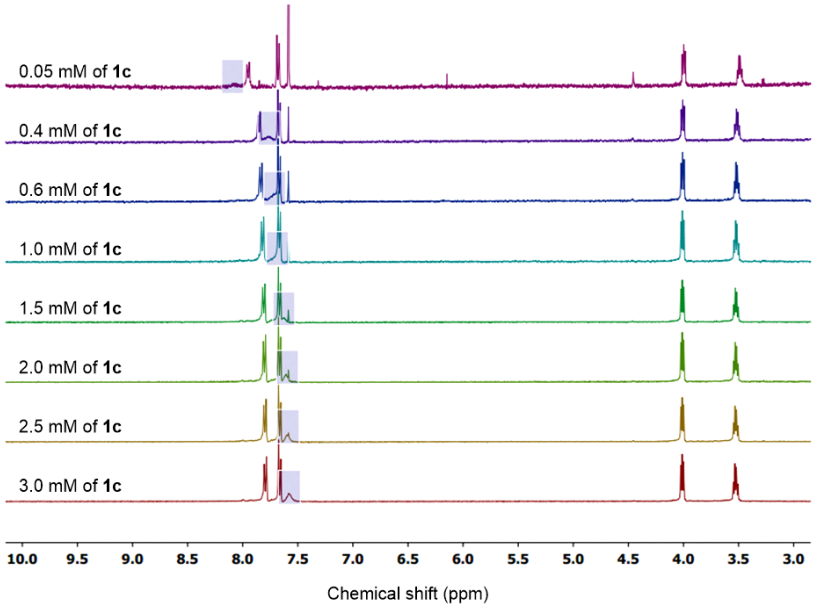



**Figure 2.7** Stacked plot for $^1$H-NMR experiment in acetonitrile-$d_3$ for compound **1c** with the successive dilution from 3.0 mM to 0.05 mM. The N-H proton chemical shifts are highlighted in blue colour.

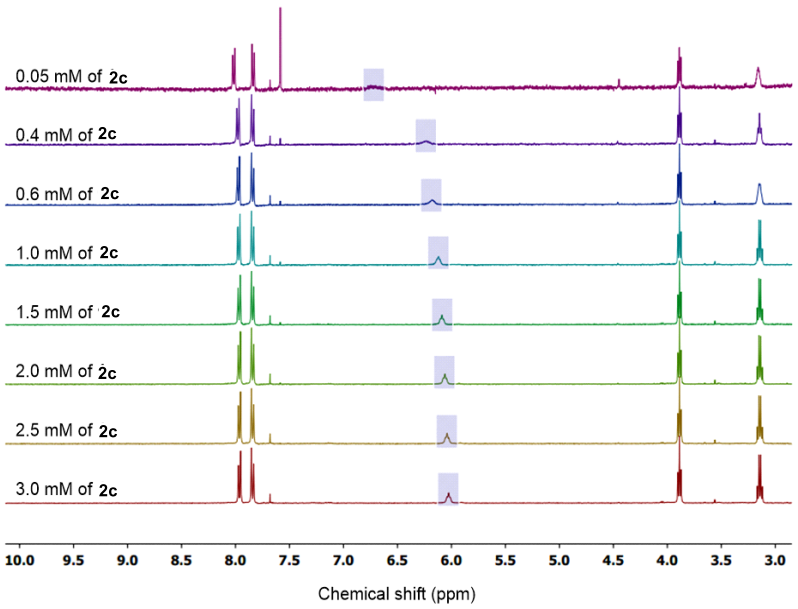


**Figure 2.8** Stacked plot for $^1$H-NMR experiment in acetonitrile-$d_3$ for compound **2c** with the successive dilution from 3.0 mM to 0.05 mM. The N-H proton chemical shifts are highlighted in blue colour.

### 2.4.5. $^1$H NMR Titration with TBACl

The proton NMR titration was done in acetonitrile-$d_3$ by successive addition of TBACl. For that, a 300 mM solution of TBACl solution in acetonitrile-$d_3$ was added in a stepwise manner to the stock solution of receptor (3 mM) in acetonitrile-$d_3$. The N–H proton chemical shift of receptor was monitored and was found to be downfield shifted with the increasing amount of TBACl up to certain limit

As self-association is there even in the much diluted solution, we have calculated the apparent association constant and the values are 32876 (± 23%) $M^{-1}$ for carboxyamide **1c** (Figure 2.9A) and 21678 (± 19%) $M^{-1}$ for sulfonamide **2c** (Figure 2.9B). The apparent dissociation constant values were calculated by fitting the $^1$H NMR titration data in the following equation.[31] The high value of error in binding constant calculation is probably due to the inaccurate TBACl stock solution concentration caused by the hygroscopic nature of the tetrabutylammonium sulfate salt.

$$y = P_3 - ((P_3 - P_1) \times (((x + P_4 + P_2) - \sqrt{(((x + P_4 + P_2)\text{^}2) - (4P_4x)))/(2P_4)))} \qquad \text{Equation 1}$$

where, x is the concentration of TBACl, y is the chemical shift upon addition of TBACl, $P_2$ is the apparent dissociation constant, $P_4$ is the concentration of receptor; $P_3$ and $P_1$ are the initial and final N-H proton chemical shift, respectively.

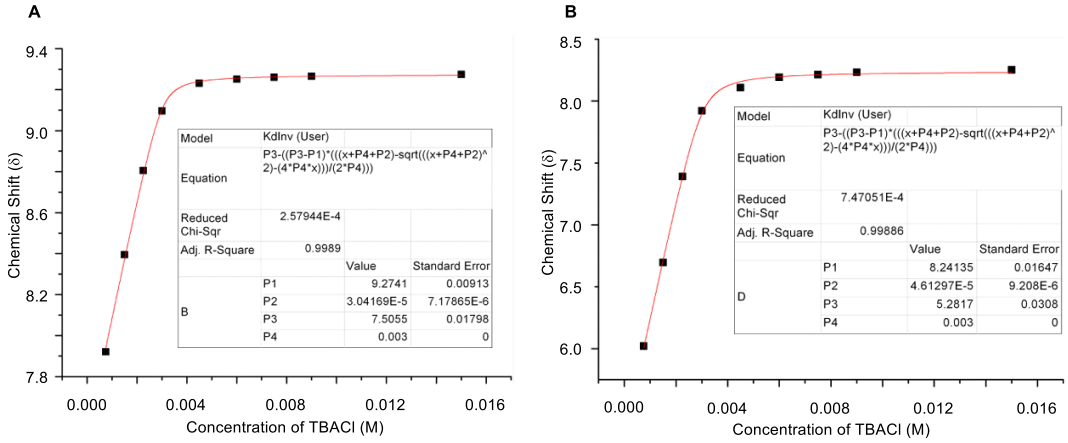



**Figure 2.9** Fit plot for apparent dissociation constant calculation from $^1$H-NMR titration data at 3.0 mM concentration for carboxyamide **1a** (**A**), and sulfonamide **2c** (**B**).

### 2.4.6. Theoretical Calculations

**Prediction of conformations:** To get an idea about the conformations of **1c**, [**1c**+$Cl^-$] complex, **2c**, and [**2c**+$Cl^-$] complex, several initial geometries of each systems were generated using the CONFLEX 8 software package[20-21] using MMFF94s force field.

For **1c**, the program generated 118 possible conformations. Among these, the top 5 conformations were very similar with Boltzmann populations 45.6886, 15.1626, 13.2945, 6.08141 and 4.79931% (i.e. 85.02642% in total) (Figure 2.10B). Therefore, the conformation with the highest Boltzmann population was taken for further geometry optimization.

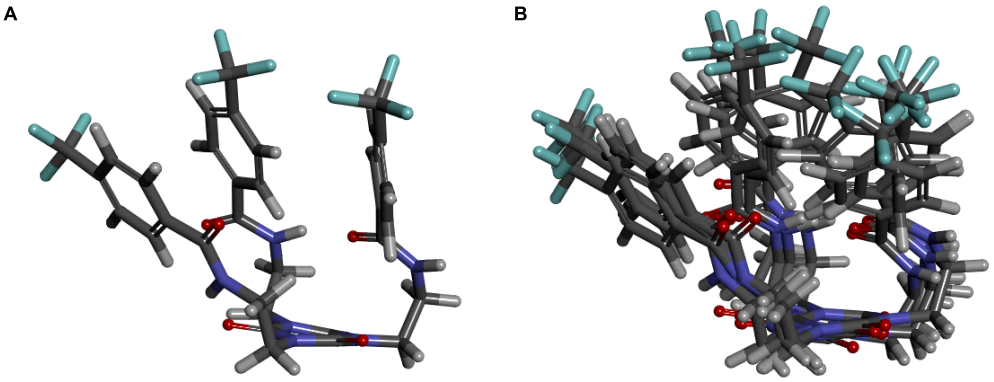



**Figure 2.10** The conformation of the highest Boltzmann populated geometry of **1c** (**A**) the overlay image of top 5 Boltzmann populated geometries of **1c** (**B**).

For [**1c**+$Cl^-$] complex, the program generated 135 possible conformations. Among these, the top 23 conformations were very similar with Boltzmann populations 8.90409, 8.77205, 8.64056, 8.50925, 5.30589, 5.27565, 5.23927, 5.20792, 5.17597, 5.14329, 5.10481, 5.07127, 2.57018, 2.55808, 2.54014, 2.52966, 2.48242, 2.47076, 2.45291, 2.44282, 0.910333, 0.903437 and 0.897125% (i.e. 99.10799% in total). (Figure 2.11B). Therefore, the conformation with the highest Boltzmann population was taken for further geometry optimization.

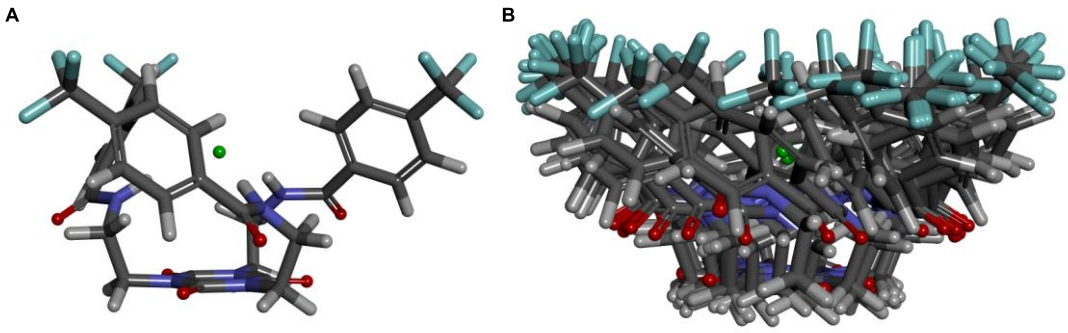


**Figure 2.11** The conformation of the highest Boltzmann populated geometry of [**1c**+$Cl^-$] (**A**) the overlay image of top 23 Boltzmann populated geometries of [**1c**+$Cl^-$] (**B**).

For **2c**, the program generated 326 possible conformations. Among these, the top 2 conformations were very similar with Boltzmann populations 20.8638 and 19.9479% (i.e. 40.8117% in total) (Figure 2.12B). The populations of other conformations were less than 5%. Therefore, the conformation with the highest Boltzmann population was taken for further geometry optimization.

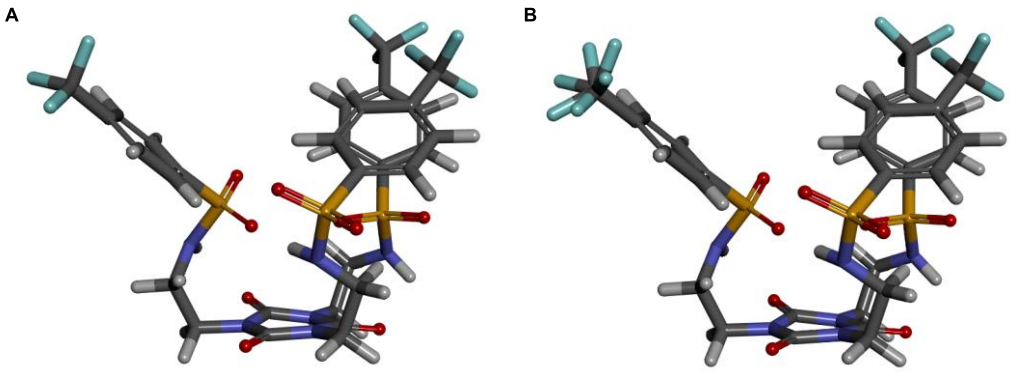



**Figure 2.12** The conformation of the highest Boltzmann populated geometry of **2c** (**A**) the overlay image of top 2 Boltzmann populated geometries of **2c** (**B**).

For [**2c**+$Cl^-$] complex, the program generated 43 possible conformations. Among these, the Boltzmann population of the most favourable conformation was 88.8617% (Figure 2.13). Therefore, this conformation was taken for further geometry optimization.

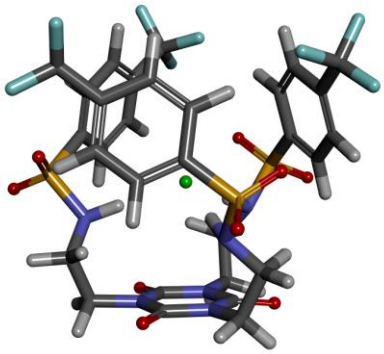


**Figure 2.13** The conformation of the highest Boltzmann populated geometry of [**2c**+$Cl^-$].

**Binding Energy Calculation:** The zero-point energy (ZPE) and basis set superposition error (BSSE)[32-33] corrected binding energy (BE) calculation for [**1c**+$Cl^-$] and [**2c**+$Cl^-$] was performed by Gaussian 09 program package at the same level. The binding energy (*BE*) was calculated using the following relation:

$BE = [HF_{[\mathbf{L}+Cl^-]} + ZPE_{[\mathbf{L}+Cl^-]} + BSSE_{[\mathbf{L}+Cl^-]}] - [HF_{\mathbf{L}} + ZPE_{\mathbf{L}}] - [HF_{Cl^-}]$ Equation 2

where, $HF_{[\mathbf{L}+Cl^-]}$ = electronic energy of [**L**+$Cl^-$] complex, $ZPE_{[\mathbf{L}+Cl^-]}$ = ZPE of [**L**+$Cl^-$] complex, $BSSE_{[\mathbf{L}+Cl^-]}$ = BSSE of [**L**+$Cl^-$] complex, $HF_{\mathbf{L}}$ = electronic energy of **L**, $ZPE_{\mathbf{L}}$ = ZPE of **L**, $HF_{Cl^-}$ = electronic energy of $Cl^-$, and **L** = receptor (i.e. either **1c** or **2c**).

**Table 1** Atomic coordinates of the optimized structure of lowest energy conformation obtained for **1c** from DFT B3LYP/6-31G geometry optimization.

| Charge = 0 | Multiplicity = 1 | | | |
|---|---|---|---|---|
| Atom # | Atom Type | x | y | z |
| 1 | C | 3.956283 | -3.192636 | -0.465851 |
| 2 | C | 4.060813 | -1.634097 | 1.447556 |
| 3 | N | 4.607031 | -2.224772 | 0.308662 |
| 4 | N | 2.812928 | -2.130361 | 1.837923 |
| 5 | N | 2.654586 | -3.509353 | -0.082149 |
| 6 | O | 4.505291 | -3.710946 | -1.452625 |
| 7 | O | 4.650146 | -0.740813 | 2.085904 |
| 8 | C | 1.292373 | -0.485538 | 3.04867 |
| 9 | H | 1.17768 | -0.038671 | 4.043269 |
| 10 | H | 1.714238 | 0.300087 | 2.407471 |
| 11 | C | 5.721641 | -0.777193 | -1.378106 |
| 12 | H | 6.704728 | -0.489187 | -1.765796 |
| 13 | H | 5.17223 | -1.276152 | -2.178472 |
| 14 | C | 1.856743 | -4.353899 | -1.014155 |
| 15 | H | 0.924502 | -4.588367 | -0.503701 |
| 16 | H | 2.418352 | -5.271623 | -1.20439 |
| 17 | C | 5.911044 | -1.741224 | -0.193877 |
| 18 | H | 6.488449 | -2.608865 | -0.518006 |
| 19 | H | 6.411555 | -1.253804 | 0.642669 |
| 20 | C | 2.263689 | -1.664927 | 3.145062 |
| 21 | H | 3.128451 | -1.366992 | 3.737252 |
| 22 | H | 1.780884 | -2.525028 | 3.614095 |
| 23 | C | 1.572041 | -3.627023 | -2.340876 |
| 24 | H | 2.506798 | -3.405156 | -2.857406 |
| 25 | H | 0.976974 | -4.306092 | -2.959512 |
| 26 | C | 2.883326 | 3.633088 | 0.934414 |
| 27 | C | 3.094179 | 1.917636 | -0.770746 |
| 28 | C | 2.222764 | 2.639839 | -1.602315 |
| 29 | C | 1.704797 | 3.864057 | -1.179587 |
| 30 | H | -4.516453 | -0.058956 | -2.069612 |

| | | | | |
|---|---|---|---|---|
| 31 | C | -3.619547 | 2.4651 | -1.627606 |
| 32 | C | -2.802559 | 1.228989 | -1.789336 |
| 33 | C | -3.437932 | -0.003917 | -1.989998 |
| 34 | C | 1.444769 | 5.650342 | 0.555902 |
| 35 | H | 1.056547 | 4.438098 | -1.831398 |
| 36 | H | 1.970505 | 2.244694 | -2.579723 |
| 37 | H | -1.941038 | -2.674323 | 2.092844 |
| 38 | H | -4.138752 | -3.338115 | 1.216197 |
| 39 | O | 2.952506 | -0.22922 | -1.874175 |
| 40 | H | -3.142314 | -2.131532 | -2.213484 |
| 41 | H | -5.428445 | 0.770957 | 1.280605 |
| 42 | C | -2.686726 | -1.907759 | 1.912903 |
| 43 | C | -2.416124 | -0.553154 | 2.173779 |
| 44 | C | -3.93362 | -2.294147 | 1.420532 |
| 45 | C | -3.420807 | 0.403861 | 1.960454 |
| 46 | C | -4.920854 | -1.327024 | 1.191806 |
| 47 | C | -4.666358 | 0.023787 | 1.464708 |
| 48 | N | 0.829553 | -2.380601 | -2.169433 |
| 49 | H | 1.355209 | -1.514072 | -2.200304 |
| 50 | C | -1.273918 | -1.112192 | -1.959442 |
| 51 | O | -1.155689 | -3.507742 | -2.054446 |
| 52 | C | -0.533964 | -2.41287 | -2.058083 |
| 53 | C | -6.205976 | -1.720948 | 0.551042 |
| 54 | H | -3.198863 | 1.44236 | 2.171718 |
| 55 | N | -0.025632 | -0.89969 | 2.570435 |
| 56 | H | -0.092759 | -1.804475 | 2.119446 |
| 57 | C | 2.0417 | 4.362367 | 0.08688 |
| 58 | H | 3.122747 | 4.01618 | 1.91885 |
| 59 | C | 3.416832 | 2.416152 | 0.503661 |
| 60 | C | -1.409906 | 1.292764 | -1.658747 |
| 61 | H | -0.927091 | 2.246849 | -1.486227 |
| 62 | O | 0.903399 | -3.359848 | 1.423433 |
| 63 | H | 4.046638 | 1.837782 | 1.173373 |
| 64 | C | 2.052556 | -3.022532 | 1.073372 |
| 65 | O | -0.964222 | 1.102586 | 3.149005 |
| 66 | C | -1.092191 | -0.054258 | 2.671802 |
| 67 | H | 0.428844 | 0.198716 | -1.638685 |
| 68 | C | -0.647435 | 0.127323 | -1.748313 |
| 69 | C | -2.67334 | -1.165902 | -2.070831 |
| 70 | N | 4.983588 | 0.431098 | -1.008926 |

| | | | | |
|---|---|---|---|---|
| 71 | H | 5.48601 | 1.166986 | -0.533157 |
| 72 | C | 3.656703 | 0.620064 | -1.259266 |
| 73 | F | 0.193429 | 5.474411 | 1.139678 |
| 74 | F | 1.267143 | 6.550179 | -0.492546 |
| 75 | F | 2.242855 | 6.277914 | 1.508362 |
| 76 | F | -6.139977 | -1.639836 | -0.852278 |
| 77 | F | -7.267173 | -0.904467 | 0.927575 |
| 78 | F | -6.570706 | -3.033071 | 0.83642 |
| 79 | F | -4.056931 | 2.652529 | -0.307656 |
| 80 | F | -4.770729 | 2.448049 | -2.409313 |
| 81 | F | -2.91096 | 3.61735 | -1.961657 |

**Table 2** Atomic coordinates of the optimized structure of lowest energy conformation obtained for [**1c**+$Cl^-$] from DFT B3LYP/6-31G geometry optimization.

Charge = -1 Multiplicity = 1

| Atom # | Atom Type | x | y | z |
|---|---|---|---|---|
| 1 | Cl | 0.012437 | -0.007344 | -0.059662 |
| 2 | C | -0.992911 | 1.026782 | 3.54255 |
| 3 | C | -0.338296 | -1.353905 | 3.558077 |
| 4 | N | -1.295979 | -0.337288 | 3.555575 |
| 5 | N | 0.994518 | -0.933878 | 3.551968 |
| 6 | N | 0.366179 | 1.348146 | 3.537867 |
| 7 | O | -1.887351 | 1.892405 | 3.555918 |
| 8 | O | -0.640509 | -2.561054 | 3.586295 |
| 9 | C | 2.171751 | -2.596145 | 2.084583 |
| 10 | H | 2.878931 | -3.428568 | 2.145173 |
| 11 | H | 1.204542 | -2.975829 | 1.748449 |
| 12 | C | -3.315534 | -0.543375 | 2.079208 |
| 13 | H | -4.391612 | -0.7317 | 2.136252 |
| 14 | H | -3.151576 | 0.478478 | 1.730202 |
| 15 | C | 0.758976 | 2.776473 | 3.45283 |
| 16 | H | 1.588217 | 2.930594 | 4.146454 |
| 17 | H | -0.104328 | 3.363758 | 3.762195 |
| 18 | C | -2.730383 | -0.711974 | 3.492707 |
| 19 | H | -3.268665 | -0.067948 | 4.191365 |
| 20 | H | -2.802844 | -1.751874 | 3.807772 |
| 21 | C | 2.03632 | -1.988502 | 3.491988 |
| 22 | H | 1.755397 | -2.768742 | 4.202595 |
| 23 | H | 2.975592 | -1.526353 | 3.792176 |

| | | | | |
|---|---|---|---|---|
| 24 | C | 1.191931 | 3.179029 | 2.031851 |
| 25 | H | 1.563155 | 4.207255 | 2.073057 |
| 26 | H | 1.995802 | 2.524713 | 1.687531 |
| 27 | C | -1.018954 | -4.206468 | -1.787827 |
| 28 | C | -2.609154 | -3.642007 | -0.041969 |
| 29 | C | -3.160593 | -4.930199 | -0.147335 |
| 30 | C | -2.65474 | -5.848966 | -1.062993 |
| 31 | H | -4.40051 | 6.071181 | -1.195203 |
| 32 | C | -5.08395 | 4.097381 | -2.914257 |
| 33 | C | -3.995921 | 4.070932 | -1.899834 |
| 34 | C | -3.755593 | 5.204192 | -1.109144 |
| 35 | C | -1.079378 | -6.439207 | -2.913946 |
| 36 | H | -3.080061 | -6.84333 | -1.134493 |
| 37 | H | -3.987403 | -5.18055 | 0.50624 |
| 38 | H | 6.499875 | -0.833986 | 0.47877 |
| 39 | H | 7.464622 | 0.782228 | -1.175106 |
| 40 | O | -4.216009 | -3.12544 | 1.664009 |
| 41 | H | -2.489175 | 6.057503 | 0.424386 |
| 42 | H | 3.478896 | 1.774747 | -2.4655 |
| 43 | C | 5.861881 | -0.256771 | -0.179367 |
| 44 | C | 4.472708 | -0.43932 | -0.071281 |
| 45 | C | 6.392535 | 0.639846 | -1.102573 |
| 46 | C | 3.615292 | 0.299419 | -0.904481 |
| 47 | C | 5.530894 | 1.374518 | -1.930322 |
| 48 | C | 4.144701 | 1.20095 | -1.831561 |
| 49 | N | 0.100133 | 3.124947 | 1.063244 |
| 50 | H | -0.029157 | 2.243811 | 0.567286 |
| 51 | C | -1.861799 | 4.077512 | -0.080295 |
| 52 | O | -0.59888 | 5.239125 | 1.597218 |
| 53 | C | -0.744547 | 4.181915 | 0.922142 |
| 54 | C | 6.098085 | 2.282749 | -2.963257 |
| 55 | H | 2.536412 | 0.194582 | -0.845361 |
| 56 | N | 2.669648 | -1.643999 | 1.095089 |
| 57 | H | 1.970862 | -1.099393 | 0.590708 |
| 58 | C | -1.577641 | -5.487149 | -1.884946 |
| 59 | H | -0.181349 | -3.930733 | -2.417806 |
| 60 | C | -1.529834 | -3.28631 | -0.868979 |
| 61 | C | -3.170396 | 2.945616 | -1.783954 |
| 62 | H | -3.361871 | 2.06779 | -2.389764 |
| 63 | O | 2.592834 | 0.745711 | 3.551039 |

| | | | | |
|---|---|---|---|---|
| 64 | H | -1.068893 | -2.305275 | -0.811545 |
| 65 | C | 1.396045 | 0.403685 | 3.539676 |
| 66 | O | 4.850821 | -2.071225 | 1.64715 |
| 67 | C | 4.006792 | -1.437516 | 0.953728 |
| 68 | H | -1.491567 | 2.055281 | -0.803862 |
| 69 | C | -2.107937 | 2.945881 | -0.876314 |
| 70 | C | -2.696873 | 5.20088 | -0.205292 |
| 71 | N | -2.739786 | -1.466523 | 1.104707 |
| 72 | H | -1.915444 | -1.143049 | 0.599751 |
| 73 | C | -3.238489 | -2.72527 | 0.97204 |
| 74 | F | 0.272234 | -6.261249 | -3.204899 |
| 75 | F | -1.750656 | -6.314719 | -4.138396 |
| 76 | F | -1.239697 | -7.773236 | -2.533585 |
| 77 | F | 5.241398 | 3.332158 | -3.290279 |
| 78 | F | 6.373883 | 1.626556 | -4.171192 |
| 79 | F | 7.30801 | 2.856363 | -2.565627 |
| 80 | F | -4.671244 | 4.640964 | -4.138879 |
| 81 | F | -6.173233 | 4.873086 | -2.510852 |
| 82 | F | -5.578412 | 2.828545 | -3.210553 |

**Table 3** Atomic coordinates of the optimized structure of lowest energy conformation obtained for **2c** from DFT B3LYP/6-31G geometry optimization.

| Charge = 0 | Multiplicity = 1 | | | |
|---|---|---|---|---|
| Atom # | Atom Type | x | y | z |
| 1 | C | -0.635294 | -4.247506 | -0.515321 |
| 2 | C | -2.9787 | -3.684561 | -0.011762 |
| 3 | N | -1.684555 | -4.060838 | 0.374893 |
| 4 | N | -3.131701 | -3.375201 | -1.372952 |
| 5 | N | -0.883546 | -3.896996 | -1.847287 |
| 6 | O | 0.467202 | -4.710445 | -0.160572 |
| 7 | O | -3.93868 | -3.653338 | 0.768957 |
| 8 | C | -4.7668 | -1.46175 | -1.648014 |
| 9 | H | -5.776314 | -1.257532 | -2.023828 |
| 10 | H | -4.759037 | -1.221493 | -0.580865 |
| 11 | C | -0.486556 | -3.220552 | 2.431294 |
| 12 | H | -0.408014 | -3.439029 | 3.501725 |
| 13 | H | 0.510935 | -3.277724 | 1.980687 |
| 14 | C | 0.208814 | -4.058534 | -2.833504 |
| 15 | H | -0.271311 | -4.124487 | -3.810666 |

| | | | | |
|---|---|---|---|---|
| 16 | H | 0.706635 | -5.006632 | -2.616373 |
| 17 | C | -1.416919 | -4.281691 | 1.823015 |
| 18 | H | -0.959501 | -5.26797 | 1.934856 |
| 19 | H | -2.387985 | -4.257944 | 2.314405 |
| 20 | C | -4.473271 | -2.960026 | -1.836839 |
| 21 | H | -5.202884 | -3.53269 | -1.261433 |
| 22 | H | -4.542513 | -3.236734 | -2.889942 |
| 23 | C | 1.225996 | -2.906297 | -2.869329 |
| 24 | H | 1.786922 | -2.981966 | -3.808691 |
| 25 | H | 0.690502 | -1.951258 | -2.885968 |
| 26 | C | 3.468618 | -0.464626 | 3.746724 |
| 27 | C | 1.150481 | -0.120873 | 3.274096 |
| 28 | C | 1.4211 | 0.947773 | 2.426505 |
| 29 | C | 2.755165 | 1.314608 | 2.239094 |
| 30 | H | 1.794083 | 2.530354 | -3.205797 |
| 31 | C | 4.402774 | 3.219736 | -3.406989 |
| 32 | C | 3.829329 | 2.06465 | -2.650475 |
| 33 | C | 2.446656 | 1.838684 | -2.687044 |
| 34 | C | 5.194952 | 0.962118 | 2.624148 |
| 35 | H | 3.004108 | 2.155071 | 1.602253 |
| 36 | H | 0.610839 | 1.484807 | 1.949765 |
| 37 | H | -2.722152 | 1.156915 | 1.399005 |
| 38 | H | -3.656447 | 3.263201 | 2.329067 |
| 39 | O | -1.5424 | 0.67254 | 3.118519 |
| 40 | H | 0.827489 | 0.555485 | -2.023695 |
| 41 | H | -4.76034 | 4.565117 | -1.633044 |
| 42 | C | -3.169158 | 1.898878 | 0.740903 |
| 43 | C | -3.243516 | 1.718637 | -0.635769 |
| 44 | C | -3.690228 | 3.090936 | 1.260241 |
| 45 | C | -3.794183 | 2.642946 | -1.519259 |
| 46 | C | -4.257984 | 4.040359 | 0.401997 |
| 47 | C | -4.310468 | 3.824315 | -0.9837 |
| 48 | N | 2.223478 | -2.923812 | -1.770801 |
| 49 | H | 2.253759 | -3.797531 | -1.234298 |
| 50 | C | 2.784636 | -0.124208 | -1.378316 |
| 51 | O | 0.52029 | -1.2792 | -0.150135 |
| 52 | S | 2.089683 | -1.621449 | -0.502111 |
| 53 | C | -4.753556 | 5.335877 | 0.961922 |
| 54 | H | -3.834044 | 2.446143 | -2.583425 |
| 55 | N | -3.844613 | -0.545242 | -2.35883 |

| | | | | |
|---|---|---|---|---|
| 56 | H | -3.375122 | -0.942782 | -3.181126 |
| 57 | C | 3.771485 | 0.60282 | 2.893304 |
| 58 | H | 4.26281 | -0.997135 | 4.254656 |
| 59 | C | 2.134693 | -0.831483 | 3.94938 |
| 60 | C | 4.686313 | 1.194024 | -1.961971 |
| 61 | H | 5.749256 | 1.396224 | -1.918062 |
| 62 | O | -2.24614 | -2.958066 | -3.465601 |
| 63 | H | 1.866097 | -1.630868 | 4.629315 |
| 64 | C | -2.092673 | -3.370292 | -2.295351 |
| 65 | O | -2.243996 | -0.82398 | -0.04547 |
| 66 | S | -2.503529 | 0.150396 | -1.33475 |
| 67 | H | 4.788926 | -0.595928 | -0.741138 |
| 68 | C | 4.158964 | 0.076048 | -1.310111 |
| 69 | C | 1.90113 | 0.728623 | -2.032207 |
| 70 | N | -1.098641 | -1.893744 | 2.287427 |
| 71 | H | -1.099406 | -1.466739 | 1.352331 |
| 72 | S | -0.648897 | -0.648703 | 3.496785 |
| 73 | F | 6.050347 | 0.555684 | 3.640151 |
| 74 | F | 5.367722 | 2.334625 | 2.458765 |
| 75 | F | 5.682113 | 0.376131 | 1.447089 |
| 76 | F | -5.26177 | 5.192025 | 2.247113 |
| 77 | F | -5.758171 | 5.894552 | 0.176559 |
| 78 | F | -3.739889 | 6.291173 | 1.041487 |
| 79 | F | 4.681844 | 2.887821 | -4.733885 |
| 80 | F | 5.596817 | 3.670558 | -2.8553 |
| 81 | F | 3.529419 | 4.302406 | -3.450833 |
| 82 | O | -0.726755 | -1.377473 | 4.958858 |
| 83 | O | -1.305589 | 0.475123 | -2.410978 |
| 84 | O | 3.100686 | -2.087227 | 0.69693 |

**Table 4** Atomic coordinates of the optimized structure of lowest energy conformation obtained for [**2c**+$Cl^-$] from DFT B3LYP/6-31G geometry optimization.

Charge = -1 Multiplicity = 1

| Atom # | Atom Type | x | y | z |
|---|---|---|---|---|
| 1 | Cl | 1.009067 | -0.001392 | 0.002036 |
| 2 | C | 4.398229 | 1.373022 | 0.395841 |
| 3 | C | 4.401415 | -1.01821 | 1.010974 |
| 4 | N | 4.378651 | 0.34282 | 1.337471 |
| 5 | N | 4.386935 | -1.318646 | -0.351995 |

| | | | | |
|---|---|---|---|---|
| 6 | N | 4.385896 | 0.975233 | -0.946173 |
| 7 | O | 4.459356 | 2.567505 | 0.739211 |
| 8 | O | 4.466282 | -1.912292 | 1.873934 |
| 9 | C | 3.101639 | -3.500322 | -0.349314 |
| 10 | H | 3.192885 | -4.52246 | -0.733739 |
| 11 | H | 3.008495 | -3.541787 | 0.740485 |
| 12 | C | 3.084894 | 1.435366 | 3.220484 |
| 13 | H | 3.171305 | 1.613162 | 4.298331 |
| 14 | H | 2.9933 | 2.400013 | 2.711488 |
| 15 | C | 4.380509 | 2.032571 | -1.98997 |
| 16 | H | 5.240053 | 1.863703 | -2.645615 |
| 17 | H | 4.495184 | 2.975528 | -1.458235 |
| 18 | C | 4.364622 | 0.71767 | 2.775093 |
| 19 | H | 5.217717 | 1.377354 | 2.959985 |
| 20 | H | 4.485418 | -0.213455 | 3.325994 |
| 21 | C | 4.379212 | -2.751072 | -0.746352 |
| 22 | H | 5.233459 | -3.237828 | -0.2663 |
| 23 | H | 4.501522 | -2.76194 | -1.82803 |
| 24 | C | 3.10843 | 2.057495 | -2.845749 |
| 25 | H | 3.199972 | 2.901925 | -3.538154 |
| 26 | H | 3.02319 | 1.133969 | -3.426944 |
| 27 | C | -2.957714 | -0.933306 | 3.031814 |
| 28 | C | -0.688092 | -0.3573 | 3.501991 |
| 29 | C | -0.23523 | -1.63358 | 3.185872 |
| 30 | C | -1.175077 | -2.580935 | 2.762919 |
| 31 | H | -0.821429 | 3.909139 | 1.851436 |
| 32 | C | -3.517274 | 3.58646 | 1.656916 |
| 33 | C | -2.507461 | 3.481384 | 0.564177 |
| 34 | C | -1.149323 | 3.692308 | 0.84206 |
| 35 | C | -3.541453 | -3.225906 | 2.247512 |
| 36 | H | -0.847933 | -3.564306 | 2.447639 |
| 37 | H | 0.819625 | -1.872834 | 3.226591 |
| 38 | H | 0.847033 | -1.860891 | -3.22401 |
| 39 | H | -0.817809 | -0.34319 | -4.307769 |
| 40 | O | 1.045142 | 0.764182 | 5.60285 |
| 41 | H | 0.846344 | 3.723041 | -0.001835 |
| 42 | H | -3.984569 | -2.252124 | -2.081013 |
| 43 | C | -0.20897 | -1.948119 | -3.002988 |
| 44 | C | -0.665348 | -2.861786 | -2.05914 |
| 45 | C | -1.147084 | -1.109787 | -3.616897 |

| | | | | |
|---|---|---|---|---|
| 46 | C | -2.002206 | -2.992319 | -1.700901 |
| 47 | C | -2.505348 | -1.24263 | -3.294911 |
| 48 | C | -2.934958 | -2.171475 | -2.335903 |
| 49 | N | 1.928595 | 2.302843 | -1.995968 |
| 50 | H | 1.597067 | 1.501457 | -1.421482 |
| 51 | C | -0.664529 | 3.21441 | -1.452398 |
| 52 | O | 1.080166 | 4.455303 | -3.476117 |
| 53 | S | 0.536431 | 3.025424 | -2.878306 |
| 54 | C | -3.513319 | -0.345234 | -3.930153 |
| 55 | H | -2.295675 | -3.687796 | -0.926096 |
| 56 | N | 1.927927 | -2.883625 | -0.995074 |
| 57 | H | 1.595905 | -1.98516 | -0.589199 |
| 58 | C | -2.531762 | -2.230261 | 2.710178 |
| 59 | H | -4.006002 | -0.668137 | 2.969127 |
| 60 | C | -2.022989 | 0.023599 | 3.429012 |
| 61 | C | -2.935415 | 3.113525 | -0.719762 |
| 62 | H | -3.985043 | 2.934651 | -0.918355 |
| 63 | O | 4.480696 | -0.655393 | -2.572719 |
| 64 | H | -2.313242 | 1.043684 | 3.64197 |
| 65 | C | 4.408966 | -0.355302 | -1.367267 |
| 66 | O | 1.074544 | -5.23791 | -2.125333 |
| 67 | S | 0.533194 | -4.005845 | -1.183943 |
| 68 | H | -2.293336 | 2.646377 | -2.736092 |
| 69 | C | -2.001192 | 2.970899 | -1.746383 |
| 70 | C | -0.209638 | 3.576628 | -0.189127 |
| 71 | N | 1.912434 | 0.567371 | 3.003679 |
| 72 | H | 1.586357 | 0.470488 | 2.020631 |
| 73 | S | 0.512541 | 0.967573 | 4.06262 |
| 74 | F | -3.803441 | -3.14314 | 0.869927 |
| 75 | F | -4.781071 | -3.041628 | 2.86583 |
| 76 | F | -3.159166 | -4.53762 | 2.489287 |
| 77 | F | -3.121575 | 0.110731 | -5.180509 |
| 78 | F | -3.788177 | 0.800129 | -3.164675 |
| 79 | F | -4.748456 | -0.977999 | -4.095336 |
| 80 | F | -4.751345 | 4.045039 | 1.187998 |
| 81 | F | -3.126731 | 4.443962 | 2.675213 |
| 82 | F | -3.794019 | 2.352922 | 2.269231 |
| 83 | O | -0.213439 | 2.413691 | 3.744334 |
| 84 | O | -0.199264 | -4.453196 | 0.224202 |
| 85 | O | -0.195609 | 2.028908 | -3.969538 |

### 2.4.7. Ion Transport Activity Studies

#### 2.4.7.1. Determination of Ion Transport Activity by HPTS Assay

We have prepared a buffer solution using autoclaved water of strength 100 mM of NaCl and 10 mM of HEPES. The pH of the solution was below 7.0 and to make the pH at around 7.0 required amount of 0.5 M NaOH solution was added. Then 1 mM of HPTS solution was prepared from solid HPTS using the above buffer solution. The stock solution for the HPTS assay was prepared from solid compound by using HPLC grade DMSO.

In a 10 mL round bottomed flask 1 mL of EYPC lipid solution (25 mg/mL in $CHCl_3$) was taken and the chloroform present in the lipid solution was evaporated by a slow stream of nitrogen gas to get a thin film of lipid. Then the trace amount of chloroform present in the lipid was evaporated by keeping it in high vacuum for about 4 h. The lipid membrane was then hydrated with 1 mL of HPTS solution (1 mM HPTS, 100 mM NaCl, 10 mM HEPES, pH 7.0) by vortexing 4–5 times over the time period of 1 h. Then the hydrated suspension was subjected through 20 freeze-thaw cycles and extrusions were done for 19 times (must be odd number) through 100 nm polycarbonate membrane. The extravesicular dyes were separated from vesicles by size exclusion column chromatography (Sephadex G-50) eluting with buffer solution (1 mM HPTS, 100 mM NaCl, 10 mM HEPES, pH 7.0). The vesicles were then diluted to 6 mL by using buffer (100 mM NaCl, 10 mM HEPES, pH 7.0) to get the concentration of 5.4 mM of EYPC-LUVs⊃HPTS, assuming no loss of lipid during gel filtration process. The vesicles contain, inside: 1 mM HPTS, 100 mM NaCl, 10 mM HEPES, pH 7.0 and outside: 100 mM NaCl, 10 mM HEPES, pH 7.0.

In a clean fluorimetric cuvette, 1975 µL of buffer solution (100 mM NaCl, 10 mM HEPES, pH 7.0), 25 µL of above prepared vesicles solution were taken and placed in a fluorescence instrument equipped with a magnetic stirrer at $t$ = 0 s. The fluorescence emission intensity of the HPTS dye, $I_t$ was measured at $\lambda_{em}$ = 510 nm (where, $\lambda_{ex}$ = 450 nm) for the time course of 0 to 350 s. At $t$ = 20 s, 20 µL of 0.5 M NaOH solution was added to the same cuvette to generate a pH gradient (ΔpH = 0.8) between intra and extra vesicular medium. Then 20 µL solution of tripodal molecules in DMSO of different concentration were added at $t$ = 100 s. At

*t* = 300 s, 25 µL of 10% triton X-100 was added to destroy all the vesicles for destructing the pH gradient.

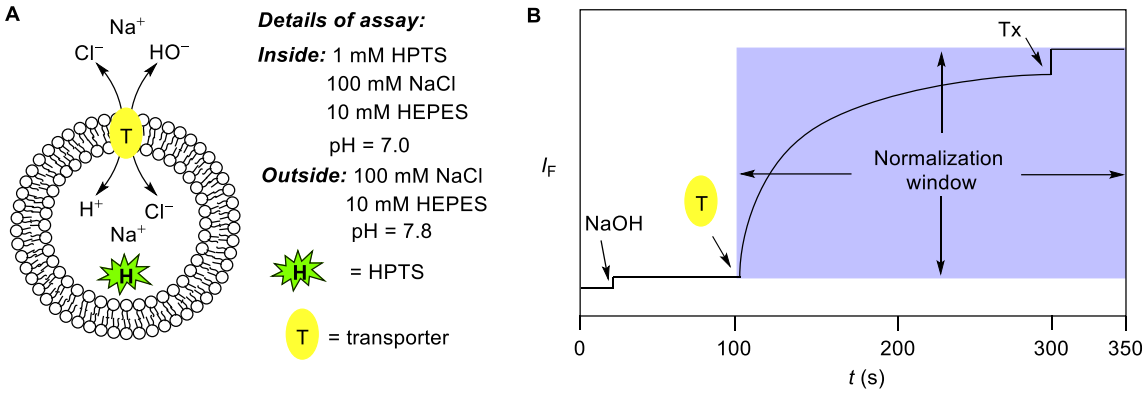



**Figure 2.14** Representation of fluorescence kinetics based HPTS assay for checking ion transport activity across EYPC-LUVs⊃HPTS (**A**), and normalization window for the same fluorescence kinetics experiment (**B**).

The fractional emission intensity (in percentage), $I_F$ (Figure 2.14B) was obtained after normalizing all the data using the following equation (Equation 3).

$$\% \text{ of } I_F = (I_t - I_0) / (I_\infty - I_0) \times 100 \qquad \text{Equation 3}$$

Where, $I_0$ is the fluorescence intensity just before the addition of the tripodal compound, $I_t$ is the fluorescence intensity at time $t$ and $I_\infty$ is the fluorescence intensity after the addition of Triton X–100.

For plotting all the data in to graph the time axis was normalized using the following equation:

$$t = t - 100 \qquad \text{Equation 4}$$

To get the relative activity for all the transporter molecules ion transport experiment was done across bilayer membrane using EYPC-LUVs⊃HPTS.

The concentration profile data was used for fitting of the "Hill equation" (Equation 5) to get the half maximal effective concentration ($EC_{50}$) and Hill coefficient ($n$).

$$Y = Y_\infty + (Y_0 - Y_\infty) / [(1 + (c / EC_{50})^n] \qquad \text{Equation 5}$$

Where, $Y_0$ is the fluorescence intensity just before the addition of the tripodal compound, $Y_\infty$ is the fluorescence intensity after addition of excess tripodal compound, and $c$ is the concentration of the compound.

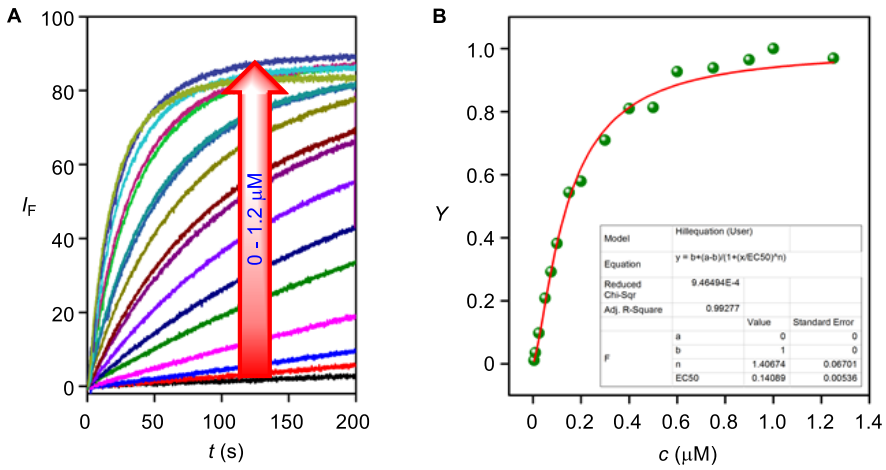



**Figure 2.15** Concentration dependent fluorescence kinetics based ion transport activity assay of compound **1f** (0–1.2 µM) across EYPC-LUVs⊃HPTS (**A**), and Hill plot of compound **1f** at $t$ = 100 s to get $EC_{50}$ and $n$ (**B**).

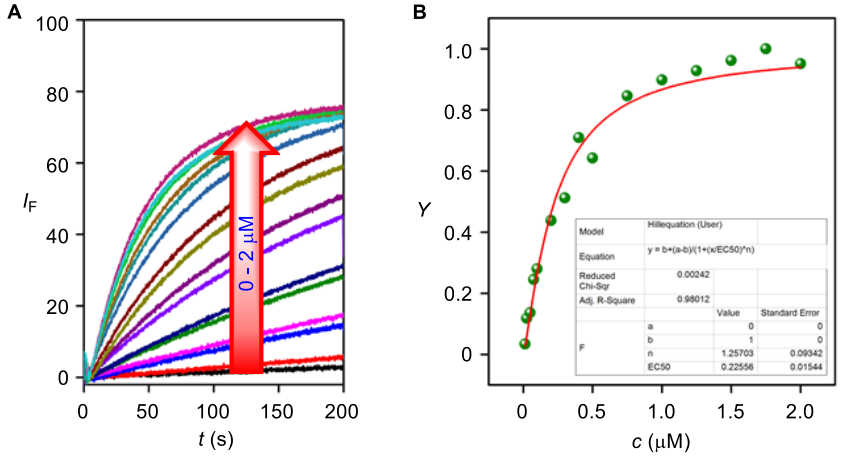



**Figure 2.16** Concentration dependent fluorescence kinetics based ion transport activity assay of compound **1c** (0–2 µM) across EYPC-LUVs⊃HPTS (**A**), and Hill plot of compound **1c** at $t$ = 100 s to get $EC_{50}$ and $n$ (**B**).

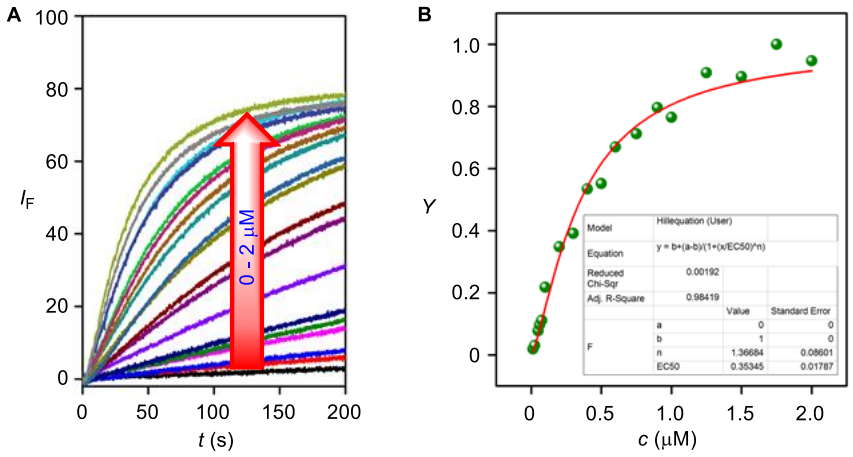



**Figure 2.17** Concentration dependent fluorescence kinetics based ion transport activity assay of compound **1e** (0–2 µM) across EYPC-LUVs⊃HPTS (**A**), and Hill plot of compound **1e** at $t$ = 100 s to get $EC_{50}$ and $n$ (**B**).

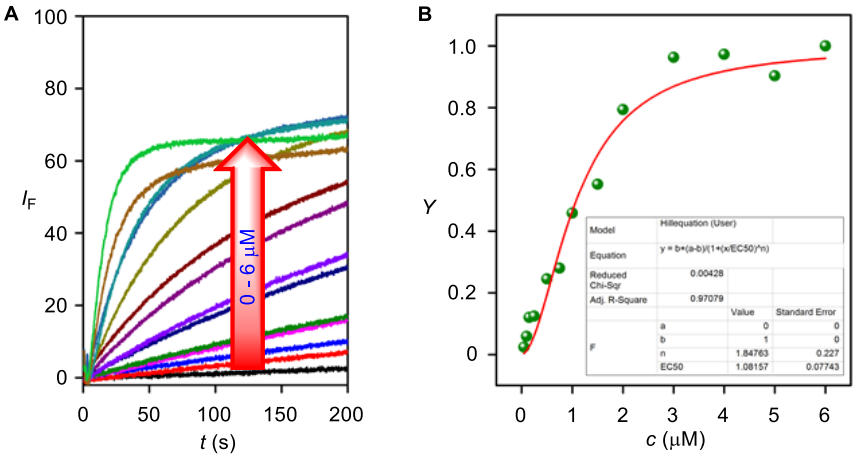



**Figure 2.18** Concentration dependent fluorescence kinetics based ion transport activity assay of compound **1d** (0–6 μM) across EYPC-LUVs⊃HPTS (**A**), and Hill plot of compound **1d** at $t$ = 100 s to get $EC_{50}$ and $n$ (**B**).

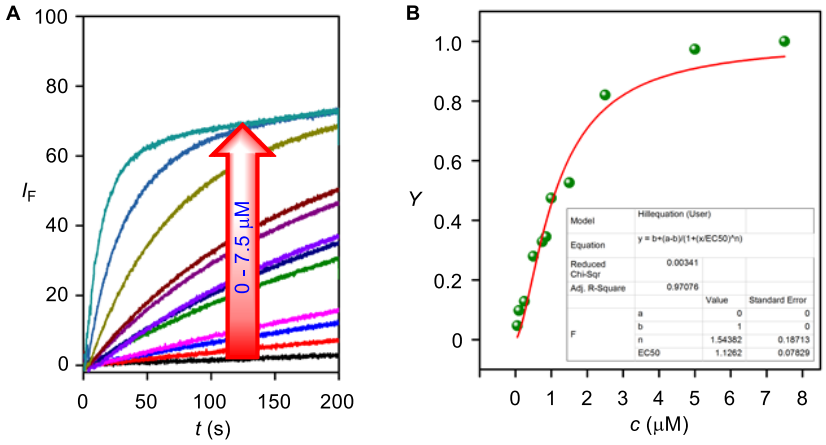



**Figure 2.19** Concentration dependent fluorescence kinetics based ion transport activity assay of compound **1a** (0–7.5 μM) across EYPC-LUVs⊃HPTS (**A**), and Hill plot of compound **1a** at $t$ = 100 s to get $EC_{50}$ and $n$ (**B**).

### 2.4.7.2. Determination of Ion Selectivity by HPTS Assay

We have prepared buffer solutions of different salts using autoclaved water of strength 100 mM of MX (where, MX = NaCl, NaBr, NaI, $NaNO_3$, NaSCN, $NaClO_4$, NaOAc, LiCl, KCl, RbCl, CsCl) and 10 mM of HEPES. The pHs of the solutions were adjusted at around 7.0 by the addition of required amount of 0.5 M NaOH solution. Then 1 mM of HPTS solution was prepared from solid HPTS using the above buffer solution. The stock solution for the HPTS assay was prepared from solid compound by using HPLC grade DMSO.

**Cation Selectivity Transport Study by HPTS Assay:** In a clean fluorimetric cuvette, 1975 μL of buffer solution (100 mM MCl, 10 mM HEPES, pH 7.0; where, $M^+$ = $Li^+$, $Na^+$, $K^+$, $Rb^+$, and $Cs^+$), 25 μL of above prepared vesicles solution were taken and placed in a fluorescence

instrument equipped with a magnetic stirrer at $t$ = 0 s. The fluorescence emission intensity of the HPTS dye, $I_t$ was measured at $\lambda_{em}$ = 510 nm (where $\lambda_{ex}$ = 450 nm) for the time course of 0 to 350 s. At $t$ = 20 s, 20 µL of 0.5 M NaOH solution was added to the same cuvette to generate a pH gradient (ΔpH = 0.8) between intra and extra vesicular medium. Then 20 µL solution of tripodal molecules in DMSO was added at $t$ = 100 s. At $t$ = 300 s, 25 µL of 10% triton X–100 was added to destroy all the vesicles for destructing the pH gradient. All the data was normalized using the Equation 3 and Equation 4.

**Anion Selectivity Transport Study by HPTS Assay:** In a clean fluorimetric cuvette, 1975 µL of buffer solution (100 mM NaX, 10 mM HEPES, pH 7.0; where, $X^-$ = $Cl^-$, $Br^-$, $I^-$, $NO_3^-$, $SCN^-$, $ClO_4^-$, and $AcO^-$), 25 µL of above prepared vesicles solution were taken and placed in a fluorescence instrument equipped with a magnetic stirrer at $t$ = 0 s. The fluorescence emission intensity of the HPTS dye, $I_t$ was measured at $\lambda_{em}$ = 510 nm (where $\lambda_{ex}$ = 450 nm) for the time course of 0 to 350 s. At $t$ = 20 s, 20 µL of 0.5 M NaOH solution was added to the same cuvette to generate a pH gradient (ΔpH = 0.8) between intra and extra vesicular medium. Then 20 µL solution of tripodal molecules in DMSO of different concentration were added at $t$ = 100 s. At $t$ = 300 s, 25 µL of 10% triton X–100 was added to destroy all the vesicles for destructing the pH gradient. All the data was normalized using the Equation 3and Equation 4.

### 2.4.7.3. Ion Transport Mechanism Study by HPTS Assay

**FCCP Assay:** In a clean fluorimetric cuvette, 1975 µL of buffer solution (100 mM NaCl, 10 mM HEPES, pH 7.0), 25 µL of above prepared vesicles solution were taken and placed in a fluorescence instrument equipped with a magnetic stirrer at $t$ = 0 s. The fluorescence emission intensity of the HPTS dye, $I_t$ was measured at $\lambda_{em}$ = 510 nm (where $\lambda_{ex}$ = 450 nm) for the time course of 0 to 350 s. At $t$ = 20 s, 20 µL of 0.5 M NaOH solution was added to the same cuvette to generate a pH gradient (ΔpH = 0.8) between intra and extra vesicular medium. Then FCCP (2.5 µM) was added at t = 50 s followed by the addition of 20 µL solution of tripodal molecule in DMSO at $t$ = 100 s. At $t$ = 300 s, 25 µL of 10% triton X-100 was added to destroy all the vesicles for destructing the pH gradient. All the data was normalized using the Equation 3 and Equation 4.

**Valinomycin Assay:** In a clean fluorimetric cuvette 1975 µL of buffer solution (100 mM KCl, 10 mM HEPES, pH 7.0), 25 µL of above prepared vesicles solution were taken and placed in a fluorescence instrument equipped with a magnetic stirrer at $t$ = 0 s. The fluorescence emission

intensity of the HPTS dye, $I_t$ was measured at $\lambda_{em}$ = 510 nm (where $\lambda_{ex}$ = 450 nm) for the time course of 0 to 350 s. At *t* = 20 s, 20 µL of 0.5 M NaOH solution was added to the same cuvette to generate a pH gradient (ΔpH = 0.8) between intra and extra vesicular medium. Then valinomycin (2.5 pM) was added at *t* = 50s followed by the addition of 20 µL solution of tripodal molecule (0.16 µM) in DMSO at *t* = 100 s. At *t* = 300 s, 25 µL of 10% triton X-100 was added to destroy all the vesicles for destructing the pH gradient. All the data was normalized using the Equation 3 and Equation 4.

#### 2.4.7.4. Determination of $Cl^-$ Transport Activity by Lucigenin Assay

We have prepared a salt solution using autoclaved water of strength 225 mM of $NaNO_3$. Then 1 mM of Lucigenin solution was prepared from solid Lucigenin using the above solution. The stock solution of the compound for the Lucigenin assay was prepared from solid compound by using HPLC grade $CH_3CN$ : $CH_3OH$ = 5 : 1.

**Vesicles Preparation:** In a 10 mL round bottomed flask 1 mL of EYPC lipid solution (25 mg/mL in $CHCl_3$) was taken and the chloroform present in the lipid solution was evaporated by a slow stream of nitrogen gas to get a thin film of lipid. Then the trace amount of chloroform present in the lipid was evaporated by keeping it in high vacuum for about 4 h. The lipid membrane was then hydrated with 1 mL of Lucigenin solution (1 mM Lucigenin, 225 mM $NaNO_3$) by vortexing 4-5 times over the time period of 1 h. Then the hydrated suspension was subjected through 20 freeze-thaw cycles and extrusions were done for 19 times through 200 nm polycarbonate membrane. The extravesicular Lucigenin dyes were separated from vesicles by size exclusion column chromatography (Sephadex G-50) using 225 mM of $NaNO_3$ solution. The vesicles were then diluted to 4 mL by using the same 225 mM of $NaNO_3$ solution to get the concentration of ~ 8 mM of EYPC-LUVs⊃Lucigenin, assuming no loss of lipid during gel filtration process. The vesicles contains, inside: 1 mM Lucigenin, 225 mM $NaNO_3$ and outside: 225 mM $NaNO_3$.

**Lucigenin Assay:** In a clean fluorimetric cuvette 1950 µL of 225 mM $NaNO_3$ solution, 25 µL of above prepared vesicles solution were taken and placed in a fluorescence instrument equipped with a magnetic stirrer at *t* = 0 s. The fluorescence emission intensity of the Lucigenin dye, $I_t$ was measured at $\lambda_{em}$ = 535 nm (where, $\lambda_{ex}$ = 455 nm) for the time course of 0 to 350 s. At *t* = 20 s, 33.3 µL of 2N NaCl solution was added to the same cuvette to generate a chloride ion concentration gradient between intra and extravesicular medium. Then 20 µL solution of tripodal molecule of different concentration were added at *t* = 100 s. At *t* = 300 s, 25 µL of

10% triton X-100 was added to destroy all the vesicles for destructing the chloride ion concentration gradient.

The fractional emission intensity, $I_F$ (Figure 2.20B) was obtained after normalizing all the data using the following equation (Equation 6).

$$\% \text{ of } I_F = (I_t - I_0) / (I_\infty - I_0) \times (-100) \qquad \text{Equation 6}$$

Where, $I_0$ is the fluorescence intensity just before the addition of the tripodal compound, $I_t$ is the fluorescence intensity at time $t$, and $I_\infty$ is the fluorescence intensity after the addition of Triton X–100.

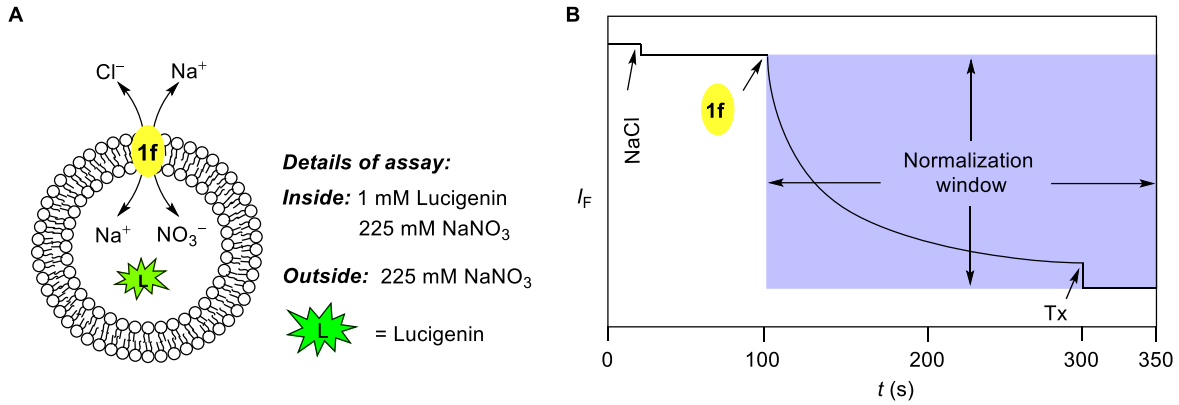
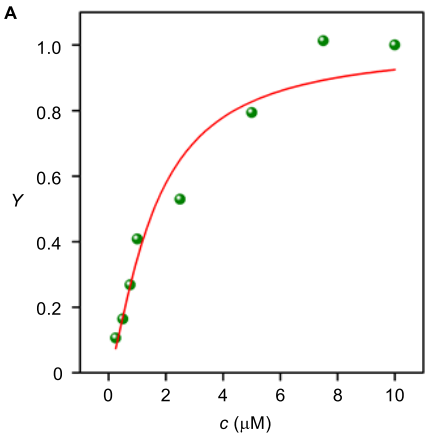



**Figure 2.20** Representation of fluorescence kinetics based Lucigenin assay for checking the chloride ion transport activity across EYPC-LUVs⊃Lucigenin (A), and normalization window for the same fluorescence kinetics experiment (B).

For plotting all the data in to graph the time axis was normalized using Equation 4, The concentration profile data was used for fitting of the "Hill equation" (Equation 5) to get the half maximal effective concentration ($EC_{50}$) and Hill coefficient ($n$).




B

| | | | |
|---|---|---|---|
| Model | Hillequation (User) | | |
| Equation | y = b+(a-b)/(1+(x/EC50)^n) | | |
| Reduced Chi-Sqr | 0.00677 | | |
| Adj. R-Square | 0.94854 | | |
| | | Value | Standard Error |
| F | a | 0 | 0 |
| | b | 1 | 0 |
| | n | 1.3632 | 0.21255 |
| | EC50 | 1.58623 | 0.21503 |

**Figure 2.21** Hill plot of compound **1f** at $t$ = 100 s to get $EC_{50}$ and $n$ (A) and table for Hill equation (B).

### 2.4.7.5. $Cl^-$ transport by Symport assay in presence of Lucigenin

In a clean fluorimetric cuvette 1950 µL of 225 mM $NaNO_3$ solution, 25 µL of above prepared vesicles solution were taken and placed in a fluorescence instrument equipped with a magnetic stirrer at $t$ = 0 s. The fluorescence emission intensity of the Lucigenin dye, $I_t$ was measured at $\lambda_{em}$ = 535 nm (where $\lambda_{ex}$ = 455 nm) for the time course of 0 to 350 s. At $t$ = 50 s, 33.3 µL of 2 N MCl (where, $M^+$ = $Li^+$, $Na^+$, $K^+$, $Rb^+$, and $Cs^+$) solution was added to the same cuvette to generate a concentration gradient of ions ($Cl^-$ and $M^+$) between intra and extra vesicular medium. Then 20 µL of 0.15 mM tripodal molecule was added at $t$ = 100 s and at, $t$ = 300 s, 25 µL of 10% triton X-100 was added to destroy all the vesicles for destructing the chloride ion concentration gradient.

### 2.4.7.6. $Cl^-$ transport by Lucigenin assay in presence of Valinomycin

In a clean fluorimetric cuvette 1950 µL of 225 mM $NaNO_3$ solution, 25 µL of above prepared vesicles solution were taken and placed in a fluorescence instrument equipped with a magnetic stirrer at $t$ = 0 s. The fluorescence emission intensity of the Lucigenin dye, $I_t$ was measured at $\lambda_{em}$ = 535 nm (where, $\lambda_{ex}$ = 455 nm) for the time course of 0 to 350 s. At $t$ = 20 s, 33.3 µL of 2 N KCl solution was added to the same cuvette to generate a concentration gradient of ions ($Cl^-$ and $K^+$) between intra and extra vesicular medium. Then valinomycin (0.5 µM) was added at $t$ = 50 s followed by the addition of 20 µL of 75 µM solution of tripodal molecule at $t$ = 100 s and at, $t$ = 300 s, 25 µL of 10% triton X-100 was added to destroy all the vesicles for destructing the chloride ion concentration gradient.

### 2.4.7.7. U-tube experiments for checking $Cl^-$ transport

In this experiment we have checked whether the chloride ion is transporting *via* mobile carrier mechanism or ion channel formation by transporter molecule. For that we have set up an experiment using a U-tube where left arm (Source arm) of the tube was filled with 7.5 mL of 500 mM NaCl solution buffered to pH 7.0 using 5mM phosphate buffer and the right arm (receiver arm) of the tube was filled with 7.5 mL of 500 mM $NaNO_3$ solution buffered to pH 7.0 using 5mM phosphate buffer. Two different salts solution in two different arm were separated by 15 mL solution of compound **1f** in $CHCl_3$ (1 mM compound **1f**, 1 mM tetrabutylammonium hexafluorophosphate ) in such a way that two salts solution never come contact with each other. Here transport of chloride ion is only possible *via* mobile carrier mechanism due to the long length of $CHCl_3$ layer, which does not allow the formation ion

channel. For checking transport activity via carrier mechanism chloride ion concentration in the receiver arm was measured by chloride ion selective electrode. The gradual increase of chloride ion concentration (Figure 2.22) was measured in a fixed time interval for the time period of 8 days, gave evidence in support of mobile carrier mechanism. In a control experiment no increase in chloride ion concentration was observed when we omitted transporter molecule **1f** keeping other conditions same.

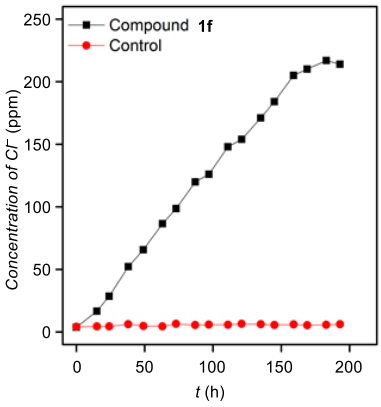



**Figure 2.22** Change of chloride ion concentration in U-tube experiment with and without using compound **1f** (1 mM).

## 2.5. NMR Spectra

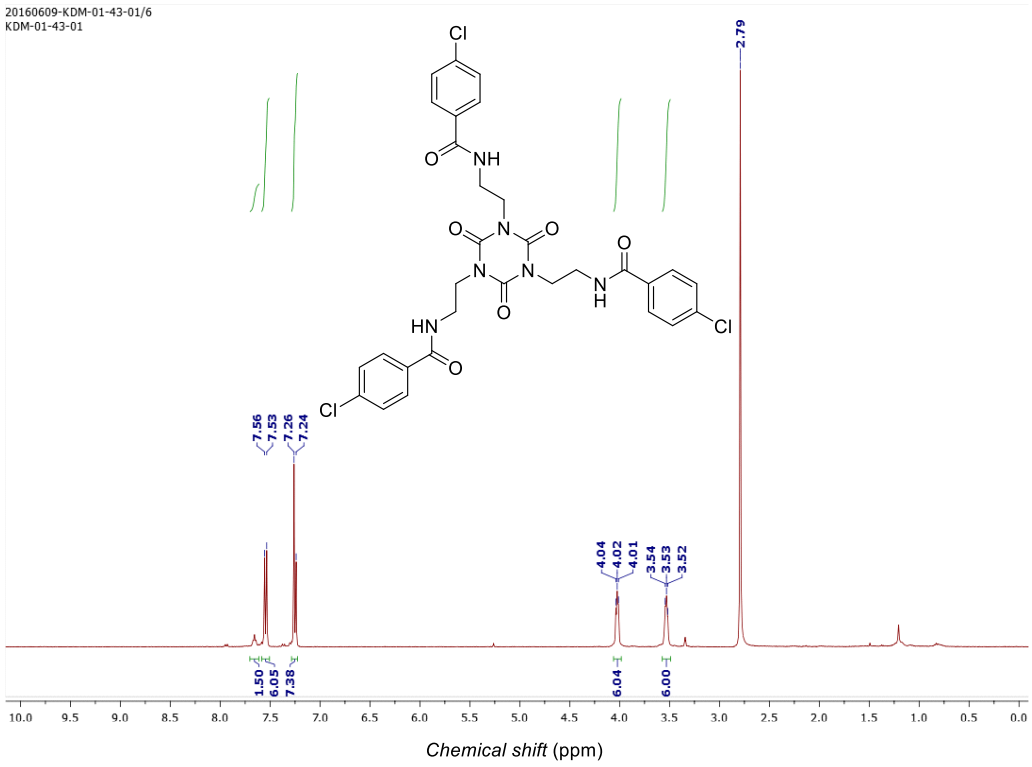



**Figure 2.23** $^{1}$H NMR spectrum of compound **1a** in $CDCl_3$:MeOH-$d_4$ = 4:1.

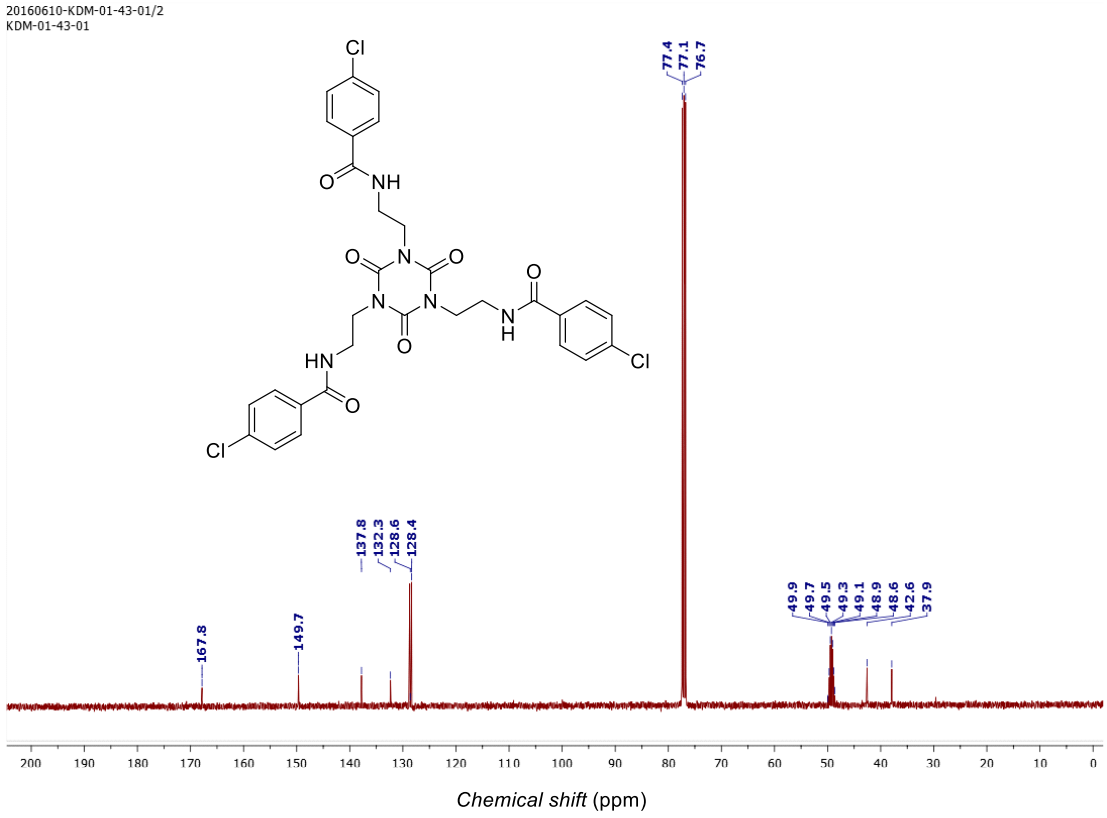



**Figure 2.24** $^{13}$C NMR spectrum of compound **1a** in $CDCl_3$:MeOH-$d_4$ = 4:1.

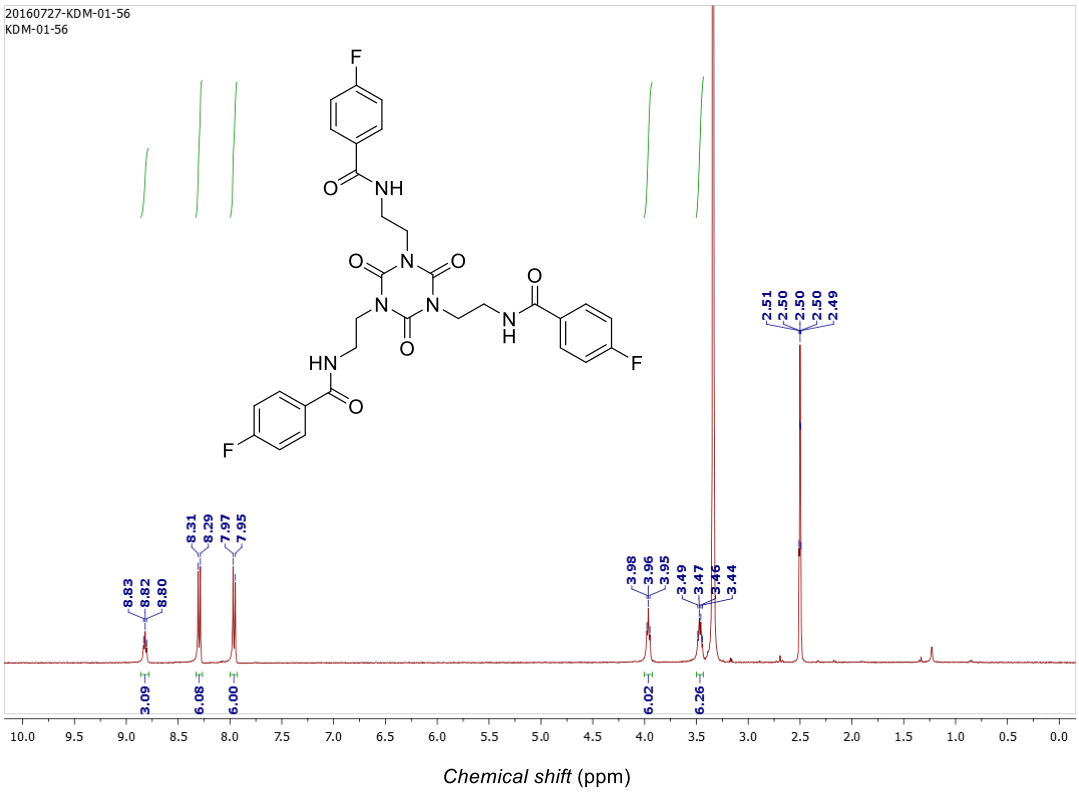



**Figure 2.25** $^{1}$H NMR spectrum of compound **1b** in DMSO-$d_6$.

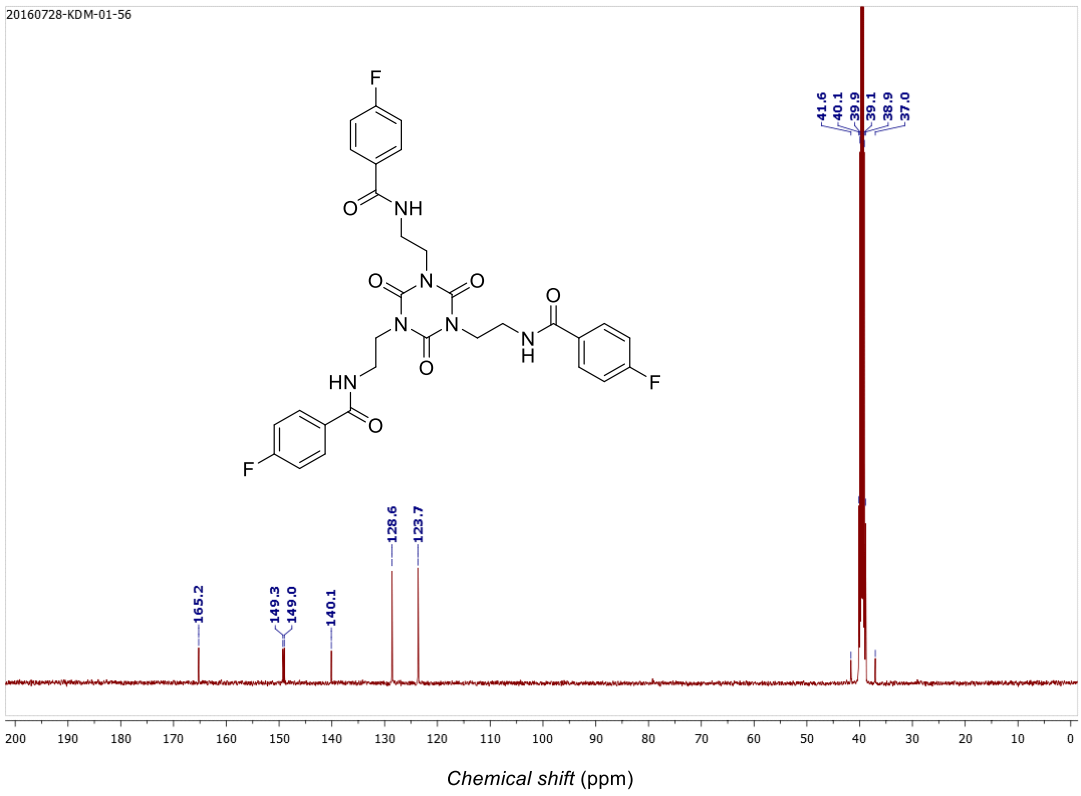



**Figure 2.26** $^{13}$C NMR spectrum of compound **1b** in DMSO-$d_6$.

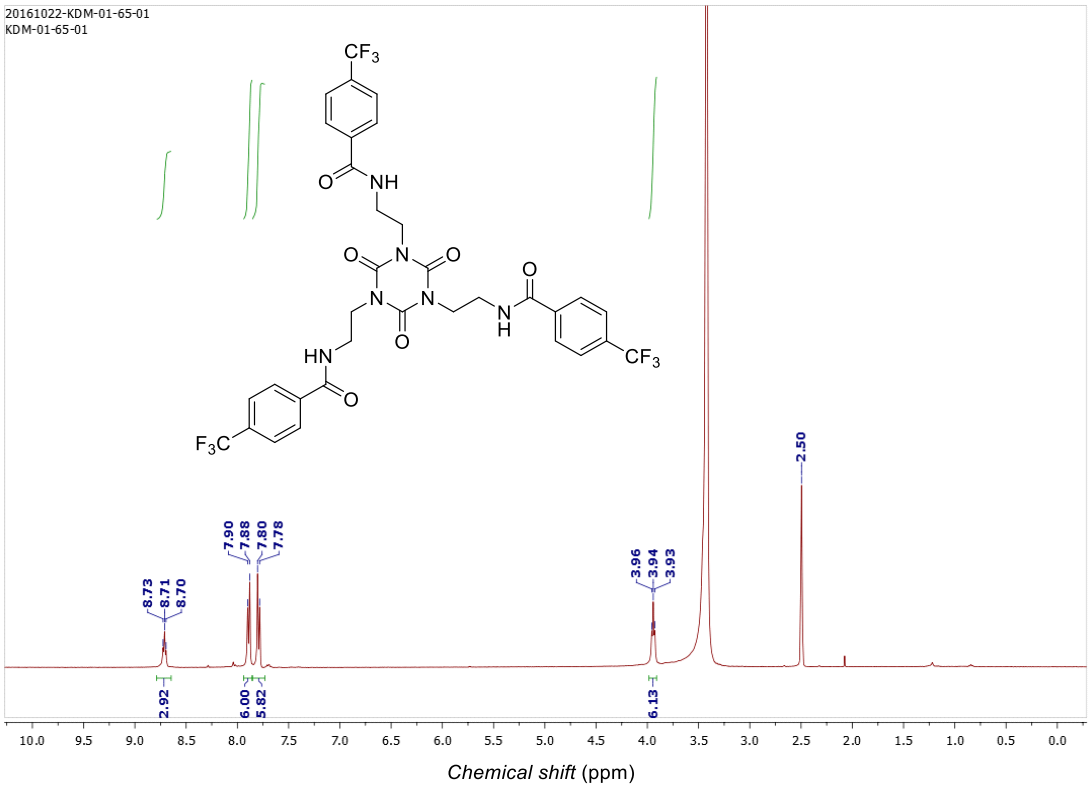



**Figure 2.27** $^{1}$H NMR spectrum of compound **1c** in DMSO-$d_6$.

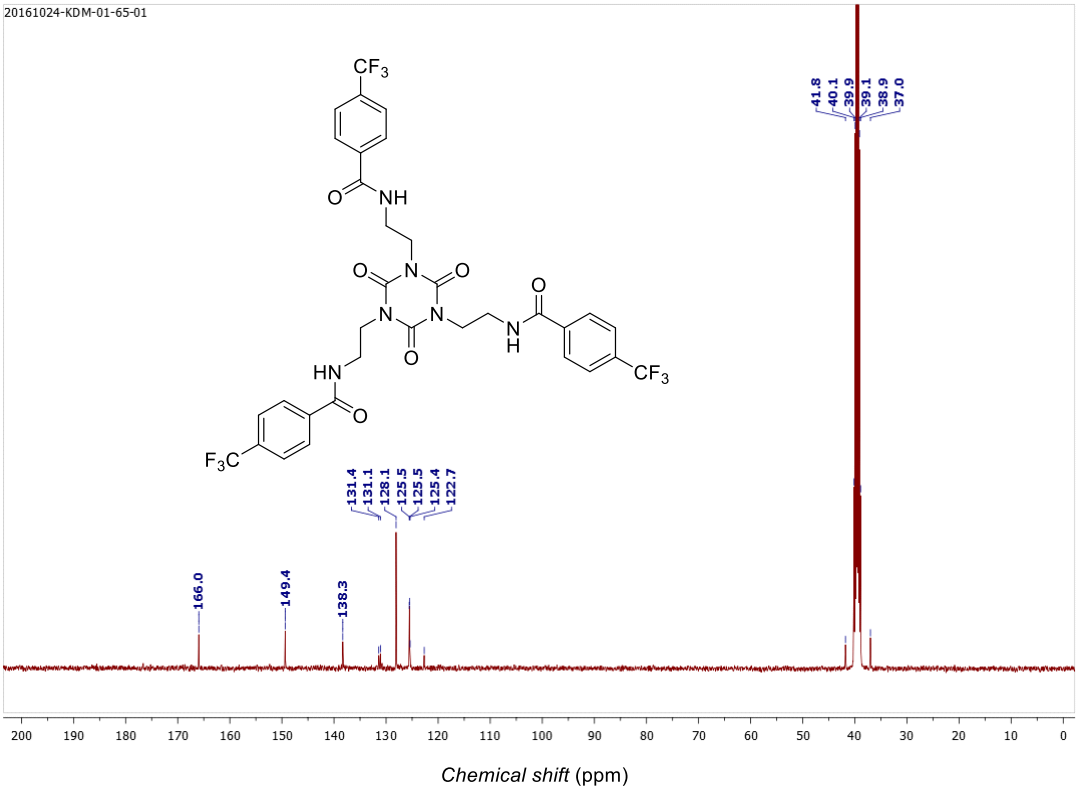



**Figure 2.28** $^{13}$C NMR spectrum of compound **1c** in DMSO-$d_6$.

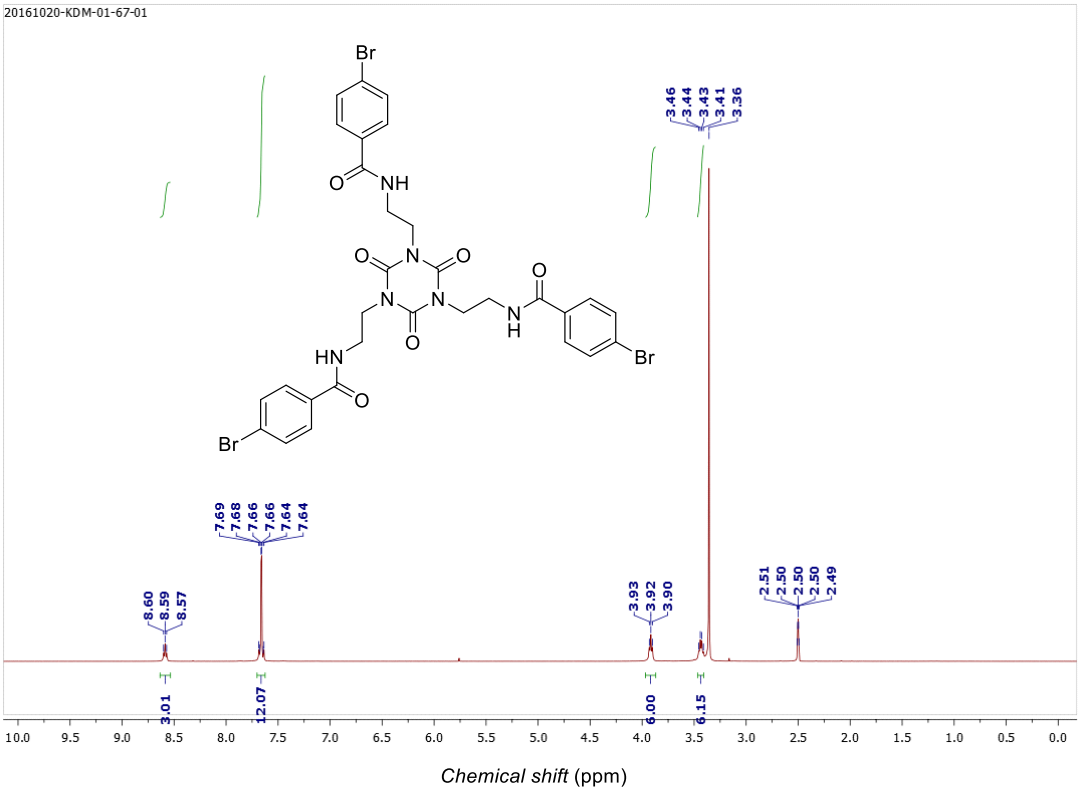



**Figure 2.29** $^{1}$H NMR spectrum of compound **1d** in DMSO-$d_6$.

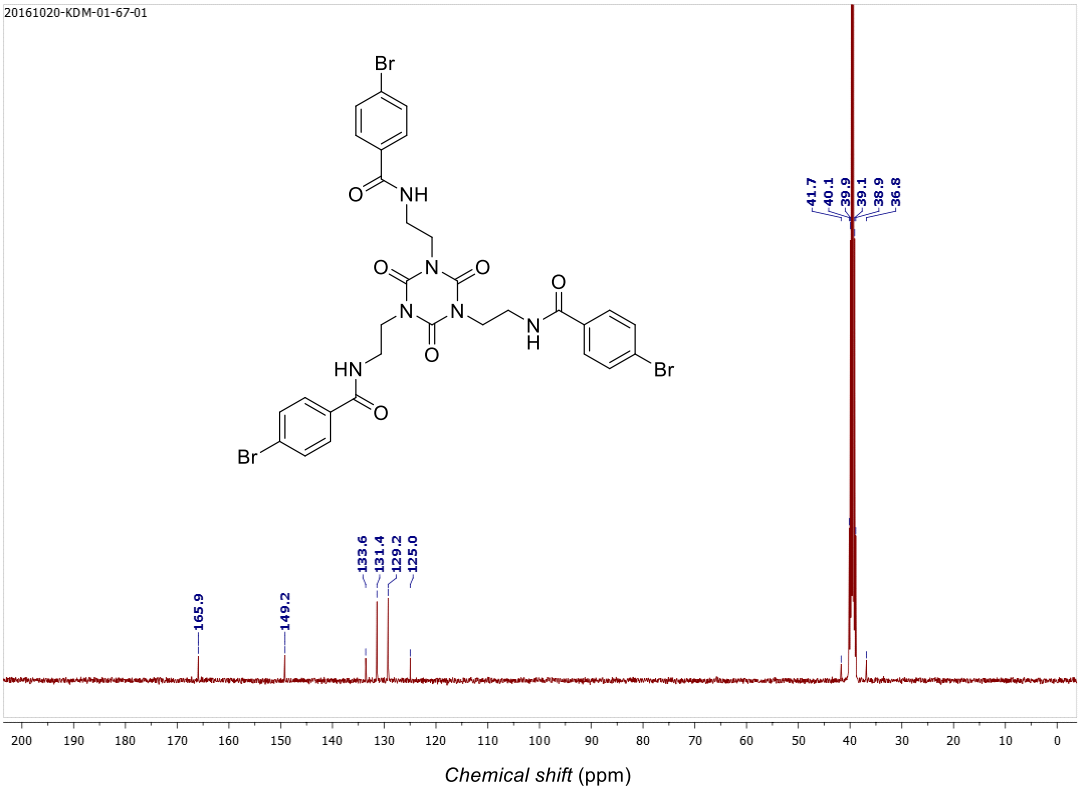



**Figure 2.30** $^{13}$C NMR spectrum of compound **1d** in DMSO-$d_6$.

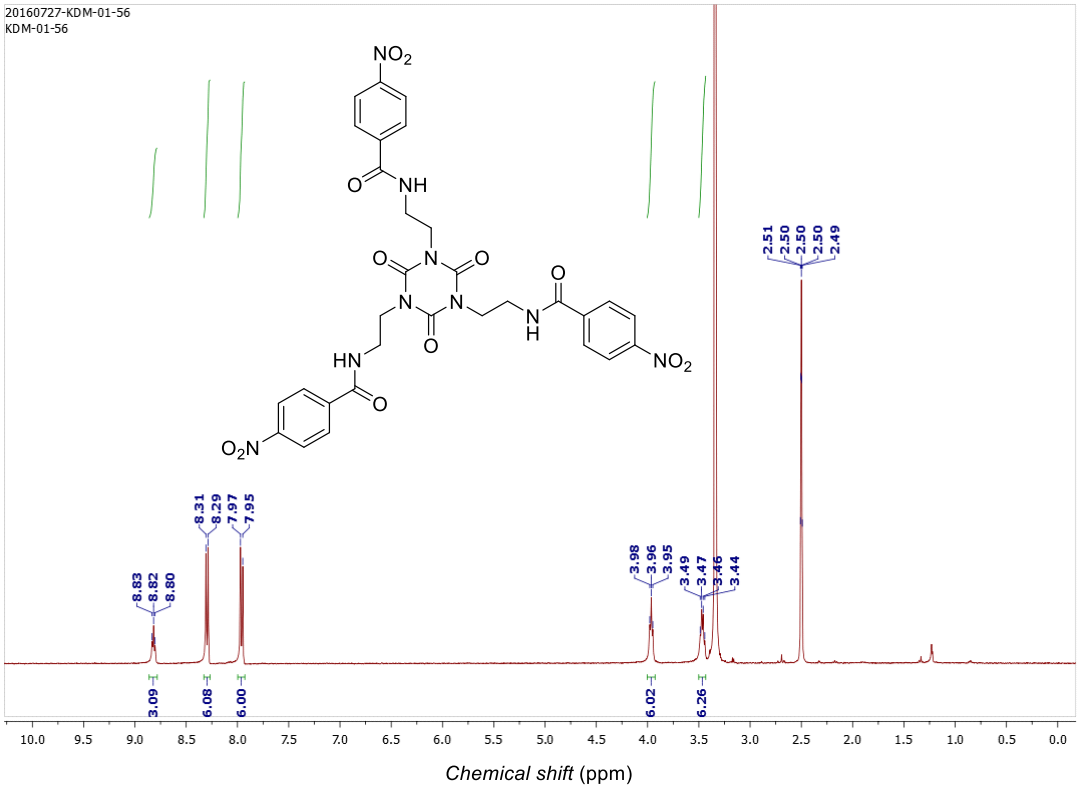



**Figure 2.31** $^{1}$H NMR spectrum of compound **1e** in DMSO-$d_6$.

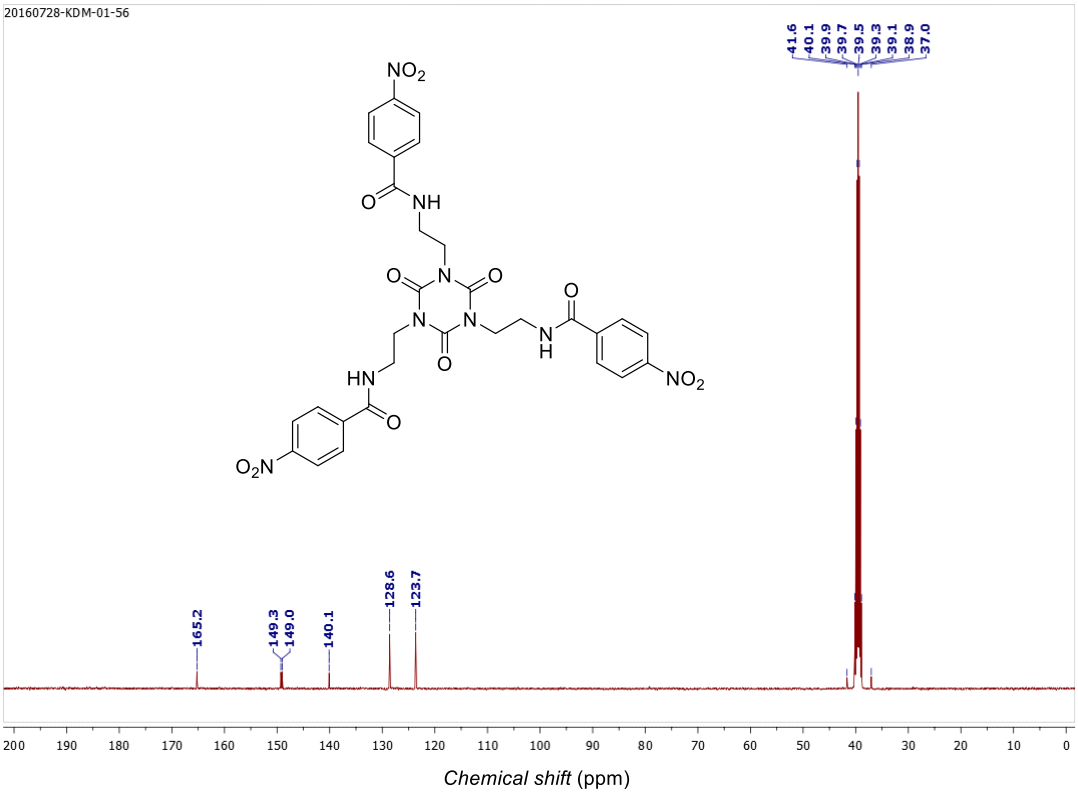



**Figure 2.32** $^{13}$C NMR spectrum of compound **1e** in DMSO-$d_6$.

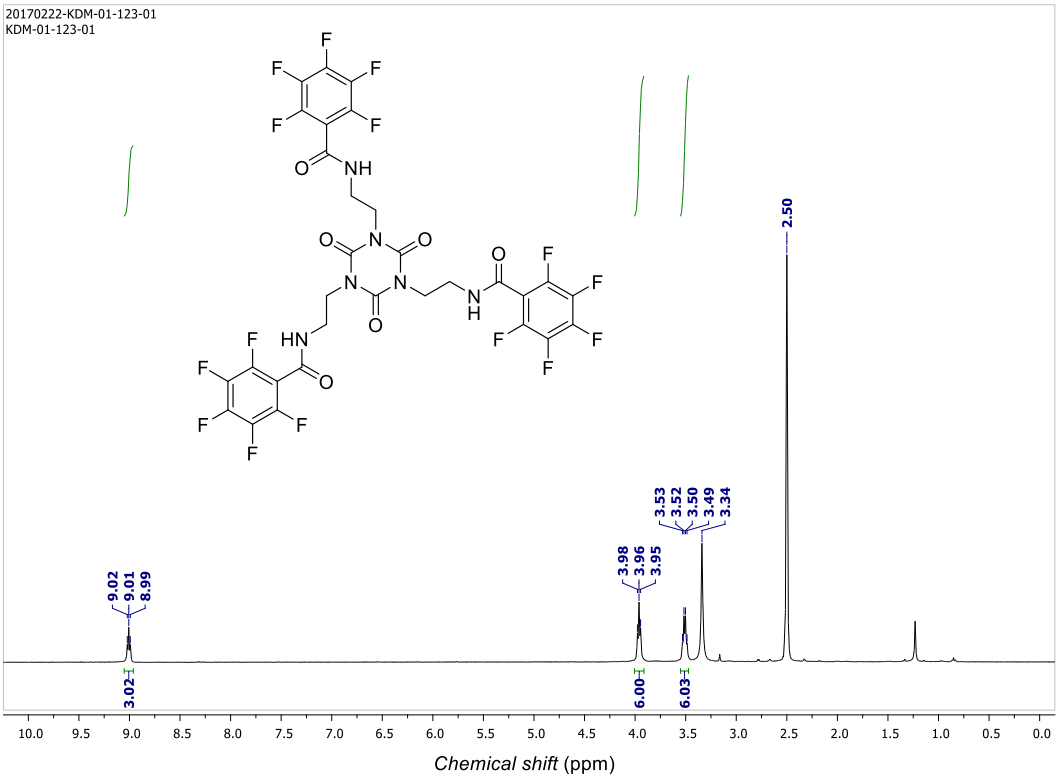



**Figure 2.33** $^{1}$H NMR spectrum of compound **1f** in DMSO-$d_6$.

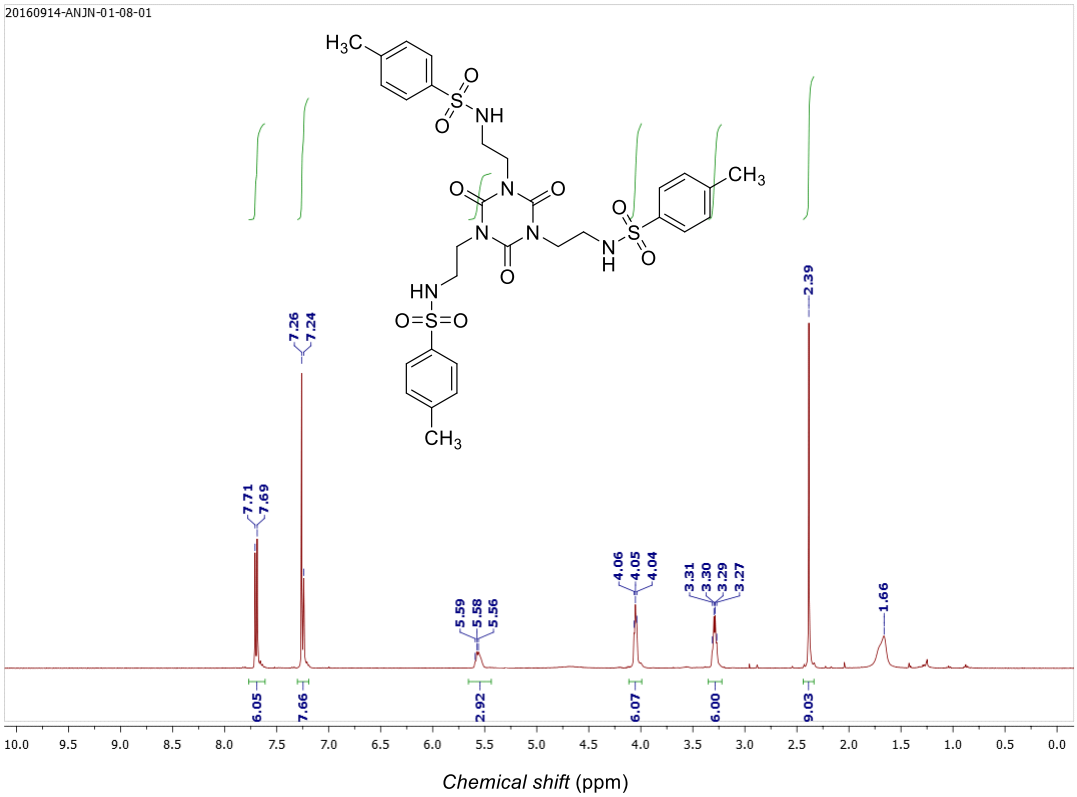



**Figure 2.34** $^{1}$H NMR spectrum of compound **2a** in $CDCl_3$.

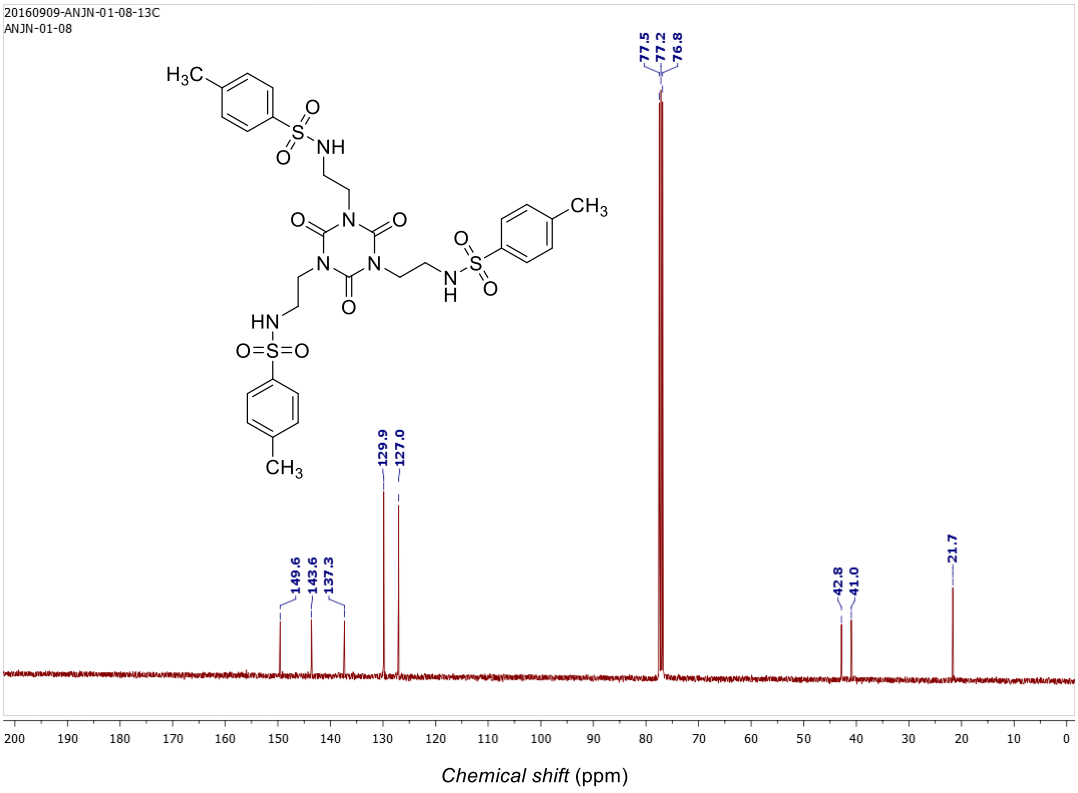



**Figure 2.35** $^{13}$C NMR spectrum of compound **2a** in $CDCl_3$.

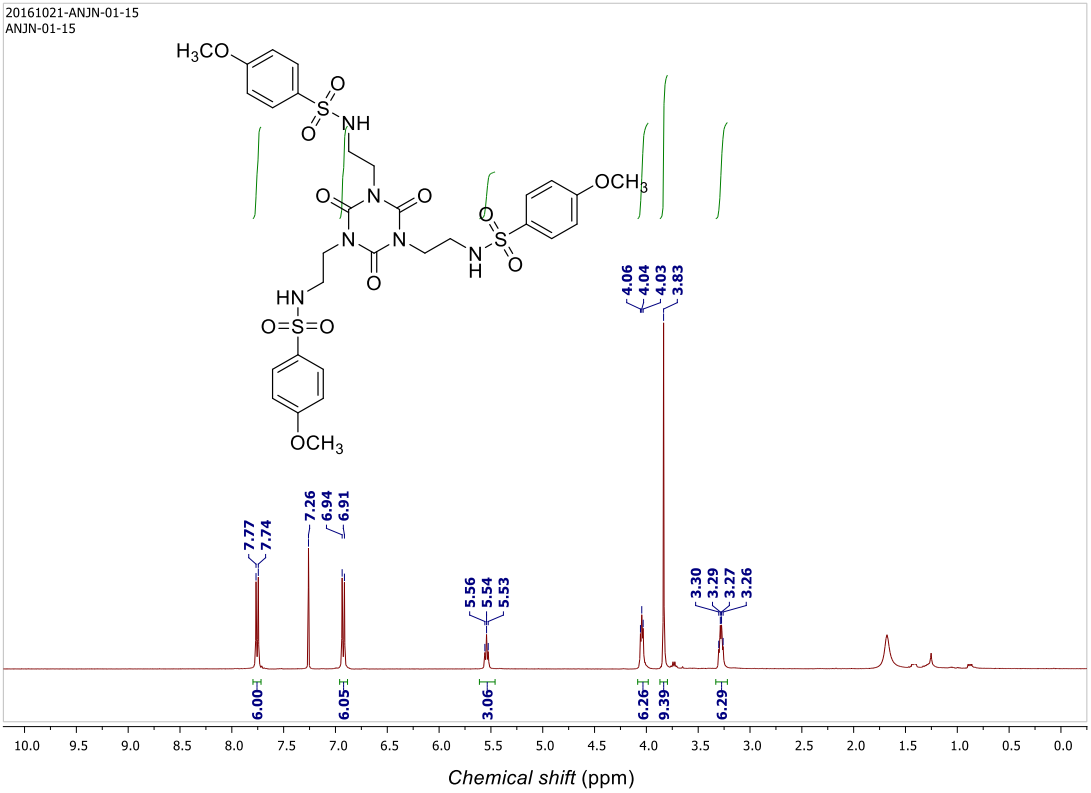



**Figure 2.36** $^{1}$H NMR spectrum of compound **2b** in $CDCl_3$.

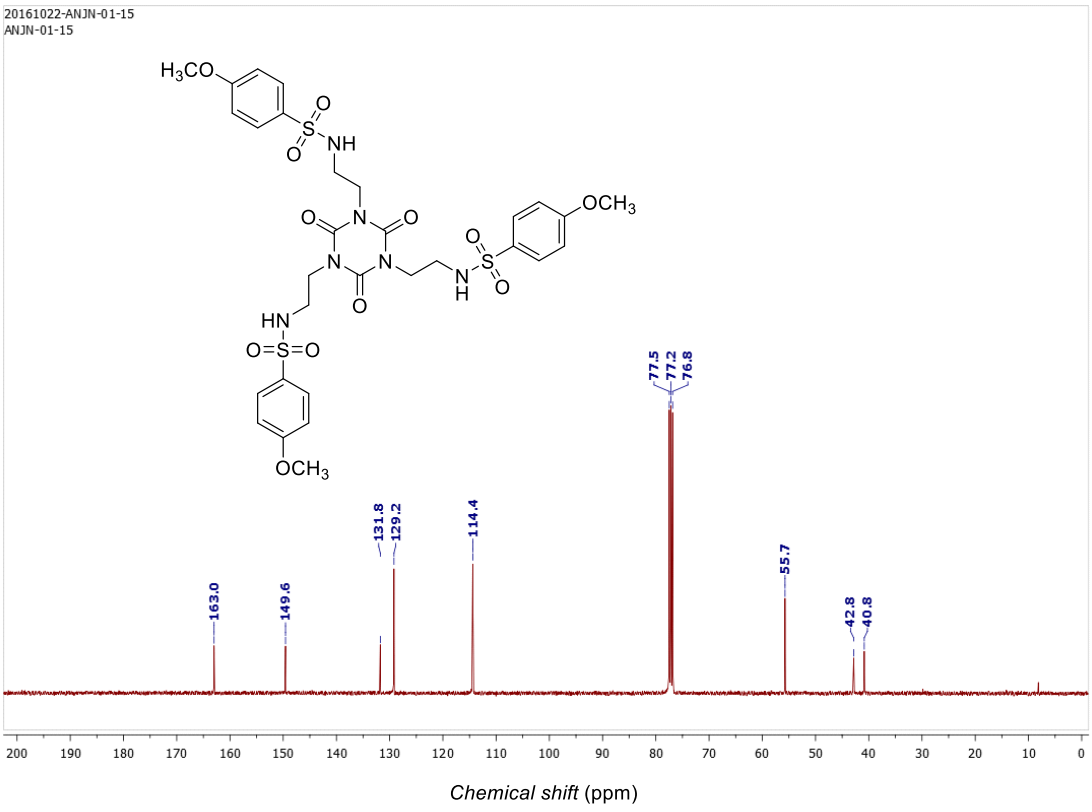



**Figure 2.37** $^{13}$C NMR spectrum of compound **2b** in $CDCl_3$.

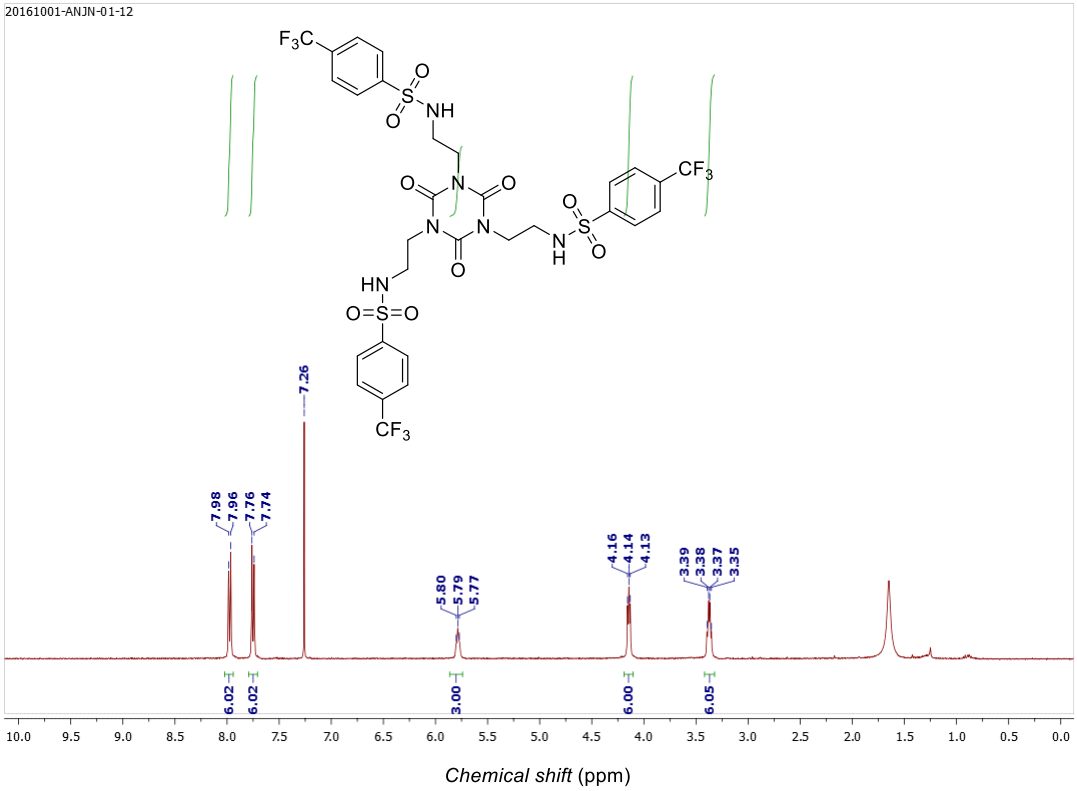



**Figure 2.38** $^{1}$H NMR spectrum of compound **2c** in $CDCl_3$.

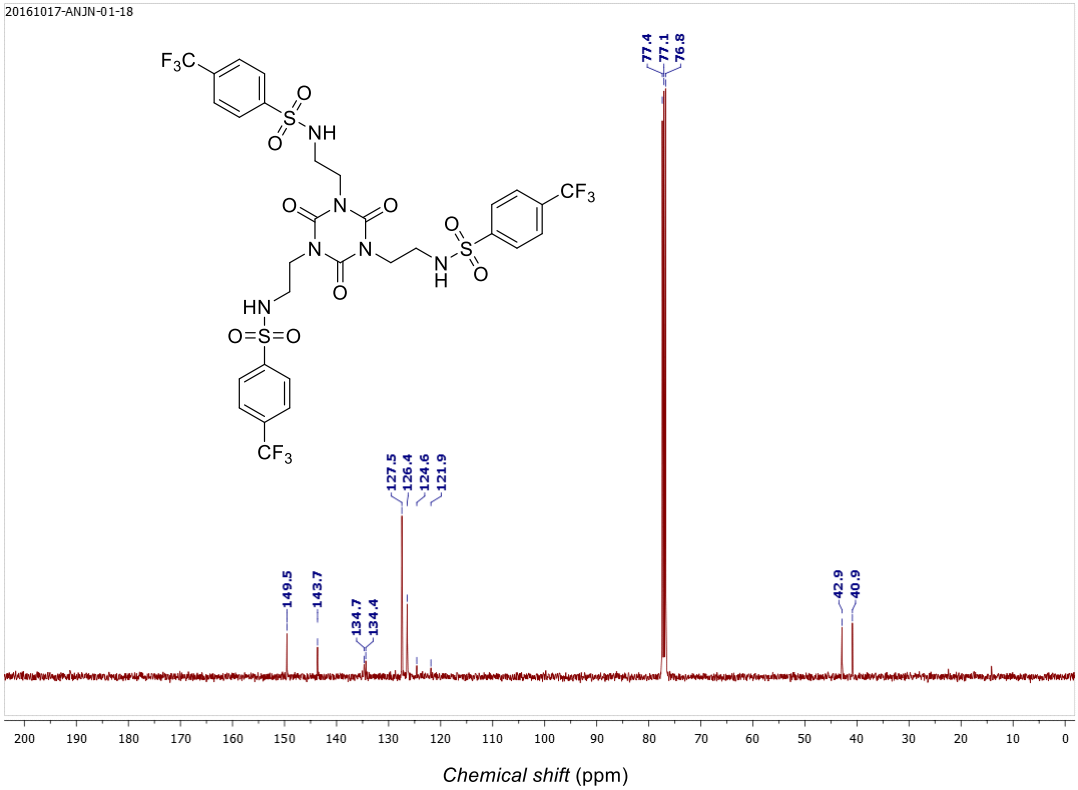



**Figure 2.39** $^{13}$C NMR spectrum of compound **2c** in $CDCl_3$.

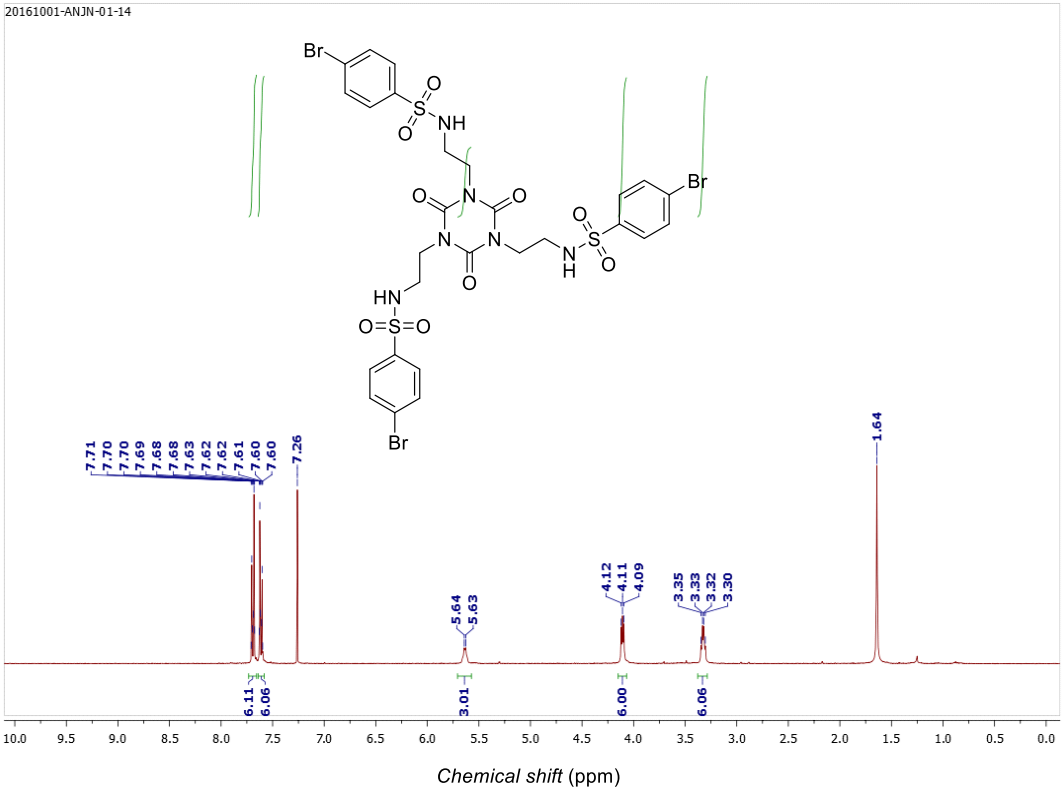



**Figure 2.40** $^{1}$H NMR spectrum of compound **2d** in $CDCl_3$.

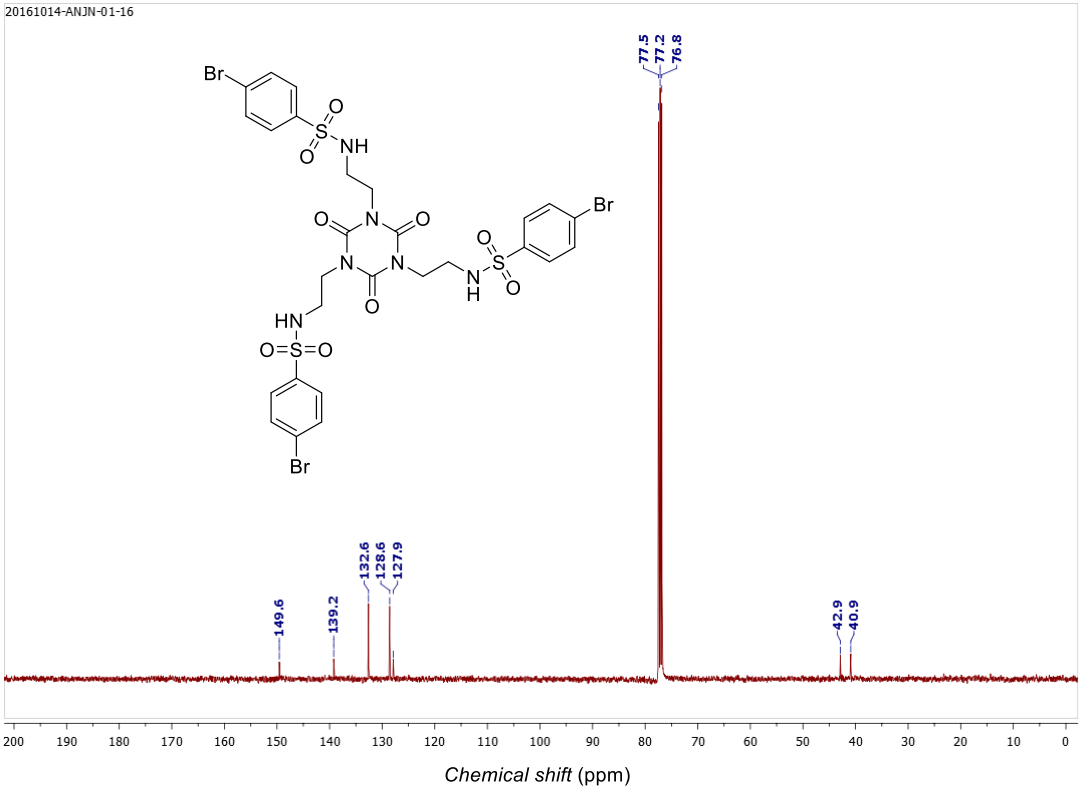



**Figure 2.41** $^{13}$C NMR spectrum of compound **2d** in $CDCl_3$.

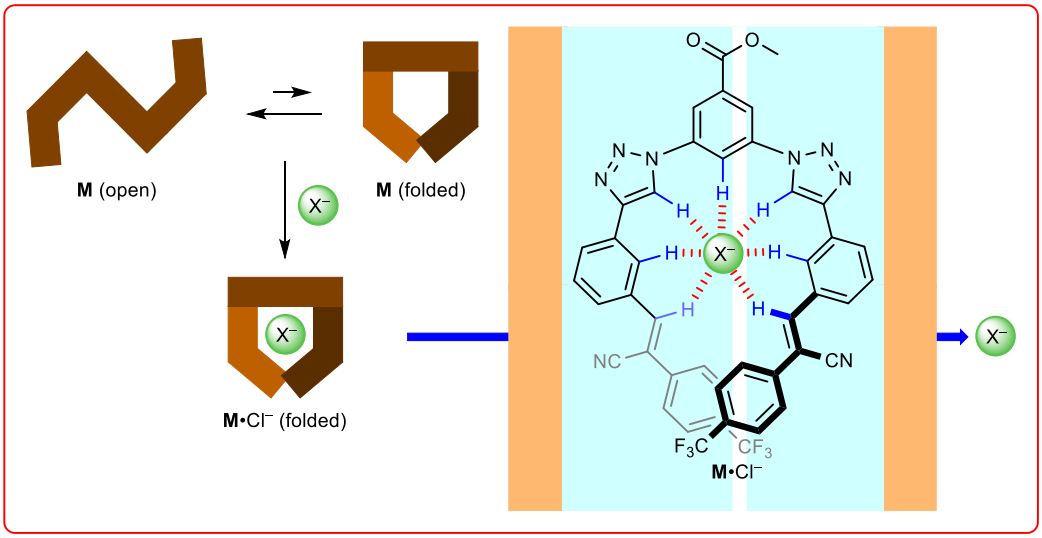
## 2.6. References


1. Cavallo, G.; Metrangolo, P.; Pilati, T.; Resnati, G.; Sansotera, M.; Terraneo, G. *Chem. Soc. Rev.* **2010**, *39*, 3772–3783.
2. Vargas Jentzsch, A.; Emery, D.; Mareda, J.; Metrangolo, P.; Resnati, G.; Matile, S. *Angew. Chem., Int. Ed.* **2011**, *50*, 11675–11678.
3. Gorteau, V.; Bollot, G.; Mareda, J.; Perez-Velasco, A.; Matile, S. *J. Am. Chem. Soc.* **2006**, *128*, 14788–14789.
4. Gorteau, V.; Bollot, G.; Mareda, J.; Matile, S. *Org. Biomol. Chem.* **2007**, *5*, 3000–3012.
5. Mareda, J.; Matile, S. *Chem. – Eur. J.* **2009**, *15*, 28–37.
6. Valiyaveettil, S.; Engbersen, J. F. J.; Verboom, W.; Reinhoudt, D. N. *Angew. Chem., Int. Ed.* **1993**, *32*, 900–901.
7. Ravikumar, I.; Lakshminarayanan, P. S.; Arunachalam, M.; Suresh, E.; Ghosh, P. *Dalton Trans.* **2009**, 4160–4168.
8. Andrews, N. J.; Haynes, C. J. E.; Light, M. E.; Moore, S. J.; Tong, C. C.; Davis, J. T.; Harrell Jr, W. A.; Gale, P. A. *Chem. Sci.* **2011**, *2*, 256–260.
9. Busschaert, N.; Gale, P. A.; Haynes, C. J. E.; Light, M. E.; Moore, S. J.; Tong, C. C.; Davis, J. T.; Harrell, J. W. A. *Chem. Commun.* **2010**, *46*, 6252–6254.
10. Winstanley, K. J.; Allen, S. J.; Smith, D. K. *Chem. Commun.* **2009**, 4299–4301.
11. Roy, A.; Saha, D.; Mukherjee, A.; Talukdar, P. *Org. Lett.* **2016**, *18*, 5864–5867.
12. Roy, A.; Saha, D.; Mandal, P. S.; Mukherjee, A.; Talukdar, P. *Chem. – Eur. J.* **2017**, *23*, 1241–1247.
13. Dutta, R.; Ghosh, P. *Eur. J. Inorg. Chem.* **2012**, *2012*, 3456–3462.
14. Hettche, F.; Hoffmann, R. W. *New J. Chem.* **2003**, *27*, 172–177.
15. Saha, T.; Hossain, M. S.; Saha, D.; Lahiri, M.; Talukdar, P. *J. Am. Chem. Soc.* **2016**, *138*, 7558–7567.
16. Ravikumar, I.; Ghosh, P. *Chem. Commun.* **2010**, *46*, 6741–6743.
17. *Marvin*, ver. 5.8.0; ChemAxon, 2012. http://www.chemaxon.com.
18. Kim, H.-J.; Kim, Y.-H.; Hong, J.-I. *Tetrahedron Lett.* **2001**, *42*, 5049–5052.
19. Datta, B. K.; Thiyagarajan, D.; Samanta, S.; Ramesh, A.; Das, G. *Org.Biomol. Chem.* **2014**, *12*, 4975–4982.
20. Goto, H.; Osawa, E. *J. Am. Chem. Soc.* **1989**, *111*, 8950–8951.

21. Goto, H.; Obata, S.; Nakayama, N.; Ohta, K. *CONFLEX 8*, CONFLEX Corporation, Tokyo, Japan, 2017.
22. Gale, P. A.; Pérez-Tomás, R.; Quesada, R. *Acc. Chem. Res.* **2013**, *46*, 2801−2813.
23. Foster, J. P.; Weinhold, F. *Journal of the American Chemical Society* **1980**, *102*, 7211−7218.
24. Kano, K.; Fendler, J. H. *Biochim. Biophys. Acta, Biomembr.* **1978**, *509*, 289−299.
25. Talukdar, P.; Bollot, G.; Mareda, J.; Sakai, N.; Matile, S. *J. Am. Chem. Soc.* **2005**, *127*, 6528−6529.
26. Roy, A.; Biswas, O.; Talukdar, P. *Chem. Commun.* **2017**, *53*, 3122−3125.
27. Shinde, S. V.; Talukdar, P. *Angew. Chem., Int. Ed.* **2017**, *56*, 4238−4242.
28. Sakai, N.; Brennan, K. C.; Weiss, L. A.; Matile, S. *J. Am. Chem. Soc.* **1997**, *119*, 8726−8727.
29. Rose, L.; Jenkins, A. T. A. *Bioelectrochemistry* **2007**, *70*, 387−393.
30. McNally, B. A.; Koulov, A. V.; Smith, B. D.; Joos, J.-B.; Davis, A. P. *Chemical Communications* **2005**, 1087−1089.
31. Thordarson, P. *Chem. Soc. Rev.* **2011**, *40*, 1305−1323.
32. Frisch, M. J. *et al.*, *Gaussian 09, Revision B.01*, Gaussian, Inc., Wallingford, CT, 2010.
33. Boys, S. F.; Bernardi, F. *Mol. Phys.* **1970**, *19*, 553−566.

*Chapter 3*

# Anion Induced Triazole Foldamers for Transport of $Cl^-$ ion across Phospholipid Membranes



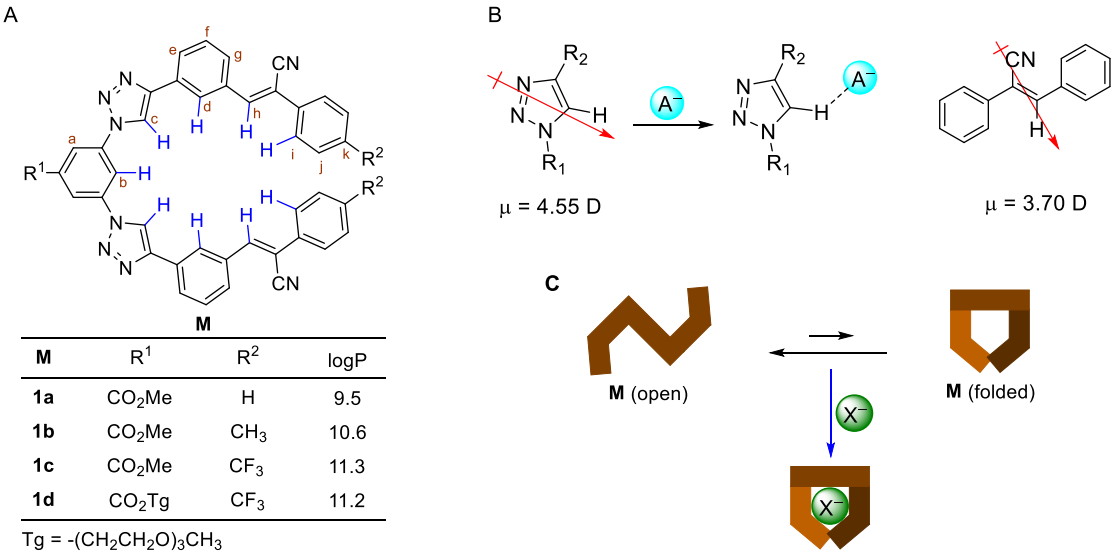
## 3.1. Introduction

The ion transport process via carrier mechanism is generally associated with three different steps such as: (a) partial or complete dehydration of ion from aqueous media followed by its capture by the receptor molecule, (b) insertion into the lipid bilayer membrane followed by transport across it, and finally (c) release of the ions into the aqueous media of other side of the membrane.[1-2] Among the steps mentioned above, the first step is heavily supported by a potent receptor that binds the anion via conventional hydrogen bonding interactions such as N–H and O–H hydrogen bonding interactions. Such types of interactions are employed for designing the receptors in chapter 2, where we have discussed on cyanuric acid-based tris-carboxyamide and tris-sulfonamide tripodal receptors for the $Cl^-$ ion recognition, where one of the type of receptors is capable of binding strongly to the chloride ion with a very high association constant of 32000 $M^{-1}$. The combined effect of three N–H···$Cl^-$, $Cl^-$···π and C–H···$Cl^-$ interactions help the receptor to bind the anion strongly. The moderate to strong hydrogen bonding interactions by such receptors employing N–H and O–H hydrogen bond donors are accrediting such moieties a selectivity and strong anion binding affinities. However, the release of anions is a real issue for such receptors due to a strong binding affinity for anions. A proper structural design of truly reversible receptors with appropriate anion binding affinity and selectivity can be achieved by taking the benefit from the fair potential of the nonconventional hydrogen bonding interactions.

In the development of neutral anion receptors, noncovalent interactions such as CH hydrogen bond,[3] halogen bond,[4] chalcogen bond,[5] pnictogen bond,[6] etc., are now receiving significant attention alongside traditional NH and OH hydrogen bonds.[7-11] Although, a single CH hydrogen bond is very weak,[12] the collective effort of multiple C–H bonds and preorganized structure of a receptor can offer efficient anion binding.[11, 13-15] In this regard, moieties such as 1,2,3-triazoles,[7] cyanostilbenes,[11] electron deficient aryls,[3] etc., with their activated CH donors, due to polarized C–H bonds, are reported to show selective chloride binding over the other halides.[8] Even though there are several sulfate receptors reported in the literature,[16-28] but very few of them are known to bind with sulfate via CH···anion interactions.[29-32] Therefore, we planned to design a receptor that can bind to sulfate and other physiologically relevant anions employing only CH···anion type interactions for the selective recognition of the anion. This type of receptors can also be used for selective transport of $Cl^-$ ion across the bilayer membranes for its fair potential as an anion receptor. Further, only a

limited number of CH hydrogen bond-based transmembrane chloride transporters consisting of 1,2,3-triazoles are reported.[33-35]

Herein, we report a family of triazole-cyanostilbene receptors **1a**–**1d** (Figure 1A) that binds to sulfate ions more efficiently than chloride ions in solution while transports chloride ions efficiently across lipid bilayer membranes. In the design of this class of receptors, we incorporated 1,2,3-triazole, cyanostilbene, and electron deficient aryl moieties to favor multivalent CH hydrogen bond interactions within the binding cavity. The system is expected to adopt a helical conformation while binding to an anion via CH hydrogen bonding interactions. The substituents at the terminal aryl groups and at the ester group were introduced to control the lipophilicity while designing these receptors.[36] The logP values, which dictate the membrane permeability of the receptors, were calculated using the Marvin Sketch program (Figure 1A).[37] The variation in the $R^1$ group from methyl ester to OTg ester makes the molecule more lipophilic, which can help the receptor to easily permeate through the lipid bilayer membrane and hence can enhance the transport activity. On the other hand, the variation at the para substituent in the terminal aromatic ring controls the lipophilicity of the transporter molecules[23, 38] and the acidity of the cyanostilbene proton, and hence enhances the binding affinity of the receptor molecules.




| M | $R^1$ | $R^2$ | logP |
|---|---|---|---|
| **1a** | $CO_2Me$ | H | 9.5 |
| **1b** | $CO_2Me$ | $CH_3$ | 10.6 |
| **1c** | $CO_2Me$ | $CF_3$ | 11.3 |
| **1d** | $CO_2Tg$ | $CF_3$ | 11.2 |

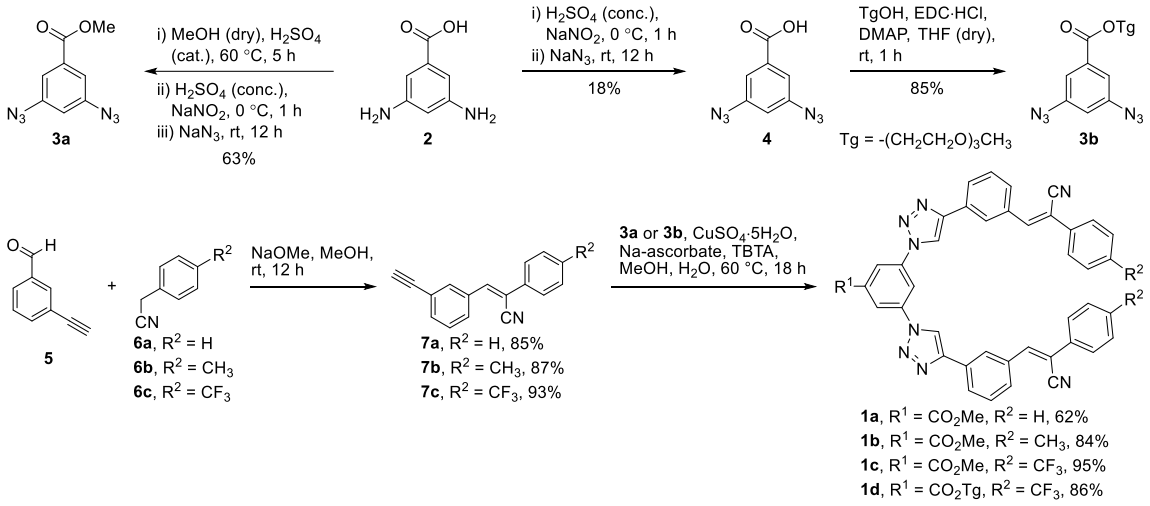
Tg = $-(CH_2CH_2O)_3CH_3$

**Figure 3.1** Chemical structures and estimated logP values of triazole-cyanostilbene receptors **1a**–**1d** (A). The dipole moment of triazole and cyanostilbene C-H protons (B). Schematic representation of conformational change and anion induced foldamer formation (C).

## 3.2. Results and Discussions

### 3.2.1. Synthesis

The triazole cyanostilbene receptors **1a**–**1d** were synthesized from 3,5-diaminobenzoic acid **2** (Scheme 1). At first, the aminobenzoic acid **2** was converted to methyl 3,5-diazidobenzoate **3a** by reacting with methanol followed by diazotization reaction (yield 63%). On the other hand, diazotization of aminobenzoic acid **2** followed by esterification gave the 3,5-diazidobenzoate **3b** in 15% overall yield. The 3-ethynylbenzaldehyde **5** was prepared following the literature reported procedure.[39] Then, 3-ethynylbenzaldehyde **5** was reacted with different benzylcyanide derivatives **6a**–**6c** to synthesize cyanostilbene molecules **7a**–**7c** via Knoevenagel condensation reaction.[40] The subsequent reaction of **7a**–**7c** with 3,5-diazidobenzoate **3a** and **3b** in the presence of $CuSO_4{\cdot}5H_2O$ and sodium ascorbate in degassed methanol/water solvent system gave the clicked product **1a**–**1d** in 62-95% yield.[10]

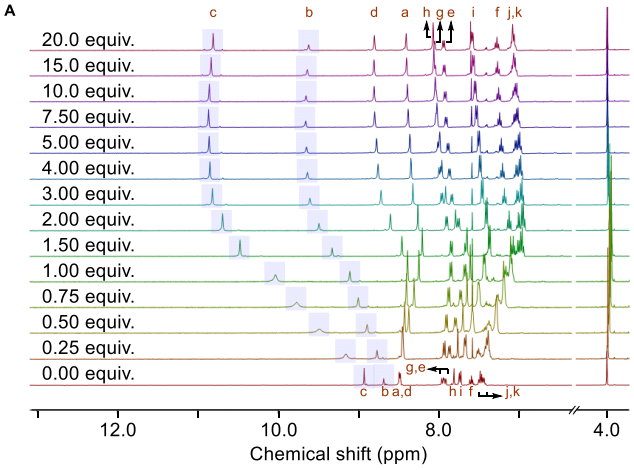



**Scheme 3.1** Synthesis of transporters **1a–1d**.

### 3.2.2. Anion Binding Studies

The binding of the receptor with different anions was investigated by performing the $^1$H NMR titrations in $CD_3CN$, and for that, we have chosen **1a** derivative for its adequate solubility in $CD_3CN$ compared to other derivatives. At first, the $^1$H NMR dilution experiment was conducted to check whether any self-aggregation is present in the receptor solution.[41] The $^1$H NMR spectra recorded in $CD_3CN$ at a concentration range from 3.0 mM to 0.06 mM confirmed no significant self-aggregation of the molecules at and below 1.0 mM of concentration (Figure 3.7). Based on this observation, 1.0 mM concentration was chosen for the $^1$H NMR titration

experiment with different anions to rule out the effect of possible self-aggregation. The addition of $(TBA)_2SO_4$ to **1a** provided significant downfield shifts of 1,2,3-triazole ($H_c$), cyanostilbene ($H_h$) and phenylene ($H_b$ and $H_d$) C–H protons (Figure 3.2A), indicating the multivalent CH···anion hydrogen bonding interactions. Among all these C–H protons, the different values of their dipole moment ($\mu_{triazole}$ = 5.0 D, $\mu_{cyanostilbene}$ = 3.7 D, $\mu_{phenylene}$ = 0.4 D) give different magnitude of C–H bonds polarization and hence gives various chemical shift change.[10-11, 42] The high dipole moment of triazole C–H helps it to bind the anion strongly (via dipole–anion interaction), whereas the phenylene C–H protons interact comparably less strongly with the anion because of the low dipole moment. On the other hand, the shielding behavior of $H_i$ proton in this experiment is due to the anisotropic effect of terminal aromatic groups, where aromatic groups are engaged in π– π stacking interaction upon anion induced foldamer formation (Figure 3.32A and 3.32B).




B

| Anion | $K_a$ |
|---|---|
| $Cl^-$ | 947 $M^{-1}$ ± 13% (1:1) |
| $Br^-$ | 269 $M^{-1}$ ± 10% (1:1) |
| $I^-$ | 26 $M^{-1}$ ± 2% (1:1) |
| $NO_3^-$ | 31 $M^{-1}$ ± 7% (1:1) |
| $SO_4^{2-}$ | 2879 $M^{-1}$ ± 22% (1:1) |
| $ClO_4^-$ | ND |
| $H_2PO_4^-$ | ND |
| $HP_2O_7^{3-}$ | 2340 $M^{-1}$ ± 18% (1:1) |
| | 2995 $M^{-2}$ ± 24% (2:1) |

**Figure 3.2** The partial stacked plot of $^1H$ NMR titration experiment (400 MHz, $CD_3CN$) for compound **1a** (1.0 mM) with the successive addition of $(TBA)_2SO_4$ at 25 ˚C (A). The binding constant values of triazole receptor **1a** with different anions (B).

The binding constant, $K_a$ = 2879 $M^{-1}$ ± 22% was calculated for sulfate by fitting $H_c$ and $H_b$ chemical shift data in 1:1 receptor to anion binding model (Figure 3.8).[43-45] The binding constant for pyrophosphate anion was calculated by fitting $H_c$ and $H_b$ chemical shift data in 2:1 receptor to anion binding model (Figure 3.20), which is found to be 2340 $M^{-1}$ ± 18% ($K_{1:1}$) and 2995 $M^{-2}$ ± 24% ($K_{2:1}$). For $Cl^-$, $Br^-$ and $I^-$, the downfield shifts were observed for $H_c$ and $H_b$ protons and $K_a$ = 947 $M^{-1}$ ± 13%, $K_a$ = 269 $M^{-1}$ ± 10%, and $K_a$ = 26 $M^{-1}$ ± 2%, respectively, were calculated from 1:1 binding model. For $NO_3^-$, the shifts were observed for $H_c$ proton, and $K_a$ = 31 $M^{-1}$ ± 7% was obtained (Figure 3.16). However, $ClO_4^-$ and $H_2PO_4^-$ did not show any

significant downfield shift for their protons and therefore, no binding constant value could be obtained (Figure 3.17 and 3.18). The strong binding affinity of the receptor towards the sulfate ion can be explained based on ion–dipole interaction and size selectivity. The dipole moment of triazole and cyanostilbene units help the C–H bonds to interact with the anions via dipole–ion interactions, where the strength of this interaction is proportional to the charge of the ions.[10] The sulfate ion having two units of negative charge interacts strongly with the receptor via ion-dipole interactions compared to that of the monovalent anions. Moreover, the excellent fitting of the sulfate anion into the receptor's folded cavity provides strong non-covalent interactions for anion binding. On the other hand, among the monovalent anion, the high charge density and better size selectivity of chloride ion help it efficiently bind with the receptor. The binding studies were performed for the triazole compound **1a** with different monovalent and multivalent anions, where most of the anions shows better fitting in 1:1 receptor to anion model. The excellent fitting of most of the anions into the receptor's folded cavity provides strong non-covalent interactions for anion binding and subsequently showed 1:1 binding ratio. On the other hand, the linear lengthy structure of pyrophosphate anion compared to the other anions, interact with two different receptor molecules with its two arm and thereby resulted in 2:1 binding ratio.

We have also performed the electrospray ionization mass spectrometry (ESI-MS) experiment of **1a** with tetrabutylammonium sulfate to know the binding affinity and stoichiometry of the receptor with the $SO_4^{2-}$. In this experiment, we have observed the peak corresponding to [**1a** + $SO_4^{2-}$ + $H^+$], which confirmed that the receptor forms a 1:1 complex with the anion. Moreover, we have not observed peak corresponding to higher order complexes. Next, we have performed a similar type of ESI-MS experiment for the receptor **1a** with tetramethylammonium chloride. Here we found the peak corresponding to [**1a** + $Cl^-$], which confirmed that the receptor forms a 1:1 complex with the $Cl^-$ ion as well.

### 3.2.3. Conformational Analysis

The conformational analysis of the receptor **1a** in the free form and the anion bound form was studied by $^1H$–$^1H$ NOESY NMR experiments. At first, the NOESY NMR data of only receptor **1a** was recorded in DMSO-$d_6$, which showed the interaction of $H_c$ proton with $H_a$, $H_b$, $H_d$, and $H_e$ protons (Figure 3.3A). These interactions are the outcome of the conformational change across aryl-triazole bonds, allowing the receptor to exist in a dynamic equilibrium of open and

closed conformations. The existence of dynamic equilibrium was further proved from computational analysis by calculating the Boltzmann populations of open and close conformations and are found to be 98.5% and 1.5%, respectively, at room temperature (Figure 3.33 and 3.34). In the presence of $SO_4^{2-}$ anion, the interactions of $H_c$ proton with $H_a$ and $H_e$ protons were disappeared (Figure 3.3B), which indicate that the receptor folds into a helical conformation upon binding with anion.

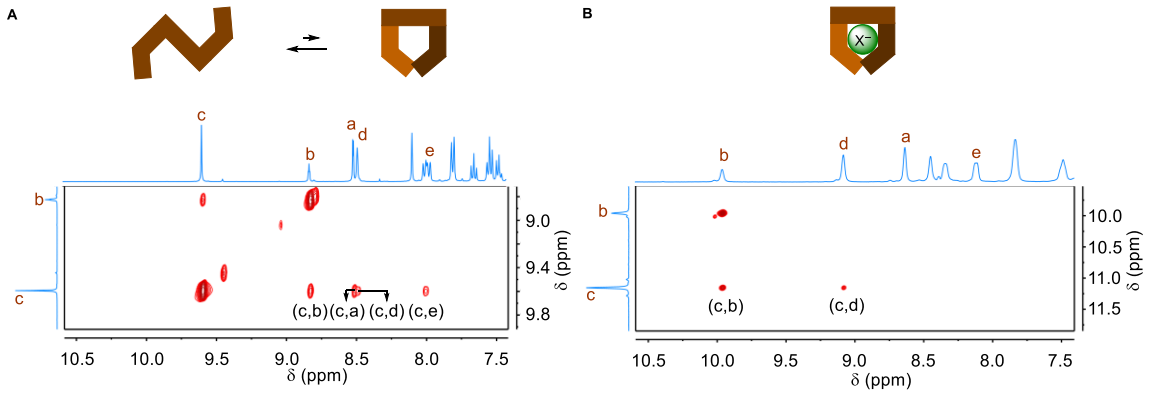



**Figure 3.3** The partial $^1$H-$^1$H NOESY NMR spectrum of free receptor **1a** (5.0 mM) (A), and receptor with $(TBA)_2SO_4$ (B) in $CD_3CN$ at 25 ˚C.

### 3.2.4. Ion Transport Activity

Moderate to good binding affinity of the receptor **1a** with different anions encouraged us to evaluate the ion transport abilities of **1a–1d**. The ion transport activity across the lipid bilayer membrane was checked by incorporating each compound with egg yolk phosphatidylcholine (EYPC) lipid (5 mol% compound-to-lipid ratio) while preparing the large unilamellar vesicles (LUVs) in a suitable salt solution buffered to pH 7.0.[46-47] Pyranine, a pH sensitive fluorescence dye, was entrapped inside the LUVs to monitor the ion transport by the receptors characterized by the enhancement of the dye fluorescence as a result of the collapse of the applied pH gradient. With isoosmolar intravesicular and extravesicular NaCl (100 mM), the comparative ion transport by receptors **1a**–**1d** (5 mol% compound to lipid) provided an activity sequence: **1c** (80.3% after 250 s of transporter addition) > **1d** (71.5% after 250 s of transporter addition) > **1b** (57.3% after 250 s of transporter addition) > **1a** (30.2% after 250 s of transporter addition). The above sequence shows the role of molecular amphiphilicity in the transport of anions (Figure 3.4A). Therefore, further studies were done using the most active transporter **1c**. When the anions in the intravesicular and extravesicular buffers were replaced with isoosmolar $Na_2SO_4$ and $Na_4P_2O_7$, no considerable fluorescence intensity increment was observed (Figure

3.4B). These results implied that the receptor is a good transporter of $Cl^-$ but fails to transport sulfate and pyrophosphate ions across the lipid bilayer membranes. The poor transport of sulfate and pyrophosphate ion by the receptor across the bilayer membrane can be explained by considering the dehydration energy of the anion. The first step of the ion transport process, i.e., the dehydration of ions, requires a significant amount of energy (dehydration energy), which has to compensate by the binding energy of the receptor with the ion. So here sulfate and pyrophosphate ions are heavily hydrated in the aqueous media compared to that of chloride ion (hydration energy, $\Delta G_h$ of sulfate = –1080 kJ $mol^{-1}$, $\Delta G_h$ of chloride = –340 kJ $mol^{-1}$) because of the high ionic charge.[48] So, taking all these things into consideration, more energy is required to dehydrate the sulfate and pyrophosphate ions, which cannot be compensated by their binding energy with the receptor molecule and hence, making it difficult for the transport across the lipid bilayer membrane.

To further compare the anion selectivity of **1c**, a variation of the anions ($Cl^-$, $Br^-$, $I^-$, $NO_3^-$, $ClO_4^-$, and $SCN^-$) in the extravesicular buffer provided a sequence: $Cl^-$ >> $Br^-$ > $NO_3^-$ > $SCN^-$ > $I^-$ > $ClO_4^-$ (Figure 3.4C). When similar studies were performed by changing the extravesicular cations ($Li^+$, $Na^+$, $K^+$, $Rb^+$, and $Cs^+$), no accountable cation selectivity was observed (Figure 3.27B).

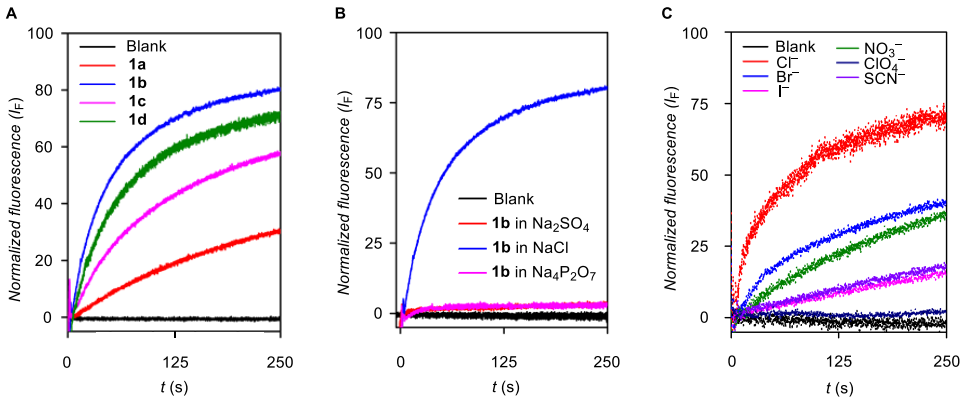



**Figure 3.4** The comparison of ion transport activities of **1a**–**1d** (5 mol% compound to lipid ratio) in NaCl buffer solution (A). The ion transport activity of **1c** (5 mol% compound to lipid ratio) across lipid bilayer in $Na_2SO_4$, NaCl, and $Na_4P_2O_7$ buffer solution (B), and ion transport activity by varying the extravesicular anions by **1c** (4 mol% transporter to lipid) across lipid bilayer membrane (C).

A further comparison of cation selectivity of **1c** was made while measuring the $Cl^-$ influx using LUVs with trapped lucigenin.[49] The variation of extravesicular cations ($Li^+$, $Na^+$, $K^+$, $Rb^+$, and $Cs^+$) provided no difference in the $Cl^-$ influx rate, indicating a concomitant $NO_3^-$

efflux associated with the quenching of fluorescence (Figure 3.5A). To further prove such mechanism, the $Cl^-$ influx was monitored in the absence and presence of valinomycin, a naturally occurring $K^+$ carrier.[50] A significantly faster $Cl^-$ influx in the presence of valinomycin, due to the cooperative effect of transporter and valinomycin confirmed the $Cl^-/NO_3^-$ antiport as the primary mechanism of ion transport by **1c** (Figure 3.5B). Further, U-tube experiments were performed to evaluate the possibility of carrier formation by **1c**.[23] In this experiment, the bilayer was substituted with a chloroform layer in which the compound **1c** (1 mM) was dissolved. Further, NaCl (500 mM) and $NaNO_3$ (500 mM) were placed in the source and receiver arms, respectively, and a time-dependent increase in $Cl^-$ concentration (ppm) in the receiver arm was monitored using the chloride ion selective electrode (ISE). Significant increase in the $Cl^-$ concentration in the receiver arm only in the presence of **1c** corroborated to a carrier-mediated ion transport mechanism (Figure 3.5C).

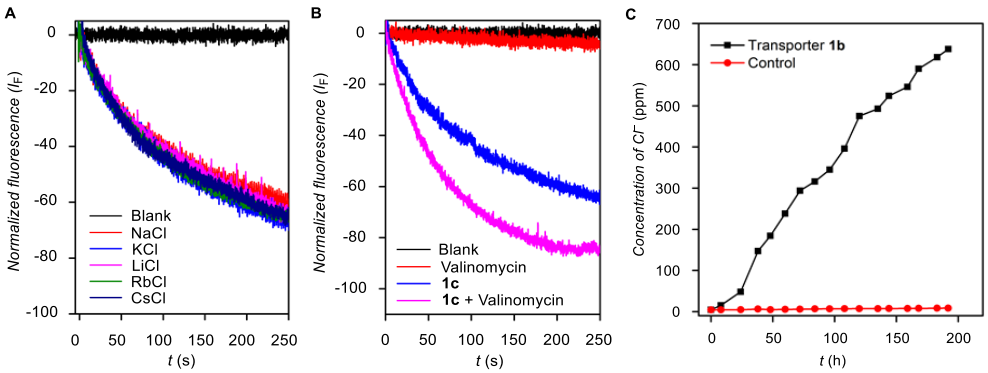



**Figure 3.5** The ion transport activity by varying the extravesicular cations in lucigenin assay (A), and the same lucigenin assay with and without valinomycin (2.5 pM, B) by **1c** (15 mol% transporter to lipid) across lipid bilayer membrane. The change of chloride ion concentration (ppm) in the U-tube experiment with transporter **1c** (1 mM) and with control experiment (C).

### 3.2.5. Geometry Optimization and Binding Energy Calculation

To correlate the anion binding interactions observed from $^1H$ NMR titration, geometry optimization studies for **1a** and **1c** with $SO_4^{2-}$ and $Cl^-$ were carried out in the gas phase, i.e., without considering any solvents or other molecules in the vicinity of the experimental object. At first, the initial geometries of [**1a**+$SO_4^{2-}$], [**1a**+$Cl^-$], [**1c**+$SO_4^{2-}$] and [**1c**+$Cl^-$] complexes were generated from the CONFLEX 8 program.[51] Subsequently, the most probable conformation of each complex obtained from this program was then optimized by using the Gaussian 09 program[52] with a B3LYP functional and 6-31G(d,p) basis set.[53] The energy-minimized structure of each complex confirmed the folded helical conformation of the

receptor. The [**1a**+$SO_4^{2-}$] (Figure 3.32A) and [**1c**+$SO_4^{2-}$] (Figure 3.6A and 3.6B) complexes confirmed the hydrogen bonding interactions of 1,2,3-triazole ($H_c$), cyanostilbene ($H_h$), and phenylene ($H_b$ and $H_d$) C–H protons with $SO_4^{2-}$. However, for [**1a**+$Cl^-$] (Figure 3.32B) and [**1c**+$Cl^-$] (Figure 3.6C and 3.6D) complexes, 1,2,3-triazole ($H_c$), and phenylene ($H_b$) C–H protons provided the necessary interactions with the anion. Moreover, π-stacking interaction between the terminal aromatic rings was also evident in each complex. The binding energies of [**1a**+$SO_4^{2-}$], [**1a**+$Cl^-$], [**1c**+$SO_4^{2-}$], and [**1c**+$Cl^-$] complexes were calculated and found to be –110.63, –45.15, –119.10, and –47.89 kcal $mol^{-1}$ respectively (see ESI). These binding energy data indicated that for a particular receptor, the binding with $SO_4^{2-}$ is more favorable than $Cl^-$.

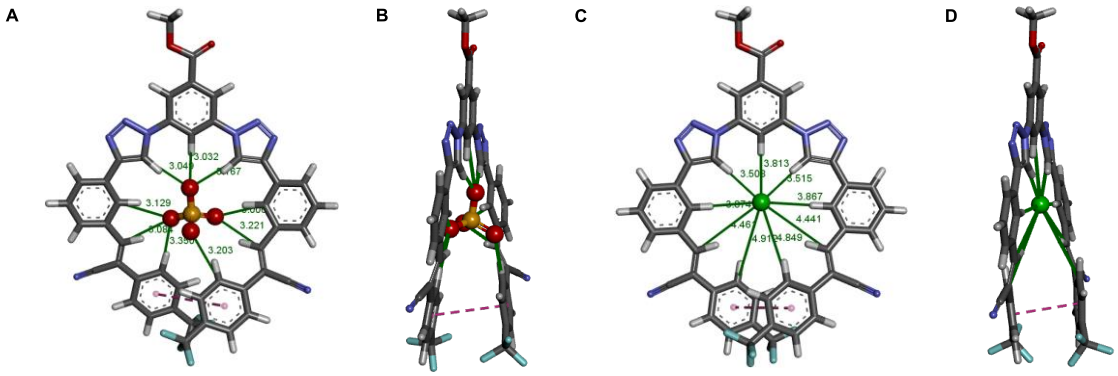



**Figure 3.6** The geometry optimized structures of [**1c**+$SO_4^{2-}$]: top view (A) and side view (B); [**1c**+$Cl^-$]: top view (C) and side view (D).

## 3.3. Conclusion

In conclusion, we have synthesized a family of triazole cyanostilbene receptors, which forms a foldameric structure while binding to different monovalent and divalent anions within its cavity. Anion recognition of each receptor was accomplished purely by multivalent CH···anion interactions. This class of receptors provided the strongest binding with $SO_4^{2-}$ followed by $Cl^-$, however, only the latter could be transported across lipid bilayer membranes. Among all receptors, the one with a *para*-$CF_3$ group on each terminal aromatic ring showed most efficient ion transport. The anion binding interactions were studied by $^1H$ NMR titration studies with different anions and also correlated by geometry optimization studies. The transporter molecules act as mobile carriers of $Cl^-$ and exchange anions via antiport mechanism.

## 3.4. Experimental Section

### 3.4.1. General Methods

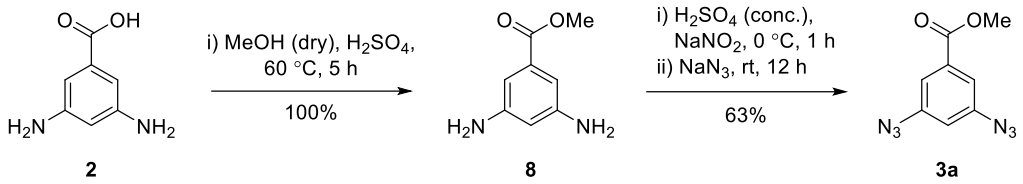
All starting materials and reagents used for the synthesis were purchased from commercial sources and used without further purification. Special precautions should be taken while adding the sodium azide to the acidic reaction mixture and handling organic azide compounds, as any misconduct in both the situation can cause a serious explosion. All $^{1}H$, $^{13}C$, and $^{19}F$ NMR spectra were recorded on either Bruker 400 MHz or Jeol 400 MHz spectrometers, where the $^{13}C$ and $^{19}F$ NMR spectra were recorded on proton-decoupled mode. High resolution mass spectra (HRMS) were acquired in the ESI (positive and negative) mode from MicroMass ESI-TOF MS spectrometer. Fluorescence spectra were recorded on a Fluoromax-4 from Horiba scientific, Jobin Yvon Edison equipped with an injector port and a magnetic stirrer. The chloride ion concentration in U-tube experiment was measured using chloride-selective electrode from Accumet.

### 3.4.2. Synthesis Procedures

**Methyl 3,5-diazidobenzoate ($C_8H_6N_6O_2$) 3a:**

At first, 2.0 g of the 3,5-diaminobenzoic acid **2** was refluxed in methanol (15 mL) for 5 h in the presence of conc. $H_2SO_4$ (0.5 mL). After completion of the reaction, solvent was evaporated to get the ester in quantitative yield and the crude product was used for the next steps without further purification. Then the ester (2.0 g, 12.04 mmol) was taken in a 250 mL round bottom flask and dissolved in 40 mL of 25% $H_2SO_4$. Then the solution was cooled to 0 ˚C and $NaNO_2$ (1.81 g, 26.24 mmol) solution in water (3 mL) was added slowly into that reaction mixture for the time period of 30 min. The solution was then stirred at 0 ˚C for about 30 min before the $NaN_3$ (3.41 g, 52.47 mmol) was added. The reaction mixture was then allowed to reach at room temperature slowly and stirred for about 24 h. After completion of the reaction, the compound was extracted in ethyl acetate (2 × 30 mL) while washing with water (20 mL). The combined organic ethyl acetate layers were evaporated to get the crude product. The crude product was then purified using silica gel column chromatography (2% ethyl acetate in petroleum ether) to obtain compound **3a** (1.8 g, 8.25 mmol) as a light yellow liquid. Yield: 63%. $^{1}H$ NMR (400 MHz, $CDCl_3$) $\delta$ 7.48 (d, $J$ = 2.1 Hz, 2H), 6.79 (t, $J$ = 2.1 Hz, 1H), 3.94 (s, 3H). $^{13}C$ NMR (101

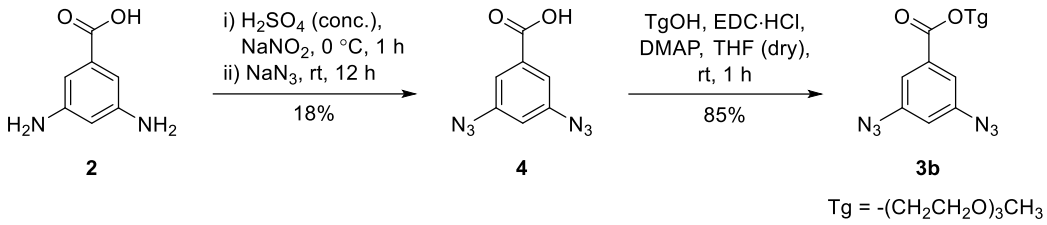
MHz, $CDCl_3$) $\delta$ 165.5, 142.4, 133.4, 116.4, 114.0, 52.8. These characterization data were matched with the reported data.[13]




**Scheme 3.2** Synthesis of compound **3a**.

**2-(2-(2-Methoxyethoxy)ethoxy)ethyl 3,5-diazidobenzoate ($C_{14}H_{18}N_6O_5$) 3b:**

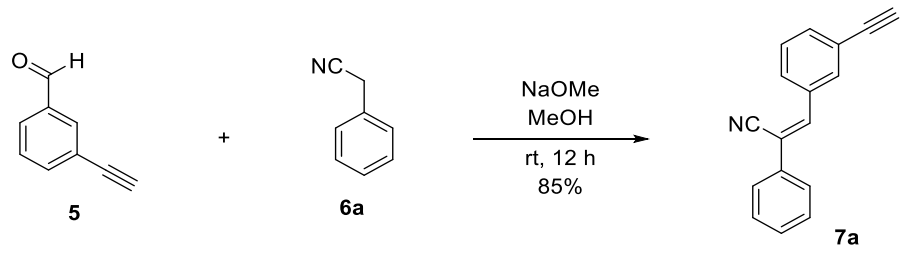
1.0 g of the 3,5-diaminobenzoic acid **2** was taken in a 250 mL round bottom flask and dissolved in 20 mL of 25% $H_2SO_4$. Then the solution was cooled to 0 ˚C and $NaNO_2$ (1.0 g, 14.46 mmol) solution in water was added slowly and stirred at 0 ˚C for about 30 min before the $NaN_3$ (1.71 g, 26.29 mmol) was added. The reaction mixture was then allowed to reach at room temperature slowly and stirred for about 24 h. After completion of the reaction, the compound was extracted in ethyl acetate (2 × 50 mL) while washing with water (30 mL). The combined organic ethyl acetate layer was then washed with brine and the solvent was evaporated to get the crude azide **4** (0.25 g, 18%). The crude product was used immediately for the next steps without further purification. The azide **4** (100 mg, 0.5 mmol) was taken in a 25 mL round bottomed flask and dissolved in dry THF. Then into that solution triethyleneglycol (80 mg, 0.50 mmol), EDC·HCl (121 mg, 0.64 mmol), and DMAP (6 mg, 0.05 mmol) were added and stirred at room temperature for 2 h. After completion of the reaction, the compound was extracted in ethyl acetate (2 × 20 mL) while washing with water (15 mL). The combined organic ethyl acetate layers were evaporated to get the crude product. The crude product was then purified using silica gel column chromatography (5% ethyl acetate in petroleum ether) to obtain compound **3b** (0.15 g, 0.42 mmol) as a colorless liquid. Yield: 85%. $^1$H NMR (400 MHz, $CDCl_3$) $\delta$ 7.49 (d, $J$ = 2.2 Hz, 2H), 6.80 (t, $J$ = 2.1 Hz, 1H), 4.53 – 4.45 (m, 2H), 3.86 – 3.79 (m, 2H), 3.74 – 3.69 (m, 2H), 3.69 – 3.66 (m, 2H), 3.66 – 3.63 (m, 2H), 3.57 – 3.52 (m, 2H), 3.37 (s, 3H). $^{13}$C NMR (101 MHz, $CDCl_3$) $\delta$ 164.6, 142.2, 133.2, 116.4, 113.7, 71.8, 70.69, 70.64, 70.59, 68.9, 64.7, 59.0. These characterization data were matched with the reported data.[54]




**Scheme 3.3** Synthesis of compound **3b**.

**General Procedure for the Synthesis of 7a, 7b, and 7c:** In a 50 mL round bottom flask, 3-ethynylbenzaldehyde **5** (250 mg, 1.92 mmol, 1.0 equiv.), and benzylcyanides **6a**–**6c** (2.11 mmol, 1.1 equiv, purchased from commercial sources) were taken and dissolved in 10 mL of dry MeOH under inert atmosphere. Then sodium methoxide (9.60 mmol, 5 equiv.) was added and reaction mixture was stirred under nitrogen atmosphere for 12 h at room temperature. The progress of reaction was monitored in between by checking the TLC. After completion of reaction, the MeOH was evaporated and the product was extracted into $CHCl_3$ (30 mL) by the washing with water (2 × 20 mL) and followed by brine solution (10 mL). The organic part was then dried over $Na_2SO_4$ and the solvent was evaporated in rotary evaporator to get crude product. The crude product was then purified using silica gel column chromatography (2–3% ethyl acetate in petroleum ether) to obtain liquid compound **7a**–**7c** in 85-93% yield.

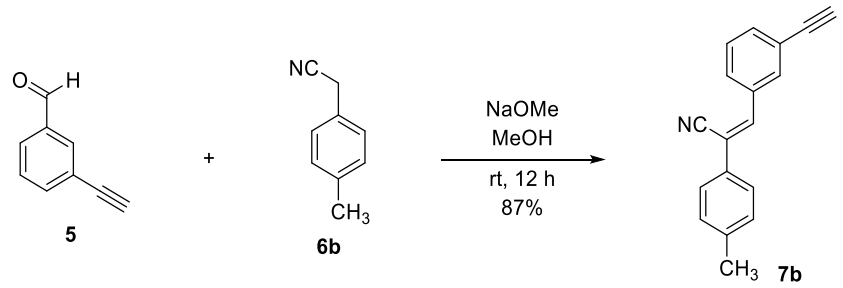
**(*Z*)-3-(3-ethynylphenyl)-2-phenylacrylonitrile ($C_{17}H_{11}N$) 7a:**




**Scheme 3.4** Synthesis of compound **7a**.

Purified by column chromatography (3 % ethyl acetate in petroleum ether). Light yellow liquid (0.37 g, 1.64 mmol). Yield: 85%. $^1$H NMR (400 MHz, $CDCl_3$) $\delta$ 7.96 (d, $J$ = 8.1 Hz, 1H), 7.91 (t, $J$ = 1.6 Hz, 1H), 7.68 (dd, $J$ = 8.2, 1.4 Hz, 2H), 7.55 (dt, $J$ = 7.7, 1.2 Hz, 1H), 7.52 – 7.38 (m, 5H), 3.14 (s, 1H). $^{13}$C NMR (101 MHz, $CDCl_3$) $\delta$ 143.0, 141.0, 134.3, 133.9, 133.2, 129.6, 129.3, 129.2, 129.1, 126.2, 123.2, 117.7, 113.0, 82.8, 78.4. HRMS (ESI) m/z: $[M + H]^+$ Calcd for $C_{17}H_{12}N$ 230.0969; Found 230.0972.

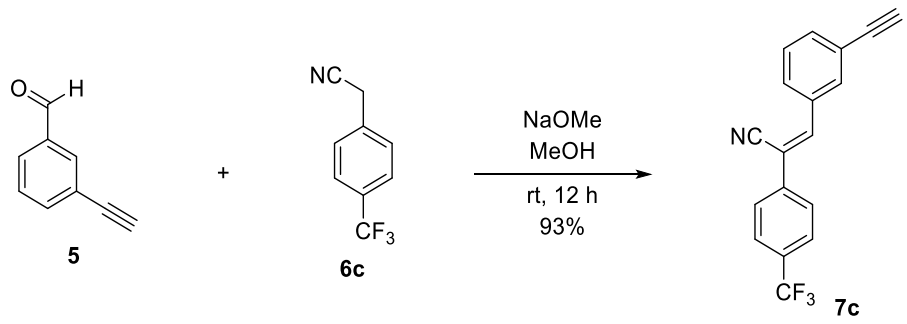
**(*Z*)-3-(3-ethynylphenyl)-2-(p-tolyl)acrylonitrile ($C_{18}H_{13}N$) 7b:**




**Scheme 3.5** Synthesis of compound **7b**.

Purified by column chromatography (2 % ethyl acetate in petroleum ether). Colourless liquid (0.41 g, 1.69 mmol). Yield: 87%. $^{1}$H NMR (400 MHz, $CDCl_3$) $\delta$ 7.94 (d, $J$ = 8.0 Hz, 1H), 7.89 (s, 1H), 7.57 (d, $J$ = 8.2 Hz, 2H), 7.53 (d, $J$ = 7.8 Hz, 1H), 7.47 – 7.37 (m, 2H), 7.26 (d, $J$ = 8.0 Hz, 2H), 3.13 (s, 1H), 2.40 (s, 3H). $^{13}$C NMR (101 MHz, $CDCl_3$) $\delta$ 140.0, 139.9, 134.2, 133.7, 133.2, 131.5, 129.9, 129.1, 129.0, 126.1, 123.1, 117.8, 113.0, 82.8, 78.3, 21.4. HRMS (ESI) m/z: $[M + H]^+$ Calcd for $C_{18}H_{14}N$ 244.1126; Found 244.1122.

**(*Z*)-3-(3-ethynylphenyl)-2-(4-(trifluoromethyl)phenyl) acrylonitrile ($C_{18}H_{10}F_3N$) 7c:**



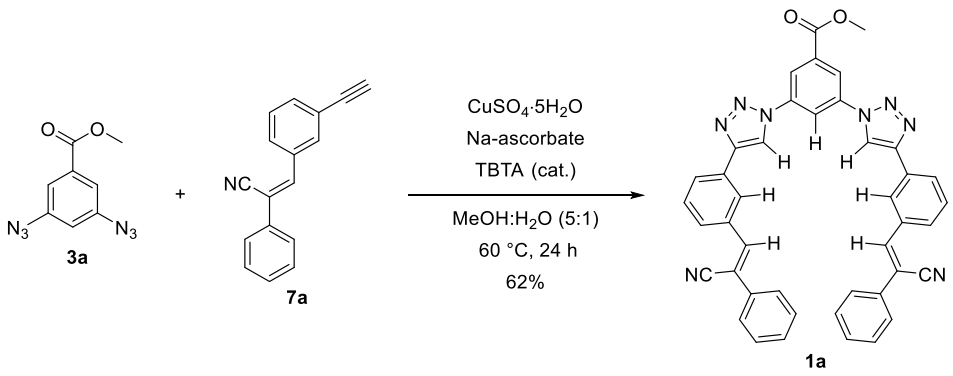

**Scheme 3.6** Synthesis of compound **7c**.

Purified by column chromatography (2 % ethyl acetate in petroleum ether). Colourless liquid (0.53 g, 1.78 mmol). Yield: 93%. $^{1}$H NMR (400 MHz, $CDCl_3$) $\delta$ 7.97 (d, $J$ = 7.9 Hz, 1H), 7.93 (s, 1H), 7.79 (d, $J$ = 8.3 Hz, 2H), 7.72 (d, $J$ = 8.4 Hz, 2H), 7.58 (dt, $J$ = 7.7, 1.2 Hz, 1H), 7.56 (s, 1H), 7.46 (t, $J$ = 7.8 Hz, 1H), 3.15 (s, 1H). $^{13}$C NMR (101 MHz, $CDCl_3$) $\delta$ 143.0, 137.7, 134.6, 133.5, 133.4, 131.5 (q, $J$ = 32.9 Hz), 129.3, 129.3, 126.5, 126.3 (q, $J$ = 3.7 Hz), 123.9 (q, $J$ = 272.3 Hz), 123.4, 117.2, 111.6, 82.6, 78.7. HRMS (ESI) m/z: $[M + H]^+$ Calcd for $C_{18}H_{11}F_3N$ 298.0843; Found 298.0845.

**General Procedure for the Synthesis of 1a, 1b, 1c, and 1d:** In a 100 mL round-bottom flask, di-azide **3a** or **3b** (0.23 mmol, 1.0 equiv.) and cyanostilbene **7a**–**7c** (0.57 mmol, 2.5 equiv.) were taken and dissolved in 20 mL of methanol:water (5 : 1) solution. The solution was then

degassed for 30 min using nitrogen gas balloon. Then into that solution $CuSO_4 \cdot 5H_2O$ (6 mg, 0.02 mmol, 0.1 equiv.), TBTA (Tris[(1-benzyl-1*H*-1,2,3-triazol-4-yl)methyl]amine; 12 mg, 0.02 mmol, 0.1 equiv.), and sodium ascorbate (9 mg, 0.05 mmol, 0.2 equiv.) were added sequentially. The whole reaction mixture was allowed to stir under nitrogen atmosphere for 24 h while heating (oil bath) at 60 °C. The progress of the reaction was monitored in between by checking the consumption of di-azide. After completion of reaction, the methanol was evaporated in rotary evaporator. The compound was then extracted into ethyl acetate while washing with water (3 × 30 mL) followed by brine solution (15 mL). The combined organic layers were evaporated to get crude product and then purified using silica gel column chromatography (30–50 % ethyl acetate in petroleum ether) to obtain compounds **1a**–**1d** in 62-95% yield.

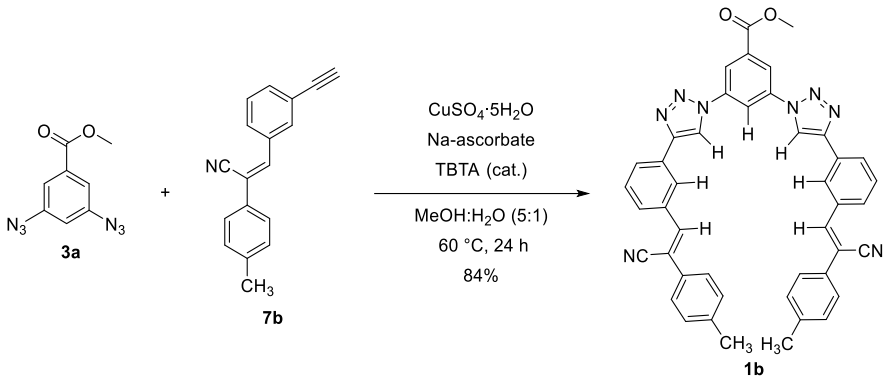
**Methyl 3,5-bis(4-(3-((*Z*)-2-cyano-2-phenylvinyl) phenyl)-1*H*-1,2,3-triazol-1-yl) benzoate ($C_{42}H_{28}N_8O_2$) 1a:**




**Scheme 3.7** Synthesis of compound **1a**.

Purified by column chromatography (50 % ethyl acetate in petroleum ether). Yellow solid (97 mg, 0.14 mmol). Yield: 62%. Mp 129–131 °C. $^1$H NMR (400 MHz, DMSO-$d_6$) $\delta$ 9.64 (s, 2H), 8.88 (s, 1H), 8.58 – 8.54 (m, 2H), 8.52 (s, 2H), 8.13 (s, 2H), 8.01 (dd, $J$ = 17.0, 7.7 Hz, 4H), 7.81 (d, $J$ = 7.5 Hz, 4H), 7.67 (t, $J$ = 7.8 Hz, 2H), 7.54 (t, $J$ = 7.5 Hz, 4H), 7.47 (t, $J$ = 7.0 Hz, 2H), 3.99 (s, 3H). $^{13}$C NMR (101 MHz, DMSO-$d_6$): $\delta$ 164.3, 147.0, 142.4, 137.7, 134.4, 133.6, 132.9, 130.5, 129.6, 129.4, 129.2, 128.23, 127.4, 126.4, 125.8, 120.2, 119.1, 117.7, 114.6, 111.1, 53.0. HRMS (ESI) m/z: $[M + H]^+$ Calcd for $C_{42}H_{29}N_8O_2$ 677.2413; Found 677.2417.

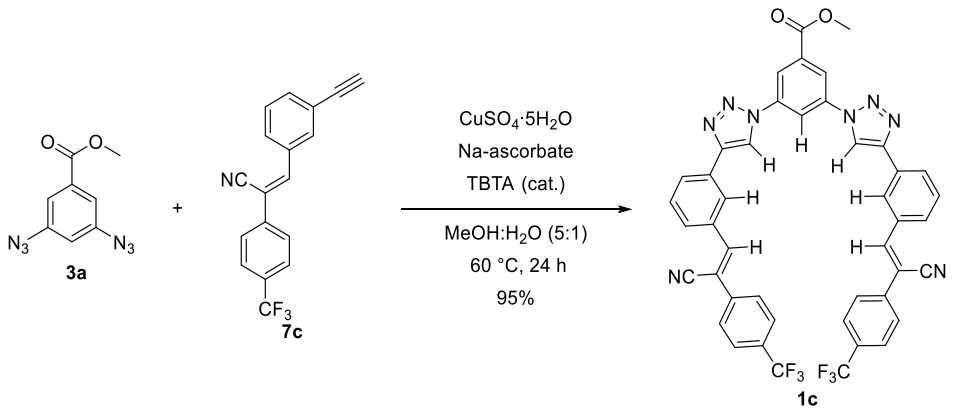
**Methyl 3,5-bis(4-(3-((*Z*)-2-cyano-2-(p-tolyl)vinyl) phenyl)-1*H*-1,2,3-triazol-1-yl) benzoate ($C_{44}H_{32}N_8O_2$) 1b:**




**Scheme 3.8** Synthesis of compound **1b**.

Purified by column chromatography (40% ethyl acetate in petroleum ether). Yellow solid (136 mg, 0.19 mmol). Yield: 84%. Mp 107–109 °C. $^{1}$H NMR (400 MHz, $CDCl_3$) $\delta$ 8.66 (t, $J$ = 1.9 Hz, 1H), 8.53 (d, $J$ = 1.9 Hz, 2H), 8.49 (s, 2H), 8.37 (s, 2H), 8.02 (d, $J$ = 7.8 Hz, 2H), 7.95 (d, $J$ = 8.0 Hz, 2H), 7.61 – 7.56 (m, 8H), 7.28 (s, 4H), 4.05 (s, 3H), 2.41 (s, 6H). $^{13}$C NMR (101 MHz, $CDCl_3$) $\delta$ 164.6, 148.3, 140.5, 139.8, 138.2, 134.6, 133.7, 131.4, 130.4, 129.9, 129.8, 129.1, 127.7, 126.9, 126.0, 120.4, 118.2, 118.1, 115.5, 112.4, 53.2, 21.4. HRMS (ESI) m/z: $[M + H]^+$ Calcd for $C_{44}H_{33}N_8O_2$ 705.2726; Found 705.2723.

**Methyl 3,5-bis(4-(3-((*Z*)-2-cyano-2-(4-(trifluoromethyl) phenyl)vinyl) phenyl)-1*H*-1,2,3-triazol-1-yl) benzoate ($C_{44}H_{26}F_6N_8O_2$) 1c:**

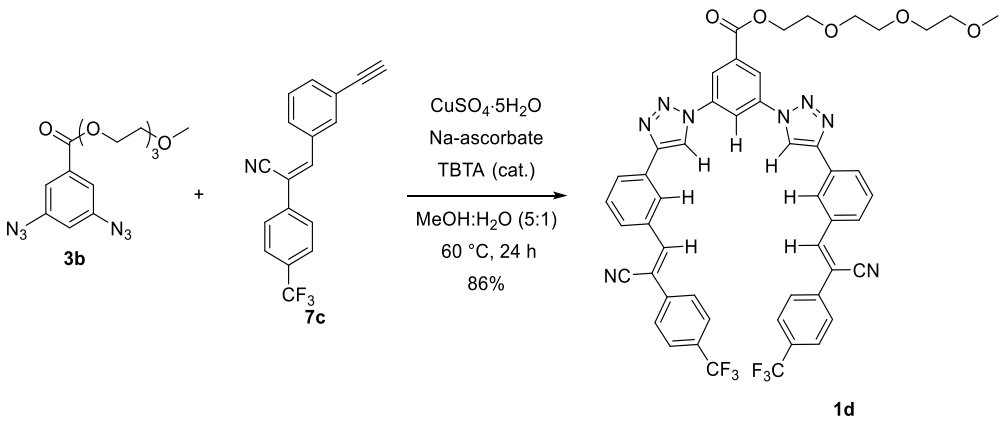



**Scheme 3.9** Synthesis of compound **1c**.

Purified by column chromatography (40% ethyl acetate in petroleum ether). White solid (178 mg, 0.22 mmol). Yield: 95%. Mp 139–141 °C. $^{1}$H NMR (400 MHz, DMSO-$d_6$) $\delta$ 9.58 (s, 2H), 8.81 (s, 1H), 8.50 (d, $J$ = 4.6 Hz, 4H), 8.25 (s, 2H), 7.99 (d, $J$ = 7.8 Hz, 8H), 7.87 (d, $J$ = 8.3 Hz, 4H), 7.65 (t, $J$ = 7.6 Hz, 2H), 3.99 (s, 3H). $^{19}$F NMR (376.6 MHz, $CDCl_3$): $\delta$ –62.77. $^{13}$C NMR (101 MHz, $CDCl_3$ : DMSO-$d_6$ = 2 : 1) $\delta$ 164.8, 148.1, 143.8, 138.2, 137.5, 134.0, 133.8,

131.3 (q, *J* = 32.7 Hz), 130.6, 129.9, 129.5, 128.5, 126.9, 126.4, 126.2 (q, *J* = 3.6 Hz), 123.8 (q, *J* = 272.2 Hz), 120.5, 118.5, 117.5, 115.6, 111.0, 53.2. HRMS (ESI) m/z: $[M + H]^+$ Calcd for $C_{44}H_{27}F_6N_8O_2$ 813.2160; Found 813.2166.

**2-(2-(2-methoxyethoxy)ethoxy)ethyl 3,5-bis(4-(3-((*Z*)-2-cyano -2-(4-(trifluoromethyl) phenyl)vinyl)phenyl)-1*H*-1,2,3-triazol-1-yl)benzoate ($C_{50}H_{38}F_6N_8O_5$) 1d:**




**Scheme 3.10** Synthesis of compound **1d**.

Purified by column chromatography (30% ethyl acetate in petroleum ether). White solid (116 mg, 0.12 mmol). Yield: 86%. Mp 98–100 °C. $^1$H NMR (400 MHz, $CDCl_3$) $\delta$ 8.74 (t, *J* = 2.1 Hz, 1H), 8.60 (s, 2H), 8.58 (d, *J* = 2.1 Hz, 2H), 8.44 (s, 2H), 8.08 (d, *J* = 7.8 Hz, 2H), 8.02 (d, *J* = 7.9 Hz, 2H), 7.84 (d, *J* = 8.2 Hz, 4H), 7.74 (d, *J* = 8.3 Hz, 4H), 7.72 (s, 2H), 7.63 (t, *J* = 7.8 Hz, 2H), 4.67 – 4.56 (m, 2H), 3.95 – 3.88 (m, 2H), 3.79 – 3.74 (m, 2H), 3.72 (d, *J* = 3.0 Hz, 2H), 3.68 – 3.62 (m, 2H), 3.56 – 3.49 (m, 2H), 3.30 (s, 3H); $^{19}$F NMR (376.6 MHz, $CDCl_3$): $\delta$ –62.74. $^{13}$C NMR (101 MHz, $CDCl_3$) $\delta$ 164.2, 148.0, 143.6, 138.2, 137.6, 134.0, 133.7, 131.4 (q, *J* = 32.9 Hz), 130.8, 129.9, 129.3, 128.5, 127.2, 126.5, 126.3 (q, *J* = 3.6 Hz), 123.9 (q, *J* = 272.2 Hz), 120.4, 118.4, 117.5, 115.7, 111.1, 72.0, 70.9, 70.7, 70.7, 69.1, 65.3, 59.0. HRMS (ESI) m/z: $[M + H]^+$ Calcd for $C_{50}H_{39}F_6N_8O_5$ 945.2947; Found 945.2948.

### 3.4.3. $^1$H NMR Dilution Studies

To check whether any self-aggregation is present in **1a**, we have recorded a series of $^1$H NMR spectra by diluting the sample from 3.0 mM to 0.06 mM. The gradual sharpness and downfield shift of the C-H protons change were observed while changing the concentration from 3.0 mM to 1.0 mM and remained same after further dilutions (Figure 3.7). These results suggested that self-aggregation is not present at and below 1.0 mM concentration. Therefore, concentration of 1.0 mM was chosen for the $^1$H NMR titration experiment to rule out the effect of plausible self-aggregation.

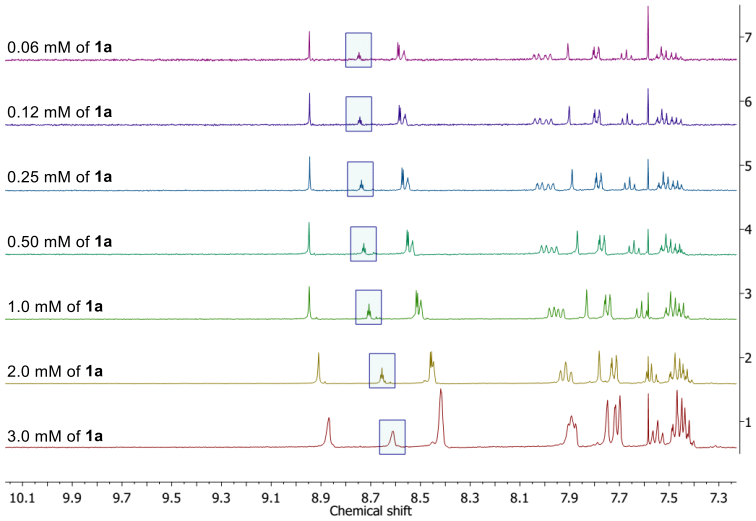



**Figure 3.7** Stacked plot for $^1$H-NMR experiment (400 MHz, acetonitrile-$d_3$) for compound **1a** with the successive dilution from 3.0 mM to 0.06 mM. The aryl C-H proton chemical shifts are inside the box.

### 3.4.4. $^1$H NMR Titration

The chemical shifts of C–H protons were fitted in the Bindfit for the calculation of the binding constant.[43] The titration data obtained from the NMR experiments were used in the Bindfit model[55] (supramolecular.org) to get the binding constant values. The binding analysis for the anions were performed in the 1:1, 1:2, and 2:1 model, where the 1:1 model has shown the best fitting in most cases (except pyrophosphate) with less amount of error. We have shown the fitting analysis data from the Bindfit model (Figure 3.8) for $SO_4^{2-}$ anion, where the 1:1 model is found to be the best-fitted one. The high hygroscopic nature of the tetrabutylammonium sulfate salt resulted the deviance while preparing the stock solution, which could be the reason for the high error value observed from the analysis. However, we have performed the titration experiment thrice, and in all three cases, similar error values were observed during the binding analysis. We could not perform the binding studies for the most active transporter **1c** due of the solubility issue.

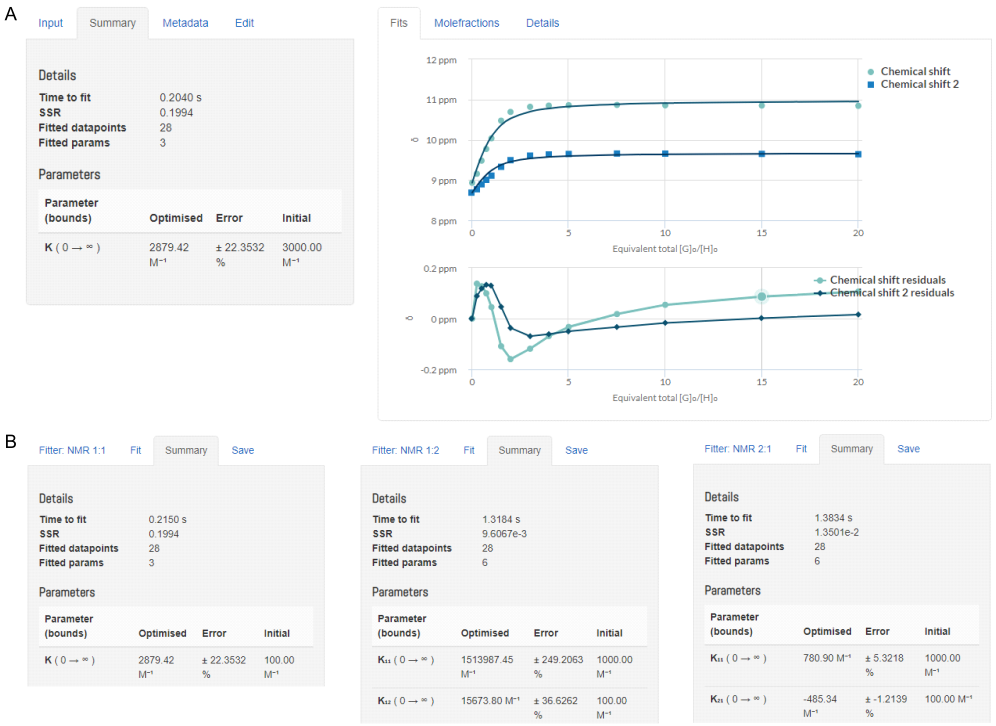



**Figure 3.8** Screenshot of the fitted data plot from supramolecular.org. The binding constant was found to be 2879 $M^{-1}$ ± 22% in 1:1 receptor **1a** to anion binding model (left side). The changing pattern of chemical shift and chemical shift residuals with the increasing equivalent $(TBA)_2SO_4$ (right side) (A). The Bindfit URL for this experiment is: http://app.supramolecular.org/bindfit/view/49fafa6f-d664-4f8e-aedf-7247ee7c0377. Screenshot of the binding constant values with their respective error in 1:1, 1:2, and 2:1 model, from supramolecular.org (B).

The high value of error (for the $SO_4^{2-}$ anion) in binding constant calculation is probably due to the inaccurate $(TBA)_2SO_4$ stock solution concentration caused by the hygroscopic nature of the tetrabutylammonium sulfate salt.

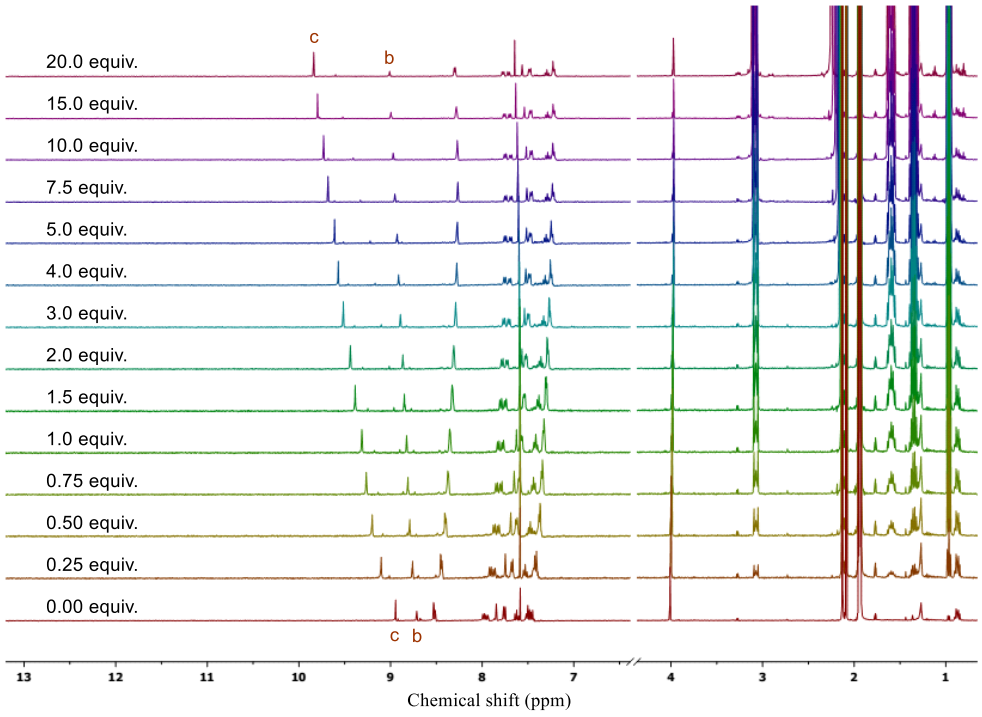



**Figure 3.9** Stacked plot for $^1$H NMR titration experiment (400 MHz, acetonitrile-$d_3$) for compound **1a** (1.0 mM) with the successive addition of TBACl.

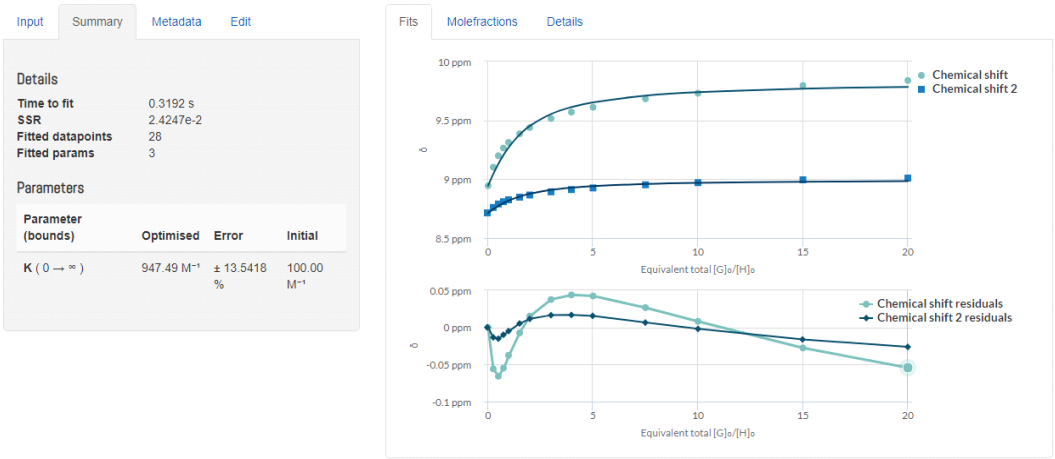



**Figure 3.10** Screenshot of the fitted data plot from supramolecular.org. The binding constant was found to be 947 $M^{-1}$ ± 13% in 1:1 receptor to anion binding model (left side). The changing pattern of chemical shift and chemical shift residuals with the increasing equivalent TBACl (right side). The Bindfit URL for this experiment is: http://app.supramolecular.org/bindfit/view/31837d8c-cd63-4480-a773-6b53434690cd.

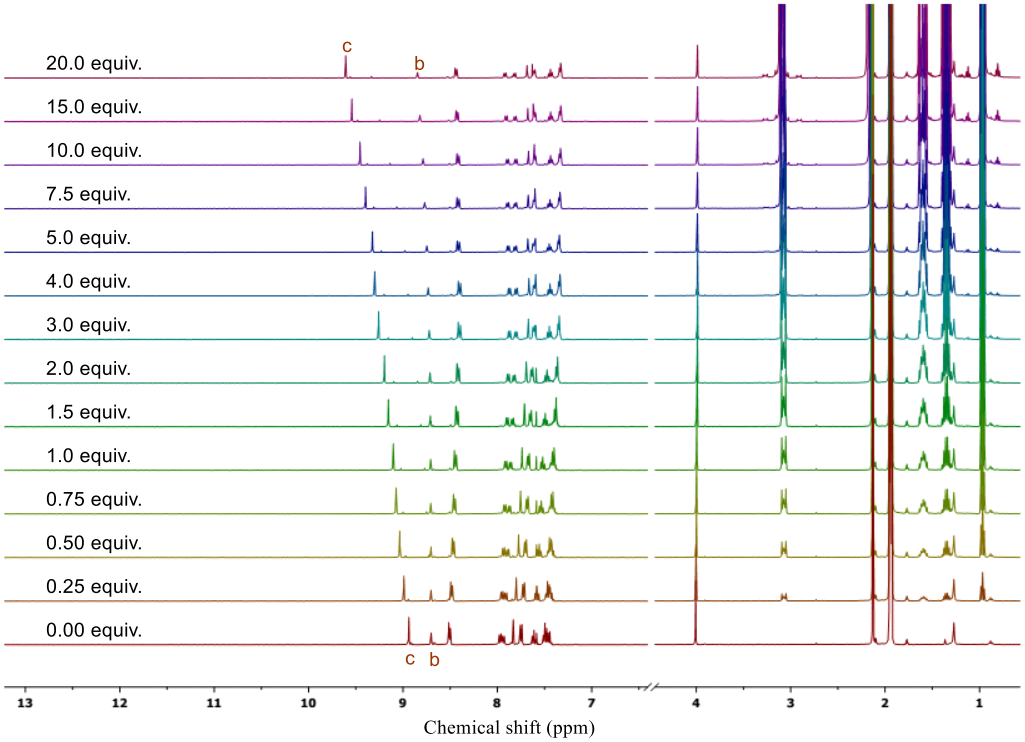



**Figure 3.11** Stacked plot for $^{1}$H NMR titration experiment (400 MHz, acetonitrile-$d_3$) for compound **1a** (1.0 mM) with the successive addition of TBABr.

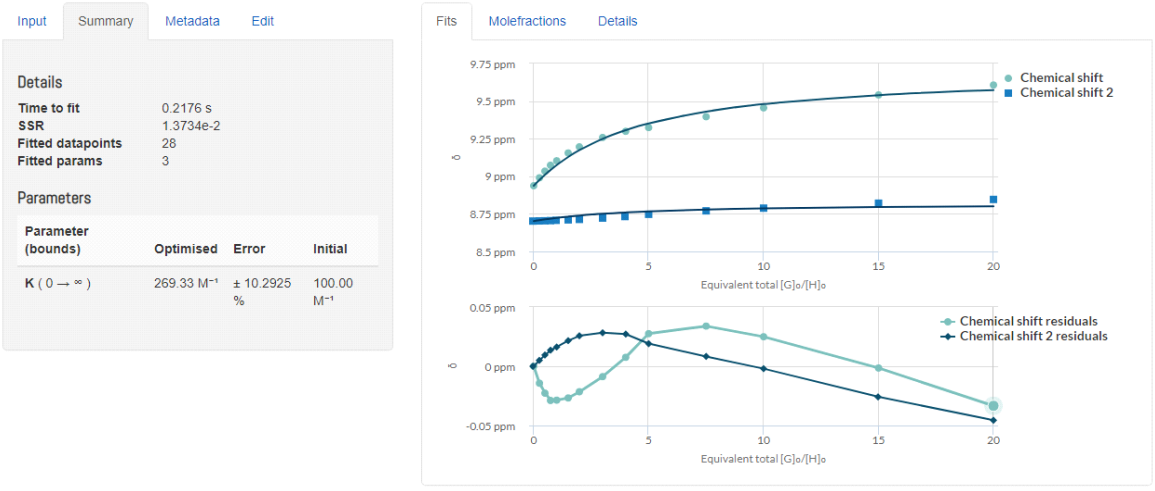



**Figure 3.12** Screenshot of the fitted data plot from supramolecular.org. The binding constant was found to be 269 $M^{-1}$ ± 10% in 1:1 receptor to anion binding model (left side). The changing pattern of chemical shift and chemical shift residuals with the increasing equivalent TBABr (right side). The Bindfit URL for this experiment is: http://app.supramolecular.org/bindfit/view/ce93819f-1f10-4e9f-925d-2f7754a46a1d.

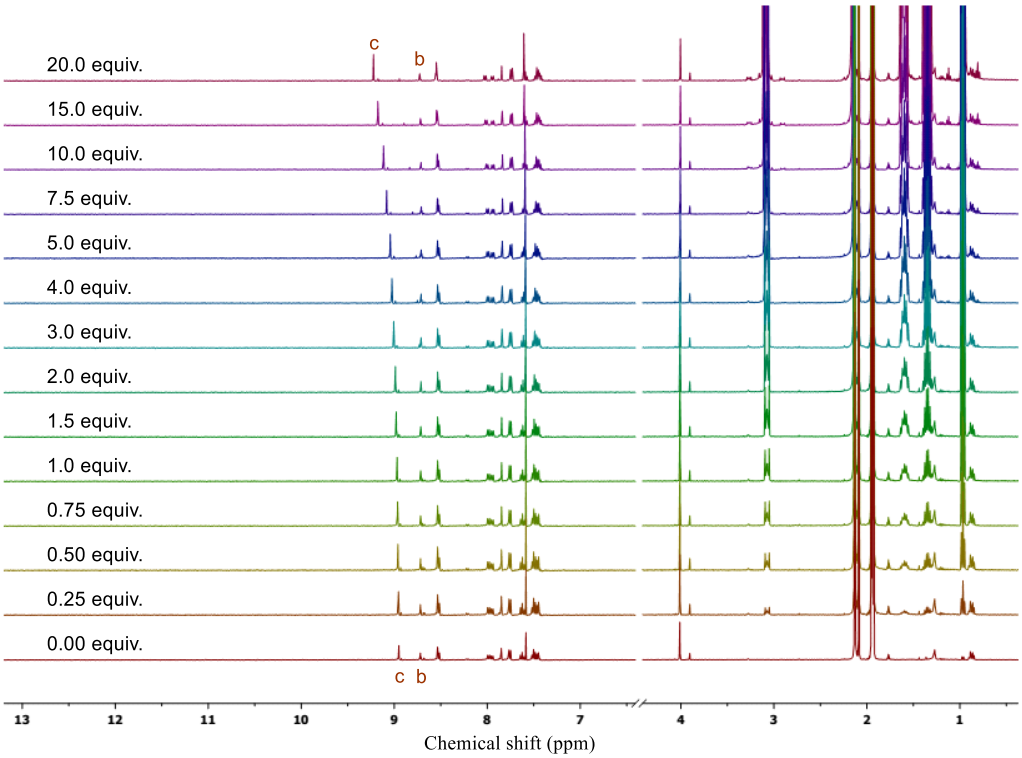



**Figure 3.13** Stacked plot for $^{1}$H NMR titration experiment (400 MHz, acetonitrile-$d_3$) for compound **1a** (1.0 mM) with the successive addition of TBAI.

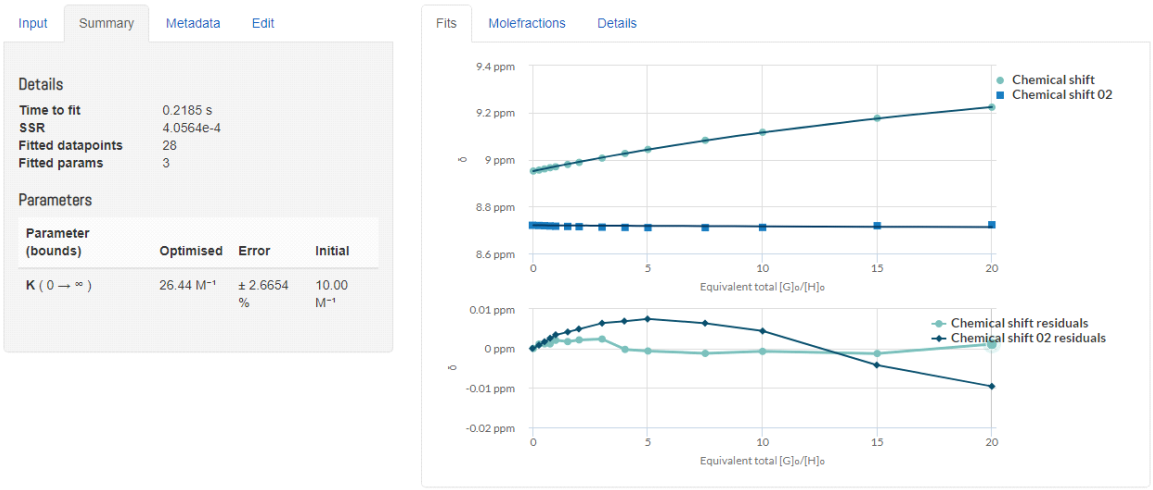



**Figure 3.14** Screenshot of the fitted data plot from supramolecular.org. The binding constant was found to be 26 $M^{-1}$ ± 2% in 1:1 receptor to anion binding model (left side). The changing pattern of chemical shift and chemical shift residuals with the increasing equivalent TBAI (right side). The Bindfit URL for this experiment is: http://app.supramolecular.org/bindfit/view/e15fca3f-234f-44c1-b100-e243961e6401.

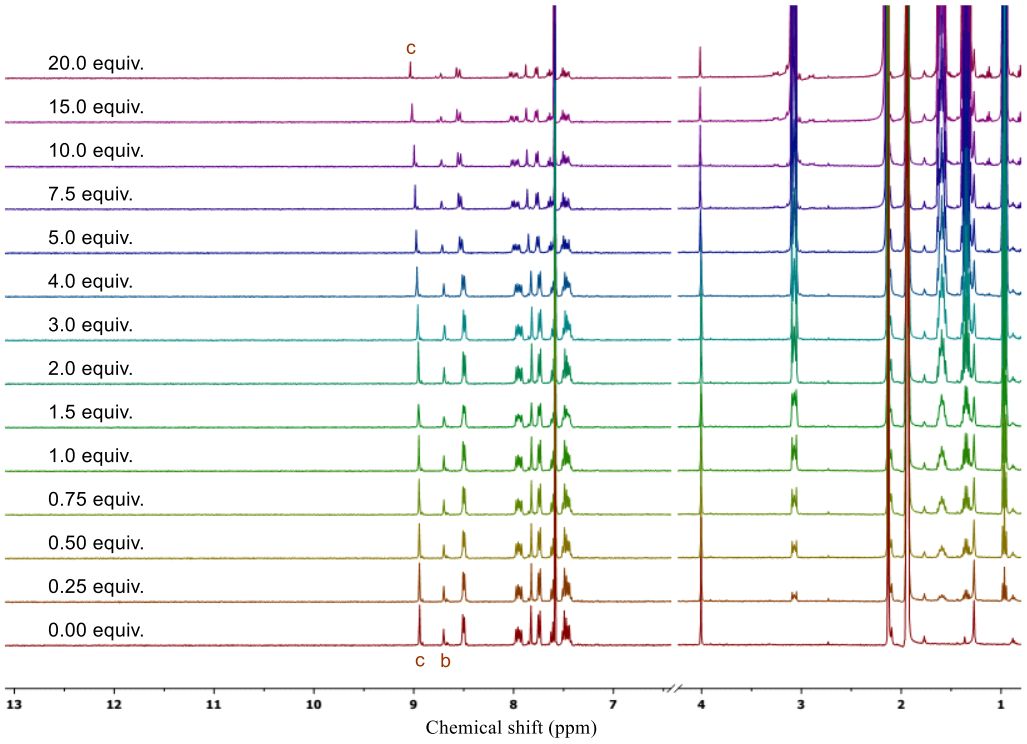



**Figure 3.15** Stacked plot for $^{1}$H NMR titration experiment (400 MHz, acetonitrile-$d_3$) for compound **1a** (1.0 mM) with the successive addition of $TBANO_3$.

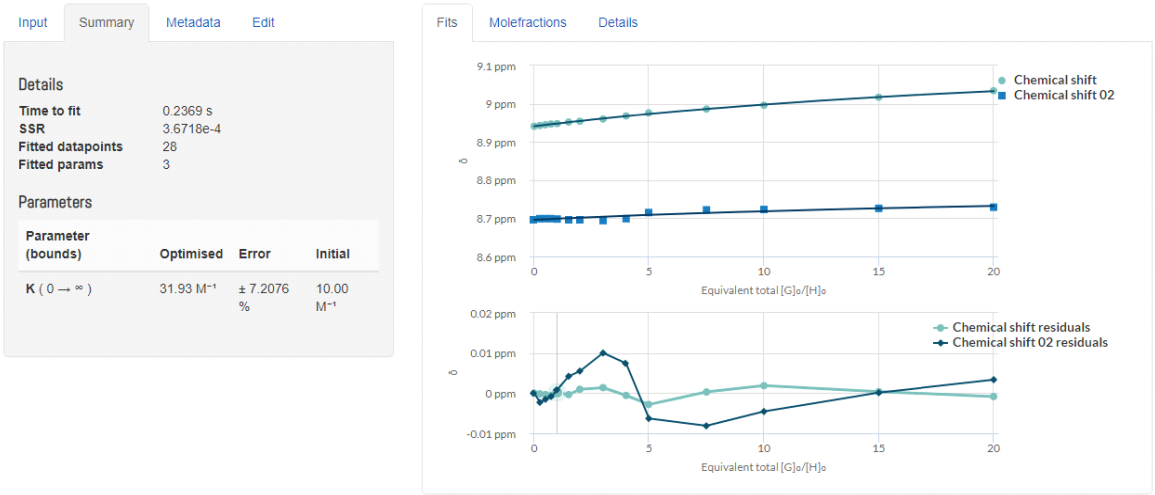



**Figure 3.16** Screenshot of the fitted data plot from supramolecular.org. The binding constant was found to be 31 $M^{-1}$ ± 7% in 1:1 receptor to anion binding model (left side). The pattern of chemical shift and chemical shift residuals with the increasing equivalent $TBANO_3$ (right side). The Bindfit URL for this experiment is: http://app.supramolecular.org/bindfit/view/a0cb5f9f-f60f-46dc-a15f-2acde718ff9a.

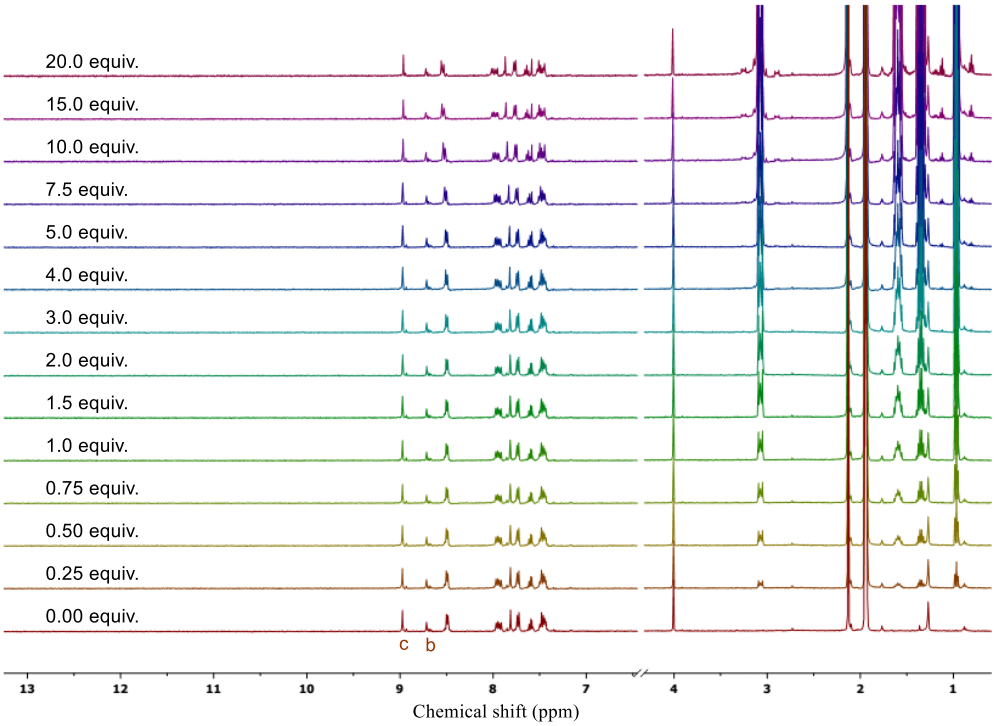



**Figure 3.17** Stacked plot for $^{1}$H NMR titration experiment (400 MHz, acetonitrile-$d_3$) for compound **1a** (1.0 mM) with the successive addition of $TBAClO_4$. No significant chemical shift change was observed for this anion.

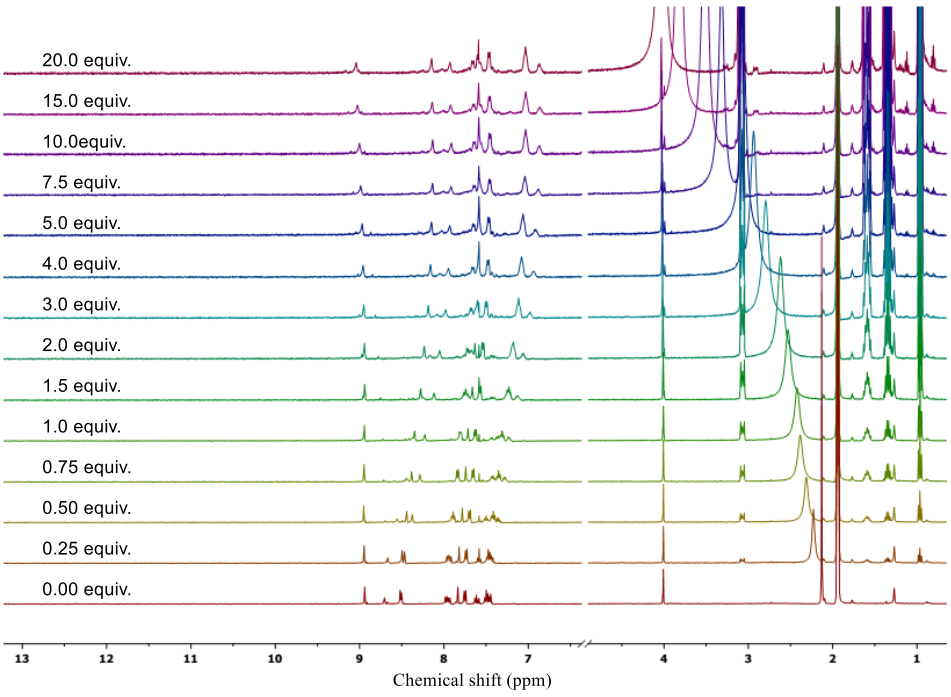



**Figure 3.18** Stacked plot for $^{1}$H NMR titration experiment in acetonitrile-$d_3$ for compound **1a** with the successive addition of $TBAH_2PO_4$. No significant chemical shift change of triazole proton was observed for this anion.

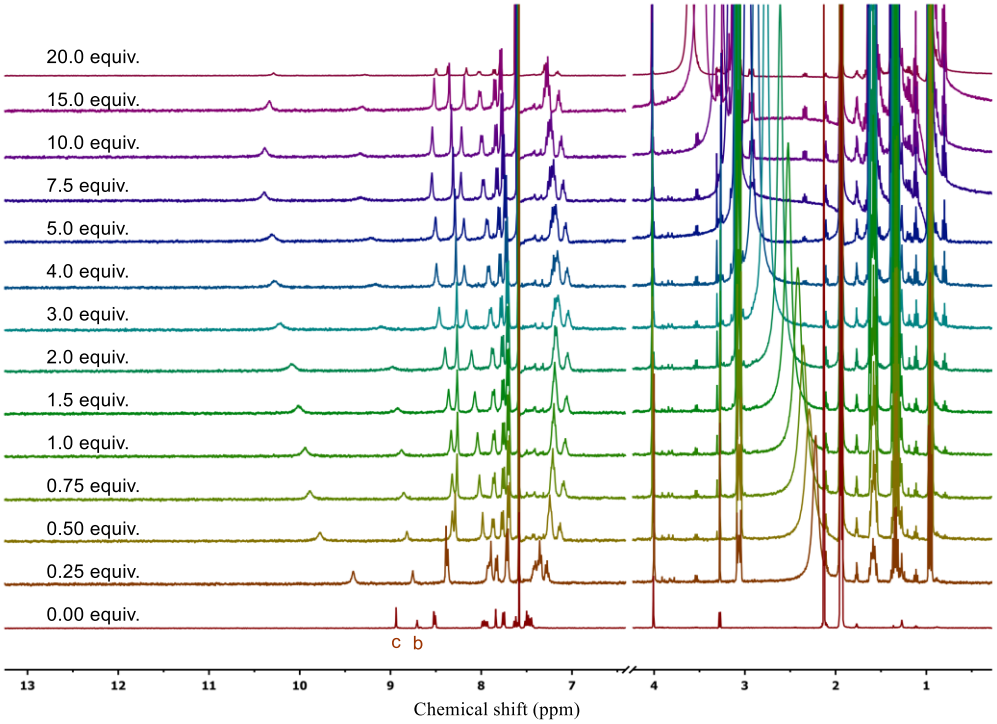



**Figure 3.19** Stacked plot for $^{1}$H NMR titration experiment in acetonitrile-$d_3$ for compound **1a** with the successive addition of $(TBA)_3HP_2O_7$.

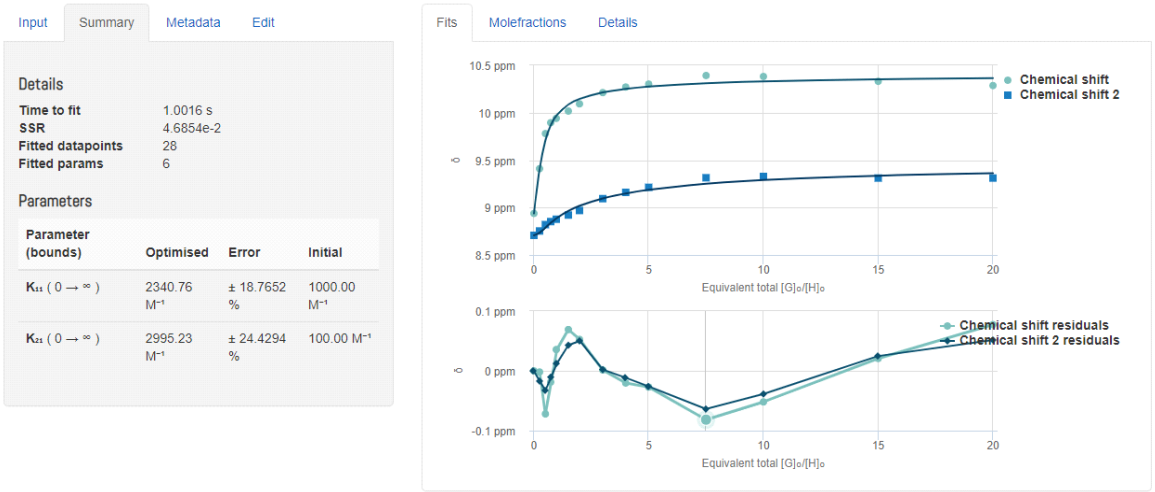



**Figure 3.20** Screenshot of the fitted data plot from supramolecular.org. The binding constant was found to be 2340 $M^{-1}$ ± 18% ($K_{1:1}$) and 2995 $M^{-1}$ ± 24% ($K_{2:1}$) in 2:1 receptor to anion binding model (left side). The pattern of chemical shift and chemical shift residuals with the increasing equivalent $(TBA)_3HP_2O_7$ (right side). The Bindfit URL for this experiment is: http://app.supramolecular.org/bindfit/view/795aeba7-f1ec-45a6-8bc4-8a054ae4dba2.

### 3.4.5. 2D NMR Studies

The conformational change across the single bond (aryl to triazole moiety) of the receptor **1a** upon anion binding was investigated by recording the $^{1}$H–$^{1}$H NOESY NMR.

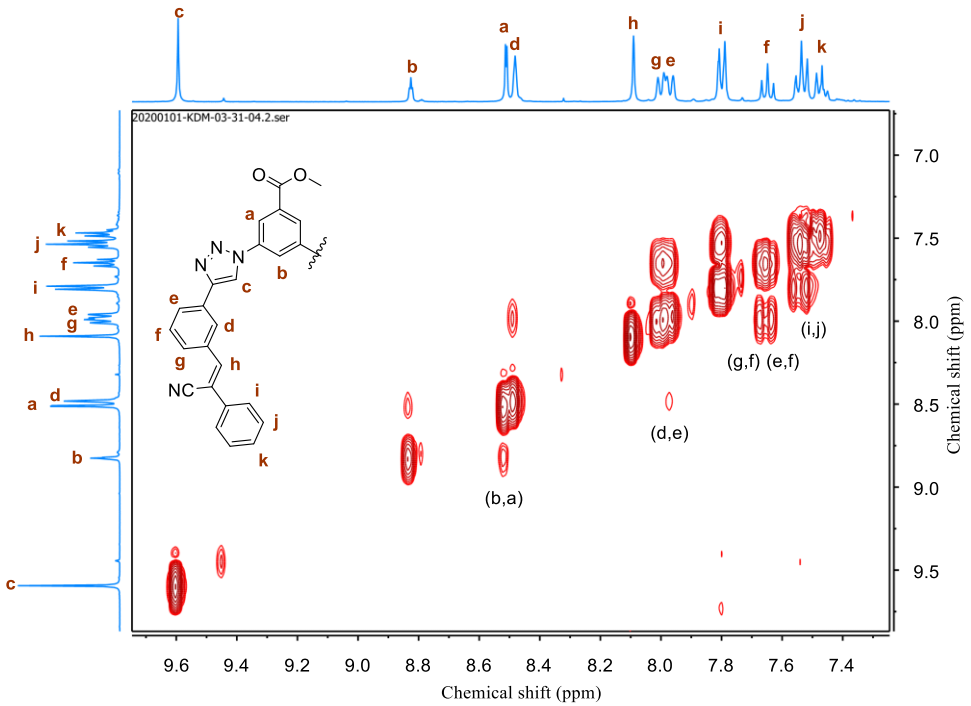



**Figure 3.21** The $^{1}H–^{1}H$ COSY NMR spectrum of **1a** (5.0 mM) at 25 ˚C (400 MHz, DMSO-$d_6$).

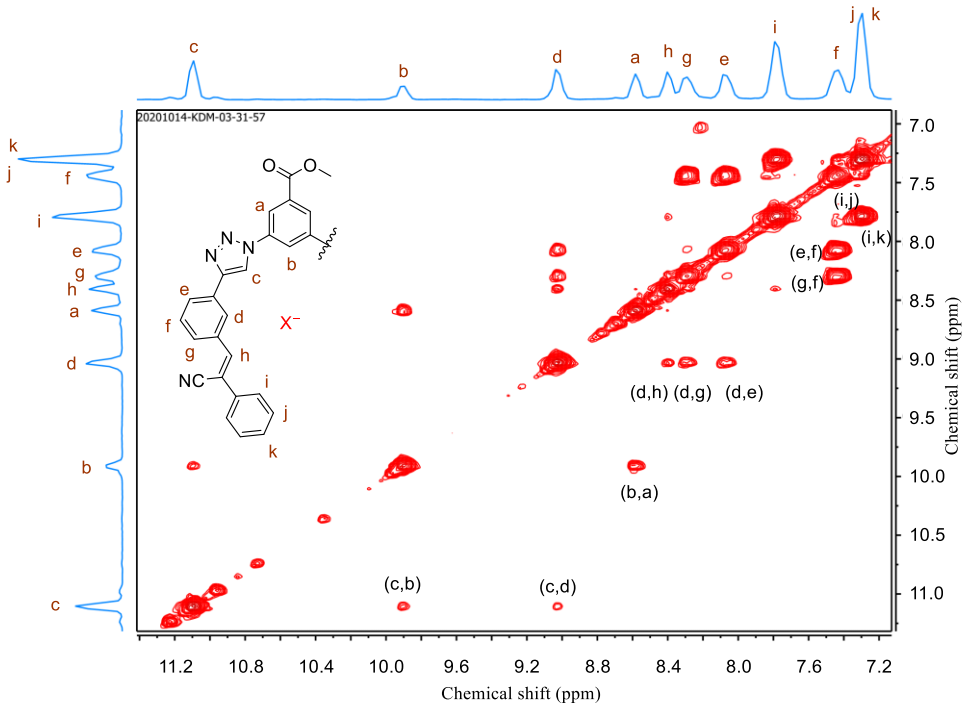



**Figure 3.22** The $^{1}H–^{1}H$ COSY NMR spectrum of **1a** (5.0 mM) with $(TBA)_2SO_4$ (1.8 equiv.) at 25 ˚C (400 MHz, DMSO-$d_6$).

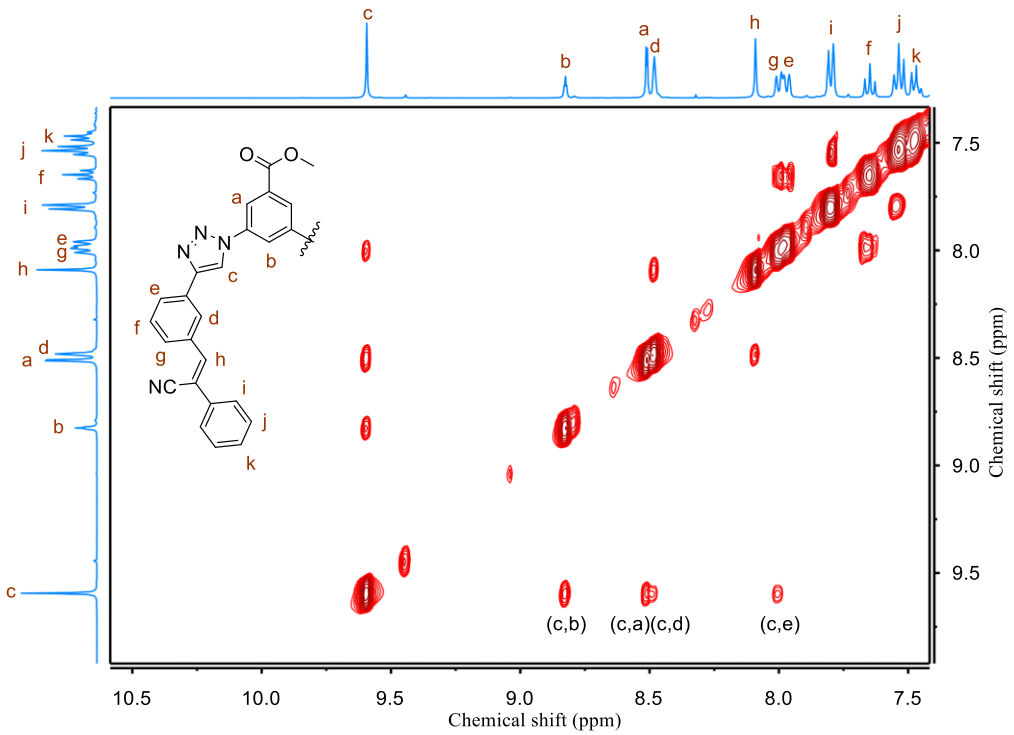



**Figure 3.23** The $^{1}H–^{1}H$ NOESY NMR spectrum of **1a** (5.0 mM) at 25 ˚C (400 MHz, DMSO-$d_6$).

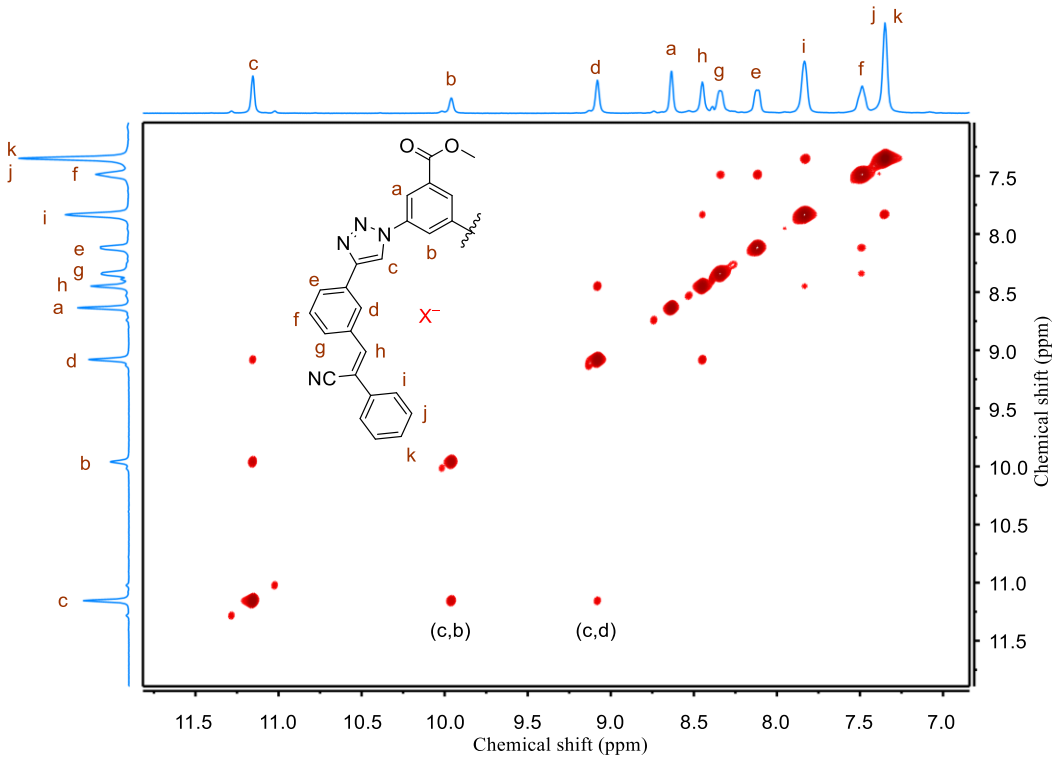



**Figure 3.24** The $^{1}H–^{1}H$ NOESY NMR spectrum of **1a** (5.0 mM) with $(TBA)_2SO_4$ (1.8 equiv.) at 25 ˚C (400 MHz, DMSO-$d_6$).

### 3.4.6. Ion Transport Activity Studies

#### 3.4.6.1. Determination of Ion Transport Activity by HPTS Assay

**HPTS assay for $SO_4^{2-}$ transport**: We have prepared a buffer solution using autoclaved water of strength 33.3 mM of $Na_2SO_4$ and 10 mM of HEPES. The pH of the solution was below 7.0 and to make the pH at around 7.0 required amount of 0.5 M NaOH solution was added. Then 1 mM of HPTS solution was prepared from solid HPTS using the above buffer solution.

In a 10 mL round bottomed flask 0.3 mL of EYPC lipid solution (25 mg/mL in $CHCl_3$) was taken and 5 mol% of transporter compound (with respect to lipid) dissolved in MeOH in $CHCl_3$ was added in to the same round bottomed flask. The entire solution was mixed properly and the organic solvent present in the solution was evaporated slowly by a slow stream of nitrogen gas to get a thin film. Then the trace amount of organic solvent present in the lipid mixture was evaporated by keeping it in high vacuum for about 5 h. The transporter incorporated lipid membrane was then hydrated with 1.0 mL of HPTS solution (1 mM HPTS, 10 mM HEPES, 33.3 mM $Na_2SO_4$, pH 7) by vortexing 5-6 times over the time period of 1.5 h. The transporter lipid hydrated suspension was then subjected through 12 freeze-thaw cycles and extrusions were done for 15 times (must be odd number) through 200 nm polycarbonate membrane. The extravesicular HPTS dye was separated from the vesicles by size exclusion column chromatography (using Sephadex G-50) eluting with buffer solution (10 mM HEPES, 33.3 mM $Na_2SO_4$, pH 7.0). The vesicles were then directly used for the assay as no changes in the transport activity were observed by diluting the eluted vesicles with buffer. The vesicles contains, inside: 1 mM HPTS, 10 mM HEPES, 33.3 mM $Na_2SO_4$, pH 7.0 and outside: 10 mM HEPES, 33.3 mM $Na_2SO_4$, pH 7.0.

In a clean fluorescence cuvette, 1900 µL of buffer solution (10 mM HEPES, 33.3 mM $Na_2SO_4$, pH 7.0), 100 µL of above prepared vesicles solution was taken and placed in a fluorescence instrument equipped with a magnetic stirrer at $t$ = 0 s. The fluorescence emission intensity ($I_t$) of the HPTS dye was measured at $\lambda_{em}$ = 510 nm (where, $\lambda_{ex}$ = 450 nm) for the time course of 0 to 350 s. At $t$ = 50 s, 20 µL of 0.5 M NaOH solution was added to the same cuvette to generate a pH gradient ($\Delta$pH = 0.8) between intra and extra vesicular medium which leads to the increase in the fluorescence intensity. Triton X-100 (25 µL of 10% solution in water) was added at $t$ = 302 s to destroy all the vesicles for destructing the pH gradient.

The fractional fluorescence emission intensity, $I_F$ (Figure 3.25B) was obtained after normalizing the data using the Equation 1.

$$I_F = (I_t - I_0) / (I_\infty - I_0) \times 100 \qquad \text{Equation 1}$$

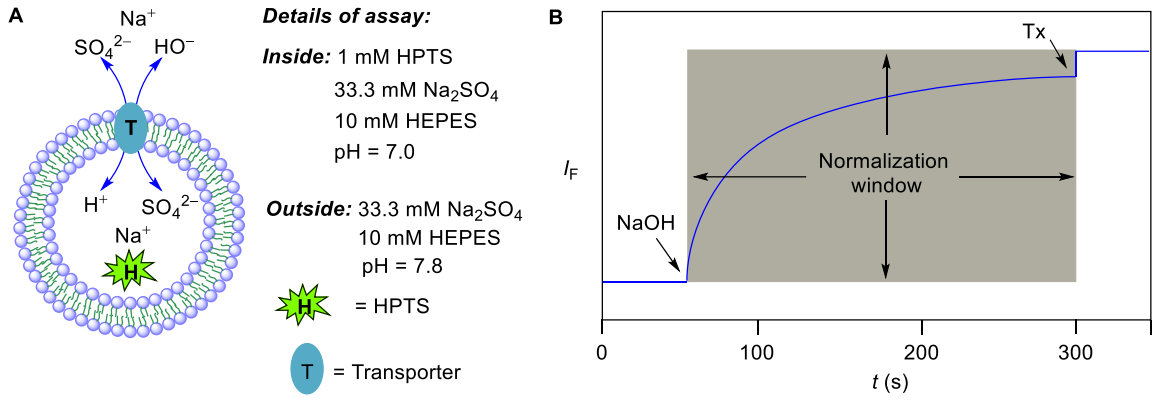



**Figure 3.25** Schematic representation of fluorescence kinetics assay for checking $SO_4^{2-}$ anion transport activity across EYPC-LUVs⊃HPTS (**A**), and normalized working window for the same experiment (**B**).

Where, $I_0$ is the initial fluorescence intensity *i.e.* before the addition of the transporter compound, $I_t$ is the fluorescence intensity at time $t$ and $I_\infty$ is the final fluorescence intensity *i.e.* after the addition of Triton X-100.

Before plotting the data the time axis was normalized using the following equation:

$$t = t - 50 \qquad \text{Equation 2}$$

No transport activity was observed in the presence of $SO_4^{2-}$ ions at 5 mol% of transporter concentration.

**HPTS assay for Pyrophosphate transport:** We have prepared a buffer solution using autoclaved water of strength 23 mM of $Na_4P_2O_7$ and 10 mM of HEPES. The pH of the solution was above 7.0 and to make the pH at around 7.0 required amount of dilute $H_2SO_4$ solution was added. Then 1 mM of HPTS solution was prepared from solid HPTS using the above buffer solution.

In a 10 mL round bottomed flask, 0.3 mL of EYPC lipid solution (25 mg/mL in $CHCl_3$) was taken and 5 mol% of transporter compound (with respect to lipid) dissolved in MeOH in $CHCl_3$ was added in to the same round bottomed flask. The entire solution was mixed properly and the organic solvent present in the solution was evaporated slowly by a slow stream of nitrogen gas to get a thin film. Then the trace amount of organic solvent present in the lipid mixture was evaporated by keeping it in high vacuum for about 5 h. The transporter incorporated lipid membrane was then hydrated with 1.0 mL of HPTS solution (1 mM HPTS, 10 mM HEPES, 23 mM of $Na_4P_2O_7$, pH 7) by vortexing 5-6 times over the time period of 1.5

h. The transporter lipid hydrated suspension was then subjected through 12 freeze-thaw cycles and extrusions were done for 15 times (must be odd number) through 200 nm polycarbonate membrane. The extravesicular HPTS dye was separated from the vesicles by size exclusion column chromatography (using Sephadex G-50) eluting with buffer solution (10 mM HEPES, 23 mM of $Na_4P_2O_7$, pH 7.0). The vesicles were then directly used for the assay as no changes in the transport activity were observed by diluting the eluted vesicles with buffer. The vesicles contains, inside: 1 mM HPTS, 10 mM HEPES, 23 mM of $Na_4P_2O_7$, pH 7.0 and outside: 10 mM HEPES, 23 mM of $Na_4P_2O_7$, pH 7.0.

In a clean fluorescence cuvette, 1900 µL of buffer solution (10 mM HEPES, 23 mM of $Na_4P_2O_7$, pH 7.0), 100 µL of above prepared vesicles solution was taken and placed in a fluorescence instrument equipped with a magnetic stirrer at $t$ = 0 s. The fluorescence emission intensity ($I_t$) of the HPTS dye was measured at $\lambda_{em}$ = 510 nm (where, $\lambda_{ex}$ = 450 nm) for the time course of 0 to 350 s. At $t$ = 50 s, 20 µL of 0.5 M NaOH solution was added to the same cuvette to generate a pH gradient (ΔpH = 0.8) between intra and extra vesicular medium which leads to the increase in the fluorescence intensity. Triton X-100 (25 µL of 10% solution in water) was added at $t$ = 302 s to destroy all the vesicles for destructing the pH gradient.

The fractional fluorescence emission intensity, $I_F$ was obtained after normalizing the data using the Equation 1. In addition, before plotting the data the time axis was normalized using the Equation 2. No transport activity was observed in the presence of pyrophosphate ions at 5 mol% of transporter concentration.

**HPTS assay for $Cl^-$ transport activity:** We have prepared a buffer solution using autoclaved water of strength 100 mM of NaCl and 10 mM of HEPES. The pH of the solution was below 7.0 and to make the pH at around 7.0 required amount of 0.5 M NaOH solution was added. Then 1 mM of HPTS solution was prepared from solid HPTS using the above buffer solution.

In a 10 mL round bottomed flask 0.3 mL of EYPC lipid solution (25 mg/mL in $CHCl_3$) was taken and 5 mol% of transporter compound (with respect to lipid) dissolved in MeOH in $CHCl_3$ was added in to the same round bottomed flask. The entire solution was mixed properly and the organic solvent present in the solution was evaporated slowly by a slow stream of nitrogen gas to get a thin film. Then the trace amount of organic solvent present in the lipid mixture was evaporated by keeping it in high vacuum for about 5 h. The transporter incorporated lipid membrane was then hydrated with 1.0 mL of HPTS solution (1 mM HPTS, 10 mM HEPES, 100 mM NaCl, pH 7.0) by vortexing 5-6 times over the time period of 1.5 h.

The transporter lipid hydrated suspension was then subjected through 12 freeze-thaw cycles and extrusions were done for 15 times (must be odd number) through 200 nm polycarbonate membrane. The extravesicular HPTS dye was separated from the vesicles by size exclusion column chromatography (using Sephadex G-50) eluting with buffer solution (10 mM HEPES, 100 mM NaCl, pH 7). The vesicles were then directly used for the assay as no changes in the transport activity were observed by diluting the eluted vesicles with buffer. The vesicles contains, inside: 5 mol% transporter, 1 mM HPTS, 10 mM HEPES, 100 mM NaCl, pH 7 and outside: 10 mM HEPES, 100 mM NaCl, pH 7.

In a clean fluorescence cuvette, 1900 µL of buffer solution (10 mM HEPES, 100 mM NaCl, pH 7), 100 µL of above prepared vesicles solution were taken and fluorescence cuvette was placed in a fluorescence instrument equipped with a magnetic stirrer at $t$ = 0 s. The fluorescence emission intensity ($I_t$) of the HPTS dye was measured at $\lambda_{em}$ = 510 nm (where, $\lambda_{ex}$ = 450 nm) for the time course of 0 to 350 s. At $t$ = 50 s, 20 µL of 0.5 M NaOH solution was added to the same cuvette to generate a pH gradient (ΔpH = 0.8) between intra and extra vesicular medium which leads to the increase in the fluorescence intensity. Triton X-100 (25 µL of 10% solution in water) was added at $t$ = 302 s to destroy all the vesicles for destructing the pH gradient.

The fractional fluorescence emission intensity, $I_F$ (Figure 3.26B) was resulted after normalizing all the data using the equation 1

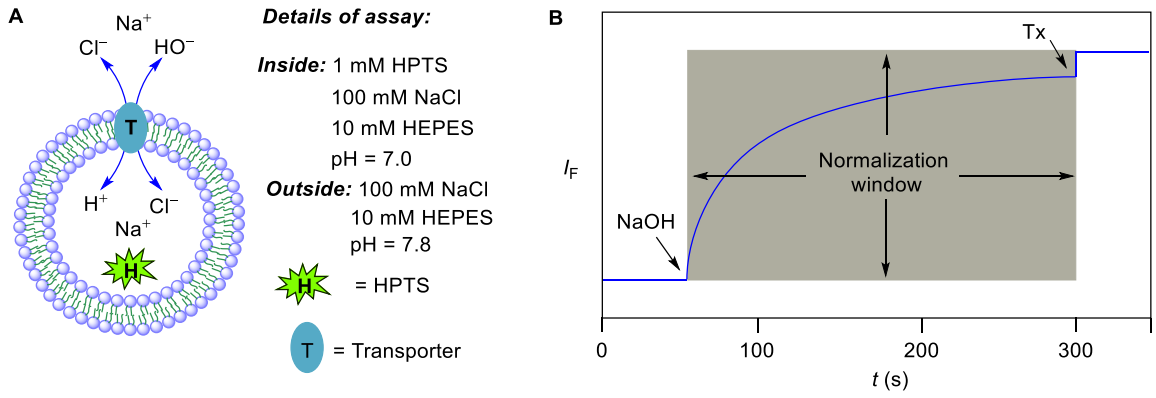



**Figure 3.26** Schematic representation of fluorescence kinetics assay for checking ion transport activity across EYPC-LUVs⊃HPTS (**A**), and normalized working window for the same experiment (**B**).

Where, $I_0$ is the initial fluorescence intensity *i.e.* before the addition of the transporter compound, $I_t$ is the fluorescence intensity at time *t* and $I_\infty$ is the final fluorescence intensity *i.e.* after the addition of Triton X-100.

We have prepared vesicles following the above mentioned procedure for three different times by incorporating three triazole derivatives at 5 mol% transporter concentrations. All three experiments results along with baseline data were plotted in a same figure to get the idea about transport efficiency.

### 3.4.6.2. Determination of Ion Selectivity by HPTS Assay

**Cation Selectivity Transport Study by HPTS Assay:** In a clean fluorescence cuvette, 1900 µL of buffer solution (100 mM MCl, 10 mM HEPES, pH 7.0; where, $M^+$ = $Li^+$, $Na^+$, $K^+$, $Rb^+$, and $Cs^+$), 100 µL of above prepared vesicles solution were taken and fluorescence cuvette was placed in a fluorescence instrument equipped with a magnetic stirrer at *t* = 0 s. The fluorescence emission intensity ($I_t$) of the HPTS dye was measured at $\lambda_{em}$ = 510 nm (where, $\lambda_{ex}$ = 450 nm) for the time course of 0 to 350 s. At *t* = 50 s, 20 µL of 0.5 M NaOH solution was added to the same cuvette to generate a pH gradient (ΔpH = 0.8) between intra and extra vesicular medium which leads to the increase in the fluorescence intensity. Triton X-100 (25 µL of 10% solution in water) was added at *t* = 302 s to destroy all the vesicles for destructing the pH gradient. All the data was normalized using the Equation 1 and Equation 2.

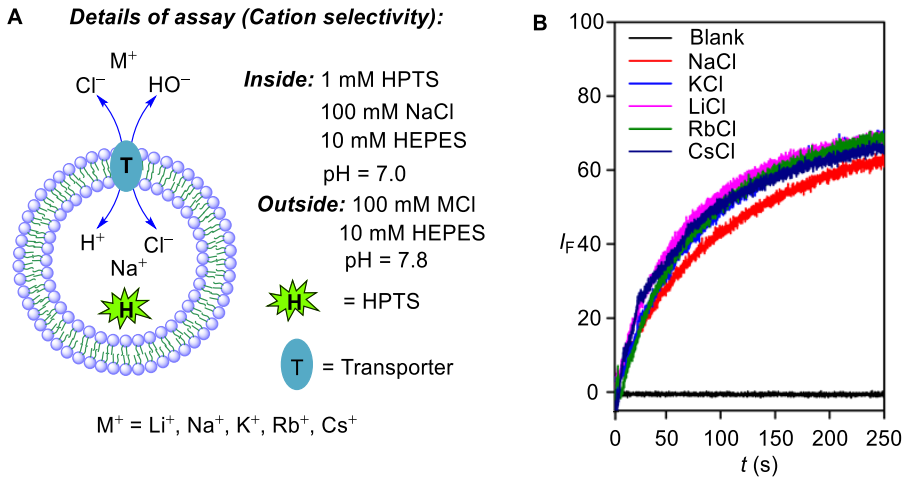



**Figure 3.27** The representation of vesicles for cation selectivity assay (A). The ion transport activities of **1c** across EYPC-LUVs⊃HPTS at 4 mol% transporter concentration by varying the extravesicular cations (B).

**Anion Selectivity Transport Study by HPTS Assay:** In a clean fluorescence cuvette, 1900 µL of buffer solution (100 mM NaX, 10 mM HEPES, pH 7.0; where, $X^-$ = $Cl^-$, $Br^-$, $I^-$, $NO_3^-$, $SCN^-$, $ClO_4^-$, and $AcO^-$), 100 µL of above prepared vesicles solution were taken and fluorescence cuvette was placed in a fluorescence instrument equipped with a magnetic stirrer at $t$ = 0 s. The fluorescence emission intensity ($I_t$) of the HPTS dye was measured at $\lambda_{em}$ = 510 nm (where, $\lambda_{ex}$ = 450 nm) for the time course of 0 to 350 s. At $t$ = 50 s, 20 µL of 0.5 M NaOH solution was added to the same cuvette to generate a pH gradient (ΔpH = 0.8) between intra and extra vesicular medium which leads to the increase in the fluorescence intensity. Triton X-100 (25 µL of 10% solution in water) was added at $t$ = 302 s to destroy all the vesicles for destructing the pH gradient. All the data was normalized using the Equation 1 and Equation 2.

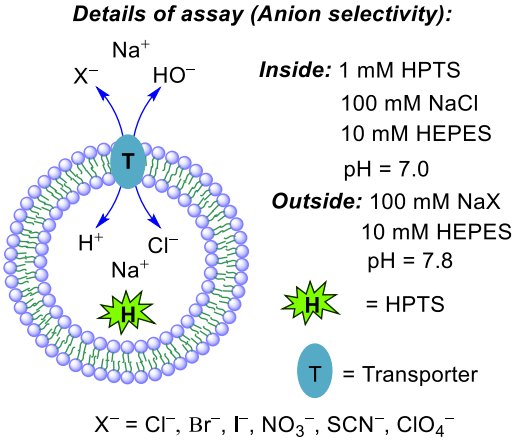



**Figure 3.28** The representation of vesicles for anion selectivity assay (A).

### 3.4.6.3. Determination of $Cl^-$ Transport Activity by Lucigenin Assay

In a 10 mL round bottomed flask 0.3 mL of EYPC lipid solution (25 mg/mL in $CHCl_3$) was taken and 15 mol% of transporter compound (with respect to lipid) dissolved in MeOH in $CHCl_3$ was added in to the same round bottomed flask. The entire solution was mixed properly and the organic solvent present in the solution was evaporated slowly by a slow stream of nitrogen gas to get a thin film. Then the trace amount of organic solvent present in the lipid mixture was evaporated by keeping it in high vacuum for about 5 h. The transporter incorporated lipid membrane was then hydrated with 1 mL of Lucigenin solution (1 mM Lucigenin, 225 mM $NaNO_3$) by vortexing 5-6 times over the time period of 1.5 h. The transporter lipid hydrated suspension was then subjected through 12 freeze-thaw cycles and extrusions were done for 15 times (must be odd number) through 200 nm polycarbonate

membrane. The extravesicular Lucigenin dye was separated from the vesicles by size exclusion column chromatography (using Sephadex G-50) eluting with buffer solution (225 mM of $NaNO_3$). The vesicles were then directly used for the assay as no changes in the transport activity were observed by diluting the eluted vesicles with buffer. The vesicles contain, inside: 1 mM Lucigenin, 225 mM of $NaNO_3$ and outside: 225 mM of $NaNO_3$.

In a clean fluorescence cuvette, 1900 µL of buffer solution (225 mM $NaNO_3$ solution), 100 µL of above prepared vesicles solution were taken and fluorescence cuvette was placed in a fluorescence instrument equipped with a magnetic stirrer at $t$ = 0 s. The fluorescence emission intensity ($I_t$) of the Lucigenin dye was measured at $\lambda_{em}$ = 535 nm (where, $\lambda_{ex}$ = 455 nm) for the time course of 0 to 350 s. At $t$ = 50 s, 33.3 µL of 2 M NaCl solution was added to the same cuvette to generate a chloride ion concentration gradient between intra and extra vesicular medium which leads to the decrease in the fluorescence intensity. Triton X-100 (25 µL of 10% solution in water) was added at $t$ = 302 s to destroy all the vesicles for destructing the chloride ion concentration gradient.

The fractional fluorescence emission intensity, $I_F$ (Figure 3.29B) was obtained after normalizing all the data using the following equation (Equation 3).

$$I_F = (I_t - I_0) / (I_\infty - I_0) \times (-100) \qquad \text{Equation 3}$$

Where, $I_0$ is the fluorescence emission intensity just before the addition of the transporter compound, $I_t$ is the fluorescence emission intensity at time $t$, and $I_\infty$ is the fluorescence emission intensity after the addition of Triton X-100.

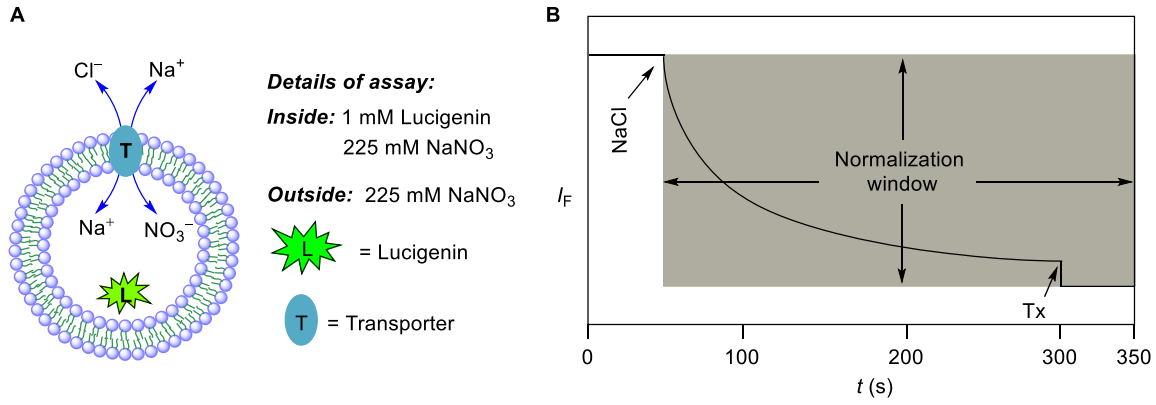



**Figure 3.29** Representation of vesicles for fluorescence kinetics based Lucigenin assay for checking the chloride anion transport activity across EYPC-LUVs⊃Lucigenin (A), and normalization window for the same fluorescence kinetics experiment (B).

For plotting all the data in to graph the time axis was normalized using Equation 2,

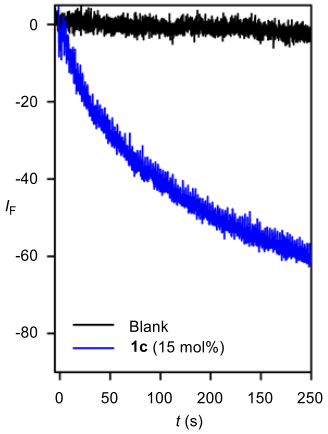



**Figure 3.30** Lucigenin assay of **1c** for chloride transport.

### 3.4.6.4. $Cl^-$ transport by Symport assay in presence of Lucigenin

In a clean fluorescence cuvette, 1900 µL of buffer solution (225 mM $NaNO_3$ solution), 100 µL of above prepared vesicles solution were taken and fluorescence cuvette were placed in a fluorescence instrument equipped with a magnetic stirrer at $t$ = 0 s. The fluorescence emission intensity ($I_t$) of the Lucigenin dye was measured at $\lambda_{em}$ = 535 nm (where, $\lambda_{ex}$ = 455 nm) for the time course of 0 to 350 s. At $t$ = 50 s, 33.3 µL of 2 M MCl (where, $M^+$ = $Li^+$, $Na^+$, $K^+$, $Rb^+$, and $Cs^+$) was added to the same cuvette to generate a chloride ion concentration gradient of ions ($Cl^-$ and $M^+$) between intra and extra vesicular medium which leads to the decrease in the fluorescence intensity. Triton X-100 (25 µL of 10% solution in water) was added at $t$ = 302 s to destroy all the vesicles for destructing the chloride ion concentration gradient.

### 3.4.6.5. $Cl^-$ transport by Lucigenin assay in presence of Valinomycin

In a clean fluorescence cuvette, 1900 µL of buffer solution (225 mM $NaNO_3$ solution), 100 µL of above prepared vesicles solution were taken and fluorescence cuvette was placed in a fluorescence instrument equipped with a magnetic stirrer at $t$ = 0 s. The fluorescence intensity of the Lucigenin dye, $I_t$ was measured at $\lambda_{em}$ = 535 nm (where, $\lambda_{ex}$ = 455 nm) for the time course of 0 to 350 s. Then valinomycin (0.6 µM) was added at $t$ = 20 s. At $t$ = 50 s, 33.3 µL of 2 N KCl solution was added to the same cuvette to generate a concentration gradient of ions ($Cl^-$ and $K^+$) between intra and extra vesicular medium which leads to the decrease in the

fluorescence intensity. Triton X-100 (25 µL of 10% solution in water) was added at $t$ = 302 s to destroy all the vesicles for destructing the chloride ion concentration gradient.

#### 3.4.6.6. U-tube experiments for checking $Cl^-$ transport

U-tube experiment was performed to check whether the chloride ion is transporting *via* mobile carrier mechanism or ion channel formation by transporter molecule. In a typical experiment, left arm (source arm) of the U-tube was filled with 7.5 mL of 500 mM NaCl solution (pH 7.0 using 5 mM phosphate buffer) and the right arm (receiver arm) of the U-tube was filled with 7.5 mL of 500 mM $NaNO_3$ solution (pH 7.0 using 5 mM phosphate buffer). Two different buffer solutions were well separated by 15 mL solution of transporter **1c** in $CHCl_3$ (1 mM compound **1c**, 1 mM tetrabutylammonium hexafluorophosphate). For the transport of anion, channel formation is not possible through the chloroform layer because of its long length. So the only possibility remaining is the carrier mechanism i.e., if we observe the transport of anion that will be only because of carrier mechanism. For checking transport activity via carrier mechanism chloride ion selective electrode was used to measure the chloride ion concentration with time in the receiver arm. A gradual increase in $Cl^-$ ion concentration (at the receiver arm) was seen by recording the data for consecutive 8 days (Figure 3.5C). No such transport can be seen in the absence of transporter molecule.

### 3.5. Theoretical Calculations

To get an idea about the conformations of **1a**, **1c**, [**1a**+$SO_4^{2-}$], [**1a**+$Cl^-$], [**1c**+$SO_4^{2-}$], and [**1c**+$Cl^-$] complex, several initial geometries of were generated from the CONFLEX 8 software package[51, 56] using MMFF94s force field. Among the several conformations, the highest Boltzmann populated structure for each complex was used for geometry optimization. The geometry optimization was carried out by Gaussian 09 program package[52] using B3LYP functional and 6-31G(d,p) basis set. For all structures (i.e. free receptors and anionic complexes), the vibrational frequency calculation during the geometry optimization shows no imaginary frequencies which indicated that all optimized structures are ground state minima. The energy-optimized structure confirmed the multivalent C–H hydrogen bonding interactions with each anion and the calculated C···$A^-$ bond distances are also in the range of known experimental hydrogen bond distances.[57]

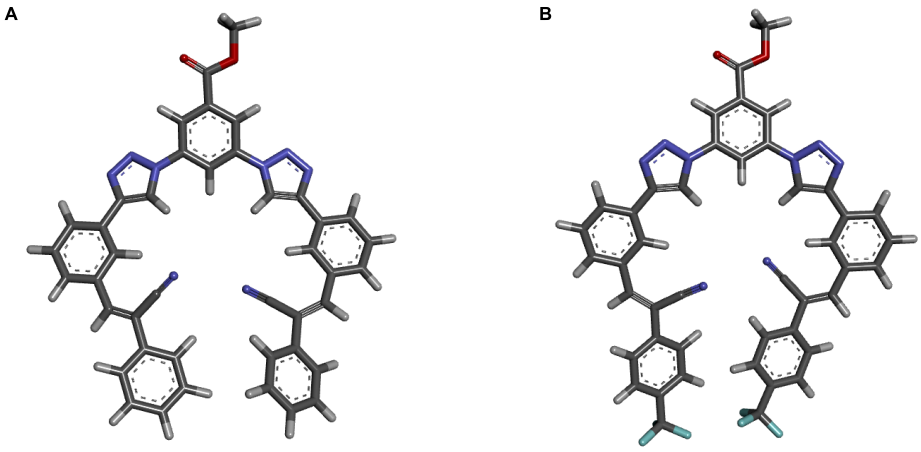



**Figure 3.31** The geometry optimized structures of **1a** (A) and **1c** (B).

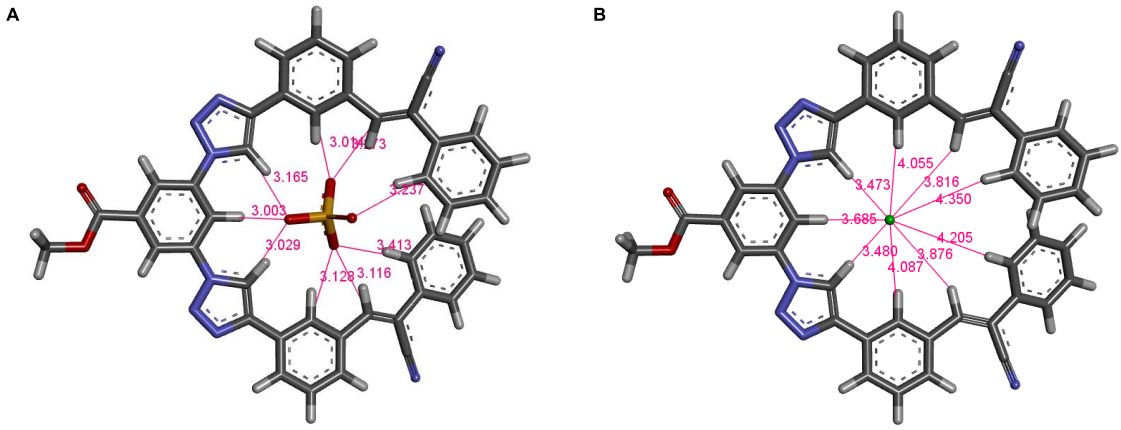



**Figure 3.32** The geometry optimized structure of [**1a**+$SO_4^{2-}$] with the C···O (in Å) bond distances (A) and [**1a**+$Cl^-$] with the C···$Cl^-$ (in Å) bond distances (B).

The Gaussian 09 program was used to calculate the zero point energy (ZPE) and basis set superposition error (BSSE)[58] corrected bonding energy of [**1a**+$SO_4^{2-}$], [**1a**+$Cl^-$], [**1c**+$SO_4^{2-}$], and [**1c**+$Cl^-$] complex which were used for the calculation of binding energy (*BE*) using the following equations.

$$BE = [HF_{[\mathbf{M}+X^-]} + ZPE_{[\mathbf{M}+X^-]} + BSSE_{[\mathbf{M}+X^-]}] - [HF_{\mathbf{M}} + ZPE_{\mathbf{M}}] - [HF_{X^-}] \quad \text{…Equation 4}$$

where, M is the receptors (i.e. **1a** or **1c**), $X^-$ is the anions (i.e. $Cl^-$ or $SO_4^{2-}$), $HF_{[\mathbf{M}+X^-]}$ = electronic energy of [**M**+$X^-$] complex, $ZPE_{[\mathbf{M}+X^-]}$ = zero point energy of [**M**+$X^-$] complex, $BSSE_{[\mathbf{M}+X^-]}$ = BSSE of [**M**+$X^-$] complex, $HF_{\mathbf{M}}$ = electronic energy of the receptor M, $ZPE_{\mathbf{M}}$ = zero point energy of the receptor **M**, $HF_{X^-}$ = electronic energy of anion $X^-$.

For all structures (i.e. free receptors and anionic complexes), the vibrational frequency calculation during the geometry optimization shows no imaginary frequencies which indicated that all optimized structures are ground state minima.

**Table 1** The electronic energy (HF), zero point energy (ZPE), basis set superposition error (BSSE) corrected energy (in Hartree unit) for all structures and complexes are calculated at the DFT B3LYP/6-31G (d, p) level of theory.

| Structures | [**1a**+$SO_4^{2-}$] | [**1a**+$Cl^-$] | [**1c**+$SO_4^{2-}$] | [**1c**+$Cl^-$] |
|---|---|---|---|---|
| $HF_{[M+X^-]}$ (in Hartree) | -2904.9004920 | -2666.0858110 | -3578.9856950 | -3340.1630220 |
| $ZPE_{[M+X^-]}$ (in Hartree) | 0.6262147 | 0.6106742 | 0.6357496 | 0.6203312 |
| $BSSE_{[M+X^-]}$ (in Hartree) | 0.0395153 | 0.0091645 | 0.0396420 | 0.0103270 |
| $HF_M$ (in Hartree) | -2205.7514789 | -2205.7514789 | -2879.8233537 | -2879.8233537 |
| $ZPE_M$ (in Hartree) | 0.6096949 | 0.6096949 | 0.6195347 | 0.6195347 |
| $HF_{X^-}$ (in Hartree) | -698.9166780 | -460.2522333 | -698.9166780 | -460.2522333 |
| BE (in Hartree) | -0.1763001 | -0.0719551 | -0.1898059 | -0.0763112 |
| BE (in kcal/mol) | -110.6299042 | -45.1524749 | -119.1048841 | -47.8859419 |

The QST2 approach was used for searching the transition states (TS) by providing the coordinates of open and close conformations, using the Synchronous Transit-Guided Quasi-Newton (QST) method at the B3LYP/6-31G(d,p) level of theory. ZPE corrected relative electronic energies are used for open and close conformations and transition states for calculating the energy barrier. The presence of one imaginary frequency in the geometry obtained from the QST2 calculation confirmed the transition state. The energy barrier for the

interconversion of the close conformations to the open conformations was 1028 $cm^{-1}$. It should be noted here that the open conformation is stable than the closed conformation by 455 $cm^{-1}$.

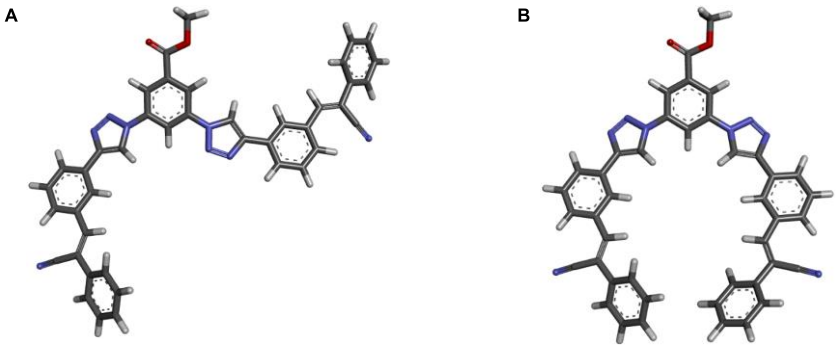



**Figure 3.33** The geometry optimized structures of open (A) and close conformation (B) of **1a**.

The significant energy barrier for the inter-conversion suggests that both the conformations should exist in the experiment. Hence, the Boltzmann population of both the conformation was calculated from the relative change in Gibbs free energies (ΔG0) of both conformations in the temperature range of 0–298 K. It can be observed from Figure 1 that the Boltzmann population of the close conformation is significantly less (~1.5 %) at room temperature and open conformation is highly populated (~98.5 %). Here is one point to note that, even though various conformations can represent the open conformation by rotating various C–C single bonds, we have considered one open conformation for our computational studies.

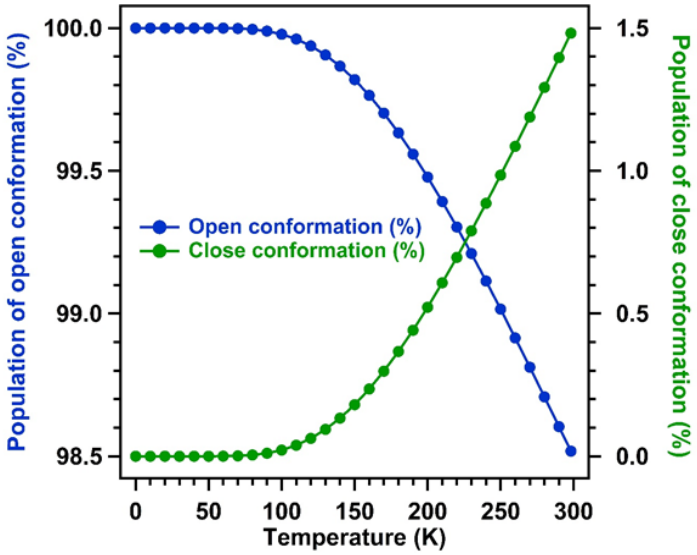



**Figure 3.34** Boltzmann populations of the open and close conformation in the temperature range of 0–298 K, calculated at the B3LYP/6-31G(d,p) level of theory.

**Table 2** Atomic coordinates of the optimized structure of lowest energy conformation obtained for **1a** from DFT B3LYP/6-31G(d,p) geometry optimization.

Charge = 0, Multiplicity = 1

| Atom # | Atom Type | x | y | z |
|---|---|---|---|---|
| 1 | C | -5.481485 | -1.284992 | -0.284396 |
| 2 | C | -4.143081 | -1.214271 | 0.107282 |
| 3 | C | -3.516610 | 0.017959 | 0.305620 |
| 4 | C | -4.240206 | 1.191384 | 0.072727 |
| 5 | C | -5.577555 | 1.144100 | -0.317940 |
| 6 | C | -6.193267 | -0.099204 | -0.482712 |
| 7 | C | -7.629742 | -0.103826 | -0.903462 |
| 8 | O | -8.279244 | 0.899667 | -1.113607 |
| 9 | O | -8.122114 | -1.353172 | -1.022775 |
| 10 | N | -3.424996 | -2.420528 | 0.324647 |
| 11 | N | -3.613971 | 2.450664 | 0.259345 |
| 12 | C | -9.502180 | -1.434359 | -1.419355 |
| 13 | C | -2.301134 | 2.786456 | 0.138104 |
| 14 | C | -2.253581 | 4.129126 | 0.460528 |
| 15 | N | -3.531305 | 4.536355 | 0.752514 |
| 16 | N | -4.349510 | 3.538126 | 0.636033 |
| 17 | N | -4.098430 | -3.566612 | 0.633296 |
| 18 | N | -3.220765 | -4.509452 | 0.763614 |
| 19 | C | -1.960540 | -4.009552 | 0.546495 |
| 20 | C | -2.086056 | -2.662420 | 0.264521 |
| 21 | C | -1.103208 | 5.037115 | 0.512301 |
| 22 | C | -0.771244 | -4.868091 | 0.608838 |
| 23 | C | 0.191476 | 4.525893 | 0.387959 |
| 24 | C | 1.318264 | 5.362353 | 0.429189 |
| 25 | C | 1.115092 | 6.741238 | 0.638553 |
| 26 | C | -0.171956 | 7.257885 | 0.763122 |

| | | | | |
|---|---|---|---|---|
| 27 | C | -1.281933 | 6.417574 | 0.697204 |
| 28 | C | -0.912870 | -6.233607 | 0.910103 |
| 29 | C | 0.206600 | -7.060881 | 0.938524 |
| 30 | C | 1.469774 | -6.543798 | 0.668493 |
| 31 | C | 1.643328 | -5.173904 | 0.383400 |
| 32 | C | 0.502851 | -4.351138 | 0.353651 |
| 33 | C | 3.003575 | -4.718215 | 0.101781 |
| 34 | C | 2.691848 | 4.874594 | 0.308264 |
| 35 | C | 3.541246 | -3.471589 | 0.005900 |
| 36 | C | 4.978562 | -3.243972 | -0.313002 |
| 37 | H | 3.706205 | -5.530703 | -0.067389 |
| 38 | H | 0.607169 | -3.302491 | 0.110681 |
| 39 | H | -1.363742 | -1.902145 | 0.014704 |
| 40 | H | -2.498372 | 0.066426 | 0.672710 |
| 41 | H | -1.546933 | 2.094338 | -0.201183 |
| 42 | H | 0.325190 | 3.458348 | 0.286630 |
| 43 | H | 3.443459 | 5.564059 | 0.685472 |
| 44 | C | 3.175870 | 3.705792 | -0.193807 |
| 45 | C | 4.627360 | 3.374332 | -0.205657 |
| 46 | C | 5.970557 | -4.141392 | 0.116263 |
| 47 | C | 7.306640 | -3.938571 | -0.221991 |
| 48 | C | 7.679681 | -2.831582 | -0.986605 |
| 49 | C | 6.704830 | -1.923877 | -1.404102 |
| 50 | C | 5.367209 | -2.123134 | -1.065766 |
| 51 | C | 5.601957 | 4.375175 | -0.354508 |
| 52 | C | 6.957367 | 4.055947 | -0.324290 |
| 53 | C | 7.364779 | 2.731282 | -0.154354 |
| 54 | C | 6.404891 | 1.726761 | -0.022216 |
| 55 | C | 5.047572 | 2.042176 | -0.053741 |
| 56 | C | 2.760826 | -2.285844 | 0.209385 |

| | | | | |
|---|---|---|---|---|
| 57 | N | 2.160226 | -1.302726 | 0.384018 |
| 58 | C | 2.309596 | 2.709381 | -0.757658 |
| 59 | N | 1.628330 | 1.894227 | -1.235584 |
| 60 | H | -5.953265 | -2.247626 | -0.422310 |
| 61 | H | -6.138318 | 2.054144 | -0.487056 |
| 62 | H | -9.731969 | -2.498325 | -1.460672 |
| 63 | H | -10.139240 | -0.929601 | -0.689536 |
| 64 | H | -9.646907 | -0.969422 | -2.397320 |
| 65 | H | 1.973898 | 7.404624 | 0.694747 |
| 66 | H | -0.312443 | 8.323593 | 0.916070 |
| 67 | H | -2.287329 | 6.811327 | 0.797433 |
| 68 | H | -1.903233 | -6.627647 | 1.108089 |
| 69 | H | 0.091578 | -8.116495 | 1.164689 |
| 70 | H | 2.337296 | -7.197912 | 0.682223 |
| 71 | H | 5.699003 | -4.986694 | 0.740765 |
| 72 | H | 8.059483 | -4.640129 | 0.124904 |
| 73 | H | 8.721722 | -2.674259 | -1.247935 |
| 74 | H | 6.981931 | -1.058947 | -1.999228 |
| 75 | H | 4.615541 | -1.414700 | -1.400612 |
| 76 | H | 5.297883 | 5.403748 | -0.521899 |
| 77 | H | 7.696156 | 4.842413 | -0.447345 |
| 78 | H | 8.421988 | 2.484123 | -0.132873 |
| 79 | H | 6.709000 | 0.692753 | 0.108479 |
| 80 | H | 4.307436 | 1.255025 | 0.057789 |

**Table 3** Atomic coordinates of the optimized structure of lowest energy conformation obtained for **1c** from DFT B3LYP/6-31G(d,p) geometry optimization.

Charge = 0, Multiplicity = 1

| Atom # | Atom Type | x | y | z |
|---|---|---|---|---|

| | | | | |
|---|---|---|---|---|
| 1 | C | -7.173921 | -0.385974 | 0.242649 |
| 2 | C | -5.839570 | -0.628167 | -0.084762 |
| 3 | C | -4.941516 | 0.424644 | -0.284714 |
| 4 | C | -5.388814 | 1.736836 | -0.113757 |
| 5 | C | -6.718387 | 2.001602 | 0.217003 |
| 6 | C | -7.606031 | 0.935677 | 0.379719 |
| 7 | C | -9.021860 | 1.269904 | 0.733451 |
| 8 | O | -9.434137 | 2.400690 | 0.889121 |
| 9 | O | -9.788379 | 0.168572 | 0.859767 |
| 10 | N | -5.394001 | -1.967943 | -0.227596 |
| 11 | N | -4.495164 | 2.826684 | -0.295505 |
| 12 | C | -11.166103 | 0.413012 | 1.193870 |
| 13 | C | -3.140703 | 2.891890 | -0.149156 |
| 14 | C | -2.823191 | 4.210213 | -0.417203 |
| 15 | N | -3.993147 | 4.867954 | -0.711880 |
| 16 | N | -4.991337 | 4.049303 | -0.642112 |
| 17 | N | -6.270768 | -2.965695 | -0.548299 |
| 18 | N | -5.594455 | -4.071276 | -0.611129 |
| 19 | C | -4.273792 | -3.821230 | -0.340484 |
| 20 | C | -4.139516 | -2.469858 | -0.085963 |
| 21 | C | -1.544488 | 4.934425 | -0.388990 |
| 22 | C | -3.233713 | -4.853573 | -0.326094 |
| 23 | C | -0.317533 | 4.273224 | -0.262685 |
| 24 | C | 0.890351 | 4.996356 | -0.200158 |
| 25 | C | 0.834207 | 6.403949 | -0.264365 |
| 26 | C | -0.380327 | 7.063847 | -0.414107 |
| 27 | C | -1.565499 | 6.338659 | -0.475626 |
| 28 | C | -3.537310 | -6.223438 | -0.294143 |
| 29 | C | -2.503842 | -7.160389 | -0.264255 |
| 30 | C | -1.171836 | -6.751506 | -0.246918 |

| | | | | |
|---|---|---|---|---|
| 31 | C | -0.846099 | -5.380432 | -0.259700 |
| 32 | C | -1.896114 | -4.454171 | -0.332227 |
| 33 | C | 0.558907 | -4.977655 | -0.226830 |
| 34 | C | 2.220732 | 4.410500 | -0.057111 |
| 35 | C | 1.110190 | -3.771507 | 0.082899 |
| 36 | C | 2.574633 | -3.512734 | 0.022366 |
| 37 | H | 1.264835 | -5.760672 | -0.495235 |
| 38 | H | -1.672301 | -3.402143 | -0.421777 |
| 39 | H | -3.295872 | -1.873090 | 0.223015 |
| 40 | H | -3.924682 | 0.227107 | -0.602404 |
| 41 | H | -2.543700 | 2.047349 | 0.155440 |
| 42 | H | -0.300361 | 3.191899 | -0.207381 |
| 43 | H | 2.988166 | 5.146456 | 0.170530 |
| 44 | C | 2.679808 | 3.133380 | -0.156158 |
| 45 | C | 4.120998 | 2.794600 | 0.014416 |
| 46 | C | 3.044331 | -2.261769 | -0.413564 |
| 47 | C | 4.409557 | -2.010754 | -0.496040 |
| 48 | C | 5.328596 | -2.994157 | -0.120097 |
| 49 | C | 4.874075 | -4.239041 | 0.320546 |
| 50 | C | 3.507636 | -4.495368 | 0.389093 |
| 51 | C | 5.129725 | 3.679998 | -0.398286 |
| 52 | C | 6.473577 | 3.357410 | -0.232481 |
| 53 | C | 6.834309 | 2.134955 | 0.336683 |
| 54 | C | 5.842673 | 1.238906 | 0.745356 |
| 55 | C | 4.500514 | 1.566100 | 0.582243 |
| 56 | C | 0.312458 | -2.652052 | 0.498740 |
| 57 | N | -0.313515 | -1.736932 | 0.856228 |
| 58 | C | 1.824813 | 2.022703 | -0.453495 |
| 59 | N | 1.181928 | 1.086098 | -0.712225 |
| 60 | H | -7.854711 | -1.214065 | 0.382193 |

| | | | | |
|---|---|---|---|---|
| 61 | H | -7.066671 | 3.018469 | 0.340666 |
| 62 | H | -11.631358 | -0.570193 | 1.251171 |
| 63 | H | -11.240422 | 0.932493 | 2.152001 |
| 64 | H | -11.643307 | 1.021939 | 0.422690 |
| 65 | H | 1.756723 | 6.974832 | -0.205609 |
| 66 | H | -0.405436 | 8.147486 | -0.473164 |
| 67 | H | -2.520461 | 6.840234 | -0.581710 |
| 68 | H | -4.575313 | -6.538185 | -0.298187 |
| 69 | H | -2.740595 | -8.219830 | -0.249625 |
| 70 | H | -0.376999 | -7.491697 | -0.214795 |
| 71 | H | 2.338887 | -1.486332 | -0.697715 |
| 72 | H | 4.761468 | -1.049704 | -0.853401 |
| 73 | C | 6.797771 | -2.670920 | -0.110827 |
| 74 | H | 5.586730 | -4.999882 | 0.618776 |
| 75 | H | 3.163316 | -5.454968 | 0.761090 |
| 76 | H | 4.865015 | 4.612130 | -0.886425 |
| 77 | H | 7.242657 | 4.041910 | -0.571809 |
| 78 | C | 8.282862 | 1.776884 | 0.536962 |
| 79 | H | 6.122258 | 0.282514 | 1.173067 |
| 80 | H | 3.737445 | 0.862600 | 0.899581 |
| 81 | F | 9.098405 | 2.516858 | -0.246544 |
| 82 | F | 8.515929 | 0.476806 | 0.257893 |
| 83 | F | 8.672303 | 1.979946 | 1.817401 |
| 84 | F | 7.152196 | -2.036241 | 1.038970 |
| 85 | F | 7.141351 | -1.851343 | -1.125888 |
| 86 | F | 7.564559 | -3.778023 | -0.196195 |

**Table 4** Atomic coordinates of the optimized structure of lowest energy conformation obtained for [**1a**+$SO_4^{2-}$] from DFT B3LYP/6-31G(d,p) geometry optimization.

Charge = –2, Multiplicity = 1

| Atom # | Atom Type | x | y | z |
|---|---|---|---|---|
| 1 | C | -5.915373 | -1.088627 | 0.14265 |
| 2 | C | -4.519793 | -1.093673 | 0.104569 |
| 3 | C | -3.793331 | 0.078595 | -0.123628 |
| 4 | C | -4.492635 | 1.277283 | -0.295024 |
| 5 | C | -5.887521 | 1.313406 | -0.266529 |
| 6 | C | -6.590428 | 0.122332 | -0.051703 |
| 7 | C | -8.074231 | 0.196114 | -0.026714 |
| 8 | O | -8.735214 | 1.205209 | -0.188785 |
| 9 | O | -8.65343 | -1.014573 | 0.20318 |
| 10 | N | -3.817389 | -2.312679 | 0.29258 |
| 11 | N | -3.759214 | 2.477193 | -0.483945 |
| 12 | C | -10.081118 | -1.002688 | 0.237597 |
| 13 | C | -2.416293 | 2.672851 | -0.373042 |
| 14 | C | -2.259662 | 4.029791 | -0.59636 |
| 15 | N | -3.496211 | 4.578928 | -0.830857 |
| 16 | N | -4.404028 | 3.650872 | -0.765716 |
| 17 | N | -4.493416 | -3.49961 | 0.3873 |
| 18 | N | -3.601495 | -4.437637 | 0.508133 |
| 19 | C | -2.346052 | -3.881204 | 0.488546 |
| 20 | C | -2.472445 | -2.509861 | 0.358171 |
| 21 | C | -1.021275 | 4.813894 | -0.539169 |
| 22 | C | -1.111263 | -4.670253 | 0.547047 |
| 23 | C | 0.193729 | 4.138449 | -0.383996 |
| 24 | C | 1.405248 | 4.82974 | -0.208224 |
| 25 | C | 1.393411 | 6.240157 | -0.260869 |
| 26 | C | 0.188858 | 6.910435 | -0.465598 |
| 27 | C | -1.017354 | 6.215094 | -0.590373 |
| 28 | C | -1.115229 | -6.037621 | 0.858523 |
| 29 | C | 0.085626 | -6.751666 | 0.874959 |

| | | | | |
|---|---|---|---|---|
| 30 | C | 1.297241 | -6.134238 | 0.572558 |
| 31 | C | 1.318834 | -4.760339 | 0.250764 |
| 32 | C | 0.107106 | -4.045019 | 0.258001 |
| 33 | C | 2.478504 | -3.956087 | -0.130997 |
| 34 | C | 2.54663 | 3.955953 | 0.064605 |
| 35 | C | 3.742638 | -4.300249 | -0.507692 |
| 36 | C | 4.742422 | -3.289706 | -0.960531 |
| 37 | H | 2.236923 | -2.891576 | -0.154346 |
| 38 | H | 0.149242 | -2.985898 | -0.003612 |
| 39 | H | -1.741486 | -1.690786 | 0.337829 |
| 40 | H | -2.700833 | 0.059859 | -0.161604 |
| 41 | H | -1.710572 | 1.871199 | -0.139128 |
| 42 | H | 0.23608 | 3.046589 | -0.401465 |
| 43 | H | 2.309466 | 2.905735 | -0.119347 |
| 44 | C | 3.790268 | 4.215835 | 0.558325 |
| 45 | C | 4.743187 | 3.124246 | 0.910997 |
| 46 | C | 6.089017 | -3.652307 | -1.141882 |
| 47 | C | 7.033361 | -2.718788 | -1.56774 |
| 48 | C | 6.652961 | -1.401147 | -1.819809 |
| 49 | C | 5.316359 | -1.031513 | -1.646998 |
| 50 | C | 4.363587 | -1.957592 | -1.229017 |
| 51 | C | 4.277223 | 1.822077 | 1.181814 |
| 52 | C | 5.183331 | 0.812199 | 1.499734 |
| 53 | C | 6.554218 | 1.071472 | 1.571544 |
| 54 | C | 7.019766 | 2.363497 | 1.323186 |
| 55 | C | 6.123191 | 3.38022 | 0.996821 |
| 56 | C | 4.180439 | -5.666318 | -0.519569 |
| 57 | N | 4.578507 | -6.763139 | -0.53515 |
| 58 | C | 4.251537 | 5.552623 | 0.796372 |
| 59 | N | 4.674003 | 6.623663 | 0.987513 |

| | | | | |
|---|---|---|---|---|
| 60 | H | -6.451948 | -2.010057 | 0.315832 |
| 61 | H | -6.418249 | 2.245478 | -0.403866 |
| 62 | H | -10.38109 | -2.033812 | 0.429199 |
| 63 | H | -10.44804 | -0.344753 | 1.03078 |
| 64 | H | -10.492752 | -0.656289 | -0.714887 |
| 65 | H | 2.309257 | 6.807238 | -0.145523 |
| 66 | H | 0.186058 | 7.997087 | -0.513269 |
| 67 | H | -1.955646 | 6.745745 | -0.719775 |
| 68 | H | -2.057667 | -6.52765 | 1.082672 |
| 69 | H | 0.074923 | -7.809911 | 1.125829 |
| 70 | H | 2.212605 | -6.713101 | 0.589008 |
| 71 | H | 6.398871 | -4.674685 | -0.945992 |
| 72 | H | 8.06888 | -3.025888 | -1.696765 |
| 73 | H | 7.386737 | -0.667964 | -2.144389 |
| 74 | H | 5.00153 | -0.009269 | -1.831799 |
| 75 | H | 3.330739 | -1.627087 | -1.12012 |
| 76 | H | 3.216881 | 1.56451 | 1.170201 |
| 77 | H | 4.794106 | -0.182587 | 1.691976 |
| 78 | H | 7.250691 | 0.274511 | 1.819405 |
| 79 | H | 8.083734 | 2.583671 | 1.378078 |
| 80 | H | 6.494143 | 4.383054 | 0.803417 |
| 81 | S | 0.68902 | 0.096572 | 0.071356 |
| 82 | O | 0.942573 | 1.259405 | -0.865561 |
| 83 | O | 1.092974 | -1.205926 | -0.607503 |
| 84 | O | 1.436163 | 0.281675 | 1.360575 |
| 85 | O | -0.828106 | 0.033481 | 0.352222 |

**Table 5** Atomic coordinates of the optimized structure of lowest energy conformation obtained for [**1a**+$Cl^-$] from DFT B3LYP/6-31G(d,p) geometry optimization.

Charge = –1, Multiplicity = 1

| Atom # | Atom Type | x | y | z |
|---|---|---|---|---|
| 1 | C | 5.937266 | 0.957614 | 0.162560 |
| 2 | C | 4.543443 | 1.000366 | 0.101590 |
| 3 | C | 3.792925 | -0.160905 | -0.090942 |
| 4 | C | 4.455605 | -1.384767 | -0.211681 |
| 5 | C | 5.847300 | -1.458299 | -0.157264 |
| 6 | C | 6.577863 | -0.279274 | 0.027511 |
| 7 | C | 8.063363 | -0.396798 | 0.082808 |
| 8 | O | 8.682455 | -1.437222 | -0.025253 |
| 9 | O | 8.669776 | 0.800515 | 0.270904 |
| 10 | N | 3.861946 | 2.239266 | 0.226787 |
| 11 | N | 3.680366 | -2.560916 | -0.381765 |
| 12 | C | 10.100306 | 0.754319 | 0.334594 |
| 13 | C | 2.329595 | -2.689786 | -0.302765 |
| 14 | C | 2.103961 | -4.032926 | -0.522050 |
| 15 | N | 3.315899 | -4.647895 | -0.723897 |
| 16 | N | 4.267895 | -3.768954 | -0.640569 |
| 17 | N | 4.549120 | 3.415849 | 0.349026 |
| 18 | N | 3.669924 | 4.369422 | 0.412653 |
| 19 | C | 2.407269 | 3.834868 | 0.329983 |
| 20 | C | 2.521579 | 2.464579 | 0.215699 |
| 21 | C | 0.824785 | -4.747963 | -0.519259 |
| 22 | C | 1.185173 | 4.643874 | 0.336176 |
| 23 | C | -0.362484 | -4.056802 | -0.244265 |
| 24 | C | -1.603582 | -4.717428 | -0.179416 |
| 25 | C | -1.642661 | -6.105320 | -0.435722 |
| 26 | C | -0.466640 | -6.787681 | -0.730867 |
| 27 | C | 0.761975 | -6.126807 | -0.766686 |
| 28 | C | 1.225436 | 6.022023 | 0.592050 |
| 29 | C | 0.047156 | 6.769565 | 0.576121 |

| | | | | |
|---|---|---|---|---|
| 30 | C | -1.179995 | 6.174290 | 0.300812 |
| 31 | C | -1.244733 | 4.789515 | 0.032251 |
| 32 | C | -0.050758 | 4.044527 | 0.062121 |
| 33 | C | -2.447381 | 4.036229 | -0.312125 |
| 34 | C | -2.744253 | -3.880651 | 0.182993 |
| 35 | C | -3.757710 | 4.393268 | -0.428562 |
| 36 | C | -4.825073 | 3.429779 | -0.822310 |
| 37 | H | -2.233029 | 2.994426 | -0.534305 |
| 38 | H | -0.097883 | 2.975219 | -0.134516 |
| 39 | H | 1.768949 | 1.679922 | 0.149139 |
| 40 | H | 2.707462 | -0.114326 | -0.143372 |
| 41 | H | 1.647879 | -1.861573 | -0.115279 |
| 42 | H | -0.331922 | -2.983743 | -0.063818 |
| 43 | H | -2.489357 | -2.824764 | 0.230452 |
| 44 | C | -4.037383 | -4.178595 | 0.494570 |
| 45 | C | -5.018554 | -3.145356 | 0.931854 |
| 46 | C | -4.645131 | 2.039208 | -0.703034 |
| 47 | C | -5.641280 | 1.155336 | -1.109450 |
| 48 | C | -6.845211 | 1.634632 | -1.630609 |
| 49 | C | -7.043534 | 3.010815 | -1.737563 |
| 50 | C | -6.046835 | 3.898542 | -1.336724 |
| 51 | C | -6.399166 | -3.369828 | 0.791203 |
| 52 | C | -7.325667 | -2.410722 | 1.196486 |
| 53 | C | -6.895575 | -1.207235 | 1.754992 |
| 54 | C | -5.526742 | -0.976128 | 1.910431 |
| 55 | C | -4.597663 | -1.933677 | 1.510894 |
| 56 | C | -4.199530 | 5.738731 | -0.202098 |
| 57 | N | -4.609007 | 6.816812 | -0.032894 |
| 58 | C | -4.549355 | -5.516463 | 0.431785 |
| 59 | N | -5.020641 | -6.581640 | 0.387726 |

| | | | | |
|---|---|---|---|---|
| 60 | H | 6.500746 | 1.867865 | 0.308799 |
| 61 | H | 6.357956 | -2.406942 | -0.253909 |
| 62 | H | 10.421257 | 1.784698 | 0.488130 |
| 63 | H | 10.430582 | 0.121921 | 1.162873 |
| 64 | H | 10.516667 | 0.357219 | -0.594935 |
| 65 | H | -2.578786 | -6.647244 | -0.408246 |
| 66 | H | -0.506605 | -7.854927 | -0.930357 |
| 67 | H | 1.679156 | -6.664592 | -0.982363 |
| 68 | H | 2.181580 | 6.491411 | 0.798141 |
| 69 | H | 0.087115 | 7.836394 | 0.777938 |
| 70 | H | -2.074162 | 6.783244 | 0.287006 |
| 71 | H | -3.731757 | 1.635632 | -0.278533 |
| 72 | H | -5.479145 | 0.088068 | -1.000557 |
| 73 | H | -7.621139 | 0.940724 | -1.940529 |
| 74 | H | -7.976166 | 3.400090 | -2.136704 |
| 75 | H | -6.213132 | 4.967211 | -1.428182 |
| 76 | H | -6.746593 | -4.303251 | 0.359568 |
| 77 | H | -8.387035 | -2.607296 | 1.072739 |
| 78 | H | -7.615745 | -0.458320 | 2.070605 |
| 79 | H | -5.177314 | -0.048041 | 2.352402 |
| 80 | H | -3.542011 | -1.740860 | 1.670358 |
| 81 | Cl | 0.112203 | -0.038831 | 0.033895 |

**Table 6** Atomic coordinates of the optimized structure of lowest energy conformation obtained for [**1c**+$SO_4^{2-}$] from DFT B3LYP/6-31G geometry optimization.

Charge = –2, Multiplicity = 1

| Atom # | Atom Type | x | y | z |
|---|---|---|---|---|
| 1 | C | 6.996734 | -1.133195 | -0.127528 |
| 2 | C | 5.601175 | -1.126779 | -0.090434 |
| 3 | C | 4.884320 | 0.051881 | 0.134083 |

| | | | | |
|---|---|---|---|---|
| 4 | C | 5.593095 | 1.245425 | 0.301677 |
| 5 | C | 6.988128 | 1.270138 | 0.273920 |
| 6 | C | 7.681342 | 0.072734 | 0.063674 |
| 7 | C | 9.166238 | 0.134704 | 0.039707 |
| 8 | O | 9.833694 | 1.140026 | 0.197295 |
| 9 | O | 9.735540 | -1.081261 | -0.183036 |
| 10 | N | 4.888365 | -2.339955 | -0.275194 |
| 11 | N | 4.868595 | 2.451197 | 0.485709 |
| 12 | C | 11.163743 | -1.081500 | -0.215836 |
| 13 | C | 3.528192 | 2.655997 | 0.366058 |
| 14 | C | 3.379227 | 4.013603 | 0.588592 |
| 15 | N | 4.617616 | 4.554662 | 0.830949 |
| 16 | N | 5.519475 | 3.620459 | 0.771594 |
| 17 | N | 5.552468 | -3.534070 | -0.361361 |
| 18 | N | 4.651687 | -4.463745 | -0.480392 |
| 19 | C | 3.402109 | -3.894598 | -0.468067 |
| 20 | C | 3.542084 | -2.524081 | -0.344665 |
| 21 | C | 2.144998 | 4.802719 | 0.522842 |
| 22 | C | 2.158259 | -4.668684 | -0.525862 |
| 23 | C | 0.929506 | 4.130319 | 0.359381 |
| 24 | C | -0.278548 | 4.824114 | 0.172455 |
| 25 | C | -0.264400 | 6.234835 | 0.224611 |
| 26 | C | 0.939775 | 6.902010 | 0.439120 |
| 27 | C | 2.143554 | 6.203614 | 0.573103 |
| 28 | C | 2.142015 | -6.037467 | -0.829743 |
| 29 | C | 0.930386 | -6.733833 | -0.845934 |
| 30 | C | -0.272897 | -6.096855 | -0.551756 |
| 31 | C | -0.273796 | -4.720701 | -0.238662 |
| 32 | C | 0.948572 | -4.024370 | -0.244026 |
| 33 | C | -1.419831 | -3.893906 | 0.131205 |

| | | | | |
|---|---|---|---|---|
| 34 | C | -1.417271 | 3.952297 | -0.113611 |
| 35 | C | -2.694737 | -4.211394 | 0.495381 |
| 36 | C | -3.674091 | -3.174723 | 0.926894 |
| 37 | H | -1.157706 | -2.833810 | 0.153253 |
| 38 | H | 0.921116 | -2.964582 | 0.014696 |
| 39 | H | 2.818787 | -1.699544 | -0.330109 |
| 40 | H | 3.792735 | 0.041971 | 0.173318 |
| 41 | H | 2.818022 | 1.860058 | 0.127431 |
| 42 | H | 0.882753 | 3.039323 | 0.379878 |
| 43 | H | -1.184669 | 2.900926 | 0.074379 |
| 44 | C | -2.654931 | 4.220029 | -0.618964 |
| 45 | C | -3.611468 | 3.136724 | -0.981001 |
| 46 | C | -5.034672 | -3.499557 | 1.069604 |
| 47 | C | -5.966022 | -2.544979 | 1.465968 |
| 48 | C | -5.554411 | -1.238440 | 1.729390 |
| 49 | C | -4.201663 | -0.902198 | 1.600004 |
| 50 | C | -3.266036 | -1.852930 | 1.207871 |
| 51 | C | -3.162144 | 1.827748 | -1.243205 |
| 52 | C | -4.074700 | 0.833403 | -1.589219 |
| 53 | C | -5.438316 | 1.121558 | -1.695615 |
| 54 | C | -5.891286 | 2.420553 | -1.445881 |
| 55 | C | -4.986752 | 3.414465 | -1.095141 |
| 56 | C | -3.163651 | -5.566689 | 0.509807 |
| 57 | N | -3.583447 | -6.655089 | 0.528457 |
| 58 | C | -3.106574 | 5.558993 | -0.862455 |
| 59 | N | -3.519797 | 6.631992 | -1.061163 |
| 60 | H | 7.526071 | -2.059421 | -0.297490 |
| 61 | H | 7.526443 | 2.198271 | 0.408557 |
| 62 | H | 11.455146 | -2.116303 | -0.400247 |
| 63 | H | 11.536636 | -0.431898 | -1.013002 |

| | | | | |
|---|---|---|---|---|
| 64 | H | 11.576690 | -0.732183 | 0.734919 |
| 65 | H | -1.177675 | 6.804300 | 0.102507 |
| 66 | H | 0.944807 | 7.988457 | 0.487079 |
| 67 | H | 3.081921 | 6.732367 | 0.709377 |
| 68 | H | 3.077346 | -6.543247 | -1.048555 |
| 69 | H | 0.926444 | -7.793402 | -1.090604 |
| 70 | H | -1.197135 | -6.661465 | -0.568668 |
| 71 | H | -5.369208 | -4.510474 | 0.858832 |
| 72 | H | -7.013949 | -2.810503 | 1.553424 |
| 73 | C | -6.537870 | -0.208862 | 2.195131 |
| 74 | H | -3.870469 | 0.112653 | 1.792835 |
| 75 | H | -2.222186 | -1.548480 | 1.124416 |
| 76 | H | -2.106971 | 1.548365 | -1.210207 |
| 77 | H | -3.701705 | -0.165268 | -1.785556 |
| 78 | C | -6.435827 | 0.059398 | -2.041236 |
| 79 | H | -6.948412 | 2.652386 | -1.530865 |
| 80 | H | -5.347189 | 4.421463 | -0.908396 |
| 81 | F | -6.496439 | -0.037780 | 3.547592 |
| 82 | F | -7.819875 | -0.543737 | 1.900529 |
| 83 | F | -6.308370 | 1.008065 | 1.656833 |
| 84 | F | -7.373004 | 0.512659 | -2.922785 |
| 85 | F | -7.136185 | -0.370965 | -0.958022 |
| 86 | F | -5.871262 | -1.032595 | -2.598465 |
| 87 | S | 0.372329 | 0.101414 | -0.063503 |
| 88 | O | 0.103713 | 1.280621 | 0.848107 |
| 89 | O | -0.031633 | -1.188208 | 0.640855 |
| 90 | O | -0.374048 | 0.255219 | -1.358431 |
| 91 | O | 1.888636 | 0.038518 | -0.335578 |

**Table 7** Atomic coordinates of the optimized structure of lowest energy conformation obtained for [**1c**+$Cl^-$] from DFT B3LYP/6-31G(d,p) geometry optimization.

Charge = –1, Multiplicity = 1

| Atom # | Atom Type | x | y | z |
|---|---|---|---|---|
| 1 | C | 7.101062 | -1.054885 | -0.174985 |
| 2 | C | 5.711223 | -1.074436 | -0.052276 |
| 3 | C | 4.991999 | 0.102749 | 0.15529 |
| 4 | C | 5.67074 | 1.321751 | 0.201603 |
| 5 | C | 7.059106 | 1.373039 | 0.08463 |
| 6 | C | 7.763743 | 0.176229 | -0.09437 |
| 7 | C | 9.247792 | 0.269825 | -0.214853 |
| 8 | O | 9.883418 | 1.304431 | -0.164346 |
| 9 | O | 9.828809 | -0.941114 | -0.390007 |
| 10 | N | 4.99013 | -2.293162 | -0.13211 |
| 11 | N | 4.902669 | 2.503947 | 0.352691 |
| 12 | C | 11.256661 | -0.91919 | -0.512527 |
| 13 | C | 3.554532 | 2.625067 | 0.242401 |
| 14 | C | 3.313376 | 3.965867 | 0.45218 |
| 15 | N | 4.516132 | 4.590434 | 0.677305 |
| 16 | N | 5.47707 | 3.716693 | 0.618863 |
| 17 | N | 5.62075 | -3.507163 | -0.14337 |
| 18 | N | 4.695244 | -4.419543 | -0.177732 |
| 19 | C | 3.459748 | -3.81902 | -0.185056 |
| 20 | C | 3.641732 | -2.452696 | -0.164079 |
| 21 | C | 2.015695 | 4.645876 | 0.41468 |
| 22 | C | 2.185484 | -4.543041 | -0.166133 |
| 23 | C | 0.861418 | 3.894435 | 0.15967 |
| 24 | C | -0.405641 | 4.494217 | 0.051943 |
| 25 | C | -0.509431 | 5.889117 | 0.246776 |
| 26 | C | 0.633573 | 6.632576 | 0.525998 |
| 27 | C | 1.891202 | 6.028959 | 0.602911 |
| 28 | C | 2.118182 | -5.936178 | -0.302104 |

| | | | | |
|---|---|---|---|---|
| 29 | C | 0.8811 | -6.58272 | -0.248968 |
| 30 | C | -0.297671 | -5.871116 | -0.046552 |
| 31 | C | -0.251751 | -4.467121 | 0.099226 |
| 32 | C | 0.996952 | -3.825279 | 0.020133 |
| 33 | C | -1.383065 | -3.584555 | 0.369428 |
| 34 | C | -1.490378 | 3.579333 | -0.290968 |
| 35 | C | -2.691979 | -3.832299 | 0.658205 |
| 36 | C | -3.652369 | -2.748305 | 1.00605 |
| 37 | H | -1.102179 | -2.533837 | 0.355825 |
| 38 | H | 1.02958 | -2.742493 | 0.126381 |
| 39 | H | 2.92741 | -1.632955 | -0.180483 |
| 40 | H | 3.914101 | 0.072165 | 0.277573 |
| 41 | H | 2.881299 | 1.797136 | 0.037065 |
| 42 | H | 0.934302 | 2.816244 | 0.030114 |
| 43 | H | -1.16976 | 2.540033 | -0.292621 |
| 44 | C | -2.79384 | 3.785874 | -0.63182 |
| 45 | C | -3.696847 | 2.675126 | -1.043151 |
| 46 | C | -3.211562 | -1.51852 | 1.527788 |
| 47 | C | -4.119495 | -0.516755 | 1.854243 |
| 48 | C | -5.489266 | -0.722203 | 1.673254 |
| 49 | C | -5.943477 | -1.939817 | 1.160433 |
| 50 | C | -5.035011 | -2.939697 | 0.833572 |
| 51 | C | -5.092229 | 2.816715 | -0.939602 |
| 52 | C | -5.947709 | 1.789143 | -1.319988 |
| 53 | C | -5.426007 | 0.59275 | -1.817818 |
| 54 | C | -4.042326 | 0.437692 | -1.932967 |
| 55 | C | -3.187537 | 1.467039 | -1.554007 |
| 56 | C | -3.236003 | -5.158591 | 0.658483 |
| 57 | N | -3.726074 | -6.216024 | 0.662291 |
| 58 | C | -3.384931 | 5.091818 | -0.627019 |

| | | | | |
|---|---|---|---|---|
| 59 | N | -3.910997 | 6.131809 | -0.629467 |
| 60 | H | 7.645615 | -1.976024 | -0.326674 |
| 61 | H | 7.587888 | 2.316007 | 0.127222 |
| 62 | H | 11.556332 | -1.958939 | -0.643631 |
| 63 | H | 11.561467 | -0.319996 | -1.374481 |
| 64 | H | 11.715198 | -0.497694 | 0.385751 |
| 65 | H | -1.46773 | 6.38835 | 0.184092 |
| 66 | H | 0.545541 | 7.704545 | 0.678979 |
| 67 | H | 2.780119 | 6.61759 | 0.804868 |
| 68 | H | 3.03506 | -6.498587 | -0.445083 |
| 69 | H | 0.837014 | -7.662367 | -0.361551 |
| 70 | H | -1.239228 | -6.402939 | -0.002134 |
| 71 | H | -2.155139 | -1.338474 | 1.694687 |
| 72 | H | -3.761487 | 0.426471 | 2.250662 |
| 73 | C | -6.481432 | 0.331272 | 2.073977 |
| 74 | H | -7.003738 | -2.096494 | 0.995862 |
| 75 | H | -5.399332 | -3.879558 | 0.432276 |
| 76 | H | -5.509086 | 3.738864 | -0.548505 |
| 77 | H | -7.019522 | 1.90718 | -1.206914 |
| 78 | C | -6.356809 | -0.494226 | -2.272591 |
| 79 | H | -3.631644 | -0.488796 | -2.317757 |
| 80 | H | -2.118547 | 1.324197 | -1.669134 |
| 81 | F | -7.448324 | -0.592665 | -1.475172 |
| 82 | F | -5.760978 | -1.706954 | -2.289746 |
| 83 | F | -6.8221 | -0.270649 | -3.528685 |
| 84 | F | -7.025508 | 0.077283 | 3.291955 |
| 85 | F | -7.518244 | 0.405541 | 1.204118 |
| 86 | F | -5.926547 | 1.561068 | 2.144491 |
| 87 | Cl | 1.183422 | 0.043963 | -0.010926 |

## 3.6. NMR Spectra

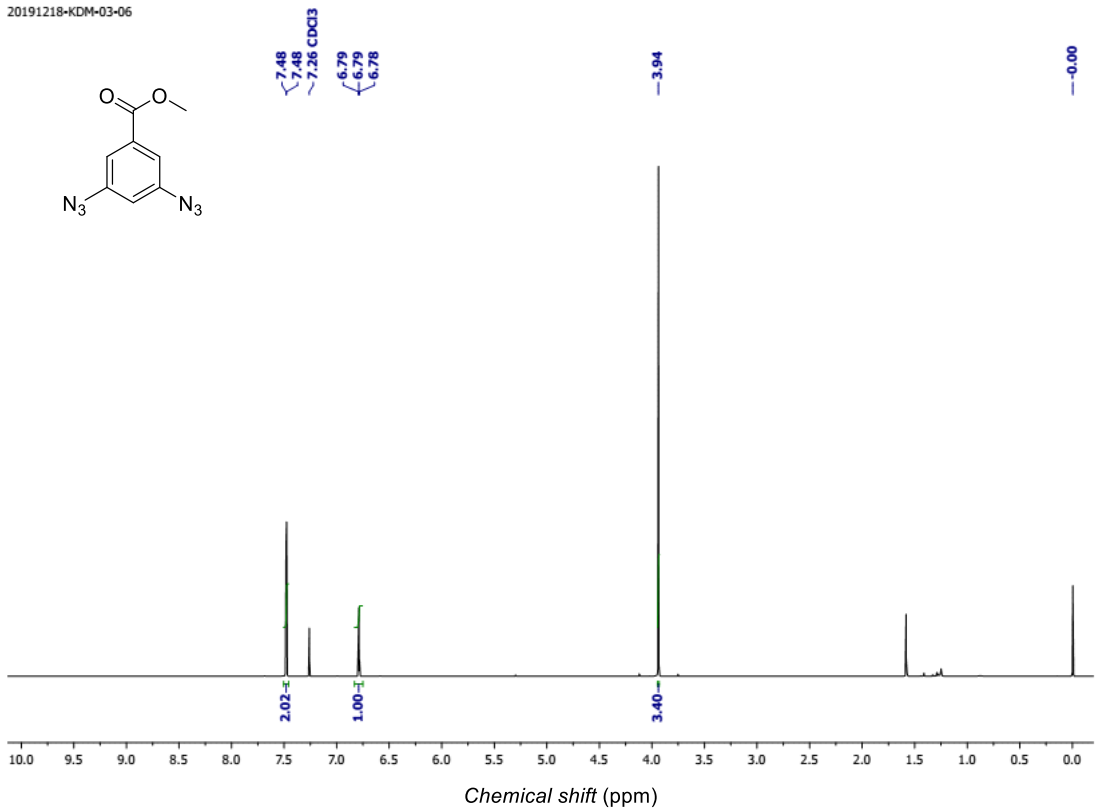



**Figure 3.35** $^{1}$H NMR spectrum of compound **3a** (400 MHz, $CDCl_3$).

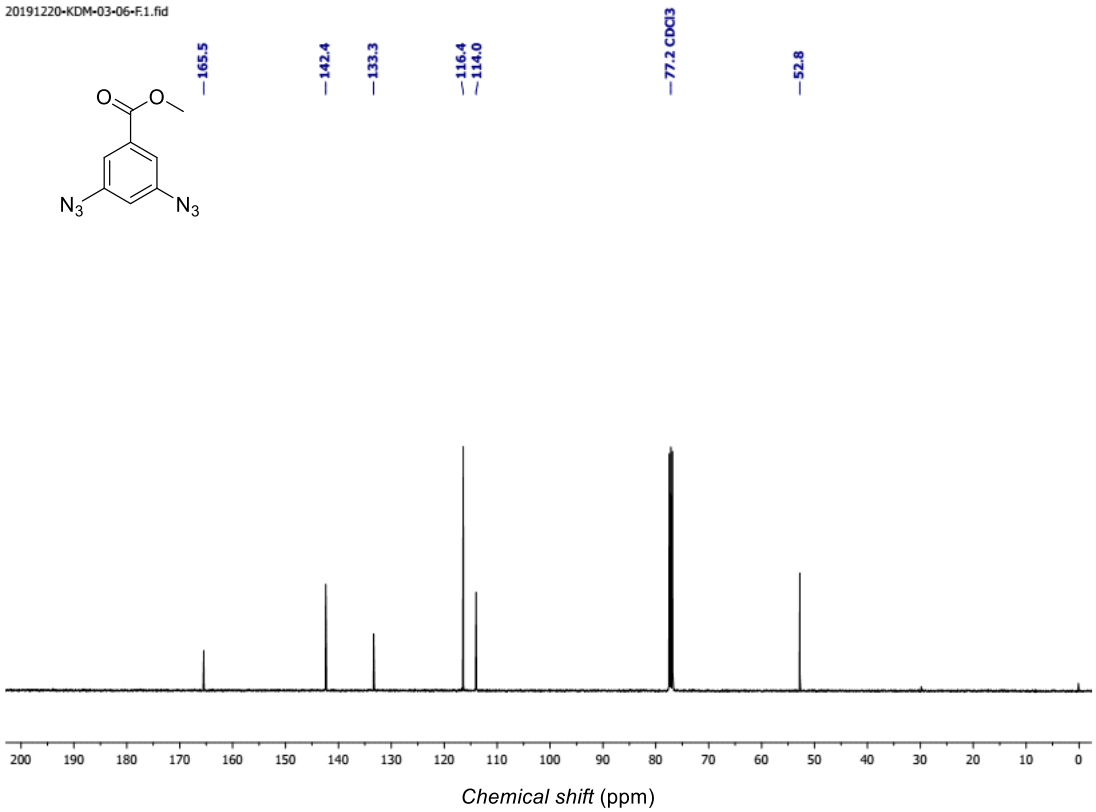



**Figure 3.36** $^{13}$C NMR spectrum of compound **3a** (101 MHz, $CDCl_3$).

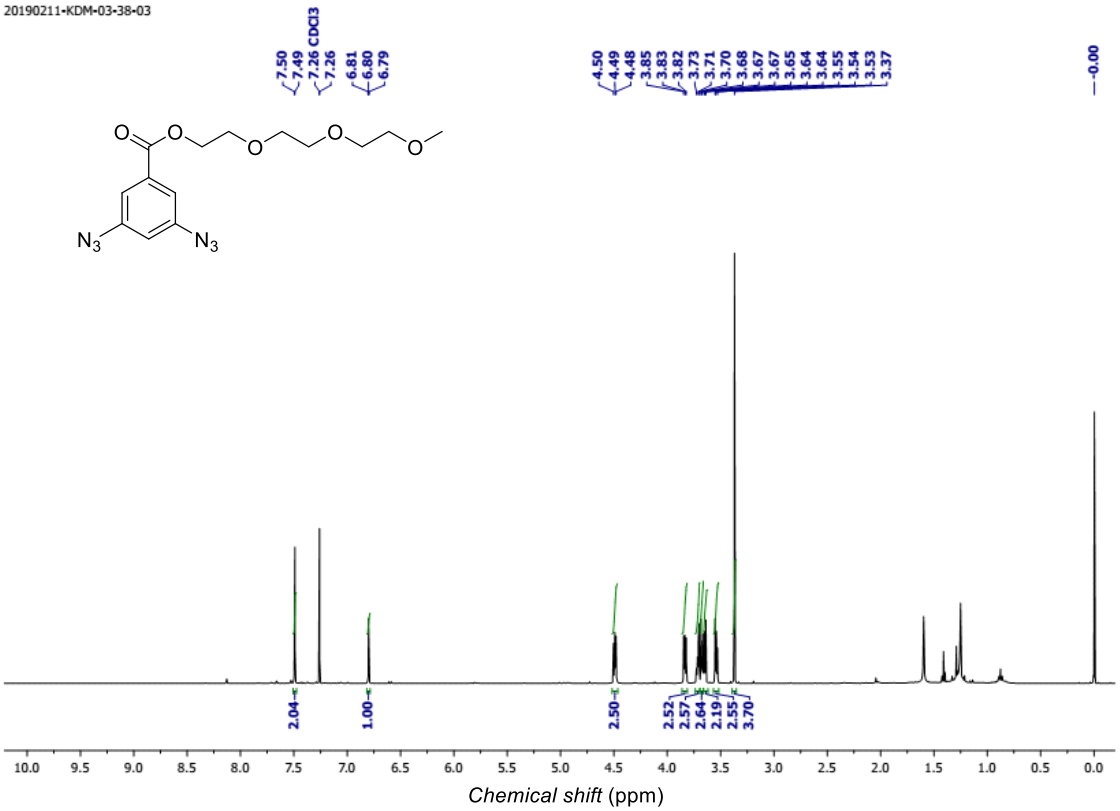



**Figure 3.37** $^{1}$H NMR spectrum of compound **3b** (400 MHz, $CDCl_3$).

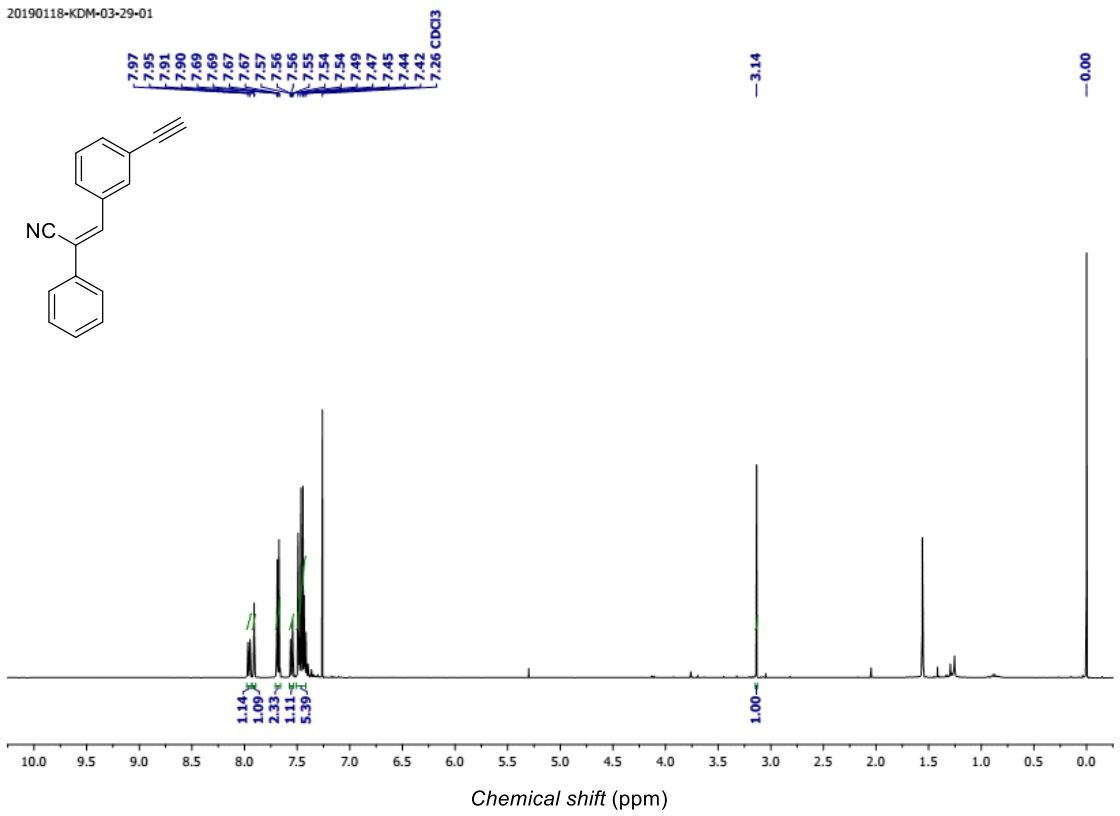



**Figure 3.38** $^{1}$H NMR spectrum of compound **7a** (400 MHz, $CDCl_3$).

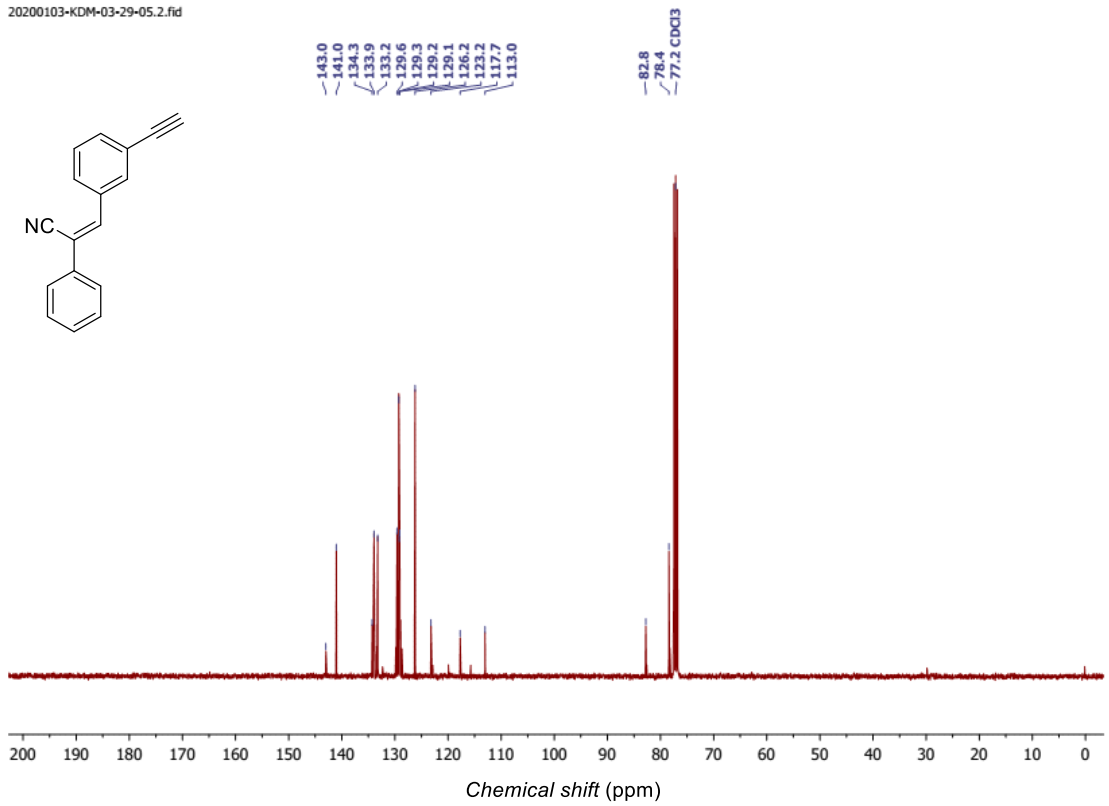



**Figure 3.39** $^{13}C$ NMR spectrum of compound **7a** (101 MHz, $CDCl_3$).

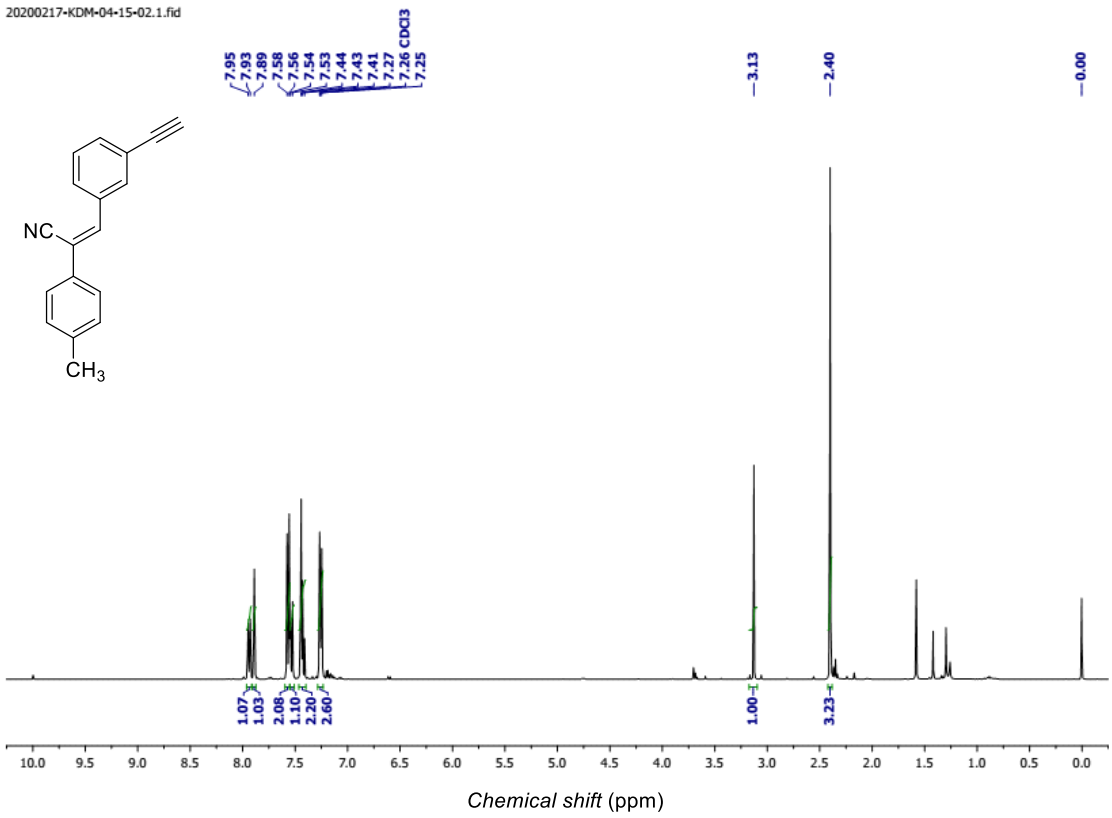



**Figure 3.40** $^{1}H$ NMR spectrum of compound **7b** (400 MHz, $CDCl_3$).

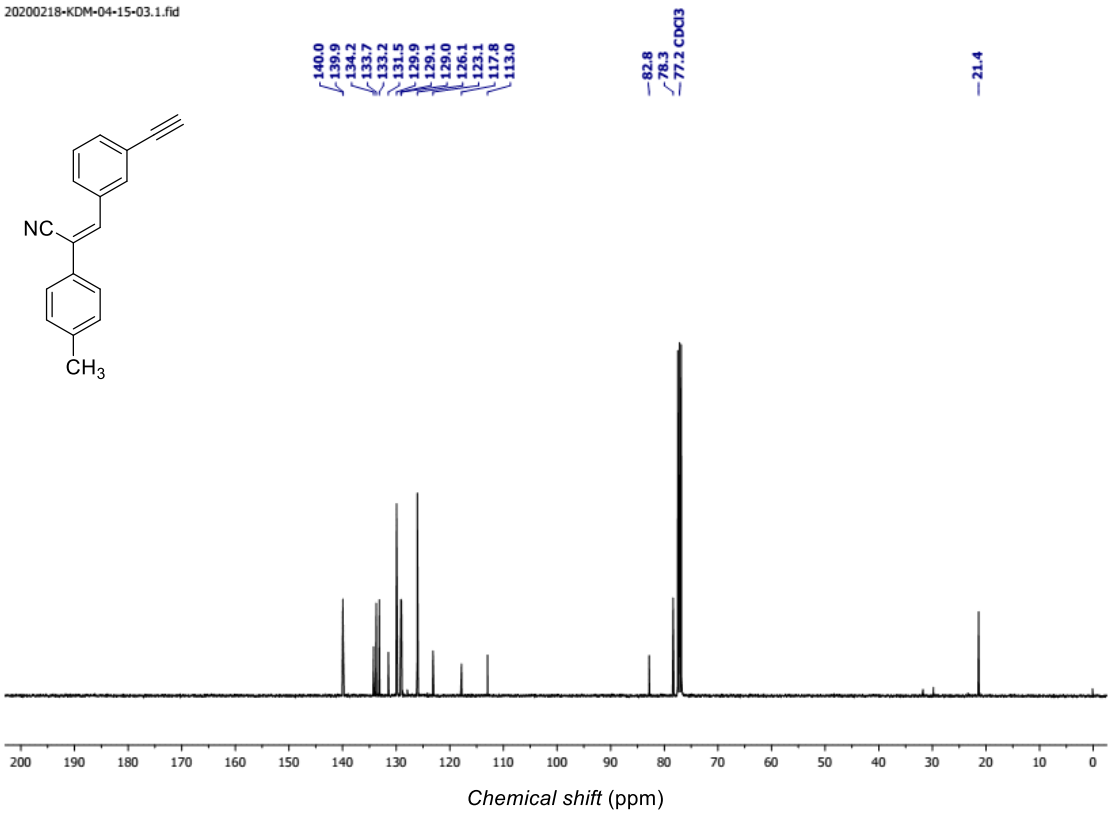



**Figure 3.41** $^{13}$C NMR spectrum of compound **7b** (101 MHz, $CDCl_3$).

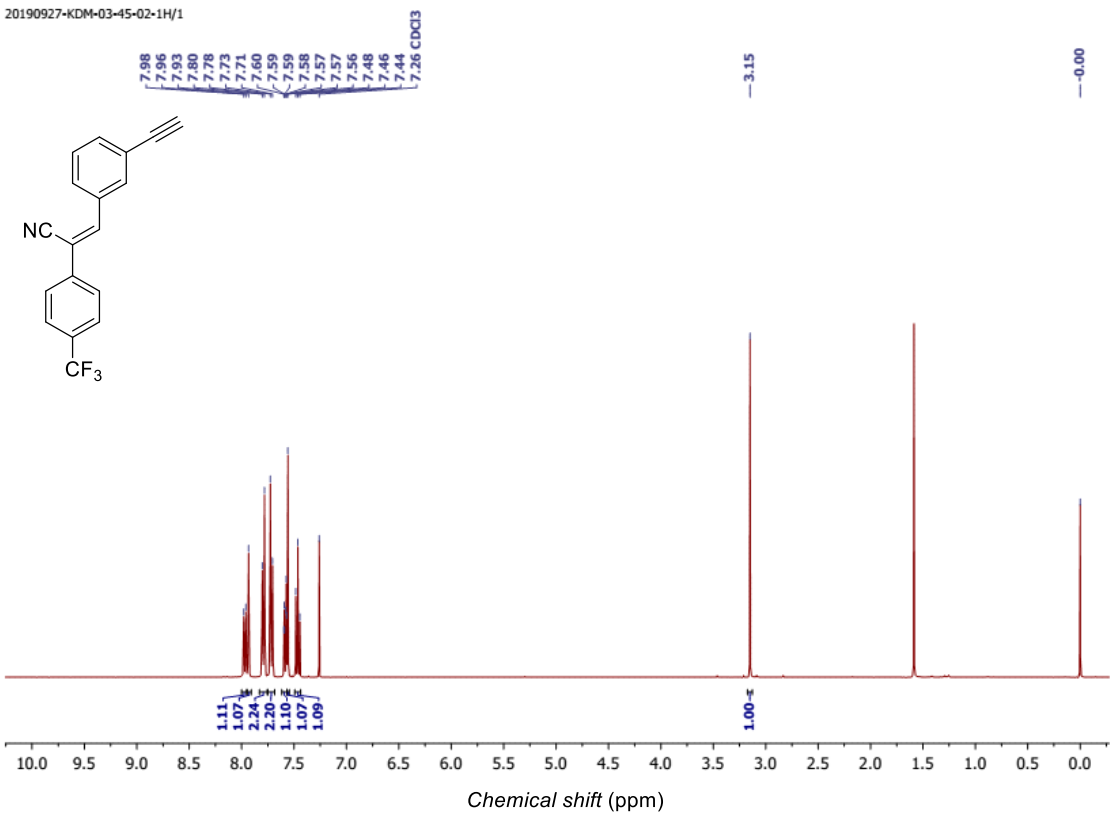



**Figure 3.42** $^{1}$H NMR spectrum of compound **7c** (400 MHz, $CDCl_3$).

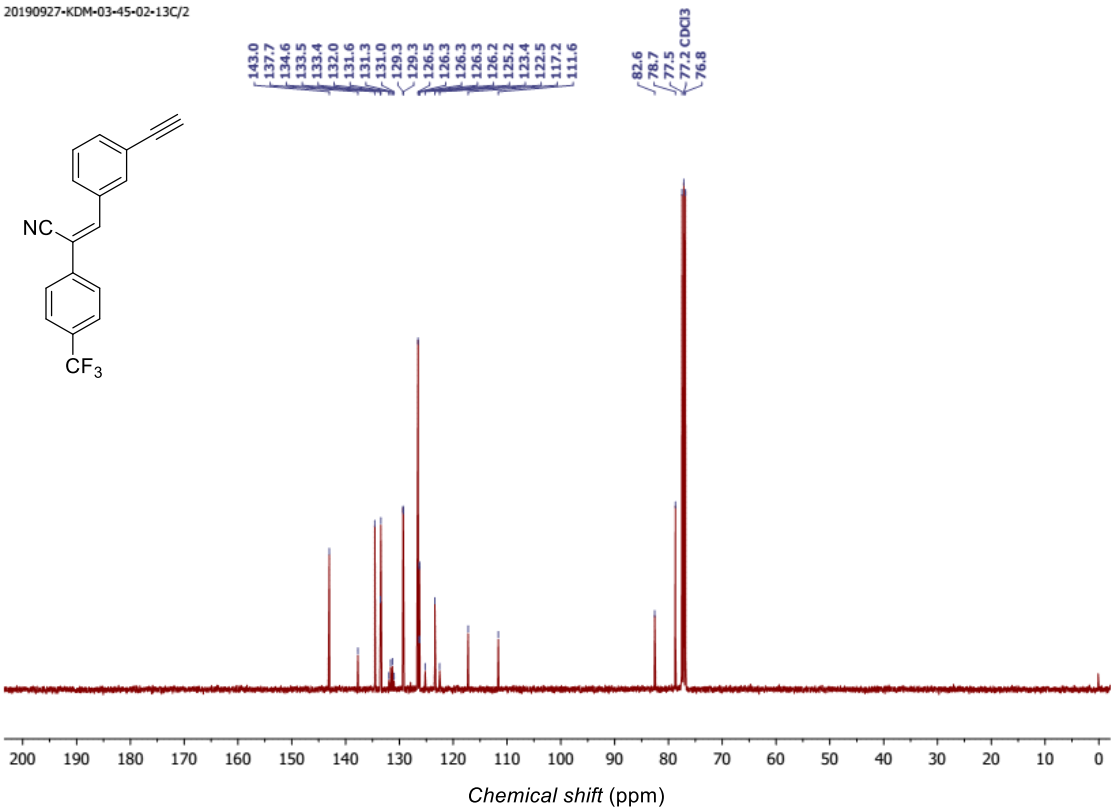



**Figure 3.43** $^{13}$C NMR spectrum of compound **7c** (101 MHz, $CDCl_3$).

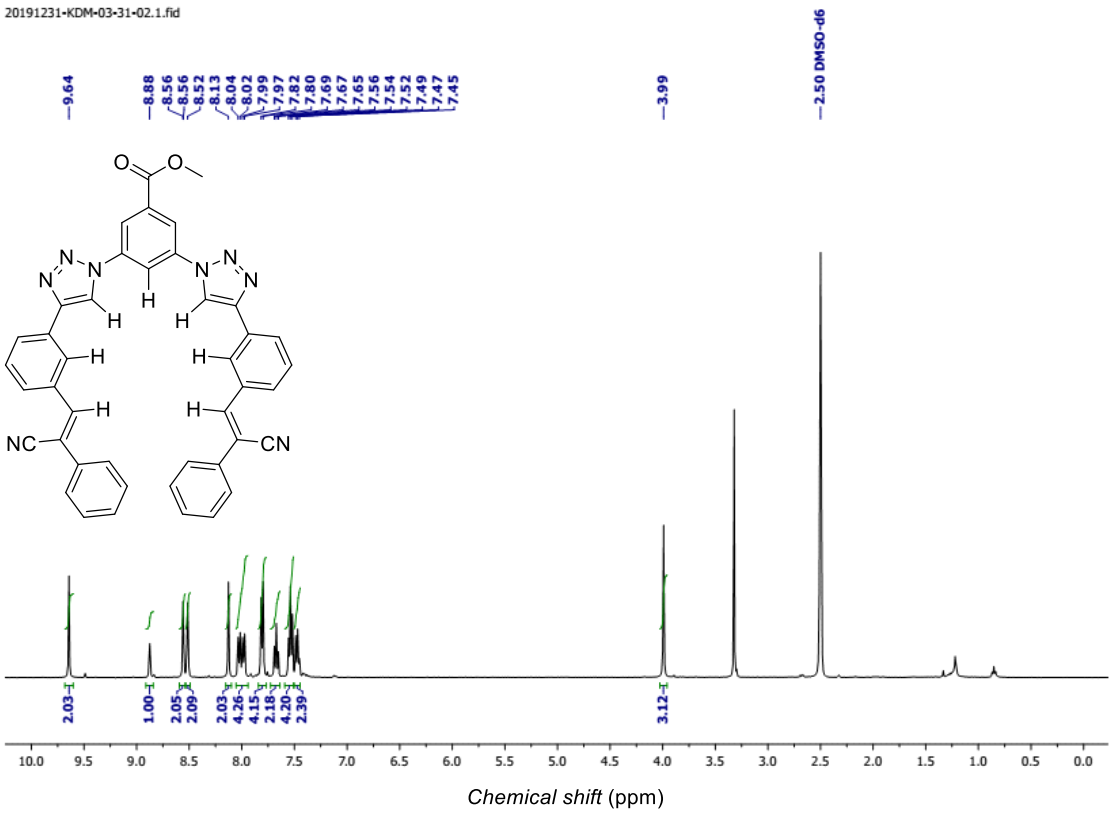



**Figure 3.44** $^{1}$H NMR spectrum of compound **1a** (400 MHz, DMSO-$d_6$).

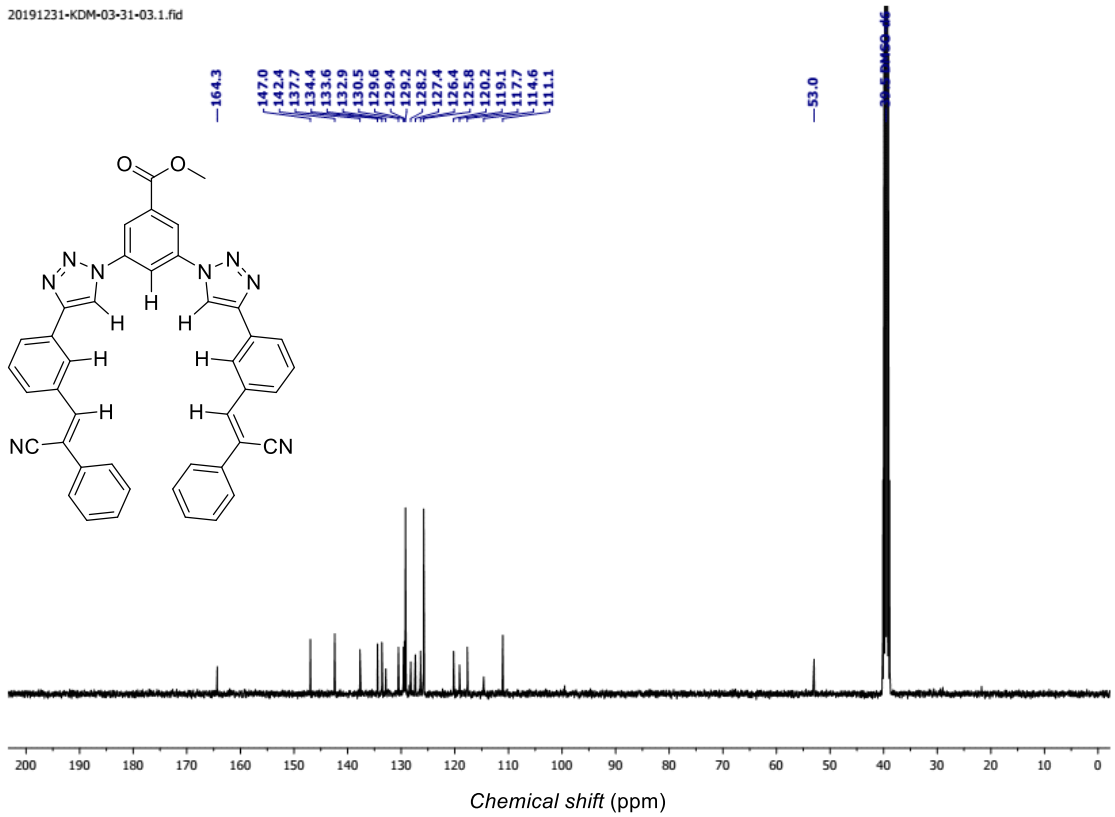



**Figure 3.45** $^{13}$C NMR spectrum of compound **1a** (101 MHz, DMSO-$d_6$).

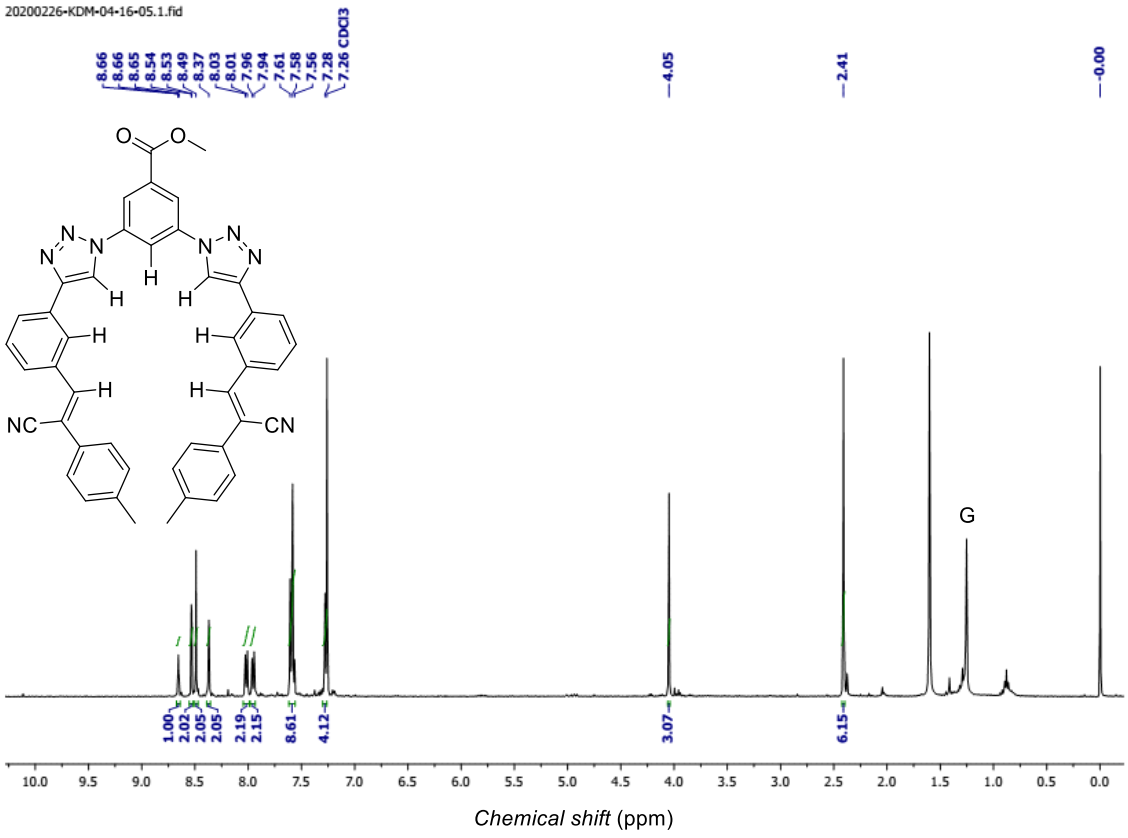



**Figure 3.46** $^{1}$H NMR spectrum of compound **1b** (400 MHz, $CDCl_3$).

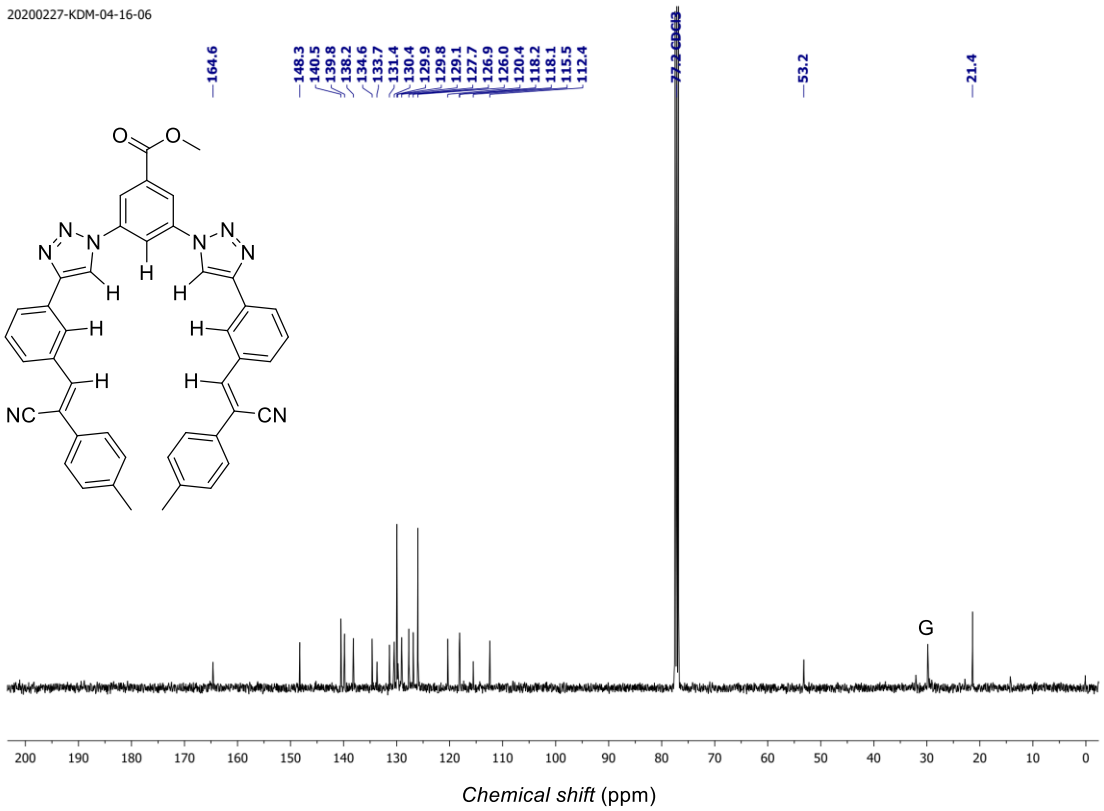



**Figure 3.47** $^{13}$C NMR spectrum of compound **1b** (101 MHz, $CDCl_3$).

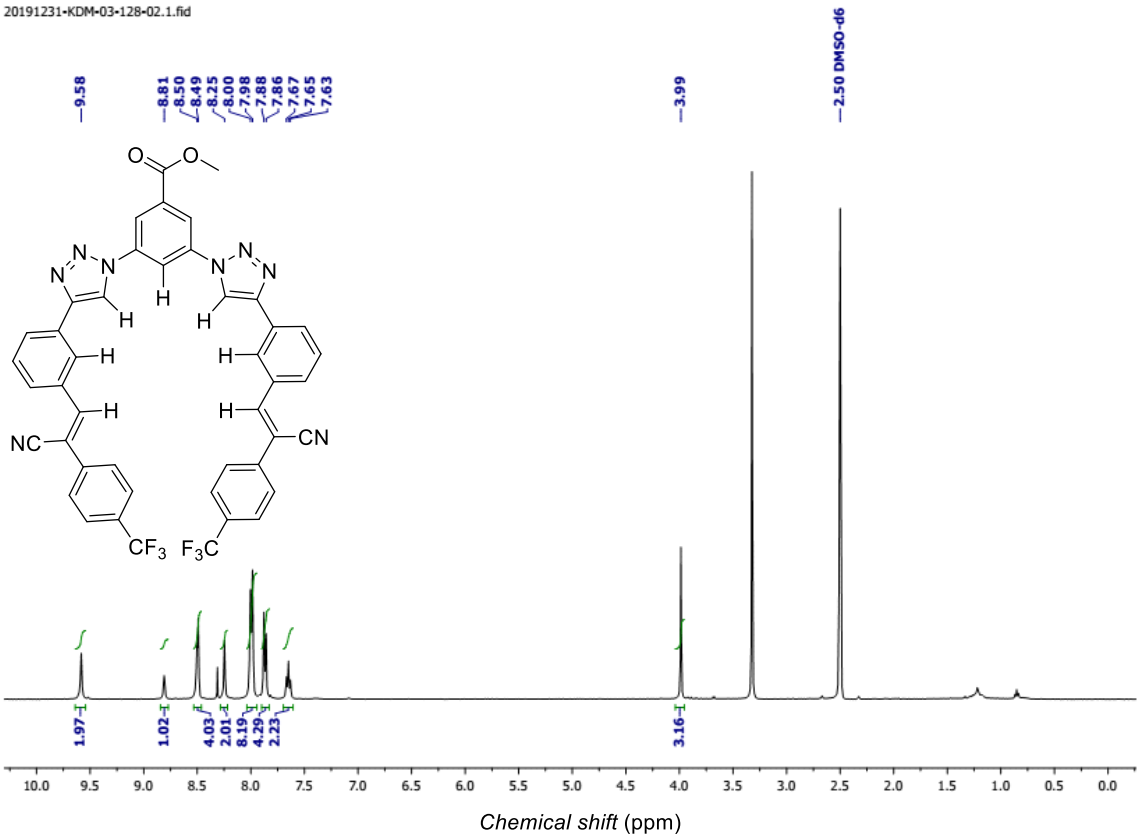



**Figure 3.48** $^{1}$H NMR spectrum of compound **1c** (400 MHz, DMSO-$d_6$).

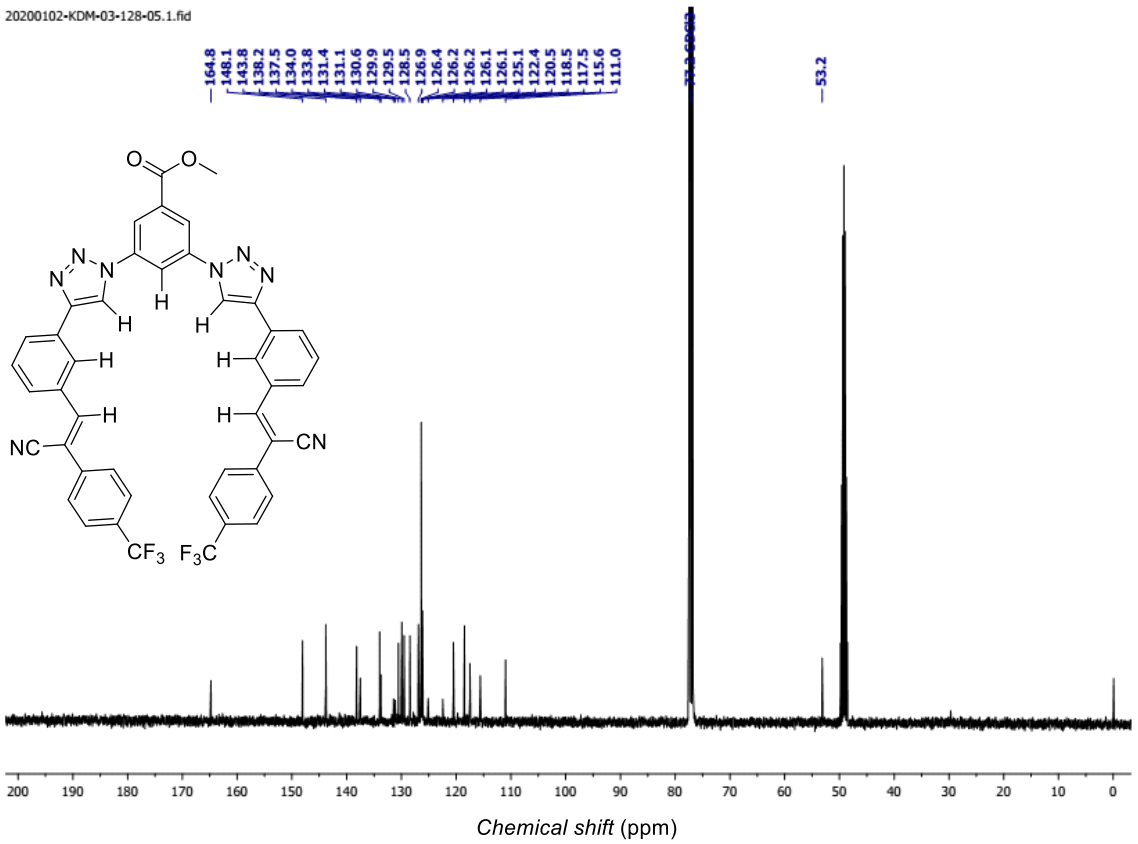



**Figure 3.49** $^{13}$C NMR spectrum of compound **1c** (101 MHz, $CDCl_3$ : DMSO-$d_6$ = 1 : 2).

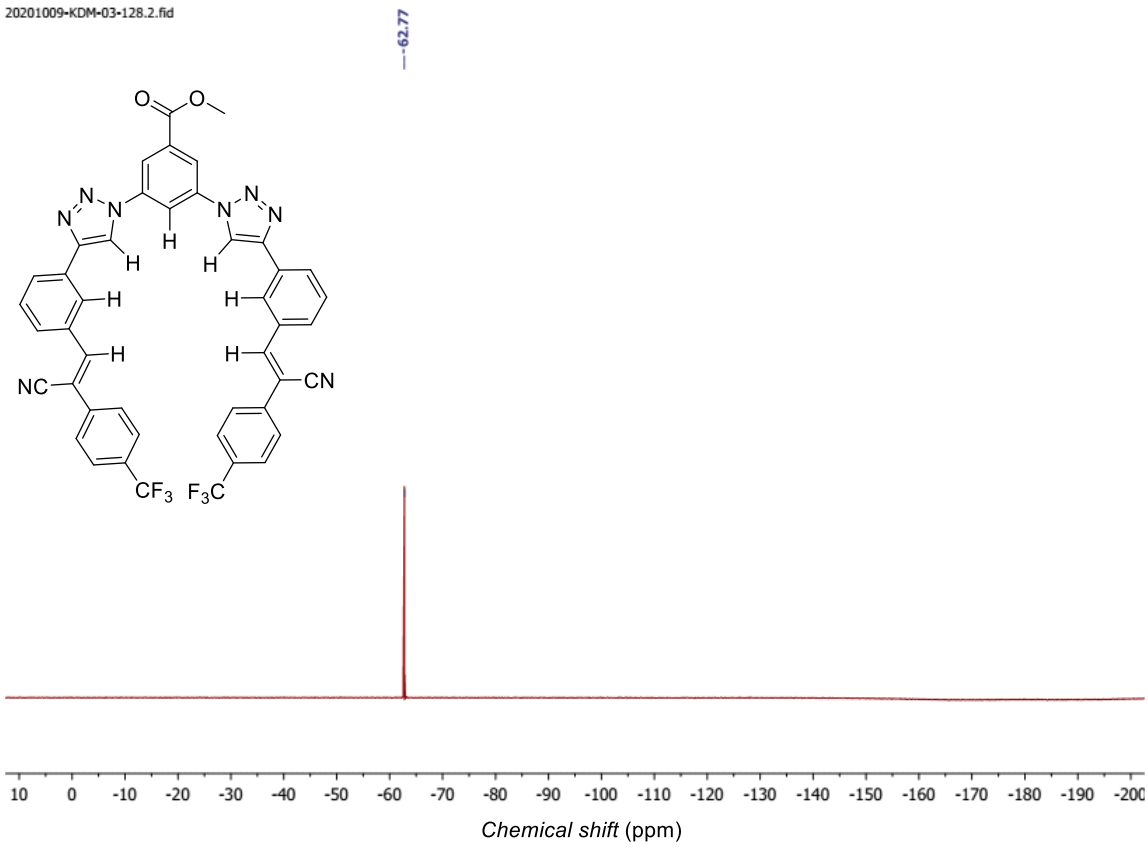



**Figure 3.50** $^{19}$F NMR spectrum of compound **1c** (376.6 MHz, $CDCl_3$).

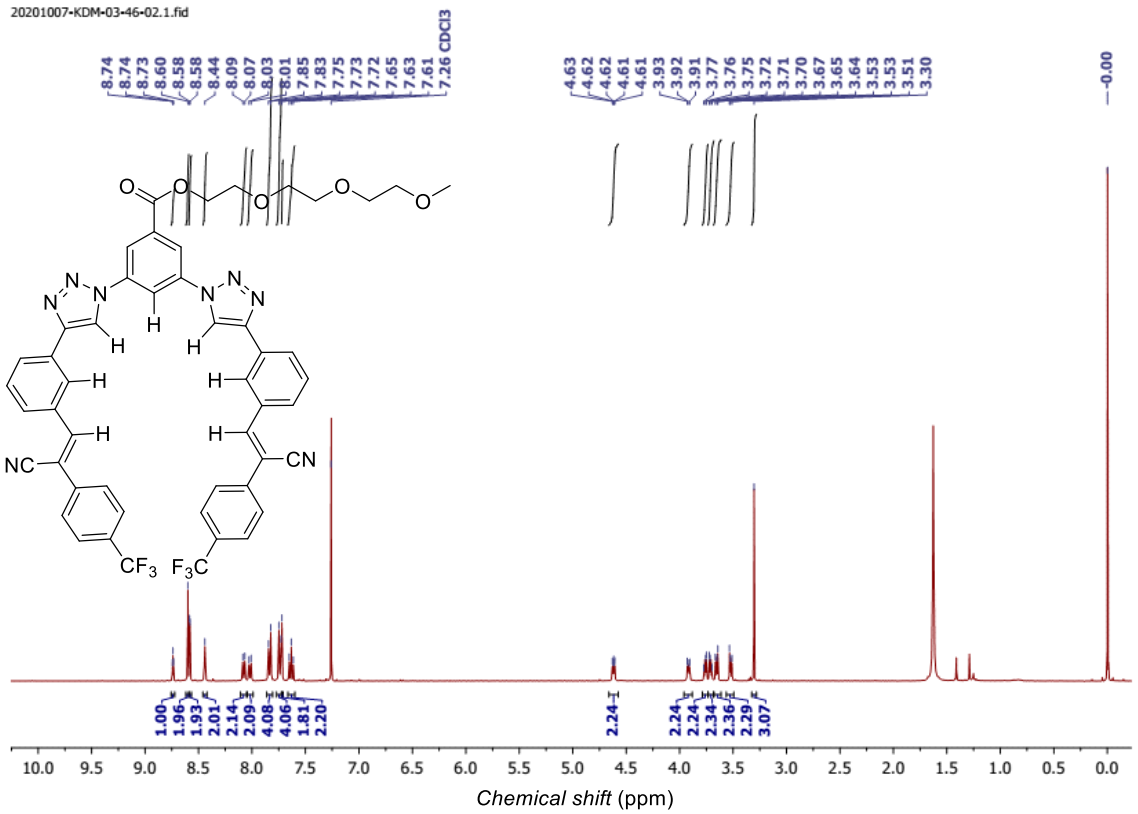



**Figure 3.51** $^{1}$H NMR spectrum of compound **1d** (400 MHz, $CDCl_3$).

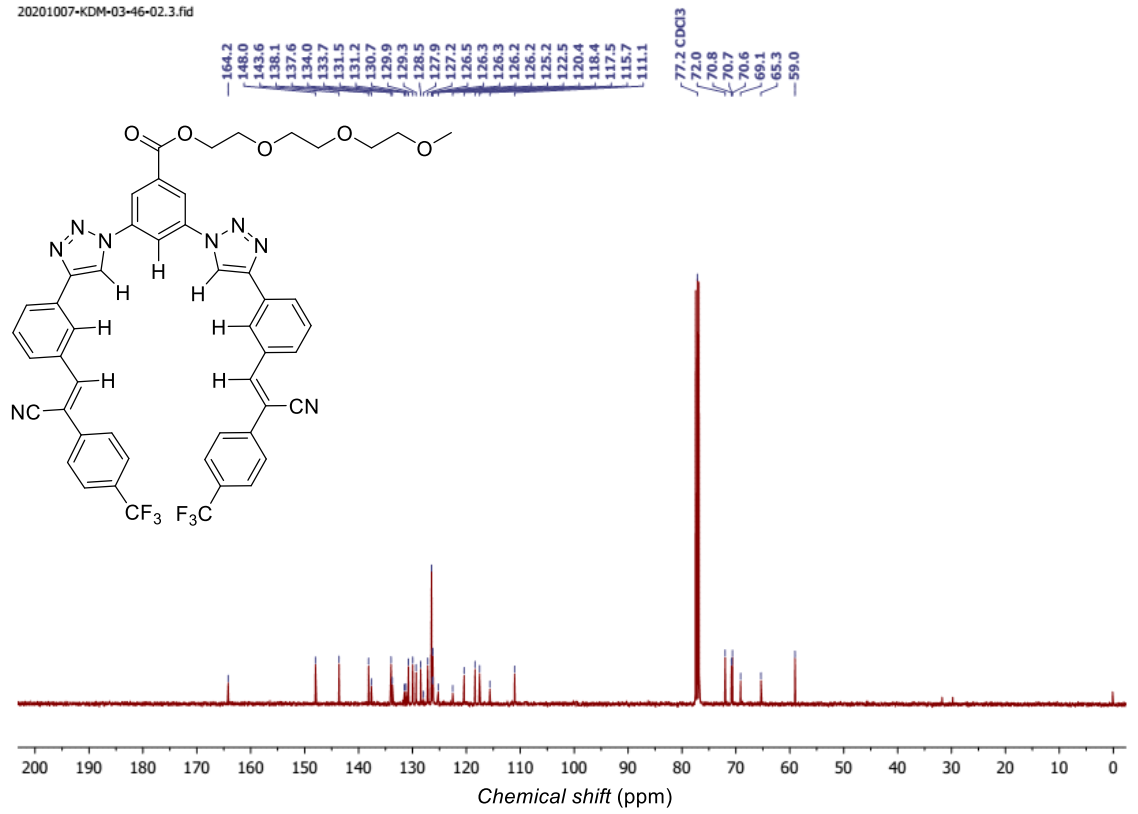



**Figure 3.52** $^{13}$C NMR spectrum of compound **1d** (101 MHz, $CDCl_3$).

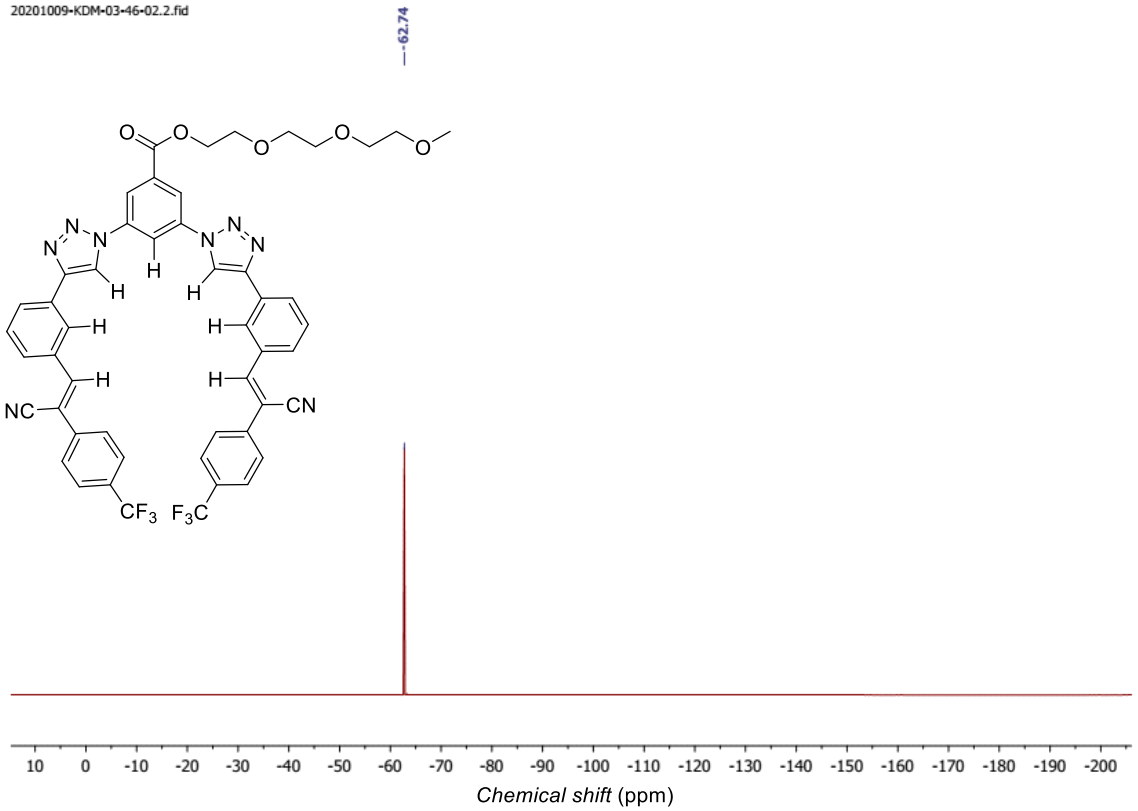



**Figure 3.53** $^{19}F$ NMR spectrum of compound **1d** (376.6 MHz, $CDCl_3$).

## 3.7. References

1. Busschaert, N.; Bradberry, S. J.; Wenzel, M.; Haynes, C. J. E.; Hiscock, J. R.; Kirby, I. L.; Karagiannidis, L. E.; Moore, S. J.; Wells, N. J.; Herniman, J.; Langley, G. J.; Horton, P. N.; Light, M. E.; Marques, I.; Costa, P. J.; Félix, V.; Frey, J. G.; Gale, P. A. *Chem. Sci.* **2013**, *4*, 3036–3045.
2. Gale, P. A.; Davis, J. T.; Quesada, R. *Chem. Soc. Rev.* **2017**, *46*, 2497–2519.
3. Berryman, O. B.; Sather, A. C.; Hay, B. P.; Meisner, J. S.; Johnson, D. W. *J. Am. Chem. Soc.* **2008**, *130*, 10895–10897.
4. Brown, A.; Beer, P. D. *Chem. Commun.* **2016**, *52*, 8645–8658.
5. Borissov, A.; Marques, I.; Lim, J. Y. C.; Félix, V.; Smith, M. D.; Beer, P. D. *J. Am. Chem. Soc.* **2019**, *141*, 4119–4129.
6. Qiu, J.; Song, B.; Li, X.; Cozzolino, A. F. *Phys. Chem. Chem. Phys.*, **2018**, *20*, 46–50.
7. Wang, Y.; Xiang, J.; Jiang, H. *Chem. – Eur. J.* **2011**, *17*, 613–619.

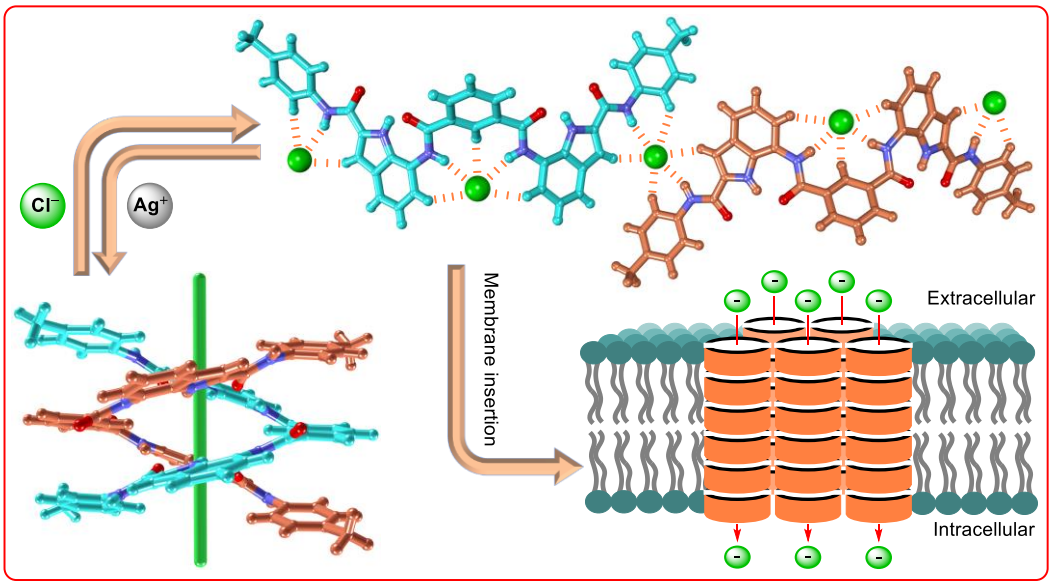
8. Fargher, H. A.; Lau, N.; Richardson, H. C.; Cheong, P. H.-Y.; Haley, M. M.; Pluth, M. D.; Johnson, D. W. *J. Am. Chem. Soc.* **2020**, *142*, 8243–8251.
9. Juwarker, H.; Lenhardt, J. M.; Castillo, J. C.; Zhao, E.; Krishnamurthy, S.; Jamiolkowski, R. M.; Kim, K.-H.; Craig, S. L. *J. Org. Chem.* **2009**, *74*, 8924–8934.
10. Li, Y.; Flood, A. H. *J. Am. Chem. Soc.* **2008**, *130*, 12111–12122.
11. Lee, S.; Chen, C.-H.; Flood, A. H. *Nat. Chem.* **2013**, *5*, 704–710.
12. Bandyopadhyay, I.; Raghavachari, K.; Flood, A. H. *ChemPhysChem* **2009**, *10*, 2535–2540.
13. Liu, Y.; Zhao, W.; Chen, C.-H.; Flood, A. H. *Science* **2019**, *365*, 159–161.
14. Juwarker, H.; Lenhardt, J. M.; Pham, D. M.; Craig, S. L. *Angew. Chem., Int. Ed.* **2008**, *47*, 3740–3743.
15. Shang, J.; Zhao, W.; Li, X.; Wang, Y.; Jiang, H. *Chem. Commun.* **2016**, *52*, 4505–4508.
16. Qin, L.; Vervuurt, S. J. N.; Elmes, R. B. P.; Berry, S. N.; Proschogo, N.; Jolliffe, K. A. *Chem. Sci.* **2020**, *11*, 201–207.
17. Qin, L.; Hartley, A.; Turner, P.; Elmes, R. B. P.; Jolliffe, K. A. *Chem. Sci.* **2016**, *7*, 4563–4572.
18. Portis, B.; Mirchi, A.; Emami Khansari, M.; Pramanik, A.; Johnson, C. R.; Powell, D. R.; Leszczynski, J.; Hossain, M. A. *ACS Omega* **2017**, *2*, 5840–5849.
19. Sessler, J. L.; Katayev, E.; Pantos, G. D.; Ustynyuk, Y. A. *Chem. Commun.* **2004**, 1276–1277.
20. Kang, S. O.; Powell, D.; Bowman-James, K. *J. Am. Chem. Soc.* **2005**, *127*, 13478–13479.
21. Ravikumar, I.; Ghosh, P. *Chem. Commun.* **2010**, *46*, 6741–6743.
22. Jia, C.; Wu, B.; Li, S.; Huang, X.; Zhao, Q.; Li, Q.-S.; Yang, X.-J. *Angew. Chem., Int. Ed.* **2011**, *50*, 486–490.
23. Busschaert, N.; Wenzel, M.; Light, M. E.; Iglesias-Hernández, P.; Pérez-Tomás, R.; Gale, P. A. *J. Am. Chem. Soc.* **2011**, *133*, 14136–14148.
24. Ravikumar, I.; Ghosh, P. *Chem. Soc. Rev.* **2012**, *41*, 3077–3098.
25. Kubik, S.; Kirchner, R.; Nolting, D.; Seidel, J. *J. Am. Chem. Soc.* **2002**, *124*, 12752–12760.
26. Rodriguez-Docampo, Z.; Eugenieva-Ilieva, E.; Reyheller, C.; Belenguer, A. M.; Kubik, S.; Otto, S. *Chem. Commun.* **2011**, *47*, 9798–9800.
27. Schaly, A.; Belda, R.; García-España, E.; Kubik, S. *Org. Lett.* **2013**, *15*, 6238–6241.

28. Sommer, F.; Marcus, Y.; Kubik, S. *ACS Omega* **2017**, *2*, 3669–3680.
29. Fatila, E. M.; Twum, E. B.; Sengupta, A.; Pink, M.; Karty, J. A.; Raghavachari, K.; Flood, A. H. *Angew. Chem., Int. Ed.* **2016**, *55*, 14057–14062.
30. Fatila, E. M.; Twum, E. B.; Karty, J. A.; Flood, A. H. *Chem. – Eur. J.* **2017**, *23*, 10652–10662.
31. Fatila, E. M.; Pink, M.; Twum, E. B.; Karty, J. A.; Flood, A. H. *Chem. Sci.* **2018**, *9*, 2863–2872.
32. Sheetz, E. G.; Qiao, B.; Pink, M.; Flood, A. H. *J. Am. Chem. Soc.* **2018**, *140*, 7773–7777.
33. Bickerton, L. E.; Sterling, A. J.; Beer, P. D.; Duarte, F.; Langton, M. J. *Chem. Sci.* **2020**, *11*, 4722–4729.
34. Chen, S.; Zhang, S.; Bao, C.; Wang, C.; Lin, Q.; Zhu, L. *Chem. Commun.* **2016**, *52*, 13132–13135.
35. Shang, J.; Si, W.; Zhao, W.; Che, Y.; Hou, J.-L.; Jiang, H. *Org. Lett.* **2014**, *16*, 4008–4011.
36. Saggiomo, V.; Otto, S.; Marques, I.; Félix, V.; Torroba, T.; Quesada, R. *Chem. Commun.* **2012**, *48*, 5274–5276.
37. *Marvin*, ver. 5.8.0; ChemAxon, 2012. http://www.chemaxon.com.
38. Smart, B. E. *J. Fluor. Chem.* **2001**, *109*, 3–11.
39. Fazio, M. A.; Lee, O. P.; Schuster, D. I. *Org. Lett.* **2008**, *10*, 4979–4982.
40. Alam, M. S.; Nam, Y.-J.; Lee, D.-U. *Eur. J. Med. Chem.* **2013**, *69*, 790–797.
41. Mondal, D.; Sathyan, A.; Shinde, S. V.; Mishra, K. K.; Talukdar, P. *Org. Biomol. Chem.* **2018**, *16*, 8690–8694.
42. Li, Y.; Pink, M.; Karty, J. A.; Flood, A. H. *J. Am. Chem. Soc.* **2008**, *130*, 17293–17295.
43. *BindFit*, http://app.supramolecular.org/bindfit/ (accessed July 2019).
44. Thordarson, P. *Chem. Soc. Rev.* **2011**, *40*, 1305–1323.
45. Ulatowski, F.; Dąbrowa, K.; Bałakier, T.; Jurczak, J. *J. Org. Chem.* **2016**, *81*, 1746–1756.
46. Bahmanjah, S.; Zhang, N.; Davis, J. T. *Chem. Commun.* **2012**, *48*, 4432–4434.
47. Saha, T.; Hossain, M. S.; Saha, D.; Lahiri, M.; Talukdar, P. *J. Am. Chem. Soc.* **2016**, *138*, 7558–7567.
48. Busschaert, N.; Karagiannidis, L. E.; Wenzel, M.; Haynes, C. J. E.; Wells, N. J.; Young, P. G.; Makuc, D.; Plavec, J.; Jolliffe, K. A.; Gale, P. A. *Chem. Sci.* **2014**, *5*, 1118–1127.

49. McNally, B. A.; Koulov, A. V.; Smith, B. D.; Joos, J.-B.; Davis, A. P. *Chem. Commun.* **2005**, 1087–1089.
50. Wu, X.; Judd, Luke W.; Howe, Ethan N. W.; Withecombe, Anne M.; Soto-Cerrato, V.; Li, H.; Busschaert, N.; Valkenier, H.; Pérez-Tomás, R.; Sheppard, David N.; Jiang, Y.-B.; Davis, Anthony P.; Gale, Philip A. *Chem* **2016**, *1*, 127–146.
51. Goto, H.; Obata, S.; Nakayama, N.; Ohta, K. *CONFLEX 8*, CONFLEX Corporation, Tokyo, Japan, 2017.
52. Frisch, M. J. *et al.*, *Gaussian 09, Revision B.01*, Gaussian, Inc., Wallingford, CT, 2010.
53. McLean, A. D.; Chandler, G. S. *J. Chem. Phys.* **1980**, *72*, 5639–5648.
54. Borissov, A.; Lim, J. Y. C.; Brown, A.; Christensen, K. E.; Thompson, A. L.; Smith, M. D.; Beer, P. D. *Chem. Commun.* **2017**, *53*, 2483–2486.
55. Brynn Hibbert, D.; Thordarson, P. *Chem. Commun.* **2016**, *52*, 12792–12805.
56. Goto, H.; Osawa, E. *J. Am. Chem. Soc.* **1989**, *111*, 8950–8951.
57. Hay, B. P.; Bryantsev, V. S. *Chem. Commun.* **2008**, 2417–2428.
58. Boys, S. F.; Bernardi, F. *Mol. Phys.* **1970**, *19*, 553–566.

*Chapter 4*

# Reversible Unwinding-Rewinding of Bis(indole) Double Helix to Chloride-coordinated Supra-molecular Polymeric Anion Channel

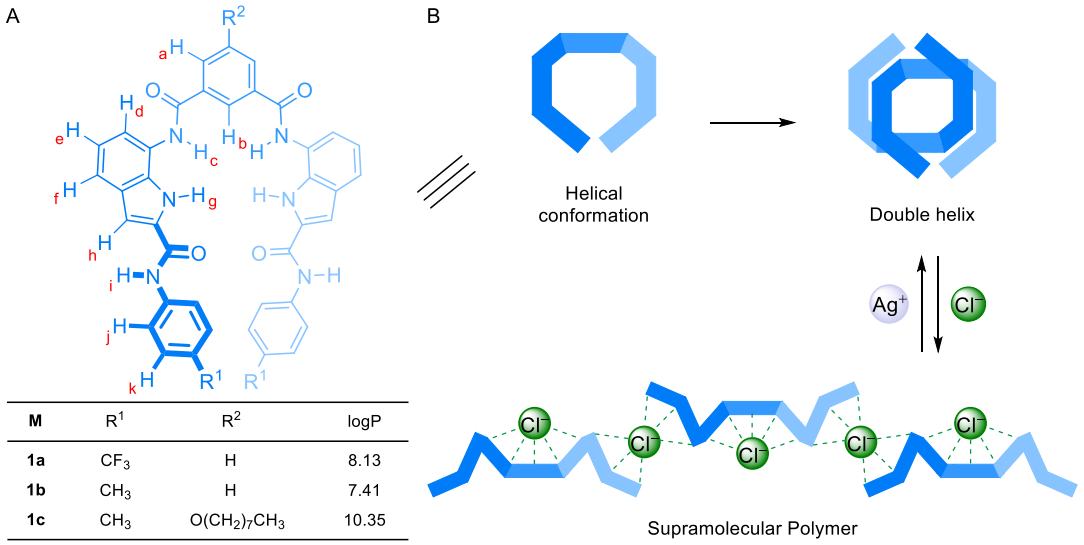


## 4.1. Introduction

We have discussed earlier that the semipermeable nature of the cell membrane allows some specific small nonpolar molecules to pass through it by preventing polar solutes such as amino acid, sugar, anions, cations, etc., which are also equally essential for the survival of the cell.[1] The ion transporters are mostly membrane-embedded protein channels or ion carriers, which play a crucial to transport the ions across the bilayer membrane for the smooth operation of the physiological process. In the previous chapters, we have discussed the transmembrane transport by cyanurate and triazole receptors, which transport the $Cl^-$ ion via a carrier mechanism. Unlike ion carriers, the ion channels form a static hydrophilic path for the ion to transport across the bilayer membrane and are very selective for different ions. The ion selectivity of the naturally occurring ion channels can be attributed to the presence of multiple ion binding sites. The lumen of the channel offers multiple binding sites for the specific ions, which allows the passage of the ions across the lipophilic membranes of the cell membrane. This characteristic can be demonstrated by reviewing the molecular-level structure of the naturally occurring chloride selective channels, i.e., the CLCs channels, which are known to transport the $Cl^-$ ion across the cell membranes with excellent selectivity. The crystal structure of the CLC channel shows the presence of three ion-binding sites creating the selectivity filter, which forms a bridge for the $Cl^-$ ions between the extra- and intracellular solutions (Figure 1.5 E).[2-3] The $Cl^-$ ions bind to all three specific sites through the noncovalent interactions with the amino acid side chains and backbone amide NH groups of α-helices, and selectivity pass through the membrane.[4]

Considering the facts as mentioned above, it can be anticipated that imposing the multiple selectivity filters in the synthetic ion channels can considerably enhance the selectivity and activity of these channels. In this regard, multiple reports are there in the literature which mimic the function of naturally occurring ion selectivity filters of ion channels. These ion channels systems are primarily self-assembled polymeric channels that form a specific path for selective transport of ions through it. For example, Matile and co-workers introduced the ion channel formation by dendritic folate molecule where the hydrogen bond directed self-assembly of guanosine unit form circular oligomers templated by a cation.[5] The circular oligomers finally form a supramolecular rosette channel for ion transport involving π–π interactions between the layers. Later, Davis and co-workers have also reported the ion channel behavior by the cation-induced polymeric channel formed by nucleoside–sterol conjugate.[6]

The guanosine moiety present in the molecule forms a G-quartet induced by $K^+$ ion, subsequently stacked via π–π interaction to create a large and stable polymeric supramolecular structure for ion transportation through bilayer membranes. However, the anion-template induced supramolecular polymeric ion channels are not reported.




| M | $R^1$ | $R^2$ | logP |
|---|---|---|---|
| **1a** | $CF_3$ | H | 8.13 |
| **1b** | $CH_3$ | H | 7.41 |
| **1c** | $CH_3$ | $O(CH_2)_7CH_3$ | 10.35 |

**Figure 4.1** Chemical structures of bis(indole) molecules **1a**–**1c** in single-stranded helical form (A) and the schematic representation of conformational change from the double helix to anion coordinated supramolecular assembly (B). The dotted lines in the bottom depiction are the representation of noncovalent bonding interactions.

Herein, we demonstrate the reversible switching of bis(indole)-based isophthalimides **1a**–**1c** between its two distinct self-assembled conformations. The compounds have multiple hydrogen bond donor and acceptor sites, including the acidic N–H and C–H bond of the indole moiety, for noncovalent interactions. With the help of these bonding sites, molecules form self-assembled double-helical conformation by employing the intermolecular hydrogen bonding interaction, whereas the treatment of $Cl^-$ ion transforms to its anion coordinated polymeric conformation. The octyloxy chain at the central aromatic ring was introduced to modulate the molecule's solubility in common organic solvents for its solution-phase characterization. On the other hand, the $CF_3$ group was presented at the para position of the terminal aromatic ring to control the lipophilicity of the molecules for its membrane transport application.

## 4.2. Results and Discussions

### 4.2.1. Synthesis

The bis(indole) molecules **1a**–**1c** were synthesized starting from 7-nitro-1*H*-indole-2-carboxylic acid **7** (Scheme 4.2, 4.3 and 4.4). At first, the indole acid **7** was synthesized in four

steps starting from 2-nitroaniline **2** following the reported literature procedure (Scheme 4.1).[7] Then the compound **7** was reacted with different *para*-substituted aryl amines **8a**–**8b** in the presence of EDC·HCl and HOBt to furnish the indole-amides **9a**–**9b** in 62-96% yield. Subsequent hydrogenation reaction of indole-amides **9a**–**9b** gave the reduced products **10a**–**10b** in quantitative yield. The products were further treated with freshly prepared isophthaloyl dichlorides[8-9] **12a**–**12b** to furnish our desired compounds **1a**–**1c** in 82-86% yield.

### 4.2.2. Double Helix Conformation

The solid-state structure of the free form of the bis(indole) foldamers was studied by single crystal X-ray analysis (Table 4.1). The suitable single crystal for X-ray analysis of **1a** was obtained from 3:2 ethyl acetate-hexane solution of the compound by slow evaporation of the solvents in the open air. In the solid state, the bis(indole) molecule **1a** forms a folded helical conformation. In this conformation, each carbonyl group attached to the indole moiety from one molecule participates in bifurcated intermolecular hydrogen bonding interaction with indole N–H ($H_g$) and amide N–H ($H_c$). There are four sets of bifurcated intermolecular hydrogen bonding interactions (Table 4.2) between two helical units of **1a**, which leads to the formation of a double helix structure [**1a**···**1a**] (Figure 4.2A). The hydrogen bond distances between N–H and carbonyl, which form a double helix structure, are ranging from 2.84 Å to 3.18 Å. Along with these interactions, the double helix structure is also stabilized by the π–π interactions between two strands with the centroid-to-centroid interaction distance ranging from 3.59 Å to 4.18 Å. Each set of the double helix was connected to its neighboring double helixes by inter-helical hydrogen bonding interaction (Figure 4.4A) of terminal amide N–H ($H_i$, facing outside) with the carbonyl group of the isophthalamide unit. We obtained the crystal structure of **1b** from 1:10 nitrobenzene-tetrahydrofuran solution, which has also shown similar intermolecular hydrogen bonding to form the double helix structure (Figure 4.2B).

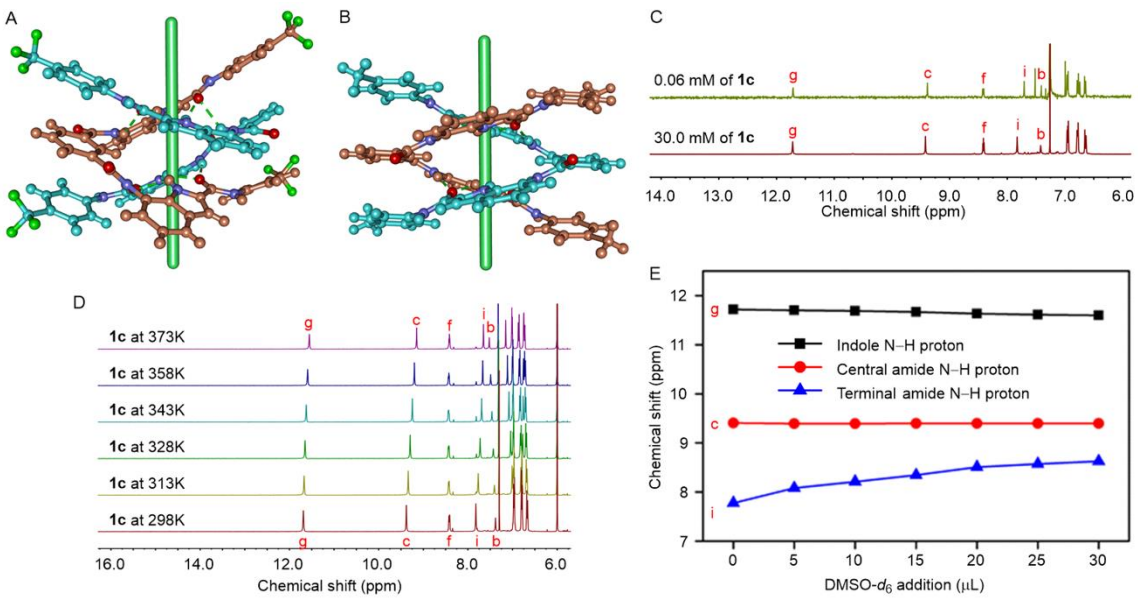



**Figure 4.2** The X-ray crystal structures of **1a** (A) and **1b** (B) forming double helix structures. Two helices in each structure are shown in two different colors, where the green rods along the helical axis are added to enhance the visibility. The solvent molecules in the crystal structure of **1a** and **1b** were omitted for clarity. The partially stacked spectra of $^1$H NMR dilution experiment of **1c** in $CDCl_3$ at 25 ˚C (C). The partially stacked spectra of $^1$H NMR experiment of **1c** in $C_2D_2Cl_4$ at variable temperature (D). The chemical shifts of The N–H protons in DMSO-$d_6$ titration of **1c** in $CDCl_3$ at 25 ˚C (E).

The formation and stability of the double helical conformation in the solution phase were studied utilizing numerous experimental technics. The formation of double helix structure by **1a** and **1b** in solution phase was confirmed by the ESI-MS experiment. Initially, a solution of **1a** and **1b** (10 μM) in $CH_2Cl_2$:$CH_3CN$ (10:1) was prepared and used for electrospray ionization mass spectrometric (ESI-MS) studies. The signal corresponding to $[2M + H]^+$ from the ESI-MS experiment (where, M is the exact mass of **1a** or **1b**) indicates the formation of the double helix in the solution phase (Figure 4.11 and 4.12). Further, to check the stability of the dimeric structure, $^1$H NMR spectroscopic studies were done, and for that compound **1c** was used due to the poor solubility of **1a** and **1b** in $CDCl_3$ (a non-hydrogen acceptor NMR solvent). At first, concentration dependent $^1$H NMR studies of **1c** from 30.0 mM to 0.06 mM of concentration in $CDCl_3$ was performed, which shows no significant changes in chemical shift of indole and amide N–H protons (i.e., $H_c$ and $H_g$). This result suggests that the N–H protons are hydrogen bonded, and the double helical conformation was stable even at a very low concentration (Figure 4.2C). To know the nature of the hydrogen bond, i.e., intramolecular or intermolecular, the DMSO-$d_6$ titration experiment was performed. The addition of DMSO-$d_6$, a hydrogen bond acceptor solvent, to a 5.0 mM solution of **1c** in $CDCl_3$ showed no significant

changes in the chemical shift of indole and amide N–H protons, i.e., $H_c$ and $H_g$ (Figure 4.2E). This result indicates the involvement of intermolecular hydrogen bonding interaction for the formation of a double helix structure. The chemical shift change ($\Delta\delta = 0.84$) of terminal N–H proton ($H_i$) was observed because of its outfacing nature, which can easily be exposed by the hydrogen bond acceptor solvent. The stability of the double helix formed by **1c** involving intermolecular hydrogen bonds was also examined by increasing the temperature up to 100 ˚C in $C_2D_2Cl_4$. This experiment resulted in a negligible change in the N–H proton chemical shift, which infers the stability of the dimer at high temperatures (Figure 4.2D).

### 4.2.3. Supramolecular Anionic Polymer Formation

The solid-state structure of **1b** with tetrabutylammonium chloride (TBACl) was obtained by slow evaporation of solvent from the solution of the receptor with salt in acetonitrile. The addition of TBACl in a receptor solution leads to conformational changes across the C (indole aryl) and N (attached to $H_c$) single bonds (Figure 4.3A), which finally binds to the $Cl^-$ with multiple hydrogen bonds (Table 4.5). Upon conformational changes, the receptor creates three anion-binding sites. The central part of the receptor binds with the $Cl^-$ ion by hydrogen bonding interactions of $H_b$, $H_c$, and $H_d$ protons ($d_{C\ or\ N\cdots Cl}$ = 3.20 Å – 3.55 Å). Whereas, the terminal binding sites are used to connect with the neighboring molecules via $Cl^-$ ion bridging by hydrogen bonding interaction of $H_h$ and $H_i$ ($d_{C\ or\ N\cdots Cl}$ = 3.29 Å – 3.46 Å) along with a weak C–H$\cdots Cl^-$ interaction with $H_j$ ($d_{C\cdots Cl}$ = 3.68 Å) for making a linear polymeric chain. Here, besides the amide N–H proton ($H_i$), the C–H proton ($H_h$) plays a crucial role in conformational change by forming the hydrogen bond with the $Cl^-$. The linear chains are connected with each other by the hydrogen bonding interaction ($d_{C\cdots O}$ = 3.22 Å – 3.26 Å) of terminal carbonyl with the terminal aryl proton and other noncovalent interactions to make a one-dimensional layer (Figure 4.3A and 4.3B). These layers are aggregated via π–π stacking interactions to form a microsheets structure (Figure 4.3B).

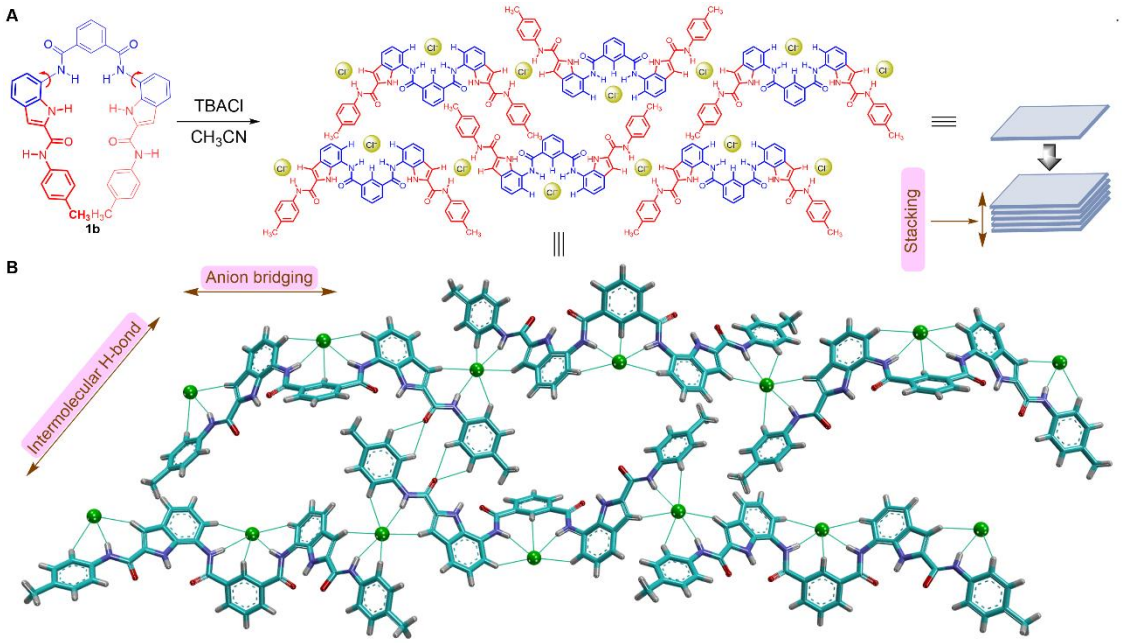



**Figure 4.3** The schematic illustration of conformational changes across the single bond followed by the formation of anion coordinated supramolecular assembly by **1b** (A). The top view of the formation of $Cl^-$ ion coordinated self-assembled architecture from the crystal structure of 1b with $Cl^-$ (B). The tetrabutylammonium cations are omitted for clarity in the solid-state representation. The light blue dotted lines in the bottom crystal structure represent the hydrogen bonding interactions.

### 4.2.4. Solid State Morphology Study

The conformational change of the bis(indole) derivative **1b** in the presence of $Cl^-$ ion from its free form was investigated by solid-state morphological studies with the help of field emission scanning electron microscopy (FESEM), atomic force microscopy (AFM), and transmission electron microscopic (TEM) technics. The FESEM analysis shows that the bis(indole) compound self-aggregates in the solid state to form a globular structure with a diameter of 230 – 400 nm (Figure 4.4B). The formation of spherical globule self-assembly by **1b** compound was further confirmed from AFM imaging (Figure 4.4D), where it has shown the curved height bar with a maximum height of 172 nm. Next, we have checked the morphology of chloride bound complex of **1b**. The FESEM image of the anionic complex has shown the multi-layered microsheets (Figure 4.4C) that were formed by the aggregation of anion coordinated polymeric chain by noncovalent interaction and π–π stacking. The flat pattern of the height bar in the AFM image of the anionic complex indicates the formation of planar aggregates. Then we recorded the TEM images of the two dissimilar conformations to get a deeper understanding of their morphology (Figure 4.4F and 4.4G). Here we observed that the free compound forms

spherical aggregates with a similar diameter, which we obtained from FESEM studies. The globular structure of **1b** is formed by the accumulation of the non-planar double helixes employing the inter-helical noncovalent interaction. The TEM image of the anionic complex shows the formation of a bigger size aggregate formed by the multiple planar microsheets.

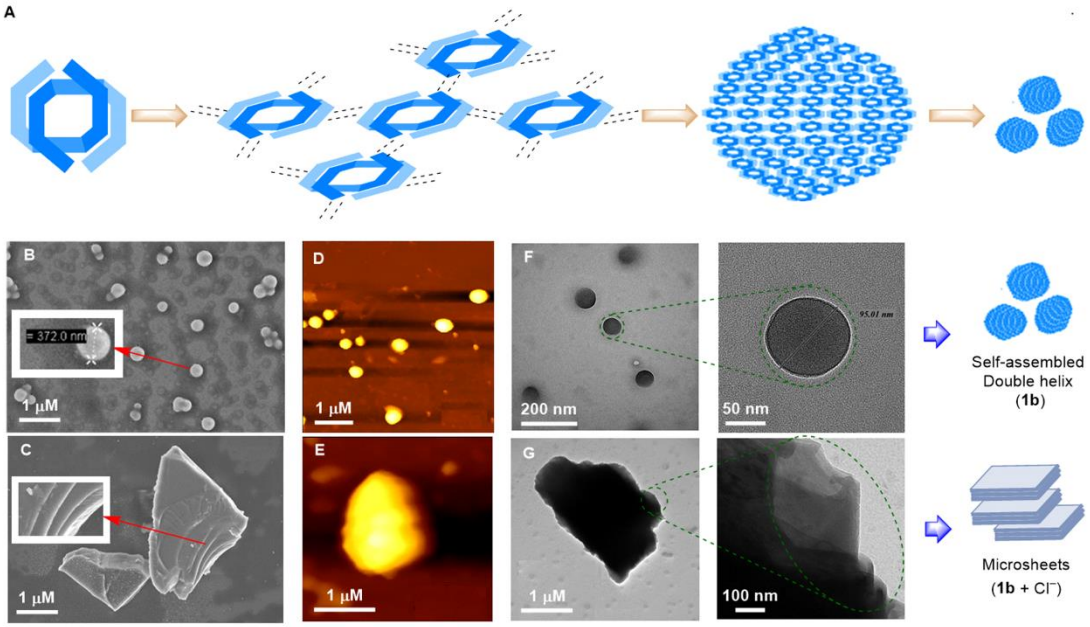



**Figure 4.4** The schematic representation of the globular assembly formation by the double helix structure (A). The globular self-assembled structure observed in FESEM (B), AFM (D), and TEM (F) microscopic technics by **1b**. The multi-layer microsheets assembly captured in FESEM (C), AFM (E), and TEM (G) microscopic technics by **1b** with TBACl.

### 4.2.5. Solution Phase Anion Binding

The formation of the $Cl^-$ ion bound polymeric complex by unwinding of the double helical structure of bis(indole) molecule **1b** in the solution phase was confirmed from ESI-MS studies (Figure 4.24). For that, a solution of **1b** (10 μM) in $CH_2Cl_2$:$CH_3OH$ (10:1) was prepared, and into that solution, 3.0 equivalents of tetramethylammonium chloride (TMACl) was added. The peaks corresponding to the different aggregated polymeric units were observed from ESI-MS experiment (Figure 4.24 and Table 4.6), which evidenced the formation of the supramolecular polymeric complex in the solution phase.

We had performed the $^1H$ NMR titration experiment of **1c** with TBACl to see the unwinding of double helix structure and subsequent formation of the anionic complex via conformational change. As the molecule has several hydrogen bond donor amide protons, the

successive addition of TBACl (0 to 40 equiv.) to a receptor solution (3.0 mM) in $CDCl_3$ leads to the slow disappearance of double helix proton signal (red star in Figure 4.5A) with the appearance of a new set of proton signal because of slow exchange between two conformations (blue sphere in Figure 4.5A). The appearance of the new set proton signal at a slightly downfield region is the outcome of receptor-anion interaction followed by the formation of an anionic complex. At intermediate TBACl concentration, the NMR signals corresponding to both sets were present. However, upon the addition of 2.0 equivalents of TBACl to the receptor solution, the proton signal corresponding to the double helix compound has completely disappeared.

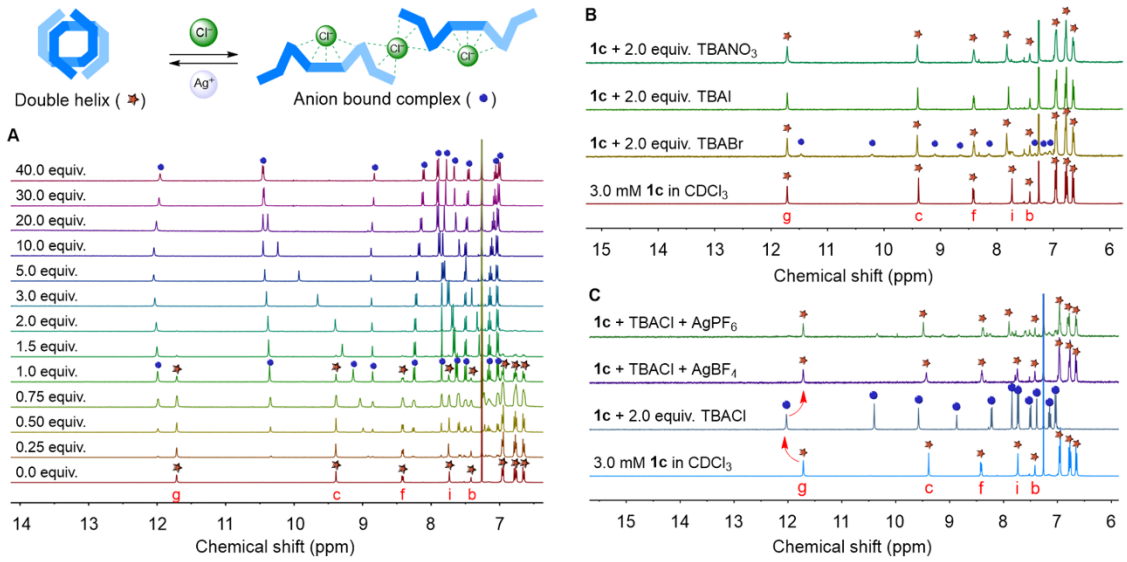



**Figure 4.5** The stacked $^1$H NMR spectra of **1c** (3.0 mM) in $CDCl_3$ at room temperature upon titrating with increasing equivalents of TBACl representing the conversion of the double helix to the anion bound complex (A). The stacked $^1$H NMR spectra of compound **1c** in $CDCl_3$ upon the addition of 2 equivalents of TBABr, TBAI, and $TBANO_3$ at room temperature (B). The stacked $^1$H NMR spectra of compound **1c** in $CDCl_3$ with the sequential addition of 2 equivalents of TBACl, and 2.5 equivalents of either $AgBF_4$ or $AgPF_6$ to monitor the reversible unwinding-rewinding process (C).

When similar anion binding studies were performed with TBABr in the solution phase, a very small amount of conversion (10%) from dimer to anionic complex was observed with the addition of 2.0 equivalents of TBA salt (Figure 4.5B). However, no accountable conversion and chemical shift change was observed when we performed similar experiments with identical equivalents of iodide and nitrate salts. These observations indicate that the conformational change is very much selective for $Cl^-$ compared to other anions. To check the reversibility of anion unwinding associated with conformational change, a series of $^1$H NMR experiments with

TBACl and silver salts were performed. We have previously observed that the addition of TBACl (2.0 equivalents) into a receptor solution of double helix leads to the complete conversion into a polymeric complex. However, the addition of silver salts (2.5 equivalents $AgBF_4$ and $AgPF_6$) to the above polymeric solution leads to the restoration of the double helix conformation (Figure 4.5C). These observations indicate that the anion unwinding and rewinding of double helical conformation is reversible and can be tuned by external stimuli such as $Cl^-$ and $Ag^+$ ions.

### 4.2.6. Ion Transport Activity across Phospholipid Bilayer Membrane

The formation of supramolecular polymeric chloride channel by bis(indole) molecule **1b** with $Cl^-$ in solid and solution state (Figure 5a) motivate us to evaluate the ion transport activity of these molecules across the lipid bilayer membrane. For a thermodynamically stable ion channel, the interactions between the ion and channel forming molecules have to be sufficiently strong to compensate for the dehydration energy of the ion.[10] The supramolecular ion channel formed through ion induced self-assembled polymeric structure can be a good option for providing a static hydrophilic path for the ions to pass through the hydrophobic lipid bilayer membrane.[5-6, 11-12]

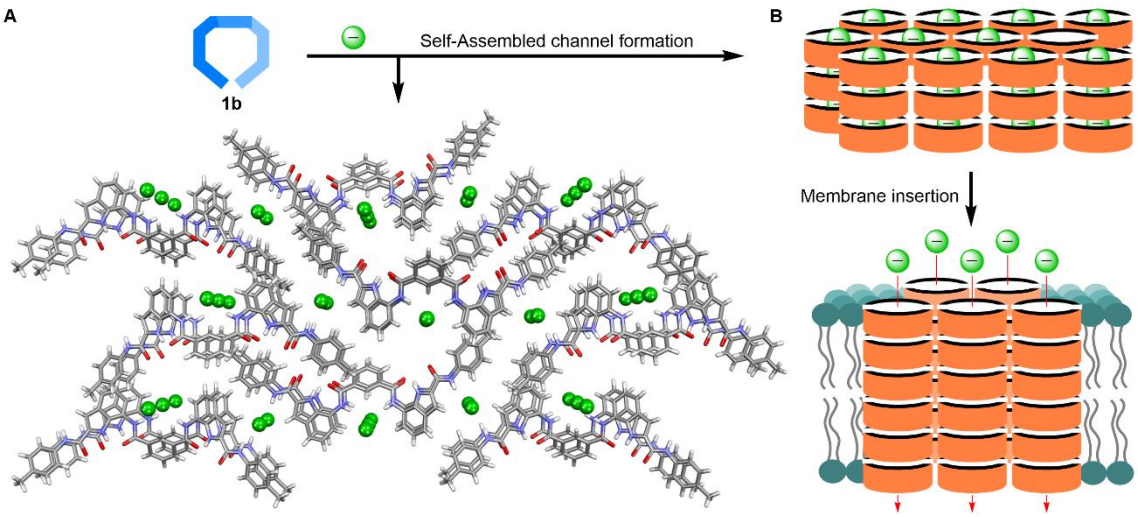



**Figure 4.6** The crystal structure of the $Cl^-$ coordinated supramolecular assembly of **1b** which stacked with a proper alignment to form an array of ion i.e. $Cl^-$ channel (here, only three layers have shown for stacking and the tetrabutylammonium cations are omitted for clarity) (A). The schematic representation of the formation of chloride channel inside the lipid bilayer membrane from a $Cl^-$ ion bound supramolecular assembly and then the transmembrane transport of $Cl^-$ ion through this supramolecular channel (B).

For example, Matile and co-workers introduced the ion channel formation by dendritic folate molecule where the hydrogen bond directed self-assembly of guanosine units form circular oligomers templated by a cation.[5] These circular oligomers finally form a supramolecular rosette channel for ion transport involving π–π interactions between the layers. Later, Davis and co-workers have also reported the ion channel behavior by the cation induced polymeric channel formed by nucleoside–sterol conjugate.[6] The guanosine moiety present in the molecule forms a G-quartet induced by $K^+$ ion, which subsequently stacked via π–π interaction to form a large and stable polymeric supramolecular structure for the transportation of ion through the lipid bilayer membrane. However, the anion-template induced supramolecular ion channel formation is not reported to date. So, to the best of our knowledge, here we are reporting the first example of anion-induced self-assembled supramolecular ion channel formation across the lipid bilayer membrane (Figure 4.6B).

At first, we evaluated the ion transport activity of the molecules **1a**–**1c** across the lipid bilayer membrane. For that, vesicles entrapped with a pH-sensitive 8-hydroxypyrene-1,3,6-trisulfonate dye (HPTS) in 100 mM NaCl solution were prepared using egg yolk phosphatidylcholine (EYPC) lipids, and a pH gradient (ΔpH = 0.8) was created between the intra- and the extra-vesicular medium.[13-16] The destruction of the pH gradient by the transporter molecules was monitored by measuring the fluorescence intensity increment of the HPTS dye with time. Under the comparable concentration of 0.07 μM, the HPTS assay showed that the methyl derivative **1b** is the most active compound (with 94% of fluorescent intensity after 200 s of transporter addition) followed by **1a** (with 84% of fluorescent intensity after 200 s of transporter addition). The alkoxy chain derivative **1c** (with 19% of fluorescent intensity after 200 s of transporter addition) was found to be the least active among the three compounds (Figure 4.7A). The above ion transport activity sequence of **1b** > **1a** > **1c** may be the outcome of the Lipinski rule, according to which the compounds with logP value close to 5 are better permeable to the lipid bilayer membrane and hence, octyl chain bearing compound **1c** with logP value of 10.35 was expected to be least active among the three molecules.[17] Subsequently, the concentration-dependent ion transport activities for the compounds **1a-1c** were evaluated across the HPTS vesicles. The concentration-dependent activity of **1b** is shown in Figure 6b. The Dose-dependent Hill analysis provides the $EC_{50}$ values of 13.7 nM, 10.9 nM and 341.5 nM for the compounds **1a**, **1b** and **1c,** respectively (Figure 4.29, 4.30 and 4.31). Compound **1b** showed the highest activity with Hill coefficient value $n \sim 1$ (Figure 4.29). The Hill coefficient

*n* value close to one indicates the formation of a thermodynamically stable ion channel across the bilayer membrane.[18-19]

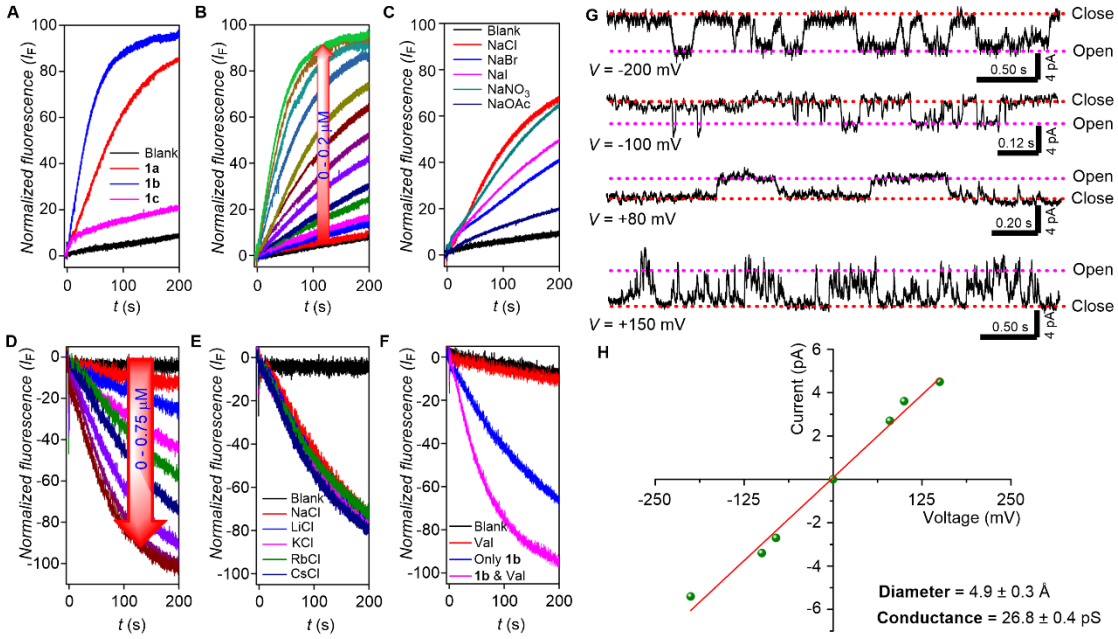



**Figure 4.7** The comparison of ion transport activities of **1a**–**1c** in the HPTS assay at 0.07 μM transporter concentration (A). The concentration dependent ion transport activity of **1b** (*c* = 0–0.2 μM) in HPTS assay (B), and the ion transport activity of **1b** (*c* = 12 nM) in the HPTS assay by varying the extravesicular anions i.e., $Cl^-$, $Br^-$, $I^-$, $NO_3^-$ and $OAc^-$ (C). The concentration dependent ion transport activity of **1b** (*c* = 0–0.75 μM) in the lucigenin assay (D). The ion transport activity of **1b** (*c* = 0.12 μM) in the lucigenin assay by varying the extravesicular cations i.e., $Li^+$, $Na^+$, $K^+$, $Rb^+$, and $Cs^+$ (E). The ion transport activity of **1b** (*c* = 0.10 μM) in the lucigenin assay in the absence and the presence of valinomycin (0.5 μM) (**F**). The single channel current traces by **1b** (*c* = 15 μM) recorded at –200 mV, –100 mV, +80 mV, and +150 mV under symmetrical KCl solution (G). The current traces vs. voltage plot of **1b** obtained from the channel opening data at different potentials (H).

To get further insights into the ion transport mechanism, the most active compound methyl bis(indole) derivative **1b** was evaluated for ion selectivity across the HPTS vesicles.[20-22] By changing the extravesicular cations ($Li^+$, $Na^+$, $K^+$, $Rb^+$, and $Cs^+$) at a 12 nM transporter concentration of **1b**, no significant change in the ion transport activity was observed (Figure 4.32), which rules out the role of cations in the ion transport process. This result excludes the possibility of $M^+/Cl^-$ symport and $M^+/H^+$ antiport mechanism out of four possible ion transport modes i.e., $Cl^-/OH^-$ antiport, $H^+/Cl^-$ symport, $M^+/Cl^-$ symport and $M^+/H^+$ antiport. However, varying the extravesicular anions ($Cl^-$, $Br^-$, $I^-$, $NO_3^-$, and $OAc^-$) makes a significant change in ion transport activity with the selectivity order of $Cl^- > NO_3^- > I^- > Br^- > OAc^-$ (Figure 4.7C),

which indicates the involvement of anions in the ion transport process with the the possible ion transport modes of either $Cl^-/OH^-$ antiport or $H^+/Cl^-$ symport.

Further, the influx of chloride ions for the most active compound **1b** was studied across the lucigenin (a chloride sensitive dye) based LUV's. Subsequently, a $Cl^-/NO_3^-$ gradient was created by applying NaCl solution in the external buffer. The destruction of concentration gradient by the transporter molecule via chloride influx was monitored by measuring the rate of the fluorescence quenching of lucigenin dye at $\lambda$ = 455 nm ($\lambda_{ex}$ = 535 nm, for lucigenin). The Dose-responsive chloride transport for **1b** is shown in figure 4.7D. The Hill analysis yielded the $EC_{50}$ value of 31.3 nM and *n* value of 1, an indication of a stable supramolecular ion channel formation (Figure 4.34). Moreover, variation of extravesicular cations ($Li^+$, $Na^+$, $K^+$, $Rb^+$, and $Cs^+$) did not affect the transport activity (Figure 4.7E), indicating no role of cations in the ion transport activity, which excludes the possibility of symport mechanism. The only possible mechanism that remains for ion transport is $Cl^-/X^-$ antiport. The direct confirmation of $Cl^-/X^-$ antiport mechanism was confirmed by valinomycin coupled lucigenin assay. The transport activity of **1b** was checked in the absence and presence of valinomycin in KCl buffer. Multifold enhancement in the ion transport activity in the presence of valinomycin indicates the cooperative effect of the transporter and valinomycin, thereby confirming an operation of an antiport mode of chloride transport through $Cl^-/NO_3^-$ exchange.

The channel formation by the transporter molecule in the lipid bilayer membrane was examined by conductance measurement experiment with the help of planar lipid bilayer workstation. In this experiment, a thin lipid bilayer membrane across a tiny aperture was formed using diphytanoylphosphatidylcholine lipid (DPhPC), which separated the *cis* and *trans* chamber filled with 1M KCl solution. The addition of the channel forming molecule **1b** in the *trans* chamber followed by the generation of potential gradient between two compartments leads to the channel opening and closing behavior which confirmed the formation of the ion channel by the transporter. The channel opening and closing events have been observed at various negative and positive potentials i.e., –200 mV, –100 mV, –80 mV, +150 mV, +100 mV, and +80 mV (Figure 4.7G and Figure 4.37). The current traces observed in these potentials were plotted against the corresponding voltage values, where the linear fit indicates the Ohomic behavior by the channel (Figure 4.7H). The conductance and diameter values were calculated using the Hille equation (Equation 5) and were found to be 26.8 ± 0.4 pS and 4.9 ± 0.3 Å, respectively.[21, 23]

## 4.3. Conclusion

In summary, we have designed and synthesized a family of bis(indole) based bio-functional molecules, which adopt a double helical conformation with the help of intermolecular hydrogen bonding and π–π stacking interactions. The FESEM, AFM, and TEM studies confirmed the formation of globular self-assembled structure in the solid phase by the **1b**, whereas the anionic complex of the molecule formed a multi-layered microsheets structure. The formation of the multi-layered structure can be corroborated with the crystal structure of the anionic complex, where conformational change with the interaction of $Cl^-$ leads to the formation of a polymeric structure, which finally self-assembled to a multi-layered architecture. This anion induced supramolecular polymeric channel structure was further utilized for the transport of ions across the lipid bilayer membrane, which was evaluated through HPTS and lucigenin based vesicular studies. The dose-dependent ion transport activity across the HPTS vesicles furnish the $EC_{50}$ value of 10.9 nM and Hill coefficient *n* value of 1, an indication of a stable supramolecular ion channel formation. Further, mechanistic ion transport studies confirmed the operation of an antiport mechanism via, $Cl^-/NO_3^-$ exchange across the lipid bilayer. The planar bilayer conductance measurement confirmed the formation of an ion channel in the lipid bilayer.

## 4.4. Experimental Section

### 4.4.1. General Methods

All reagents used for the synthesis were purchased either from Sigma-Aldrich, Avra, TCI, Spectrochem, and used without further purification. Dry solvents e.g., THF, $CHCl_3$, $CH_2Cl_2$ and MeOH used for the synthesis, were purchased from Merck and used without further drying. All the dry reactions were placed in oven-dried apparatus under nitrogen atmospheric conditions. The progress and completion of the reaction were monitored by performing thin layer chromatography experiments where the plates were visualized either by short wave UV light or by different staining reagents (Ninhydrin, PMA, etc.). Column chromatography for purification of the compound was performed using distilled organic solvents on silica gel (100-200 mesh).

### 4.4.2. Physical Measurements

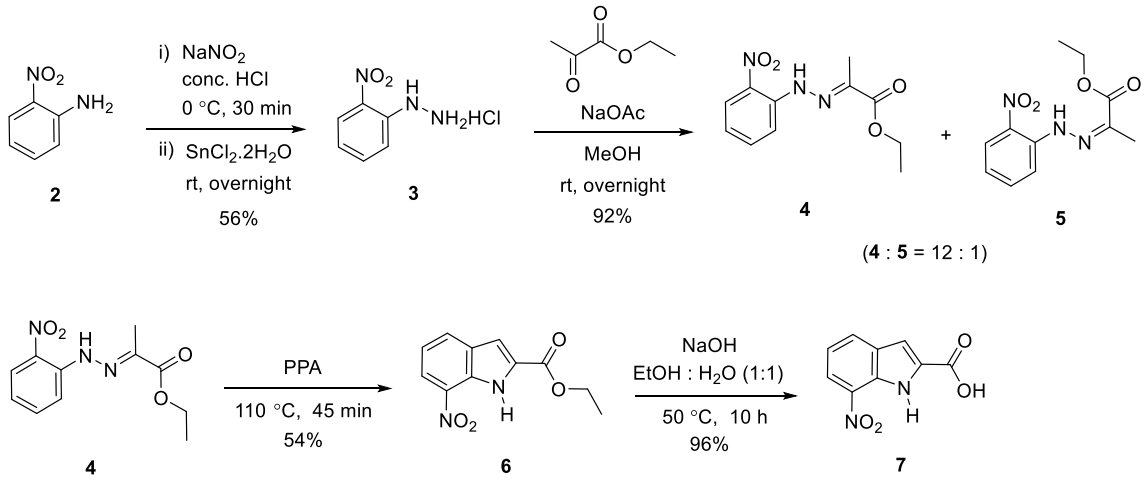
All $^1H$ and $^{13}C$ NMR spectra were recorded on either Bruker 400 MHz or Jeol 400 MHz NMR spectrometers. The chemical shifts ($\delta$) in ppm were referenced to the residual signal of either by deuterium solvents ($^1H$ NMR $CDCl_3$: $\delta$ 7.26 ppm; $^{13}C$ NMR $CDCl_3$: $\delta$ 77.2 ppm; $^1H$ NMR

$C_2D_2Cl_4$: $\delta$ 6.00 ppm; $^{13}C$ NMR $C_2D_2Cl_4$: $\delta$ 73.8 ppm; $^1H$ NMR DMSO-$d_6$: $\delta$ 2.5 ppm; $^{13}C$ NMR DMSO-$d_6$: $\delta$ 39.5 ppm). The multiplicities of the peaks are s (singlet), d (doublet), t (triplet), q (quartet), dd (doublet of doublet), m (multiplet). The high-resolution mass spectra (HRMS) were acquired from MicroMass ESI-TOF MS spectrometer and were acquired in the ESI (+ve or –ve) mode. Fluorescence spectra were recorded on a Fluoromax-4 from Horiba scientific, Jobin Yvon Edison equipped with an injector port and a magnetic stirrer. The experimental data obtained from fluorescence were processed in Origin 8.5 software. Planar lipid bilayer conductance measurements were carried out on a workstation from Warner instrument, USA. The single crystal X-ray data were collected on a Bruker Smart Apex Duo diffractometer using Mo Kα radiation for all the compounds at either 100 K or 150 K temperature. The field emission scanning electron microscopy (FESEM) images data were obtained using FEI Quanta 3D dual beam ESEM at 3.0 kV. The atomic force microscopy (AFM) images were recorded using Nano Wizard Atomic Force Microscopy. The high-resolution transmission electron microscopy (HRTEM) images were acquired on Jeol USA JEM-2200 FS transmission electron microscope.

### 4.4.3. Synthesis of Compounds

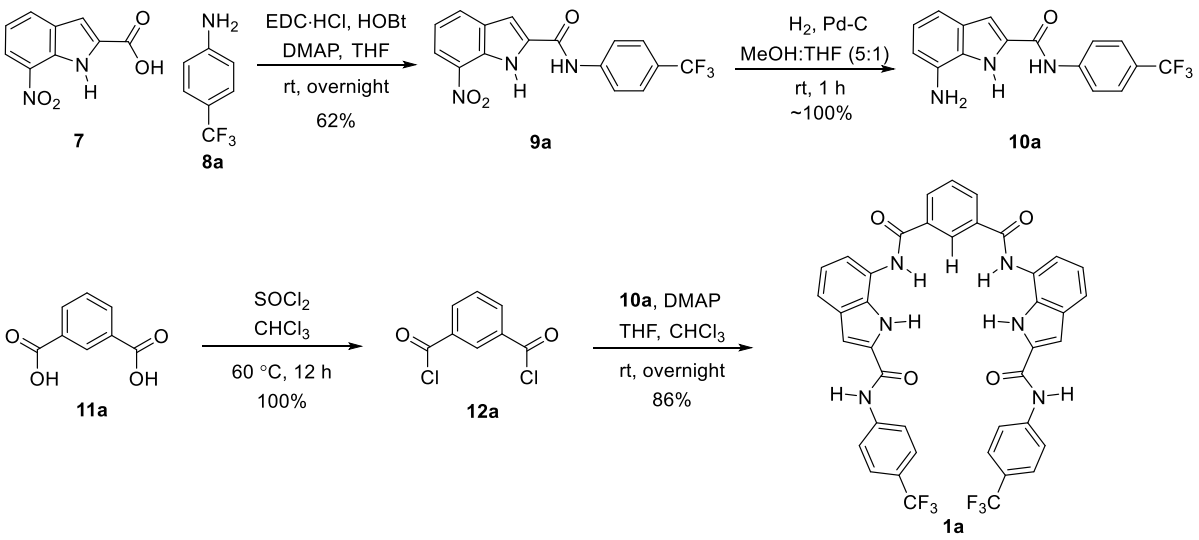
#### 4.4.3.1. Preparation of 7-Nitro-1*H*-indole-2-carboxylic acid 7 ($C_9H_6N_2O_4$)

For the preparation of the 7-Nitro-1*H*-indole-2-carboxylic acid **7** we have followed the reported literature procedure (Scheme 4.1).[7]




**Scheme 4.1** Preparation of the 7-Nitro-1*H*-indole-2-carboxylic acid **7**.

#### 4.4.3.2. Synthesis of bis(indole) compound 1a




**Scheme 4.2** Synthesis of compound **1a**.

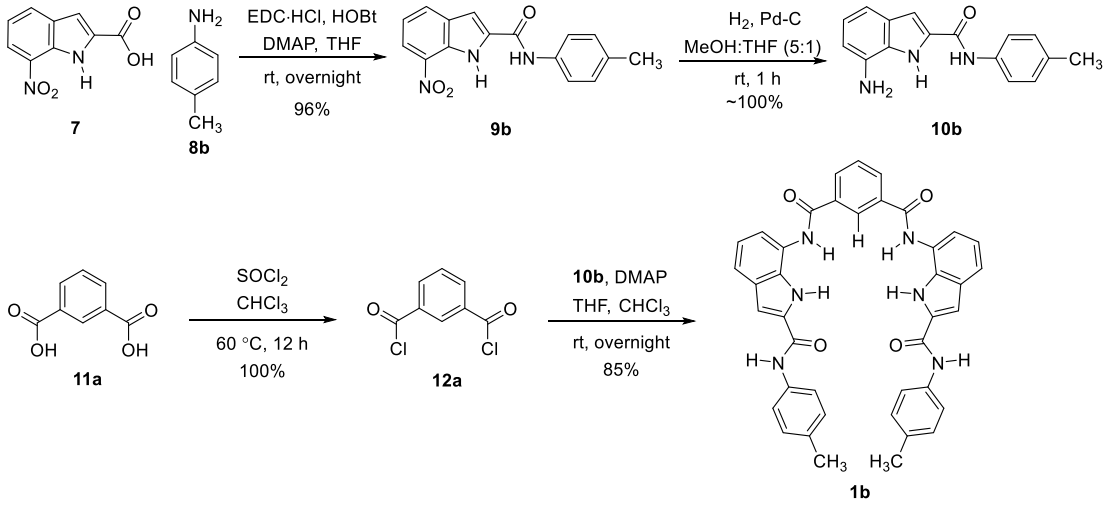
**Synthesis of 7-nitro-*N*-(4-(trifluoromethyl)phenyl)-1*H*-indole-2-carboxamide 9a ($C_{16}H_{10}F_3N_3O_3$):** In a 50 mL round bottom flask 7-Nitro-1*H*-indole-2-carboxylic acid **7** (0.40 g, 1.94 mmol) and *p*-(trifluoromethyl)aniline **8a** (0.34 g, 2.13 mmol) were taken and dissolved in 8 mL of dry THF. Then into the reaction mixture HOBt (0.29 g, 2.13 mmol), EDC·HCl (0.48 g, 2.52 mmol) and DMAP (0.55 g, 4.46 mmol) were added sequentially. The reaction mixture was then stirred overnight at room temperature under an inert atmosphere. After completion of the reaction, the reaction mixture was washed with water (2 × 30 mL) and followed by brine solution (1 × 20 mL) while extracting the compound in $CHCl_3$ (80 mL). The organic layer was then dried over $Na_2SO_4$ and the solvent was evaporated in a rotary evaporator to get the crude product. The crude product was purified by silica gel column chromatography using ethyl acetate in petroleum ether (1 : 4) as a solvent system to get the pure amide **9a** in 62% yield (0.42 g, 1.22 mmol). **$^1$H NMR (400 MHz, DMSO-*d*$_6$):** $\delta$ 11.59 (s, 1H), 10.96 (s, 1H), 8.28 (dd, *J* = 7.7, 5.7 Hz, 2H), 8.03 (d, *J* = 8.5 Hz, 2H), 7.78 (d, *J* = 8.6 Hz, 2H), 7.66 (s, 1H), 7.37 (t, *J* = 7.9 Hz, 1H); **$^{13}$C NMR (101 MHz, DMSO-*d*$_6$):** $\delta$ 158.5, 142.2, 134.0, 133.2, 130.9, 130.8, 129.1, 126.1 (q, *J* = 3.5 Hz), 124.3 (q, *J* = 271.5 Hz), 123.9 (q, *J* = 31.9 Hz), 121.6, 120.2, 120.1, 108.0; **HRMS (ESI):** Calcd. $C_{16}H_{11}F_3N_3O_3$ $[M+H]^+$: 350.0752, Found: 350.0748.

**Synthesis of 7-amino-*N*-(4-(trifluoromethyl)phenyl)-1*H*-indole-2-carboxamide 10a ($C_{16}H_{12}F_3N_3O$):** In a 100 mL round bottomed flask the indole-amide **9a** (0.41 g, 1.17 mmol) was dissolved in 25 mL of MeOH:THF (5 : 1) solvent and then the solution was degassed for 30 min using $N_2$ gas balloon. Then one pinch of Pd-C (10%) was added into that and the solution was stirred under $H_2$ gas balloon for 1 h at room temperature. After completion of the

reaction, the reaction mixture was passed through celite bed while washing with MeOH. The crude product was then purified by silica gel column chromatography using ethyl acetate in petroleum ether (1 : 3) as a solvent system to get the pure amine **10a** in quantitative yield (0.37 g, 1.17 mmol). **$^1$H NMR (400 MHz, DMSO-*d*$_6$):** $\delta$ 11.43 (s, 1H), 10.47 (s, 1H), 8.05 (d, *J* = 8.5 Hz, 2H), 7.74 (d, *J* = 8.7 Hz, 2H), 7.39 (d, *J* = 2.1 Hz, 1H), 6.89 (d, *J* = 7.9 Hz, 1H), 6.84 – 6.76 (m, 1H), 6.41 (d, *J* = 8.1 Hz, 1H), 5.44 (s, 2H); **$^{13}$C NMR (101 MHz, DMSO-*d*$_6$):** $\delta$ 160.3, 142.8, 134.5, 129.8, 127.8, 126.9, 126.0 (q, *J* = 3.8 Hz), 124.4 (q, *J* = 271.3 Hz), 123.3 (q, *J* = 32.0 Hz), 121.4, 119.8, 109.4, 106.2, 105.0; **HRMS (ESI):** Calcd. $C_{16}H_{13}F_3N_3O$ $[M+H]^+$: 320.1010, Found: 320.1010.

**Synthesis of *N*$^1$,*N*$^3$-bis(2-((4-(trifluoromethyl)phenyl)carbamoyl)-1*H*-indol-7-yl)isophthalamide 1a ($C_{40}H_{26}F_6N_6O_4$):** In a 25 mL round bottomed flask 40 mg of isopthalic acid **11a** (0.24 mmol) was taken and refluxed it for 10 h in the presence of 5 mL of $CHCl_3$:$SOCl_2$ (1:1). After completion of the reaction, volatiles were evaporated and dried in high vacuum for 30 min. Then the acid chloride **12a** was dissolved in 8 mL of dry $CHCl_3$ and added drop wise to a solution of **10a** (0.16 g, 0.49 mmol) and DMAP (0.08 g, 0.60 mmol) in 4 mL of dry THF. The reaction mixture was then stirred at room temperature for overnight under inert atmosphere. After completion of the reaction, the reaction mixture was washed with water (2 × 15 mL) while extracting the compound in $CHCl_3$ (60 mL). The organic layer was then dried over $Na_2SO_4$ and the solvent was evaporated in a rotary evaporator to get the crude product. The crude product was then purified by silica gel column chromatography using ethyl acetate in petroleum ether (2 : 3) as a solvent system to get the pure amide **1a** in 86% yield (0.16 g, 0.21 mmol). **$^1$H NMR (400 MHz, DMSO-*d*$_6$):** $\delta$ 11.92 (s, 2H), 10.61 (s, 2H), 10.40 (s, 2H), 8.66 (s, 1H), 8.27 (dd, *J* = 7.7, 1.6 Hz, 2H), 8.04 (d, *J* = 8.6 Hz, 4H), 7.98 (d, *J* = 7.7 Hz, 2H), 7.79 (t, *J* = 7.7 Hz, 1H), 7.74 (d, *J* = 8.8 Hz, 4H), 7.58 (d, *J* = 2.1 Hz, 2H), 7.56 (d, *J* = 8.1 Hz, 2H), 7.15 (t, *J* = 7.8 Hz, 2H); **$^{13}$C NMR (101 MHz, DMSO-*d*$_6$):** $\delta$ 165.6, 160.0, 142.6, 135.3, 131.0, 130.9, 129.3, 128.6, 128.6, 127.6, 126.0 (q, *J* = 3.7 Hz), 124.4 (q, *J* = 271.3 Hz), 124.2, 123.5 (q, *J* = 32.1 Hz), 120.4, 119.9, 118.4, 116.7, 105.2; **$^{19}$F NMR (376.6 MHz, DMSO-*d*$_6$)**: $\delta$ –60.34; **HRMS (ESI):** Calcd. $C_{40}H_{27}F_6N_6O_4$ $[M+H]^+$: 769.1997, Found: 769.1991.

### 4.4.3.3. Synthesis of bis(indole) compound 1b




**Scheme 4.3** Synthesis of compound **1b**.

**Synthesis of 7-nitro-*N*-(*p*-tolyl)-1*H*-indole-2-carboxamide 9b ($C_{16}H_{13}N_3O_3$):** In a 50 mL round bottom flask 7-Nitro-1*H*-indole-2-carboxylic acid **7** (0.60 g, 2.91 mmol) and *p*-toluidine **8b** (0.31 g, 2.91 mmol) were taken and dissolved in 10 mL of dry THF. Then into the reaction mixture HOBt (0.43 g, 3.20 mmol), EDC·HCl (0.73 g, 3.78 mmol) and DMAP (0.90 g, 7.28 mmol) were added sequentially. The reaction mixture was then stirred overnight at room temperature under an inert atmosphere. After completion of the reaction, the reaction mixture was washed with water (2 × 30 mL) and followed by brine solution (1 × 20 mL) while extracting the compound in $CHCl_3$ (100 mL). The organic layer was then dried over $Na_2SO_4$ and the solvent was evaporated in a rotary evaporator to get the crude product. The crude product was purified by silica gel column chromatography using ethyl acetate in petroleum ether (1 : 4) as a solvent system to get the pure amide **9b** in 96% yield (0.83 g, 2.80 mmol). **$^1$H NMR (400 MHz, DMSO-$d_6$):** $\delta$ 11.51 (s, 1H), 10.60 (s, 1H), 8.26 (t, $J$ = 7.4 Hz, 2H), 7.68 (d, $J$ = 8.3 Hz, 2H), 7.60 (d, $J$ = 1.9 Hz, 1H), 7.37 (d, $J$ = 7.9 Hz, 1H), 7.21 (d, $J$ = 8.3 Hz, 2H), 2.30 (s, 3H); **$^{13}$C NMR (101 MHz, DMSO-$d_6$):** $\delta$ 157.9, 135.9, 134.6, 133.1, 130.9, 130.7, 129.2, 129.1, 128.9, 121.3, 120.3, 120.0, 107.2, 20.5; **HRMS (ESI):** Calcd. $C_{16}H_{14}N_3O_3$ $[M+H]^+$: 296.1034, Found: 296.1035.

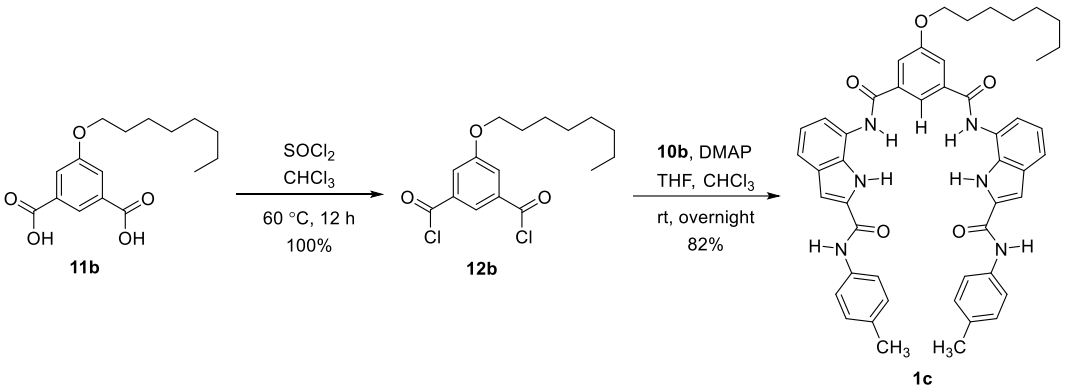
**Synthesis of 7-amino-*N*-(*p*-tolyl)-1*H*-indole-2-carboxamide 10b ($C_{16}H_{15}N_3O$):** In a 100 mL round bottomed flask, the indole-amide **9b** (0.80 g, 2.71 mmol) was dissolved in 40 mL of MeOH:THF (5 : 1) solvent and then the solution was degassed for 30 min using $N_2$ gas balloon. Then one pinch of Pd-C (10%) was added into that and the solution was stirred under an $H_2$

gas balloon for 1 h at room temperature. After completion of the reaction, the reaction mixture was passed through celite bed while washing with MeOH. The crude product was then purified by silica gel column chromatography using ethyl acetate (1 : 3) in petroleum ether as a solvent system to get the pure amine **10b** in quantitative yield (0.71 g, 2.71 mmol). **$^1$H NMR (400 MHz, DMSO-*d*$_6$):** $\delta$ 11.34 (s, 1H), 10.06 (s, 1H), 7.69 (d, *J* = 8.3 Hz, 2H), 7.31 (d, *J* = 1.9 Hz, 1H), 7.17 (d, *J* = 8.3 Hz, 2H), 6.87 (d, *J* = 7.9 Hz, 1H), 6.80 (t, *J* = 7.6 Hz, 1H), 6.39 (d, *J* = 7.2 Hz, 1H), 5.41 (s, 2H), 2.29 (s, 3H).; **$^{13}$C NMR (101 MHz, DMSO-*d*$_6$):** $\delta$ 159.8, 136.5, 134.5, 132.4, 130.5, 129.1, 127.9, 126.6, 121.2, 120.2, 109.3, 106.0, 104.0, 20.5; **HRMS (ESI):** Calcd. $C_{16}H_{16}N_3O$ $[M+H]^+$: 266.1293, Found: 266.1296.

**Synthesis of *N*$^1$,*N*$^3$-bis(2-(*p*-tolylcarbamoyl)-1*H*-indol-7-yl)isophthalamide 1b ($C_{40}H_{32}N_6O_4$):** In a 25 mL round bottomed flask, 80 mg of isopthalic acid **11a** (0.48 mmol) was taken and refluxed it for 10 h in the presence of 8 mL of $CHCl_3$:$SOCl_2$ (1:1). After completion of the reaction, volatiles were evaporated and dried in high vacuum for 30 min. Then the acid chloride **12a** was dissolved in 12 mL of dry $CHCl_3$ and added drop wise to a solution of **10b** (0.26 g, 0.72 mmol) and DMAP (0.15 g, 1.20 mmol) in 6 mL of dry THF. The reaction mixture was then stirred at room temperature for overnight under inert atmosphere. After completion of the reaction, the reaction mixture was washed with water (2 × 20 mL) while extracting the compound in $CHCl_3$ (80 mL). The organic layer was then dried over $Na_2SO_4$ and the solvent was evaporated in a rotary evaporator to get the crude product. The crude product was then purified by silica gel column chromatography using ethyl acetate in petroleum ether (2 : 3) as a solvent system to get the pure amide **1b** in 85% yield (0.27 g, 0.41 mmol). **$^1$H NMR (400 MHz, DMSO-*d*$_6$):** $\delta$ 11.82 (s, 2H), 10.40 (s, 2H), 10.22 (s, 2H), 8.67 – 8.62 (m, 1H), 8.26 (dd, *J* = 7.8, 1.7 Hz, 2H), 7.96 (d, *J* = 7.6 Hz, 2H), 7.78 (t, *J* = 7.8 Hz, 1H), 7.68 (d, *J* = 8.4 Hz, 4H), 7.53 (d, *J* = 7.9 Hz, 2H), 7.50 (d, *J* = 2.0 Hz, 2H), 7.17 (d, *J* = 8.3 Hz, 4H), 7.13 (t, *J* = 7.9 Hz, 2H), 2.28 (s, 6H); **$^{13}$C NMR (101 MHz, DMSO-*d*$_6$):** $\delta$ 165.6, 159.4, 136.3, 135.3, 132.6, 131.6, 131.0, 129.1, 129.0, 128.7, 128.5, 127.6, 124.2, 120.3, 120.2, 118.2, 116.3, 104.3, 20.5; **HRMS (ESI):** Calcd. $C_{40}H_{33}N_6O_4$ $[M+H]^+$: 661.2563, Found: 661.2559.

#### 4.4.3.4. Synthesis of bis(indole) compound 1c

For the preparation of the 5-(octyloxy)isophthalic acid **11b**, we have followed the reported literature procedure.[8]




**Scheme 4.4** Synthesis of compound **1c**.

**Synthesis of 5-(octyloxy)-*N*$^1$,*N*$^3$-bis(2-(*p*-tolylcarbamoyl)-1*H*-indol-7-yl)isophthalamide 1b ($C_{48}H_{48}N_6O_5$):** In a 50 mL round bottomed flask, 82 mg of 5-(octyloxy)isophthalic acid **11b** (0.28 mmol) was taken and refluxed it for 10 h in the presence of 10 mL of $CHCl_3$:$SOCl_2$ (1:1). After completion of the reaction, volatiles were evaporated and dried in high vacuum for 30 min. Then the acid chloride **12b** was dissolved in 10 mL of dry $CHCl_3$ and added drop wise to a solution of **10b** (0.15 g, 0.56 mmol) and DMAP (0.09 g, 0.74 mmol) in 8 mL of dry THF. The reaction mixture was then stirred at room temperature for overnight under inert atmosphere. After completion of the reaction, the reaction mixture was washed with water (2 × 30 mL) while extracting the compound in $CHCl_3$ (100 mL). The organic layer was then dried over $Na_2SO_4$ and the solvent was evaporated in a rotary evaporator to get the crude product. The crude product was then purified by silica gel column chromatography using ethyl acetate in petroleum ether as a solvent system to get the pure amide **1c** in 82% yield (0.18 g, 0.23 mmol). **$^1$H NMR (400 MHz, $CDCl_3$):** $\delta$ 11.71 (s, 2H), 9.38 (s, 2H), 8.42 (dd, $J$ = 5.9, 2.8 Hz, 2H), 7.71 (s, 2H), 7.42 (s, 1H), 7.03 – 6.88 (m, 6H), 6.78 (d, $J$ = 8.2 Hz, 4H), 6.74 (d, $J$ = 1.7 Hz, 2H), 6.65 (d, $J$ = 8.2 Hz, 4H), 3.99 – 3.78 (m, 2H), 2.16 (s, 6H), 1.99 – 1.81 (m, 2H), 1.53 – 1.32 (m, 12H), 0.99 – 0.91 (m, 3H); **$^{13}$C NMR (101 MHz, $C_2D_2Cl_4$):** $\delta$ 166.3, 160.5, 159.3, 135.6, 134.1, 132.9, 128.6, 128.5, 128.0, 127.9, 123.4, 120.4, 120.1, 118.9, 116.8, 115.5, 115.3, 105.2, 77.3, 67.9, 36.6, 33.7, 29.6, 29.3, 26.2, 24.7, 20.7; **HRMS (ESI):** Calcd. $C_{48}H_{49}N_6O_5$ $[M+H]^+$: 789.3764, Found: 789.3754.

### 4.4.4. Crystallographic Measurement and Analysis

The single crystal suitable for X-ray analysis for both complexes **1a** and **1b** were obtained by slow evaporation of ethyl acetate or THF/nitrobenzene solution of the respective compounds. The crystal structure of **1b** with tetrabutylammonium chloride (TBACl) (i.e. **1b′**) was obtained

by slow evaporation of solvent from the solution of the receptor with salt in acetonitrile. The single crystal X-ray data were collected on a Bruker Smart Apex Duo diffractometer using Mo Kα radiation for both the compounds at 100 K and 150 K, respectively. Olex 2[24] graphical interface was used with ShelXT[25] to solve the structures using intrinsic phasing and refined with ShelXL[26] with full matrix least square minimization on $F^2$. All non-hydrogen atoms were refined anisotropically, except for those in minor disordered parts. Compound **1a** has water molecules as a solvent and two of them have been modelled, but neither hydrogen atoms were added nor anisotropic refinement was not done on them due to disorder. The other two water molecules could not be modelled properly, so the solvent mask procedure in Olex 2 was adopted, which showed an electron count of 24, which roughly corresponds to two water molecules and four hydrogen atoms which were not added to the modelled oxygen atoms of the water molecule. Crystallographic parameters for compounds **1a, 1b** and **1b_Cl** are summarised in Table S1. The chemical formula of compound **1a** was obtained through a combination of single crystal X-ray, elemental analysis (Table S3).

**Table 4.1** Crystallographic data for complexes **1a**, **1b**, and **1b_Cl**, where **1b_Cl** is the crystal structure of **1b** with tetrabutylammonium chloride.

| Compound | **1a** | **1b** | **1b_Cl** |
|---|---|---|---|
| Temperature / K | 100 K | 150 K | 100 K |
| Empirical Formula | $C_{44}H_{38}F_6N_6O_8$ | $C_{96}H_{84}N_{14}O_{14}$ | $C_{72}H_{104}Cl_2N_8O_4$ |
| Formula Weight [g mol$^{-1}$] | 892.74 | 1657.77 | 1216.53 |
| crystal system | Triclinic | Monoclinic | Monoclinic |
| space group | P-1 | $P2_1/c$ | $P2_1/c$ |
| a [Å] | 15.449(6) | 14.4042(18) | 8.473(5) |
| b [Å] | 17.681(5) | 31.388(4) | 19.988(10) |
| c [Å] | 18.086(6) | 19.119(3) | 39.95(2) |
| α [°] | 104.982(9) | 90 | 90 |
| β [°] | 114.745(9) | 110.283(3) | 92.665(15) |
| γ [°] | 96.945(10) | 90 | 90 |
| cell V [Å$^3$] | 4184(2) | 8108.1(19) | 6759(6) |
| Z | 4 | 4 | 4 |
| reflections collected | 38645 | 175747 | 96815 |
| independent reflections, $R_{int}$ | 16972/0.1571 | 13927/0.2325 | 13989 |
| Data/restrains/parameters | 16972/0/1129 | 13927/0/1124 | 13989/2/773 |
| goodness-of-fit | 1.055 | 1.038 | 1.024 |
| final *R* indices [I > 2σ(I)]: $R_1$, $wR_2$ | 0.1242, 0.3099 | 0.0790, 0.1385 | 0.0968, 0.2223 |
| CCDC no. | 2101675 | 2101678 | 2101679 |

$R_1 = \Sigma||F_o| - |F_c||/\Sigma|F_o|$ and $wR_2 = |\Sigma w(|F_o|^2 - |F_c|^2)|/\Sigma|w(F_o)^2|^{1/2}$

**Table 4.2** Hydrogen bonding interactions present in complex **1a** at 100 K.

| D– H···A | D–H(Å) | H···A(Å) | D···A (Å) | <D-H-A(°) | Symmetry# |
|---|---|---|---|---|---|
| C6—H6A···O7 | 0.93 | 2.59 | 2.9466(11) | 103 | 0 |
| C26—H26···O6 | 0.93 | 2.56 | 2.9942(12) | 109 | 0 |
| C37—H37···O5 | 0.93 | 2.24 | 2.8404(110 | 122 | 0 |
| C55—H55···O2 | 0.93 | 2.26 | 2.7818(11) | 115 | 0 |
| C61—H61···O2 | 0.93 | 2.44 | 2.7503(11) | 100 | 0 |
| C66—H66···O3 | 0.93 | 2.34 | 2.9085(11) | 119 | 0 |
| C75—H75···O4 | 0.93 | 2.32 | 2.8813(11) | 119 | 0 |
| N5—H5···O5 | 0.86 | 2.09 | 2.8388(11) | 145 | 1 |
| N8—H8···O1 | 0.86 | 2.29 | 2.8830(11) | 126 | 1 |
| N9—H9···O1 | 0.86 | 2.12 | 2.9510(11) | 161 | 1 |
| N10—H10···O4 | 0.86 | 2.32 | 3.0345(12) | 141 | 1 |
| N11—H11···O4 | 0.86 | 2.12 | 2.9579(11) | 166 | 1 |
| C23—H23···O1 | 0.93 | 2.48 | 3.2355(13) | 139 | 1 |
| C59—H59···O7 | 0.93 | 2.56 | 3.4197(13) | 155 | 1 |
| C84— | 0.96 | 2.38 | 3.2233(13) | 146 | 1 |
| N7—H7···O12 | 0.86 | 2.14 | 2.9634(12) | 161 | 2 |
| C67—H67···O3 | 0.93 | 2.42 | 3.3283(13) | 164 | 3 |
| N6—H6···O8 | 0.86 | 2.28 | 3.1085(12) | 1625 | 4 |
| C71—H71···O8 | 0.93 | 2.59 | 3.3289(13) | 136 | 4 |
| N12—H12···O6 | 0.86 | 2.14 | 2.9530(11) | 157 | 5 |
| C35—H35···O6 | 0.93 | 2.58 | 3.2811(13) | 132 | 5 |
| C76—H76···O2 | 0.93 | 2.23 | 3.1537(12) | 170 | 5 |
| #(0) x,y,z; (1) x,y,1+z; (2) 1-x,-y,1-z; (3) 1-x,-y,-z; (4) 1-x,1-y,-z; (5) 1-x,1-y,1-z | | | | | |

**Table 4.3** The elemental analysis of Compound **1a**.

| Sr. No. | Theoretical % | | | | Observed % | | | |
|---|---|---|---|---|---|---|---|---|
| 1 | C% | N% | H% | S% | C% | N% | H% | S% |
| | 59.19 | 9.41 | 4.29 | 0.0 | 58.88 | 8.41 | 3.81 | 0.0 |

**Table 4.4** Hydrogen bonding interactions present in complex **1b** at 150 K.

| D– H···A | D–H(Å) | H···A(Å) | D···A (Å) | <D-H-A(°) | Symmetry# |
|---|---|---|---|---|---|
| N10—H10···N11 | 0.86 | 2.61 | 2.9343(5) | 109 | 0 |
| C15—H15···O2 | 0.93 | 2.30 | 2.8785(5) | 120 | 0 |
| C27—H27···O3 | 0.93 | 2.30 | 2.8292(4) | 115 | 0 |
| C37—H37···O4 | 0.93 | 2.42 | 2.8334(4) | 107 | 0 |
| C46—H46···O5 | 0.93 | 2.56 | 2.9531(5) | 106 | 0 |
| C55—H55···O6 | 0.93 | 2.28 | 2.8560(4) | 120 | 0 |
| C67—H67···O7 | 0.93 | 2.40 | 2.9405(5) | 117 | 0 |
| C75—H75···O8 | 0.93 | 2.57 | 2.9444(5) | 105 | 0 |
| N11—H11···O4 | 0.86 | 2.61 | 2.9343(5) | 103 | 1 |
| C19—H19···O5 | 0.93 | 2.52 | 3.0930(5) | 120 | 1 |
| C19—H19···O8 | 0.93 | 2.44 | 3.2663(5) | 148 | 1 |
| O14— | 0.85 | 1.87 | 2.7117(4) | 173 | 1 |
| C46—H46···O10 | 0.93 | 2.49 | 3.3588(5) | 155 | 2 |
| C14—H14A···O3 | 0.85 | 1.91 | 2.7309(4) | 161 | 3 |
| C31—H31···O6 | 0.93 | 2.57 | 3.3942(5) | 148 | 4 |
| N12—H12···O7 | 0.86 | 2.12 | 2.9446(5) | 162 | 5 |
| C41—H41A···O9 | 0.96 | 2.49 | 3.3212(5) | 146 | 6 |
| C50—H50···O14 | 0.93 | 2.37 | 3.2108(5) | 150 | 6 |
| #(0) x,y,z; (1) 1/2+x,1/2-y,1/2+z; (2) 1+x,y,z; (3) 1-x,1-y,1-z; (4) 1/2+x,1/2-y,-1/2+z; (5) -1/2+x,1/2-y,-1/2+z; (6) 1/2-x,-1/2+y,1/2-z | | | | | |

**Table 4.5** Hydrogen bonding interactions present in complex **1b_Cl** at 100 K.

| D– H···A | D–H(Å) | H···A(Å) | D···A (Å) | <D-H-A(°) | Symmetry# |
|---|---|---|---|---|---|
| N2—H2···O2 | 0.86 | 2.08 | 2.6858(16) | 127 | 0 |
| N5—H5···O3 | 0.86 | 2.12 | 2.7195(16) | 126 | 0 |
| C6—H6A···O1 | 0.93 | 2.33 | 2.8857(17) | 118 | 0 |
| C33—H33···O4 | 0.93 | 2.34 | 2.8964(17) | 118 | 0 |
| C89—H89B···Cl1 | 0.97 | 2.71 | 3.477(2) | 136 | 0 |
| C97—H97A···Cl2 | 0.97 | 2.6 | 3.542(2) | 164 | 0 |
| N3—H3···Cl2 | 0.86 | 2.35 | 3.1877(19) | 163 | 1 |
| N4—H4···Cl2 | 0.86 | 2.40 | 3.2213(19) | 160 | 1 |
| C105— | 0.97 | 2.69 | 3.630(2) | 164 | 1 |
| C14—H14···Cl2 | 0.93 | 2.8 | 3.551(2) | 138 | 1 |
| C25—H25···Cl2 | 0.93 | 2.73 | 3.506(2) | 142 | 1 |
| C143—H143···Cl2 | 0.93 | 2.75 | 3.3014(19) | 119 | 1 |
| N1—H1···Cl1 | 0.86 | 2.41 | 3.2328(19) | 159 | 2 |
| C10—H10···Cl1 | 0.93 | 2.64 | 3.459(2) | 147 | 2 |
| C97—H97B···O1 | 0.97 | 2.37 | 3.2755(19) | 155 | 2 |
| N6—H6···Cl1 | 0.86 | 2.44 | 3.2900(19) | 168 | 3 |
| C30—H30···Cl1 | 0.93 | 2.59 | 3.455(2) | 156 | 3 |
| C34—H34···O4 | 0.93 | 2.59 | 3.2038(19) | 124 | 3 |
| #(0) x,y,z; (1) 1+x,y,z; (2) 1-x,-1/2+y,1/2-z; (3) 1-x,1-y,-z | | | | | |

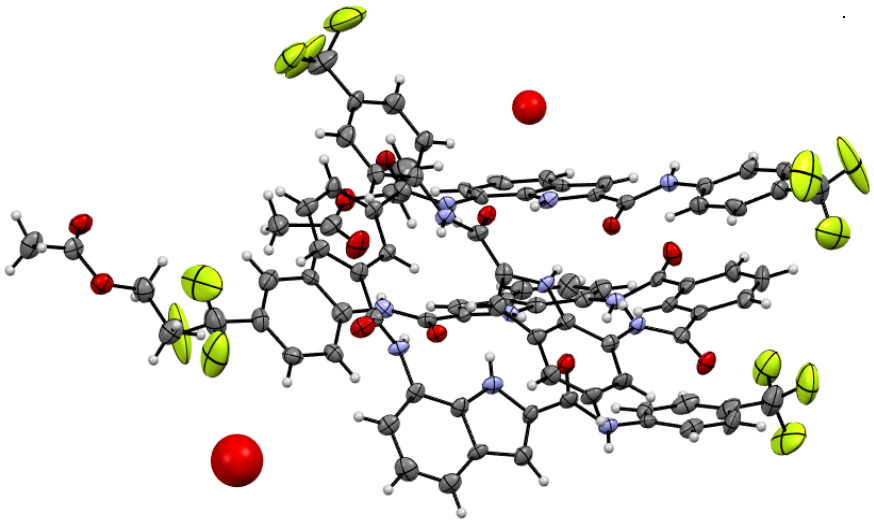


**Figure 4.8** The ORTEP diagram of compound **1a** where the ellipsoids are shown with 50% probability.

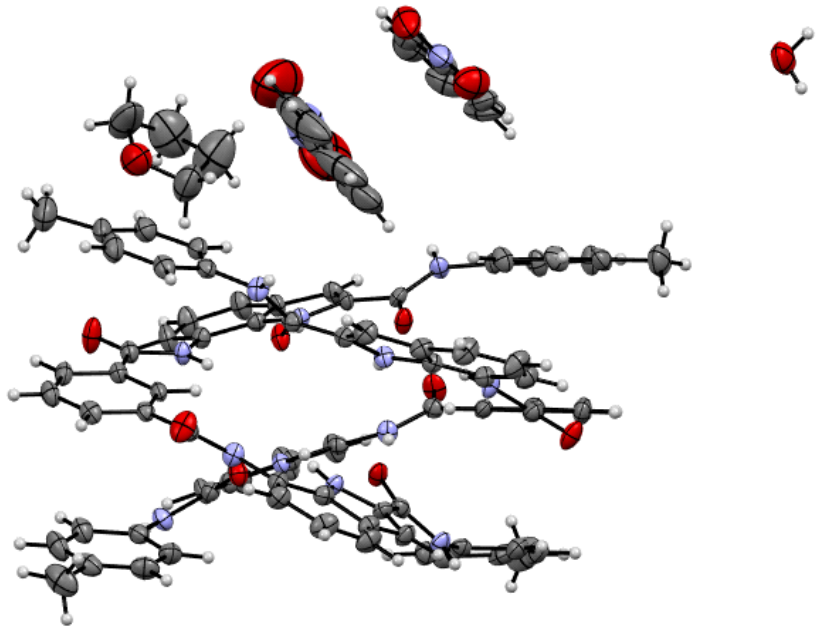


**Figure 4.9** The ORTEP diagram of compound **1b** where the ellipsoids are shown with 50% probability.

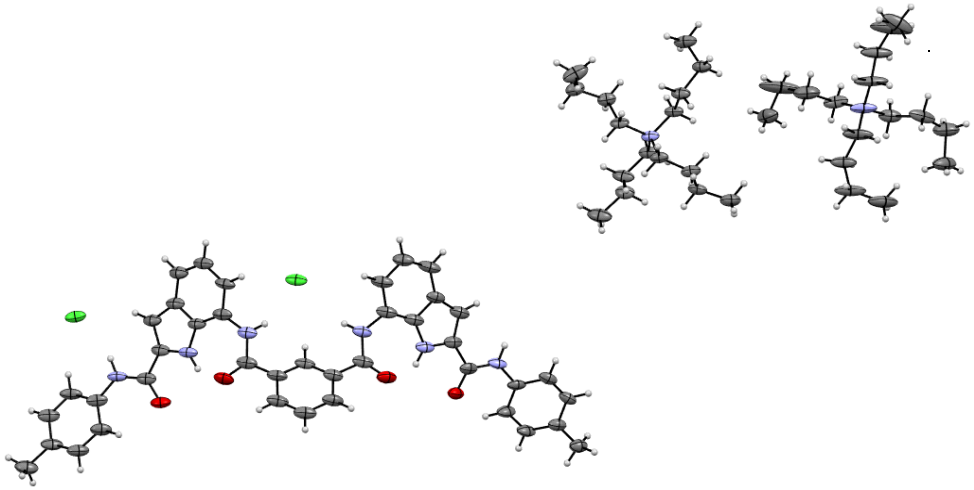


**Figure 4.10** The ORTEP diagram of compound **1b** with tetrabutylammonium chloride (TBACl) where the ellipsoids are shown with 50% probability.

### 4.4.5. ESI-MS Experiment for 1a and 1b

The formation of the double helical structure by the bis(indole) molecules **1a** and **1b** in the solution phase was confirmed from ESI-MS studies. For that, we have prepared a solution of compound (10 μM) in $CH_2Cl_2$:$CH_3CN$ (10:1) and used it for Electrospray Ionization Mass Spectrometric (ESI-MS) studies in positive mode. The peaks corresponding to $[2M + H]^+$

and/or $[2M + Na]^+$ were observed from ESI-MS experiments (where, M is the exact mass of compound), which evidenced the formation of double helix structure in the solution phase.

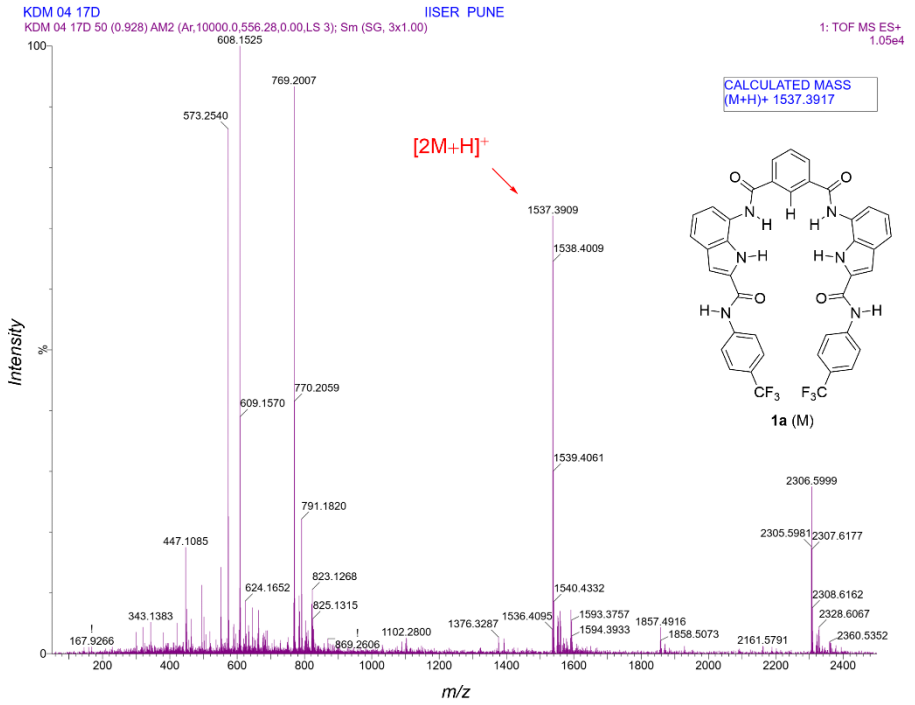



**Figure 4.11** The ESI-MS spectrum of **1a** in positive mode, where dimeric peak is marked in red color.

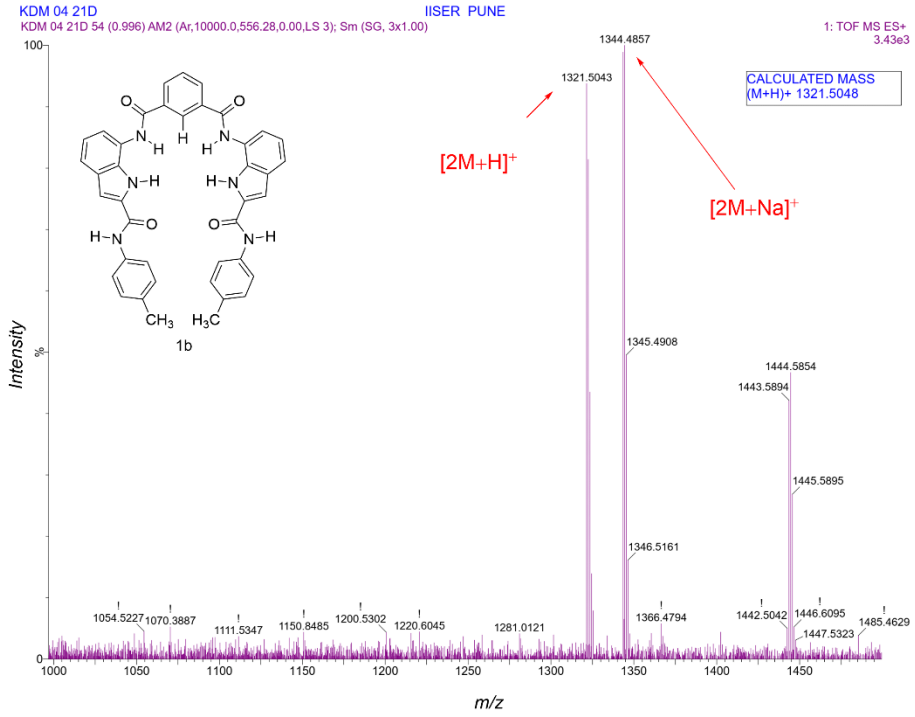



**Figure 4.12** The ESI-MS spectrum of **1b** in positive mode, where dimeric peak is marked in red color.

### 4.4.6. Solution Phase NMR Studies

The stability of the double-helical assembly by the bis(indole) derivative was confirmed from different NMR experiment technics.

#### 4.4.6.1. 2D NMR Studies

We have performed all the solution phase studies using **1c** derivative as the **1b** derivative is not soluble in $CDCl_3$. Before performing the solution phase studies, we have assigned the proton by analyzing the 2D NMR data.

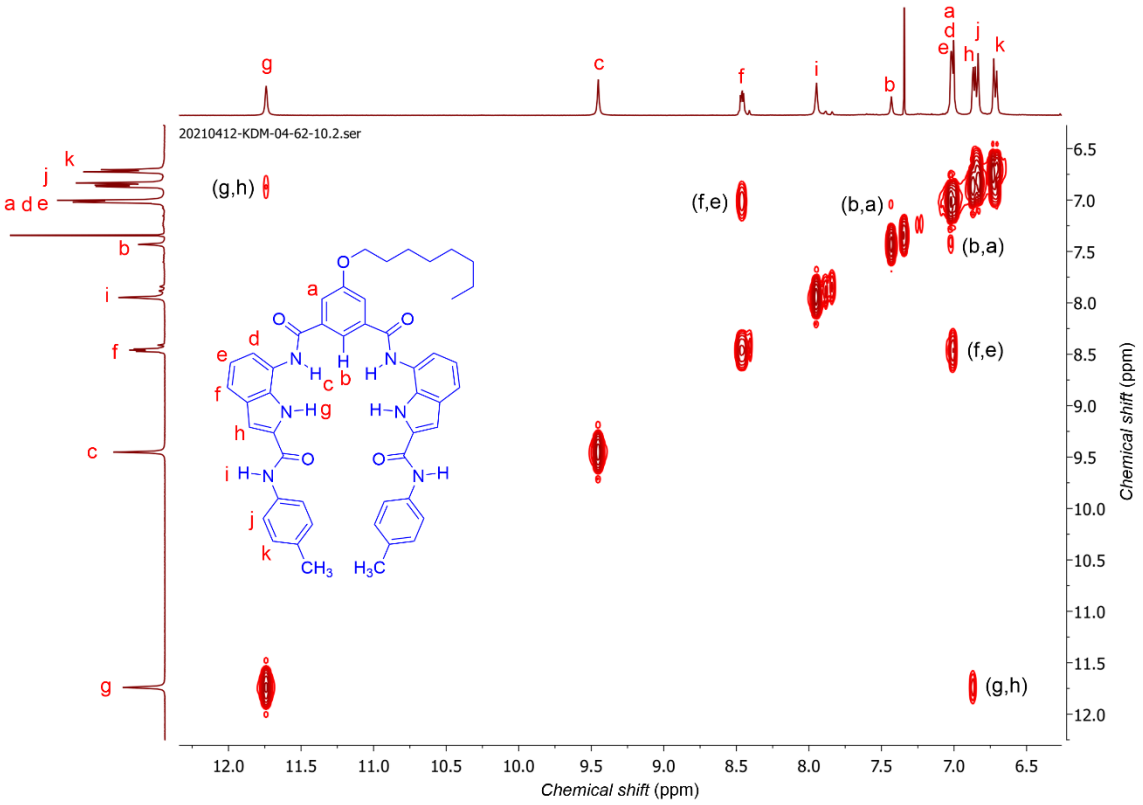



**Figure 4.13** The $^1H$-$^1H$ COSY NMR spectrum of **1c** (5.0 mM) at 25 ˚C (400 MHz, $C_2D_2Cl_4$).

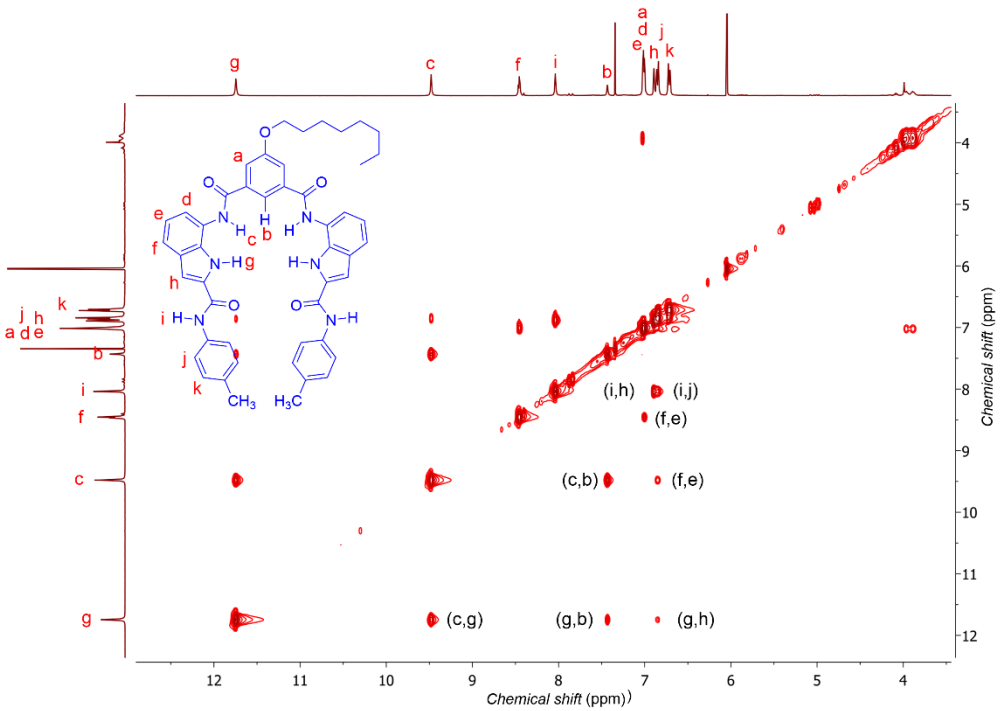



**Figure 4.14** The $^{1}$H-$^{1}$H NOESY NMR spectrum of **1c** (5.0 mM) at 25 ˚C (400 MHz, $C_2D_2Cl_4$).

### 4.4.6.2. Concentration Dependent NMR Studies of 1c

We have performed a series of $^{1}$H NMR spectra of **1c** by diluting the sample from 30.0 mM to 0.06 mM in $CDCl_3$.

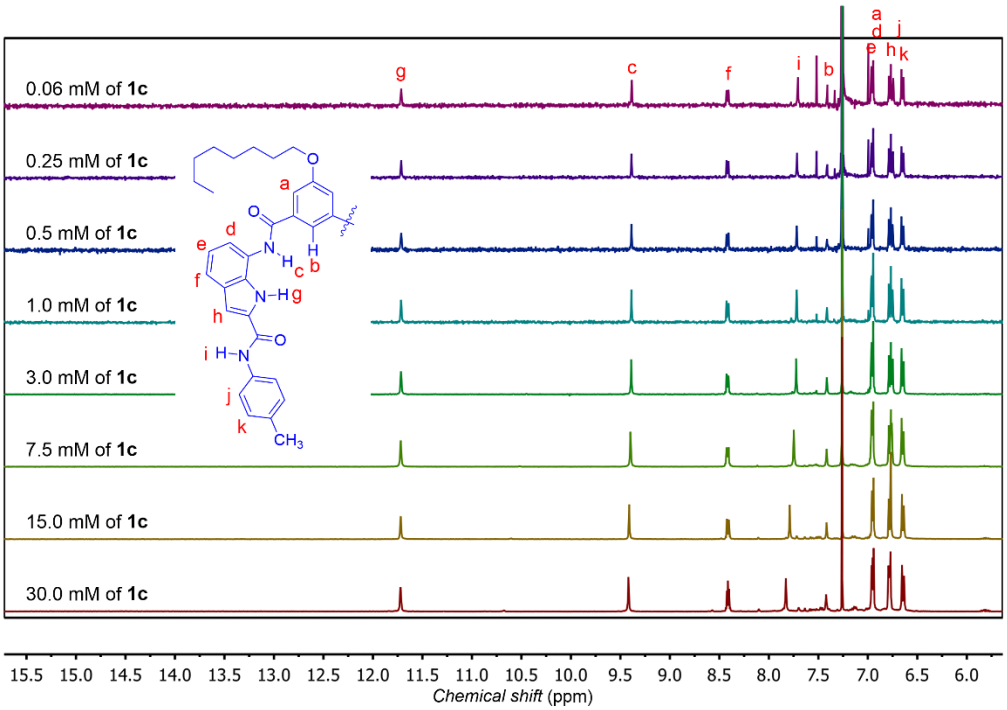



**Figure 4.15** The **s**tacked plot for $^{1}$H-NMR experiment for compound **1c** with the successive dilution from 30.0 mM to 0.06 mM at 25 ˚C (400 MHz, $CDCl_3$).

### 4.4.6.3. DMSO-$d_6$ Titration of 1c

We have performed the DMSO titration to check the stability of the double-helical assembly in the presence of a hydrogen bond acceptor solvent. For that, we have prepared a 0.5 mL solution of **1c** (5 mM) in $CDCl_3$ and recorded the $^1H$ NMR spectrum of it. Then we have recorded a series of $^1H$ NMR spectra with the successive addition of DMSO-$d_6$ (0-30 mL) at room temperature.

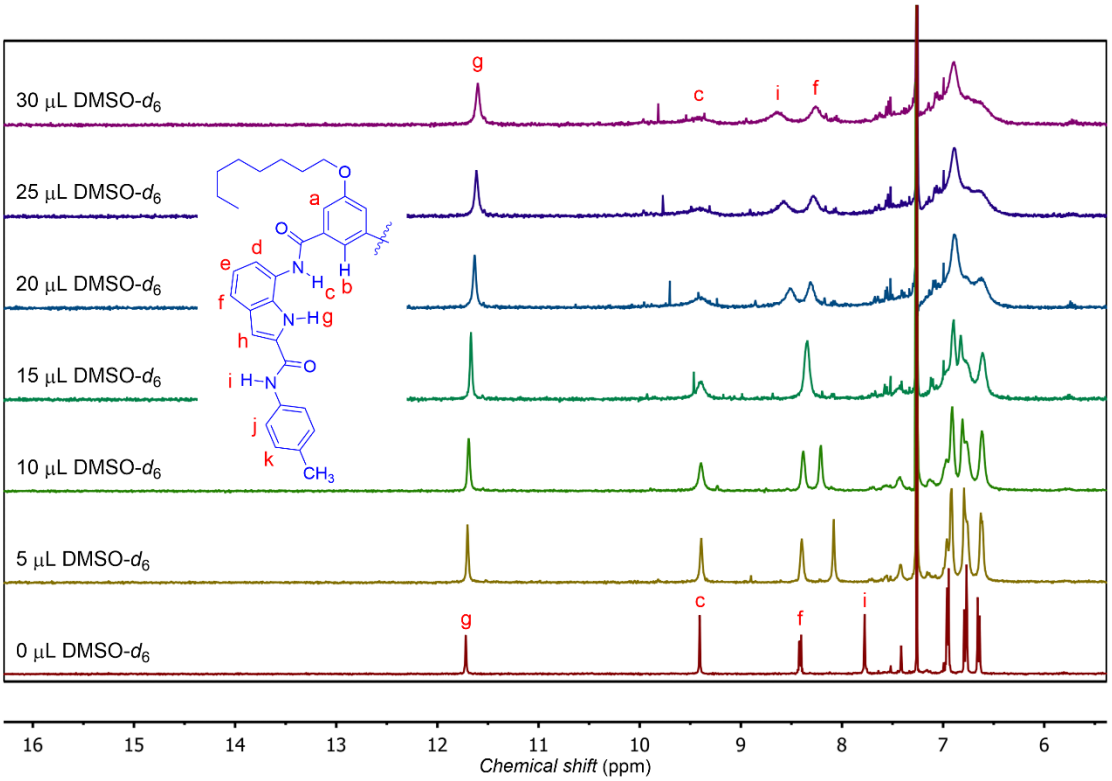



**Figure 4.16** The Stacked plot for $^1H$-NMR titration experiment for compound **1c** in $CDCl_3$ (0.5 mL) with the successive addition of DMSO-$d_6$ (0-30 μL) at 25 ˚C (400 MHz).

### 4.4.6.4. Variable Temperature NMR Experiment of 1c

We have performed the variable temperature $^1H$ NMR experiments to check the stability of the double-helical assembly at high temperatures. For that, we have prepared a 0.5 mL solution of **1c** (5 mM) in $C_2D_2Cl_4$ (boiling point 146 ˚C) and recorded the $^1H$ NMR spectrum of it. Then we have recorded a series of $^1H$ NMR spectra while increasing the recording temperature from 298K to 373K.

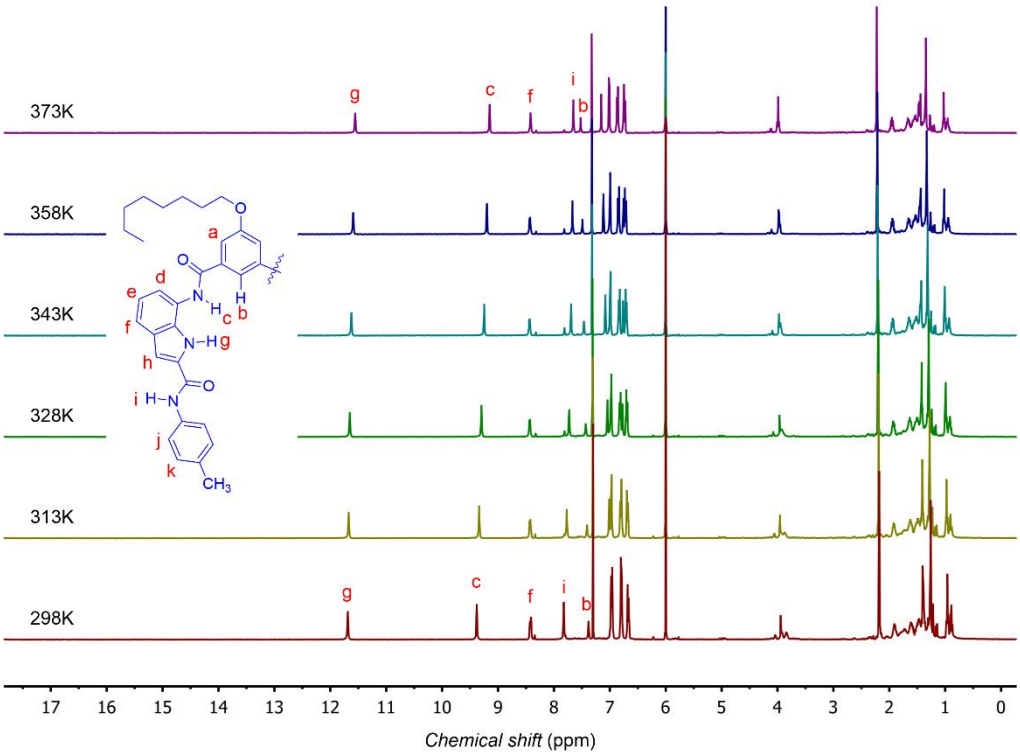



**Figure 4.17** The **s**tacked plot of variable temperature $^{1}$H NMR experiment (298K to 373K) for compound **1c** in $C_2D_2Cl_4$.

### 4.4.7. Field Emission Scanning Electron Microscopy (FESEM)

#### 4.4.7.1. FESEM Studies for Free Compound 1b

The surface morphology of the compound in solid state was examined by FESEM studies. For that, compound **1b** was dissolved in $CHCl_3$/THF to prepare a 150 μM solution. The compound solution was drop-casted on a silicon wafer, dried, and then used for FESEM studies.

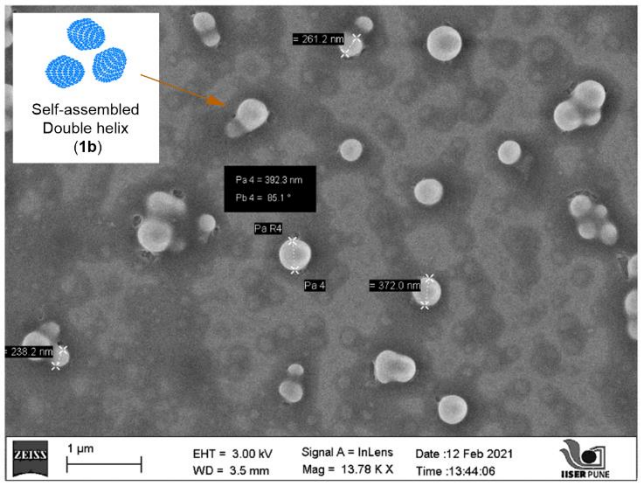



**Figure 4.18** The FESEM image of free compound **1b**.

### 4.4.7.2. FESEM Studies for Compound 1b with 2.0 and 6.0 Equivalent of TBACl

For that, compound **1b** was dissolved in $CHCl_3$/THF to prepare a 150 μM solution, and into that solution, 2.0 and 6.0 equivalents of TBACl was added separately in two solutions. The compound solutions were drop-casted on a silicon wafer, dried and then used for FESEM studies.

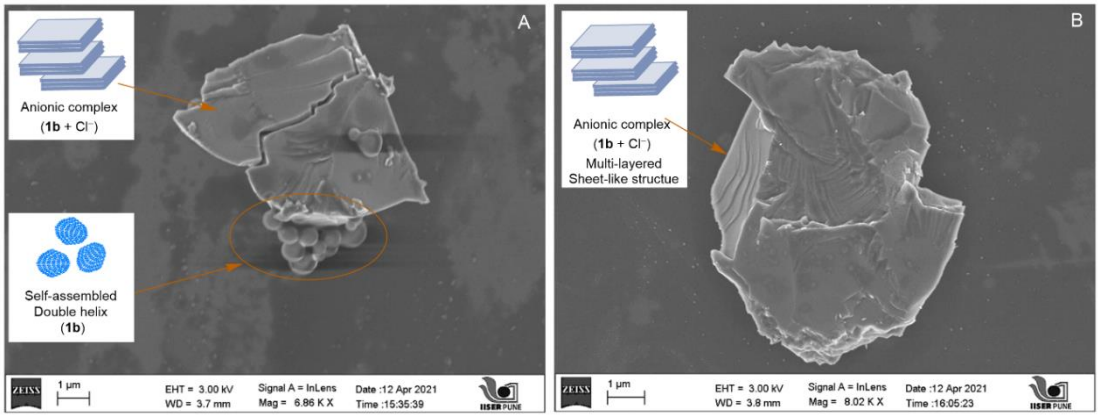



**Figure 4.19** The FESEM images of compound **1b** with 2.0 (A) and 6.0 (B) equivalents of TBACl.

## 4.4.8. Atomic Force Microscopy (AFM)

### 4.4.8.1. AFM Studies for Free Compound 1b

A 100 μM solution the compound **1b** was prepared in $CHCl_3$/THF. The compound solution was then drop-casted on a silicon wafer, dried and then used for AFM studies.

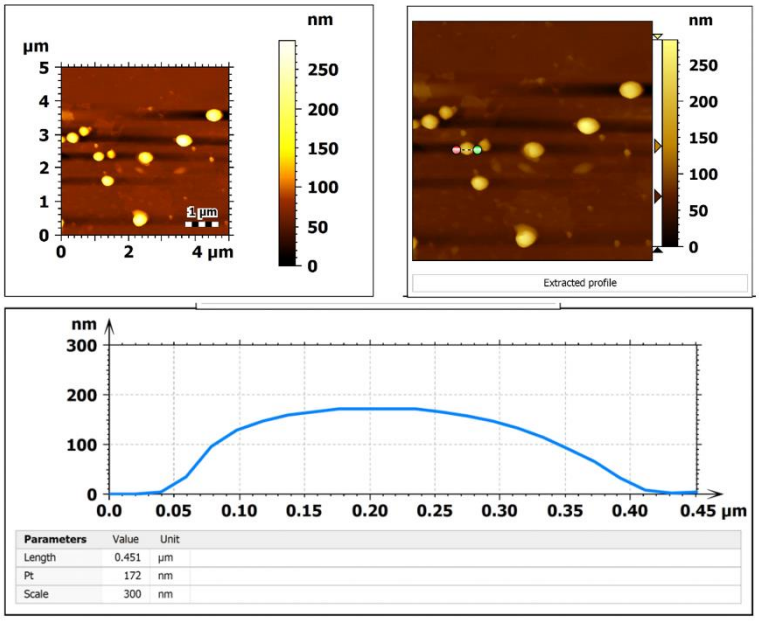



**Figure 4.20** The AFM image of free compound **1b**.

### 4.4.8.2. AFM Studies for Compound with 6.0 Equivalent of TBACl

A 100 μM solution of compound **1b** was prepared in $CHCl_3$/THF, and into that solution, 6.0 equivalents of TBACl was added. The compound solutions were then drop-casted on a silicon wafer, dried and then used for AFM studies.

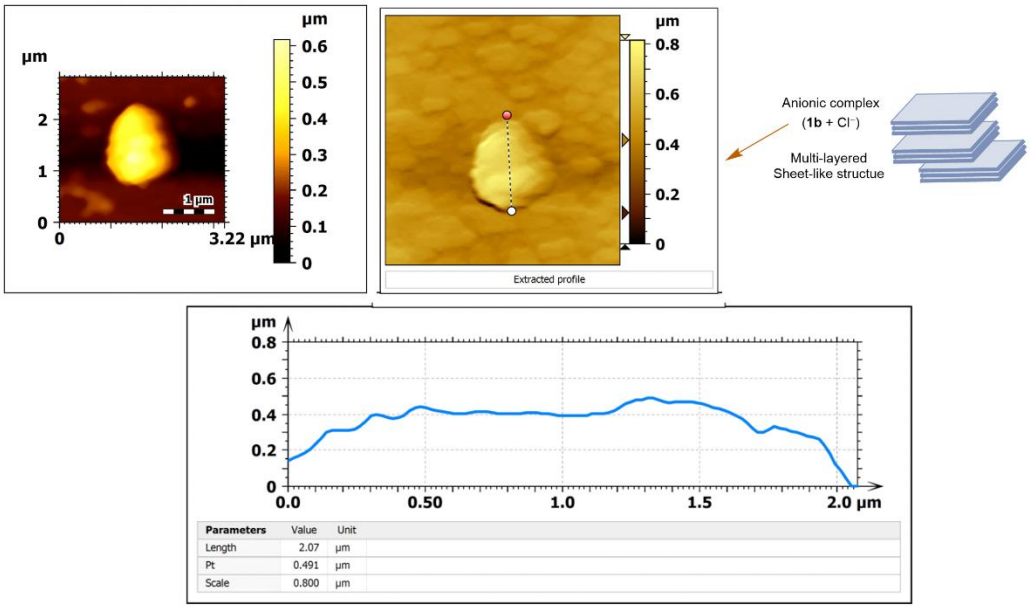



**Figure 4.21** The AFM image of compound **1b** with 6.0 equivalents of TBACl.

## 4.4.9. High-Resolution Transmission Electron Microscopy (HRTEM)

### 4.4.9.1. HRTEM Studies for Free Compound 1b

An 80 μM solution of compound **1b** was prepared in $CHCl_3$/THF. The compound solution was then drop-casted on a TEM grid, dried and then used for HRTEM imaging.

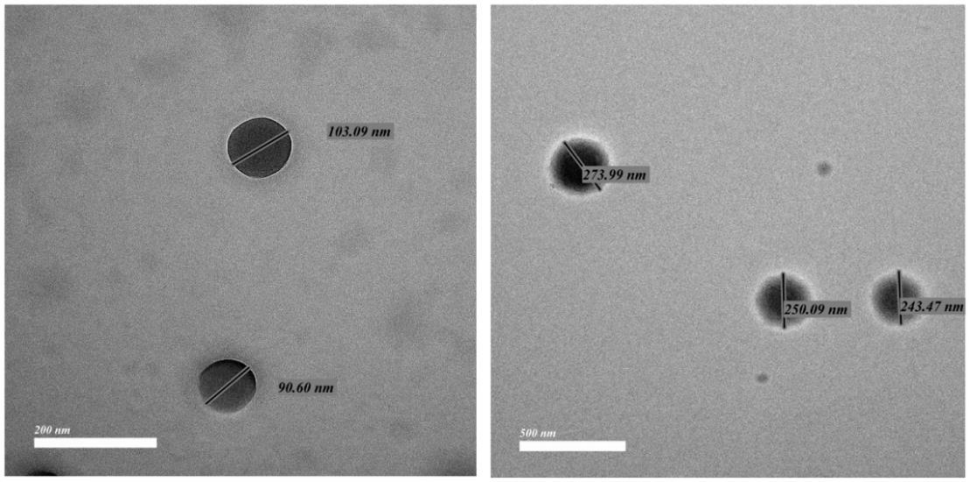



**Figure 4.22** The HRTEM images of free compound **1b**.

### 4.4.9.2. HRTEM Studies for Compound with 6.0 Equivalent of TBACl

An 80 μM solution, compound **1b** was prepared in $CHCl_3$/THF, and into that solution, 6.0 equivalents of TBACl was added. The compound solutions were then drop-casted on a TEM grid, dried and then used for HRTEM studies.

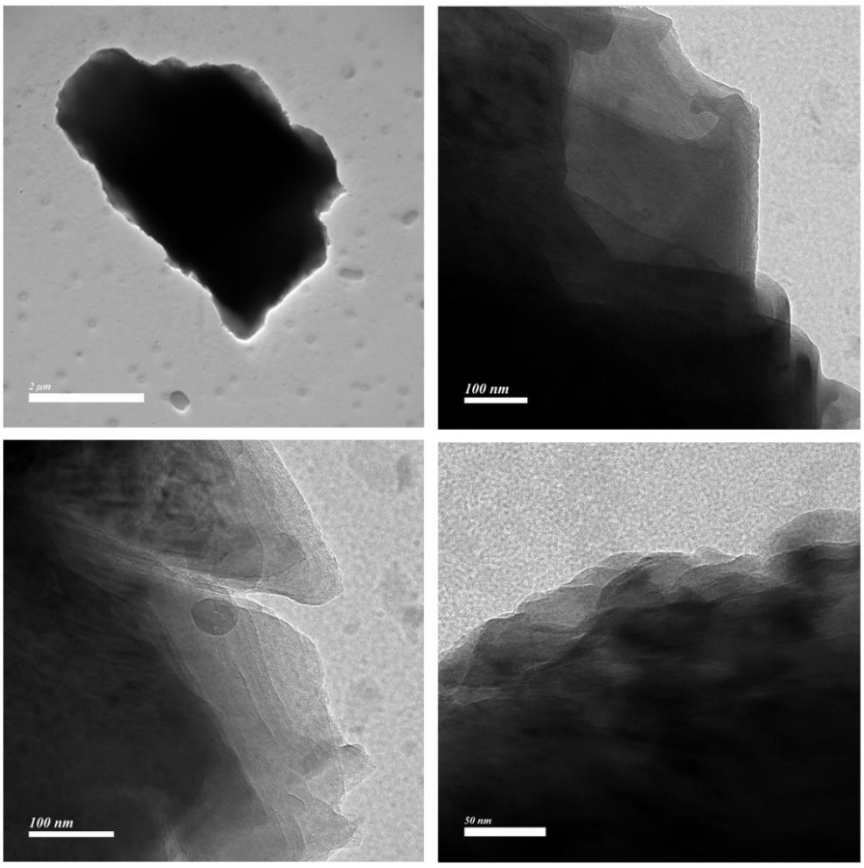



**Figure 4.23** The HRTEM images of compound **1b** with 6.0 equivalents of TBACl.

### 4.4.10. ESI-MS Spectrum of $Cl^-$ bound Complex of 1b

The formation of the $Cl^-$ ion bound complex by unwinding of the double helical structure of bis(indole) molecule **1b** in the solution phase was confirmed from ESI-MS studies. For that, we have prepared a solution of **1b** (10 μM) in $CH_2Cl_2$:$CH_3OH$ (10:1) and, into that solution, 3.0 equivalents of tetramethylammonium chloride (TMACl) was added. The peaks corresponding to the different aggregated polymeric units were observed from ESI-MS experiment and are listed in the below table (Table S6; where, M is the exact mass of **1b**), which evidenced the formation of a supramolecular polymeric complex in the solution phase.

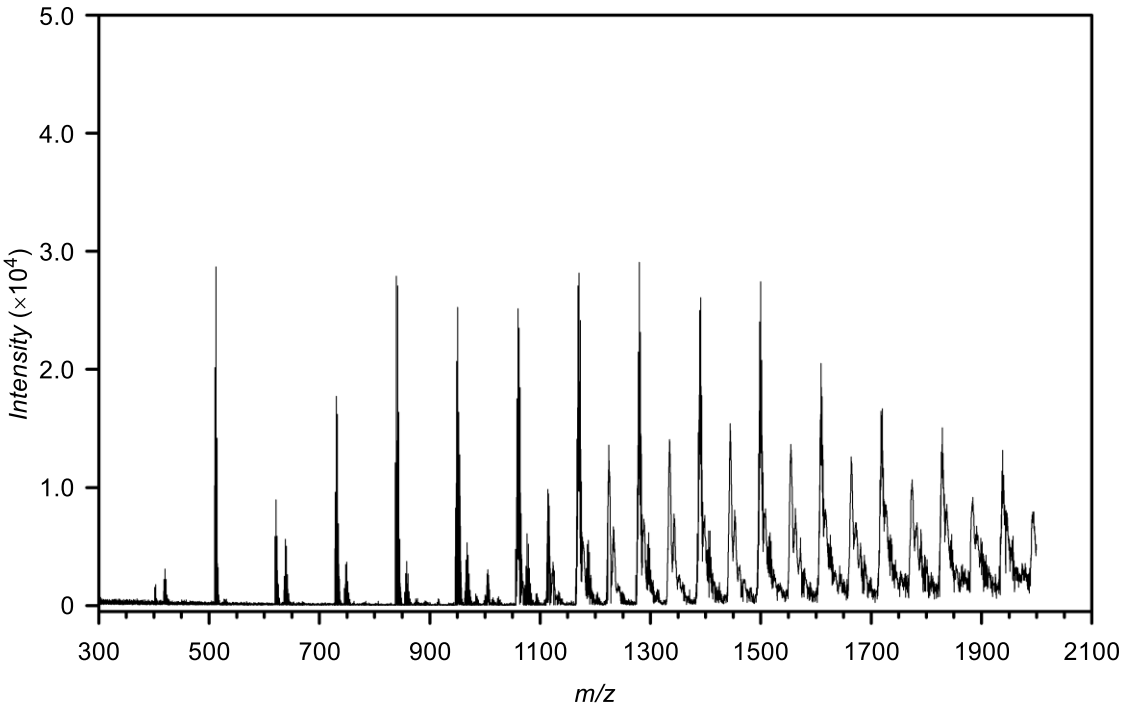



**Figure 4.24** The ESI-MS spectrum of **1b** with $Cl^-$ in negative mode.

**Table 4.6** Calculated and observed ESI-MS mass of **1b** with $Cl^-$ (where M = **1b**).

| Sr. No. | Complex | m/z | Sr. No. | Complex | m/z |
|---|---|---|---|---|---|
| 1 | $[5M+9Cl]^{9-}$ | 401.77 | 37 | $[5M+11Cl+8Na]^{3-}$ | 1289.94 |
| 2 | $[4M+7Cl]^{7-}$ | 412.25 | 38 | $[2M+Cl]^-$ | 1355.47 |
| 3 | $[5M+11Cl+2K]^{9-}$ | 418.20 | 39 | $[5M+12Cl+9K]^{3-}$ | 1357.17 |
| 4 | $[5M+12Cl+3Na]^{9-}$ | 421.09 | 40 | $[4M+3Cl+Na]^{2-}$ | 1384.45 |
| 5 | $[5M+7Cl]^{7-}$ | 506.58 | 41 | $[2M+2Cl+H]^-$ | 1391.44 |
| 6 | $[2M+6Cl+3H]^{3-}$ | 511.11 | 42 | $[4M+7Cl+5H]^{2-}$ | 1445.41 |
| 7 | $[5M+8Cl+H]^{7-}$ | 511.72 | 43 | $[4M+5Cl+3H]^{2-}$ | 1409.43 |
| 8 | $[5M+9Cl+2H]^{7-}$ | 516.85 | 44 | $[2M+4Cl+3H]^-$ | 1463.40 |
| 9 | $[4M+13Cl+8H]^{5-}$ | 620.73 | 45 | $[4M+5Cl+3K]^{2-}$ | 1466.36 |
| 10 | $[5M+12Cl+6H]^{6-}$ | 621.15 | 46 | $[2M+5Cl+4H]^-$ | 1499.37 |
| 11 | $[5M+9Cl+3K]^{6-}$ | 622.14 | 47 | $[4M+7Cl+5Na]^{2-}$ | 1500.36 |
| 12 | $[5M+10Cl+4Na]^{6-}$ | 623.82 | 48 | $[4M+11Cl+9H]^{2-}$ | 1517.36 |
| 13 | $[5M+12Cl+6Na]^{6-}$ | 643.14 | 49 | $[4M+13Cl+11H]^{2-}$ | 1553.34 |
| 14 | $[5M+11Cl+5K]^{6-}$ | 646.78 | 50 | $[2M+7Cl+6H]^-$ | 1571.33 |

| | | | | | |
|---|---|---|---|---|---|
| 15 | $[5M+8Cl+3Na]^{5-}$ | 729.99 | 51 | $[2M+4Cl+3K]^{-}$ | 1577.25 |
| 16 | $[2M+4Cl+2H]^{2-}$ | 731.19 | 52 | $[4M+11Cl+9Na]^{2-}$ | 1616.28 |
| 17 | $[2M+5Cl+3H]^{2-}$ | 749.18 | 53 | $[2M+6Cl+5Na]^{-}$ | 1645.26 |
| 18 | $[5M+10Cl+5Na]^{5-}$ | 753.18 | 54 | $[4M+13Cl+11Na]^{2-}$ | 1674.24 |
| 19 | $[2M+7Cl+5Na]^{2-}$ | 840.12 | 55 | $[4M+11Cl+9K]^{2-}$ | 1688.15 |
| 20 | $[5M+4Cl]^{4-}$ | 860.28 | 56 | $5M+3Cl+Na]^{2-}$ | 1714.57 |
| 21 | $[5M+10Cl+6Na]^{4-}$ | 947.22 | 57 | $[5M+4Cl+2H]^{2-}$ | 1721.57 |
| 22 | $[4M+6Cl+3H]^{3-}$ | 951.28 | 58 | $[5M+3Cl+K]^{2-}$ | 1722.56 |
| 23 | $[5M+9Cl+5K]^{4-}$ | 952.69 | 59 | $[2M+6Cl+5K]^{-}$ | 1725.11 |
| 24 | $[4M+7Cl+4H]^{3-}$ | 963.27 | 60 | $[5M+5Cl+3H]^{2-}$ | 1739.56 |
| 25 | $[4M+5Cl+2K]^{3-}$ | 964.59 | 61 | $[5M+4Cl+2Na]^{2-}$ | 1743.55 |
| 26 | $[5M+10Cl+6K]^{4-}$ | 971.17 | 62 | $[4M+13Cl+11K]^{2-}$ | 1762.08 |
| 27 | $[5M+12Cl+8K]^{4-}$ | 1008.14 | 63 | $[5M+5Cl+3Na]^{2-}$ | 1772.53 |
| 28 | $[3M+4Cl+2H]^{2-}$ | 1061.32 | 64 | $[5M+7Cl+5H]^{2-}$ | 1775.53 |
| 29 | $[3M+5Cl+3H]^{2-}$ | 1079.31 | 65 | $[2M+7Cl+6K]^{-}$ | 1799.04 |
| 30 | $[3M+7Cl+5H]^{2-}$ | 1115.28 | 66 | $[5M+7Cl+5Na]^{2-}$ | 1830.49 |
| 31 | $[3M+10Cl+8H]^{2-}$ | 1169.25 | 67 | $[5M+11Cl+9H]^{2-}$ | 1847.49 |
| 32 | $[5M+6Cl+3H]^{3-}$ | 1171.36 | 68 | $[5M+7Cl+5K]^{2-}$ | 1870.41 |
| 33 | $[5M+7Cl+4H]^{3-}$ | 1183.35 | 69 | $[5M+9Cl+7Na]^{2-}$ | 1888.45 |
| 34 | $[5M+5Cl+2K]^{3-}$ | 1184.67 | 70 | $[5M+8Cl+6K]^{2-}$ | 1907.38 |
| 35 | $[5M+9Cl+6K]^{3-}$ | 1283.24 | 71 | $[5M+9Cl+7K]^{2-}$ | 1944.34 |
| 36 | $[3M+9Cl+7K]^{2-}$ | 1284.10 | 72 | $[5M+11Cl+9Na]^{2-}$ | 1946.41 |

### 4.4.11. Solution Phase Anion Binding

#### $^1$H NMR Titration of Compound 1c with TBACl

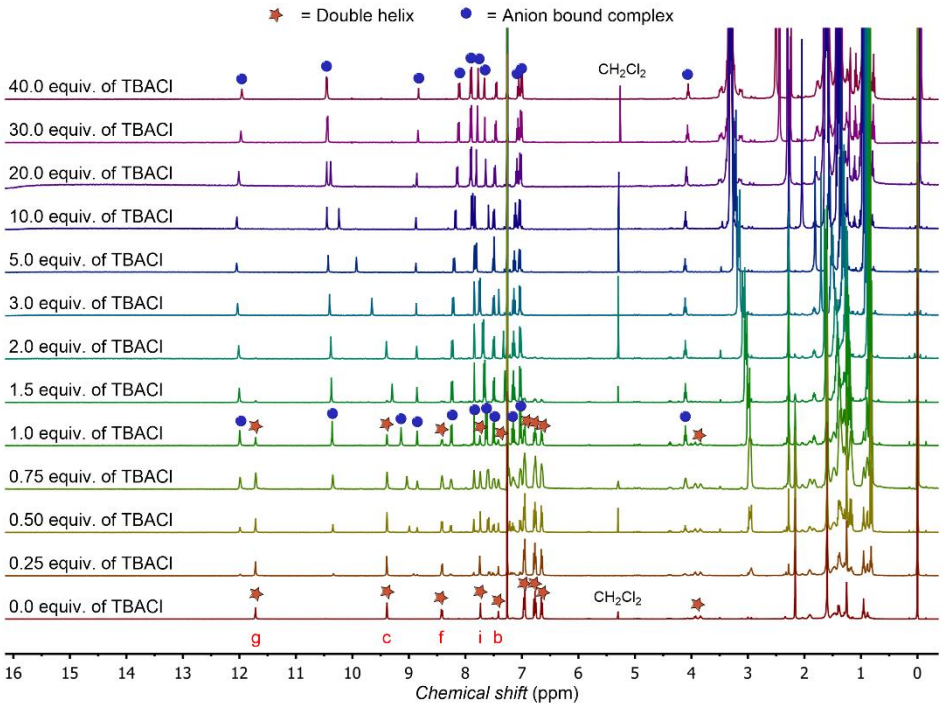



**Figure 4.25** The stacked plot of $^1$H NMR titration of compound **1c** in $CDCl_3$ with the successive addition of TBACl at room temperature (400 MHz).

#### $^1$H NMR Titration of Compound 1c with TBABr, TBAI, and $TBANO_3$

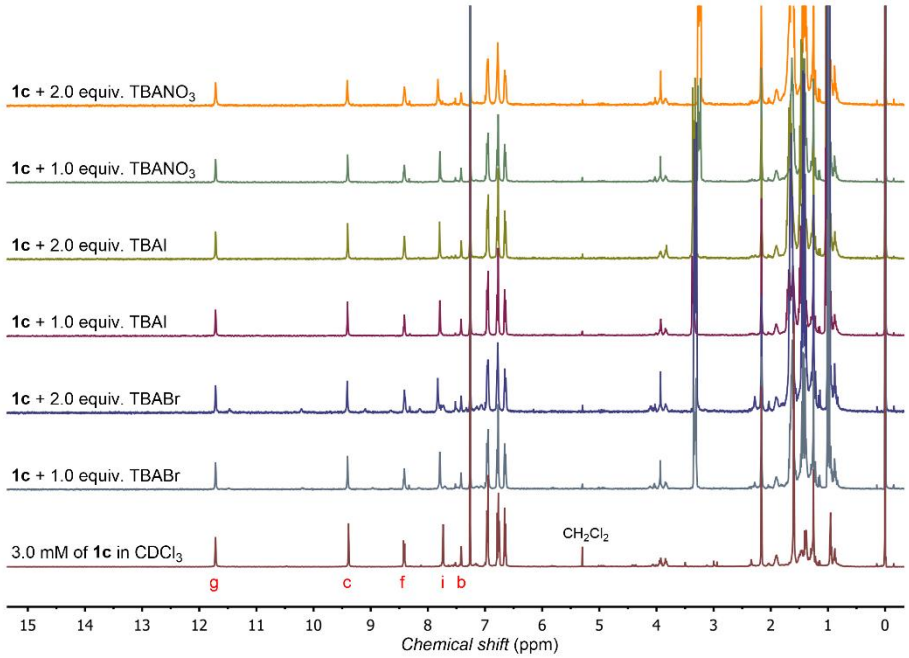



**Figure 4.26** The stacked plot of $^1$H NMR of compound **1c** in $CDCl_3$ with different equivalents of TBABr, TBAI, and $TBANO_3$ at room temperature (400 MHz).

**Anion Binding Reversibility of Anionic Complex by $AgBF_4$ and $AgPF_6$**

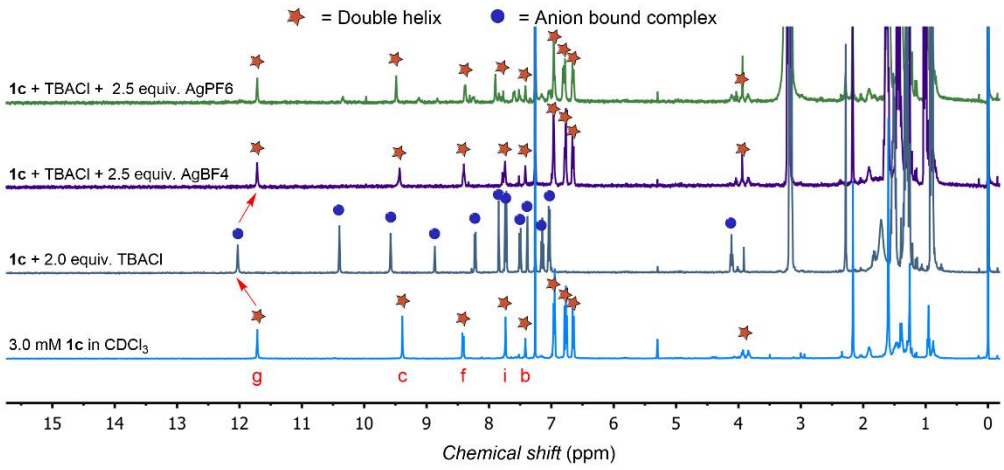



**Figure 4.27** The stacked plot of $^1$H NMR of compound **1c** in $CDCl_3$ with the addition of 2 equivalents of TBACl and then the addition of 2.5 equivalents of silver salts for checking anion binding reversibility at room temperature (400 MHz).

### 4.4.12. 2D-DOSY NMR Experiment of Bis(indole) Compound 1c

To check the aggregation behaviour, we have performed the 2D-DOSY NMR experiment for the free and anionic complex of the receptor in $CHCl_3$ solution. At first 2D-DOSY NMR spectrum was recorded for the 5.0 mM solution of the free bis(indole) compound **1c**, which provided the diffusion coefficient value of 5.96 (± 0.03) × $10^{-6}$ $cm^2/s$ (Figure 4.28). With the addition of 3.0 equivalent TBACl salt in the same 5.0 mM receptor solution leads the decrement of diffusion coefficient value, which is found to be 4.25 (± 0.02) × $10^{-6}$ $cm^2/s$ (Figure 4.29). This decrease in the diffusion coefficient value supports the polymer structure formation in the solution phase, which has formed by the conversion of the double helix form to monomeric unit and subsequent formation of polymeric aggregates.

Further, the 2D-DOSY NMR spectra were recorded at higher concentrations of receptor with 3.0 equivalent of TBACl. And from these experiments the diffusion coefficient values have been calculated and the values are 3.14 (± 0.02) × $10^{-6}$ $cm^2/s$ and 2.64 (± 0.02) × $10^{-6}$ $cm^2/s$ for 14 mM and 20 mM concentration of receptor (with 3.0 equivalent of TBACl), respectively (Figure 4.30 and 4.31).

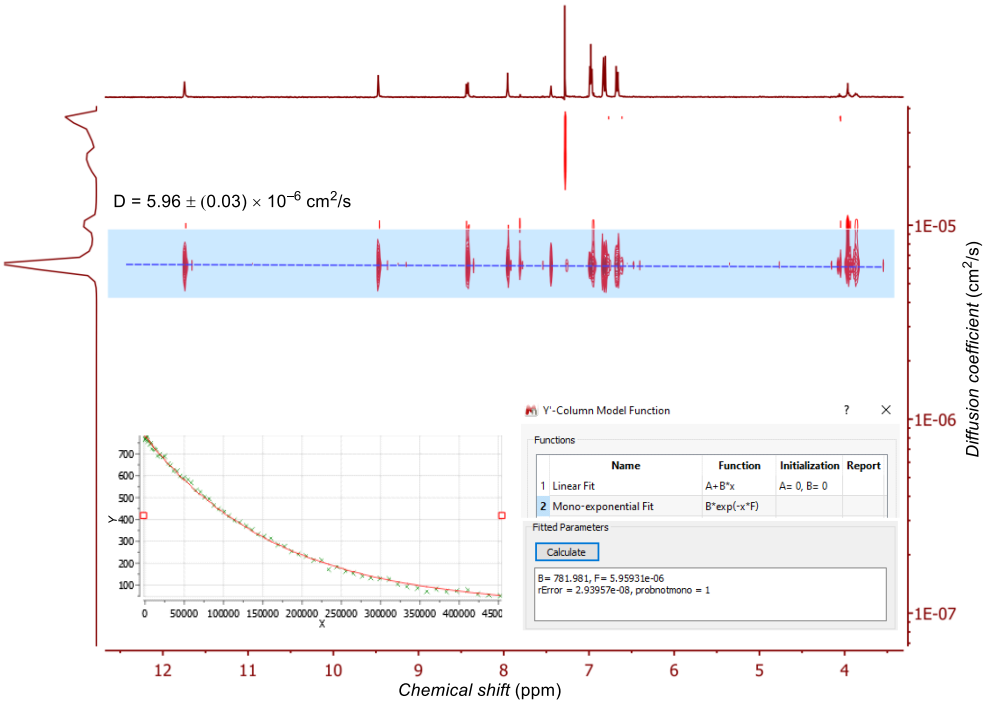



**Figure 4.28** The 2D DOSY NMR spectrum of bis(indole) compound **1c** (5 mM) in $CHCl_3$ at 25 ºC. Two sub-figures in the bottom sections are the screenshots of the processed data. The diffusion coefficient value for this compound in the above-mentioned condition is 5.96 (± 0.03) × $10^{-6}$ $cm^2/s$.

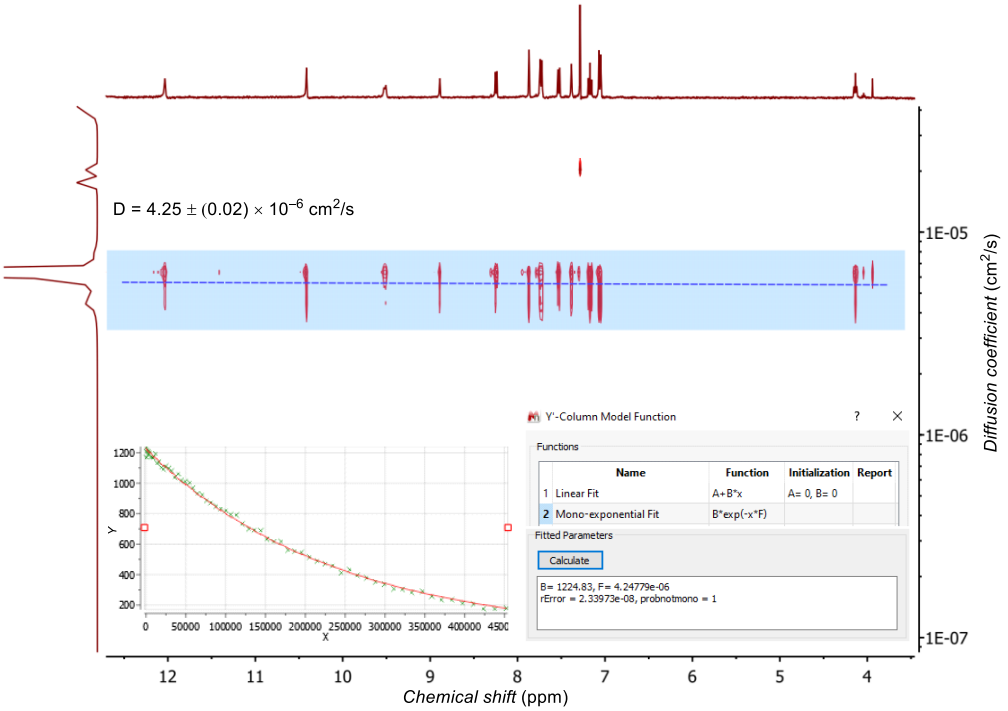



**Figure 4.29** The 2D DOSY NMR spectrum of bis(indole) compound **1c** (5 mM) with 3 equiv. of TBACl in $CHCl_3$ at 25 ºC. Two sub-figures in the bottom sections are the screenshots of the processed data. The diffusion coefficient value for this compound in the above-mentioned condition is 4.25 (± 0.02) × $10^{-6}$ $cm^2/s$.

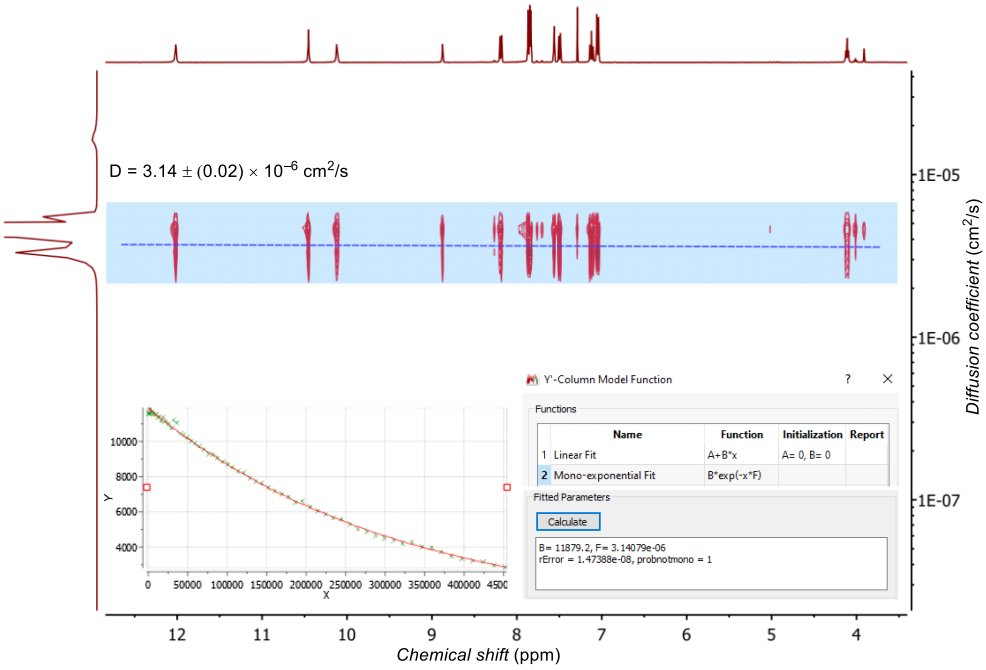



**Figure 4.30** The 2D DOSY NMR spectrum of bis(indole) compound **1c** (14 mM) with 3 equiv. of TBACl in $CHCl_3$ at 25 ºC. Two sub-figures in the bottom sections are the screenshots of the processed data. The diffusion coefficient value for this compound in the above-mentioned condition is 3.14 (± 0.02) × $10^{-6}$ $cm^2/s$.

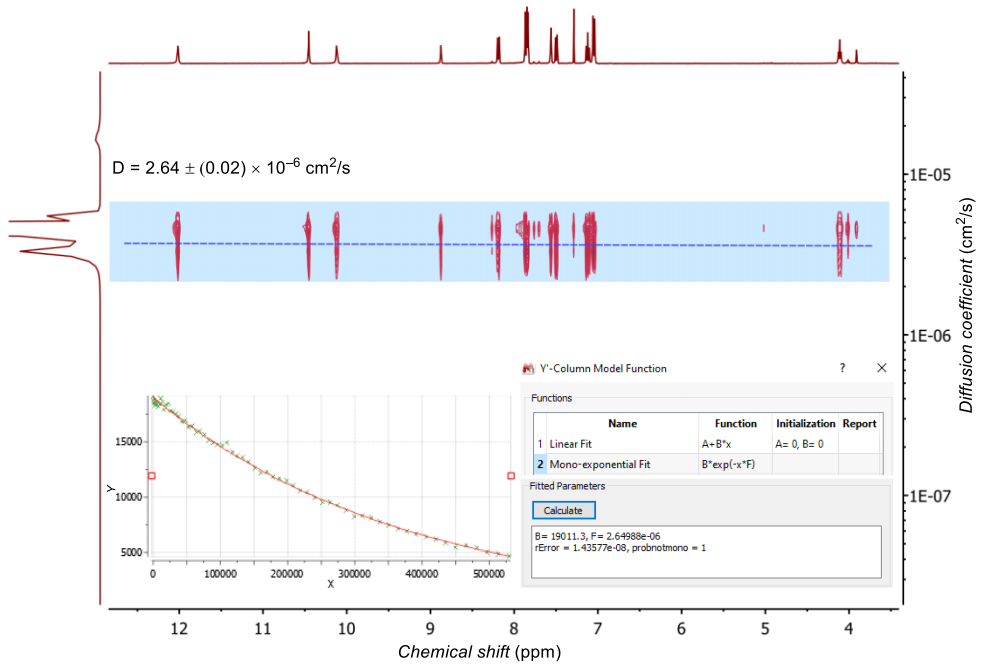



**Figure 4.31** The 2D DOSY NMR spectrum of bis(indole) compound **1c** (20 mM) with 3 equiv. of TBACl in $CHCl_3$ at 25 ºC. Two sub-figures in the bottom sections are the screenshots of the processed data. The diffusion coefficient value for this compound in the above-mentioned condition is 2.64 (± 0.02) × $10^{-6}$ $cm^2/s$.

### 4.4.13. Ion Transport Studies

#### 4.4.13.1. HPTS Assay for Checking Ion Transport Activity

We have prepared a salt solution using autoclaved water of strength 100 mM of NaCl and 10 mM of HEPES. Initially, the pH of the solution was below 7.0 and to make the pH at around 7.0 required amount of NaOH (0.5 M) solution was added. Then HPTS solution of 1 mM was prepared from solid HPTS using the above mentioned buffer solution. The stock solution of the transporter for the HPTS assay was prepared using HPLC grade DMSO.

At first, 1 mL of EYPC lipid solution (25 mg/mL in chloroform) was taken in a 10 mL round bottomed flask. The chloroform present in the lipid solution was then evaporated by a slow stream of nitrogen gas while rotating the round bottomed flask to get a thin film of lipid inside it. Then the trace amount of chloroform present in the lipid was evaporated by drying it in a high vacuum for about 5 h. The thin film of lipid was hydrated with HPTS solution (1 mM HPTS, 10 mM HEPES, 100 mM NaCl, pH 7) while vortexing 4-5 times over the time period of 1 h. Then the hydrated vesicles suspension was subjected through 15 freeze-thaw cycles and extrusions were done for 19 times (must be odd number) using 100 nm polycarbonate membrane. The extravesicular dye was separated from vesicles by size exclusion column chromatography (using Sephadex G-50 gel) eluting with buffer solution (10 mM HEPES, 100 mM NaCl, pH 7). After collecting the vesicles from the column, these were diluted to 6 mL using aforementioned buffer (10 mM HEPES, 100 mM NaCl, pH 7) to get the concentration of ~ 5.5 mM of EYPC-LUVs⊃HPTS, assuming no loss of lipid throughout the process. The vesicles compositions, inside: 1 mM HPTS, 10 mM HEPES, 100 mM NaCl, pH 7 and outside: 10 mM HEPES, 100 mM NaCl, pH 7. Final vesicles concentration: ~ 65 μM.

In a clean cuvette, 1975 μL of buffer solution (10 mM HEPES, 100 mM NaCl, pH 7), 25 μL of HPTS trapped vesicles solution were taken and placed in a fluorescence instrument equipped with a magnetic stirrer. The fluorescence emission intensity of the HPTS dye, $I_t$ was measured at $\lambda_{em}$ = 510 nm (where, $\lambda_{ex}$ = 450 nm) for 350 s. For each reading, the start time of the instrument was considered as $t$ = 0 s. Then at $t$ = 20 s, 20 μL of 0.5 M NaOH solution was added to the same cuvette to generate a pH gradient (ΔpH = 0.8) between intra and extra vesicular medium. Then 20 μL solution of transporters in DMSO of different concentrations were added at $t$ = 100 s. At $t$ = 300 s, 10% triton X-100 (25 μL) was added to destroy all the vesicles for the destructing of the pH gradient.

The fractional emission intensity (in percentage), $I_F$ (Figure 4.32B) was calculated after normalizing all the data using the following equation (Equation 1).

$$\% \text{ of } I_F = (I_t - I_0) / (I_\infty - I_0) \times 100 \qquad \text{Equation 1}$$

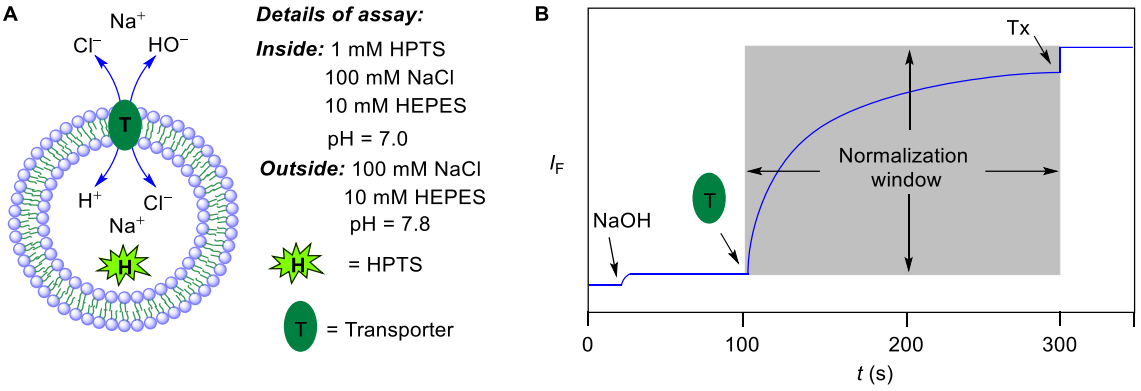



**Figure 4.32** Schematic representation of fluorescence kinetics assay for checking ion transport activity across EYPC-LUVs⊃HPTS (**A**), and normalized working window for the same experiment (**B**).

where, $I_0$ is the initial fluorescence intensity *i.e.* before the addition of the transporter compound, $I_t$ is the fluorescence intensity at time $t$ and $I_\infty$ is the final fluorescence intensity *i.e.* after the addition of Triton X-100.

Before plotting the data the time axis was normalized using the following equation:

$$t = t - 100 \qquad \text{Equation 2}$$

The concentration dependent ion transport activity data was used for fitting of the "Hill equation" (Equation 3) to get the $EC_{50}$ value *i.e.*, half maximal effective concentration and Hill coefficient ($n$).

$$Y = Y_\infty + (Y_0 - Y_\infty) / [(1 + (c / EC_{50})^n] \qquad \text{Equation 3}$$

where, $Y_0$ is the initial fluorescence intensity *i.e.* before the addition of the transporter molecule, $Y_\infty$ is the fluorescence intensity after addition of excess transporter molecule, and $c$ is the concentration of the transporter in the same assay condition.

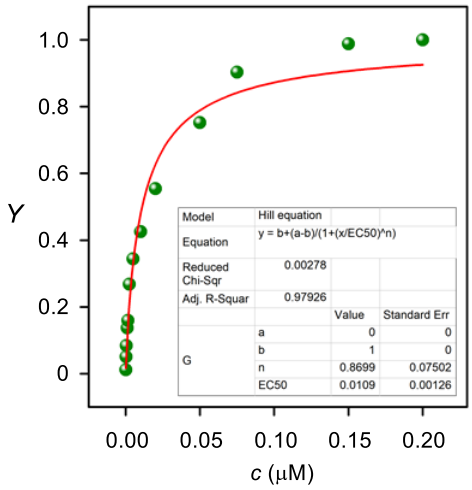



**Figure 4.33** The Hill plot of transporter **1b** at $t$ = 100 s to get $EC_{50}$ and Hill coefficient.

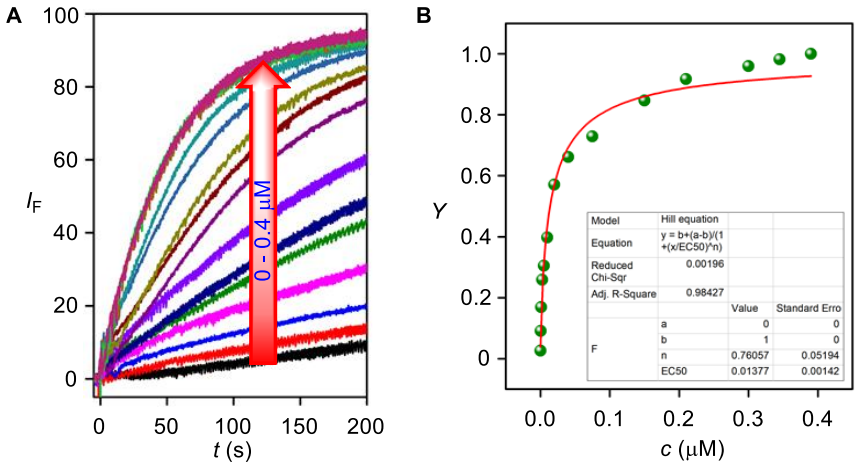



**Figure 4.34** Concentration dependent ion transport activity assay of transporter **1a** (0–0.4 μM) across EYPC-LUVs⊃HPTS (**A**), and Hill plot of transporter **1a** at $t$ = 100 s to get $EC_{50}$ and Hill coefficient (**B**).

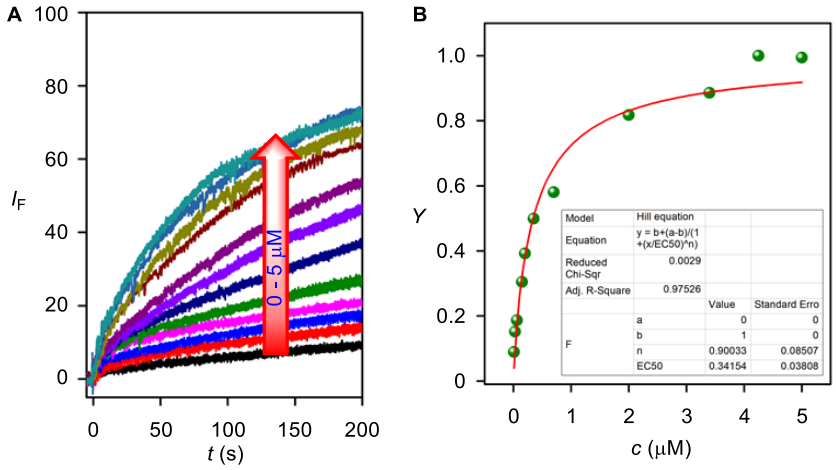



**Figure 4.35** Concentration dependent ion transport activity assay of transporter **1c** (0–5 μM) across EYPC-LUVs⊃HPTS (**A**), and Hill plot of transporter **1c** at $t$ = 100 s to get $EC_{50}$ and Hill coefficient (**B**).

### 4.4.13.2.HPTS Assay for Checking Ion Selectivity

We have prepared different buffer solutions using autoclaved water of strength 100 mM of MX (where, MX = NaCl, NaBr, NaI, $NaNO_3$, NaOAc, LiCl, KCl, RbCl, CsCl) and 10 mM of HEPES. The pH of the solutions was adjusted to 7.0 by the addition of NaOH solution (0.5 M). The stock solution for the ion selectivity assay was prepared from solid transporter compound by using HPLC grade DMSO.

We have prepared the vesicles for the ion selectivity assay following the same procedure as mentioned earlier.

**Description of HPTS Assay for Cation Selectivity:** In a clean cuvette, 1975 µL of buffer solution (10 mM HEPES, 100 mM MCl, pH 7; where, $M^+ = Na^+$, $Li^+$, $K^+$, $Rb^+$, and $Cs^+$), 25 µL of HPTS trapped vesicles solution were taken and placed in a fluorescence instrument equipped with a magnetic stirrer. The fluorescence emission intensity of the HPTS dye, $I_t$ was measured at $\lambda_{em}$ = 510 nm (where $\lambda_{ex}$ = 450 nm) for 350 s. The start time of the instrument for each reading was considered as $t$ = 0 s. Then at $t$ = 20 s, 20 µL NaOH solution (0.5 M) was added to the same cuvette to generate a pH gradient (ΔpH = 0.8) between intra and extra vesicular medium. Then 20 µL solution of the transporter in DMSO was added at $t$ = 100 s. At $t$ = 300 s, 10% triton X-100 (25 µL) was added to destroy all the vesicles for the destructing of the pH gradient. All the data were normalized using Equation 1 and Equation 2.

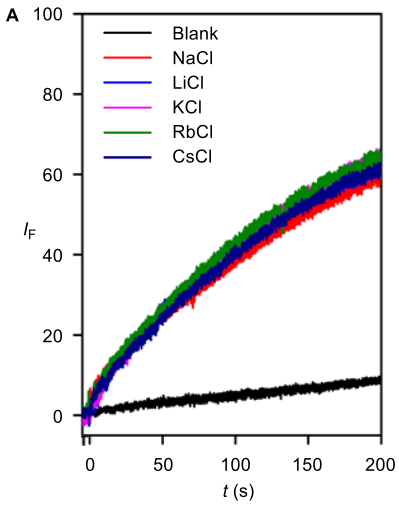



**Figure 4.36** The ion transport activity by the transporter **1b** (12 nM) across EYPC-LUVs⊃HPTS by changing the extravesicular cations.

**Description of HPTS Assay for Anion Selectivity:** In a clean cuvette, 1975 µL of buffer solution (10 mM HEPES, 100 mM NaX, pH 7; where, $X^- = Cl^-$, $Br^-$, $I^-$, $NO_3^-$, $ClO_4^-$, $SCN^-$, and $AcO^-$), 25 µL of HPTS trapped vesicles solution were taken and placed in a fluorescence instrument equipped with a magnetic stirrer. The fluorescence emission intensity of the HPTS dye, $I_t$ was measured at $\lambda_{em}$ = 510 nm (where $\lambda_{ex}$ = 450 nm) for 350 s. For each reading, the start time of the instrument was considered as $t$ = 0 s. Then at $t$ = 20 s, 20 µL NaOH solution (0.5 M) was added to the same cuvette to generate a pH gradient (ΔpH = 0.8) between intra and extra vesicular medium. Then 20 µL solution of the transporter in DMSO was added at $t$ = 100 s. At $t$ = 300 s, 10% triton X-100 (25 µL) was added to destroy all the vesicles for the destructing of the pH gradient. All the data was normalized using Equation 1 and Equation 2.

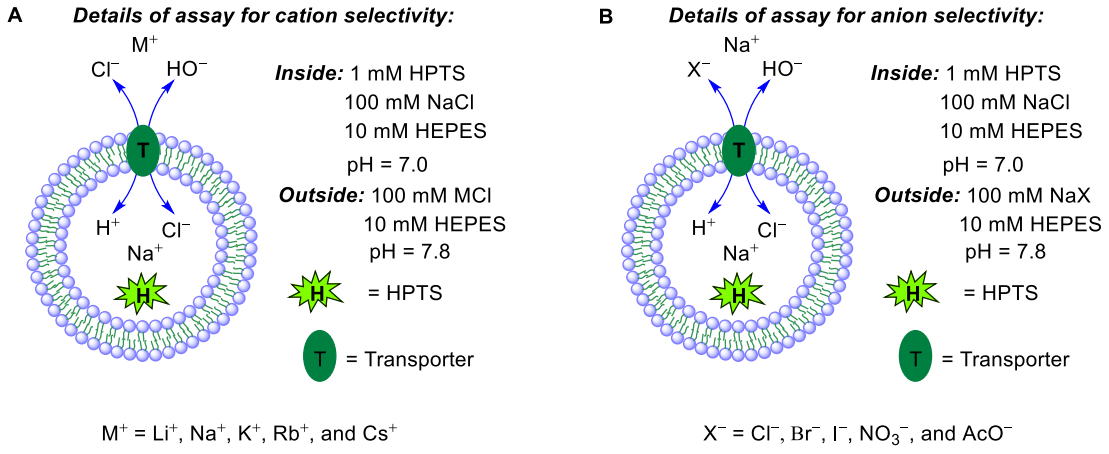



**Figure 4.37** Schematic representation of fluorescence kinetics assay for checking ion selectivity across EYPC-LUVs⊃HPTS. Cation selectivity assay (A), and anion selectivity assay (B).

### 4.4.13.3. Lucigenin Assay for Checking $Cl^-$ Transport Activity

We have prepared a 225 mM $NaNO_3$ salt solution using autoclaved water. Then 1 mM Lucigenin solution was prepared using the 225 mM $NaNO_3$ solution. The stock solution of the transporter for the Lucigenin assay was prepared from solid compound by using HPLC grade $CH_3CN$ : $CH_3OH$ (6 : 1) solution.

At first, 1 mL of EYPC lipid solution (25 mg/mL in chloroform) was taken in a 10 mL round bottomed flask. The chloroform present in the lipid solution was then evaporated by a slow stream of nitrogen gas while rotating the round bottomed flask to get a thin film of lipid inside it. Then the last trace amount of chloroform present in the lipid was evaporated by drying it in a high vacuum for about 5 h. The thin film of lipid was hydrated with 1 mL of Lucigenin solution (1 mM Lucigenin, 225 mM $NaNO_3$) while vortexing 4-5 times by keeping 10 mins of the gap in between it. Then the hydrated vesicles suspension was subjected to 15 freeze-thaw

cycles and extrusions were done for 19 times (must be odd number) using 200 nm polycarbonate membrane. The extravesicular dye was separated from vesicles by size exclusion column chromatography (using Sephadex G-50 gel) eluting with buffer solution (225 mM $NaNO_3$). After collecting the vesicles from the column, these were diluted to 4 mL by using the aforementioned buffer (225 mM $NaNO_3$) to get the concentration of ~ 8 mM of EYPC-LUVs⊃Lucigenin, assuming no loss of lipid throughout the process. The vesicles compositions, inside: 1 mM Lucigenin, 225 mM $NaNO_3$ and outside: 225 mM $NaNO_3$.

In a clean cuvette, 1950 µL of salt solution (225 mM $NaNO_3$), 50 µL of lucigenin trapped vesicles solution were taken and placed in a fluorescence instrument equipped with a magnetic stirrer. The fluorescence emission intensity of the Lucigenin dye, $I_t$ was measured at $\lambda_{em}$ = 535 nm (where, $\lambda_{ex}$ = 455 nm) for 350 s. For each reading, the start time of the instrument was considered as $t$ = 0 s. Then at $t$ = 50 s, 33 µL of 2N NaCl solution was added to the cuvette for generating a $Cl^-$ concentration gradient across the lipid bilayer. Then 20 µL solution of transporters in ACN : MeOH (6 : 1) solvent of different concentrations were added at $t$ = 100 s. At $t$ = 300 s, 10% triton X-100 (25 µL) was added to destroy all the vesicles for the destructing of the $Cl^-$ concentration gradient.

The fractional emission intensity (in percentage), $I_F$ was calculated after normalizing all the data using the following equation (Equation 4).

$$\% \text{ of } I_F = (I_t - I_0) / (I_\infty - I_0) \times (-100) \qquad \text{Equation 4}$$

where, $I_0$ is the initial fluorescence intensity *i.e.,* just before the addition of the transporter solution, $I_t$ is the fluorescence intensity at time *t*, and $I_\infty$ is the final fluorescence intensity *i.e.,* after the addition of Triton X-100.

Before plotting the data, the time axis was normalized using Equation 2. The concentration dependent ion transport activity data was used for fitting the "Hill equation" (Equation 3) to get the $EC_{50}$ value *i.e.,* half maximal effective concentration and the Hill coefficient ($n$).

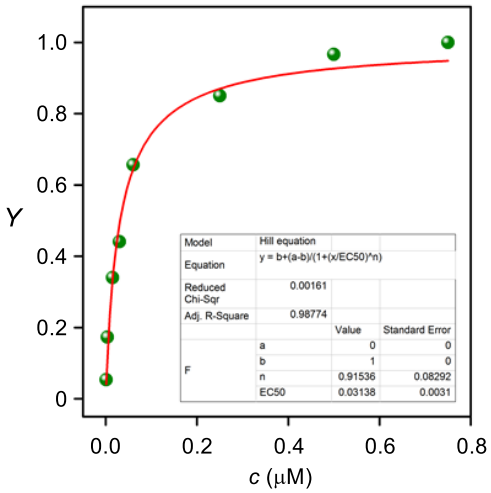



**Figure 4.38** Hill plot of transporter **1b** at $t$ = 100 s to get half-maximal effective concentration ($EC_{50}$) and Hill coefficient.

**Lucigenin Assay for Checking Symport Mechanism:** In a clean cuvette, 1950 µL of salt solution (225 mM $NaNO_3$), 50 µL of lucigenin trapped vesicles solution were taken and placed inside the measurement compartment of a fluorescence instrument equipped with a magnetic stirrer. The fluorescence emission intensity of the Lucigenin dye, $I_t$ was measured at $\lambda_{em}$ = 535 nm by exciting at 455 nm for 350 s. For each reading, the start time of the instrument was considered as $t$ = 0 s. Then at $t$ = 50 s, 33 µL of 2 N MCl (where, $M^+$ = $Na^+$, $Li^+$, $K^+$, $Rb^+$, and $Cs^+$) was added to the cuvette for generating a $Cl^-$ and $M^+$ concentration gradient across the lipid bilayer. Then 20 µL solution of transporters in ACN : MeOH (6 : 1) solvent was added at $t$ = 100 s. At $t$ = 300 s, 10% triton X-100 (25 µL) was added to destroy all the vesicles for the destructing of the $Cl^-$ and $M^+$ concentration gradient.

Before plotting the data, the time axis was normalized using Equation 2.

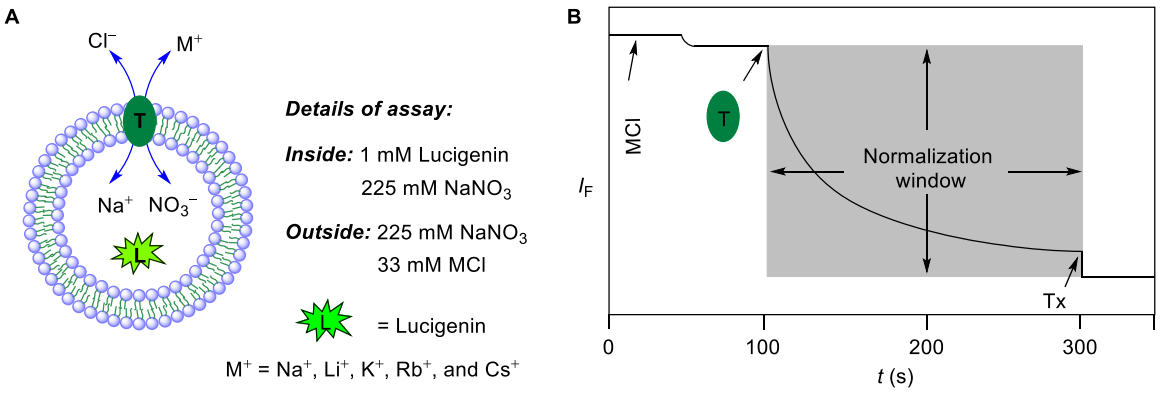



**Figure 4.39** Schematic representation of fluorescence kinetics assay for checking symport mechanism across EYPC-LUVs⊃Lucigenin (A), and normalized working window for the same experiment (B).

**Lucigenin Assay for Checking Antiport Mechanism in the Presence of Valinomycin:** In a clean cuvette, 1950 µL of salt solution (225 mM $NaNO_3$), 50 µL of lucigenin trapped vesicles solution were taken and placed inside the measurement compartment of a fluorescence instrument equipped with a magnetic stirrer. The fluorescence emission intensity of the Lucigenin dye, $I_t$ was measured at $\lambda_{em}$ = 535 nm by exciting at 455 nm for 350 s. For each reading, the start time of the instrument was considered as $t$ = 0 s. Then at $t$ = 50 s, 33 µL of 2 N KCl was added to the cuvette for generating a $Cl^-$ and $K^+$ concentration gradient across the lipid bilayer. The valinomycin (0.5 µM) was added at $t$ = 50 s. Then 20 µL solution of transporters in ACN : MeOH (6 : 1) solvent was added at $t$ = 100 s. At $t$ = 300 s, 10% triton X-100 (25 µL) was added to destroy all the vesicles for the destructing of the $Cl^-$ and $K^+$ concentration gradient.

Before plotting the data, the time axis was normalized using Equation 2.

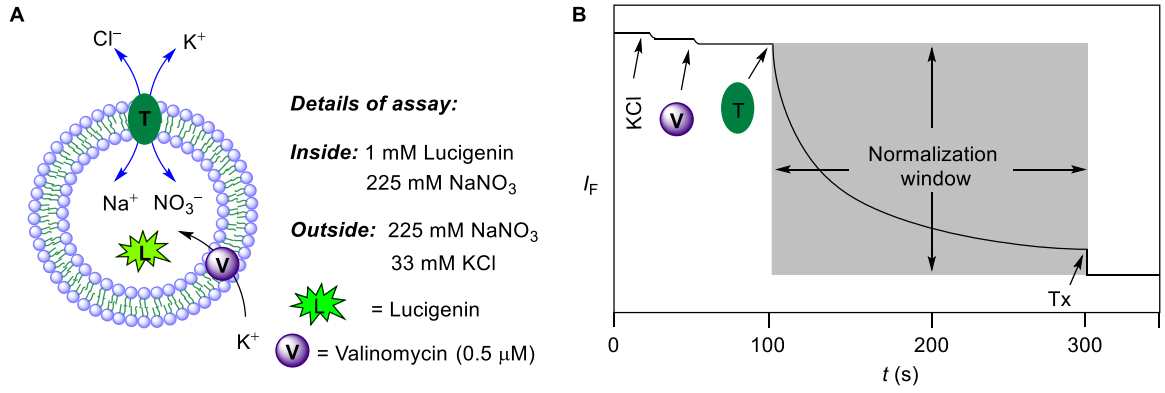



**Figure 4.40** Schematic representation of fluorescence kinetics assay for checking antiport mechanism in the presence of Valinomycin across EYPC-LUVs⊃Lucigenin (A), and normalized working window for the same experiment (B).

### 4.4.14. Planner Bilayer Conductance Measurement

The conductance measurement across the bilayer lipid membrane was done with the help of Warner instrument (USA). For that, a solution of diphytanoylphosphatidylcholine lipid (DPhPC; Avanti Polar Lipids) was prepared by dissolving it in *n*-decane of concentration 20 mg/mL. Then this solution was used to form a bilayer membrane across an aperture of 150 µm diameter in a polystyrene cup (Warner Instrument, USA). Both the *cis* and *trans* chambers of the instrument were filled with symmetrical solution, containing 1 M KCl. The *trans* chamber was held at virtual ground, whereas the *cis* chamber was connected to the BC *535* head–stage (Warner Instrument, USA) via matched Ag-AgCl electrodes. Then the channel forming

molecule **1b** was added (15 μM) to the trans chamber, and the solution was stirred with an inbuilt magnetic stirred for 20 min. The formation of the channel through the lipid bilayer was conformed from channel opening and closing events while applying different voltages using pClamp9 software (Molecular probes, USA). The currents were low pass filtered at 1 kHz using pClamp9 software (Molecular probes, USA) and analog-to-digital converter (Digidata 1440A, Molecular Devices).

The channel opening and closing events at positive, as well as negative potentials, were analyzed by pClamp software (v. 10.6). A complete trace comprised of a series of opening and closing events for the time period of 2 h was recorded and a small portion of the trace is presented here.

The channel diameter was calculated using the equation (Hille equation) mentioned below.

$$1/g = (l + \pi d/4)(4\rho/\pi d^2) \qquad \text{Equation 5}$$

where, $g$ = corrected conductance (calculated by multiplying measured single channel conductance with the Sansom's correction factor), $l$ = length of the ion channel (34 Å), and $\rho$ = resistivity of the KCl solution ($\rho$ = 10.1 Ω·cm).

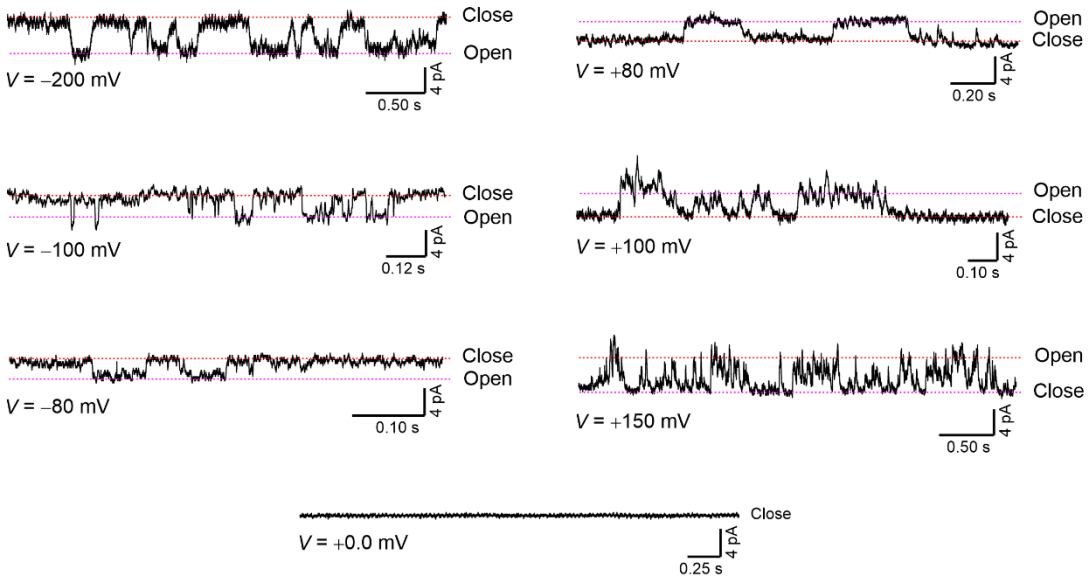



**Figure 4.41** The single channel current traces by **1b** (15 μM) recorded at various negative and positive potentials under symmetrical KCl solution.

## 4.5. NMR Spectra of Compounds

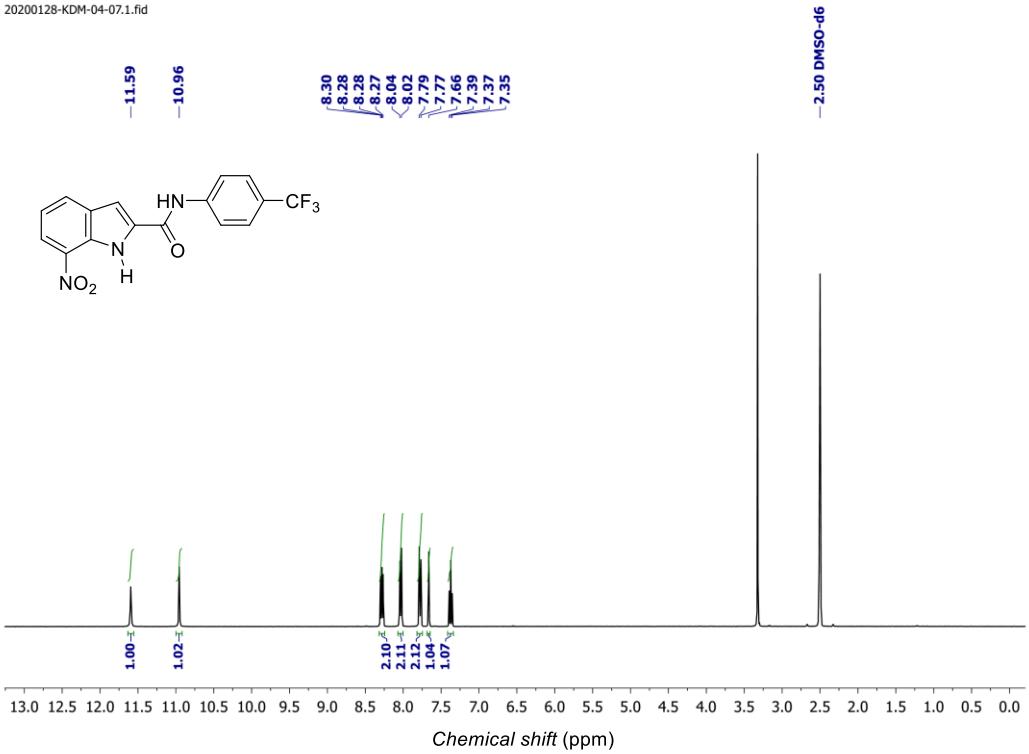



**Figure 4.42** $^{1}$H NMR spectrum of compound **9a** in DMSO-$d_6$.

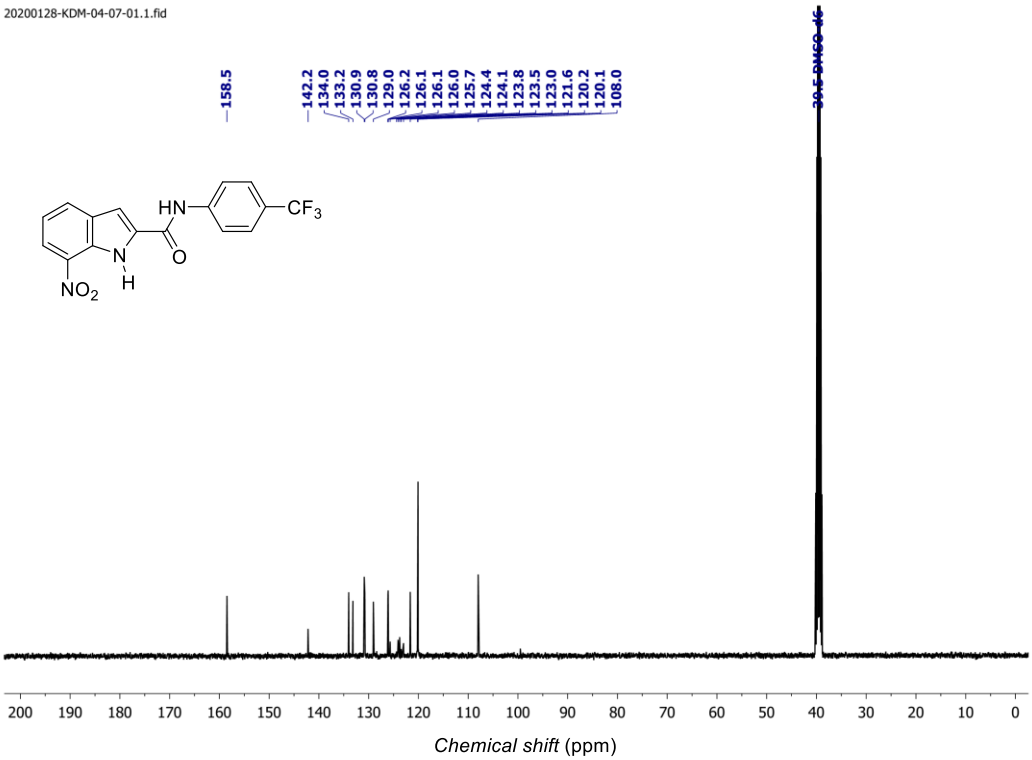



**Figure 4.43** $^{13}$C NMR spectrum of compound **9a** in DMSO-$d_6$.

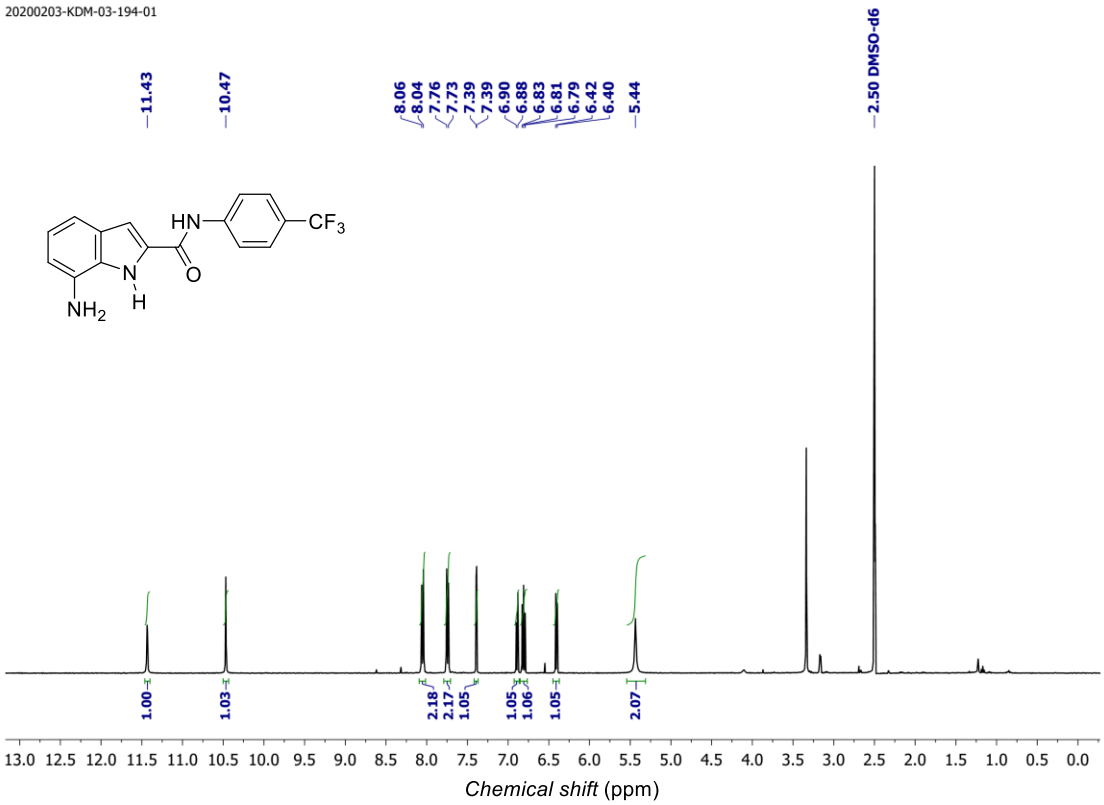



**Figure 4.44** $^{1}$H NMR spectrum of compound **10a** in DMSO-$d_6$.

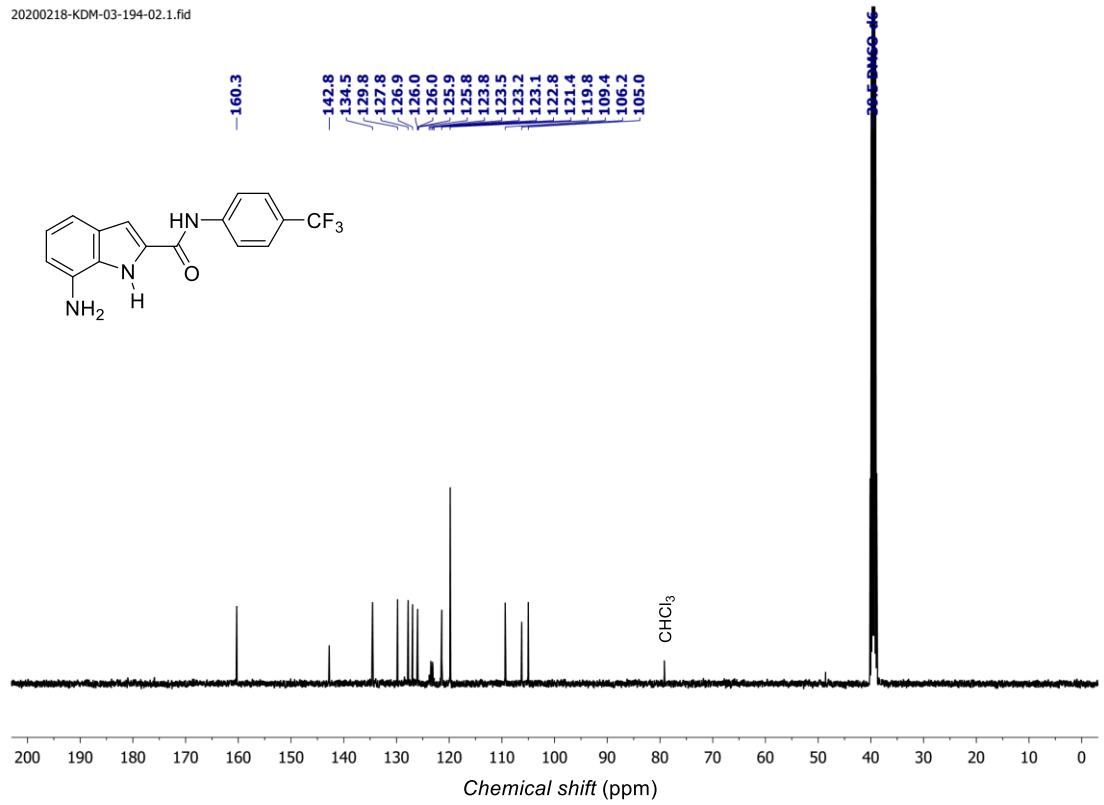



**Figure 4.45** $^{13}$C NMR spectrum of compound **10a** in DMSO-$d_6$.

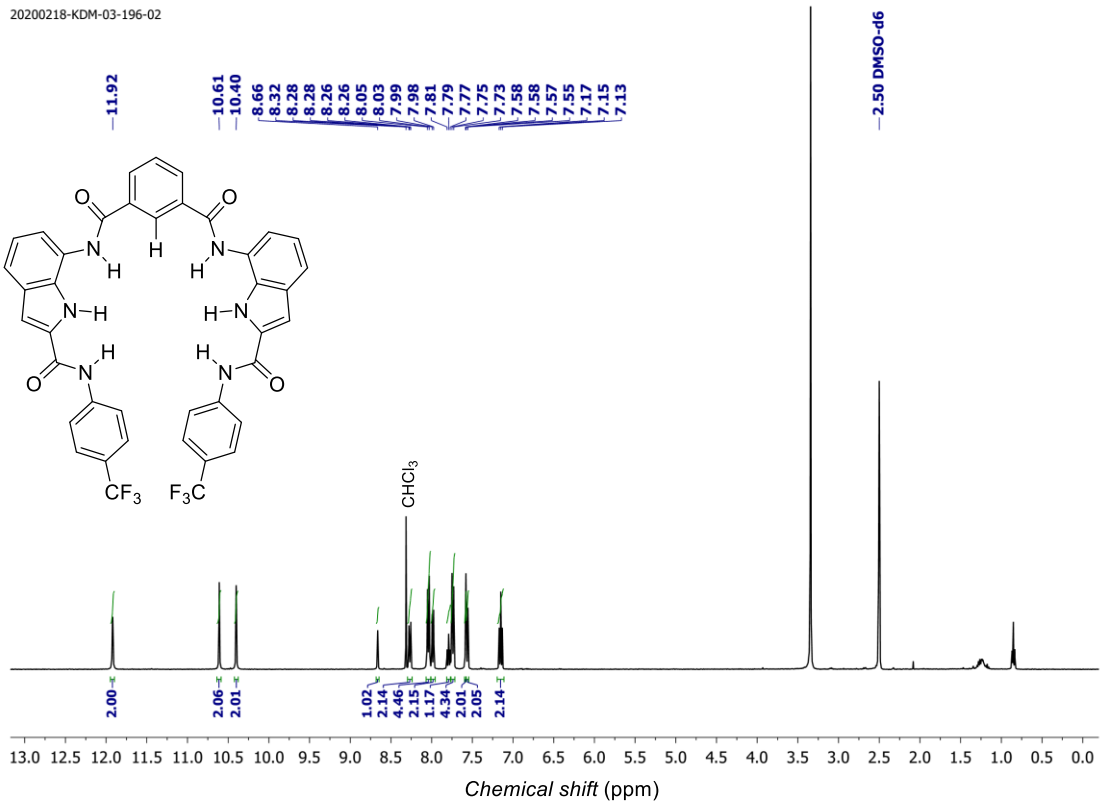



**Figure 4.46** $^{1}$H NMR spectrum of compound **1a** in DMSO-$d_6$.

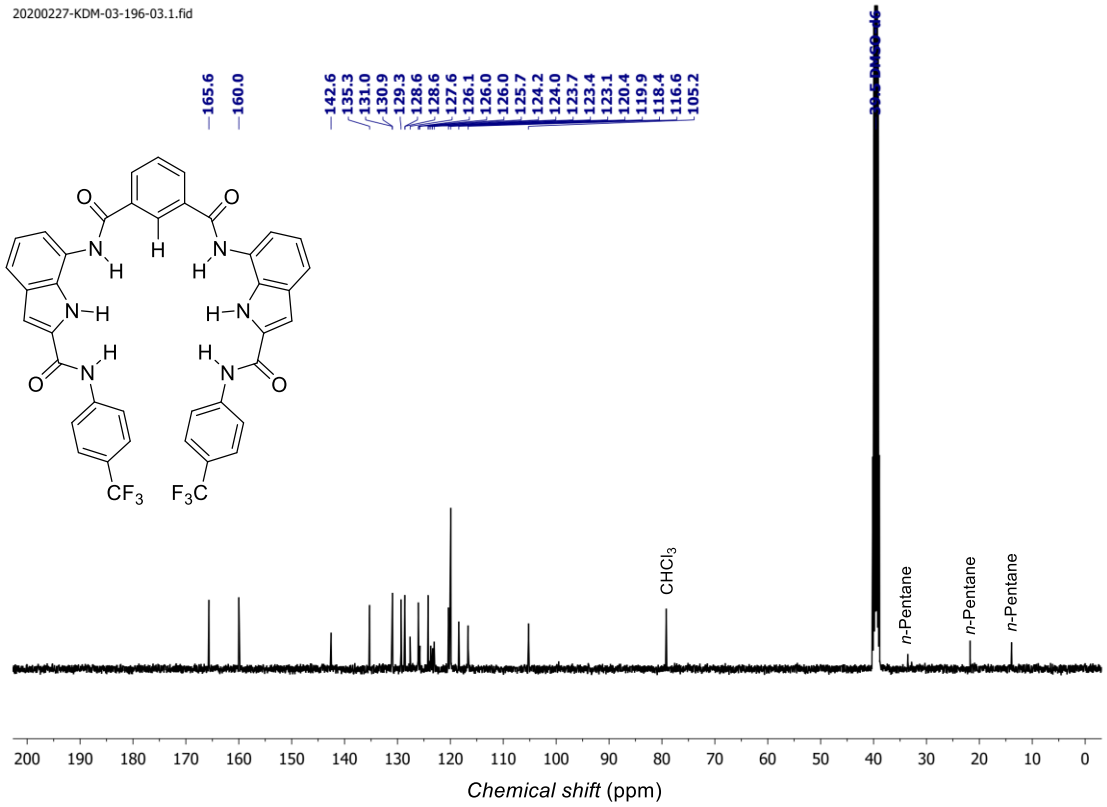



**Figure 4.47** $^{13}$C NMR spectrum of compound **1a** in DMSO-$d_6$.

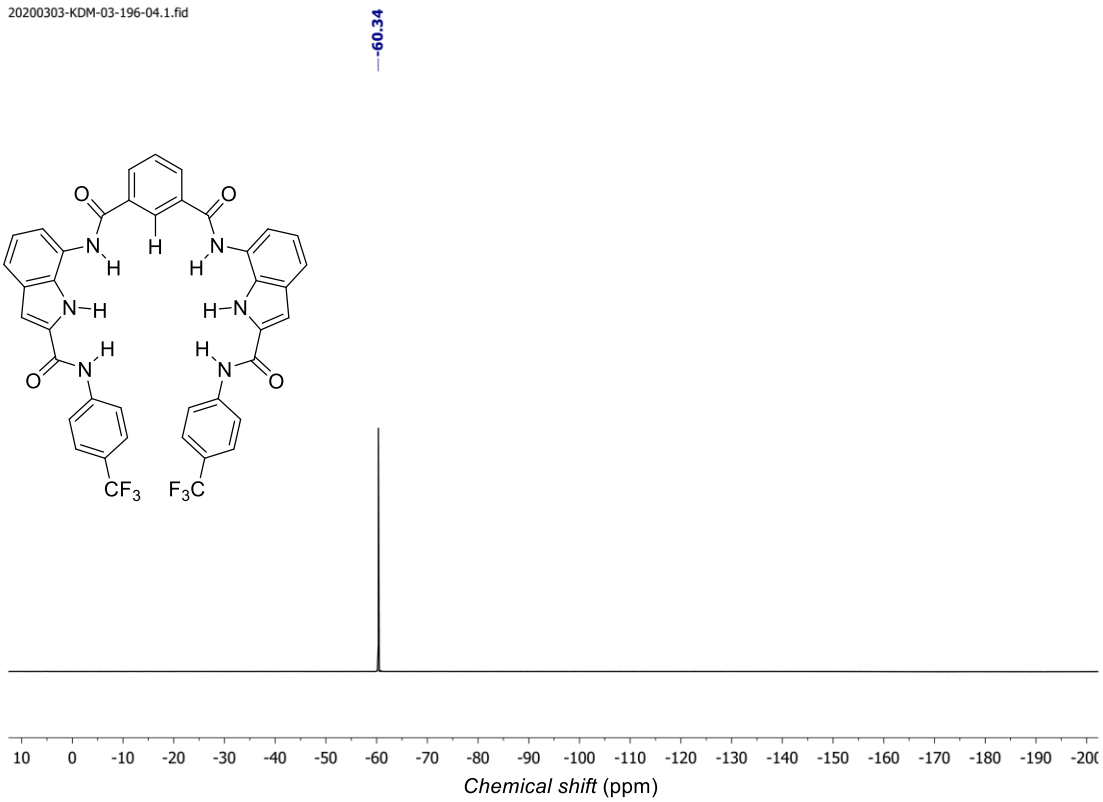



**Figure 4.48** $^{19}$F NMR spectrum of compound **1a** in DMSO-$d_6$.

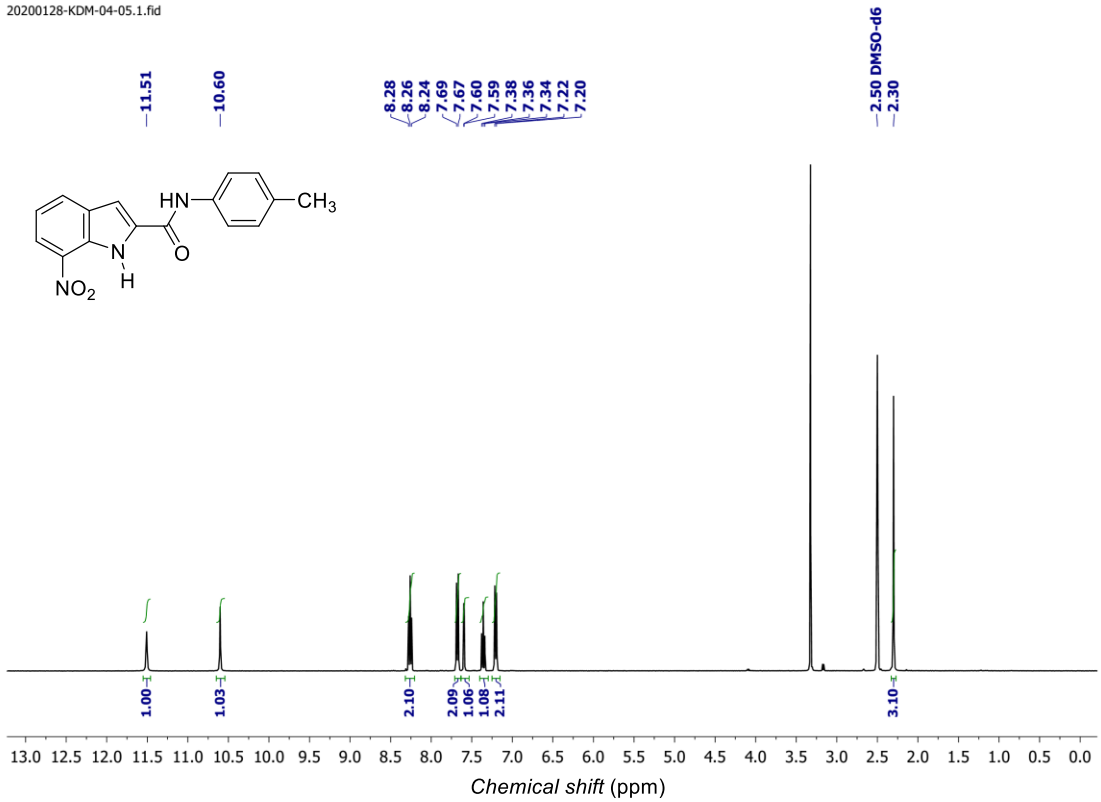



**Figure 4.49** $^{1}$H NMR spectrum of compound **9b** in DMSO-$d_6$.

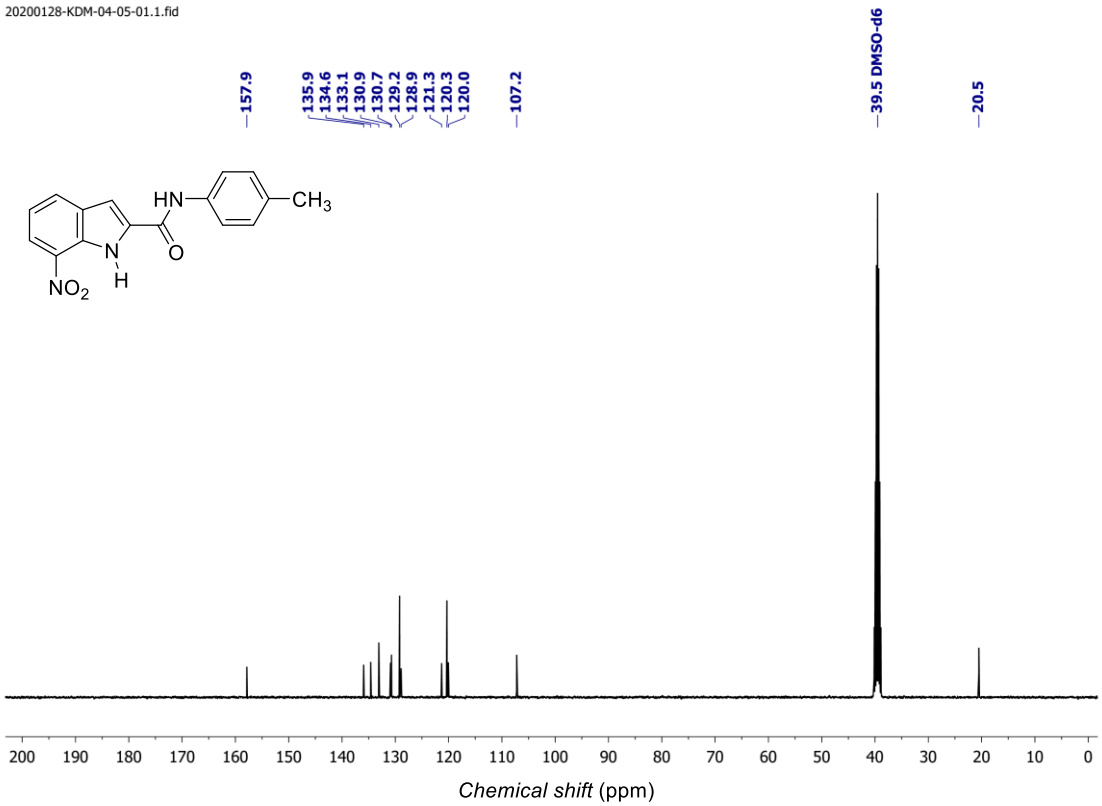



**Figure 4.50** $^{13}$C NMR spectrum of compound **9b** in DMSO-$d_6$.

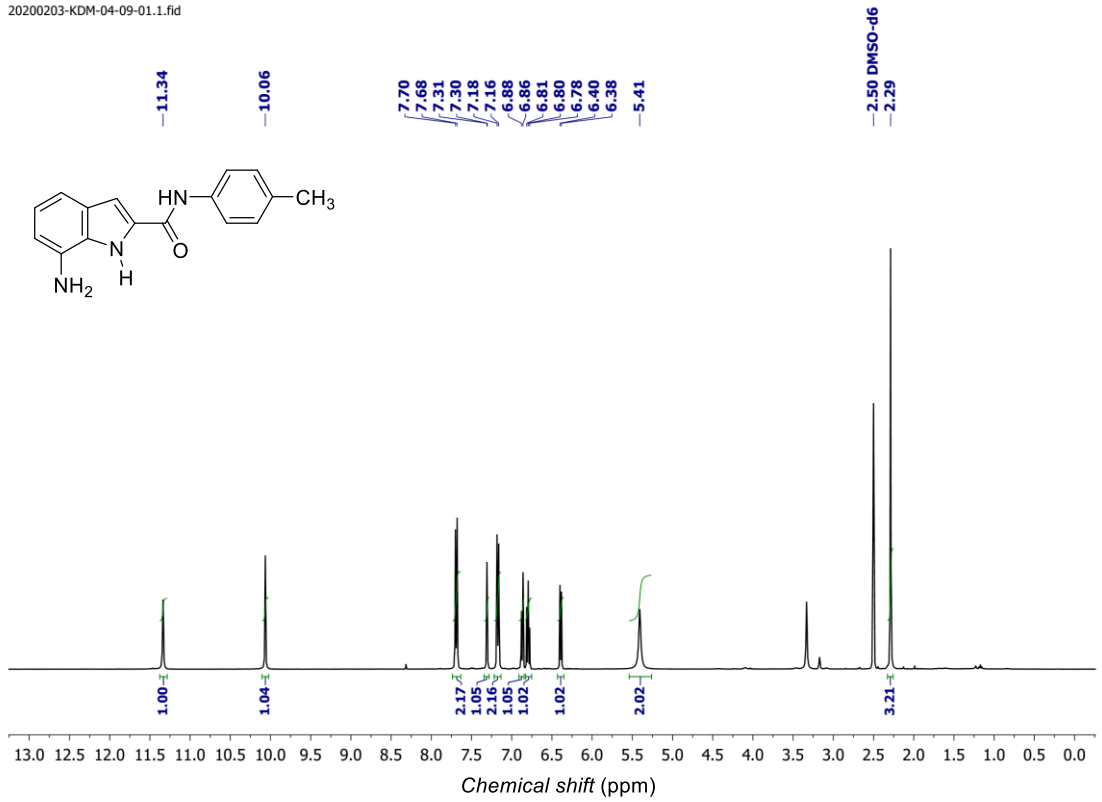



**Figure 4.51** $^{1}$H NMR spectrum of compound **10b** in DMSO-$d_6$.

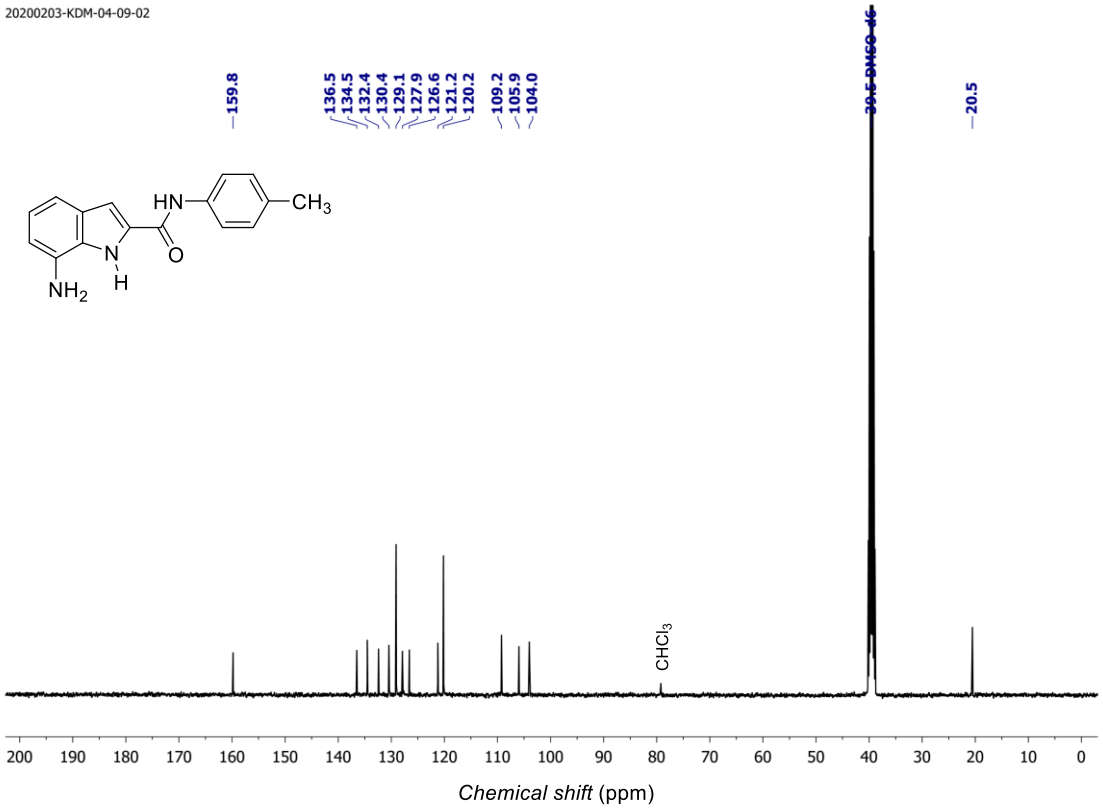



**Figure 4.52** $^{13}$C NMR spectrum of compound **10b** in DMSO-$d_6$.

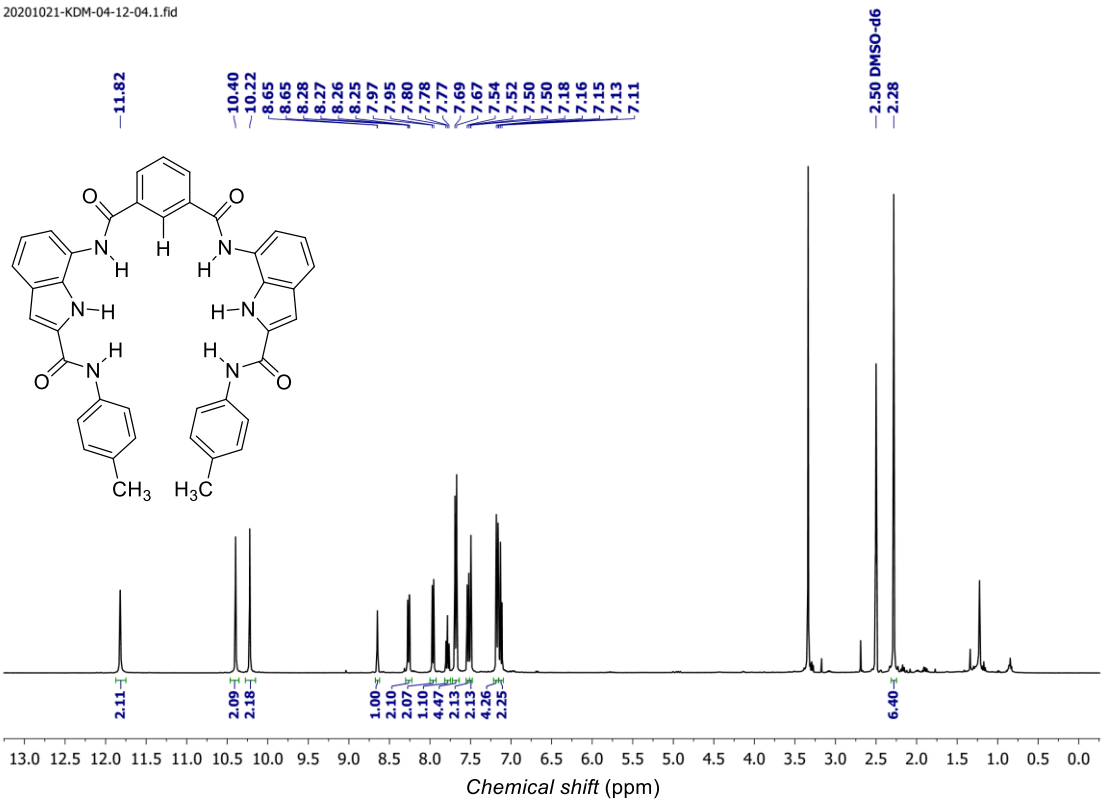



**Figure 4.53** $^{1}$H NMR spectrum of compound **1b** in DMSO-$d_6$.

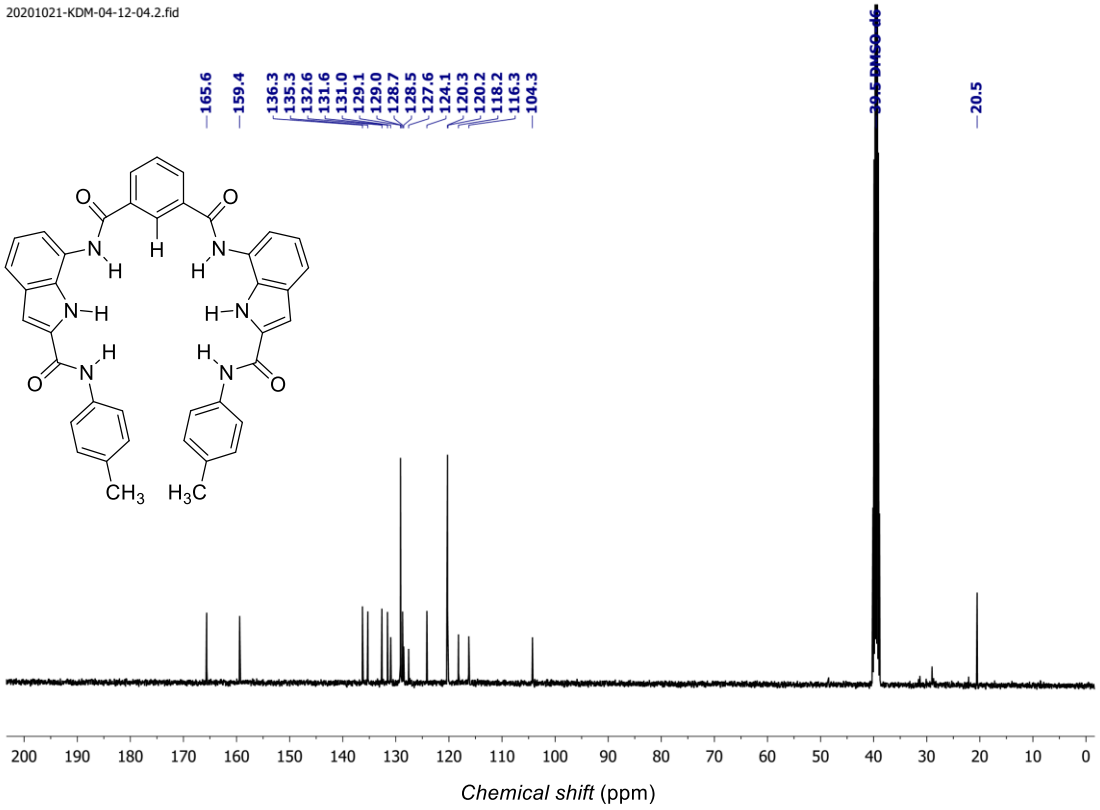



**Figure 4.54** $^{13}$C NMR spectrum of compound **1b** in DMSO-$d_6$.

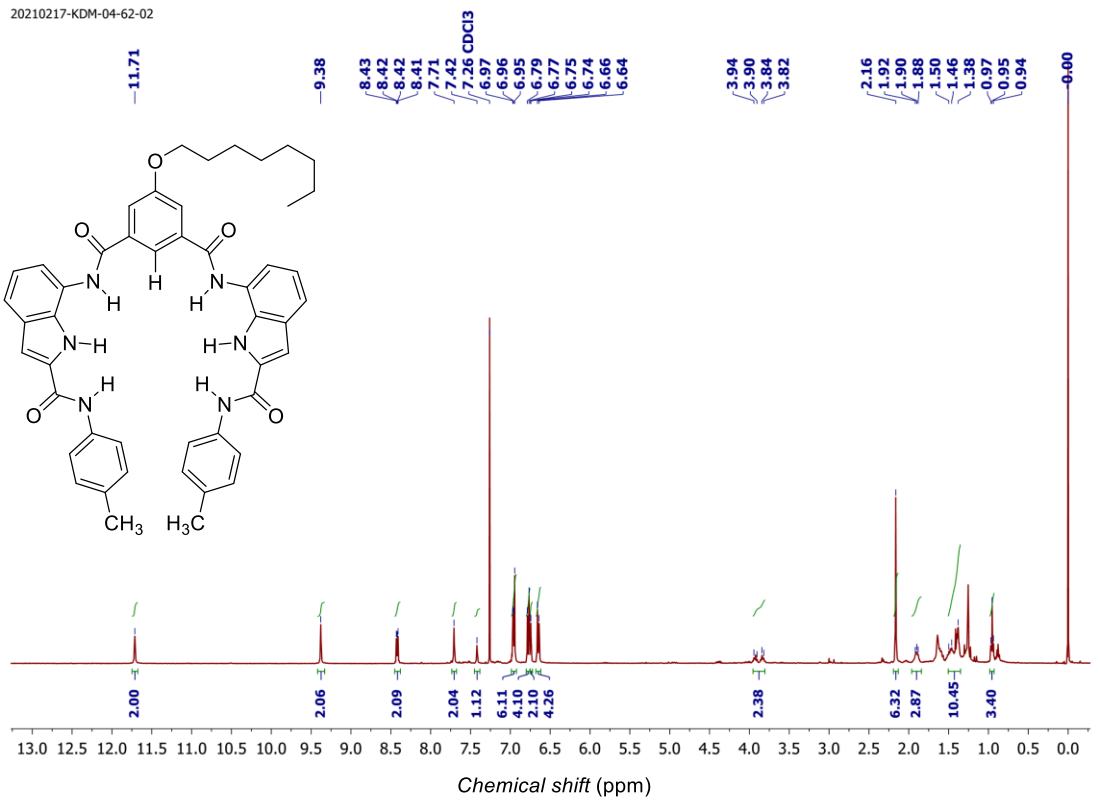



**Figure 4.55** $^{1}$H NMR spectrum of compound **1c** in $CDCl_3$.

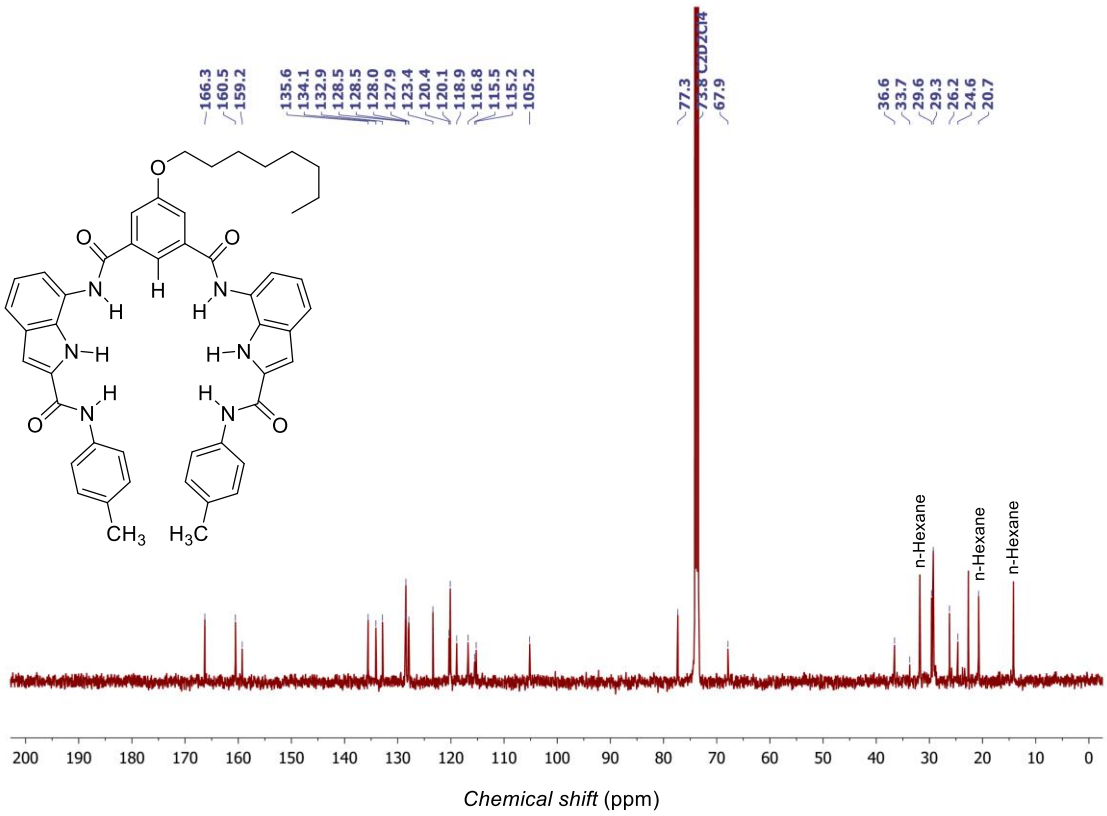



**Figure 4.56** $^{13}C$ NMR spectrum of compound **1c** in $C_2D_2Cl_4$.

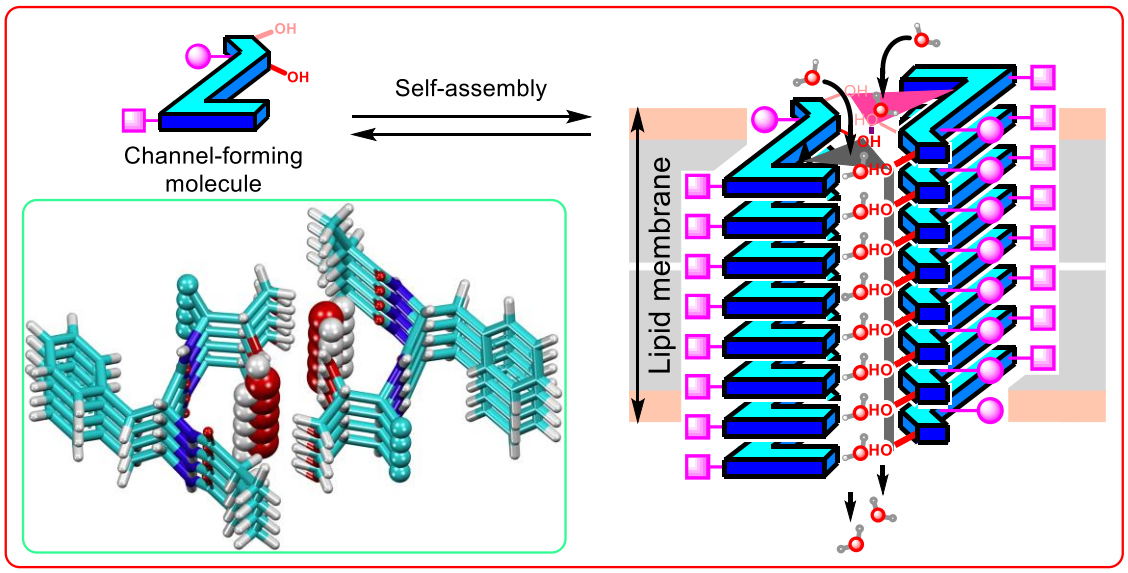
## 4.6. References


1. Fyles, T. M. *Chem. Soc. Rev.* **2007**, *36*, 335–347.
2. Dutzler, R.; Campbell Ernest, B.; MacKinnon, R. *Science* **2003**, *300*, 108–112.
3. Dutzler, R. *FEBS Lett.* **2007**, *581*, 2839–2844.
4. Maduke, M.; Miller, C.; Mindell, J. A. *Annu. rev. biophys. biomol. struct.* **2000**, *29*, 411–438.
5. Sakai, N.; Kamikawa, Y.; Nishii, M.; Matsuoka, T.; Kato, T.; Matile, S. *J. Am. Chem. Soc.* **2006**, *128*, 2218–2219.
6. Ma, L.; Melegari, M.; Colombini, M.; Davis, J. T. *J. Am. Chem. Soc.* **2008**, *130*, 2938–2939.
7. Xiong, L.; Zhu, X.-L.; Gao, H.-W.; Fu, Y.; Hu, S.-Q.; Jiang, L.-N.; Yang, W.-C.; Yang, G.-F. *J. Agric. Food Chem.* **2016**, *64*, 4830–4837.
8. Lal, G.; Lee, S. J.; Spasyuk, D. M.; Shimizu, G. K. H. *Chem. Commun.* **2018**, *54*, 1722–1725.
9. Lim, W. L.; Oo, C. W.; Kobayashi, T. *J. Appl. Polym. Sci.* **2015**, *132*.

10. Wang, C.; Yang, H.; Xiang, Y.; Pang, S.; Bao, C.; Zhu, L. *Front. Chem.* **2021**, *9*.
11. Kumar, Y. P.; Das, R. N.; Kumar, S.; Schütte, O. M.; Steinem, C.; Dash, J. *Chem. – Eur. J.* **2014**, *20*, 3023–3028.
12. August, D. P.; Borsley, S.; Cockroft, S. L.; della Sala, F.; Leigh, D. A.; Webb, S. J. *J. Am. Chem. Soc.* **2020**, *142*, 18859–18865.
13. Moore, S. J.; Haynes, C. J. E.; Gonzalez, J.; Sutton, J. L.; Brooks, S. J.; Light, M. E.; Herniman, J.; Langley, G. J.; Soto-Cerrato, V.; Perez-Tomas, R.; Marques, I.; Costa, P. J.; Felix, V.; Gale, P. A. *Chem. Sci.* **2013**, *4*, 103–117.
14. Shinde, S. V.; Talukdar, P. *Angew. Chem., Int. Ed.* **2017**, *56*, 4238–4242.
15. Mondal, D.; Sathyan, A.; Shinde, S. V.; Mishra, K. K.; Talukdar, P. *Org. Biomol. Chem.* **2018**, *16*, 8690–8694.
16. Zeng, F.; Liu, F.; Yuan, L.; Zhou, S.; Shen, J.; Li, N.; Ren, H.; Zeng, H. *Org. Lett.* **2019**, *21*, 4826–4830.
17. Lipinski, C. A.; Lombardo, F.; Dominy, B. W.; Feeney, P. J. *Adv. Drug Deliv. Rev.* **2001**, *46*, 3–26.
18. Saha, T.; Dasari, S.; Tewari, D.; Prathap, A.; Sureshan, K. M.; Bera, A. K.; Mukherjee, A.; Talukdar, P. *J. Am. Chem. Soc.* **2014**, *136*, 14128–14135.
19. Litvinchuk, S.; Bollot, G.; Mareda, J.; Som, A.; Ronan, D.; Shah, M. R.; Perrottet, P.; Sakai, N.; Matile, S. *J. Am. Chem. Soc.* **2004**, *126*, 10067–10075.
20. Li, Z.; Yu, X.-H.; Chen, Y.; Yuan, D.-Q.; Chen, W.-H. *J. Org. Chem.* **2017**, *82*, 13368–13375.
21. Saha, T.; Gautam, A.; Mukherjee, A.; Lahiri, M.; Talukdar, P. *J. Am. Chem. Soc.* **2016**, *138*, 16443–16451.
22. Roy, A.; Gautam, A.; Malla, J. A.; Sarkar, S.; Mukherjee, A.; Talukdar, P. *Chem. Commun.* **2018**, *54*, 2024–2027.
23. Ishida, H.; Qi, Z.; Sokabe, M.; Donowaki, K.; Inoue, Y. *J. Org. Chem.* **2001**, *66*, 2978–2989.
24. Dolomanov, O. V.; Bourhis, L. J.; Gildea, R. J.; Howard, J. A. K.; Puschmann, H. *J. Appl. Cryst.* **2009**, *42*, 339–341.
25. Sheldrick, G. *Acta Cryst.* **2015**, *C71*, 3–8.
26. Sheldrick, G. *Acta Cryst.* **2015**, *A71*, 3–8.

*Chapter 5*

# Peptide Backbone-based 1,2-Diol Transports Water via Self-Assembled Barrel Rosette Water Channel



## 5.1. Introduction

Even though 71% of the earth's surface is covered by water,[1] over more than one-third of the world's population faces severe freshwater scarcity because only a tiny percentage of the total is available as accessible freshwater.[2-4] This shortage of freshwater is not only incompetent to meet the drinking water issue, but it also pushes humankind to get infected with severe life-threatening diseases due to inadequate sanitation.[5-8] To solve this crisis, scientists have come up with various water purification techniques where 90% of the water purification plants use reverse osmotic (RO) technique for the desalination of seawater.[9-11] In this regard, reverse osmosis membrane or, more precisely, the artificial water channels (AWCs), which have the ability to transport water selectively by excluding the salts and protons from the seawater, have an essential role.[12] However, one disadvantage of this technique is that the desalination process is high energy-consuming.[13-15] Therefore, an extremely sophisticated membrane material is required, which can complete the process by consuming less energy and making the process economical and available to all.[16-17]

In nature, aquaporin-based protein channels are available, which are known to transport water across lipid bilayer membranes with high permeability and permselectivity.[18-21] However, the lack of stability and compatibility of aquaporins outside the cellular environment delimit its widespread use for water purification applications.[22] Therefore, the development of biomimetic artificial water channels (AWCs) is fundamentally essential for studying their water transport behavior and can be useful for medical and water purification purposes.[12, 23]

Over the past decade, various AWCs based on unimolecular and supramolecular systems have been reported to achieve superfast water transport across the bilayer membranes.[24-37] Some of them have even shown ultrafast water transport rates. For example, carbon nanotube porins (CNTPs) transport water across the bilayer membrane with a transport rate of 6 times than that of Aqp1, a natural water channel protein.[30, 38] However, it also transports monovalent cations such as $Na^+$, $K^+$, and proton.[39] Nevertheless, the exclusion of salts and protons by the channel forming substrate is an indispensable criterion for water purification application.[40] In this regards, Barboiu, Hou, and their co-workers have made a tremendous effort to develop synthetic channels for selective water transport, where the studies were further extended by Kumar, Zeng, and their co-workers. Aquafoldamer-based water channel designed by Zeng and co-workers has shown water permeability rate 50% of Aquaporin Z (AqpZ), and it excludes salts during the transport process.[34-35, 37] In another report,

Kumar and co-workers has reported peptide-appended hybrid[4]arenes (PAH[4]s) based water transport system which transport water (water permeability > $10^9$ $H_2O$ $s^{-1}$ $channel^{-1}$) with comparable transport rate of AQPs while excluding salts.[33] The I-quartet and the hydroxyl-based water channels reported by Barboiu and co-workers has shown selective and fast water permeation across the bilayer membrane.[32, 36, 41]

As mentioned earlier, most artificial water channels have shown water permeability slightly less or close to aquaporins, but very few have demonstrated good water-salt permselectivity.[42] The lack of water selectivity mechanism (like aquaporins) in most synthetic channels makes them less selective for water over the ions.[36] Therefore, the proper structural design of the channel, which can interact with the water molecules selectively and softly, can show excellent water transport behavior with high salt rejection. Moreover, the absence of intermolecular hydrogen bonding interactions between two water molecules in the same water array can restrict the Grotthuss mechanism for proton transport, which is essential for showing good water channel behavior.[43-45] However, getting permselectivity while achieving superfast permeability is still an exciting and challenging task in the water purification science.

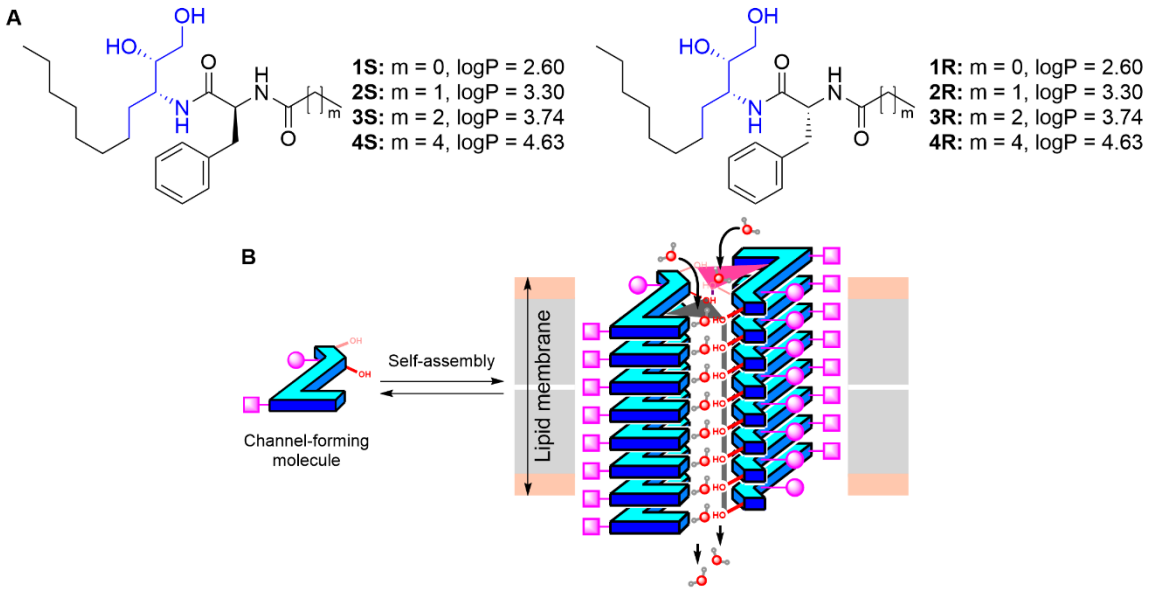



**Figure 5.1** Chemical structures and the calculated logP values of peptide 1,2-diol **1S**–**4S** and **1R**–**4R** (A). Schematic representation of the self-assembled water channel formation by transporter molecules in the lipid bilayer membrane (B).

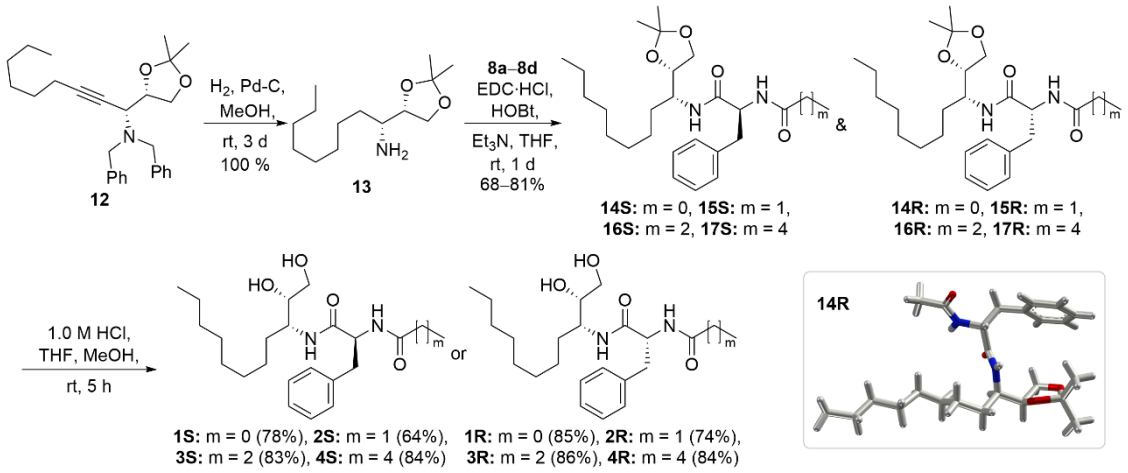
Herein, we report the peptide backbone-based 1,2-diol systems **1S**-**4S** and **1R**-**4R** (Figure 5.1A) that form dimeric rosette assembly that offers a double water channel in the bilayer membrane. The molecules were designed to have multiple hydrogen bond donor and

acceptor sites such as O–H, N–H, C=O, etc., for efficient noncovalent interactions. We expected that these systems would self-aggregate into a stacked sheet by a parallel one-dimensional array of monomers utilizing the intermolecular C=O···H–N bonding interactions. Two such one-dimensional sheets would bundle up via intermolecular hydrogen bonding interaction through hydroxyl groups and water molecules to form a water channel (Figure 5.1B). The chirality of the phenylalanine α-carbon was varied for generating two different series. The octyl and alkyl chains were introduced to the monomers to tune the membrane permeability,[42] which was estimated by calculating the logP values of each compound using Marvin Sketch program (Figure 5.1A).[46] Moreover, we expected that the dimeric rosette assembly would offer adequate channel pore and strong noncovalent interactions for water recognition by excluding the salts and hence increase the water-salt permselectivity.

## 5.2. Results and Discussions

### 5.2.1. Synthesis

The synthesis of the channel forming molecules was started from *L*-phenylalanine and *D*-mannitol. At first, the *L*-phenylalanine was converted to its amide analogs **8a**-**8d** by reacting with different aliphatic carboxylic acids following the reported literature protocol (Scheme S1).[47] On the other hand, *D*-mannitol was converted to acetonide protected dibenzylamine derivative **12** in three steps following the literature protocol of our previous report (Scheme S2).[48-49] The hydrogenation of dibenzyl derivative **12** in the presence of Pd-C led to the debenzylation and reduction of triple bond for the formation of acetonide-protected amine **13** in quantitative yield. Then, the amine **13** was reacted with different *L*-phenylalanine derivatives **8a**-**8d** via EDC·HCl assisted coupling reaction to form amides **14S**-**17S**. Surprisingly, the diastereomeric compounds **14R**-**17R** were also formed almost in equal amounts due to the inversion of configuration at phenylalanine α-carbon. Each *S*- and *R*-configuration product was isolated separately by column chromatography. The formation of the *R*-configuration product was confirmed from the crystal structure of **14R** (Scheme 5.1). Subsequently, all the acetonide-protected amides were separately treated with dilute HCl for the deprotection of the acetonide group to furnish the desired free diol compounds **1S**-**4S** and **1R**-**4R** in 64-86% yield (Scheme 5.1).




**Scheme 5.1** The synthetic scheme of peptide 1,2-diol **1S**–**4S** and **1R**–**4R**. The X-ray crystal structure of **14R**, obtained from a nitrobenzene solution of the protected compound (bottom right position, inside the box).

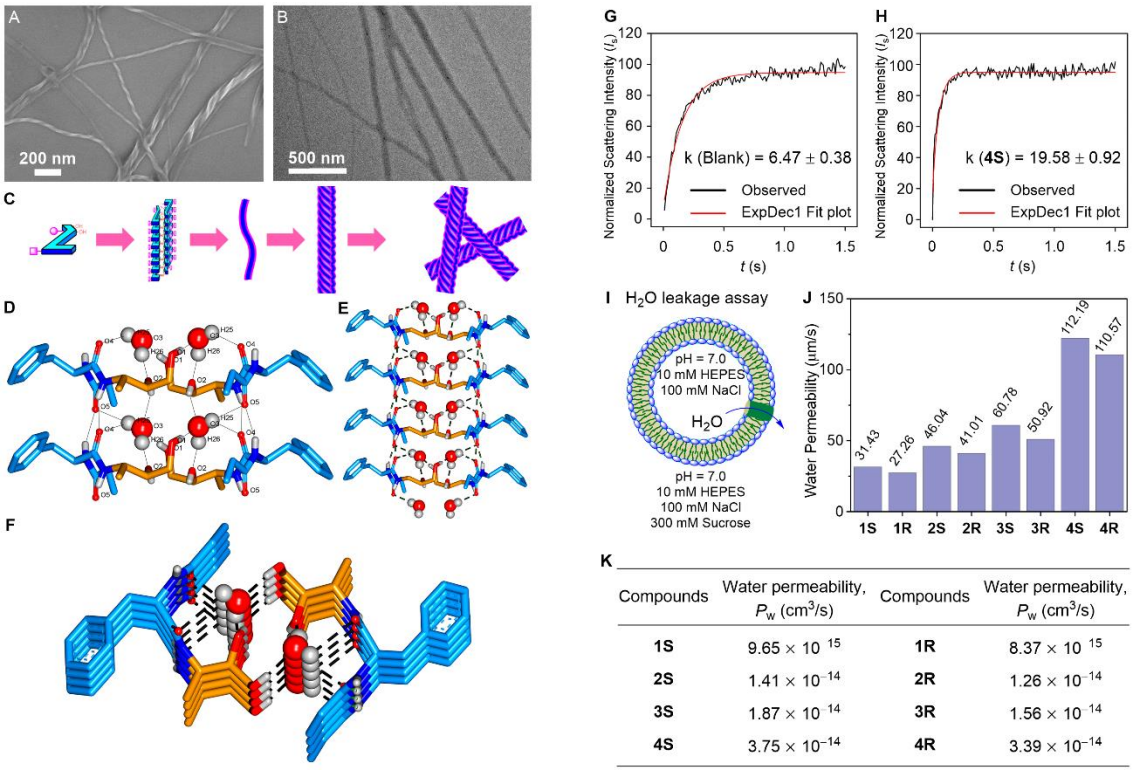
### 5.2.2. Morphology Analysis

After synthesizing all the desired derivatives, we performed the experiments for morphological studies. At first, field emission scanning electron microscopy (FESEM) images for **4S** and **4R** were recorded using chloroform (Figure 5.6A and 5.7A), where no specific self-aggregated pattern was observed. However, when we performed the same experiments for these compounds by preparing the sample in moist methanol, self-aggregated left-handed helical fibril morphology was observed for each compound (Figure 5.2A and 5.6B for **4S** and Figure 5.7B for **4R**). These observations indicate that the designed systems can form self-aggregated assembly, where a polar protic solvent assists the assembled states. Such a fibril formation can be rationalized by considering the intermolecular hydrogen bonding interactions between the peptide backbones to form sheet structures followed by the self-aggregation via water molecules bridging to create a continuous chain, where multiple chains of this type bundled up for the formation of a left-handed helical fibril (Figure 5.2A and 5.2C). The fibril formation was further confirmed from transmission electron microscopy (TEM) studies for **4S** and **4R**, where the samples were prepared in moist methanol (Figure 5.2B and 5.8).

### 5.2.3. Solid-state Structure Analysis

Good quality crystals of **2R**, suitable for solid-state single crystal X-ray analysis, were obtained by dissolving the compound in moist methanol followed by slow evaporation. In the solid-state, multiple monomer units participate in the parallel self-aggregation process via intermolecular amide C=O···H–N hydrogen bonding interactions to form one-dimensional stacked sheets. Further, two such one-dimensional sheets bundle up antiparallelly through

water-bridged hydrogen bonds. In this assembly, each water molecule forms one C=O···H–OH hydrogen bond with the phenylalanine carbonyl of one monomer, and a second C=O···H–OH hydrogen bond with the terminal eathylamide carbonyl of the next monomer of the same sheet (Figure 5.2D). Moreover, it also forms two C–O···H–OH hydrogen bonds, one with the secondary hydroxyl carbon of the first monomer, and the other with a monomer from the second sheet C–O···H–OH hydrogen bond with the primary hydroxyl carbon of a monomer from the second sheet. Interestingly, the presence of two distinct water channels was evident




K

| Compounds | Water permeability, $P_w$ ($cm^3$/s) | Compounds | Water permeability, $P_w$ ($cm^3$/s) |
|---|---|---|---|
| **1S** | $9.65 \times 10^{-15}$ | **1R** | $8.37 \times 10^{-15}$ |
| **2S** | $1.41 \times 10^{-14}$ | **2R** | $1.26 \times 10^{-14}$ |
| **3S** | $1.87 \times 10^{-14}$ | **3R** | $1.56 \times 10^{-14}$ |
| **4S** | $3.75 \times 10^{-14}$ | **4R** | $3.39 \times 10^{-14}$ |

**Figure 5.2** The FESEM (A) and TEM (B) images of self-aggregated **4S** compound (prepared from 100 μM solution in methanol) with the cartoon representation of probable self-aggregating pattern for obtained morphology (C). The crystal structure of **2R** with water molecules forming the self-assembled water channel:2 × 2 layers top view H-bonding interaction distances (D), 2 × 4 layers lateral view (E), and 2 × 4 layers top view (F). The dashed lines in the crystal structure are the representation of the hydrogen bonding interactions between the channel-forming molecules and water molecules. The light scattering intensity *versus* time plot of blank DOPC vesicles (G) and DOPC vesicles with **4S** (H, lipid to transporter ratio = 50 : 1) recorded on a stopped-flow instrument for measuring water permeability. The representation of vesicles for water leakage assay (I) and the comparison of corrected water permeability, $P_w$ (corrected from blank, in μm/s and $cm^3$/s unit) of all transporters (J, K) at 50:1 lipid to transporter ratio.

within the cavity created by the two sheets. Moreover, the water molecules of each channel (i.e., in the same water array) are well separated (4.93 Å) to restrict the proton transport as per our proposed design. Finally, two antiparallelly aggregated sheets are ensembled in a way that

allows all the polar groups either face inwardly or interact with each other to favor the assembly, whereas the hydrophobic phenyl and alkyl units are outwardly directed, which can help it to be inserted inside the bilayer easily.

### 5.2.4. Water Permeability Studies across Lipid Bilayer Membrane

The surprising results from the solvent dependent morphology studies and water channel formation by **2R** in the solid-state encouraged us to assess the water transport permeability and selectivity by the transporter molecules across the phospholipid bilayer membrane. For that, a stopped-flow light scattering instrument was used for measuring the light scattering intensity of the vesicles suspension at a millisecond scale. At first, large unilamellar vesicles (LUVs) with a diameter of ~ 150 nm were prepared using DOPC lipid by incorporating each channel forming compound (molar channel-to-lipid ratio, mCLRs = 1 : 50) in 100 mM NaCl solution buffered to 7.0 using HEPES (Figure 5.2I).[34-35] When such a vesicle suspension is exposed suddenly to an equal volume of 300 mM sucrose solution, it leads to the shrinkage of the vesicles by outwardly directed water leakage through the water channels. This event subsequently leads to the change in light scattering intensity of the vesicles suspension. For each compound, a significant change in light scattering intensity compared to the blank sample was observed, and the rate constant value was also calculated (Figure 5.2G, 5.2H, 5.11A–5.11K). Further, the rate constant value was used to calculate the water permeability value.[33, 50] All our molecules **1S**–**4S** and **1R**–**4R** were found to transport the water across the bilayer membrane (Figure 5.2H and 5.2J) and the permeability values calculated using the recently updated model,[33, 50-51] considering the osmolyte concentration correction factor and the values are 30.2 (± 2.8%), 35.4 (± 3.5%), 40.6 (± 7.3%), 62.3 (± 4.7%), 28.8 (± 0.6%), 33.6 (± 5.8%), 37.1 (± 5.9%), and 58.17 (± 6.9%) μm/s, respectively. We assume that the 8 layers of self-assembled system (2 × 8 layers) forms a single channel structure. The **4S** channel exhibited the highest water transport rate with the permeability value of $1.51 \times 10^{-14}$ $cm^3/s$ compared to the **4R** channel, for which the estimated permeability value is $1.34 \times 10^{-14}$ $cm^3/s$. Further, these water permeability values were used to calculate the single channel water permeability, and the values are $5.05 \times 10^8$, $4.48 \times 10^8$water molecules/s per channel for **4S** and **4R**, respectively, indicating **4S** as the most efficient water channel forming molecule (Figure 5.2J, and Table 2). The data indicate that the efficiency of the water channels increases when a longer hydrophobic alkyl tail is present, indicating that the higher logP value contributes to better membrane permeability of the channel. It is also apparent that the activity

of an *S*-configuration product is higher than the corresponding *R*-configuration product. This may be attributed to the better self-assembly of the *S*-configuration molecules.

### 5.2.5. Water Permselectivity Studies across Lipid Bilayer Membrane

As discussed earlier that the salt exclusion is the essential criteria for water purification application of the water channel system. The salt exclusion behavior by the channel molecules while transporting the water was confirmed by performing the water leakage assay in different osmolytes other than sucrose.[35, 52] Here, we have calculated the reflection coefficient value for our system, where the reflection coefficient is the water permeability ratio of the channel in NaCl and sucrose solution. We observed the reflection coefficient value 0.98 (Figure 5.12), which is close to 1, indicating that the water permeability value remains unaltered while shifting from sucrose solution to NaCl solution. This observation also confirmed the salt exclusion capability of our water channel system.

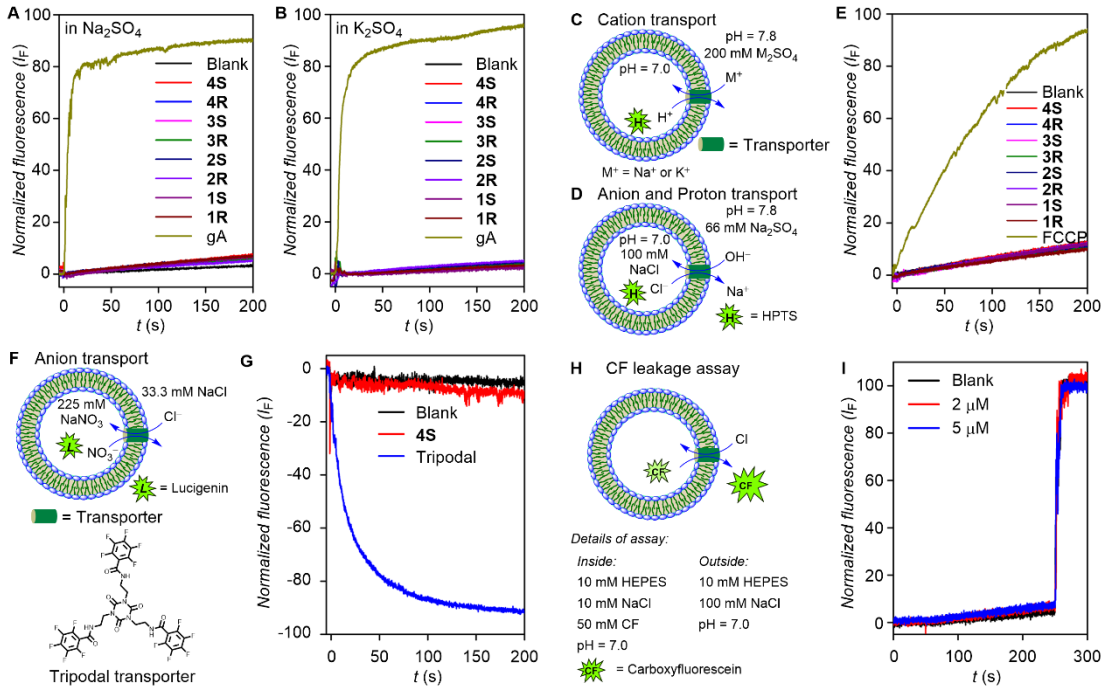



**Figure 5.3** The $Na^+$ (A) and $K^+$ (B) transport activities of gramicidin (0.1 μM) and channel molecules (2 μM) in HPTS assay across EYPC-LUVs⊃HPTS. The vesicular representations and assay details of cation transport (C) and anion transport (D) experiments. The $H^+$ transport activities of FCCP (0.2 μM) and water channel-forming molecules (2 μM) in HPTS assay across the EYPC-LUVs⊃HPTS (E). The vesicular representation (F) and anion transport activities in lucigenin assay across the EYPC-LUVs⊃Lucigenin by tripodal transporter (2 μM) and water channel molecules (2 μM) (G).The assay details (H) and normalized fluorescence intensity plot by **4S** (2 and 5 μM concentration) of CF leakage assay (I).

### 5.2.6. Ion Transport Studies across Lipid Bilayer Membrane

The cation transport activity of the water channel-forming molecules across the bilayer membrane was evaluated following the standard ion transport experiment protocol.[35, 53-55] For that, we have prepared large unilamellar vesicles using EYPC lipid by entrapping pH-sensitive 8-hydroxypyrene-1,3,6-trisulfonic acid trisodium salt (HPTS, 1.0 mM), a fluorescent dye, in 10 mM HEPES buffer (pH = 7.0). The vesicles were then suspended in 200 mM $Na_2SO_4$ solution, and a pH gradient (ΔpH = 0.8) was applied between the intra- and the extra-vesicular medium (Figure 5.3C). Then the fluorescence intensity change of the HPTS dye was monitored with time after the addition of transporter molecules. None of our diol molecules has shown the fluorescence intensity increment at 2.0 μM of transporter concentration (Figure 5.3A), whereas gramicidin A (gA, a natural cationophore) has shown significant transport activity (~ 90%) even at 20 times diluted concentration (0.1 μM). These results indicate that our water channel molecules cannot transport $Na^+$ across the bilayer membrane. When a similar experiment was performed for each compound by suspending the vesicles in $K_2SO_4$ solution, no significant transport activity was observed (Figure 5.3B and 5.3C), which indicates that the 1,2-diol systems are not transporting the $K^+$ ions either.

Next, anion and proton transport activities of the 1,2-diol compounds across the bilayer membrane were evaluated preparing HPTS vesicles (Figure 5.3D). Here, no significant transport activity was observed by these compounds, whereas carbonyl cyanide-4-(trifluoromethoxy)phenylhydrazone (FCCP, a proton carrier) showed significant transport activity (~ 92%) even at the one-tenth concentration (Figure 5.3E). These observations indicate that the 1,2-diol compounds are incapable of transporting anions and protons. Additionally, the anion influx by **4S** was also evaluated across large unilamellar EYPC vesicles by entrapping lucigenin dye.[56-57] Under intravesicular $NaNO_3$ (225 mM) and extravesicular $NaNO_3$ (225 mM) and NaCl (33.3 mM), no destruction of chloride gradient in the presence of **4S** was observed (Figure 5.3F and 5.3G). On the contrary, a reported tripodal chloride transporter showed excellent chloride influx activity (~88%) under comparable conditions. Therefore, the inability of **4S** for transporting anions was further established. The carboxyfluorescein (CF) leakage assay,[58] using 2 and 5 μM concentrations of **4S** resulted in no release of CF dye (Figure 5.3H and 5.3I), which indicates that the membrane integrity is preserved in the presence of the compounds and also rules out any possibility of pore formation.

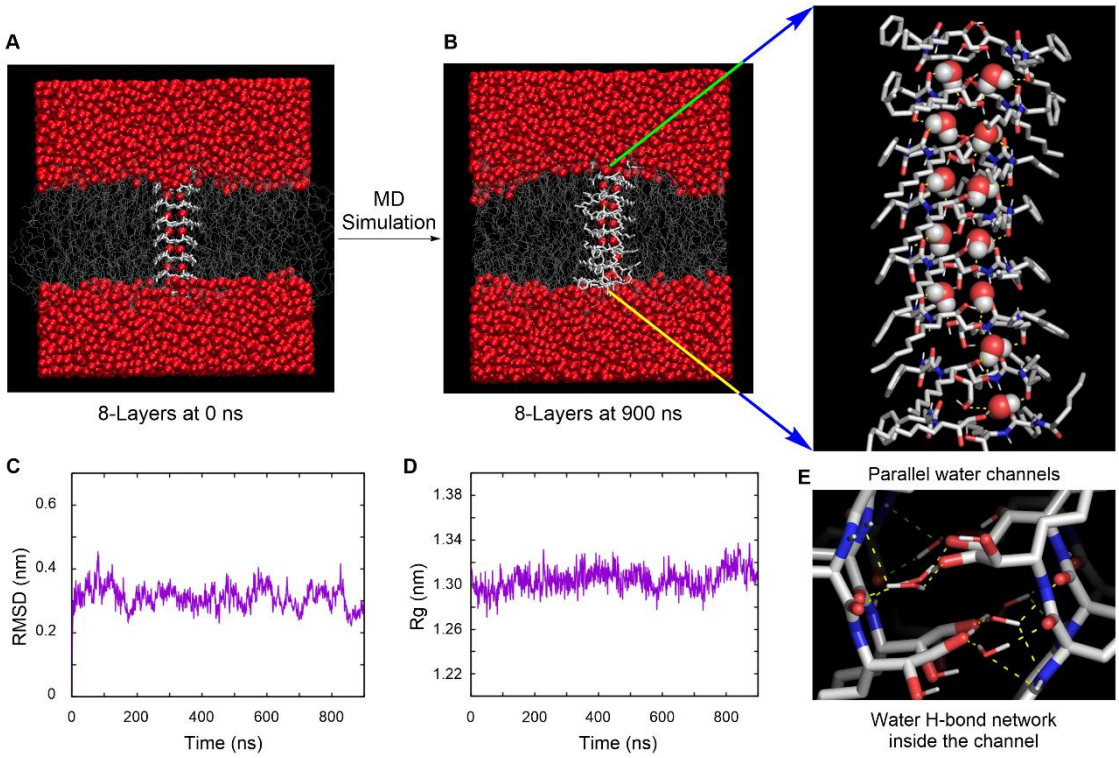



**Figure 5.4** Snapshot from MD simulation of 2 × 8 layers of **4R** synthetic channel at initial point, i.e., 0 ns (A) and at the completion of the simulation .i.e. 900 ns (B). Also shown is a closed view image of the equilibrated synthetic channel. The presence of two distinct water files inside the layer is evident. The RMSD (C) and radius of gyration (D) of 2 × 8 layers **4R** channel. The snapshot highlighting the water hydrogen bond network inside the channel (E). Color code: membrane hydrophobic cores are shown in thin white lines, the synthetic channel are represented via white licorice representation. In figure B, the water oxygen and hydrogen atoms are shown by red and white space-filling representation, respectively. In figure E, the same color code is maintained for water, except a licorice representation is rendered.

### 5.2.7. Molecular Dynamics Simulations Studies

The excellent water channel properties of the 1,2-diol system encouraged us to carry out computational studies to get atomistic insight into the channel architecture and water transport mechanism. The marginal difference in water transport properties between **4S** and **4R** and, most importantly, the availability of crystallographic coordinates of *R*-configuration product with water, prompted us to focus on simulating the **4R** superstructure and water permeation through it. The self-assembly pattern obtained from the crystal structure of **2R** with water was used to generate the 2 × 8 layers (i.e., 8 layers of 2 molecules) assemblies of **4R**. The assembly of **4R** was generated by elongating each ethyl chain with a pentyl one.

The figure 5.4A and 5.4B, respectively, demonstrate the representative snapshot of membrane-embedded 2 × 8 layers assembly of **4R** at the initial and completion of the computer simulation after about microsecond (900 ns) long time-evolution. The visual inspection of the snapshot indicates that the simulations maintain stable superstructure during the time period at ambient pressure (1 bar) and temperature (298 K). Unlike previous investigations, which required the introduction of an order of magnitude larger lateral pressures or restraining forces for maintaining a stable synthetic channel,[32, 36] the current simulation was found to produce a structurally integrated channel inside the phospholipid bilayer at the ambient condition of 1 bar pressure. This is further demonstrated by a steady time profile of root-mean-squared deviation (RMSD) of the 2 × 8 layers assembly relative to the crystal structure (Figure 5.4C). A low RMSD of 0.3 nm from the crystal structure and a steady trend radius of gyration ($R_g$) profile (Figure 5.4D) with an average $R_g$ fluctuating around 1.3 nm further provides credence to the stability of 2 × 8 layers superstructure.

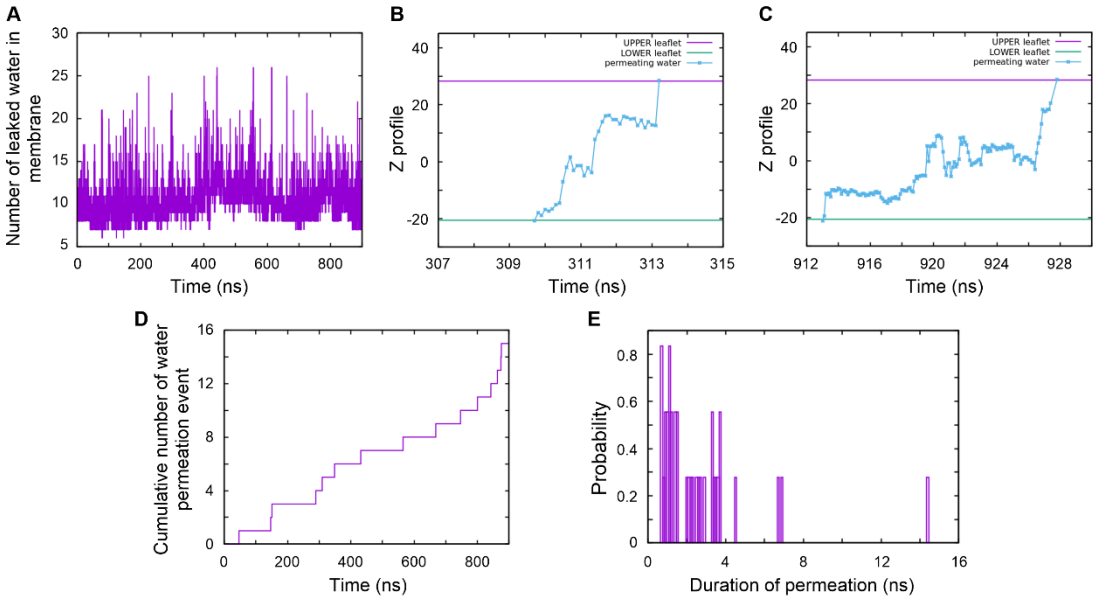



**Figure 5.5** Water permeation analysis across 2 × 8 layers of **4R** superstructure: Time profile of number of leaked waters inside the membrane (A). The time profiles of two representative water permeation events through channels (B and C), the cumulative time profiles of water permeation events (D), and the distribution of time-span for water permeation events (E).

We had also explored the effect of the number of layers on the overall integrity of the superstructure. Figure 5.16A and 5.16B compare the representative snapshot of superstructures across 2 × 7 layers and 2 × 9 layers, respectively. As depicted from steady RMSD and Rg profiles (Figure 5.16C and 5.16D), the overall assembly remains stable in these two cases as

well. However, when compared across all three cases (2 × 7 layers, 2 × 8 layers and 2 × 9 layers), the registry and overall orientation of 2 × 8 layers assembly inside the membrane are found to be relatively optimal. Hence, we proceeded with simulation trajectories of 2 × 8 layers for subsequent analysis of water permeation dynamics inside the channel.

A close-view representation of the synthetic channel (see an enlarged snapshot of Figure 5.4B) highlighted the distinct presence of two parallel, non-intersecting water wires inside the synthetic channel. A molecular-level characterization of the inner architecture of water inside the simulated channel indicated the water molecule is forming an intricate hydrogen bond network (Figure 5.4E) with the phenylalanine carbonyl oxygen, the diol (or hydroxyl) moiety and also with the amide nitrogen of the channel-forming molecules. The organization of inner water molecules is majorly guided by the integrity of the superstructure. However, there is no hydrogen bond between the water molecules present inside the channel. The visual inspection of MD simulation trajectory had indicated significant water leakage inside the phospholipid bilayer, as induced by synthetic channel. A quantitative analysis of water leakage events (see method) provided further insights into the dynamical behavior of water molecules in a lipid bilayer environment. Figure 5.5A shows the time profile of the number of water molecules leaked inside the membrane, suggesting significant water transport via the channel at ambient pressure and temperature. Very interestingly, tracking the movement of leaked water molecules, revealed multiple water permeation events during the period of simulation. Figures 5.5B and 5.5C depict two representative water-permeation events in which the water molecules make a full pass across the membrane from one of the leaflets to the other leaflet. The characterization of the simulation trajectory indicated a regular occurrence of water permeation events during the simulation period (Figure 5.5D). However, the duration of such water permeation events are not uniform. In fact, as shown in figure 5.5E, the duration of water permeation is quite heterogeneous, ranging from as low as 2 ns to as large as 14 ns. Overall, the extent of water leakage and water permeation via maintaining two distinct files of water wires inside a single superstructure, dictates a highly efficient synthetic water channel. The observation of two coexisting parallel water wires inside the channel formed by **4R** is considerably distinct, when compared with previous investigations, which either have reported either single water wire or more disordered water structure inside the channel.

The quantitative value of water/salt selectivity were estimated from MD simulation studies[35] in the presence of NaCl salt, where total 7247 water molecules were present on both

sides of the lipid bilayer, and the salt concentration was maintained at 0.10 M by adding 12 atoms of $Na^+$ and 12 atoms of $Cl^-$ ions. In the transport simulation, a total of 52223223 water entry events upto the $1/8^{th}$ (the first layer; till 4.79 Å) of the water channel was recorded in a time scale of 900 ns. Out of this, 16 molecules of water were found to successfully transport across the bilayer membrane within this time scale. Additionally, we have not observed any transport of either of the $Na^+$ and $Cl^-$ ion across the bilayer membrane. The transport selectivity (water/$Na^+$ or water/$Cl^-$) was calculated from that data for $Na^+$ and $Cl^-$ ion, and are 5223223/(7247/12), i.e. 8649.

## 5.3. Conclusion

In conclusion, we have designed and synthesized peptide diol-based water channel systems, which form two distinct water channels in a single self-assembled structure by employing intermolecular hydrogen bonding interactions between the hydroxyl group and amide side chain with the water molecules. The experimental analysis revealed that the molecules are able to transport the water across the lipid bilayer membrane with the highest permeability rate of $1.25 \times 10^9$ water molecules/s/channel, observed for the **4S** derivative. Most importantly, the precise single-channel diameter of 2.5 Å allows only water molecules selectively to pass through it while excluding the $Na^+$, $Cl^-$, and $H^+$, which are also confirmed from experimental and computational studies. The MD simulation studies for **4R** superstructure confirmed the formation of stable water channel assembly inside the bilayer membrane at ambient temperature and pressure, and more importantly, it transports the water through its channel pore. The superfast water transport rate and salt exclusion behavior of the self-assembled channels can be applied in various applications, including the development of biomimetic RO membranes.

## 5.4. Experimental Section

### 5.4.1. General Methods

All reagents used for the synthesis were purchased from Sigma-Aldrich, Avra, TCI, Spectrochem, Alfa Aesar and used without further purification. Dry solvents, e.g., Toluene, Acetone, THF, $CH_2Cl_2$, and MeOH used for the synthesis, were purchased from Rankem, Merck and used without further drying. All the dry reactions were placed in oven-dried apparatus under atmospheric nitrogen conditions. The progress and completion of the reactions were monitored by performing thin layer chromatography experiments where the plates were

visualized either by short-wave UV light or by different staining reagents (Ninhydrin, PMA, etc.). Column chromatography for purification of the compound was performed using distilled organic solvents on silica gel (100–200 or 230–400 mesh). HEPES buffer, HPTS dye, Triton X-100, Lucigenin dye, NaOH, and inorganic salts (NaCl, $NaNO_3$, KCl, LiCl, CsCl, NaBr, NaI, etc.) were used in molecular biology grade purchased from Sigma-Aldrich. Egg yolk phosphatidylcholine (EYPC) lipid (25 mg/mL in chloroform), mini-extruder, and polycarbonate membranes (100 and 200 nm) were obtained from Sigma-Aldrich (Avanti Polar Lipids).

### 5.4.2. Physical Measurements

All $^1H$ and $^{13}C$ NMR spectra were recorded either on Bruker 400 MHz and Jeol 400 MHz spectrometers. The chemical shifts ($\delta$) in ppm were referenced to the residual signal of deuterium solvents ($^1H$ NMR $CDCl_3$: $\delta$ 7.26 ppm; $^{13}C$ NMR $CDCl_3$: $\delta$ 77.2 ppm; $^1H$ NMR DMSO-$d_6$: $\delta$ 2.5 ppm; $^{13}C$ NMR DMSO-$d_6$: $\delta$ 39.5 ppm). The multiplicities of the peaks are s (singlet), d (doublet), t (triplet), q (quartet), dd (doublet of doublet), m (multiplet). High-resolution mass spectra (HRMS) were acquired in the ESI (+ve) mode. The measurement of pH during preparation of buffer solution was done by pH meter purchased from Hanna instruments. Fluorescence spectra were recorded on a Fluoromax-4 from Horiba scientific, Jobin Yvon Edison equipped with an injector port and a magnetic stirrer. The experimental data obtained from fluorescence were processed in Origin 8.5 software. The field emission scanning electron microscopy (FESEM) images were obtained using FEI Quanta 3D dual beam ESEM at 3.0 kV. The high-resolution transmission electron microscopy (HRTEM) images were acquired on the Jeol USA JEM-2200 FS transmission electron microscope. The dynamic light scattering (DLS) measurement experiment was performed using the Nano ZS-90 setup from the Malvern instrument with a 636 nm laser as a light source. The light scattering intensity was measured at a 90° angle by the detector and used further to calculate the diameter of the vesicles following the Stokes-Einstein equation.

### 5.4.3. Synthesis of Compounds

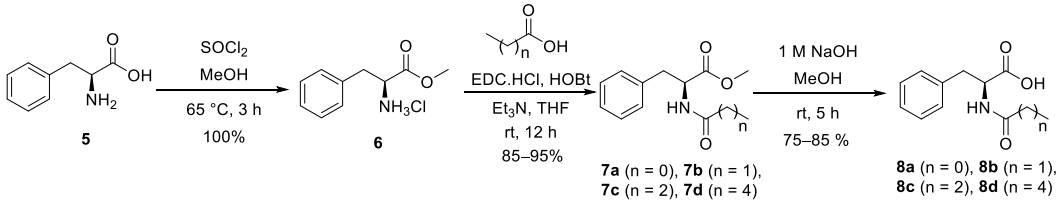
#### 5.4.3.1. Preparation of phenylalanine derivatives 8a–8d.

To prepare the phenylalanine derivatives **8a**–**8d**, we have followed the reported literature procedure with slight modifications.[47] For the preparation of the methyl ester **6**, the *L*-phenylalanine **5** (1.24 g, 7.51 mmol) and methanol (90 mL) were taken in a 250 mL round

bottom flask. The amino acid suspension was cooled to 0 °C by keeping it on an ice bath, and then $SOCl_2$ (2 mL) was added slowly to avoid the spontaneous heat generation. Then the reaction mixture was refluxed under stirring condition for about 6 h under an inert atmosphere. After completion of the reaction, volatiles were evaporated to get the corresponding ester as a hydrochloride salt **6** in quantitative yield. Next, the methyl ester was used for the coupling reaction with different alkyl chains containing carboxylic acid to form the amides **7a**–**7d**.

In a 50 mL round bottom flask, methyl ester **6** (0.50 g, 2.32 mmol) and carboxylic acid (2.55 mmol) were taken and dissolved by 15 mL of dry THF. Then HOBt (0.38 g, 2.78 mmol), triethylamine (1 mL, 7.20 mmol), and EDC·HCl (0.54 g, 2.78 mmol) were added sequentially to the reaction mixture. The reaction mixture was then stirred at room temperature overnight under an inert atmosphere. After completion, the reaction mixture was washed sequentially with water and brine by extracting the compounds in $CH_2Cl_2$. Then the organic solvent was evaporated to yield the amide compounds **7a**–**7d** in moderate to good yield. The amide compounds were then used for the next steps without further purification.

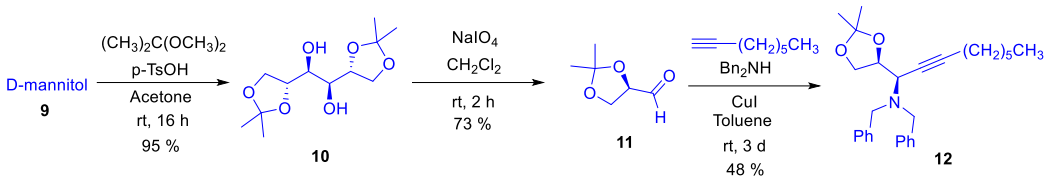
The hydrolysis reaction was done in the presence of sodium hydroxide as a base. For that, in a 25 mL round bottom flask, amides **7a**–**7d** (1.80 mmol) were taken and dissolved in 10 mL of THF : MeOH (1 : 1) solution. Then, NaOH (0.15 g, 3.62 mmol) was added into that reaction mixture by dissolving it in 2 mL of water. The reaction mixture was then heated at 65 °C for 5 h. After completion of the reaction, the reaction solution was cooled, acidified with 1 M HCl, and washed with water by extracting the compound in ethyl acetate (EtOAc). Then the volatiles solvents were evaporated to get the crude compound which was then purified by column chromatography to obtain the pure acid compounds **8a**–**8d** in 75-85% yield. $^1$H NMR spectra of the compounds were matched with the reported spectra.




**Scheme 5.2** Preparation of the acid derivatives **8a**–**8d**.

### 5.4.3.2. Preparation of diol-protected compound 12.

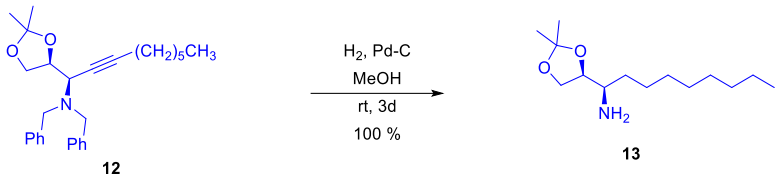
For the preparation of molecule **12,** we have followed the literature procedure reported from our group.[48-49]




**Scheme 5.3** Preparation of the diol-protected compound **12**.

### 5.4.3.3. Synthesis procedure for diol-protected amine 13.

In a 100 mL round bottom flask, 2.0 g of diol-protected compound **12** was taken and dissolved in 30 mL of MeOH. The compound solution was then degassed for about 1 h using an $N_2$ gas balloon. Then into that degassed solution one small pinch of 10% Pd-C was added. The reaction mixture was then stirred under a hydrogen gas balloon for 3 days at room temperature. After completion of the reaction, the whole solution was passed through a celite bed while washing with MeOH. Then the solvent was evaporated to get the amine **13** as a colorless sticky liquid in quantitative yield.

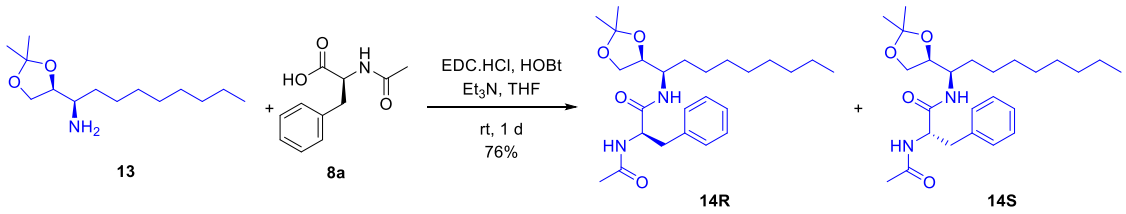



**Scheme 5.4** Synthesis of compound **13**.

**Yield:** 100%; **$^1$H NMR (400 MHz, $CDCl_3$):** $\delta$ 4.03 – 3.96 (m, 1H), 3.87 (q, $J$ = 6.8 Hz, 1H), 3.66 (dd, $J$ = 8.1, 7.0 Hz, 1H), 2.69 (t, $J$ = 7.5 Hz, 1H), 1.41 (s, 3H), 1.34 (s, 3H), 1.32 – 1.17 (m, 14H), 0.86 (t, $J$ = 6.8 Hz, 3H); **$^{13}$C NMR (101 MHz, $CDCl_3$ : MeOH-$d_4$ = 4 : 1):** $\delta$ 109.1, 80.4, 67.1, 54.2, 34.1, 31.9, 29.8, 29.6, 29.4, 26.8, 26.1, 25.5, 22.8, 14.2; **HRMS (ESI):** Calcd. $C_{14}H_{30}NO_2$ $[M+H]^+$: 244.2276, Found: 244.2281.

### 5.4.3.4. Synthesis of the compound 1R, 1S, 2R, 2S, 3R, 3S, 4R and 4S

**14R** and **14S:**



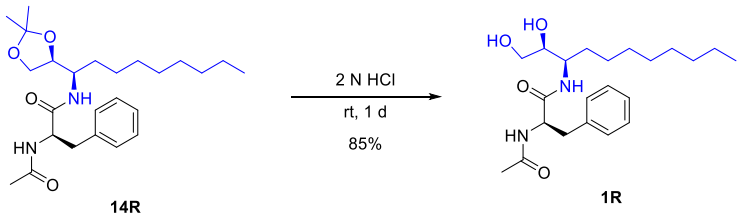

**Scheme 5.5** Synthesis of compound **14R** and **14S**.

In a 25 mL round bottom flask, the amine **13** (0.14 g, 0.58 mmol) was taken and dissolved in 6 mL of dry THF. Then into the reaction mixture acetyl-*L*-phenylalanine **8a** (0.12 g, 0.58 mmol), HOBt (0.08 g, 0.58 mmol) and triethylamine (0.5 mL) were added. At last, EDC·HCl (0.13 g, 0.69 mmol) was added, and the reaction mixture was then stirred at room temperature overnight under an inert atmosphere. After completion of the reaction, the reaction mixture was washed with water (3 × 10 mL) and then with a solution of brine (1 × 10 mL), after which it was extracted in $CHCl_3$ (50 mL). The organic layer was then dried over $Na_2SO_4$, and the solvent was evaporated in a rotary evaporator to get the crude product. The crude product was purified by silica gel column chromatography using ethyl acetate (EtOAc) in petroleum ether (PE) as a solvent system. Two diastereomeric amide compounds **14R** and **14S** were collected separately in 37% yield (**14R** in 45% EtOAc/PE) and 39% yield (**14S** 75% EtOAc/PE).

**(*R*)-2-acetamido-*N*-((*R*)-1-((*S*)-2,2-dimethyl-1,3-dioxolan-4-yl)nonyl)-3-phenylpropan-amide ($C_{25}H_{40}N_2O_4$) 14R: $^1$H NMR (400 MHz, $CDCl_3$):** $\delta$ 7.33 – 7.18 (m, 5H), 6.11 – 5.96 (m, 2H), 4.64 (q, *J* = 7.7 Hz, 1H), 4.07 (td, *J* = 7.0, 2.0 Hz, 1H), 3.90 (q, *J* = 8.4 Hz, 1H), 3.82 (dd, *J* = 8.2, 6.7 Hz, 1H), 3.20 (t, *J* = 7.8 Hz, 1H), 3.11 (dd, *J* = 13.7, 7.6 Hz, 1H), 3.01 (dd, *J* = 13.8, 6.5 Hz, 1H), 1.96 (s, 3H), 1.67 – 1.60 (m, 2H), 1.55 – 1.43 (m, 2H), 1.29 (s, 3H), 1.29 (s, 3H),1.27 – 1.24 (m, 2H), 0.87 (t, *J* = 6.8 Hz, 1H); **$^{13}$C NMR (101 MHz, $CDCl_3$):** $\delta$ 171.1, 170.1, 136.5, 129.4, 128.8, 127.2, 109.1, 76.6, 66.2, 55.0, 49.5, 38.2, 33.1, 32.0, 29.6, 29.5, 29.4, 26.4, 26.1, 25.2, 23.2, 22.8, 14.2; **HRMS (ESI):** Calcd. $C_{25}H_{41}N_2O_4$ $[M+H]^+$: 433.3066, Found: 433.3068.

**(*S*)-2-acetamido-*N*-((*R*)-1-((*S*)-2,2-dimethyl-1,3-dioxolan-4-yl)nonyl)-3-phenylpropan-amide ($C_{25}H_{40}N_2O_4$) 14S: $^1$H NMR (400 MHz, $CDCl_3$):** $\delta$ 7.33 – 7.22 (m, 5H), 6.20 (d, *J* = 7.9 Hz, 1H), 5.69 (d, *J* = 9.5 Hz, 1H), 4.68 – 4.58 (m, 1H), 4.10 (t, *J* = 7.6 Hz, 1H), 3.96 – 3.82 (m, 2H), 3.49 – 3.41 (m, 1H), 3.14 (dd, *J* = 13.6, 5.6 Hz, 1H), 2.98 (dd, *J* = 13.7, 8.6 Hz, 1H), 1.98 (s, 3H), 1.46 – 1.32 (m, 2H), 1.30 (s, 3H), 1.27 (s, 3H), 1.25 – 1.11 (m, 12H), 0.89 (t, *J* = 6.8 Hz, 3H); **$^{13}$C NMR (101 MHz, $CDCl_3$):** $\delta$ 170.9, 170.0, 136.9, 129.4, 128.9, 127.2, 109.2, 76.6, 66.3, 54.9, 49.6, 38.5, 33.0, 32.0, 29.8, 29.6, 29.4, 26.2, 26.1, 24.9, 23.3, 22.8, 14.3; **HRMS (ESI):** Calcd. $C_{25}H_{41}N_2O_4$ $[M+H]^+$: 433.3066, Found: 433.3055.

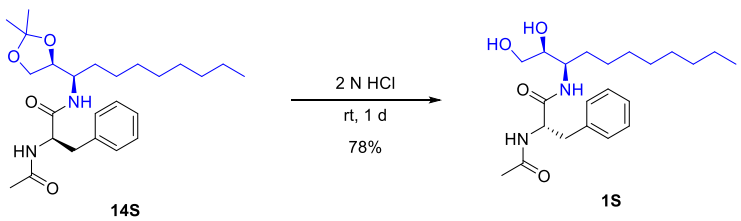
**(*R*)-2-acetamido-*N*-((2*S*,3*R*)-1,2-dihydroxyundecan-3-yl)-3-phenylpropanamide ($C_{22}H_{36}N_2O_4$) 1R:**




**Scheme 5.6** Synthesis of compound **1R**.

In a 25 mL round bottom flask, compound **14R** (0.06 g, 0.14 mmol) was taken and dissolved in 3 mL of THF : MeOH (1 : 1) solution. Then into that solution, 2 mL of 2 N HCl was added and the reaction mixture was then stirred at room temperature overnight. After completion of the reaction, the reaction solution was neutralized by the dilute $NaHCO_3$ solution. The neutralized solution was then washed with water and brine by extracting the compound in ethyl acetate (EtOAc). The organic layer was dried over $Na_2SO_4$ and the solvent was then evaporated to get the crude product. The crude product was purified by silica gel column chromatography using methanol in chloroform (3% MeOH/$CHCl_3$) solvent system to obtain pure product **1R** as a white solid in 85% yield. **$^1$H NMR (400 MHz, DMSO-$d_6$):** $\delta$ 8.11 (d, $J$ = 8.5 Hz, 1H), 7.45 (d, $J$ = 9.0 Hz, 1H), 7.30 – 7.12 (m, 5H), 4.72 (d, $J$ = 5.2 Hz, 1H), 4.53 – 4.45 (m, 1H), 4.38 (t, $J$ = 5.7 Hz, 1H), 3.82 – 3.69 (m, 1H), 3.46 – 3.39 (m, 1H), 3.23 – 3.09 (m, 2H), 2.98 (dd, $J$ = 13.8, 4.6 Hz, 1H), 2.72 (dd, $J$ = 13.7, 10.1 Hz, 1H), 1.73 (s, 3H), 1.49 – 1.37 (m, 2H), 1.27 – 1.21 (d, $J$ = 4.6 Hz, 12H), 0.91 – 0.81 (m, 3H); **$^{13}$C NMR (100 MHz, DMSO-$d_6$):** $\delta$ 171.5, 169.0, 138.1, 129.1, 128.0, 126.2, 72.3, 62.9, 54.2, 49.9, 39.5, 37.7, 31.3, 30.9, 29.1, 29.1, 28.7, 25.8, 22.4, 22.1, 14.0; **HRMS (ESI):** Calcd. $C_{22}H_{37}N_2O_4$ $[M+H]^+$: 393.2753, Found: 393.2740.

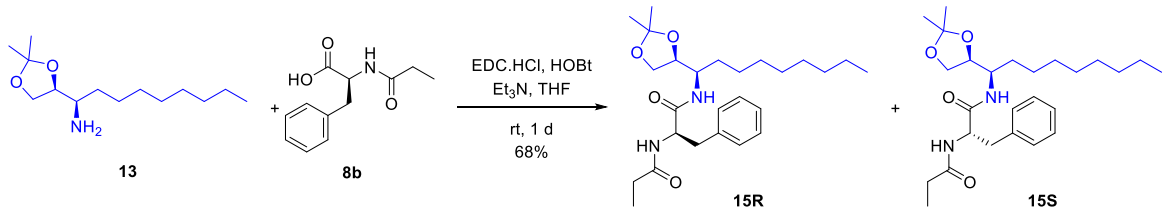
**(*S*)-2-acetamido-*N*-((2*S*,3*R*)-1,2-dihydroxyundecan-3-yl)-3-phenylpropanamide ($C_{22}H_{36}N_2O_4$) 1S:**




**Scheme 5.7** Synthesis of compound **1S**.

In a 25 mL round bottom flask compound **14S** (0.07 g, 0.16 mmol) was taken and dissolved in 4 mL of THF : MeOH (1 : 1) solution. Then into that solution, 3 mL of 2 N HCl was added and the reaction mixture was then stirred at room temperature overnight. After completion of the reaction, the reaction solution was neutralized by the dilute $NaHCO_3$ solution. The neutralized solution was then washed with water and brine by extracting the compound in ethyl acetate (EtOAc). The organic layer was dried over $Na_2SO_4$ and the solvent was then evaporated to get the crude product. The crude product was purified by silica gel column chromatography using methanol in chloroform (4% MeOH/$CHCl_3$) solvent system to obtain pure product **1S** as a white solid in 78% yield. **$^1$H NMR (400 MHz, DMSO-*d*$_6$):** $\delta$ 8.10 (d, *J* = 8.4 Hz, 1H), 7.62 (d, *J* = 9.0 Hz, 1H), 7.29 – 7.20 (m, 4H), 7.19 – 7.12 (m, 1H), 4.72 (d, *J* = 4.8 Hz, 1H), 4.53 (td, *J* = 9.3, 5.3 Hz, 1H), 4.40 (t, *J* = 5.9 Hz, 1H), 3.73 (q, *J* = 8.7 Hz, 1H), 3.47 – 3.40 (m, 1H), 3.21 (td, *J* = 6.2, 2.0 Hz, 2H), 2.92 (dd, *J* = 13.6, 5.3 Hz, 1H), 2.71 (dd, *J* = 13.5, 9.6 Hz, 1H), 1.74 (s, 3H), 1.37 (q, *J* = 7.6 Hz, 2H), 1.30 – 1.08 (m, 12H), 0.88 – 0.80 (m, 3H); **$^{13}$C NMR (100 MHz, DMSO-*d*$_6$):** $\delta$ 171.7, 168.9, 138.0, 129.2, 128.0, 126.2, 72.5, 62.9, 54.2, 49.7, 38.0, 31.3, 30.7, 29.0, 28.9, 28.7, 25.6, 22.5, 22.1, 14.0; **HRMS (ESI):** Calcd. $C_{22}H_{37}N_2O_4$ $[M+H]^+$: 339.2753, Found: 339.2756.

**15R** and **15S:**




**Scheme 5.8** Synthesis of compound **15R** and **15S**.

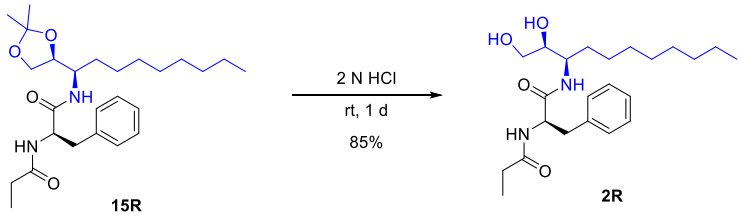
In a 25 mL round bottom flask, the amine **13** (0.18 g, 0.74 mmol) was taken and dissolved in 7 mL of dry THF. Then into the reaction mixture propionyl-L-phenylalanine **8b** (0.17 g, 0.77 mmol), HOBt (0.10 g, 0.74 mmol) and triethylamine (0.5 mL) were added. At last, EDC·HCl (0.17 g, 0.89 mmol) was added, and the reaction mixture was then stirred at room temperature overnight under an inert atmosphere. After completion of the reaction, the reaction mixture was washed with water (2 × 10 mL) and followed by brine solution (1 × 10 mL) by extracting the compound in $CHCl_3$ (60 mL). The organic layer was then dried over $Na_2SO_4$, and the solvent was evaporated in a rotary evaporator to get the crude product. The crude product was purified by silica gel column chromatography using ethyl acetate (EtOAc) in petroleum ether (PE) as a solvent system. Two diastereomeric amide compounds **15R** and

**15S** were collected separately in 35% yield (**15R** in 25% EtOAc/PE) and 33% yield (**15S** 40% EtOAc/PE).

**(*R*)-*N*-((*R*)-1-((*S*)-2,2-dimethyl-1,3-dioxolan-4-yl)nonyl)-3-phenyl-2-propionamido-propanamide ($C_{26}H_{42}N_2O_4$) 15R: $^1$H NMR (400 MHz, $CDCl_3$):** *δ* 7.34 – 7.15 (m, 5H), 6.00 (dd, *J* = 32.6, 8.6 Hz, 2H), 4.65 (q, *J* = 7.8 Hz, 1H), 4.06 (t, *J* = 7.0 Hz, 1H), 3.90 (q, *J* = 8.4 Hz, 1H), 3.83 (t, *J* = 7.4 Hz, 1H), 3.21 (t, *J* = 7.8 Hz, 1H), 3.16 – 3.08 (m, 1H), 3.01 (dd, *J* = 13.7, 6.6 Hz, 1H), 2.18 (q, *J* = 7.6 Hz, 2H), 1.53 – 1.44 (m, 2H), 1.29 (s, 3H), 1.28 (s, 3H), 1.27 – 1.12 (m, 12H), 1.09 (t, *J* = 7.6 Hz, 3H), 0.87 (t, *J* = 6.3 Hz, 3H); **$^{13}$C NMR (101 MHz, $CDCl_3$):** *δ* 173.8, 171.2, 136.6, 129.4, 128.8, 127.2, 109.1, 77.2, 76.7, 66.3, 54.8, 49.5, 38.1, 33.1, 32.0, 29.8, 29.7, 29.5, 29.4, 26.4, 26.1, 25.2, 22.8, 14.2, 9.8; **HRMS (ESI):** Calcd. $C_{26}H_{43}N_2O_4$ $[M+H]^+$: 447.3222, Found: 447.3219.

**(*S*)-*N*-((*R*)-1-((*S*)-2,2-dimethyl-1,3-dioxolan-4-yl)nonyl)-3-phenyl-2-propionamido-propanamide ($C_{26}H_{42}N_2O_4$) 15S: $^1$H NMR (400 MHz, $CDCl_3$):** *δ* 7.32 – 7.20 (m, 5H), 6.19 (d, *J* = 7.6 Hz, 1H), 5.74 (d, *J* = 9.4 Hz, 1H), 4.66 (td, *J* = 8.2, 5.8 Hz, 1H), 4.10 (t, *J* = 6.8 Hz, 1H), 3.94 – 3.83 (m, 1H), 3.44 (dd, *J* = 8.2, 7.0 Hz, 1H), 3.14 (dd, *J* = 13.7, 5.8 Hz, 1H), 2.99 (dd, *J* = 13.7, 8.5 Hz, 1H), 2.21 (q, *J* = 7.6 Hz, 2H), 1.29 (s, 3H), 1.27 (s, 3H), 1.26 – 1.15 (m, 14H), 1.11 (t, *J* = 7.6 Hz, 3H), 0.89 (t, *J* = 6.9 Hz, 3H); **$^{13}$C NMR (101 MHz, $CDCl_3$):** *δ* 173.7, 171.0, 136.9, 129.4, 128.9, 127.2, 109.2, 76.7, 66.4, 54.7, 49.6, 38.6, 33.1, 32.0, 29.8, 29.7, 29.6, 29.4, 26.3, 26.1, 24.9, 22.8, 14.3, 9.8; **HRMS (ESI):** Calcd. $C_{26}H_{43}N_2O_4$ $[M+H]^+$: 447.3222, Found: 447.3219.

**(*R*)-*N*-((2*S*,3*R*)-1,2-dihydroxyundecan-3-yl)-3-phenyl-2-propionamidopropanamide ($C_{23}H_{38}N_2O_4$) 2R:**

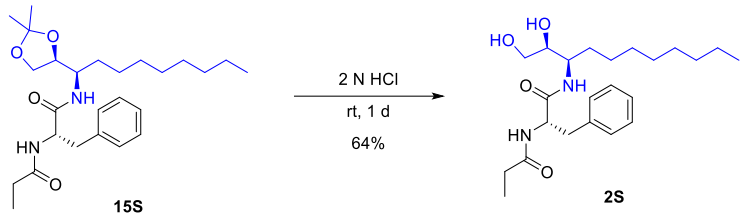



**Scheme 5.9** Synthesis of compound **2R**.

In a 25 mL round bottom flask, compound **15R** (0.08 g, 0.18 mmol) was taken and dissolved in 4 mL of THF : MeOH (1 : 1) solution. Then into that solution, 3 mL of 2 N HCl was added and the reaction mixture was then stirred at room temperature overnight. After completion of the reaction, the reaction solution was neutralized by the dilute $NaHCO_3$

solution. The neutralized solution was then washed with water and brine by extracting the compound in ethyl acetate (EtOAc). The organic layer was dried over $Na_2SO_4$ and the solvent was then evaporated to get the crude product. The crude product was purified by silica gel column chromatography using methanol in chloroform (3% MeOH/$CHCl_3$) solvent system to obtain pure product **2R** as a white solid in 74% yield. **$^1$H NMR (400 MHz, DMSO-*d*$_6$):** $\delta$ 7.99 (d, *J* = 8.5 Hz, 1H), 7.56 (d, *J* = 9.1 Hz, 1H), 7.29 – 7.13 (m, 5H), 4.73 (d, *J* = 4.3 Hz, 1H), 4.53 (td, *J* = 9.4, 5.2 Hz, 1H), 4.39 (bs, 1H), 3.74 (q, *J* = 6.7 Hz, 1H), 3.43 (bs, 1H), 3.21 (bs, 2H), 2.94 (dd, *J* = 13.6, 5.2 Hz, 1H), 2.72 (dd, *J* = 13.5, 9.7 Hz, 1H), 2.02 (q, *J* = 7.6 Hz, 2H), 1.38 (q, *J* = 7.4 Hz, 2H), 1.30 – 1.10 (m, 12H), 0.87 (t, *J* = 7.6 Hz, 3H), 0.84 (t, *J* = 6.8 Hz, 3H); **$^{13}$C NMR (101 MHz, DMSO-*d*$_6$):** $\delta$ 172.7, 171.6, 138.0, 129.2, 127.9, 126.1, 72.5, 62.9, 54.0, 49.7, 37.9, 31.3, 30.8, 28.9, 28.9, 28.7, 28.3, 25.6, 22.1, 14.0, 9.9; **HRMS (ESI):** Calcd. $C_{23}H_{39}N_2O_4$ $[M+H]^+$: 407.2909, Found: 407.2901.

**(*S*)-*N*-((2*S*,3*R*)-1,2-dihydroxyundecan-3-yl)-3-phenyl-2-propionamidopropanamide ($C_{23}H_{38}N_2O_4$) 2S:**

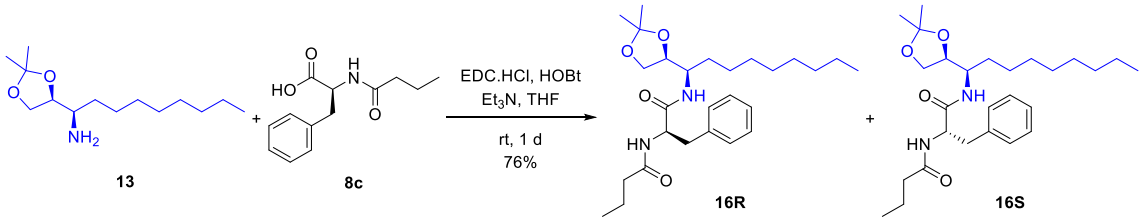



**Scheme 5.10** Synthesis of compound **2S**.

In a 25 mL round bottom flask compound **15S** (0.07 g, 0.16 mmol) was taken and dissolved in 4 mL of THF : MeOH (1 : 1) solution. Then into that solution, 3 mL of 2 N HCl was added and the reaction mixture was then stirred at room temperature overnight. After completion of the reaction, the reaction solution was neutralized by the dilute $NaHCO_3$ solution. The neutralized solution was then washed with water and brine by extracting the compound in ethyl acetate (EtOAc). The organic layer was dried over $Na_2SO_4$ and the solvent was then evaporated to get the crude product. The crude product was purified by silica gel column chromatography using methanol in chloroform (4% MeOH/$CHCl_3$) solvent system to obtain pure product **2S** as a white solid in 64% yield. **$^1$H NMR (400 MHz, DMSO-*d*$_6$):** $\delta$ 7.99 (d, *J* = 8.5 Hz, 1H), 7.56 (d, *J* = 9.0 Hz, 1H), 7.27 – 7.15 (m, 5H), 4.73 (d, *J* = 4.8 Hz, 1H), 4.53 (td, *J* = 9.4, 5.2 Hz, 1H), 4.39 (t, *J* = 5.9 Hz, 1H), 3.74 (q, *J* = 6.5 Hz, 1H), 3.47 – 3.40 (m, 1H), 3.21 (td, *J* = 6.0, 3.0 Hz, 2H), 2.95 (dd, *J* = 13.6, 5.2 Hz, 1H), 2.72 (dd, *J* = 13.5, 9.7 Hz, 1H), 2.02 (q, *J* = 7.8, 7.2 Hz, 2H), 1.38 (q, *J* = 7.6 Hz, 2H), 1.27 – 1.18 (m, 12H), 0.87 (t, *J* = 7.6 Hz, 3H), 0.85 (t, *J* = 6.8

Hz, 3H); **$^{13}$C NMR (100 MHz, DMSO-*d*$_6$):** $\delta$ 172.7, 171.6, 138.0, 129.2, 127.9, 126.1, 72.5, 62.9, 54.0, 49.7, 37.9, 31.3, 30.8, 28.9, 28.9, 28.7, 28.3, 25.6, 22.1, 14.0, 9.9; **HRMS (ESI):** Calcd. $C_{23}H_{39}N_2O_4$ $[M+H]^+$: 407.2909, Found: 407.2901.

**16R and 16S:**



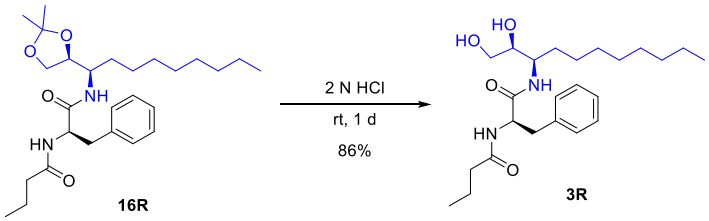

**Scheme 5.11** Synthesis of compounds **16R** and **16S**.

In a 50 mL round bottom flask, the amine **13** (0.27 g, 1.13 mmol) was taken and dissolved in 10 mL of dry THF. Then into the reaction mixture butyryl-*L*-phenylalanine **8c** (0.26 g, 1.13 mmol), HOBt (0.15 g, 1.13 mmol) and triethylamine (1 mL) were added. At last, EDC·HCl (0.26 g, 1.35 mmol) was added, and the reaction mixture was then stirred at room temperature overnight under an inert atmosphere. After completion of the reaction, the reaction mixture was washed with water (3 × 10 mL) and followed by brine solution (1 × 10 mL) by extracting the compound in $CHCl_3$ (40 mL). The organic layer was then dried over $Na_2SO_4$, and the solvent was evaporated in a rotary evaporator to get the crude product. The crude product was purified by silica gel column chromatography using ethyl acetate (EtOAc) in petroleum ether (PE) as a solvent system. Two diastereomeric amide compounds **16R** and **16S** were collected separately in 38% yield (**16R** in 25% EtOAc/PE) and 38% yield (**16S** 40% EtOAc/PE).

***N*-((*R*)-1-(((*R*)-1-((*S*)-2,2-dimethyl-1,3-dioxolan-4-yl)nonyl)amino)-1-oxo-3-phenyl-propan-2-yl)butyramide ($C_{27}H_{44}N_2O_4$) 16R: $^1$H NMR (400 MHz, $CDCl_3$):** $\delta$ 7.32 – 7.18 (m, 5H), 6.09 (bs, 1H), 6.01 (bs, 1H), 4.67 (q, *J* = 7.5 Hz, 1H), 4.06 (td, *J* = 7.1, 2.1 Hz, 1H), 3.90 (dd, *J* = 17.5, 8.4 Hz, 1H), 3.82 (dd, *J* = 8.2, 6.6 Hz, 1H), 3.20 (t, *J* = 7.8 Hz, 1H), 3.12 (dd, *J* = 13.7, 7.6 Hz, 1H), 2.99 (dd, *J* = 13.8, 6.8 Hz, 1H), 2.13 (dd, *J* = 16.0, 8.8 Hz, 2H), 1.66 – 1.53 (m, 2H), 1.29 (s, 3H), 1.28 (s, 3H), 1.27 – 1.17 (m, 14H), 0.87 (td, *J* = 7.2, 2.0 Hz, 6H); **$^{13}$C NMR (101 MHz, $CDCl_3$):** $\delta$ 173.1, 171.2, 136.6, 129.4, 128.8, 127.2, 109.1, 76.8, 66.3, 54.7, 49.4, 38.6, 38.2, 33.2, 32.0, 29.6, 29.6, 29.4, 26.4, 26.1, 25.2, 22.8, 19.1, 14.2, 13.7; **HRMS (ESI):** Calcd. $C_{27}H_{45}N_2O_4$ $[M+H]^+$: 461.3379, Found: 461.3377.

***N*-((*S*)-1-(((*R*)-1-((*S*)-2,2-dimethyl-1,3-dioxolan-4-yl)nonyl)amino)-1-oxo-3-phenylpropan-2-yl)butyramide ($C_{27}H_{44}N_2O_4$) 16S**: **$^1$H NMR (400 MHz, $CDCl_3$):** $\delta$ 7.34 – 7.18 (m, 5H), 6.17 (d, *J* = 6.7 Hz, 1H), 5.73 (d, *J* = 9.1 Hz, 1H), 4.66 (td, *J* = 8.1, 6.0 Hz, 1H), 4.09 (td, *J* = 6.8, 1.9 Hz, 1H), 3.93 – 3.86 (m, 2H), 3.44 (dd, *J* = 8.2, 7.0 Hz, 1H), 3.14 (dd, *J* = 13.7, 5.9 Hz, 1H), 2.99 (dd, *J* = 13.7, 8.5 Hz, 1H), 2.15 (td, *J* = 7.4, 2.5 Hz, 2H), 1.67 – 1.55 (m, 2H), 1.45 – 1.32 (m, 4H), 1.28 (s, 3H), 1.27 (s, 3H), 1.26 – 1.13 (m, 10H), 0.88 (td, *J* = 7.2, 2.3 Hz, 6H); **$^{13}$C NMR (101 MHz, $CDCl_3$):** $\delta$ 172.9, 171.0, 136.9, 129.4, 128.9, 127.2, 109.2, 77.4, 76.7, 66.4, 54.7, 49.5, 38.6, 33.1, 32.0, 29.8, 29.6, 29.4, 26.3, 26.1, 24.9, 22.8, 19.1, 14.3, 13.8; **HRMS (ESI):** Calcd. $C_{27}H_{45}N_2O_4$ $[M+H]^+$: 461.3379, Found: 461.3376.

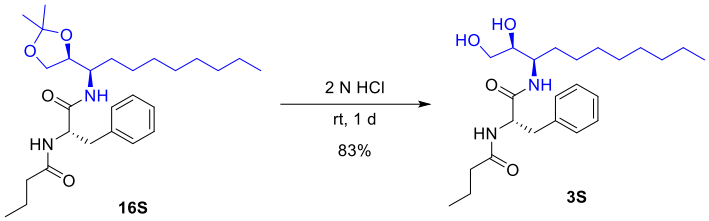
***N*-((*R*)-1-(((*2S,3R*)-1,2-dihydroxyundecan-3-yl)amino)-1-oxo-3-phenylpropan-2-yl) butyramide ($C_{24}H_{40}N_2O_4$) 3R:**




**Scheme 5.12** Synthesis of compound **3R**.

In a 25 mL round bottom flask, compound **16R** (0.10 g, 0.22 mmol) was taken and dissolved in 5 mL of THF : MeOH (1 : 1) solution. Then into that solution, 2 mL of 2 N HCl was added and the reaction mixture was then stirred at room temperature overnight. After completion of the reaction, the reaction solution was neutralized by the dilute $NaHCO_3$ solution. The neutralized solution was then washed with water and brine by extracting the compound in ethyl acetate (EtOAc). The organic layer was dried over $Na_2SO_4$ and the solvent was then evaporated to get the crude product. The crude product was purified by silica gel column chromatography using methanol in chloroform (2% MeOH/$CHCl_3$) solvent system to obtain pure product **3R** as a white solid in 86% yield. **$^1$H NMR (400 MHz, DMSO-$d_6$):** $\delta$ 8.04 (d, *J* = 8.6 Hz, 1H), 7.37 (d, *J* = 9.1 Hz, 1H), 7.29 – 7.12 (m, 5H), 4.71 (d, *J* = 5.1 Hz, 1H), 4.51 (td, *J* = 9.9, 4.6 Hz, 1H), 4.37 (t, *J* = 5.7 Hz, 1H), 3.77 (dd, *J* = 16.4, 8.5 Hz, 1H), 3.42 (q, *J* = 6.2 Hz, 1H), 3.23 – 3.09 (m, 2H), 2.99 (dd, *J* = 13.7, 4.6 Hz, 1H), 2.73 (dd, *J* = 13.7, 10.3 Hz, 1H), 1.98 (t, *J* = 7.4 Hz, 2H), 1.46 – 1.13 (m, 14H), 0.85 (t, *J* = 6.8 Hz, 3H), 0.70 (t, *J* = 7.4 Hz, 3H); **$^{13}$C NMR (100 MHz, DMSO-$d_6$):** $\delta$ 171.8, 171.5, 138.1, 129.1, 128.0, 126.1, 79.2, 72.2, 62.9, 53.9, 49.8, 39.5, 37.5, 37.09, 31.5, 31.3, 31.1, 29.1, 28.7, 25.7, 22.1, 18.6, 14.0, 13.4; **HRMS (ESI):** Calcd. $C_{24}H_{41}N_2O_4$ $[M+H]^+$: 421.3066, Found: 421.3063.

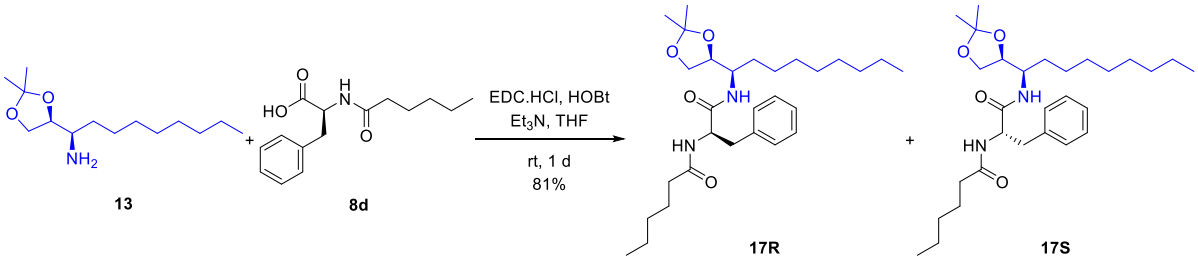
***N*-((*S*)-1-(((*2S,3R*)-1,2-dihydroxyundecan-3-yl)amino)-1-oxo-3-phenylpropan-2-yl) butyramide ($C_{24}H_{40}N_2O_4$) 3S:**




**Scheme 5.13** Synthesis of compound **3S**.

In a 25 mL round bottom flask, compound **16S** (0.12 g, 0.26 mmol) was taken and dissolved in 6 mL of THF : MeOH (1 : 1) solution. Then into that solution, 3 mL of 2 N HCl was added and the reaction mixture was then stirred at room temperature overnight. After completion of the reaction, the reaction solution was neutralized by the dilute $NaHCO_3$ solution. The neutralized solution was then washed with water and brine by extracting the compound in ethyl acetate (EtOAc). The organic layer was dried over $Na_2SO_4$ and the solvent was then evaporated to get the crude product. The crude product was purified by silica gel column chromatography using methanol in chloroform (2.5% MeOH/$CHCl_3$) solvent system to obtain pure product **3S** as a white solid in 83% yield. **$^1$H NMR (400 MHz, DMSO-$d_6$):** $\delta$ 8.01 (d, $J$ = 8.5 Hz, 1H), 7.55 (d, $J$ = 9.0 Hz, 1H), 7.29 – 7.11 (m, 5H), 4.74 (d, $J$ = 4.7 Hz, 1H), 4.55 (td, $J$ = 9.6, 5.1 Hz, 1H), 4.39 (t, $J$ = 5.9 Hz, 1H), 3.75 (q, $J$ = 8.6 Hz, 1H), 3.48 – 3.40 (m, 1H), 3.26 – 3.16 (m, 2H), 2.95 (dd, $J$ = 13.6, 5.1 Hz, 1H), 2.72 (dd, $J$ = 13.6, 9.9 Hz, 1H), 1.99 (t, $J$ = 7.4 Hz, 2H), 1.46 – 1.31 (m, 4H), 1.28 – 1.11 (m, 12H), 0.88 – 0.81 (m, 3H), 0.70 (t, $J$ = 7.4 Hz, 3H); **$^{13}$C NMR (100 MHz, DMSO-$d_6$):** $\delta$ 171.8, 171.7, 138.0, 129.2, 127.9, 126.1, 79.2, 72.4, 62.9, 54.0, 49.7, 39.5, 37.9, 37.1, 31.6, 31.3, 30.8, 28.9, 28.7, 25.6, 22.1, 18.6, 14.0, 13.4; **HRMS (ESI):** Calcd. $C_{24}H_{41}N_2O_4$ $[M+H]^+$: 421.3066, Found: 421.3057.

**17R** and **17S:**



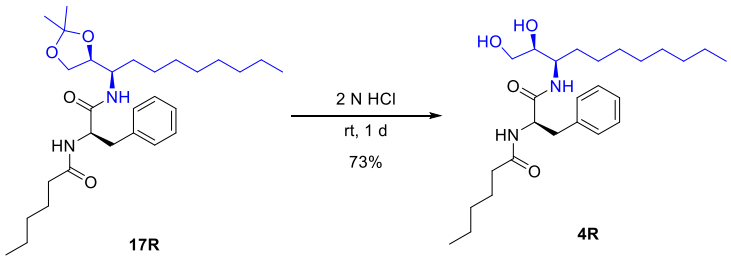

**Scheme 5.14** Synthesis of compound **17R** and **17S**.

In a 50 mL round bottom flask, the amine **13** (0.30 g, 1.23 mmol) was taken and dissolved in 12 mL of dry THF. Then into the reaction mixture, hexanoyl-*L*-phenylalanine **8d** (0.32 g, 1.23 mmol), HOBt (0.17 g, 1.23 mmol), and triethylamine (1 mL) were added. At last, EDC·HCl (0.29 g, 1.48 mmol) was added, and the reaction mixture was then stirred at room temperature overnight under an inert atmosphere. After completion of the reaction, the reaction mixture was washed with water (3 × 10 mL) and then with a solution of brine (1 × 10 mL), after which it was extracted in $CHCl_3$ (50 mL). The organic layer was then dried over $Na_2SO_4$, and the solvent was evaporated in a rotary evaporator to get the crude product. The crude product was purified by silica gel column chromatography using ethyl acetate (EtOAc) in petroleum ether (PE) as a solvent system. Two diastereomeric amide compounds **17R** and **17S** were collected separately in 40% yield (**17R** in 20% EtOAc/PE) and 41% yield (**17S** 25% EtOAc/PE).

***N*-((*R*)-1-(((*R*)-1-((*S*)-2,2-dimethyl-1,3-dioxolan-4-yl)nonyl)amino)-1-oxo-3-phenyl-propan-2-yl)hexanamide ($C_{29}H_{48}N_2O_4$) 17R**: **$^1$H NMR (400 MHz, $CDCl_3$):** $\delta$ 7.32 – 7.19 (m, 5H), 6.11 – 6.02 (m, 1H), 5.97 (t, *J* = 7.9 Hz, 1H), 4.66 (dd, *J* = 15.0, 7.6 Hz, 1H), 4.06 (td, *J* = 7.1, 2.1 Hz, 1H), 3.90 (dd, *J* = 17.2, 8.7 Hz, 1H), 3.83 (dd, *J* = 8.2, 6.7 Hz, 1H), 3.24 – 3.17 (m, 1H), 3.12 (dd, *J* = 13.8, 7.6 Hz, 1H), 3.00 (dd, *J* = 13.8, 6.8 Hz, 1H), 2.14 (dd, *J* = 14.5, 6.9 Hz, 2H), 1.61 – 1.54 (m, 2H), 1.53 – 1.46 (m, 2H), 1.29 (s, 3H), 1.29 (s, 3H), 1.27 – 1.19 (m, 16H), 0.86 (t, *J* = 7.1 Hz, 6H); **$^{13}$C NMR (101 MHz, $CDCl_3$):** $\delta$ 173.2, 171.2, 136.6, 129.4, 128.8, 127.2, 109.1, 76.7, 66.3, 54.7, 49.4, 38.1, 36.7, 33.2, 32.0, 31.4, 29.6, 29.6, 29.4, 26.4, 26.1, 25.4, 25.2, 22.8, 22.5, 14.3, 14.0; **HRMS (ESI):** Calcd. $C_{29}H_{49}N_2O_4$ $[M+H]^+$: 489.3692, Found: 489.3691.

***N*-((*S*)-1-(((*R*)-1-((*S*)-2,2-dimethyl-1,3-dioxolan-4-yl)nonyl)amino)-1-oxo-3-phenyl-propan-2-yl)hexanamide ($C_{29}H_{48}N_2O_4$) 17S**: **$^1$H NMR (400 MHz, $CDCl_3$):** $\delta$ 7.33 – 7.21 (m, 5H), 6.14 (d, *J* = 7.3 Hz, 1H), 5.72 (d, *J* = 9.3 Hz, 1H), 4.65 (td, *J* = 8.1, 6.0 Hz, 1H), 4.09 (td, *J* = 6.7, 1.6 Hz, 1H), 3.94 – 3.80 (m, 2H), 3.49 – 3.39 (m, 1H), 3.14 (dd, *J* = 13.7, 5.9 Hz, 1H), 2.99 (dd, *J* = 13.7, 8.4 Hz, 1H), 2.16 (td, *J* = 7.4, 2.4 Hz, 2H), 1.64 – 1.51 (m, 2H), 1.45 – 1.30 (m, 4H), 1.28 (s, 3H), 1.27 (s, 3H), 1.26 – 1.12 (m, 14H), 0.92 – 0.84 (m, 6H); **$^{13}$C NMR (101 MHz, $CDCl_3$):** $\delta$ 173.1, 171.0, 136.9, 129.4, 128.9, 127.2, 109.1, 76.7, 66.4, 54.7, 49.5, 38.6, 36.7, 33.1, 32.0, 31.5, 29.6, 29.4, 26.3, 26.1, 25.4, 24.9, 22.8, 22.5, 14.3, 14.0; **HRMS (ESI):** Calcd. $C_{29}H_{49}N_2O_4$ $[M+H]^+$: 489.3692, Found: 489.3691.

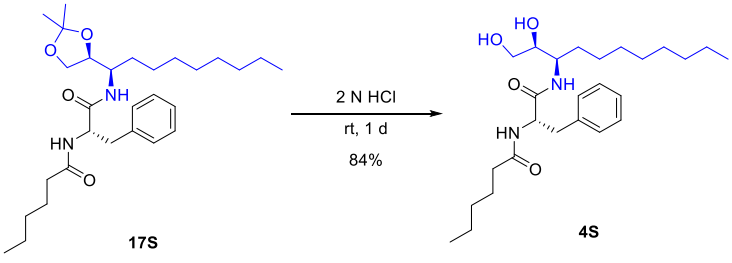
**_N_-((_R_)-1-(((2_S_,3_R_)-1,2-dihydroxyundecan-3-yl)amino)-1-oxo-3-phenylpropan-2-yl) hexanamide ($C_{26}H_{44}N_2O_4$) 4R:**




**Scheme 5.15** Synthesis of compound **4R**.

In a 25 mL round bottom flask, compound **17R** (0.16 g, 0.32 mmol) was taken and dissolved in 6 mL of THF : MeOH (1 : 1) solution. Then into that solution, 3 mL of 2 N HCl was added and the reaction mixture was then stirred at room temperature overnight. After completion of the reaction, the reaction solution was neutralized by the dilute $NaHCO_3$ solution. The neutralized solution was then washed with water and brine by extracting the compound in ethyl acetate (EtOAc). The organic layer was dried over $Na_2SO_4$ and the solvent was then evaporated to get the crude product. The crude product was purified by silica gel column chromatography using methanol in chloroform (2% MeOH/$CHCl_3$) solvent system to obtain pure product **4R** as a white solid in 73% yield. **$^1$H NMR (400 MHz, DMSO-$d_6$):** $\delta$ 8.04 (d, $J$ = 8.5 Hz, 1H), 7.35 (d, $J$ = 9.1 Hz, 1H), 7.29 – 7.08 (m, 5H), 4.71 (bs, 1H), 4.50 (td, $J$ = 10.0, 4.7 Hz, 1H), 4.37 (bs, 1H), 3.77 (q, $J$ = 8.3, 7.5 Hz, 1H), 3.42 (d, $J$ = 5.6 Hz, 1H), 3.25 – 3.08 (m, 2H), 2.99 (dd, $J$ = 13.8, 4.6 Hz, 1H), 2.73 (dd, $J$ = 13.7, 10.3 Hz, 1H), 1.99 (t, $J$ = 7.2 Hz, 2H), 1.48 – 1.30 (m, 4H), 1.29 – 1.12 (m, 14H), 1.11 – 0.98 (m, 2H), 0.85 (t, $J$ = 6.7 Hz, 3H), 0.80 (t, $J$ = 7.3 Hz, 3H); **$^{13}$C NMR (100 MHz, DMSO-$d_6$):** $\delta$172.0, 171.5, 138.2, 129.1, 128.0, 126.1, 79.2, 72.2, 62.9, 53.9, 49.8, 37.5, 35.2, 31.4, 31.1, 30.7, 29.1, 28.7, 25.8, 24.9, 22.1, 21.9, 14.0, 13.8; **HRMS (ESI):** Calcd. $C_{26}H_{45}N_2O_4$ $[M+H]^+$: 449.3379, Found: 449.3381.

**_N_-((_S_)-1-(((2_S_,3_R_)-1,2-dihydroxyundecan-3-yl)amino)-1-oxo-3-phenylpropan-2-yl) hexanamide ($C_{26}H_{44}N_2O_4$) 4S:**




**Scheme 5.16** Synthesis of compound **4S**.

In a 25 mL round bottom flask, compound **17S** (0.24 g, 0.50 mmol) was taken and dissolved in 8 mL of THF : MeOH (1 : 1) solution. Then into that solution, 4 mL of 2N HCl was added and the reaction mixture was then stirred at room temperature overnight. After completion of the reaction, the reaction solution was neutralized by the dilute $NaHCO_3$ solution. The neutralized solution was then washed with water and brine by extracting the compound in ethyl acetate (EtOAc). The organic layer was dried over $Na_2SO_4$ and the solvent was then evaporated to get the crude product. The crude product was purified by silica gel column chromatography using methanol in chloroform (2.5% MeOH/$CHCl_3$) solvent system to obtain pure product **4S** as a white solid in 84% yield. **$^1$H NMR (400 MHz, DMSO-*d*$_6$):** $\delta$ 8.01 (d, *J* = 8.5 Hz, 1H), 7.54 (d, *J* = 9.1 Hz, 1H), 7.31 – 7.11 (m, 5H), 4.74 (bs, 1H), 4.61 – 4.49 (m, 1H), 4.38 (bs, 1H), 3.75 (q, *J* = 7.0 Hz, 1H), 3.44 (bs, 1H), 3.27 – 3.14 (m, 2H), 2.95 (dd, *J* = 13.6, 4.9 Hz, 1H), 2.72 (dd, *J* = 13.3, 9.8 Hz, 1H), 2.00 (t, *J* = 7.3 Hz, 2H), 1.43 – 1.31 (m, 4H), 1.28 – 1.12 (m, 14H), 1.09 – 1.01 (m, 2H), 0.82 (dt, *J* = 17.4, 6.9 Hz, 6H); **$^{13}$C NMR (100 MHz, DMSO-*d*$_6$):** $\delta$ 171.9, 171.8, 138.0, 129.2, 127.9, 126.1, 79.2, 72.4, 62.9, 54.0, 49.7, 39.5, 37.9, 35.2, 31.3, 30.8, 30.6, 29.0, 28.7, 25.6, 24.9, 22.1, 21.9, 14.0, 13.8; **HRMS (ESI):** Calcd. $C_{26}H_{45}N_2O_4$ $[M+H]^+$: 449.3379, Found: 449.3385.

### 5.4.4. Field Emission Scanning Electron Microscopy (FESEM)

#### 5.4.4.1. FESEM Studies for Compound 4S in $CHCl_3$ and MeOH

The surface morphology followed by the aggregation pattern of the compound **4S** in solid-state was examined by field emission scanning electron microscopy (FESEM) studies. For that, the compound **4S** was dissolved in $CHCl_3$ or moist MeOH to prepare a 100 μM solution. The compound solution was drop-casted on a silicon wafer, dried, and then used for FESEM studies.

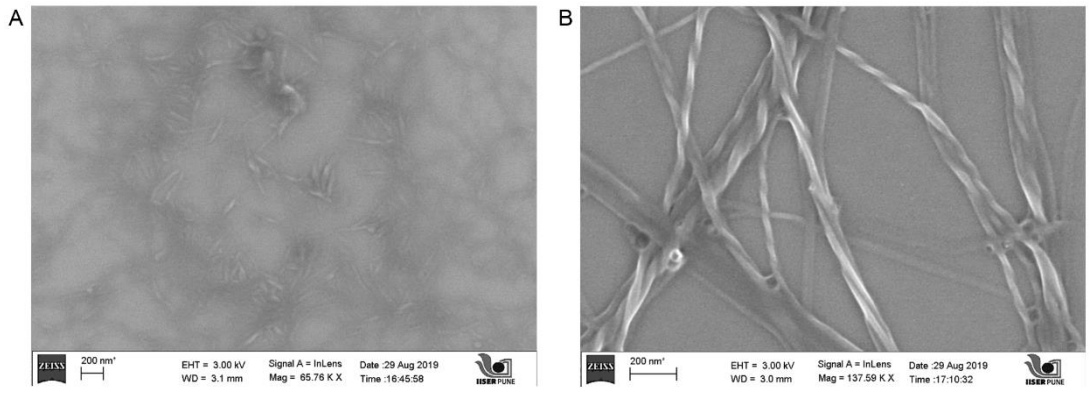



**Figure 5.6** The FESEM image of compound **4S** from $CHCl_3$ (A) and MeOH (B) solution.

### 5.4.4.2. FESEM Studies for Compound 4R in $CHCl_3$ and MeOH

The surface morphology followed by the aggregation pattern of the compound **4R** in the solid state was examined by field emission scanning electron microscopy (FESEM) studies. For that, the compound **4R** was dissolved in $CHCl_3$ or moist MeOH to prepare a 150 μM solution. The compound solution was drop-casted on a silicon wafer, dried, and then used for FESEM studies.

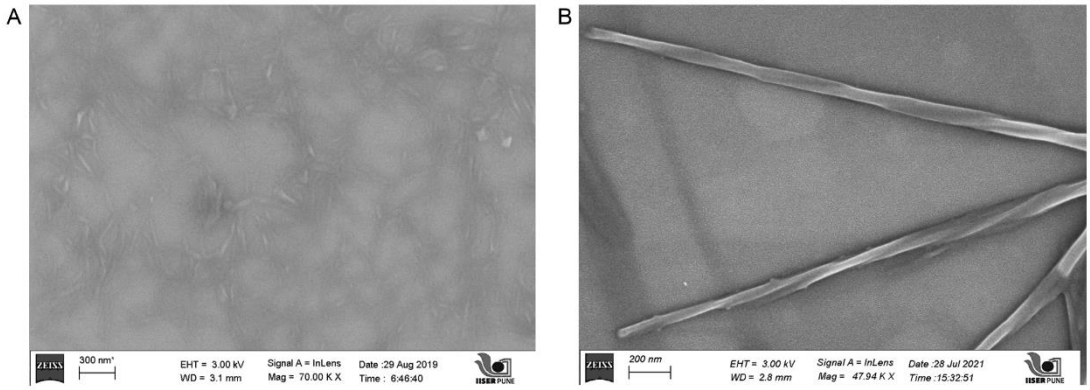



**Figure 5.7** The FESEM image of compound **4R** from $CHCl_3$ (A) and moist MeOH (B) solution.

### 5.4.5. High-Resolution Transmission Electron Microscopy (HRTEM)

A 100 μM solution of the compounds **4S** and **4R** were prepared in moist MeOH. The compound solution was then drop-casted on a TEM grid, dried, and then used for HRTEM imaging.

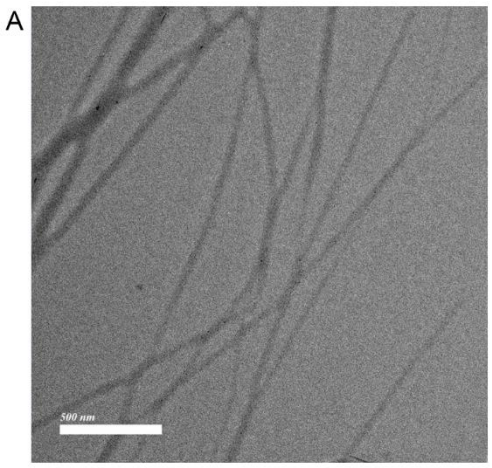



**Figure 5.8** The HRTEM images of free compound **4R**.

### 5.4.6. Crystallographic Measurement and Analysis

The single crystal suitable for X-ray analysis for **2R** was obtained by slow evaporation of moist methanol solution of the respective compounds. On the other hand, the **14R** crystallizes from nitrobenzene and acetonitrile solution (1:10) as a pale yellow crystal. The single-crystal X-ray data were collected on a Bruker Smart Apex Duo diffractometer using Mo Kα radiation for both the compounds either at 100 K, and 150 K. Olex 2[59] graphical interface were used with ShelXT[60] to solve the structures using intrinsic phasing and refined with ShelXL[61] with full matrix least square minimization on $F^2$. All non-hydrogen atoms were refined anisotropically, except for those in minor disordered parts. Crystallographic parameters for compounds **2R** and **14R** are summarised in Table 1.

**Table 1** Crystallographic data for complexes **2R** and **14R**

| Compound | **2R** | **14R** |
|---|---|---|
| Temperature / K | 100 K | 150 K |
| Empirical Formula | $C_{23}H_{40}N_2O_5$ | $C_{25}H_{40}N_2O_4$ |
| Formula Weight [g $mol^{-1}$] | 424.57 | 432.59 |
| crystal system | monoclinic | triclinic |
| space group | C 2 | P-1 |
| a [Å] | 37.83(2) | 9.3339(19) |
| b [Å] | 4.929(3) | 9.6044(18) |
| c [Å] | 12.845(7) | 14.535(3) |
| α [°] | 90 | 81.540(6) |
| β [°] | 97.014(13) | 78.191(6) |
| γ [°] | 90 | 89.814(6) |
| cell V [$Å^3$] | 2377(2) | 1261.1(4) |
| Z | 4 | 2 |
| reflections collected | 13714 | 16669 |
| independent reflections, $R_{int}$ | 4026 | 4296 |
| Data/restrains/parameters | 4026/1/287 | 4296/6/284 |
| goodness-of-fit | 0.996 | 1.035 |
| final *R* indices [$I > 2\sigma(I)$]: $R_1$, $wR_2$ | 0.0668, 0.1355 | 0.0938, 0.2134 |
| CCDC no. | 2122390 | 2122389 |

$R_1 = \Sigma||F_o| - |F_c||/\Sigma|F_o|$ and $wR_2 = |\Sigma w(|F_o|^2 - |F_c|^2)|/\Sigma|w(F_o)^2|^{1/2}$

### 5.4.6.1. ORTEP Diagram of Compound 2R

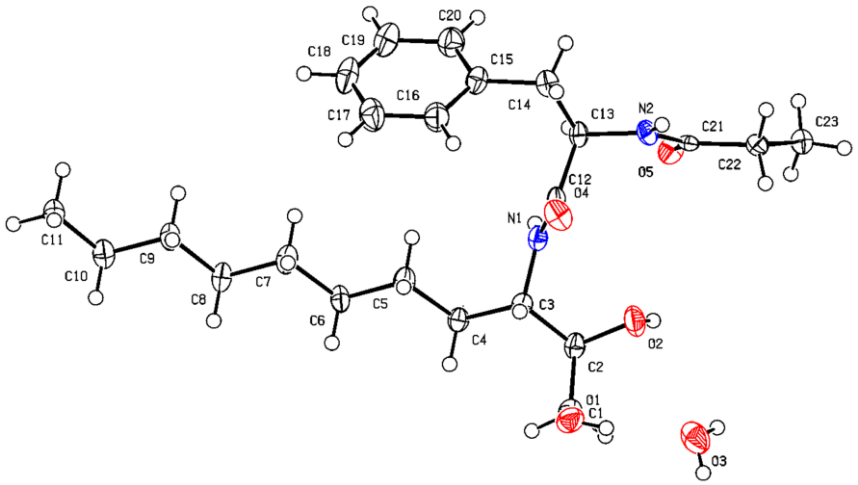



**Figure 5.9** The ORTEP diagram of compound **2R** where the ellipsoids are shown with 50% probability.

### 5.4.6.2. ORTEP Diagram of Compound 14R

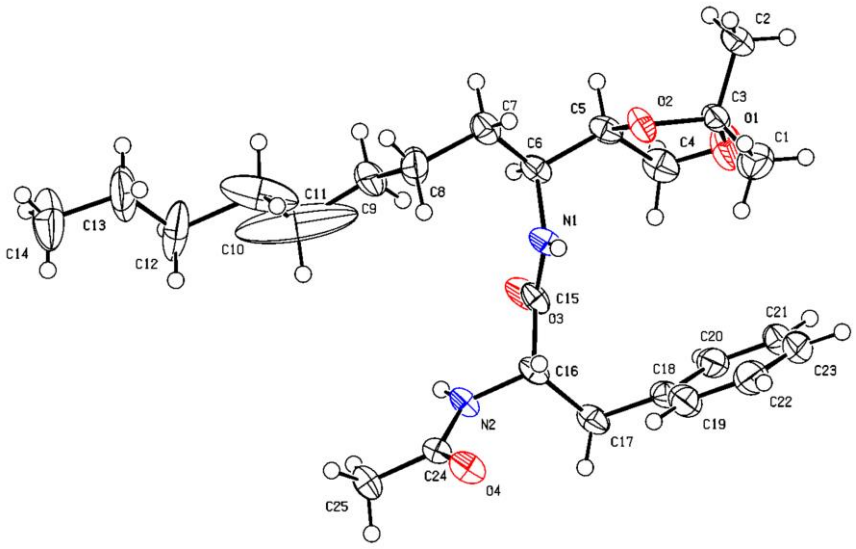



**Figure 5.10** The ORTEP diagram of compound **14R** where the ellipsoids are shown with 50% probability.

### 5.4.7. Water Transport Studies

### 5.4.7.1. Stopped-flow Experiments for Checking Water Transport Activity

**HEPES Buffer Preparation for Experiments**

We have prepared a salt solution using autoclaved water of strength 100 mM of NaCl and 10 mM of HEPES. Initially, the pH of the solution was below 7.0, and to make the pH at around 7 required amount of NaOH (0.5 M) solution was added.

**Vesicles Preparation for Permeability Assay**[34-35]

At first, 0.25 mL of DOPC lipid solution (25 mg/mL in chloroform) was taken in a 10 mL round-bottomed flask, and into that required amount of channel-forming molecule (mol% compound with respect to lipid) in chloroform was added. The chloroform in the compound-lipid solution was then evaporated by a slow stream of nitrogen gas while slowly rotating the round-bottomed flask to get a thin film of lipid inside it. Then the trace amount of chloroform present in the compound-lipid was evaporated by drying it in a high vacuum for about 8 h. The thin film of lipid was hydrated with buffer solution (10 mM HEPES, 100 mM NaCl, pH 7.0), and then sonication followed by vortexing was done 4-5 times (2 minutes each) over the period of 1 h. Then the hydrated vesicles suspension was subjected to 15 freeze-thaw cycles (liquid nitrogen and 55 ˚C temperature water bath), and extrusions were done 19 times (must be odd number) using 200 nm polycarbonate membrane. The extruded vesicles were then diluted to 6 mL using the buffer as mentioned above (10 mM HEPES, 100 mM NaCl, pH 7.0) to get the desired concentration (mol% of compound with respect to lipid), assuming no loss of lipid throughout the process. The vesicles compositions, inside: 10 mM HEPES, 100 mM NaCl, pH 7.0 and outside: 10 mM HEPES, 100 mM NaCl, pH 7.0.

**Description of Stopped-flow Experiments for Water Transport Studies**

The above-mentioned vesicles solution was exposed to an equal volume of 300 mM Sucrose solution (300 mM Sucrose, 10 mM HEPES, 100 mM NaCl, pH 7.0), which leads to the shrinkage of the vesicles due to the outwardly directed water transport through the water channel. The sudden shrinkage of the size of the vesicle has then directed to change in light scattering intensity with time (90˚ angle recorded at 600 nm wavelength), which was monitored on a stopped-flow instrument (SFM 400 and MOS 450 from Biologic Science Instruments). The light scattering intensity was plotted against time by fitting the following exponential decay equation (Equation 1).

$$y = A.exp(-kx) + y_0 \qquad \text{Equation 1}$$

where $x$ is the time, $y$ is the light scattering intensity change, and $k$ is the exponential coefficient for the light scattering change.

This exponential coefficient value, $k$ was used to calculate the osmotic permeability value, $P_f$ following the below equation:

$$P_f = \frac{k}{\frac{S}{V_o} \times V_w \times \Delta_{osm}} \qquad \text{Equation 2}$$

where $P_f$ is the osmotic permeability, $k$ is the exponential coefficient, $S$ is the initial surface area of the vesicles, $V_0$ is the initial volume of the vesicles, $V_w$ is the molar volume of water, $\Delta_{osm}$ is the change in osmolarity of the vesicular suspension after the addition of sucrose solution.

The corrected water permeability, $P_w$ by the water channel molecules were calculated by subtracting the exponential coefficient value a compound from the exponential coefficient value of the blank data from the following equation:

$$P_w = (P_{f(compound)} - P_{f(blank)}) \times \frac{S}{N} \qquad \text{Equation 3}$$

where $P_w$ is the corrected water permeability, $P_{f(compound)}$ is the osmotic permeability of the compounds, $P_{f(blank)}$ is the osmotic permeability of the blank vesicles, $S$ is the surface area of the vesicles, and $N$ is the number of self-aggregated channels per vesicles and can be calculated from the Equation 4.

Each channel aggregate consists of 16 peptide-diol molecules (2 × 8 layered assembly has shown optimal channel formation in MD simulation studies, discussed latter) with a cross-sectional area of nearly 2.6 $nm^2$ (alkyl chain attached to peptide group less significantly differ the area calculation). The lipid molecule has a cross-sectional area of 0.34 $nm^2$ and the lipid bilayer has a thickness of ca. 5 nm. The 'unit area' was calculated based on one channel aggregate. The number of 'unit areas' is equivalent to the number of self-aggregated channels per vesicles ($N$). The $N$ can be calculated from the following equation:

$$N = \frac{SA_{total}}{SA_{unit}} = \frac{2\pi r^2 + 2\pi(r-5)^2}{A_{channel} + \left(\frac{1-x}{x}\right) \times 0.34} \qquad \text{Equation 4}$$

where $SA_{total}$ is the total surface area of a vesicles; $SA_{unit}$ is the 'unit area'; $A_{channel}$ is the cross-sectional area of a single channel aggregate; $x$ is the corrected mCLR considering each channel aggregate is made up of 16 peptide-diol molecules. The number of single channel aggregates per liposome can then be used to calculate the single channel permeability ($P_w$) following equation 3. Please note, in our system the single channel water permeability is the sum of the water permeability of two water arrays in a single self-assembled system.

We have re-calculated the water permeability values utilizing the recently reported equation considering the intra- and extra-vesicular osmolyte concentrations correction factor.

$$P_{f(corrected)} = \frac{k}{\frac{S}{V_0} \times V_w} \times \frac{C_{in,t=0} + C_{out}}{2 \times {C_{out}}^2} \qquad \text{Equation 5}$$

where $C_{in,\,t=0}$ is the change in osmolyte concentration inside the vesicles at $t = 0$ and $C_{out}$ is the osmolyte concentration outside the vesicles.

The $P_{f(corrected)}$ values obtained from Equation 5, considering the osmolyte concentration correction factor, was further used to calculate the corrected water permeability and single channel permeability for all channel forming molecules following the Equation 3 and 4.

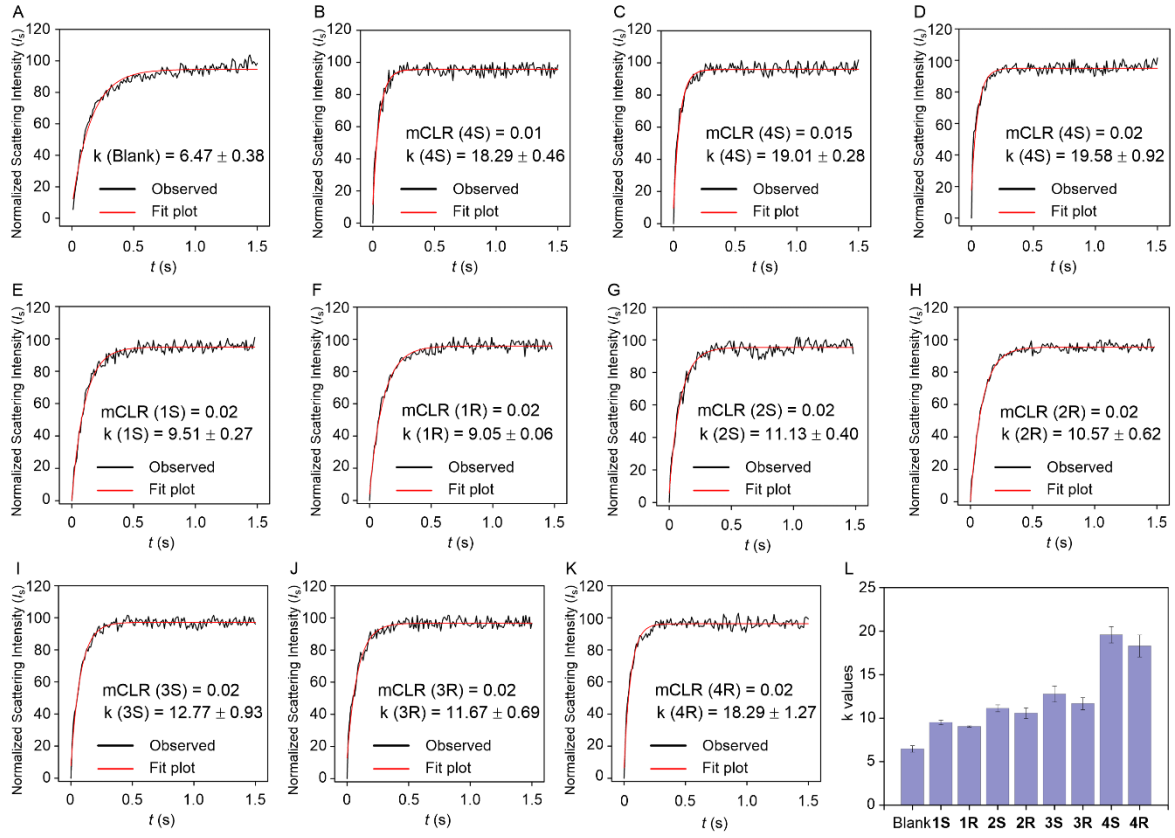



**Figure 5.11** Kinetic curves for water permeability measurement of blank (A), channel **4S** at different mCLRs (B, C, and D), channel **1S** (E), channel **1R** (F), channel **2S** (G), channel **2R** (H), channel **3S** (I), channel **3R** (J), and channel **4R** (K). The comparison of exponential coefficient values of blank, **1S**-**4S**, and **1R**-**4R** (**L**). All the data are triplicated and used to calculate rate constants with their standard deviation values for each compound.

### 5.4.7.2. Estimation of insertion efficiency[50]

The insertion efficiency of peptide 1,2-diol channels in the vesicles was measured using the UV-Vis spectroscopic technique. At first, we have prepared different sets of vesicles (without extrusion, following the process mentioned above) for each compound by inserting the channel forming molecules (mCLR 0.005 to 0.03) and measured the UV-Vis absorbance intensity. These intensity values were used to generate a calibration curve, which has been shown to follow a linear pattern. Next, we prepared a similar type of vesicles (with extrusion, following the process mentioned above) by inserting the channel-forming molecules (mCLR 0.02) and measured the UV-Vis absorbance intensity. This absorbance intensity was used to calculate the actual concentration of the compound (corrected mCLR, after the extrusion process) from the calibration curve. Following these methods, we have calculated the percentage of insertion efficiency (ratio of corrected concentration and initial concentration) for **4S** and **4R**, and the corrected concentrations for these channels were used to calculate the single-channel permeability. The insertion efficiency of **4S** and **4R** are found to be 84% (0.0168/0.02) and 86% (0.0172/0.02), respectively.

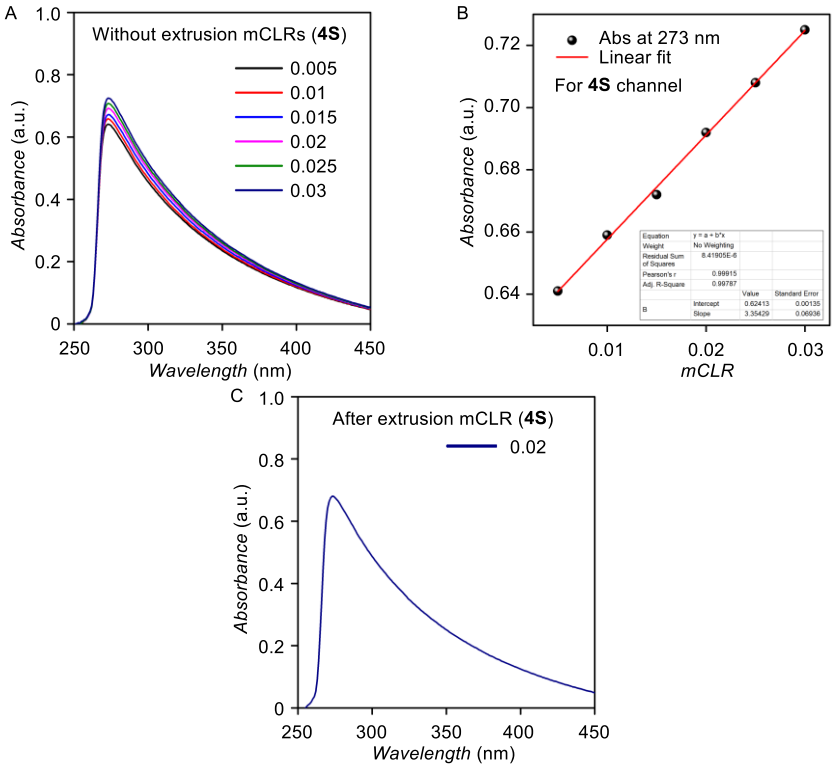



**Figure 5.12** Determination of actual loading of channel-forming compounds in vesicles using UV–Vis spectroscopy. The UV-Vis absorbance intensity of vesicles (without extrusion) with increasing concentration of **4S** (A), Calibration plot (B), and the absorbance intensity of vesicles (with extrusion) with **4S** (mCLR 0.02, C).

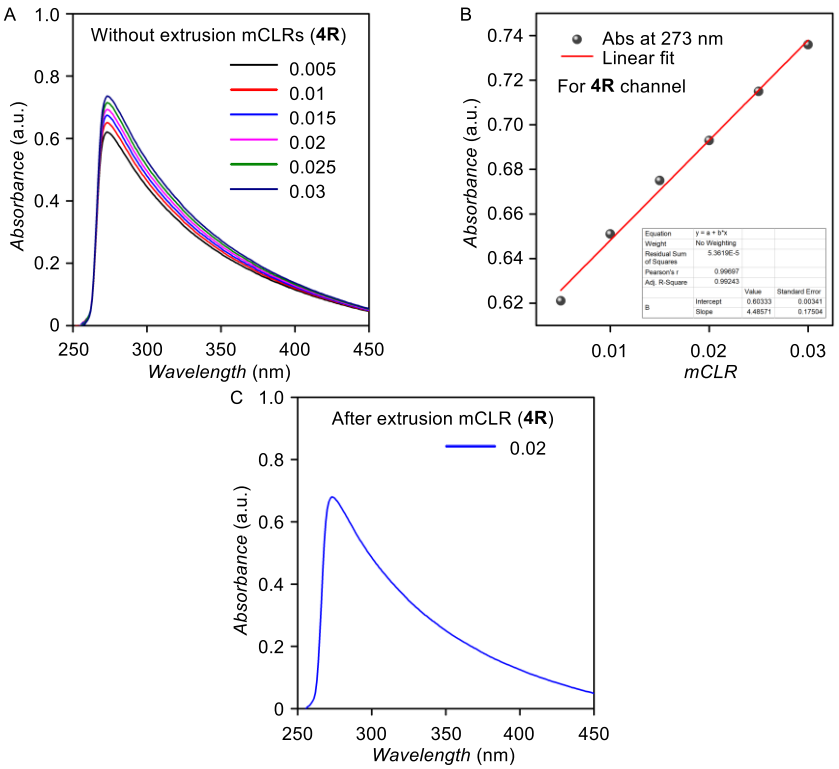



**Figure 5.13** Determination of actual loading of channel-forming compounds in vesicles using UV–Vis spectroscopy. The UV-Vis absorbance intensity of vesicles (without extrusion) with increasing concentration of **4R** (A), Calibration plot (B), and the absorbance intensity of vesicles (with extrusion) with **4R** (mCLR 0.02, C).

**Table 2.** Water permeability calculation tables for compounds **1S**-**4S**, and **1R**-**4R** with corrected mCLRs and without considering the osmolyte concentration correction factor.

| Channels | Exponential coefficient ($k$) | Water permeability, ($P_f$, μm/s) | Corrected water permeability, ($P_f$, μm/s) | Water permeability ($P_w$, $cm^3/s$) | Water permeability/channel (water molecules/s) |
|---|---|---|---|---|---|
| Blank | 6.47 | 54.28 | 0.00 | - | - |
| **1S** | 9.51 | 85.71 | 31.43 | - | - |
| **1R** | 9.05 | 81.54 | 27.26 | - | - |
| **2S** | 11.13 | 100.32 | 46.04 | - | - |
| **2R** | 10.57 | 95.29 | 41.01 | - | - |
| **3S** | 12.77 | 115.06 | 60.78 | - | - |
| **3R** | 11.67 | 105.20 | 50.92 | - | - |
| **4S** | 19.58 | 176.47 | 122.19 | $4.47 \times 10^{-14}$ | $1.49 \times 10^{9}$ |
| **4R** | 18.29 | 164.85 | 110.57 | $3.95 \times 10^{-14}$ | $1.32 \times 10^{9}$ |

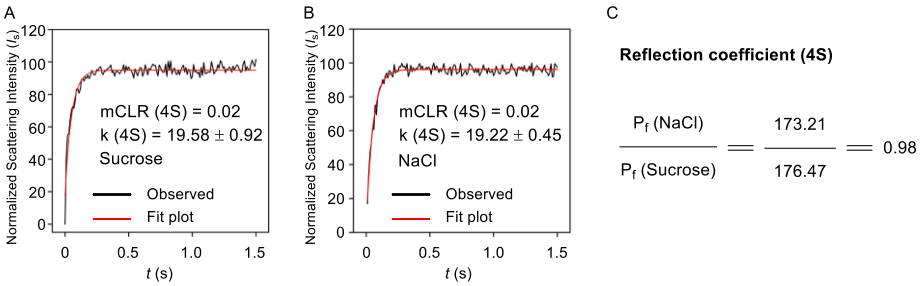



**Figure 5.14** Comparison of water permeability of **4S** in 300 mM sucrose (A) and 250 mM NaCl solution (B). The reflection coefficient value of **4S** (C).

**Table 3.** Water permeability calculation tables for compounds **1S**-**4S**, and **1R**-**4R** with corrected mCLRs and considering the osmolyte concentration correction factor.

| Channels | Exponential coefficient ($k$) | Water permeability, ($P_f$, μm/s) | Corrected water permeability, ($P_f$, μm/s) | Water permeability ($P_w$, $cm^3/s$) | Water permeability/channel (water molecules/s) |
|---|---|---|---|---|---|
| Blank | 6.47 | 19.48 | 0.00 | - | - |
| **1S** | 9.51 | 30.24 | 10.75 | - | - |
| **1R** | 9.05 | 28.77 | 9.28 | - | - |
| **2S** | 11.13 | 35.39 | 15.91 | - | - |
| **2R** | 10.57 | 33.62 | 14.13 | - | - |
| **3S** | 12.77 | 40.60 | 21.11 | - | - |
| **3R** | 11.67 | 37.12 | 17.63 | - | - |
| **4S** | 19.58 | 62.27 | 42.78 | $1.51 \times 10^{-14}$ | $5.05 \times 10^{8}$ |
| **4R** | 18.29 | 58.17 | 38.68 | $1.34 \times 10^{-14}$ | $4.48 \times 10^{8}$ |

## 5.4.8. Ion Transport Studies[37]

### 5.4.8.1. Cation Transport Studies in HPTS Assay

**HEPES Buffer, HPTS Solution, and Stock Solution Preparation for Assay**

We have prepared a buffer solution using autoclaved water of 10 mM HEPES (pH 7.0) and this buffer was used to prepare a salt solution of strength 200 mM of $M_2SO_4$ ($M^+$ = $Na^+$ and $K^+$). Initially, the pH of the buffer solution was below 7 and to make the pH at around 7, the required amount of MOH (0.5 Molar, $M^+$ = $Na^+$ and $K^+$) solution was added. Then HPTS solution of 1 mM was prepared from solid HPTS using the above-mentioned HEPES buffer solution

(without salt). The stock solution of the transporter for the HPTS assay was prepared using HPLC grade DMSO.

**Vesicles Preparation for Cation Transport Assay**

At first, 1.0 mL of EYPC lipid solution (25 mg/mL in chloroform) was taken in a 10 mL round-bottomed flask. The chloroform present in the lipid solution was then evaporated by a slow stream of nitrogen gas while rotating the round-bottomed flask to get a thin film of lipid inside it. Then the trace amount of chloroform present in the lipid was evaporated by drying it in a high vacuum for about 8 h. The thin film of lipid was hydrated with HPTS solution (1.0 mM HPTS, 10 mM HEPES, pH 7.0) while vortexing 4-5 times over the period of 1 h. Then the hydrated vesicles suspension was subjected to 15 freeze-thaw cycles, and extrusions were done 19 times (must be an odd number) using a 100 nm polycarbonate membrane. The extravesicular dye was separated from vesicles by size exclusion column chromatography (using Sephadex G-50 gel) eluting with buffer solution (10 mM HEPES, pH 7). After collecting, the vesicles from the column were diluted to 6 mL using buffer (10 mM HEPES, pH 7.0) to get the concentration of ~ 5.5 mM of EYPC-LUVs⊃HPTS, assuming no loss of lipid throughout the process. The vesicles compositions, inside: 1 mM HPTS, 10 mM HEPES, pH 7.0 and outside: 10 mM HEPES, pH 7.0.

**Description of Cation Transport Study**

In a clean cuvette, 1975 µL of buffer solution (10 mM HEPES, 200 mM of $M_2SO_4$ ($M^+ = Na^+$ and $K^+$), pH 7.0), 25 µL of HPTS trapped vesicles solution were taken and placed in a fluorescence instrument equipped with a magnetic stirrer. The fluorescence emission intensity of the HPTS dye, $I_t$ was measured at $\lambda_{em}$ = 510 nm (where, $\lambda_{ex}$ = 450 nm) for 350 s. For each reading, the start time of the instrument was considered as $t$ = 0 s. Then at $t$ = 20 s, 20 µL of 0.5 M NaOH solution was added to the same cuvette to generate a pH gradient (ΔpH = 0.8) between intra and extra vesicular medium. Then 20 µL solution of transporters in DMSO of different concentrations were added at $t$ = 100 s. At $t$ = 300 s, 10% triton X-100 (25 µL) was added to destroy all the vesicles to destruct the pH gradient.

The fractional emission intensity (in percentage), $I_F$ (Figure 5.15B) was calculated after normalizing all the data using the following equation (Equation 6).

$$\% \text{ of } I_F = (I_t - I_0) / (I_\infty - I_0) \times 100 \qquad \text{Equation 6}$$

where, $I_0$ is the initial fluorescence intensity *i.e.*, before the addition of the transporter compound, $I_t$ is the fluorescence intensity at time $t$ and $I_\infty$ is the final fluorescence intensity *i.e.*, after the addition of Triton X-100.

Before plotting the data, the time axis was normalized using the following equation:

$$t = t - 100 \qquad \text{Equation 7}$$

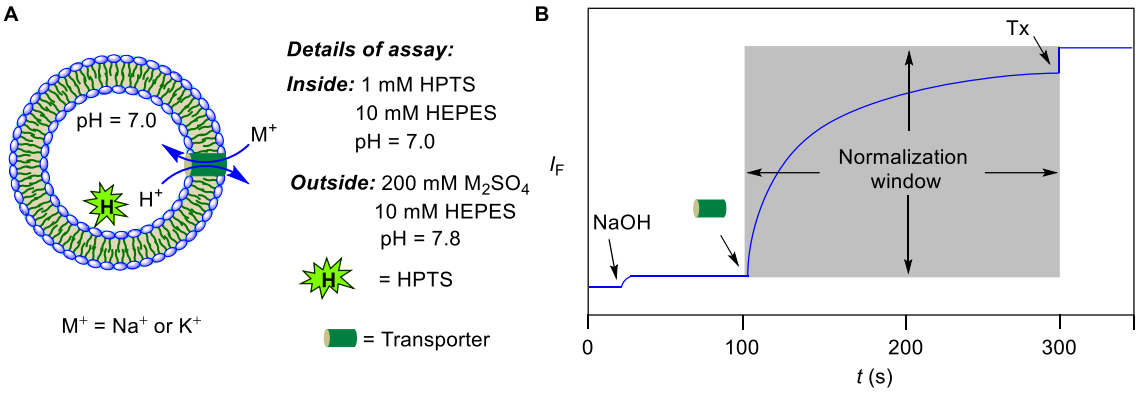



**Figure 5.15** Schematic representation of fluorescence kinetics assay for checking cation transport activity across EYPC-LUVs⊃HPTS (**A**), and normalized working window for the same experiment (**B**).

### 5.4.8.2. Proton and Anion Transport Studies in HPTS Assay

**HEPES Buffer, HPTS Solution and Stock Solution Preparation for Assay**:

We have prepared a buffer solution using autoclaved water of 10 mM HEPES (pH 7.0) and this buffer was used to prepare a salt solution of strength 100 mM of NaCl and 66 mM of $Na_2SO_4$. Initially, the pH of the buffer solution was below 7.0, and to make the pH at around 7.0, the required amount of NaOH (0.5 M) solution was added. Then HPTS solution of 1.0 mM was prepared from solid HPTS using the above-mentioned HEPES buffer solution (100 mM of NaCl). The stock solution of the transporter for the HPTS assay was prepared using HPLC grade DMSO.

**Vesicles Preparation for Proton and Anion Transport Assay**

At first, 1 mL of EYPC lipid solution (25 mg/mL in chloroform) was taken in a 10 mL round-bottomed flask. The chloroform present in the lipid solution was then evaporated by a slow stream of nitrogen gas while rotating the round-bottomed flask to get a thin film of lipid inside it. Then the trace amount of chloroform present in the lipid was evaporated by drying it in a high vacuum for about 8 h. The thin film of lipid was hydrated with HPTS solution (1.0 mM

HPTS, 100 mM NaCl, 10 mM HEPES, pH 7.0) while vortexing 4-5 times over the period of 1 h. Then the hydrated vesicles suspension was subjected to 15 freeze-thaw cycles, and extrusions were done 19 times (must be an odd number) using a 100 nm polycarbonate membrane. The extravesicular dye was separated from vesicles by size exclusion column chromatography (using Sephadex G-50 gel) eluting with buffer solution (10 mM HEPES, 100 mM NaCl, pH 7.0). After collecting, the vesicles from the column were diluted to 6 mL using the buffer as mentioned above (10 mM HEPES, 100 mM NaCl, pH 7) to get the concentration of ~ 5.5 mM of EYPC-LUVs⊃HPTS, assuming no loss of lipid throughout the process. The vesicles compositions, inside: 1.0 mM HPTS, 10 mM HEPES, 100 mM NaCl, pH 7.0 and outside: 10 mM HEPES, 100 mM NaCl, pH 7.0.

**Description of Proton and Anion Transport Study**

In a clean cuvette, 1975 µL of buffer solution (10 mM HEPES, 66 mM of $Na_2SO_4$, pH 7.0), 25 µL of HPTS trapped vesicles solution were taken and placed in a fluorescence instrument equipped with a magnetic stirrer. The fluorescence emission intensity of the HPTS dye, $I_t$ was measured at $\lambda_{em}$ = 510 nm (where $\lambda_{ex}$ = 450 nm) for 350 s. For each reading, the start time of the instrument was considered as $t$ = 0 s. Then at $t$ = 20 s, 20 µL of 0.5 M NaOH solution was added to the same cuvette to generate a pH gradient (ΔpH = 0.8) between intravesicular and extravesicular media. Then 20 µL solution of transporters in DMSO of different concentrations were added at $t$ = 100 s. At $t$ = 300 s, 10% Triton X-100 (25 µL) was added to destroy all the vesicles to destruct the pH gradient.

The fractional emission intensity (in percentage), $I_F$ (Figure 5.16B) was calculated after normalizing all the data using the following equation (Equation 8).

$$\% \text{ of } I_F = (I_t - I_0) / (I_\infty - I_0) \times 100 \qquad \text{Equation 8}$$

where, $I_0$ is the initial fluorescence intensity, *i.e.,* before the addition of the transporter compound, $I_t$ is the fluorescence intensity at time $t$, and $I_\infty$ is the final fluorescence intensity, *i.e.,* after the addition of Triton X-100.

Before plotting the data, the time axis was normalized using the following equation:

$$t = t - 100 \qquad \text{Equation 9}$$

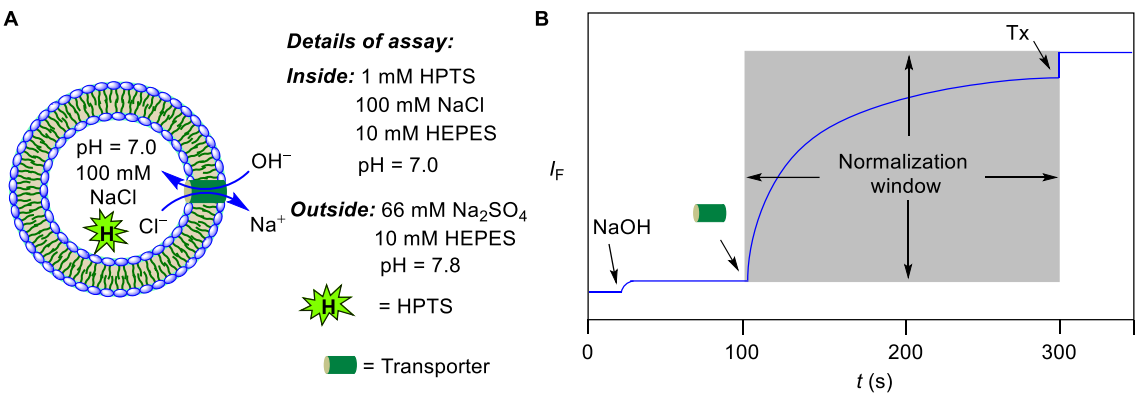



**Figure 5.16** Schematic representation of fluorescence kinetics assay for checking proton and anion transport activity across EYPC-LUVs⊃HPTS (**A**), and normalized working window for the same experiment (**B**).

### 5.4.8.3. Lucigenin Assay for Checking $Cl^-$ Transport Activity

#### Salt and Stock Solution Preparation for Lucigenin Assay

We have prepared a 225 mM $NaNO_3$ salt solution using autoclaved water. Then 1.0 mM Lucigenin solution was prepared using the 225 mM $NaNO_3$ solution. The stock solution of the transporter for the Lucigenin assay was prepared from a solid compound by using HPLC grade $CH_3CN$ : $CH_3OH$ (10 : 1) solution.

#### Vesicles Preparation Procedure for Lucigenin Assay

At first, 1.0 mL of EYPC lipid solution (25 mg/mL in chloroform) was taken in a 10 mL round-bottomed flask. The chloroform present in the lipid solution was then evaporated by a slow stream of nitrogen gas while rotating the round-bottomed flask to get a thin film of lipid inside it. Then the last trace amount of chloroform present in the lipid was evaporated by drying it in a high vacuum for about 8 h. The thin film of lipid was hydrated with 1 mL of Lucigenin solution (1.0 mM Lucigenin, 225 mM $NaNO_3$) while vortexing 4-5 times for 2 min with a time interval of 10 min. Then the hydrated vesicles suspension was subjected to 15 freeze-thaw cycles, and extrusions were done 19 times (must be an odd number) using a 200 nm polycarbonate membrane. The extravesicular dye was separated from vesicles by size exclusion column chromatography (using Sephadex G-50 gel) eluting with $NaNO_3$ solution (225 mM). After collecting, the vesicles from the column were diluted to 4 mL using the buffer as mentioned above (225 mM $NaNO_3$) to get the concentration of ~8 mM of EYPC-LUVs⊃Lucigenin, assuming no loss of lipid throughout the process. The vesicles compositions, inside: 1.0 mM Lucigenin, 225 mM $NaNO_3$ and outside: 225 mM $NaNO_3$.

**Description of Lucigenin Assay**

In a clean cuvette, 1950 µL of salt solution (225 mM $NaNO_3$), 50 µL of lucigenin trapped vesicles solution were taken and placed in a fluorescence instrument equipped with a magnetic stirrer. The fluorescence emission intensity of the Lucigenin dye, $I_t$ was measured at $\lambda_{em}$ = 535 nm (where $\lambda_{ex}$ = 455 nm) for 350 s. For each reading, the start time of the instrument was considered as $t$ = 0 s. Then at $t$ = 50 s, 33 µL of 2N NaCl solution was added to the cuvette for generating a $Cl^-$ concentration gradient across the lipid bilayer. Then 20 µL solution of transporters in ACN : MeOH (6 : 1) solvent of different concentrations were added at $t$ = 100 s. At $t$ = 300 s, 10% Triton X-100 (25 µL) was added to destroy all the vesicles to destruct the $Cl^-$ concentration gradient.

The fractional emission intensity (in percentage), $I_F$ (Figure 5.17B) was calculated after normalizing all the data using the following equation (Equation 10).

$$\% \text{ of } I_F = (I_t - I_0) / (I_\infty - I_0) \times (-100) \qquad \text{Equation 10}$$

where, $I_0$ is the initial fluorescence intensity, *i.e.*, just before the addition of the transporter solution, $I_t$ is the fluorescence intensity at time $t$, and $I_\infty$ is the final fluorescence intensity, *i.e.*, after the addition of Triton X-100.

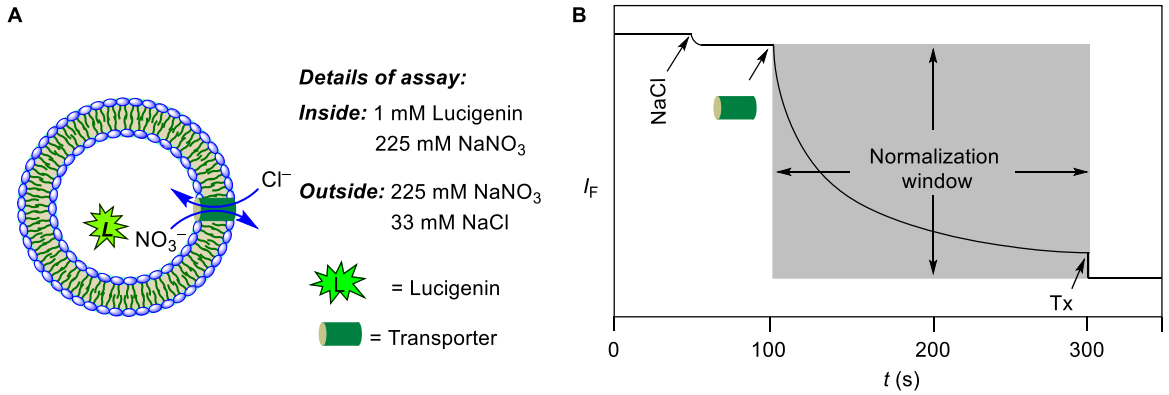



**Figure 5.17** Schematic representation of fluorescence kinetics assay for checking $Cl^-$ ion transport selectivity across EYPC-LUVs⊃Lucigenin (A), and normalized working window for the same experiment (B).

Before plotting the data, the time axis was normalized using Equation 9,

### 5.4.8.4. Carboxyfluorescein (CF) Leakage Assay

**Vesicles Preparation for CF Leakage Assay**[58]

At first, 0.5 mL of EYPC lipid solution (25 mg/mL in chloroform) was taken in a 10 mL round-bottomed flask. The chloroform present in the lipid solution was then evaporated by a slow stream of nitrogen gas while rotating the round-bottomed flask to get a thin film of lipid inside it. Then the trace amount of chloroform present in the lipid was evaporated by drying it in a high vacuum for about 8 h. The thin film of lipid was hydrated with CF solution (50 mM CF, 10 mM NaCl, 10 mM HEPES, pH 7.0) while vortexing 4-5 times over the period of 1 h. Then the hydrated vesicles suspension was subjected to 15 freeze-thaw cycles and extrusions were done 19 times (must be an odd number) using a 200 nm polycarbonate membrane. The extravesicular dye was separated from vesicles by size exclusion column chromatography (using Sephadex G-50 gel) eluting with buffer solution (10 mM HEPES, 100 mM NaCl, pH 7). After collecting, the vesicles from the column were diluted to 3 mL using buffer (10 mM HEPES, 100 mM NaCl, pH 7) to get the concentration of ~ 5.5 mM of EYPC-LUVs⊃CF, assuming no loss of lipid throughout the process. The vesicles compositions, inside: 50 mM CF, 10 mM HEPES, 10 mM NaCl, pH 7.0 and outside: 10 mM HEPES, 100 mM NaCl, pH 7.0.

**Description of CF Leakage Assay**

In a clean cuvette, 1975 µL of buffer solution (10 mM HEPES, 100 mM NaCl, pH 7.0), 25 µL of CF trapped vesicles solution were taken and placed in a fluorescence instrument equipped with a magnetic stirrer. The fluorescence emission intensity of the CF dye, $I_t$ was measured at $\lambda_{em}$ = 517 nm (where, $\lambda_{ex}$ = 492 nm) for 350 s. For each reading, the start time of the instrument was considered as $t$ = 0 s. Then at $t$ = 50 s, 20 µL of channel molecule in DMSO of different concentrations were added at $t$ = 100 s. At $t$ = 250 s, 10% Triton X-100 (25 µL) was added to destroy all the vesicles to destruct the concentration gradient.

The fractional emission intensity (in percentage), $I_F$ was calculated after normalizing all the data using the following equation (Equation 11).

$$\% \text{ of } I_F = (I_t - I_0) / (I_\infty - I_0) \times 100 \qquad \text{Equation 11}$$

where, $I_0$ is the initial fluorescence intensity, *i.e.*, before the addition of the transporter compound, $I_t$ is the fluorescence intensity at time $t$ and $I_\infty$ is the final fluorescence intensity, *i.e.*, after the addition of Triton X-100.

### 5.4.9. MD Simulation Setup

The current experiments obtained the **4R** 2 × 8 layered synthetic channel atomistic coordinates from the crystal structure of **2R**. The coordinates of the 8-layered channel was initially minimized using MAESTRO (https://www.schrodinger.com/products/maestro), which was subsequently used for computer simulation of the membrane-constituted channel. We used the CHARMM-GUI Membrane builder[62] (https://www.charmmgui.org/?doc=input/membrane-.bilayer), an online webserver for assembling the channel inside a DOPC (1,2-Dioleoyl-sn-glycero-3-phosphocholine) phospholipid bilayer for subsequent MD simulation. The synthetic channel was modelled using the general AMBER force field (GAFF)[63-65] and the DOPC lipid parameters were obtained from the CHARMM36m force field.[66-68] Total 144 DOPC lipids were used to construct the bilayer by keeping 72 lipids in each of the upper and lower membrane leaflets. The salt concentration was maintained at 0.10 M by adding 12 atoms of $Na^+$ and 12 atoms of $Cl^-$ ions. The whole assembly was solvated by introducing a total of 7247 water molecules on both sides of the lipid bilayer. The water was modelled by TIP3P-charmm[69] water molecules. The total system size was 42853 particles and a rectangular box was used with dimensions 7.14 × 7.14 × 8.01 $nm^3$. The assembled system was minimized using the steepest-decent algorithm under restraints. Then the system was further subjected to restrained MD simulations in multiple stages and in each consecutive stage, the restraints were gradually reduced in each step. The temperature was set to 298.15 K and a Berendsen thermostat[70] was used during the equilibration. Initial random velocities were assigned to each atom, generated according to Maxwell-Boltzmann distribution of velocities at that temperature.

Finally, the production MD simulations were performed in an NPT ensemble using the leapfrog integrator with a 2-fs time step. The Verlet cutoff scheme[71] was employed throughout the simulation with the Lenard Jones interaction extending to 1.2 nm with dispersion corrections. The electrostatic interactions were implemented with a short-range electrostatic cutoff at 1.2 nm, and long-range interactions were treated by Particle Mesh Ewald summation[72] with cubic interpolation and in a Fourier-grid space of 0.16 nm. The neighbor lists were updated every 20 steps. All bond lengths involving hydrogen atoms of the lipids and the ligands were constrained using the LINCS algorithm[73] and water molecules were kept rigid using the SETTLE[74] approach. The average temperature is maintained at 298.15 K by coupling solute, membrane, and solvent separately to the Nose-Hoover thermostat[75] with a relaxation constant of 1.0 ps. The pressure was controlled at 1 bar by Parrinello-Rahman barostat[76] with a time constant of 5 ps and compressibility of 4.5 * 10 -5 bar with semi-isotropic coupling (XY and

Z directions coupled separately) to achieve tensionless bilayer. The system was periodic in all three directions. Two independent trajectories each of duration 0.9 microseconds were produced using GROMACS 2019 version.[77-78] The trajectory was saved at every 100 ps for the analysis.

The stability of the synthetic channel was ascertained by computing the Radius of gyration of the assembled structure and Root-mean-squared deviation (RMSD) from the crystal structure. The simulation trajectory was also analyzed via investigating the dynamical nature of water leakage and permeation event inside the membrane. Towards, we used an algorithm by Carlos et al.[79] For this purpose, the time profile of z-coordinate of each water molecule was individually tracked. A water molecule was considered to be 'leaked' if it has moved at least till the centre of the bilayer. Similarly, a successful permeation event of the water molecule is ascertained if the water molecule has completed a full pass from one of the leaflets to the other through the bilayer.

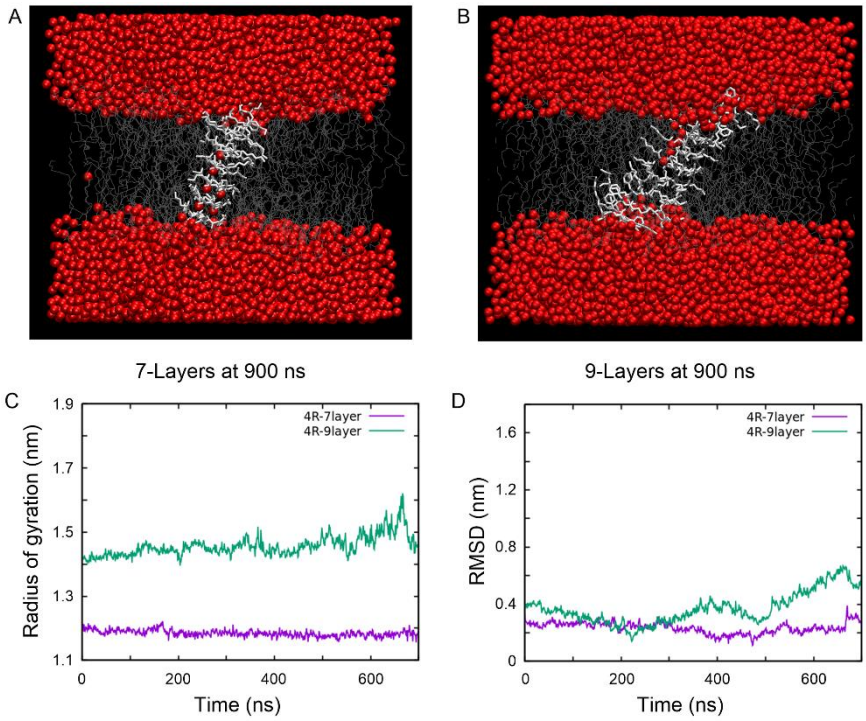



**Figure 5.18** Assessing the optimal number of layer: Simulated Snapshot of superstructure with 2 × 7 layers (a) and 2 × 8 layers (b) after 900 ns of MD simulation. Same colour code as used figure 5.4 has been used. Time profile of radius of gyration (c) and RMSD (d) for both these superstructures are also shown.

## 5.5. NMR spectra of Compounds

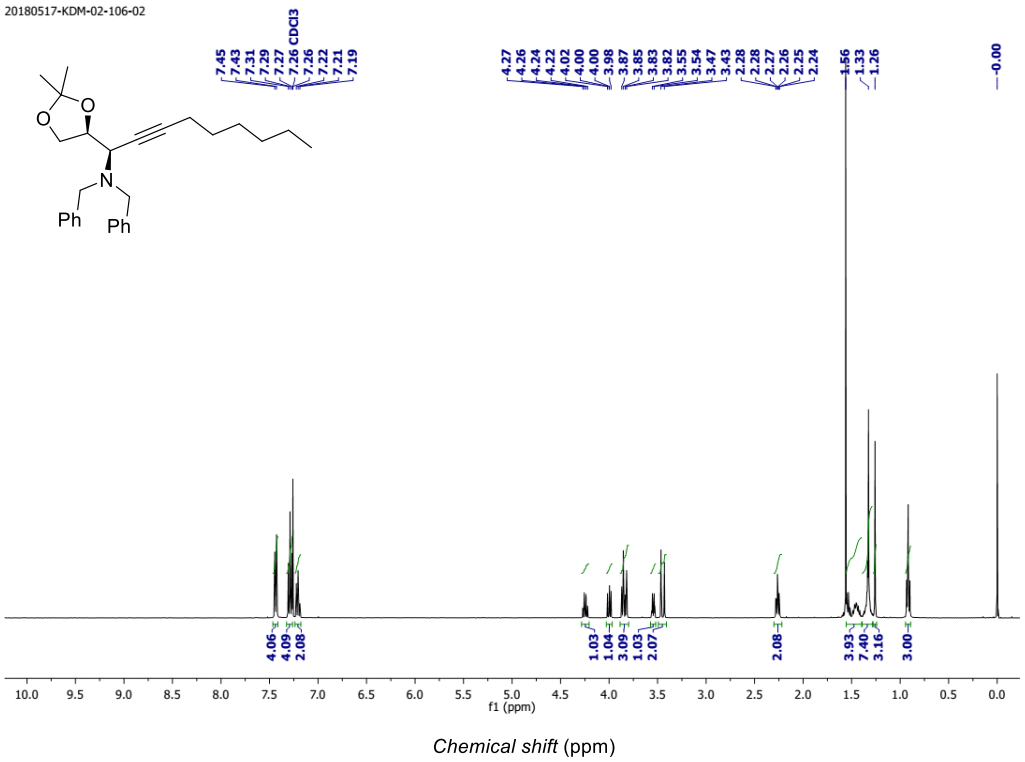



**Figure 5.19** $^{1}$H NMR spectrum of compound **12** in $CDCl_3$.

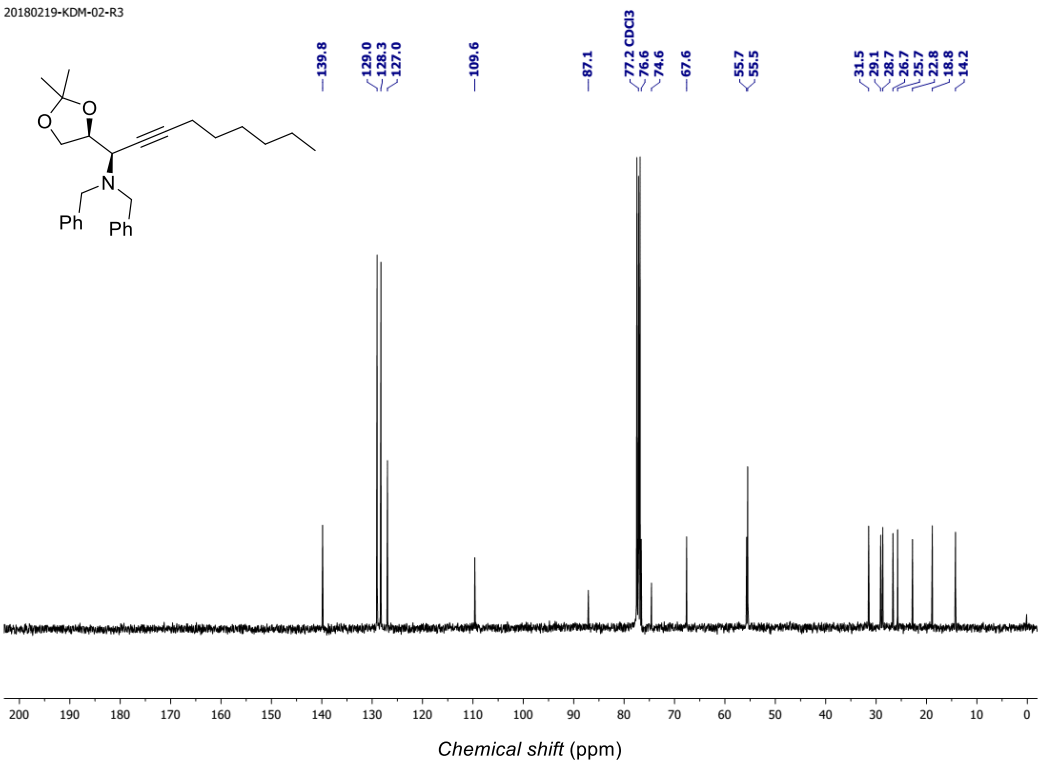



**Figure 5.20** $^{13}$C NMR spectrum of compound **12** in $CDCl_3$.

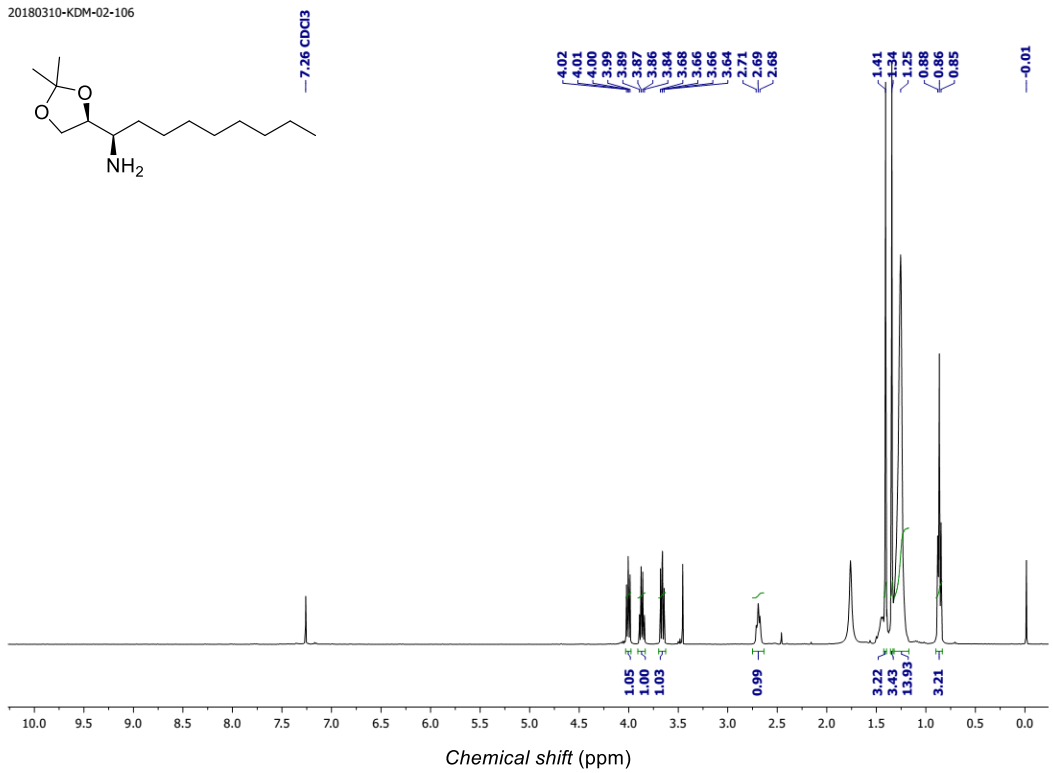



**Figure 5.21** $^{1}$H NMR spectrum of compound **13** in $CDCl_3$.

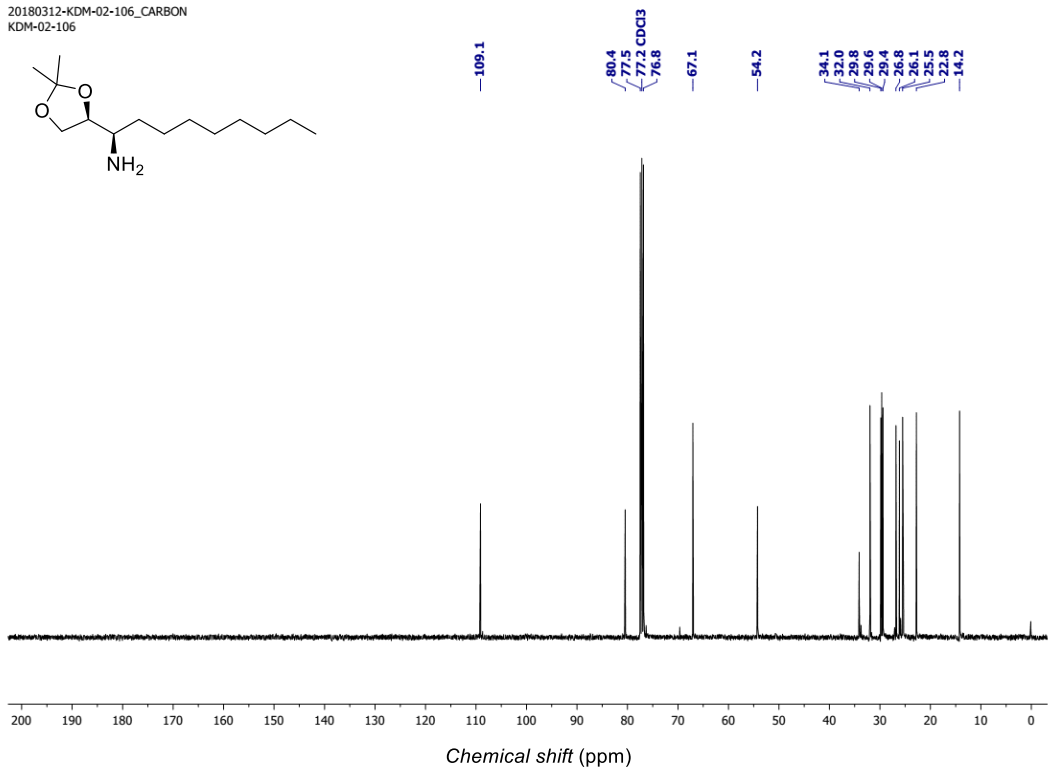



**Figure 5.22** $^{13}$C NMR spectrum of compound **13** in $CDCl_3$.

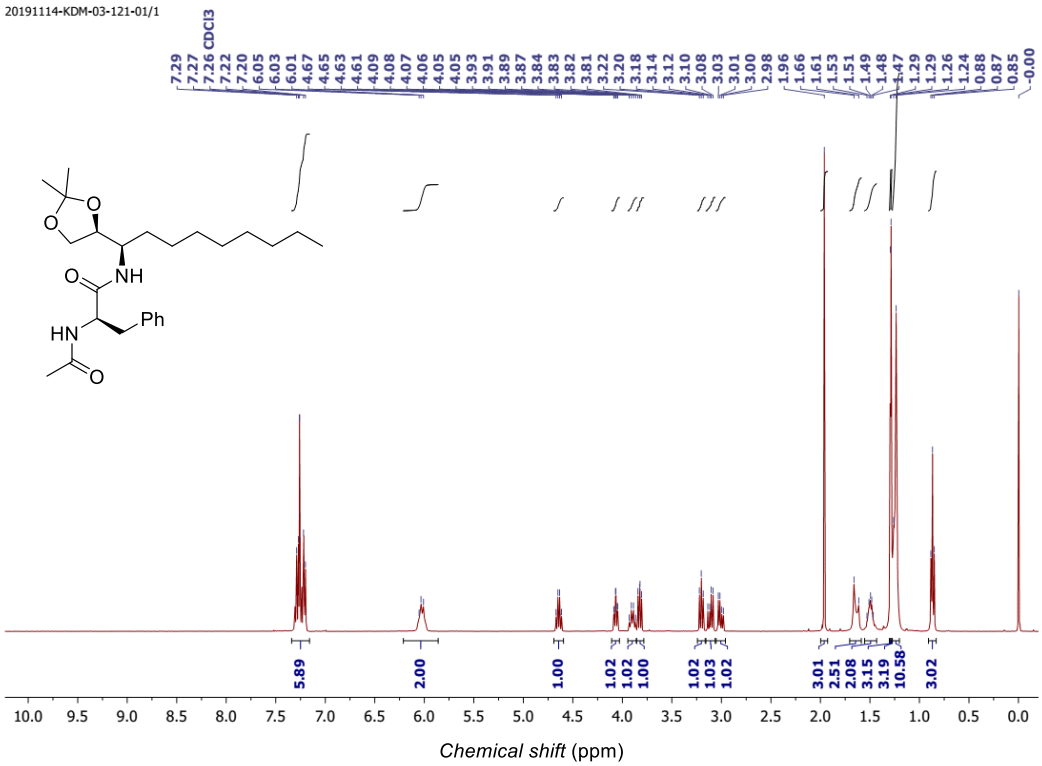



**Figure 5.23** $^{1}$H NMR spectrum of compound **14R** in $CDCl_3$.

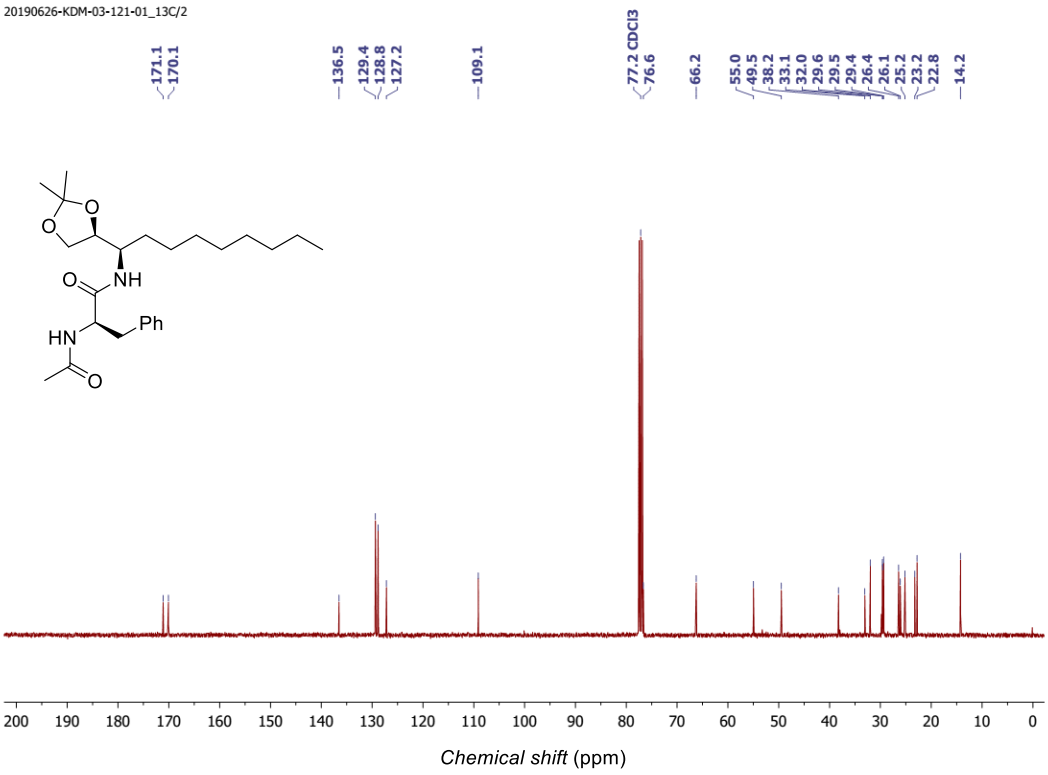



**Figure 5.24** $^{13}$C NMR spectrum of compound **14R** in $CDCl_3$.

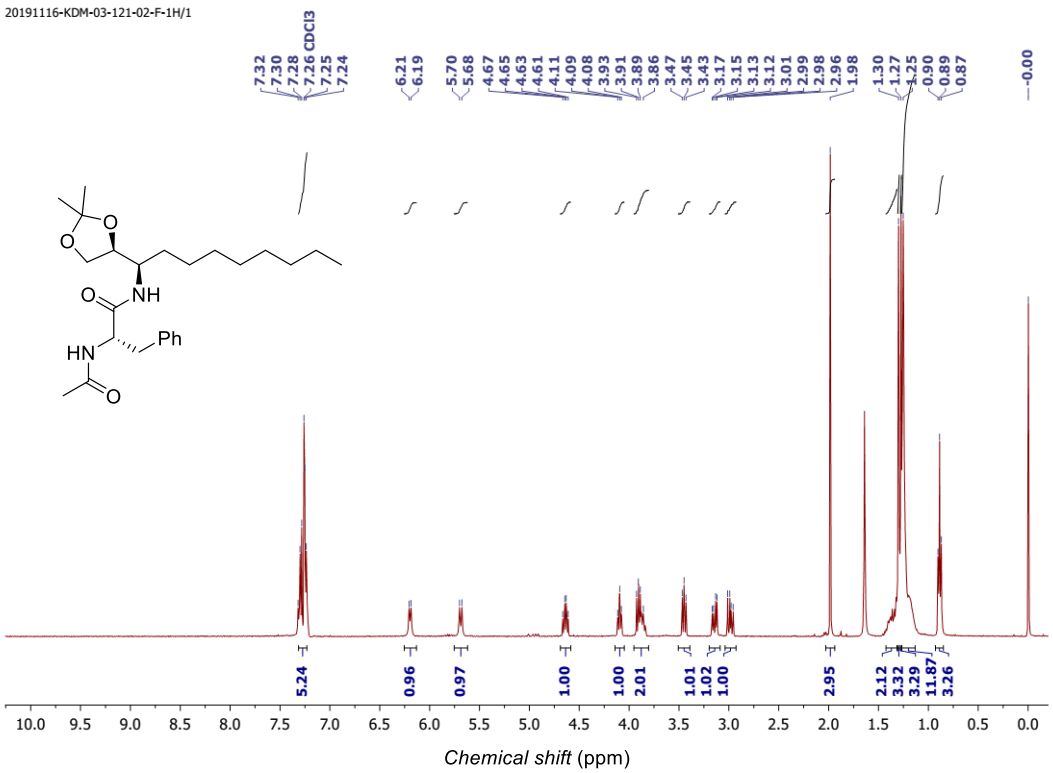



**Figure 5.25**. $^{1}$H NMR spectrum of compound **14S** in $CDCl_3$.

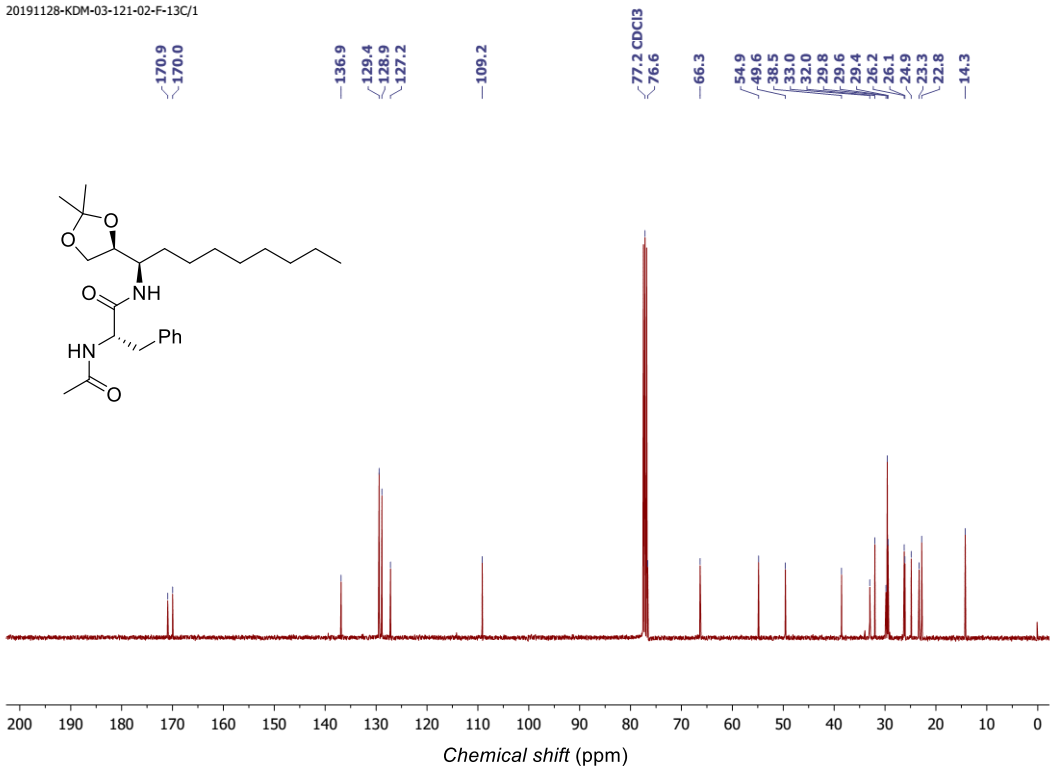



**Figure 5.26** $^{13}$C NMR spectrum of compound **14S** in $CDCl_3$.

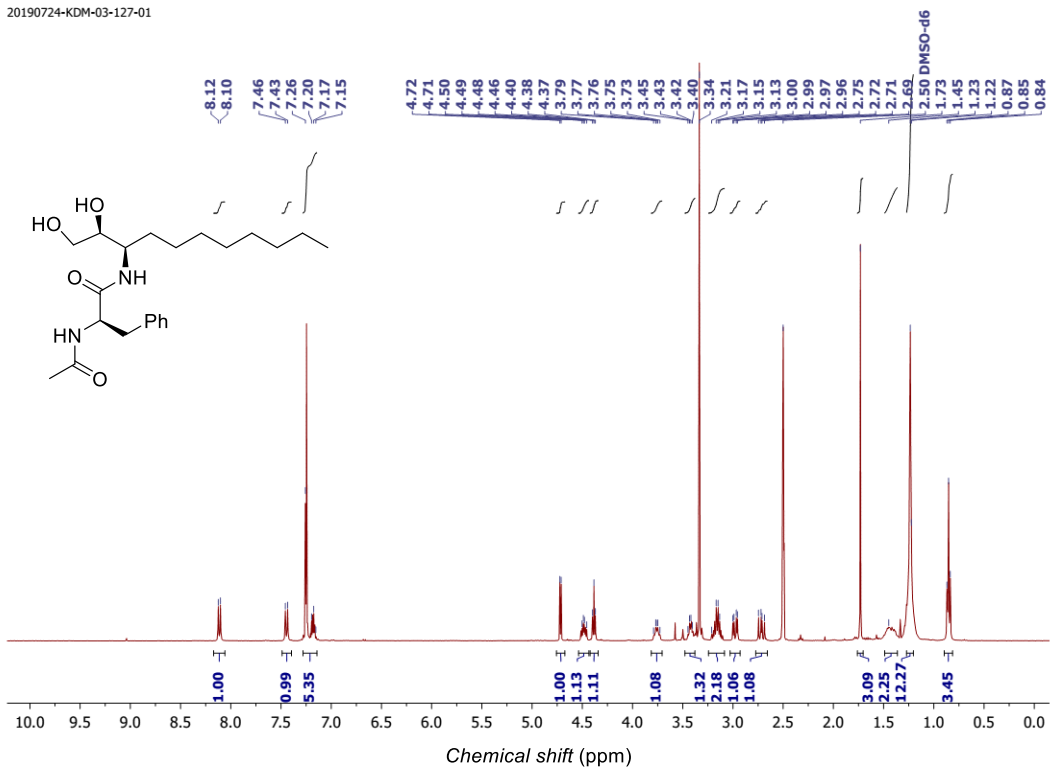



**Figure 5.27** $^{1}$H NMR spectrum of compound **1R** in DMSO-$d_6$.

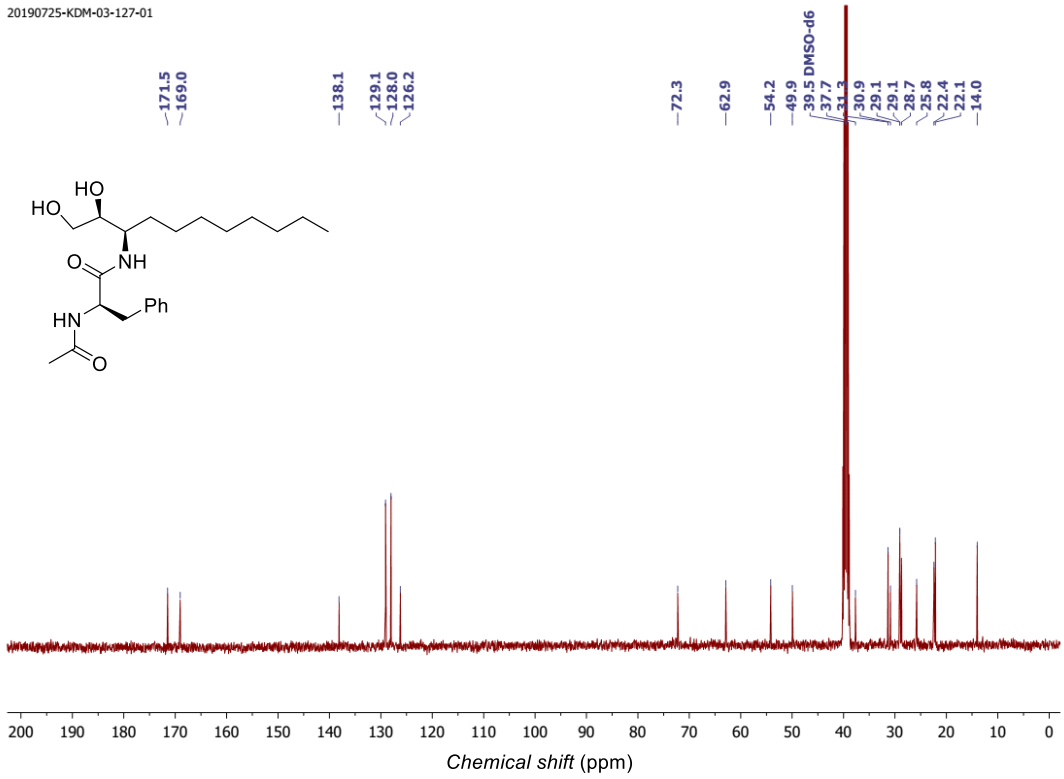



**Figure 5.28** $^{13}$C NMR spectrum of compound **1R** in DMSO-$d_6$.

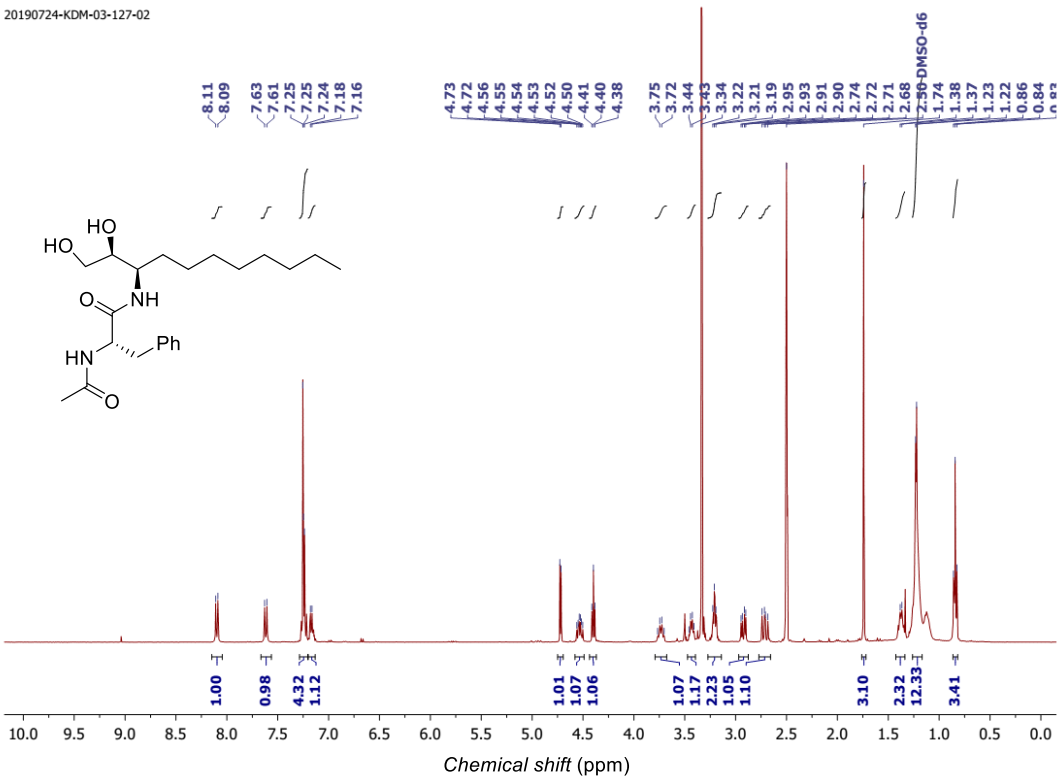



**Figure 5.29** $^{1}$H NMR spectrum of compound **1S** in DMSO-$d_6$.

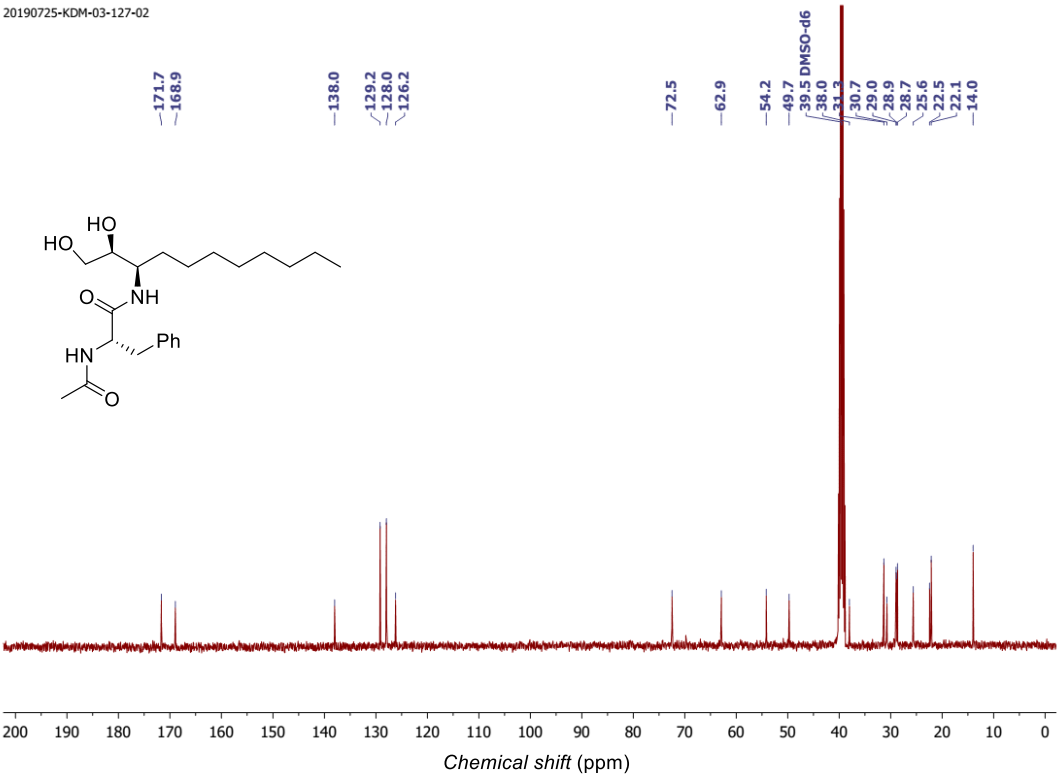



**Figure 5.30** $^{13}$C NMR spectrum of compound **1S** in DMSO-$d_6$.

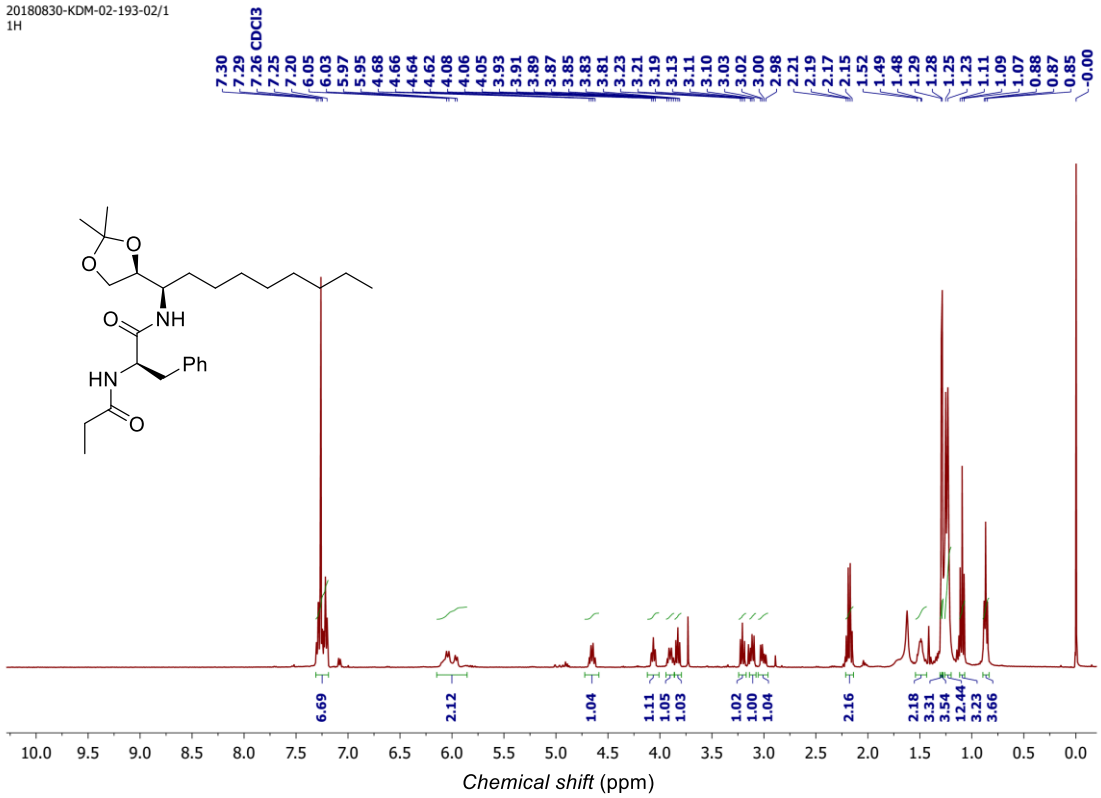



**Figure 5.31** $^{1}H$ NMR spectrum of compound **15R** in $CDCl_3$.

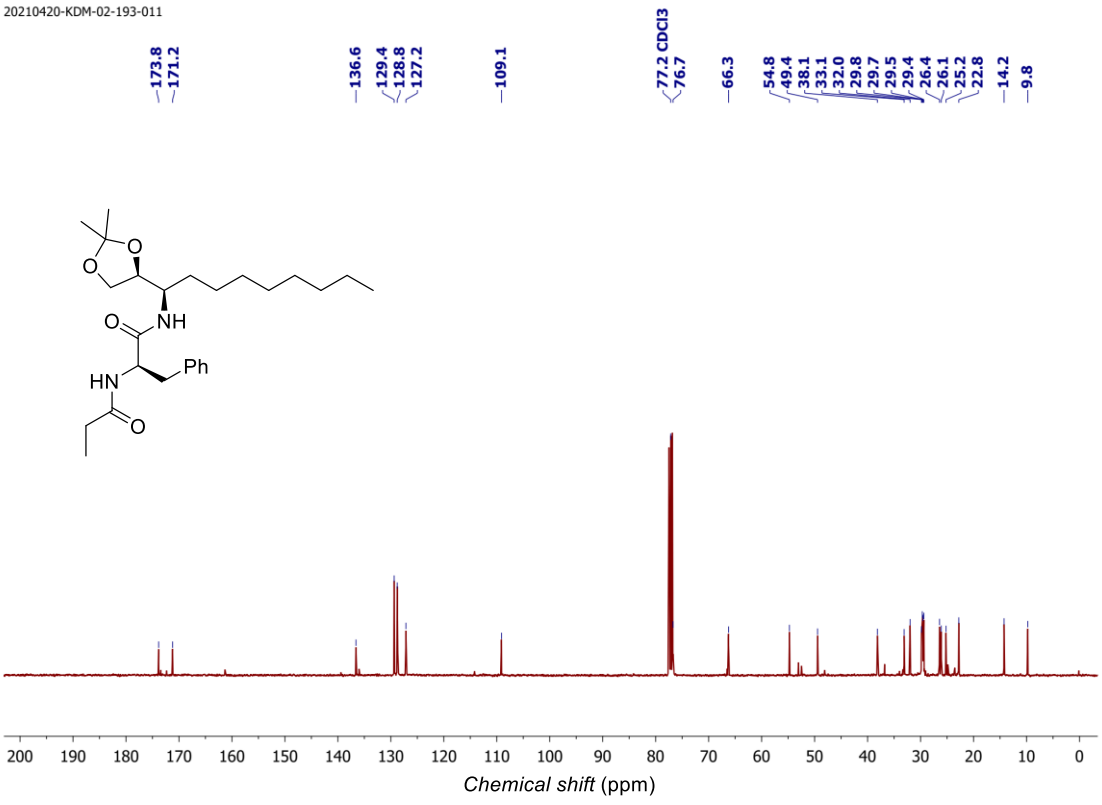



**Figure 5.32** $^{13}C$ NMR spectrum of compound **15R** in $CDCl_3$.

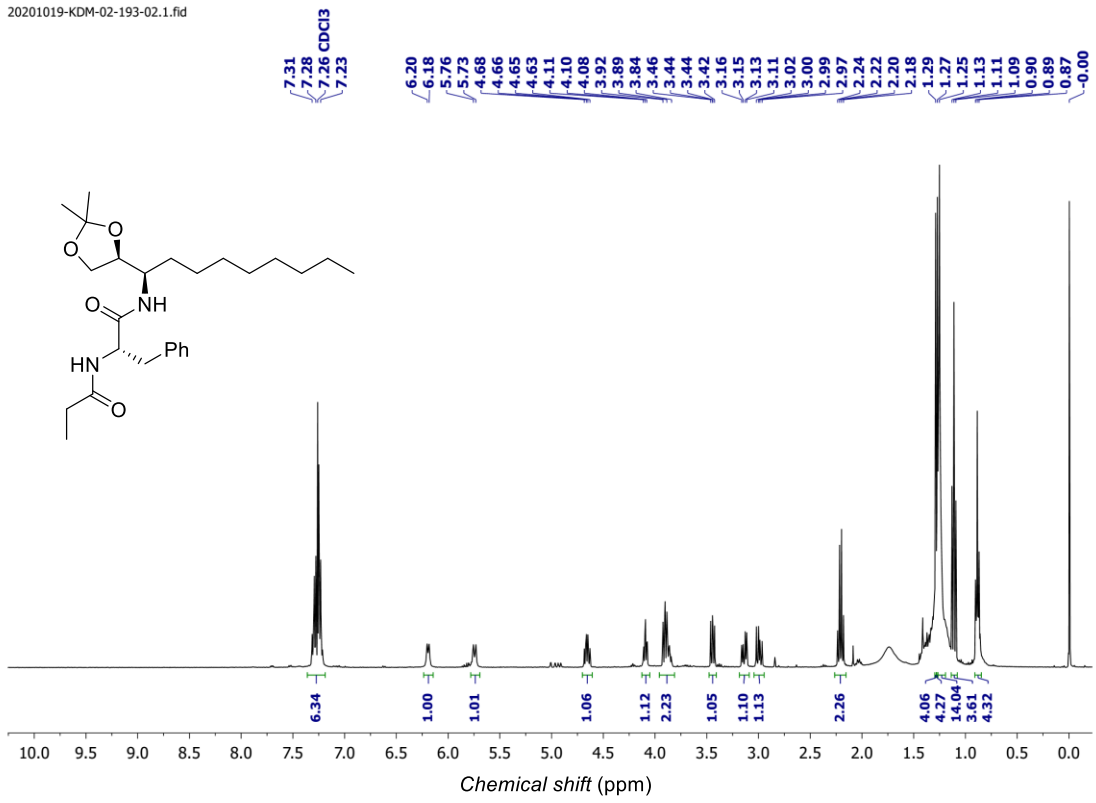



**Figure 5.33** $^{1}$H NMR spectrum of compound **15S** in $CDCl_3$.

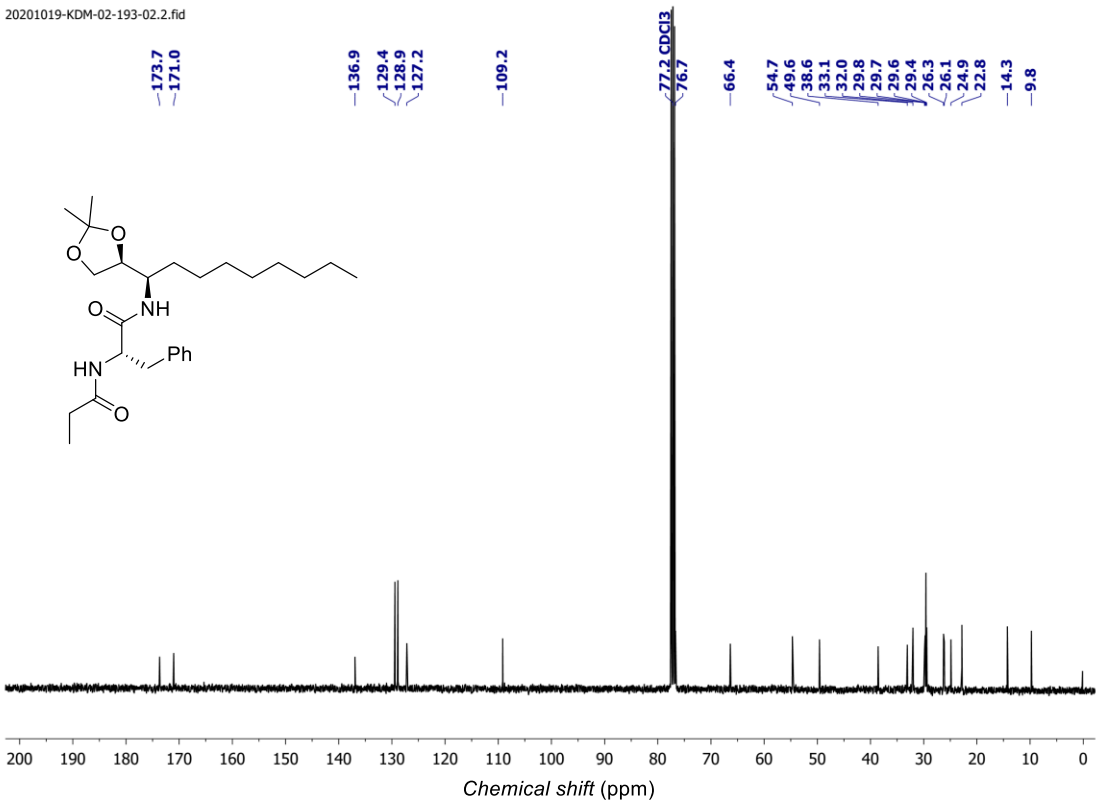



**Figure 5.34** $^{13}$C NMR spectrum of compound **15S** in $CDCl_3$.

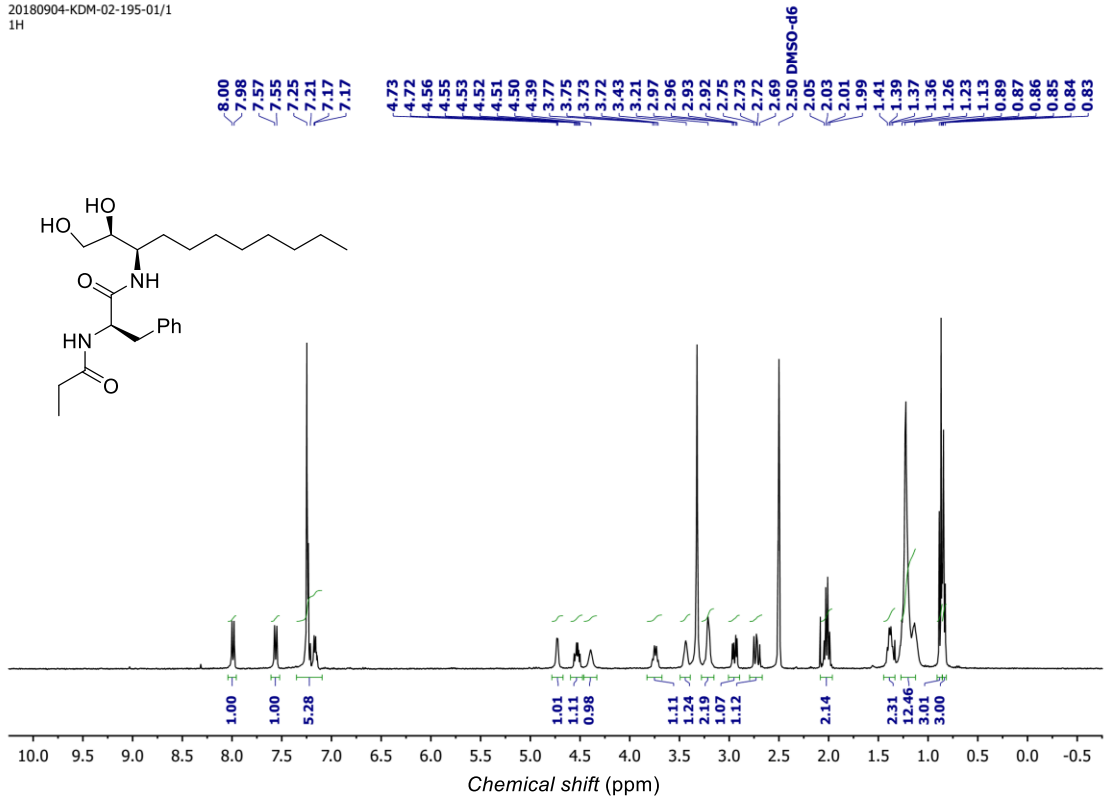



**Figure 5.35** $^{1}$H NMR spectrum of compound **2R** in DMSO-$d_6$.

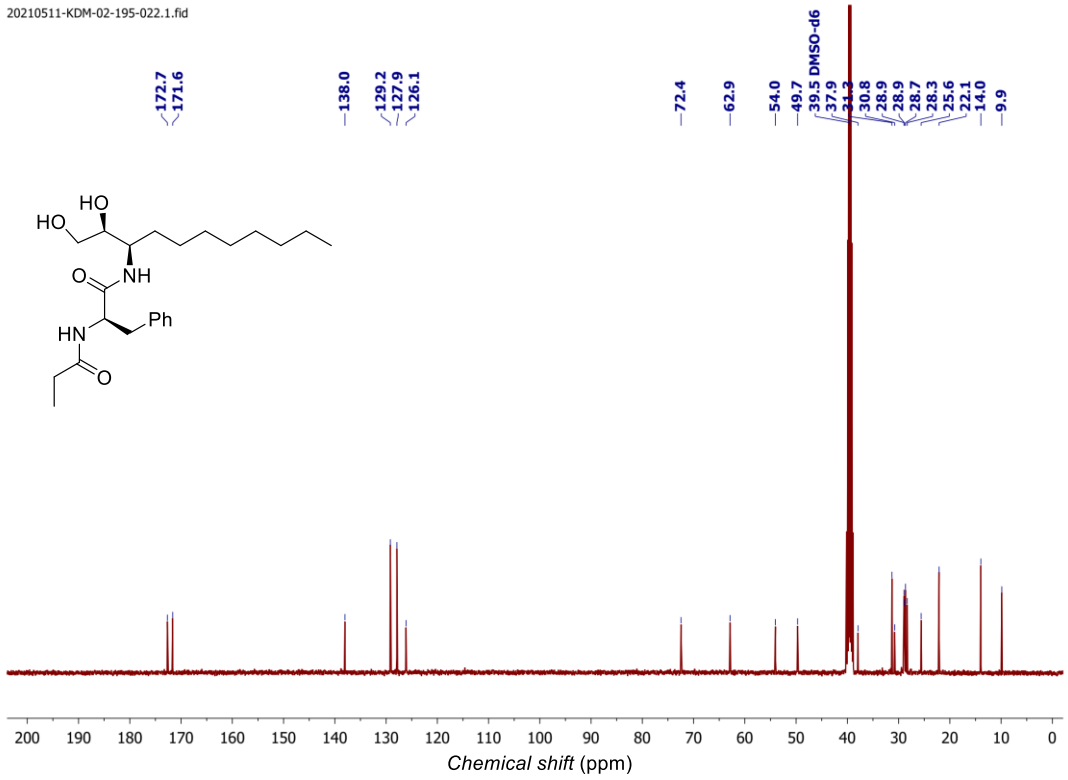



**Figure 5.36** $^{13}$C NMR spectrum of compound **2R** in DMSO-$d_6$.

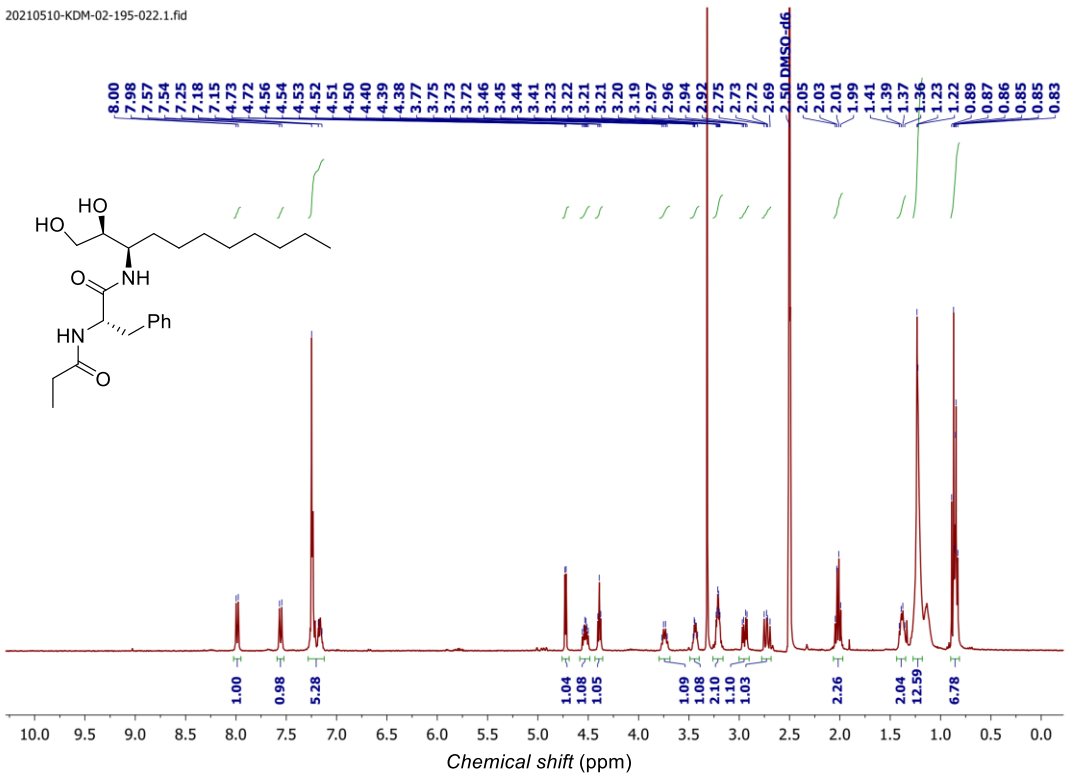



**Figure 5.37** $^{1}$H NMR spectrum of compound **2S** in DMSO-$d_6$.

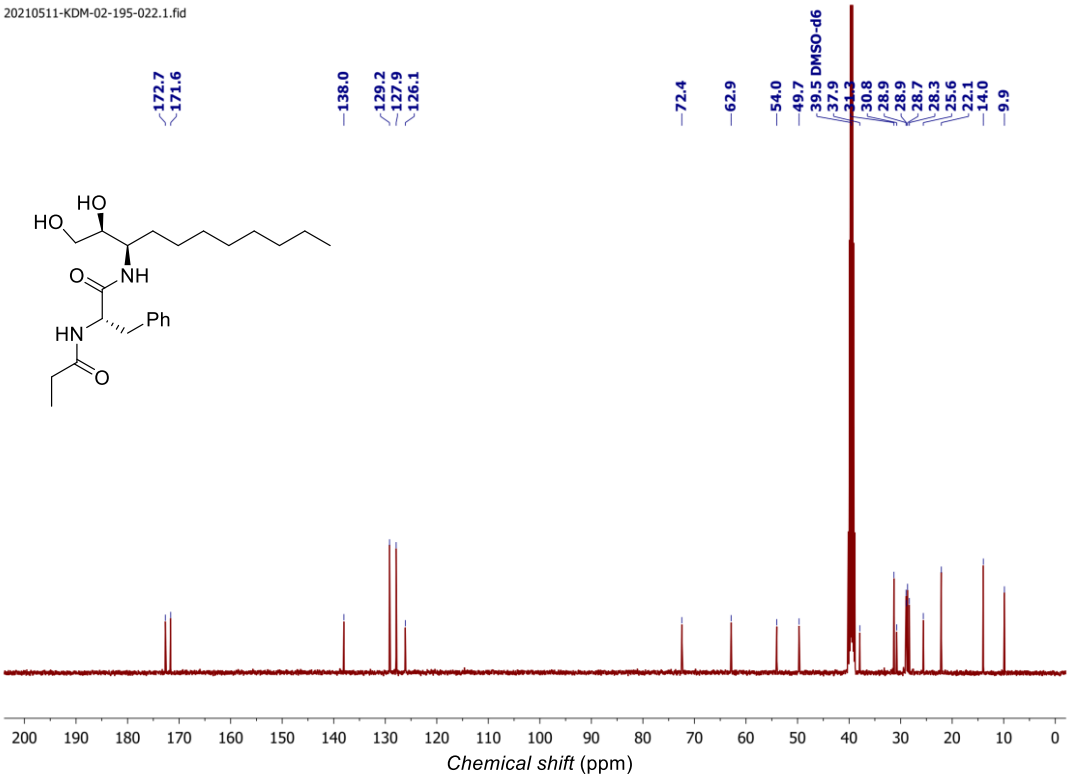



**Figure 5.38** $^{13}$C NMR spectrum of compound **2S** in DMSO-$d_6$.

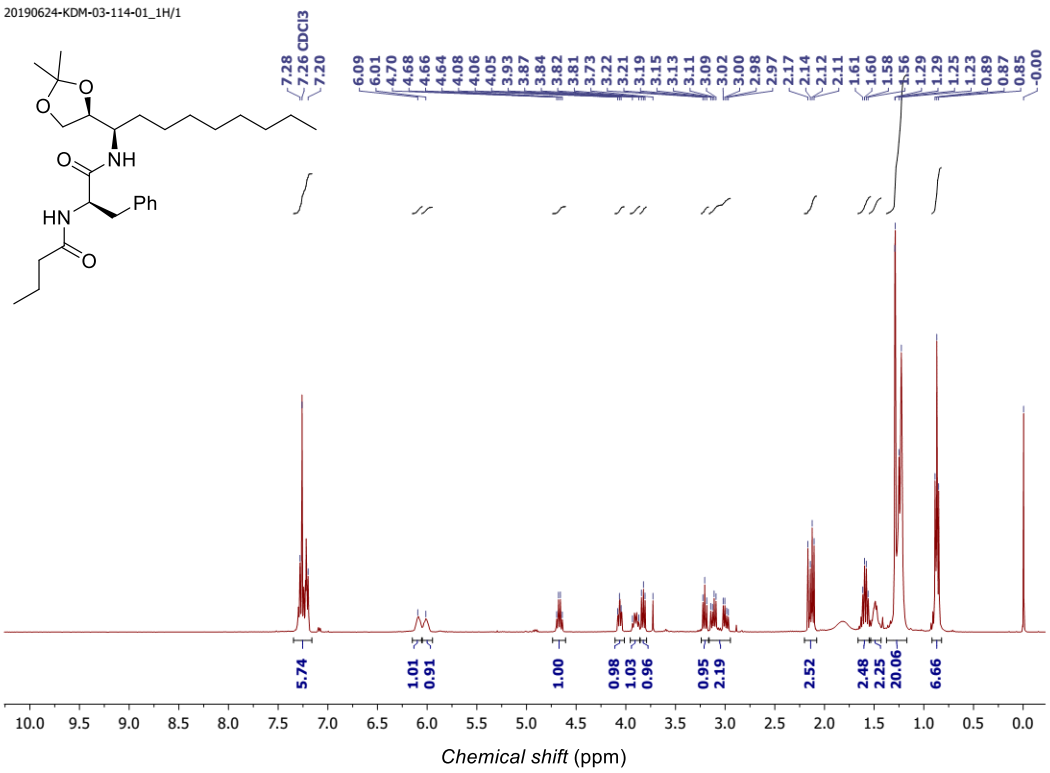



**Figure 5.39** $^{1}$H NMR spectrum of compound **16R** in $CDCl_3$.

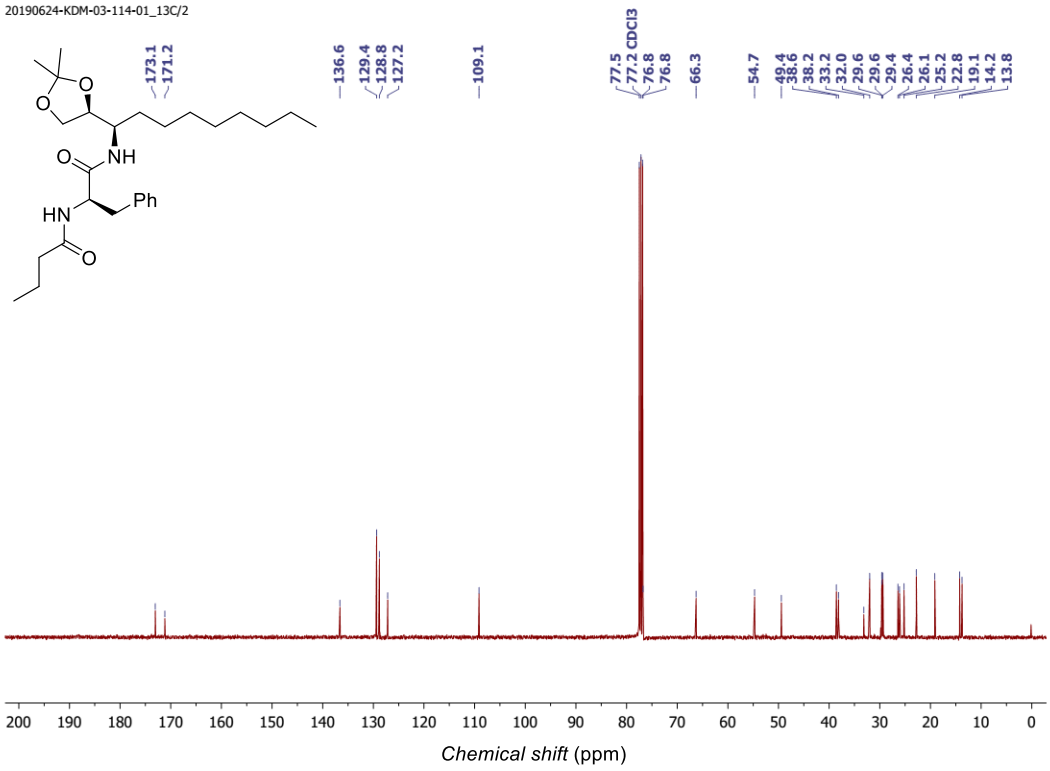



**Figure 5.40** $^{13}$C NMR spectrum of compound **16R** in $CDCl_3$.

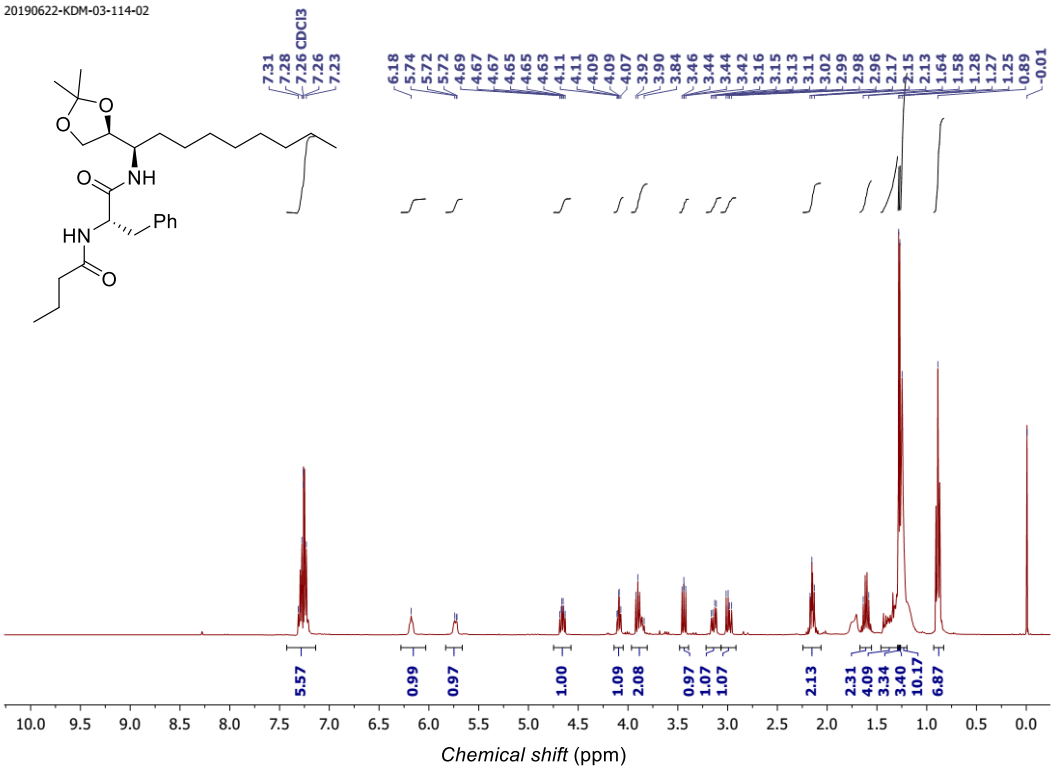



**Figure 5.41** $^{1}$H NMR spectrum of compound **16S** in $CDCl_3$.

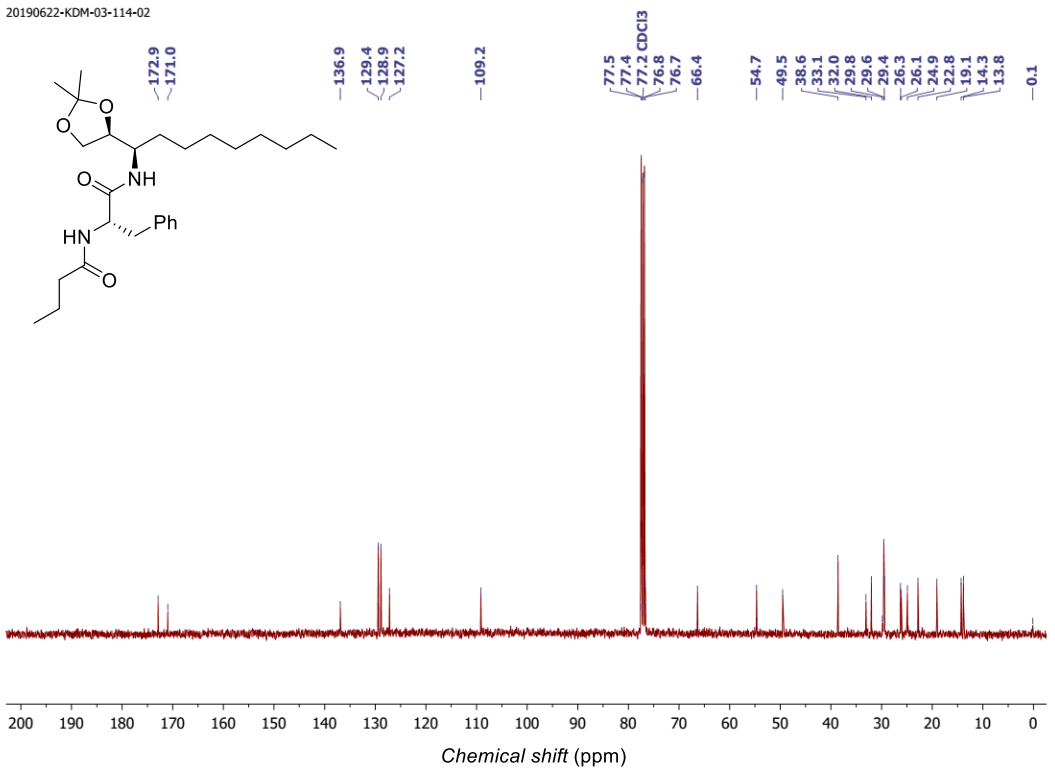



**Figure 5.42** $^{13}$C NMR spectrum of compound **16S** in $CDCl_3$.

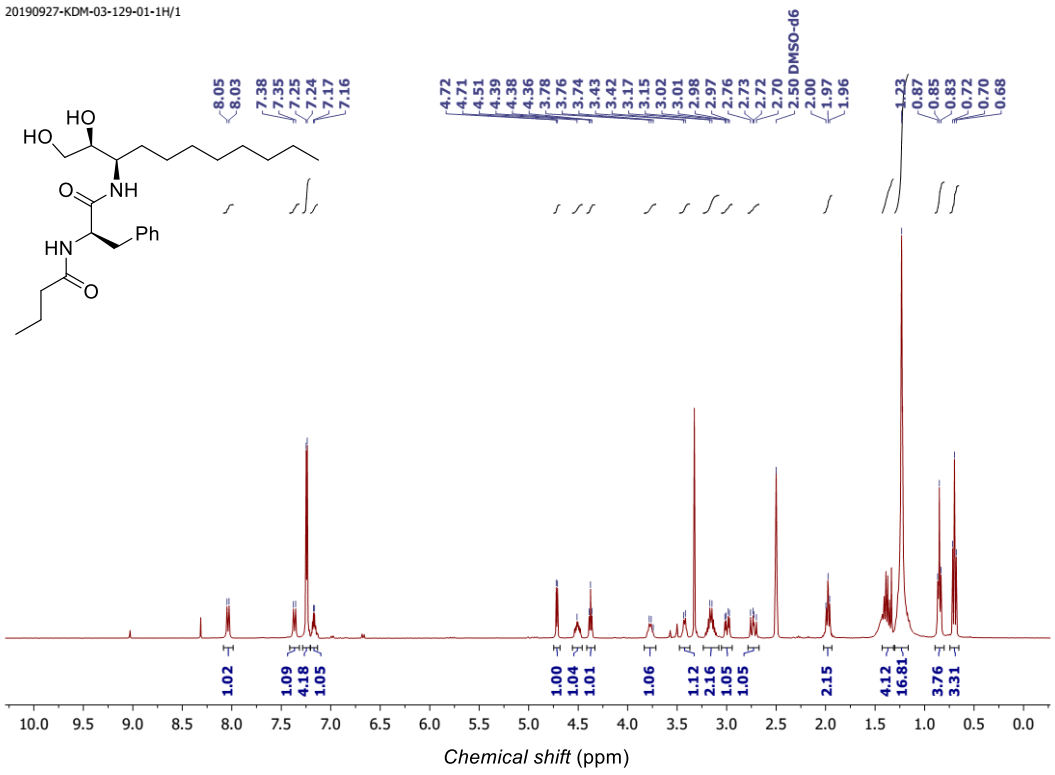



**Figure 5.43** $^{1}$H NMR spectrum of compound **3R** in DMSO-$d_6$.

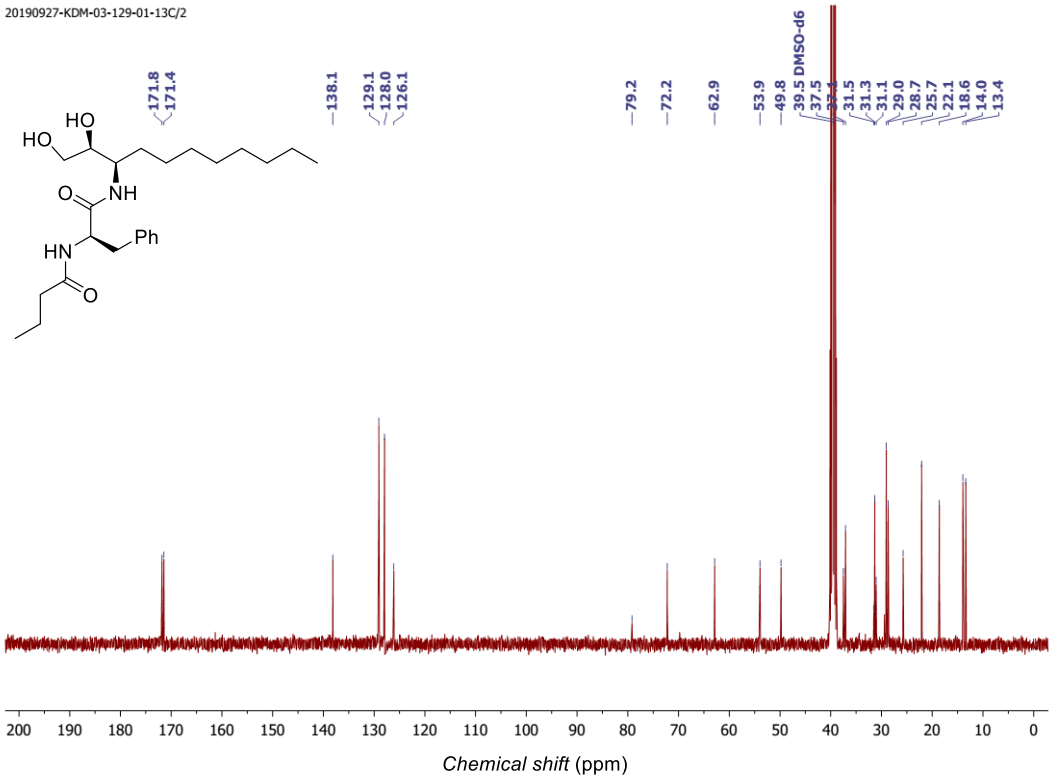



**Figure 5.44** $^{13}$C NMR spectrum of compound **3R** in DMSO-$d_6$.

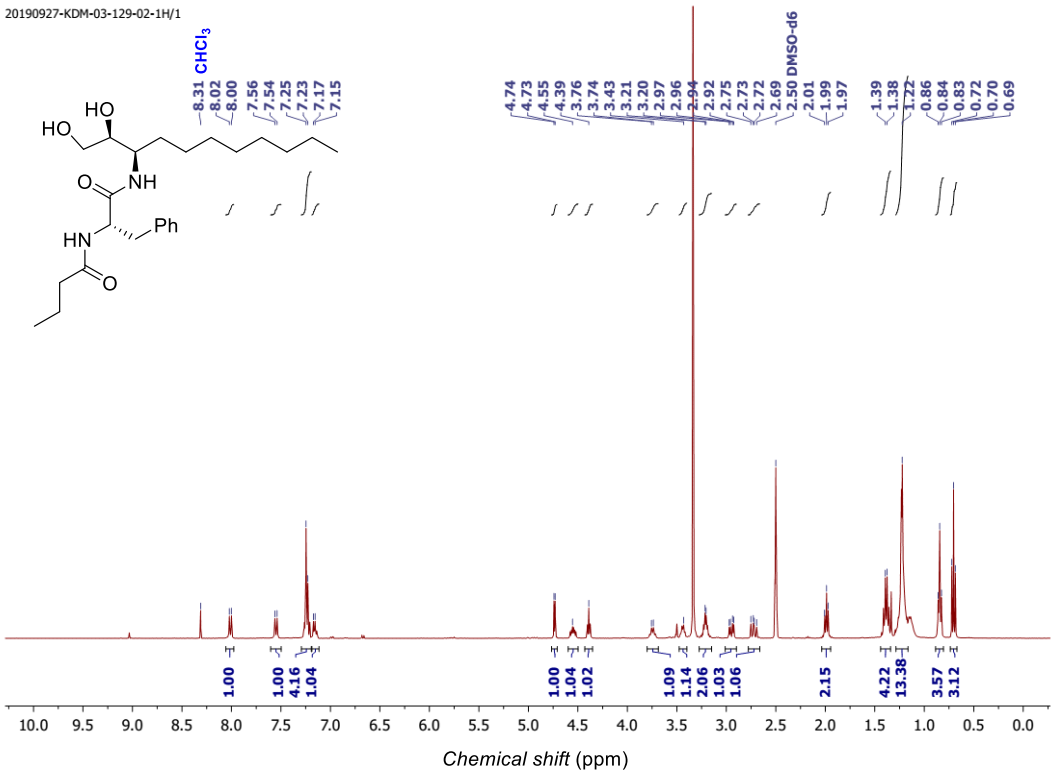



**Figure 5.45** $^{1}$H NMR spectrum of compound **3S** in DMSO-$d_6$.

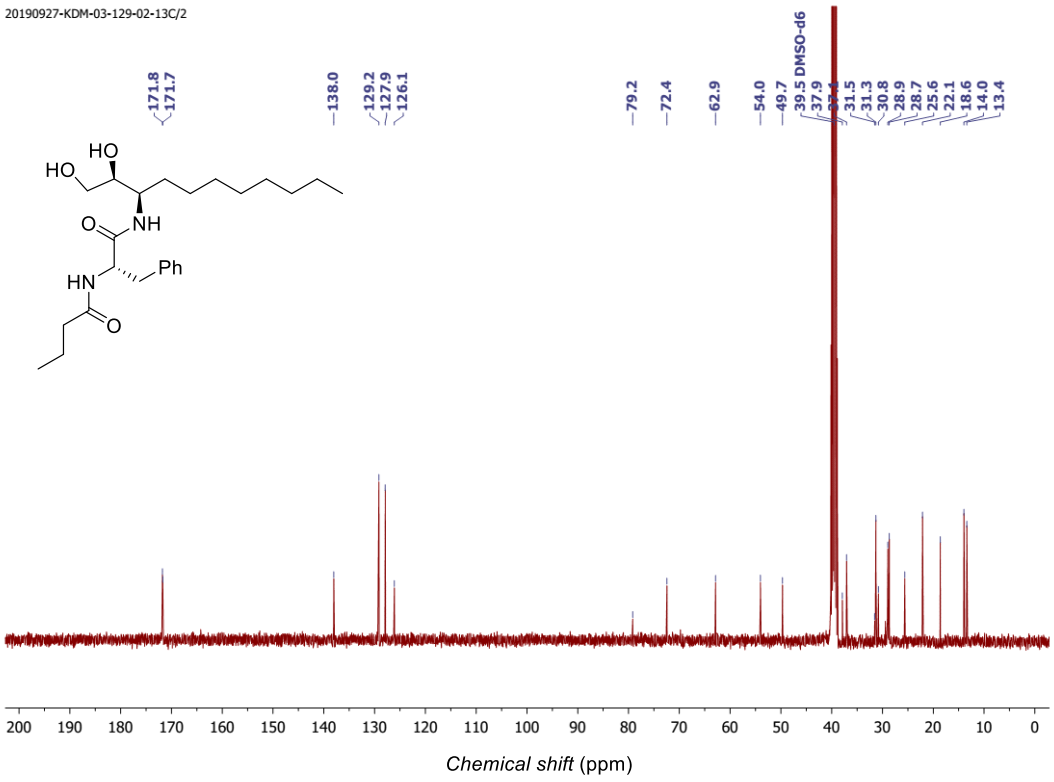



**Figure 5.46** $^{13}$C NMR spectrum of compound **3S** in DMSO-$d_6$.

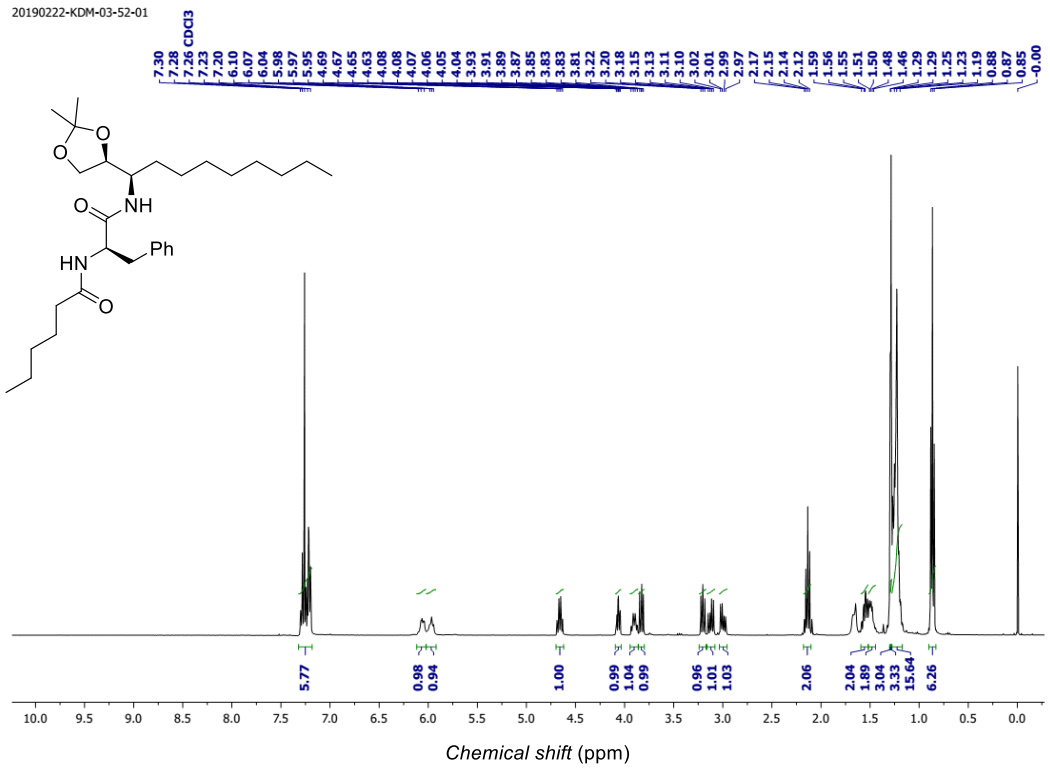



**Figure 5.47** $^{1}$H NMR spectrum of compound **17R** in $CDCl_3$.

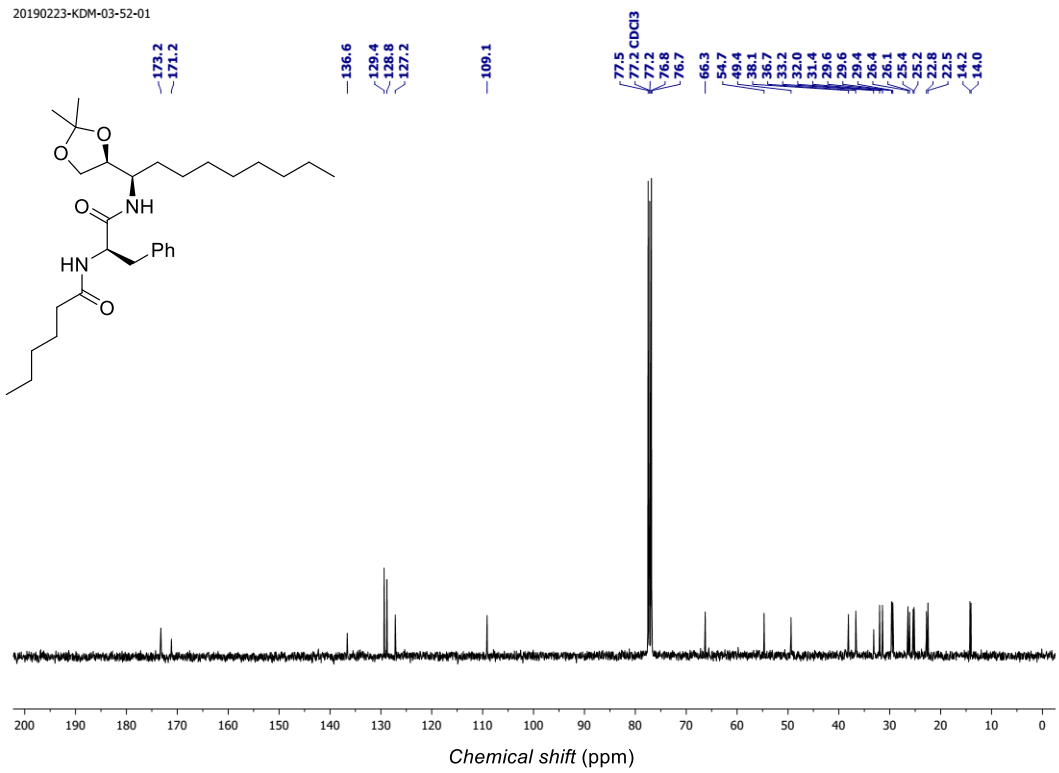



**Figure 5.48** $^{13}$C NMR spectrum of compound **17R** in $CDCl_3$.

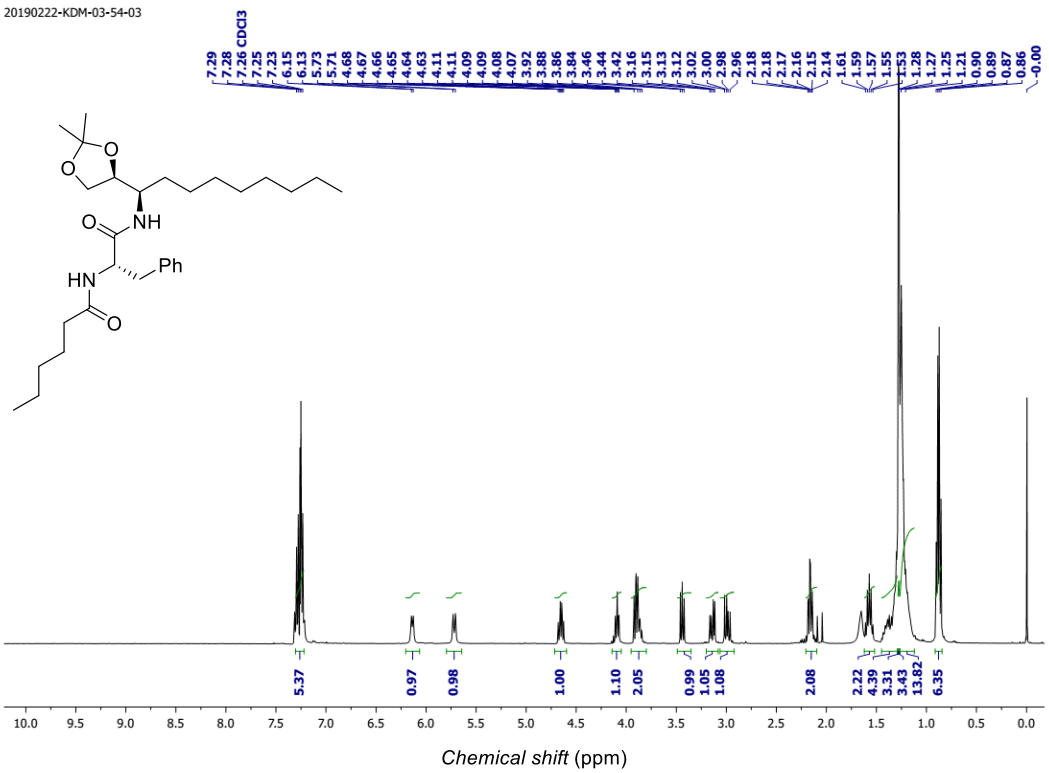



**Figure 5.49** $^{1}$H NMR spectrum of compound **17S** in $CDCl_3$.

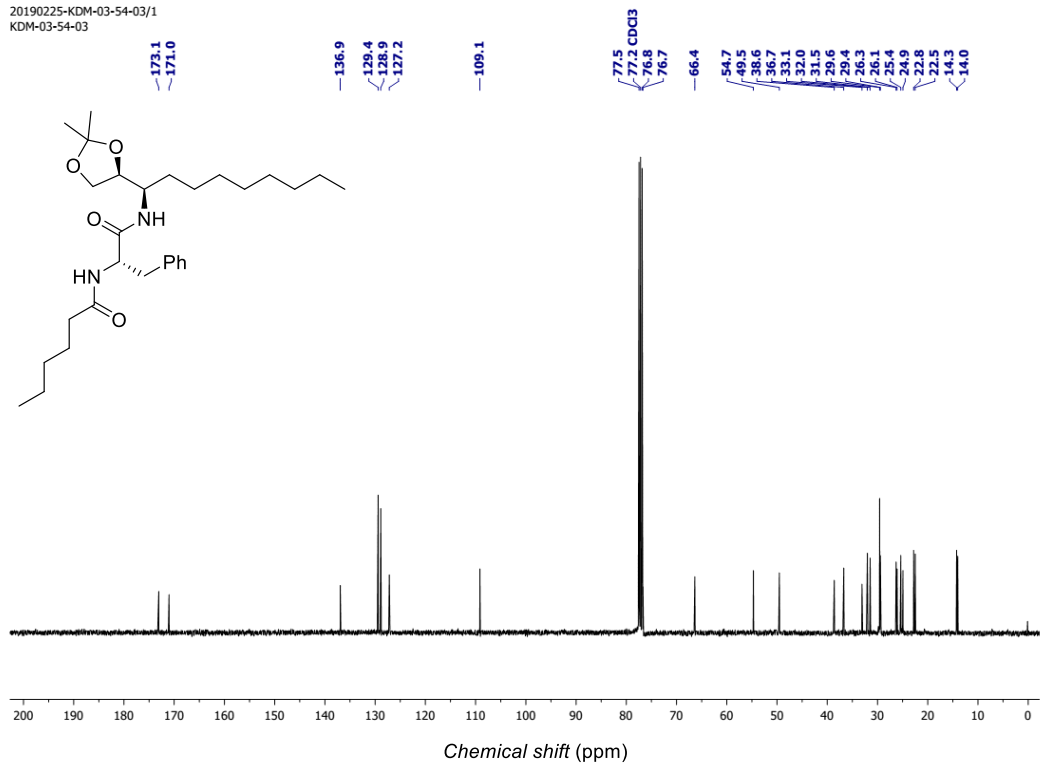



**Figure 5.50** $^{13}$C NMR spectrum of compound **17S** in $CDCl_3$.

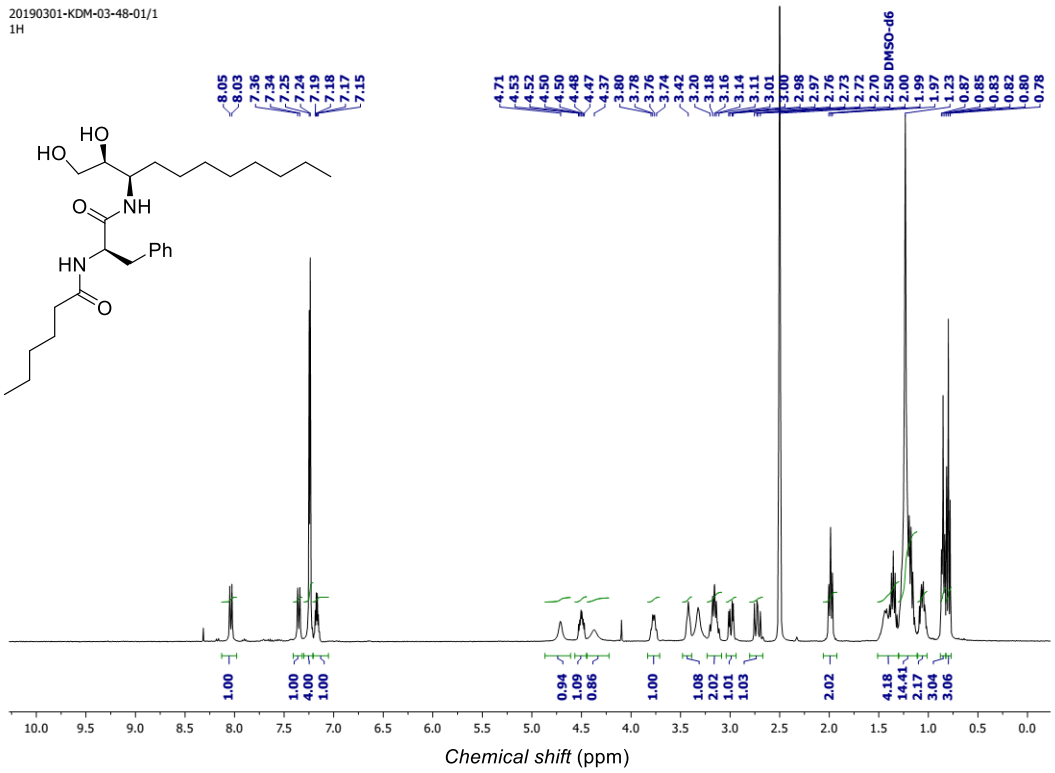



**Figure 5.51** $^{1}$H NMR spectrum of compound **4R** in DMSO-$d_6$.

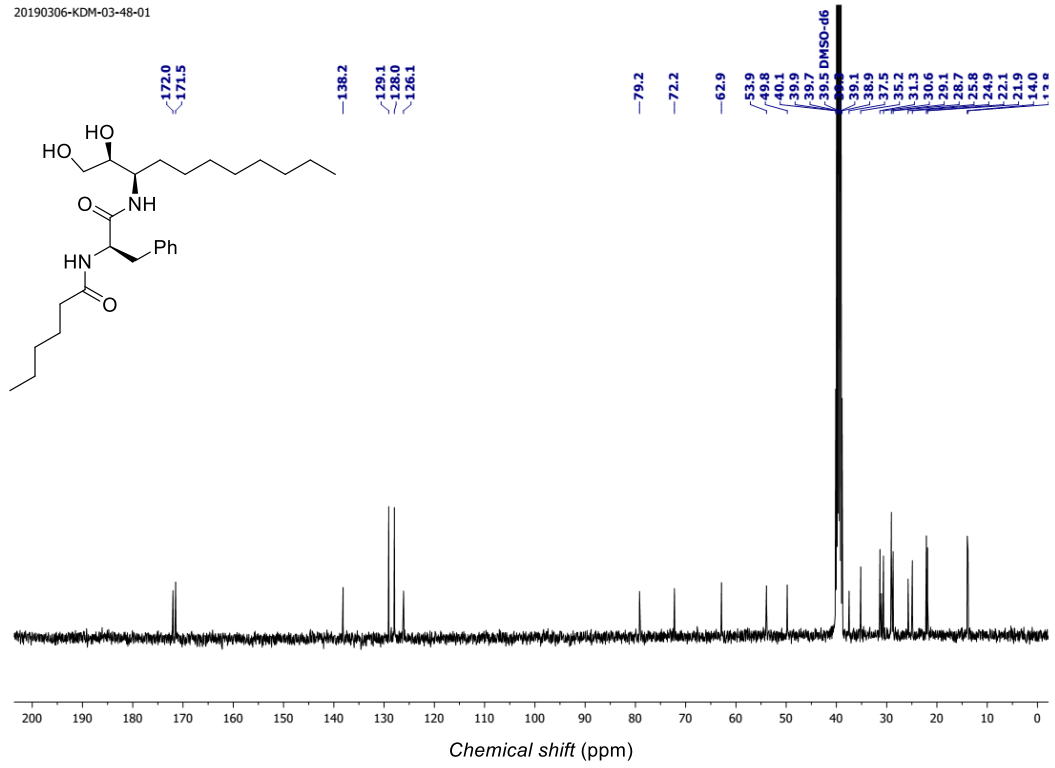



**Figure 5.52** $^{13}$C NMR spectrum of compound **4R** in DMSO-$d_6$.

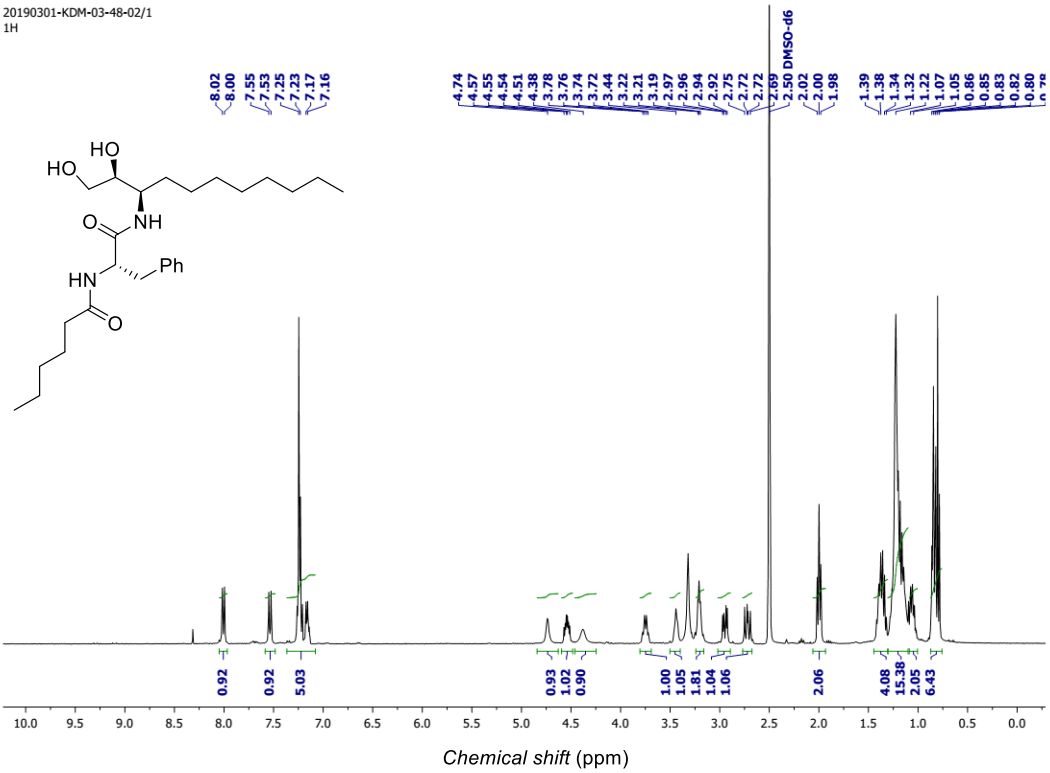



**Figure 5.53** $^{1}$H NMR spectrum of compound **4S** in DMSO-$d_6$.

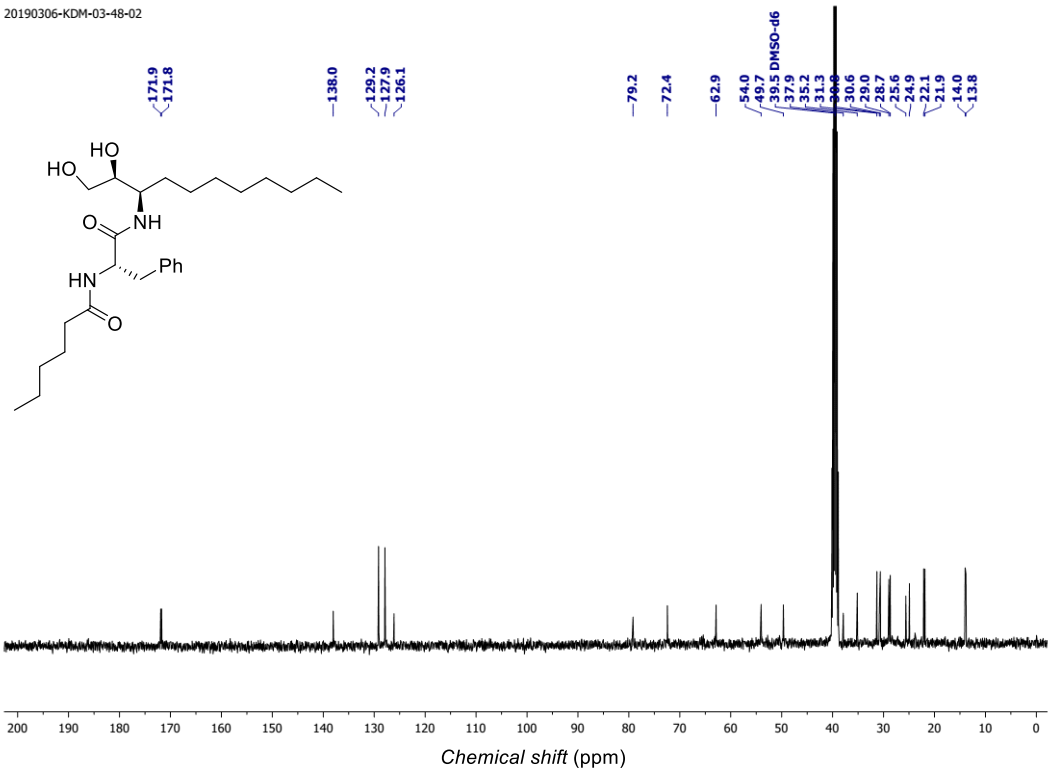



**Figure 5.54** $^{13}$C NMR spectrum of compound **4S** in DMSO-$d_6$.

## 5.6. References


1. Genda, H. *Geochem. J.* **2016**, *50*, 27–42.
2. Czajkowski, A.; Remiorz, L.; Pawlak, S.; Remiorz, E.; Szyguła, J.; Marek, D.; Paszkuta, M.; Drabik, G.; Baron, G.; Paduch, J.; Antemijczuk, O. *Appl. Sci.* **2021**, *11*, 4081.
3. Eliasson, J. *Nature* **2015**, *517*, 6.
4. Service, R. F. *Science* **2006**, *313*, 1088–1090.
5. Byker, E. J.; Ezelle-Thomas, V. *J. Res. Child. Educ.* **2021**, *35*, 268–280.
6. Prüss-Ustün, A.; Wolf, J.; Bartram, J.; Clasen, T.; Cumming, O.; Freeman, M. C.; Gordon, B.; Hunter, P. R.; Medlicott, K.; Johnston, R. *Int. J. Hyg. Environ. Health* **2019**, *222*, 765–777.
7. Mara, D.; Lane, J.; Scott, B.; Trouba, D. *PLoS Med.* **2010**, *7*, e1000363.
8. Shannon, M. A.; Bohn, P. W.; Elimelech, M.; Georgiadis, J. G.; Mariñas, B. J.; Mayes, A. M. *Nature* **2008**, *452*, 301–310.
9. Park, K.; Kim, J.; Yang, D. R.; Hong, S. *J. Membr. Sci.* **2020**, *595*, 117607.
10. Petersen, R. J. *J. Membr. Sci.* **1993**, *83*, 81–150.
11. Greenlee, L. F.; Lawler, D. F.; Freeman, B. D.; Marrot, B.; Moulin, P. *Water Res.* **2009**, *43*, 2317–2348.
12. Barboiu, M.; Gilles, A. *Acc. Chem. Res.* **2013**, *46*, 2814–2823.
13. Semiat, R. *Environ. Sci. Technol.* **2008**, *42*, 8193–8201.
14. Pérez-Zuñiga, G.; Rivas-Perez, R.; Sotomayor-Moriano, J.; Sánchez-Zurita, V. *Processes* **2020**, *8*, 1100.
15. Dodge, B. F.; Eshaya, A. M., Thermodynamics of Some Desalting Processes. In *Adv. Chem. Ser.*, American Chemical Society: 1960; Vol. 27, pp 7–20.
16. El-Sayed, Y. M. *Desalination* **2001**, *134*, 129–158.
17. Peñate, B.; García-Rodríguez, L. *Desalination* **2012**, *284*, 1–8.
18. Tajkhorshid, E.; Nollert, P.; Jensen, M.; Miercke, L. J.; O'Connell, J.; Stroud, R. M.; Schulten, K. *Science* **2002**, *296*, 525–530.
19. Murata, K.; Mitsuoka, K.; Hirai, T.; Walz, T.; Agre, P.; Heymann, J. B.; Engel, A.; Fujiyoshi, Y. *Nature* **2000**, *407*, 599–605.
20. Agre, P. *Angew. Chem., Int. Ed.* **2004**, *43*, 4278–4290.
21. Borgnia, M. J.; Kozono, D.; Calamita, G.; Maloney, P. C.; Agre, P. *J. Mol. Biol.* **1999**, *291*, 1169–1179.

22. Hélix-Nielsen, C. *Membranes (Basel)* **2018**, *8*, 44–59.
23. Verkman, A. S. *Curr. Biol.* **2013**, *23*, R52–R55.
24. Kaucher, M. S.; Peterca, M.; Dulcey, A. E.; Kim, A. J.; Vinogradov, S. A.; Hammer, D. A.; Heiney, P. A.; Percec, V. *J. Am. Chem. Soc.* **2007**, *129*, 11698–11699.
25. Le Duc, Y.; Michau, M.; Gilles, A.; Gence, V.; Legrand, Y.-M.; van der Lee, A.; Tingry, S.; Barboiu, M. *Angew. Chem., Int. Ed.* **2011**, *50*, 11366–11372.
26. Barboiu, M. *Angew. Chem., Int. Ed.* **2012**, *51*, 11674–11676.
27. Hu, X.-B.; Chen, Z.; Tang, G.; Hou, J.-L.; Li, Z.-T. *J. Am. Chem. Soc.* **2012**, *134*, 8384–8387.
28. Shen, Y.-x.; Si, W.; Erbakan, M.; Decker, K.; De Zorzi, R.; Saboe, P. O.; Kang, Y. J.; Majd, S.; Butler, P. J.; Walz, T.; Aksimentiev, A.; Hou, J.-l.; Kumar, M. *Proc. Natl. Acad. Sci. U. S. A.* **2015**, *112*, 9810–9815.
29. Zhao, H.; Sheng, S.; Hong, Y.; Zeng, H. *J. Am. Chem. Soc.* **2014**, *136*, 14270–14276.
30. Tunuguntla, R. H.; Henley, R. Y.; Yao, Y. C.; Pham, T. A.; Wanunu, M.; Noy, A. *Science* **2017**, *357*, 792–796.
31. Kocsis, I.; Sorci, M.; Vanselous, H.; Murail, S.; Sanders, S. E.; Licsandru, E.; Legrand, Y. M.; van der Lee, A.; Baaden, M.; Petersen, P. B.; Belfort, G.; Barboiu, M. *Sci. Adv.* **2018**, *4*, eaao5603.
32. Licsandru, E.; Kocsis, I.; Shen, Y.-x.; Murail, S.; Legrand, Y.-M.; van der Lee, A.; Tsai, D.; Baaden, M.; Kumar, M.; Barboiu, M. *J. Am. Chem. Soc.* **2016**, *138*, 5403–5409.
33. Song, W.; Joshi, H.; Chowdhury, R.; Najem, J. S.; Shen, Y.-x.; Lang, C.; Henderson, C. B.; Tu, Y.-M.; Farell, M.; Pitz, M. E.; Maranas, C. D.; Cremer, P. S.; Hickey, R. J.; Sarles, S. A.; Hou, J.-l.; Aksimentiev, A.; Kumar, M. *Nat. Nanotechnol.* **2020**, *15*, 73–79.
34. Shen, J.; Fan, J.; Ye, R.; Li, N.; Mu, Y.; Zeng, H. *Angew. Chem., Int. Ed.* **2020**, *59*, 13328–13334.
35. Shen, J.; Ye, R.; Romanies, A.; Roy, A.; Chen, F.; Ren, C.; Liu, Z.; Zeng, H. *J. Am. Chem. Soc.* **2020**, *142*, 10050–10058.
36. Huang, L.-B.; Hardiagon, A.; Kocsis, I.; Jegu, C.-A.; Deleanu, M.; Gilles, A.; van der Lee, A.; Sterpone, F.; Baaden, M.; Barboiu, M. *J. Am. Chem. Soc.* **2021**, *143*, 4224–4233.

37. Roy, A.; Shen, J.; Joshi, H.; Song, W.; Tu, Y.-M.; Chowdhury, R.; Ye, R.; Li, N.; Ren, C.; Kumar, M.; Aksimentiev, A.; Zeng, H. *Nat. Nanotechnol.* **2021**, *16*, 911–917.
38. Li, Y.; Li, Z.; Aydin, F.; Quan, J.; Chen, X.; Yao, Y. C.; Zhan, C.; Chen, Y.; Pham, T. A.; Noy, A. *Sci. Adv.* **2020**, *6*, eaba9966.
39. Tunuguntla, R. H.; Allen, F. I.; Kim, K.; Belliveau, A.; Noy, A. *Nat. Nanotechnol.* **2016**, *11*, 639–644.
40. Song, W.; Kumar, M. *Curr. Opin. Chem. Eng.* **2019**, *25*, 9–17.
41. Murail, S.; Vasiliu, T.; Neamtu, A.; Barboiu, M.; Sterpone, F.; Baaden, M. *Faraday Discuss.* **2018**, *209*, 125–148.
42. Huang, L.-B.; Di Vincenzo, M.; Ahunbay, M. G.; van der Lee, A.; Cot, D.; Cerneaux, S.; Maurin, G.; Barboiu, M. *J. Am. Chem. Soc.* **2021**, *143*, 14386–14393.
43. de Groot, B. L.; Frigato, T.; Helms, V.; Grubmüller, H. *J. Mol. Biol.* **2003**, *333*, 279-293.
44. Kosinska Eriksson, U.; Fischer, G.; Friemann, R.; Enkavi, G.; Tajkhorshid, E.; Neutze, R. *Science* **2013**, *340*, 1346–1349.
45. Marx, D. *ChemPhysChem* **2006**, *7*, 1848–1870.
46. *Marvin, ver. 5.8.0;* ChemAxon, 2012. http://www.chemaxon.com.
47. Sadhasivam, B.; Rigana, M. F.; Rukmanikrishnan, B.; Muthusamy, S. *Polym. Bull.* **2018**, *75*, 829–849.
48. Deshmukh, S. C.; Talukdar, P. *J. Org. Chem.* **2014**, *79*, 11215–11225.
49. Deshmukh, S. C.; Roy, A.; Talukdar, P. *Org. Biomol. Chem.* **2012**, *10*, 7536–7544.
50. Yuan, Y. D.; Dong, J.; Liu, J.; Zhao, D.; Wu, H.; Zhou, W.; Gan, H. X.; Tong, Y. W.; Jiang, J.; Zhao, D. *Nat. Commun.* **2020**, *11*, 4927.
51. Hannesschläger, C.; Barta, T.; Siligan, C.; Horner, A. *Sci. Rep.* **2018**, *8*, 8516.
52. Meinild, A.-K.; Klaerke, D. A.; Zeuthen, T. *J. Biol. Chem.* **1998**, *273*, 32446–32451.
53. Moore, S. J.; Haynes, C. J. E.; Gonzalez, J.; Sutton, J. L.; Brooks, S. J.; Light, M. E.; Herniman, J.; Langley, G. J.; Soto-Cerrato, V.; Perez-Tomas, R.; Marques, I.; Costa, P. J.; Felix, V.; Gale, P. A. *Chem. Sci.* **2013**, *4*, 103–117.
54. Mondal, D.; Sathyan, A.; Shinde, S. V.; Mishra, K. K.; Talukdar, P. *Org. Biomol. Chem.* **2018**, *16*, 8690–8694.
55. Ye, R.; Ren, C.; Shen, J.; Li, N.; Chen, F.; Roy, A.; Zeng, H. *J. Am. Chem. Soc.* **2019**, *141*, 9788–9792.

56. Busschaert, N.; Wenzel, M.; Light, M. E.; Iglesias-Hernández, P.; Pérez-Tomás, R.; Gale, P. A. *J. Am. Chem. Soc.* **2011**, *133*, 14136–14148.
57. Saha, T.; Dasari, S.; Tewari, D.; Prathap, A.; Sureshan, K. M.; Bera, A. K.; Mukherjee, A.; Talukdar, P. *J. Am. Chem. Soc.* **2014**, *136*, 14128–14135.
58. Roy, A.; Gautam, A.; Malla, J. A.; Sarkar, S.; Mukherjee, A.; Talukdar, P. *Chem. Commun.* **2018**, *54*, 2024–2027.
59. Dolomanov, O. V.; Bourhis, L. J.; Gildea, R. J.; Howard, J. A. K.; Puschmann, H. *J. Appl. Cryst.* **2009**, *42*, 339–341.
60. Sheldrick, G. *Acta Cryst.* **2015**, *C71*, 3–8.
61. Sheldrick, G. *Acta Cryst.* **2015**, *A71*, 3–8.
62. Jo, S.; Kim, T.; Iyer, V. G.; Im, W. *J. Comput. Chem.* **2008**, *29*, 1859–1865.
63. Wang, J.; Wolf, R. M.; Caldwell, J. W.; Kollman, P. A.; Case, D. A. *J. Comput. Chem.* **2004**, *25*, 1157–1174.
64. Wang, J.; Wolf, R. M.; Caldwell, J. W.; Kollman, P. A.; Case, D. A. *J. Comput. Chem.* **2005**, *26*, 114–114.
65. Sprenger, K. G.; Jaeger, V. W.; Pfaendtner, J. *J. Phys. Chem. B* **2015**, *119*, 5882–5895.
66. Brooks, B. R.; Brooks Iii, C. L.; Mackerell Jr, A. D.; Nilsson, L.; Petrella, R. J.; Roux, B.; Won, Y.; Archontis, G.; Bartels, C.; Boresch, S.; Caflisch, A.; Caves, L.; Cui, Q.; Dinner, A. R.; Feig, M.; Fischer, S.; Gao, J.; Hodoscek, M.; Im, W.; Kuczera, K.; Lazaridis, T.; Ma, J.; Ovchinnikov, V.; Paci, E.; Pastor, R. W.; Post, C. B.; Pu, J. Z.; Schaefer, M.; Tidor, B.; Venable, R. M.; Woodcock, H. L.; Wu, X.; Yang, W.; York, D. M.; Karplus, M. *J. Comput. Chem.* **2009**, *30*, 1545–1614.
67. Klauda, J. B.; Venable, R. M.; Freites, J. A.; O'Connor, J. W.; Tobias, D. J.; Mondragon-Ramirez, C.; Vorobyov, I.; MacKerell, A. D.; Pastor, R. W. *J. Phys. Chem. B* **2010**, *114*, 7830–7843.
68. Huang, J.; Rauscher, S.; Nawrocki, G.; Ran, T.; Feig, M.; de Groot, B. L.; Grubmüller, H.; MacKerell, A. D. *Nat. Methods* **2017**, *14*, 71–73.
69. MacKerell, A. D.; Bashford, D.; Bellott, M.; Dunbrack, R. L.; Evanseck, J. D.; Field, M. J.; Fischer, S.; Gao, J.; Guo, H.; Ha, S.; Joseph-McCarthy, D.; Kuchnir, L.; Kuczera, K.; Lau, F. T. K.; Mattos, C.; Michnick, S.; Ngo, T.; Nguyen, D. T.; Prodhom, B.; Reiher, W. E.; Roux, B.; Schlenkrich, M.; Smith, J. C.; Stote, R.; Straub, J.; Watanabe, M.; Wiórkiewicz-Kuczera, J.; Yin, D.; Karplus, M. *J. Phys. Chem. B* **1998**, *102*, 3586–3616.

70. Berendsen, H. J. C.; Postma, J. P. M.; van Gunsteren, W. F.; DiNola, A.; Haak, J. R. *J. Chem. Phys.* **1984**, *81*, 3684–3690.
71. Páll, S.; Hess, B. *Comput. Phys. Commun.* **2013**, *184*, 2641–2650.
72. Darden, T.; York, D.; Pedersen, L. *J. Chem. Phys.* **1993**, *98*, 10089–10092.
73. Hess, B.; Bekker, H.; Berendsen, H. J. C.; Fraaije, J. G. E. M. *J. Comput. Chem.* **1997**, *18*, 1463–1472.
74. Miyamoto, S.; Kollman, P. A. *J. Comput. Chem.* **1992**, *13*, 952–962.
75. Evans, D. J.; Holian, B. L. *J. Chem. Phys.* **1985**, *83*, 4069–4074.
76. Parrinello, M.; Rahman, A. *J. Appl. Phys.* **1981**, *52*, 7182–7190.
77. Abraham, M. J.; Murtola, T.; Schulz, R.; Páll, S.; Smith, J. C.; Hess, B.; Lindahl, E. *SoftwareX* **2015**, *1–2*, 19–25.
78. Abraham, M. J.; Spoel, D.; Lindahl, E.; Hess, B., GROMACS User Manual version 2019, http://www.gromacs.org.
79. Camilo, C. R. S.; Ruggiero, J. R.; de Araujo, A. S. *bioRxiv* **2021**, 2021.01.20.427278.

# *Overall Conclusion*

*In the overall conclusion, we have developed small molecules based systems that transport the essential solutes across the bilayer membrane via either carrier or channel mechanism. In chapters 2 and 3, we discussed tripodal and foldamer-based anion receptors, which showed an excellent binding affinity for the $Cl^-$ ion, confirmed from NMR binding and DFT calculation studies. The ion transport studies of all these receptors were evaluated across various lipid membranes and found to transport the $Cl^-$ ion selectively via the carrier mechanism. In chapter 4, we have demonstrated the reversible switchable behavior of a bis(indole)-based system. This bis(indole) system formed a double helix in solid and solution state and converted to a supramolecular channel with the addition of $Cl^-$ ion. The ion transport activity by this series of molecules has shown excellent activity via the formation of a channel inside the membrane. In the final chapter, we have developed peptide 1,2-diol water channel systems for selective translocation of water across phospholipid membranes. This system showed excellent water permeability across the DOPC membrane and can be applied in various applications, including the development of biomimetic RO membranes.*

